CO_2 Capture by Aqueous Absorption

Summary of Fourth Quarterly Progress Reports 2014

by Gary T. Rochelle

Supported by the Texas Carbon Management Program

and the

Industrial Associates Program for CO_2 Capture by Aqueous Absorption

McKetta Department of Chemical Engineering

The University of Texas at Austin

January 31, 2015

Introduction

This research program is focused on the technical obstacles to the deployment of CO_2 capture from flue gas by alkanolamine absorption/stripping. The objective is to develop and demonstrate evolutionary improvements to monoethanolamine (MEA) absorption/stripping for CO_2 capture from gas-fired and coal-fired flue gas. The Texas Carbon Management Program and the Industrial Associates Program for CO_2 Capture by Aqueous Absorption support 17 graduate students. Most of these students have prepared detailed quarterly progress reports for the period October 1 to December 31, 2014.

Conclusions

Thermodynamics and Rates

1. In dilute aqueous solution imidazole (IMI), 2-ethyl-imidazole (2E-IMI), and proprietary amine 4X have higher volatility than PZ but lower volatility than MEA. 2-(isopropylamine)ethanol (IPAE), bis(2-methoxyethyl)amine (BMEA), 1,2-dimethylimidazole (1,2-DM-IMI), and 2PDE have higher volatility than AMP.
2. Loaded 5 m PZ/5 m 2E-IMI has an amine partial pressure similar to 8 m PZ at 45 °C, but lower at 65 °C.
3. Adding IMI to 5 m PZ decreases the CO_2 capacity. Adding 2M-IMI or 2E-IMI maintains the CO_2 capacity. Adding 4X increases the CO_2 capacity. 5 m PZ/2.5 m 2E-IMI has almost the same CO_2 capacity as 5 m PZ/5 m 2E-IMI. However, 5 m PZ/5 m 4X has significantly higher CO_2 capacity than 5 m PZ/2 m 4X and 4 m PZ/2 m 4X.
4. Adding 5 m IMI or 5 m 2E-IMI to 5 m PZ maintains its high CO_2 absorption rate, while adding 5 m 4X decreases the CO_2 absorption rate by 30%, although the rate of the blend is still comparable to 8 m PZ, which is much higher than 7 m MEA.
5. Although 5 m PZ/2 m 2E-4M-IMI and 5 m PZ/2.5 m 2E-IMI have a lower absorption rate than 5 m PZ at low CO_2 partial pressure, their absorption rate at high CO_2 partial pressure is comparable to 5 m PZ. The CO_2 absorption rate of 5 m PZ/2 m 4X and 4 m PZ/2 m 4X is lower than 5 m PZ, but still higher than 8 m PZ.
6. Assuming that viscosity normalized capacity has the same effect as absorption rate on the overall CO_2 capture cost, 5 m PZ/5 m IMI, 5 m PZ/5 m 2E-IMI, 5 m PZ/2.5 m 2E-IMI,

5 m PZ/2 m 2E-4M-IMI, 5 m PZ/2 m 4X, and 4 m PZ/2 m 4X have similar CO_2 capture cost to 5 m PZ, but lower cost than 8 m PZ, 5 m PZ/5 m MDEA, or 5 m PZ/5 m 4X.

7. No precipitate was observed for the selected PZ-based blends at rich CO_2 loading. In loaded solution, 5 m PZ has 5–10 °C lower melting transition temperatures than 8 m PZ at the same CO_2 partial pressure. All the selected amines, except for 2E-4M-IMI, can lower the melting transition temperature of 5 m PZ by 3–7 °C, with more significant effect at low CO_2 partial pressure.
8. For unloaded 5 m PZ-based blends, different components have different abilities to solubilize PZ: glycerol > ethylene glycol > IMI > 2E-IMI > dimethyl sulfoxide > triethylenediamine = 2-methylpiperazine.

Modeling

An updated shortcut method was developed using a two-step energy balance around an adiabatic (no intercooling) absorber and several observations from rigorous rate-based modeling to estimate the transition lean loading for each flue gas application where a temperature-related pinch formed. In 8 m PZ the transition loading is given as:

NGCC: Actual = 0.21–0.22 vs. Predicted (NEW) = 0.219
Coal: Actual = 0.18–0.20 vs. Predicted (NEW) = 0.176
Steel: Actual = 0.17–0.19 vs. Predicted (NEW) = 0.169

Thirteen papers were found providing correlations of heat transfer coefficient and pressure drop of plate-and-frame exchangers. The corrugation angle is the primary design variable, which produces turbulence and enhances that at 30º. The dependence of the pressure drop per unit length on the heat transfer coefficient is 0.35–0.40. The dependence of the viscosity on the cross exchanger cost is 0.35–0.40. Compared to 8 m PZ, the effect of lower viscosity of 5 m PZ can reduce the cross exchanger cost by 30%.

In a hybrid-parallel process combining amine scrubbing with membrane technology, the CO_2 concentration in the flue gas is enriched to 23.4% and removal level is increased to 95%. At these conditions 5 m MDEA/5 m PZ offers higher CO_2 capacity but a lower absorption rate than 5 m PZ. Compared to 5 m PZ, absorber costs increase by 50% and advanced flash stripper (including the cross exchanger) costs decrease by 47%. The total equipment costs go down by 13%. Equivalent work using 5 m MDEA/5 m PZ (32.69 kJ/mol CO_2) is less than using 5 m PZ (33.28 kJ/mol CO_2).

As the 5 m PZ/5 m MDEA CO_2 rich loading varies from 0.34 to 0.37, the optimum lean loading increases from 0.19 to 0.21 mol/equivalent PZ CO_2, and the minimum total equivalent work decreases from 32.8 kJ/mol CO_2 to 31.6 kJ/mol CO_2., both lower than that of 5 m PZ.

The mass transfer properties of conventional structured packing are given by:

$$\frac{a_e}{a_P} = 1.41\left[\left(\frac{\rho_L}{\sigma}\right) g^{1/3} \left(\frac{u_L}{a_P}\right)^{4/3}\right]^{0.116}$$

$$k_L = 3.08\ E-3 * u_L^{0.72} M^{0.42} a_P^{-1.15}$$

$$k_G = 9.6E-3 * u_G^{0.54} M^{0.29} a_P^{-0.5}$$

k_g' for CO_2/H_2O/NaOH/glycerol has been measured with 0.3 M NaOH at 20, 30, and 40 °C. k_g' initially increases about 25% when glycerol increases to 15 wt % because of the catalytic effect

of glycerol, and then decreases about 70% when glycerol increases to 80 wt % because of the effect of elevated μ_L on mass transfer.

Neither the modified Andrade equation nor the Jones-Dole electrolyte correlation represents loaded amine viscosity.

P and PI controllers can effectively control the in-and-out intercooled absorber with advanced flash stripper when the CO_2 delivery rate to the compressor is specified. The total equivalent work of the plant is slow to reach steady state in this feedback control strategy, and bypass ratios have not been optimized. The amine concentration controller is difficult to tune because concentration has a very slow response time. Using the bypass ratios to control temperatures around the cross exchangers caused instability.

Solvent Management

Degradation of PZ-promoted MDEA is initiated by a S_N2 substitution involving free and protonated amine. The dominant initial degradation pathway involves free PZ attacking the methyl group of protonated MDEA, forming 1-MPZ and DEA.

The less dominant pathway involves MDEA attacking protonated MDEA, forming the quaternary amine salt DMDEAm and DEA. This pathway is the principal degradation pathway for MDEA degradation in the absence of PZ. DEA and DMDEAm can account for about 90% of the amine loss initially and eventually begin to approach equilibrium in MDEA degradation.

The rate constant of PZ attacking MDEAH+ is $1.5*10^{-6}$ kg/mol/s at 150 °C and MDEA attacking MDEAH+ is $0.12*10^{-6}$ kg/mol/s in the presence of PZ.

Thermal degradation of the tertiary amine in 3.2 m tertiary amine/1.6 m PZ, 0.22 mol CO_2/equiv amine, 135 ^oC

Amine	k_1 (hr^{-1}*e5)	E_a (kJ/mol)
AMP	5.9	130
4 m AMP	6.7	140
AMPD	21.3	100
TRIS	17.9	100
PM	294.4	110
PE	21.3	110
tBuAE	3.5	100

Amine oxidation at absorber conditions (70 ^oC, 98 kPa O_2, 2 kPa CO_2, 0.4 mM Fe, 0.2 mM Mn, 0.1 mM Ni, 0.05 mM Cr) occurs with rate constants: MEA/k_1 = 0.015 hr^{-1} , DEA/k_2 = 3e-6 hr/mM, and MAE/k_2 = 3e-6 hr/mM.

Nitrite accumulation in oxidation decreases in the following order:

a. Primary amines with 2 carbons between the amino group and the neighboring group that is either an ether or hydroxyl, as seen in MEA, BAE, and DGA®.

b. Primary diamines with an even number of carbons between the two amino groups, as seen in HMDA and DAB.
c. Secondary amines with 2 carbons between the amino group and neighboring functional groups, as seen in DEA and MAE.

Hydrogen peroxide was reacted with 8 m PZ. 0.03 moles of ammonia are initially produced per mole of peroxide reacted with PZ. Similar amounts of formate and ethylenediamine are also produced. Decreasing metal concentration and adding Inh A did not affect the initial rate of ammonia production via peroxide oxidation in PZ, but did reduce formate accumulation by a factor of 3. N_2O was also produced by peroxide oxidation, at 2 to 3 orders of magnitude less than ammonia.

The effect of heat stable salts on solvent viscosity was quantified. Sulfate has the strongest effect, and longer-chained carboxylic acids have an increasing effect on viscosity.

NO_2 irreversibly reacts with PZ at a 1:1.5 stoichiometry.

Inlet NO_2 costs 0.15–0.45 \$/MT CO_2/ppm NO_2 in PZ degradation and waste disposal costs.

Pre-scrubbing NO_2 using an existing NaOH scrubber and a triethanolamine additive can save on degradation costs. Simultaneously scrubbing 5 ppm NO_2 and 50 ppm SO_2 with 80 mM TEA additive in a 7 m column saves 0.97 \$/MT CO_2.

At 50 ppm inlet SO_2 and 5 ppm NO_2, n-nitrosopiperazine can be reduced by a factor of 10 with no net cost.

In stainless steel 316 cylinders at 150 °C, 5 m ethylenediamine is 93 times as corrosive as its 3 carbon analog, diaminopropane, and 10 m monoethanolamine is 34 times as corrosive as its 3 carbon analog, aminopropanol.

In stainless steel 316 cylinders at 150 °C, a 2.67 m 2-piperidinemethanol (PM), 1.33 m PZ solution is 72 times more corrosive than a 2.67 m 2-piperidineethanol (PE), 1.33 m PZ solution. There is a two-carbon backbone between the nitrogen and the alcohol functional group in PM, whereas there is a three-carbon backbone between the nitrogen and alcohol functional group in PE. This is the same trend of corrosivity decreasing with chain length seen in the linear amines.

Laboratory Safety

All experimental work is performed under the Laboratory Safety Guidelines (http://www.utexas.edu/safety/ehs/lab/manual/) of the University of Texas. The laboratory personnel have all completed four safety training courses certified by the University: general lab safety, hazardous materials, fire extinguisher, and site specific safety. Routine personal safety protection includes safety glasses, lab coats, gloves, long pants, and closed-toe shoes. Goggles are used for specific hazardous operations. Food and drink are prohibited in the laboratories. Safety inspections of all labs are conducted by a different student every month. The University Office of Environmental Health and Safety conducts random safety evaluations of each lab, usually about twice a year. An industrial visitor conducts a safety evaluation of each lab once per year. A Standard Operating Procedure is followed for three of our major experiments.

Most of the experimental work with amines is conducted in exhaust hoods. Ventilated gas cabinets are used with cylinders of nitrogen mixed with ammonia, NO, NO_2, and SO_2. All work

on undiluted nitrosamine samples is contained in one laboratory that has no desks assigned to students for continuous occupancy. We have developed a standard operating procedure to be used in an experiment with closed cylinders of amine solution heated to 175 ^{o}C in convection ovens. These experiments are also contained in the nitrosamines lab.

Dr. Rochelle is the Chairman of the Safety Committee of the Department of Chemical Engineering. The committee meets once a month to review safety issues and safety experiences, and to address initiatives for improving safety.

1. Aqueous Piperazine Blends for CO_2 Capture *p. 14*

by Yang Du

Thermally stable PZ-based blends selected last quarter (T_{max} >140 °C) were screened further this quarter for volatility, CO_2 capacity and absorption rate, viscosity, and solvent solubility. 2-(Isopropylamino)ethanol (IPAE), bis(2-methoxyethyl)amine (BMEA), 1,2-dimethylimidazole (1,2-DM-IMI), and 2-piperidinoethanol (2PDE) have higher Henry's law constants than 2-amino-2-methyl-1-propanol (AMP), and thus are excluded from future consideration. Imidazole (IMI), 2-ethyl-imidazole (2E-IMI), and the proprietary amine 4X have higher Henry's law constants than PZ but lower Henry's law constants than monoethanolamine (MEA). Loaded 5 m PZ/5 m 2E-IMI has a similar amine partial pressure to 8 m PZ at 45 °C, but lower partial pressure at 65 °C.

Adding IMI to 5 m PZ (pKa = 7.0) decreases the CO_2 capacity. Adding 2-methyl-imidazole (2M-IMI, pKa = 7.9) or 2E-IMI (pKa = 8.0) maintains the CO_2 capacity. Adding 4X (pKa = 9.4) increases the CO_2 capacity. 5 m PZ/2.5 m 2E-IMI has almost the same CO_2 capacity as 5 m PZ/5 m 2E-IMI. However, 5 m PZ/5 m 4X has significantly greater CO_2 capacity than 5 m PZ/2 m 4X or 4 m PZ/2 m 4X.

Blending 5 m IMI or 5 m 2E-IMI with 5 m PZ maintains the high CO_2 absorption rate of PZ. Blending 5 m 4X with 5 m PZ decreases its CO_2 absorption rate by 30%, although the rate of the blend is still comparable to 8 m PZ, which is much higher than 7 m MEA. The relatively low absorption rate of 5 m PZ/5 m 4X is caused by its high viscosity. Although 5 m PZ/2 m 2-ethyl-4-methyl-imidazole (2E-4M-IMI) and 5 m PZ/2.5 m 2E-IMI have lower absorption rate than 5 m PZ at low CO_2 partial pressure, their absorption rate at high CO_2 partial pressure is comparable to 5 m PZ. The CO_2 absorption rate of 5 m PZ/2 m 4X and 4 m PZ/2 m 4X is lower than 5 m PZ, but still higher than 8 m PZ.

Assuming that normalized capacity has the same effect as absorption rate on the overall CO_2 capture cost, 5 m PZ/5 m IMI, 5 m PZ/5 m 2E-IMI, 5 m PZ/2.5 m 2E-IMI, 5 m PZ/2 m 2E-4M-IMI, 5 m PZ/2 m 4X, and 4 m PZ/2 m 4X have similar CO_2 capture cost to 5 m PZ, but lower cost than 8 m PZ, 5 m PZ/5 m MDEA, or 5 m PZ/5 m 4X.

Unlike 8 m PZ, which precipitates when CO_2 loading reaches 0.44 mol CO_2/equiv PZ, no precipitate was observed for any of the selected PZ-based blends at rich CO_2 loading. In loaded solution, 5 m PZ has 5–10 °C lower melting transition temperatures than 8 m PZ at the same CO_2 partial pressure. All the selected amines except 2E-4M-IMI can lower the melting transition temperature of 5 m PZ by 3–7 °C, with a more significant effect at low CO_2 partial pressure. For unloaded 5 m PZ-based blends, different components have different abilities to solubilize PZ:

glycerol > ethylene glycol > IMI > 2E-IMI > dimethyl sulfoxide > triethylenediamine = 2-methylpiperazine.

5 m PZ/2 m 4X, 4 m PZ/2 m 4X, 5 m PZ/5 m IMI, and 5 m PZ/2.5 m IMI are superior solvents for CO_2 capture from coal-fired flue gas, showing comparable CO_2 absorption performance, and solvent stability to 5 m PZ, but better solvent solubility.

In addition, phase separation was observed in 5 m PZ/5 m 2E-4M-IMI solution, while 5 m PZ/5 m 2E-IMI only show phase separation in CO_2 loaded systems at low temperature.

2. CO_2 solubility and mass transfer rates by the wetted wall column p. 30

by Lynn Li

This report is the Introduction to a Ph.D. dissertation. The phenomenon of climate change is the main environmental issue facing our world today. The current world economy is mostly powered by energy stored in various types of fossil fuels. As fossil fuels are converted into usable energy, such as electricity, large amounts of CO_2 are generated as a byproduct and released into the atmosphere. The accumulation of the emitted CO_2 in the atmosphere is the cause of climate change. The current methods of extracting energy from fossil fuels (mostly combustion) must be adapted to minimize the impact of human activities on the environment. This need to reduce CO_2 emissions offers a potential market for new technologies and innovations.

The focus of this work is the amine scrubbing process, specifically in its application for CO_2 capture from coal-fired power plants. This chapter provides the relevant background for the application of this engineering research work. First, the reality of climate change and its main cause being the production of energy are discussed. A closer look at the energy and electric power sector in the U.S. demonstrates the significance of coal-fired power plants as a category for energy production and CO_2 emission. Next, the technology of carbon capture and sequestration (CCS) with amine scrubbing is discussed and proposed as the solution for CO_2 emission reduction from coal power plants. Last, the specific scope of this work, which examines the role of amine structure on the performance of the amine scrubbing process, will be presented.

3. CO_2 absorption rate measurement of 5 m Piperazine p. 50

In order to compare the CO_2 absorption rate of 5 m piperazine (PZ) with that of previously measured solvents, the Wetted Wall Column (WWC) repeatability was checked. Absorption rates were measured at three different loadings across the lean and rich operating range at a temperature of 40 ºC. The absorption rates (k_g') measured, together with new findings from Du under the same conditions, confirmed the k_g' measured by Dugas in 2009 with less than 10% difference. The k_g' of 5 m PZ was approximately 30% higher than that of 8 m PZ.

4. Absorber Intercooling Evaluation p. 55

by Darshan Sachde

In previous work, a shortcut method using an energy balance around the absorber was developed to predict the lean loading for each flue gas application where a temperature-related mass transfer pinch becomes limiting and intercooling is necessary to achieve maximum solvent capacity. The method only requires the use of a thermodynamic model for flash calculations and eliminates the need for the rigorous rate-based modeling to identify conditions for maximum

intercooling benefit. The method was updated significantly to improve prediction accuracy by accounting explicitly for the solvent contributions to the energy balance (i.e., ability of the solvent to carry or "trap" heat in the column). The updated method provides estimates of the gas and solvent outlet temperatures, total heat capacity of each phase, maximum temperature in the column, and the transition lean loading. The new approach successfully predicted outlet temperatures and total heat capacity for all three applications. The maximum temperature and transition lean loading estimates were improved significantly over the previous method for coal and steel applications (within ~2% of actual values). The accuracy of the predictions for the NGCC application was not significantly improved, however. The energy balance for the NGCC application was particularly sensitive to assumptions made to eliminate the rate-based portion of the model (CO_2 removed at the bulge). A correction to represent the appropriate CO_2 removal at the bulge yielded a much better estimate of maximum temperature and lean loading (within 1% of actual values). Future work will focus on providing a simplified method of addressing the removal at the bulge to ensure the shortcut approach is robust for all applications.

5. Modeling and Optimization of Advanced Stripper Configurations p. 70

by Yu-Jeng Lin

The lean/rich amine cross exchanger is one of the cost centers in the amine scrubbing process, and accounts for 20–30% of the capital cost. To reduce the cost, heat transfer performance can be enhanced by increasing pressure drop or reducing solvent viscosity.

A literature review on empirical correlations of heat transfer and pressure drop for plate-and-frame exchangers is presented in this report. The corrugation angle is the primary design geometry, which is typically designed at 30–60^o. The heat transfer coefficient at 60^o is almost double that at 30^o; however, the pressure drop at a large corrugation angle is also greater. The dependence of the pressure drop per unit length on the heat transfer coefficient is 0.35–0.40, which implies that the heat transfer coefficient will increase 30% by doubling the pressure drop per unit length.

The cost associated with the optimization of the cross exchanger has been developed as a function of the fluid velocity, the physical properties, the exponents of the empirical correlations and the pricing parameters. The dependence of viscosity on the exchanger cost is 0.3–0.4. A lower concentration of PZ, 5 m PZ, has been proposed to provide better solid solubility. Compared with 8 m PZ, the lower viscosity of 5 m PZ reduces the exchanger cost by around 30%, which nearly cancels out the increase in cost caused by the reduced capacity.

6. Absorber performance with 5 m MDEA/5 m PZ p. 83

by Yue Zhang

In a hybrid-parallel process combining amine scrubbing with membrane technology, the CO_2 concentration in the flue gas is enriched to 23.4% and removal level is increased to 95% (Case 19). This work simulates absorber performance of Case 19 with the Independence model for 5 molal (m) PZ and 5 m MDEA/5 m PZ in Aspen Plus®. Different intercooling configurations and absorber operating conditions have been tested to achieve better absorber performance and minimize stripper energy use.

5 m MDEA/5 m PZ offers higher CO_2 capacity but a lower absorption rate than 5 m PZ. Compared to 5 m PZ, absorber costs increase by 50% and advanced flash stripper costs decrease by 47%. The total equipment costs go down by 13%.

7. Stripper Performance and Equipment Costs using 5 m PZ and MDEA/PZ and Design of Ammonia Purging System *p. 92*

by Junyuan Ding

Also supported by a Phillips 66 Fellowship.

In previous work, four cases whose inlet CO_2 concentration and CO_2 removal rate were given by MTR (Cases 13, 14, 18-1, and 19-1) were simulated using 5 m piperazine (PZ) based on absorber performance. Due to the outstanding energy properties of aqueous PZ, including high CO_2 capacity, high thermal stability, moderately high viscosity, oxidative degradation resistance, and low volatility in CO_2-loaded solutions, it is a superior solvent for CO_2 capture by amine scrubbing. 5 m PZ minimizes the precipitation problem that the more viscous 8 m PZ causes in the solvent loop.

Since 5 m MDEA/5 m PZ has a greater CO_2 capacity than 5 m PZ, Case 18-MDEA/PZ (Case 18-2) and Case 19-MDEA/PZ (Cases 19-2, 19-3, and 19-4) using 5 m MDEA/5 m PZ stripping at 120 °C were studied to reduce the heat duty compared with Case 18-1 (rich loading of 0.401 mol CO_2/mol N and lean loading of 0.227 mol CO_2/mol N) and Case 19-1 (rich loading of 0.411 mol CO_2/mol N and lean loading of 0.303 mol CO_2/mol N) using 5 m PZ. The base-case stripping configuration was the advanced flash with warm rich bypass and cold rich exchanger bypass. The Independence model for MDEA/PZ in Aspen Plus® was used to simulate the stripping performance. Equipment costs for Cases 18 and 19 using 5 m PZ and 5 m MDEA/5 m PZ were analyzed according to the economic part of the Frailie dissertation.

Previous work optimized stripping using 5 m PZ with rich loading from 0.37 to 0.43 mol CO_2/mol N. In this work, 5 m MDEA/5 m PZ with a wide range of rich loading stripping at 150 °C was studied to simulate the stripper energy performance of a similar tertiary amine.

8. Packing characterization: hydraulic and mass transfer results overview

p. 105

by Chao Wang

In this chapter, three mass transfer models are developed. The database includes eleven structured packings with surface area ranging from 125 m^2/m^3 to 500 m^2/m^3 and corrugation angle from 45 degree to 70 degree, and three random packings from Raschig Super Ring family. The experimental systems use the absorption/desorption from aqueous solvents with liquid physical properties close to those of pure water.

The three mass transfer correlations developed in this work are:

$$\frac{a_e}{a_P} = 1.41\left[\left(\frac{\rho_L}{\sigma}\right) g^{1/3} \left(\frac{u_L}{a_P}\right)^{4/3}\right]^{0.116}$$

$$k_L = 3.08\,E-3 * u_L^{0.72} M^{0.42} a_P^{-1.15}$$

$$k_G = 9.6\,E-3 * u_G^{0.54} M^{0.29} a_P^{-0.5}$$

where:

a_e is the effective mass transfer area, (m^2/m^3);
a_P is the total surface area, (m^2/m^3);
ρ_L is the liquid density, (kg/m^3);
σ is the liquid phase surface tension, (N/m);
g is the gravity constant, (9.8 m/s^2);
u_L is the superficial liquid velocity, (m/s);
k_L is the liquid film mass transfer coefficient, (m/s);
M is the mixing point density, (pts/m^3);
k_G is the gas film mass transfer coefficient, (m/s);
u_G is the superficial gas velocity, (m/s).

The dimensionless k_L and k_G models for structured packings are:

$$Sh_L = 4.24 * \mathrm{Re}_L^{0.72} Mi^{0.42} Sc_L^{0.5}, \; k_L = Sh_L a_P D_L$$

$$Sh_G = 0.83 * \mathrm{Re}_G^{0.58} Mi^{0.3} Sc_G^{0.5}, \; k_G = Sh_G a_P D_G$$

where:

the dimensionless number Sh, Re, Mi, and Sc are defined in Equations (5-18) to (5-22).

The effective area model uses the basic form of the Tsai model (2010). Liquid superficial velocity over packing total area (u_L/a_P) is used as the liquid flow rate per wetted perimeter instead of (Q/L_P). Thus the applied range of this area model is extended to include hybrid packings and random packings. The experimental coefficient is changed from 1.34 to 1.41 which provides a better fit of the larger database. The wetted area varies with liquid rate to the 0.155 power and is independent of the corrugation angle and the mixing point density (Mi).

A new concept, Mixing Points Density (M), is introduced to represent the packing geometry effect on k_L and k_G. For regular structured packing, M can be calculated from basic packing geometries (channel base B, crimp height h, and corrugation angle). If these characteristic lengths data are not available, an alternative method to calculate mixing point density from a_P and θ is provided (Equation 5-33). For random packing, calculated M (M_{kL} or M_{kG}) is used to fit mass transfer models. The average deviation for experimental data and k_L model is 17%, and for k_G model is 8%.

Mass transfer models developed in this work are compared with literature models. The models have good consistency with models developed from aqueous absorption systems. There are significant differences between models developed in this work and models developed from hydrocarbon systems (distillation systems).

9. Effect of liquid viscosity on the liquid film mass transfer coefficient in packed columns *p. 134*

by Di Song

In this quarter, the reaction kinetics (k_g') of CO_2/NaOH/H_2O/glycerol was measured in the wetted wall column (WWC) with elevated NaOH concentration (0.3 M). The trend of k_g' as a function of glycerol concentration follows exactly that for the cases with 0.1 M NaOH. Models of the overall reaction rate constant (k_{Alk}) and surface alkalinity depletion were modified based on the new k_g' data. A detailed research plan for experiment in the pilot-scale air/water column was proposed.

10a. Kinetic Modeling of 4 m 2MPZ/4 m PZ and 4 m AMP/2 m PZ *p. 146*

by Brent Sherman

Also supported by CCSI

Three different projects addressed generic modeling methods, the effect of viscosity, and economics. A rigorous plate-and-frame heat exchanger economic tool was coded in Aspen Plus® using a calculator block. This brings the previous offline rigor online, enabling optimization of the exchangers. The online and offline calculations agree on average within 2% with a maximum deviation of 10%. A 2-piperadineethanol thermodynamic model was constructed using analogs from the AMP eNRTL Aspen Plus® model. This is the first step in proving the hypothesis that hindered amines enhance the rate of CO_2 absorption through increasing the solubility of CO_2 in solution. The 2PE model was used as an opportunity to investigate ways to correlate viscosity. This investigation showed that the best method is the semi-empirical modified Weiland equation rather than the internal correlations that are available in Aspen Plus®.

10b. 2MPZ CO_2 Capture Simulation User Manual *p. 162*

11. Time Scale Analysis of Amine Scrubbing *p. 274*

by Matt Walters
Co-supervised by Thomas Edgar

Proportional (P) and proportional integral (PI) controllers were demonstrated to be effective in regulating a low-fidelity model of an advanced amine scrubbing process configuration to the desired set point. P controllers were used for level control, and PI controllers were used for temperature and concentration control. The primary objective of the control strategy is to maintain a constant delivery rate of CO_2 to the compressor, in contrast to previous work which controlled the CO_2 removal rate in the absorber. The water balance is maintained by controlling the top temperature of the water wash and allowing for water makeup or bleed from the water wash recycle loop. A desired L/G ratio in the absorber is used to set the solvent circulation flowrate. This simple feedback control structure produces a slow, stable response but is not optimal. It is difficult to tune the bypass ratios around the main cross exchanger, because there is significant loop interaction and energy recovery. The bypass ratios were set to constant values in this work to avoid instability from the competing control loops. The concentration controller is also difficult to tune because of the slow nature of the response. The current tuning is too aggressive and resulted in oscillations in the amine concentration.

12. Amine Degradation *p. 285*

by Omkar Namjoshi

The degradation of PZ-promoted MDEA in the presence of H^+ is presented in this chapter and is modeled as a function of protonated and free amine species. Prior thermal degradation studies in the literature have not explicitly accounted for the presence of protonated species in degradation. This is representative of the initial degradation rate of PZ-promoted MDEA as it is initiated by a free amine attacking a protonated amine. A degradation pathway is proposed based on the product degradation slate and validated using rate measurements and fitting kinetic parameters to proposed rate laws. Degradation under acidified conditions is then compared to degradation in the presence of CO_2 and finally used to model degradation based on the design initial concentration and lean CO_2 loading from a process design perspective.

12a. Thermal Degradation of Sterically Hindered Amines Blended with Piperazine *p. 316*

by Daniel Hatchell, Undergraduate research assistant

This report presents thermal degradation data for six sterically hindered amine (SHA) blends with piperazine (PZ): 1-amino-2-methyl-1-propanol (AMP), 2-amino-2-methyl-1,3-propanediol (AMPD), 2-amino-2-(hydroxymethyl)-1,3-propanediol (TRIS), 2-(*tert*-butylamino)ethanol (tBuAE), 2-piperadinemethanol (PM), and 2-piperadineethanol (PE). The SHA/PZ blends were prepared with 3.2 m SHA/1.6 m PZ and loaded 0.22 mol CO_2/mol alkalinity. These solutions were degraded at 135 ºC, 150 ºC, and 165 ºC. Concentrations of both species over time were plotted to determine degradation rate constants and reaction activation energies. 4 m AMP/2 m PZ with the same CO_2-loading was degraded under the three temperatures to test the effect of concentration on degradation rate. 3.2 m AMP/1.6 m PZ was loaded with acid instead of CO_2 and degraded at 165 ºC to determine the role of CO_2.

AMP/PZ and tBuAE/PZ are the most stable blends, followed by AMPD/PZ, then TRIS/PZ and PE/PZ, and finally PM/PZ. These degradation reactions follow first-order rate kinetics. Concentration does not affect degradation rate at lower temperature but appears to at 165 ºC. Acid-loaded AMP/PZ undergoes significantly less degradation than CO_2-loaded AMP/PZ.

12b. Oxidative Degradation of Amines *p. 327*

by Hanbi Liu, Undergraduate research assistant

The oxidative degradation of diamines in a stirred reactor was measured at 70 °C, 98 kPa O_2, and 2 kPa CO_2. Diethanolamine (DEA) and methylaminoethanol (MAE) at an initial concentration of 5 m, 10 m ethanolamine (MEA), and a 5 m MEA/2.5 m propylenediamine (PDA), at initial loading of 0.4 mol CO_2/mol alkalinity and initial metals concentration of 0.4 mM Fe, 0.2 mM Mn, 0.1 mM Ni, and 0.05 mM Cr, were oxidatively degraded. The purpose of these experiments was to study the structural effect of amines on their degradation rates.

Approximately 78% of MEA, 69% of DEA, and 63% of MAE were lost after 300 hours run time. Only 8% of MEA was lost from MEA/PDA at the same conditions. DEA degradation follows 2nd order kinetics with a rate constant of $3*10^{-6}$ 1/(mmol/kg-hr). MAE degradation follows 2nd order kinetics with a rate constant of $1*10^{-6}$ 1/(mmol/kg-hr). MEA degradation follows 1st order kinetics with a rate constant of 0.015 1/(mmol/kg-hr).

13. Aerosol Observation and Separation in Amine-Based CO_2 Capture *p. 334*

by Matt Beaudry

Amine emissions in aerosol form are a significant problem for amine-based CO_2 capture plants. Unarrested soot and condensed hydrolyzed SO_3 travel through the absorber while collecting water and amine. Conventional water wash columns are ineffective at removing the amine once it is captured in the aerosols. While Brownian diffusion units have proven to be fairly effective at reducing amine emissions, cyclonic separators offer the potential for improved capture performance with a simpler system at a lower cost. A swirl tube cyclonic separator has been designed and will be implemented in both the Aerosol Growth Column and the PRC Pilot Plant. The flexibility of the design will allow for capture of aerosols at controllable sizes. Another

aerosol sampling system has been designed to utilize centrifugal forces to control the size of particles sampled by FTIR analysis. It is hoped that this will provide similar data to the PDI with more robust and less expensive equipment

14. Amine Degradation in Pilot Plants *p. 343*

by Paul Nielsen

PZ was oxidized by reaction with hydrogen peroxide at absorber conditions in the HGF apparatus. An initial rate of 0.03 moles ammonia was observed per mole of peroxide added regardless of PZ concentration, dissolved metal concentration, or the presence of the free radical scavenger Inhibitor A (Inh A). However, PZ solvent without Inh A and with high metal concentration had a greater rate of ammonia generation after some oxidation had already occurred. Formate accumulation was also reduced by a factor of 3 in solvent containing Inh A. Ammonia was produced at a lower rate relative to formate in peroxide oxidation compared to previous experiments in the HTOR cyclic oxidation apparatus. Oxidation at high temperature may produce a relatively greater amount of ammonia per mole of amine oxidized. N_2O was also observed from peroxide oxidation. This species has not been previously quantified as an oxidation product in cyclic oxidation experiments.

A simplified correlation for the effect of heat stable salts on MEA and PZ viscosity was developed. Sulfate, formate, and acetate are expected to have the greatest effect on solvent viscosity in a carbon capture facility, with nitrate having a much lesser effect. Therefore, limiting amine oxidation, scrubbing SO_x before the absorber, and solvent reclaiming will be the most important strategies to control solvent viscosity in a capture plant.

15. NO_2 Absorption into Aqueous Amines and Sulfite *p. 354*

by Nathan Fine

This quarter, a techno-economic evaluation was performed for simultaneously scrubbing NO_2 and SO_2 out of the flue gas upstream of the CO_2 scrubber using a NaOH scrubber with a triethanolamine (TEA) additive. Costs of NO_2 penetration into PZ are \$0.15–\$0.45/MT CO_2/ppm NO_2 due to the reaction of PZ with NO_2 as well as the cost of reclaiming and waste disposal. There is also an additional hidden cost for NO_2 penetration since n-nitrosopiperazine (PZNO), an intermediate product of NO_2 absorption, is carcinogenic. A base case NaOH scrubber at pH 8.0 with 7 m of Mellapak 250X and a gas superficial velocity of 1.5 m/s was analyzed with different TEA feed rates. As the feed rate of TEA increases, the concentration of TEA in the scrubber increases, which allows for greater NO_2 absorption. The optimal NO_2 removal occurs when the costs of increasing the TEA feed balance with diminishing returns on NO_2 removal. This corresponds to 86% removal and 80 mM circulating TEA for a gas inlet of 5 ppm NO_2 and 50 ppm SO_2. As inlet SO_2 increases, the purge rate must also increase so that sodium sulfate does not precipitate out of solution. The optimal TEA and removal decreases at higher purge rates, yielding 62% removal and 20 mM circulating TEA for a gas inlet of 5 ppm NO_2 and 300 ppm SO_2. Savings from NO_2 removal decrease with decreasing inlet NO_2, making pre-scrubbing economical only when inlet NO_2 is greater than around 2 ppm. Finally, analysis was performed with varying height and TEA at a constant 90% NO_2 removal. At 50 ppm inlet SO_2, the additional cost for TEA and height of the column balance with the savings of NO_2 removal, so PZNO concentration can decrease by a factor of 10 without any net cost to the

process. At 300 ppm inlet SO_2, TEA scrubbing costs an additional \$1.20/MT CO_2, leaving room for technology improvement.

16. Ion Exchange for Metals Removal from Amine Solutions p. 365

by Kent Fischer

A series of experiments was conducted to determine the relationships between amine structure and corrosivity. These experiments were conducted in 316 stainless steel Swagelok® cylinders, which were placed into 150 °C ovens and heated, causing corrosion of the cylinder and degradation of the amine. A series of linear amines was tested to determine the effect of chain length on amine corrosivity, and a series of hindered amines blended with piperazine (PZ) was screened. Corrosion was measured by determination of the amount of dissolved metal in solution using ICP-OES.

Attachments

Presentations from the October research review meeting, as well as papers presented at GHGT-12, will be made available in a separate document.

Aqueous piperazine blend for CO_2 Capture

Quarterly Report for October 1 – December 31, 2014

by Yang Du

Supported by the Texas Carbon Management Program

McKetta Department of Chemical Engineering

The University of Texas at Austin

January 31, 2015

Abstract

Thermally stable PZ-based blends selected last quarter (T_{max} >140 °C) were screened further this quarter for volatility, CO_2 capacity and absorption rate, viscosity, and solvent solubility. 2-(Isopropylamino)ethanol (IPAE), bis(2-methoxyethyl)amine (BMEA), 1,2-dimethylimidazole (1,2-DM-IMI), and 2-piperidinoethanol (2PDE) have higher Henry's law constants than 2-amino-2-methyl-1-propanol (AMP), and thus are excluded from future consideration. Imidazole (IMI), 2-ethyl-imidazole (2E-IMI), and the proprietary amine 4X have higher Henry's law constants than PZ but lower Henry's law constants than monoethanolamine (MEA). Loaded 5 m PZ/5 m 2E-IMI has a similar amine partial pressure to 8 m PZ at 45 °C, but lower partial pressure at 65 °C.

Adding IMI to 5 m PZ (pKa = 7.0) decreases the CO_2 capacity. Adding 2-methyl-imidazole (2M-IMI, pKa = 7.9) or 2E-IMI (pKa = 8.0) maintains the CO_2 capacity. Adding 4X (pKa = 9.4) increases the CO_2 capacity. 5 m PZ/2.5 m 2E-IMI has almost the same CO_2 capacity as 5 m PZ/5 m 2E-IMI. However, 5 m PZ/5 m 4X has significantly greater CO_2 capacity than 5 m PZ/2 m 4X or 4 m PZ/2 m 4X.

Blending 5 m IMI or 5 m 2E-IMI with 5 m PZ maintains the high CO_2 absorption rate of PZ. Blending 5 m 4X with 5 m PZ decreases its CO_2 absorption rate by 30%, although the rate of the blend is still comparable to 8 m PZ, which is much higher than 7 m MEA. The relatively low absorption rate of 5 m PZ/5 m 4X is caused by its high viscosity. Although 5 m PZ/2 m 2-ethyl-4-methyl-imidazole (2E-4M-IMI) and 5 m PZ/2.5 m 2E-IMI have lower absorption rate than 5 m PZ at low CO_2 partial pressure, their absorption rate at high CO_2 partial pressure is comparable to 5 m PZ. The CO_2 absorption rate of 5 m PZ/2 m 4X and 4 m PZ/2 m 4X is lower than 5 m PZ, but still higher than 8 m PZ.

Assuming that normalized capacity has the same effect as absorption rate on the overall CO_2 capture cost, 5 m PZ/5 m IMI, 5 m PZ/5 m 2E-IMI, 5 m PZ/2.5 m 2E-IMI, 5 m PZ/2 m 2E-4M-IMI, 5 m PZ/2 m 4X, and 4 m PZ/2 m 4X have similar CO_2 capture cost to 5 m PZ, but lower cost than 8 m PZ, 5 m PZ/5 m MDEA, or 5 m PZ/5 m 4X.

Unlike 8 m PZ, which precipitates when CO_2 loading reaches 0.44 mol CO_2/equiv PZ, no precipitate was observed for any of the selected PZ-based blends at rich CO_2 loading. In loaded solution, 5 m PZ has 5–10 °C lower melting transition temperatures than 8 m PZ at the same CO_2

partial pressure. All the selected amines except 2E-4M-IMI can lower the melting transition temperature of 5 m PZ by 3–7 °C, with a more significant effect at low CO_2 partial pressure. For unloaded 5 m PZ-based blends, different components have different abilities to solubilize PZ: glycerol > ethylene glycol > IMI > 2E-IMI > dimethyl sulfoxide > triethylenediamine = 2-methyl-piperazine.

5 m PZ/2 m 4X, 4 m PZ/2 m 4X, 5 m PZ/5 m IMI, and 5 m PZ/2.5 m IMI are superior solvents for CO_2 capture from coal-fired flue gas, showing comparable CO_2 absorption performance, and solvent stability to 5 m PZ, but better solvent solubility.

In addition, phase separation was observed in 5 m PZ/5 m 2E-4M-IMI solution, while 5 m PZ/5 m 2E-IMI only show phase separation in CO_2 loaded systems at low temperature.

Introduction

Amine scrubbing has shown the most promise for effective capture of CO_2 from coal-fired flue gas. Concentrated piperazine (PZ) has the most outstanding properties for low partial pressure CO_2 capture (large cyclic CO_2 capacity, high CO_2 absorption rate, high solvent stability, and low volatility), but its industrial application is limited by its low solubility in water. PZ-based amine blends, such as PZ/AMP, PZ/MDEA, and PZ/2MPZ have gained attention due to their superior overall performance for CO_2 capture by absorption/stripping, but better solvent solubility than straight PZ (Li et al., 2013). However, these blended amines still have problems, such as the high volatility of AMP, low solvent stability of MDEA, and high viscosity of 2MPZ, that limit their industrial application. To find a better amine to blend with PZ, 36 commercially available amines were screened for their thermal stability last quarter. Several thermally stable amines were screened further this quarter by measuring their volatility, CO_2 capacity and absorption rate, viscosity, and solvent solubility.

Experimental Methods

Solution preparation

Aqueous PZ/second amine was prepared by melting anhydrous PZ in a mixture of water and the second amine, and gravimetrically sparging CO_2 (99.5%, Matheson Tri Gas, Basking Ridge, NJ) to achieve the desired CO_2 concentration. The concentration of CO_2 was determined by total inorganic carbon (TIC) analysis, described by Freeman (2011).

Viscosity measurement

Viscosity of PZ/second amine was measured using a Physica MCR 300 cone-and-plate rheometer (Anton Paar GmbH, Graz, Austria). The method was described by Freeman (2011). The average value and standard deviation calculated from 10 individual measurements for each sample was reported.

CO_2 absorption rate and solubility

CO_2 absorption rate and equilibrium partial pressure in PZ/second amine were measured at 40 °C using the wetted wall column (WWC), which counter-currently contacted an aqueous PZ/second amine solution with a saturated N_2/CO_2 stream on the surface of a stainless steel rod with a known surface area to simulate CO_2 absorption in an absorber. A detailed description of the wetted wall column measurements has been given by Chen (2011).

Amine volatility

Amine volatility was measured in a stirred reactor coupled with a hot gas FTIR analyzer (Fourier Transform Infrared Spectroscopy, Temet Gasmet Dx-4000). This was the same method and apparatus used by Nguyen (2013) to measure amine volatility and CO_2 partial pressure in loaded solutions.

Safety considerations

For the screening test, the MSDS for each new amine should be read for proper solvent storage. Flammable amines should only be stored in the "flammables" cabinet.

Results and discussion

Amine Volatility

Figure 1 shows the amine Henry's law constants in water of 2-(Isopropylamino)ethanol (IPAE), bis(2-methoxyethyl)amine (BMEA), 1,2-dimethylimidazole (1,2-DM-IMI), and 2-piperidinoethanol (2PDE), 2-ethyl-imidazole (2E-IMI), and 4X. The partial pressure of 0.3–1 m amines at normal operating temperatures (40–70 °C) were measured using FTIR. The Henry's law constants were calculated by assuming the activity coefficients of these diluted solutions are 1. IPAE, BMEA, 1,2-DM-IMI, and 2PDE have higher Henry's law constants than 2-amino-2-methyl-1-propanol (AMP), and thus are excluded from future consideration. 2E-IMI and 4X have higher Henry's law constants than PZ but lower Henry's law constants than monoethanolamine (MEA) (Nguyen, 2013). Figure 2 shows the amine partial pressure of loaded 5 m PZ/5 m 2E-IMI at normal operating temperatures compared to 8 m PZ and 7 m MEA. Loaded 5 m PZ/5 m 2E-IMI has a similar amine partial pressure to 8 m PZ at 45 °C, but lower partial pressure at 65 °C. Both 8 m PZ and 5 m PZ/5 m 2E-IMI have lower amine partial pressure than 7 m MEA. The data also demonstrate the expected trend that amine partial pressure increases with increasing temperature.

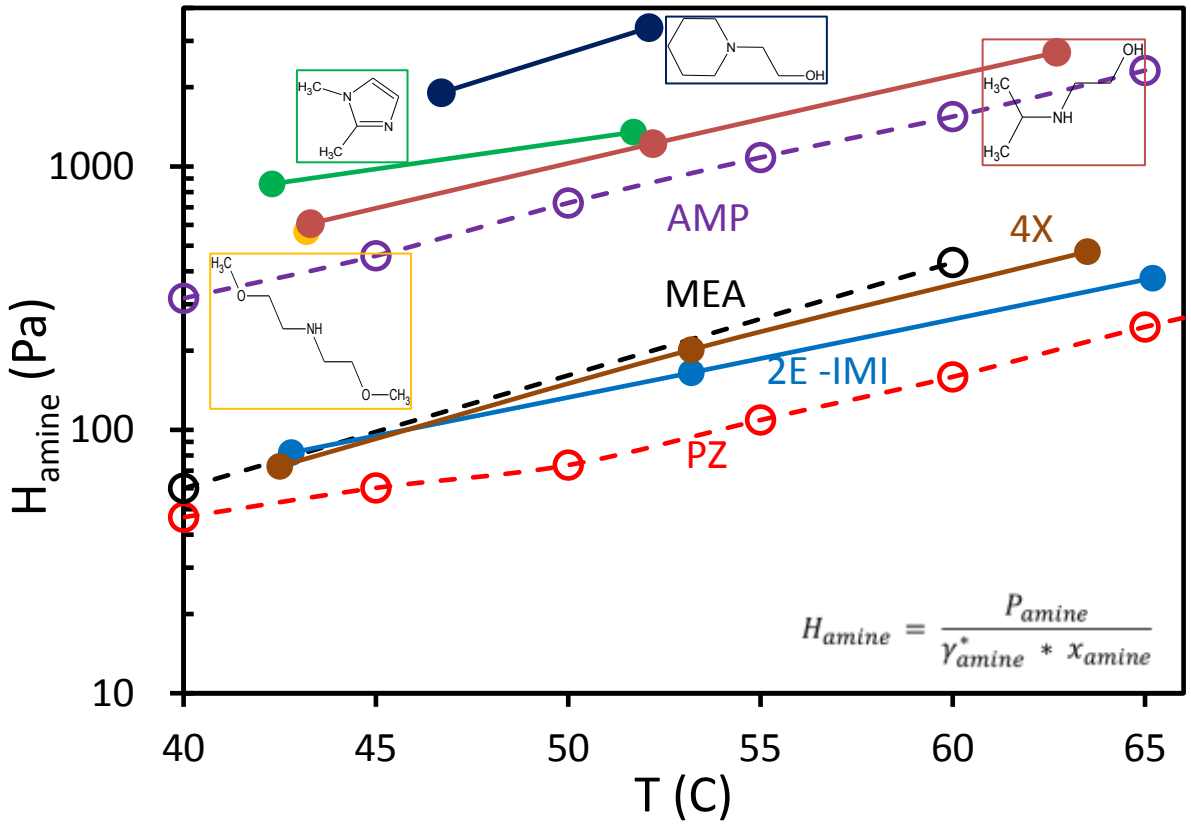

Figure 1: Henry's law constants of unloaded IPAE, 1,2-DM-IMI, BMEA, 2PDE, 2E-IMI, and 4X, compared to PZ, MEA, and AMP.

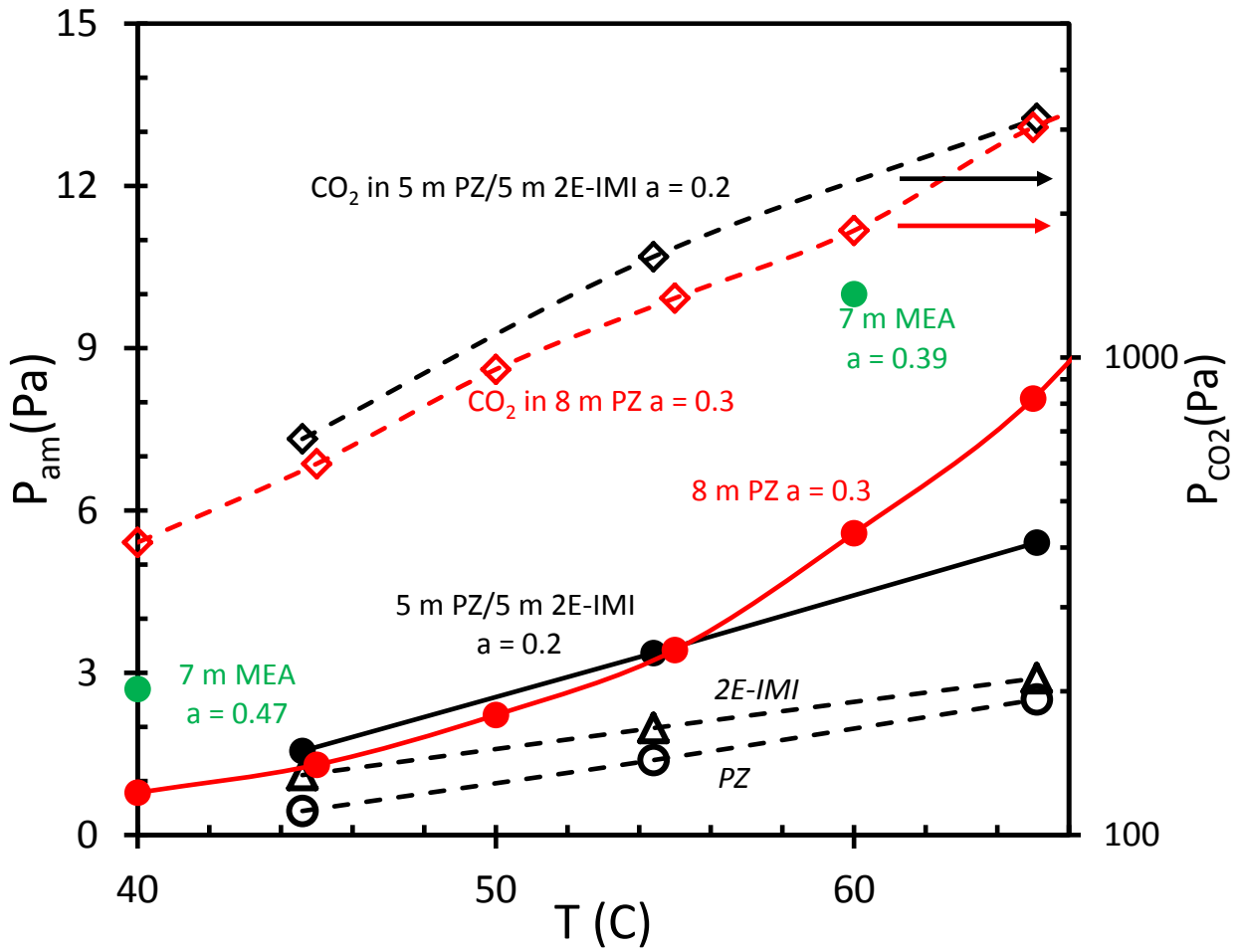

Figure 2: Partial pressure of loaded 5 m PZ/5 m 2E-IMI, compared to loaded 8 m PZ and 7 m MEA.

Viscosity

Figure 3 shows the viscosity of selected PZ-based blends at 40 °C compared to 5 m PZ and 8 m PZ at the same CO_2 partial pressure. 5 m PZ/5 m 4X has 50% higher viscosity than 8 m PZ. The viscosity of 5 m PZ/5 m 2E-IMI is twice as high as 5 m PZ, while the viscosity of 5 m PZ/5 m IMI is only 20% higher than 5 m PZ. As expected, viscosity is a strong function of amine concentration. The viscosity of 8 m PZ is three times as high as 5 m PZ. The viscosity of 5 m PZ/2 m 4X, 4 m PZ/2 m 4X, and 5 m PZ/2 m 2E-4M-IMI is 50–70% higher than 5 m PZ.

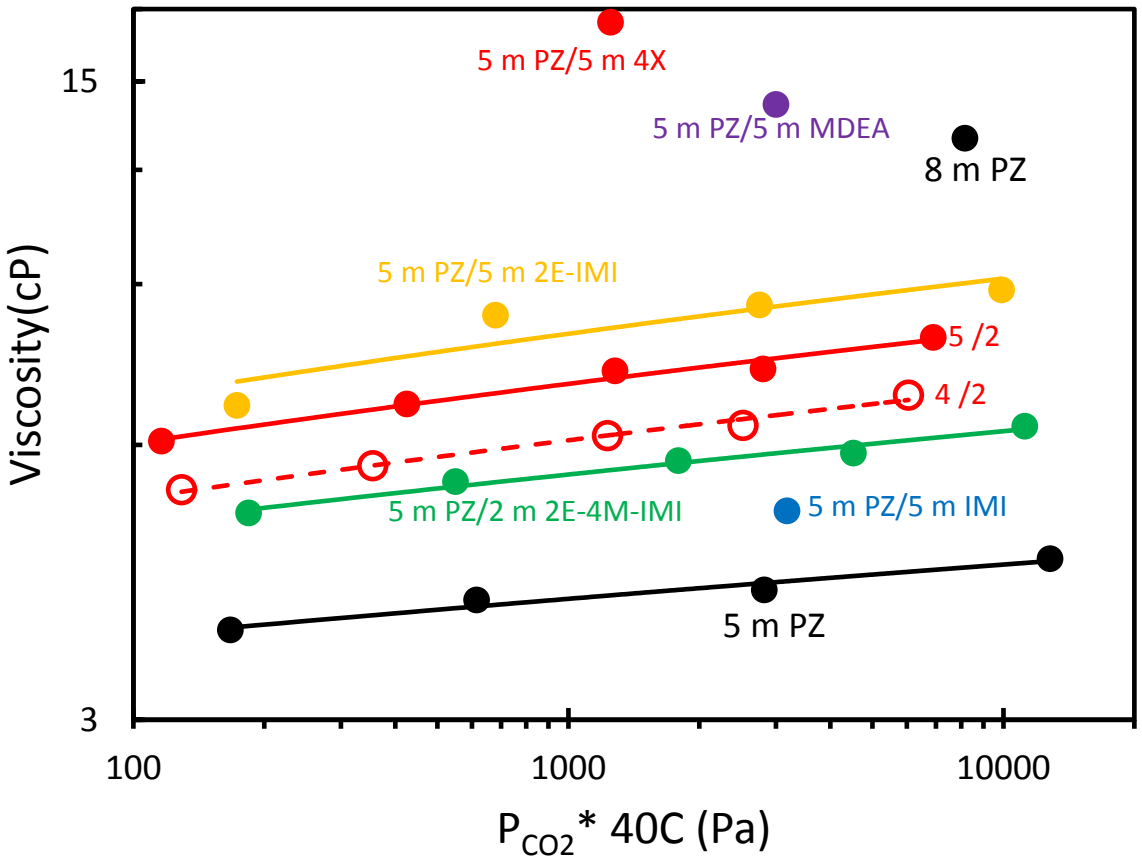

Figure 3: Viscosity at 40 °C of selected PZ-based blends, compared to 5 m PZ and 8 m PZ.

CO_2 capacity and rate

The CO_2 solubility in loaded 5 m PZ/5 m IMI, 5 m PZ/5 m 2M-IMI, 5 m PZ/5 m 2E-IMI, 5 m PZ/5 m 2E-4M-IMI, 5 m PZ/5 m 4X, 5 m PZ/2.5 m 2M-IMI, 5 m PZ/2.5 m 2E-IMI, 5 m PZ/2 m 2E-4M-IMI, 5 m PZ/2 m 4X, and 4 m PZ/2 m 4X was measured at 40 °C using the WWC. Figure 4 shows the CO_2 solubility for 5 m PZ/5 m amine blends. Blending IMI (pKa = 7.0) decreases the CO_2 capacity of PZ. Blending 2M-IMI, (pKa = 7.9) or 2E-IMI (pKa = 8.0) maintains the CO_2 capacity of PZ. Blending 4X (pKa = 9.4) increases the CO_2 capacity of PZ.

Figure 5 shows the effect of amine ratio in blends on their CO_2 capacity. 5 m PZ/2.5 m 2E-IMI has almost the same CO_2 capacity as 5 m PZ/5 m 2E-IMI. However, 5 m PZ/5 m 4X has significantly higher CO_2 capacity than 5 m PZ/2 m 4X or 4 m PZ/2 m 4X.

Blending 5 m IMI or 5 m 2E-IMI with 5 m PZ maintains the high CO_2 absorption rate of PZ. Blending 5 m 4X with 5 m PZ decreases its CO_2 absorption rate by 30%, although the rate of the blend is still comparable to 8 m PZ, which is much higher than 7 m MEA (Figure 6a). The relatively low absorption rate of 5 m PZ/5 m 4X is caused by its high viscosity. Although 5 m PZ/2 m 2E-4M-IMI and 5 m PZ/2.5 m 2E-IMI have lower absorption rate than 5 m PZ at low CO_2 partial pressure, their absorption rate at high CO_2 partial pressure is comparable to 5 m PZ. The CO_2 absorption rate of 5 m PZ/2 m 4X and 4 m PZ/2 m 4X is lower than 5 m PZ, but still higher than 8 m PZ (Figure 6b).

Figure 7 shows the normalized CO_2 capacity and average absorption rate at 40 °C for selected PZ-based blends, compared to 5 m PZ, 8 m PZ, and 7 m MEA. The normalized CO_2 capacity is defined in Equation 1 to consider the effect of viscosity on the heat cost in the process (Li et al., 2013).

$$\text{Normalized CO2 Capacity} = \frac{\text{Capacity}}{\left(\mu_{\text{mid}} / 10\ \text{cP}\right)^{0.25}} \quad (1)$$

The average absorption rate is defined in Equation 2 (Li et al., 2013).

$$k'_{g\ avg} = \frac{Flux_{CO_2,LM}}{(P_{CO_2} - P^*_{CO_2})_{LM}} = \frac{(Flux_{CO_2,top} - Flux_{CO_2,bottom}) / Ln(Flux_{CO_2,top} / Flux_{CO_2,bottom})}{(P_{CO_2,top} - P^*_{CO_2,lean}) - (P_{CO_2,bottom} - P^*_{CO_2,rich}) / Ln\left(\frac{P_{CO_2,top} - P^*_{CO_2,lean}}{P_{CO_2,bottom} - P^*_{CO_2,rich}}\right)} \quad (2)$$

Assuming that normalized capacity has the same effect as absorption rate on the overall CO_2 capture cost, 5 m PZ/5 m IMI, 5 m PZ/5 m 2E-IMI, 5 m PZ/2.5 m 2E-IMI, 5 m PZ/2 m 2E-4M-IMI, 5 m PZ/2 m 4X, and 4 m PZ/2 m 4X have similar CO_2 capture cost to 5 m PZ, but lower cost than 8 m PZ, 5 m PZ/5 m MDEA, or 5 m PZ/5 m 4X.

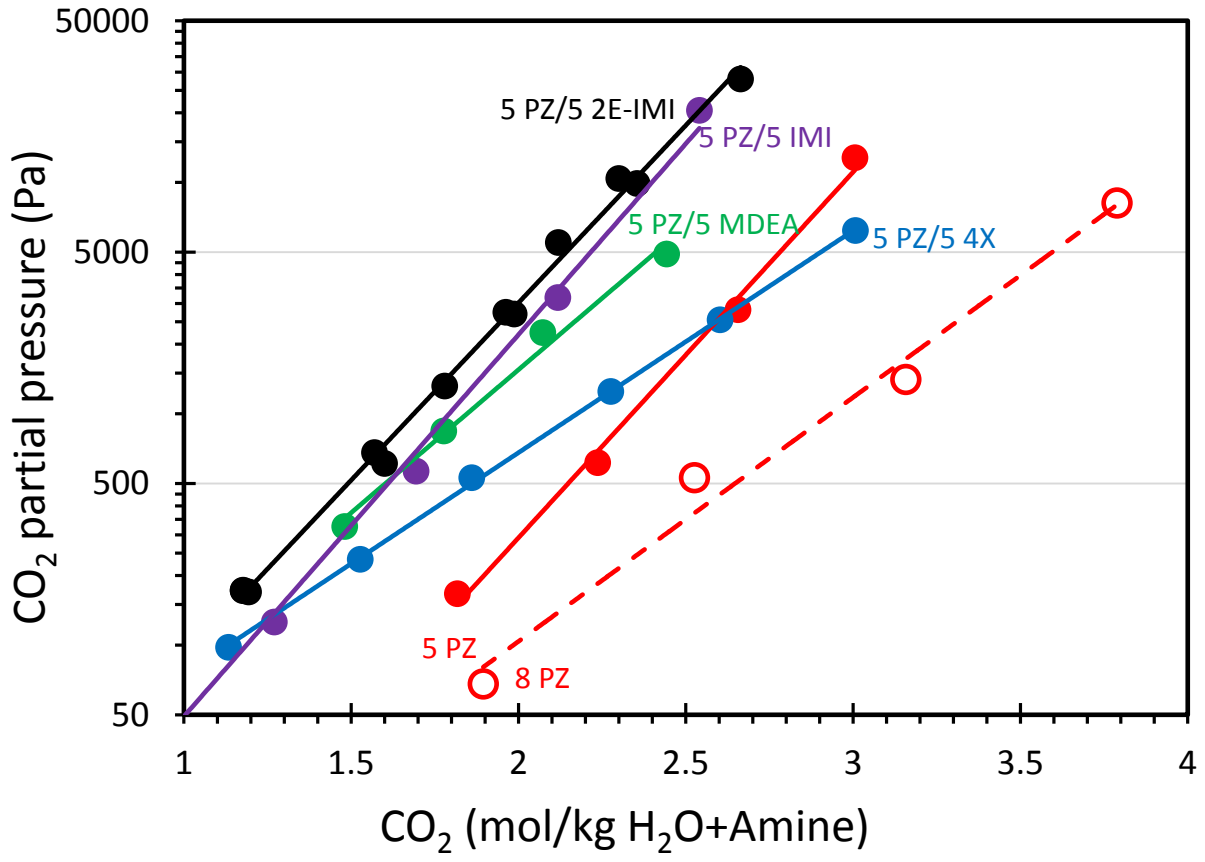

Figure 4: CO_2 solubility at 40°C for 5 m PZ/5 m amine blends, compared to 5 m PZ and 8 m PZ.

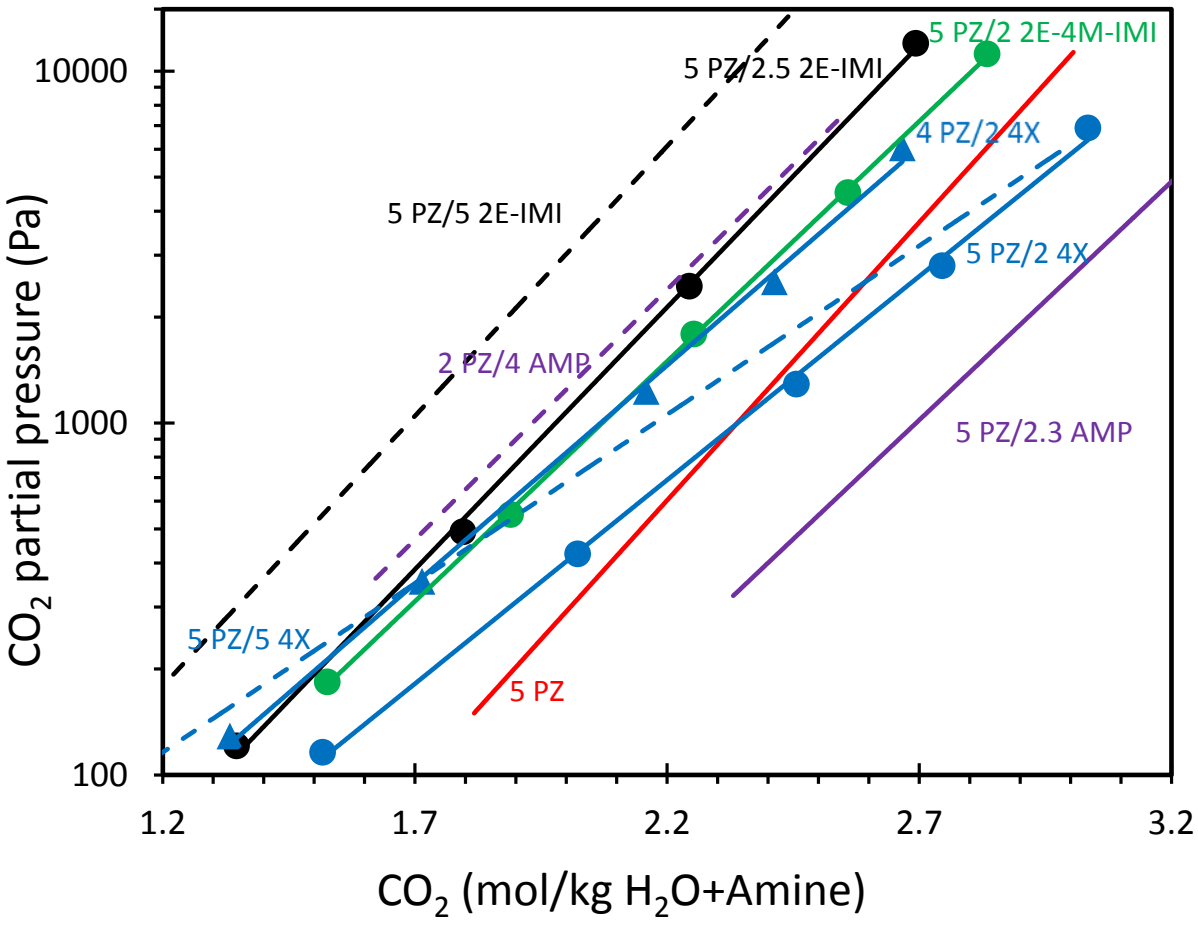

Figure 5: The effect of amine ratio in blends on their CO_2 capacity at 40 °C.

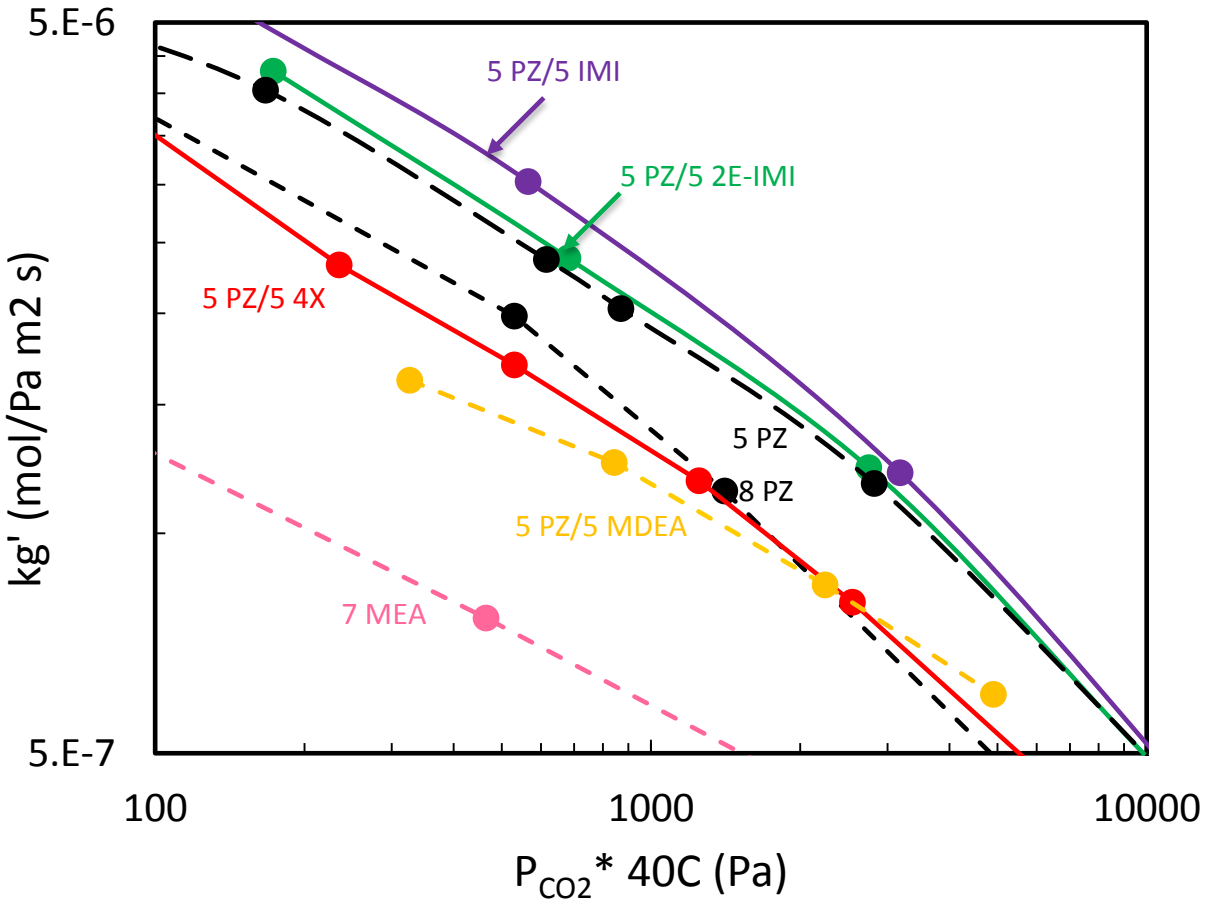

Figure 6a: Mass transfer coefficients (kg') in 5 m PZ/5 m second amine blends at 40 °C, compared to 7 m MEA, 5 m PZ, and 8 m PZ.

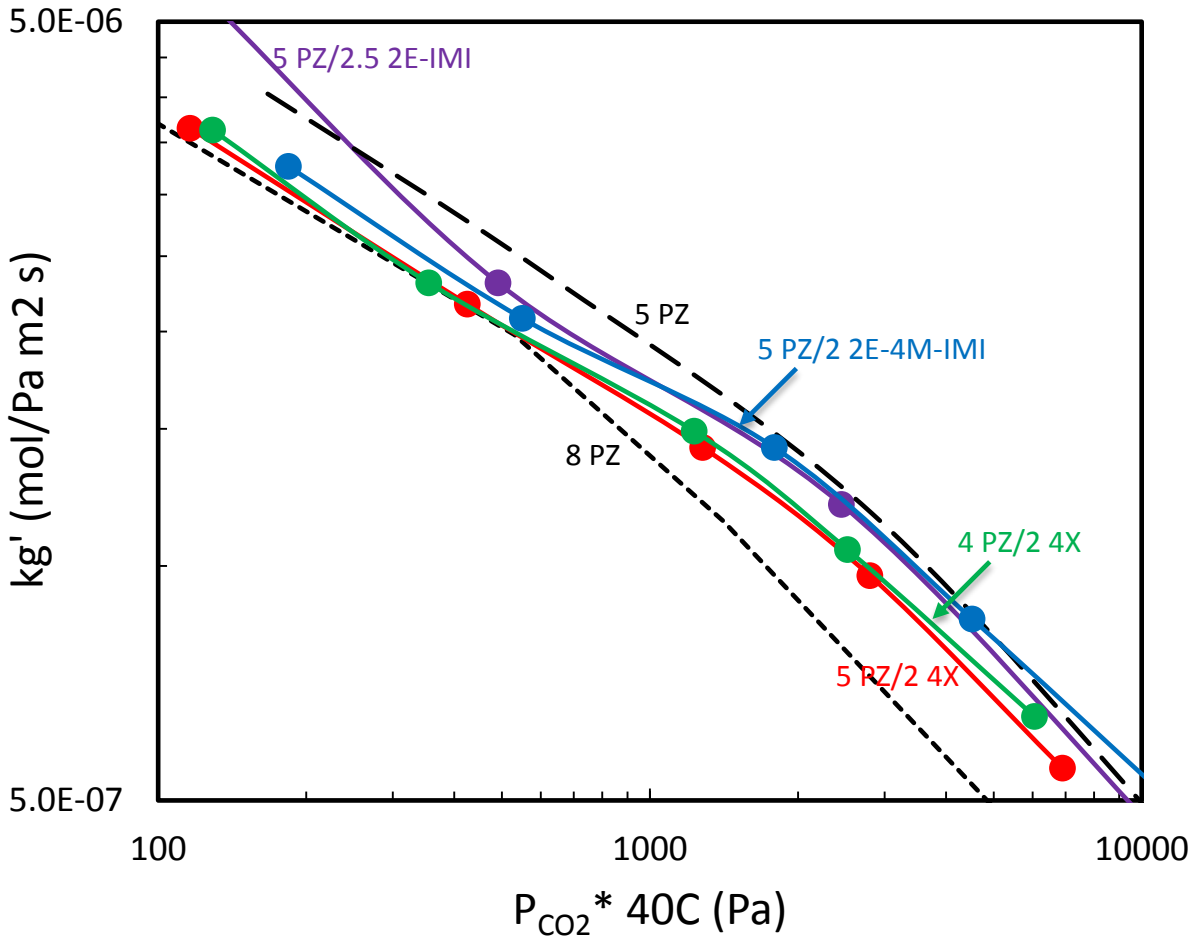

Figure 6b: Mass transfer coefficients (kg') in 5 m PZ/2 m 4X, 4 m PZ/2 m 4X, 5 m PZ/2.5 m 2E-IMI, and 5 m PZ/2 m 2E-4M-IMI at 40 °C, compared to 5 m PZ and 8 m PZ.

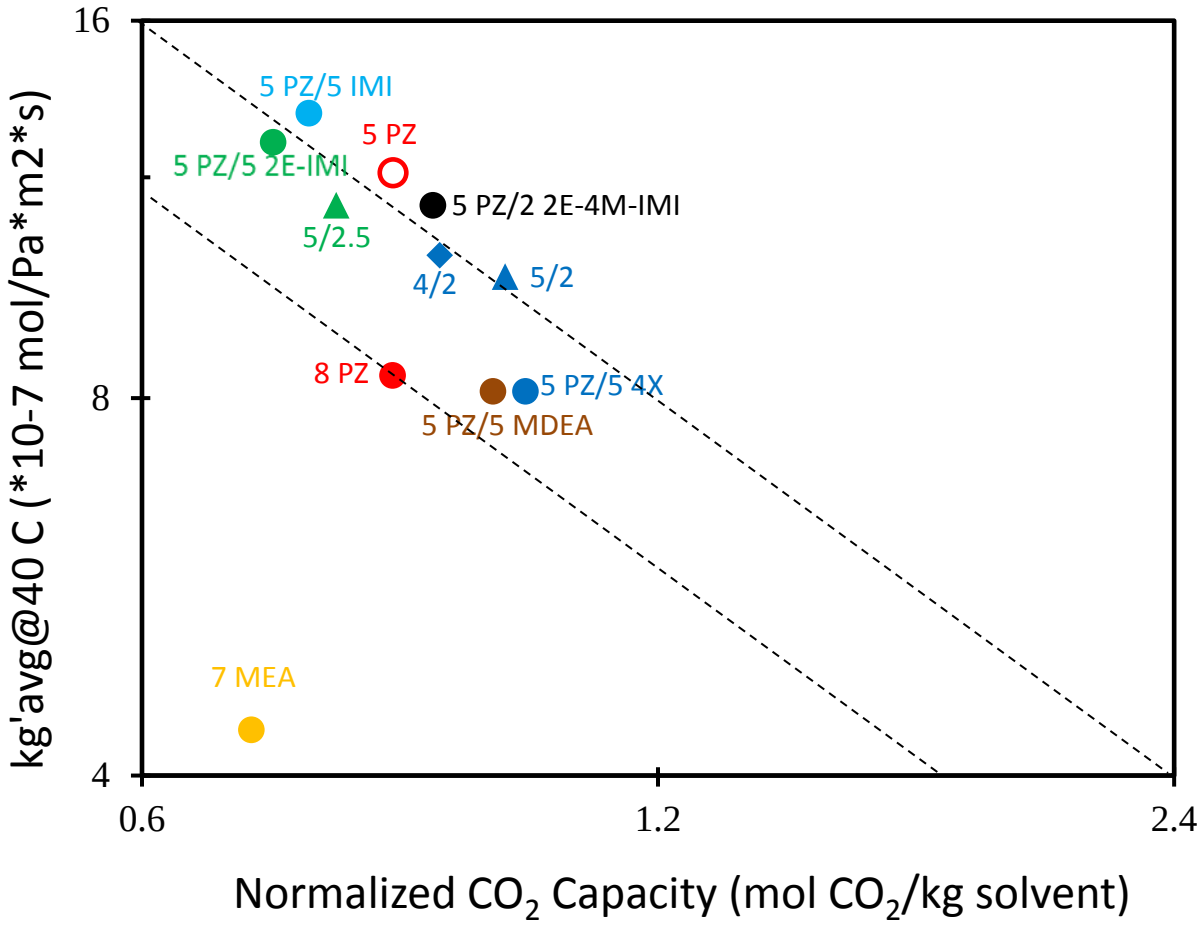

Figure 7: Normalized CO_2 capacity and average mass transfer coefficients (kg') at 40 °C for selected PZ-based blends, compared to 5 m PZ, 8 m PZ, and 7 m MEA.

Solvent solubility of PZ/imidazoles

The melting transition temperatures of unloaded 5 m PZ-based blends are shown in Figure 8. Different components have different abilities to solubilize PZ: glycerol > ethylene glycol > IMI > 2E-IMI > dimethyl sulfoxide > triethylenediamine = 2-methyl-piperazine.

The melting transition temperature of selected PZ-based blends over a range of CO_2 loading and CO_2 partial pressure are shown in Figures 9, 10a, and 10b. The transition temperature for 5 m PZ, and 8 m PZ from Freeman (2011) is shown for comparison. Unlike 8 m PZ, which precipitates when CO_2 loading reaches 0.44 mol CO_2/equiv PZ, no precipitate was observed for all the selected PZ-based blends at rich CO_2 loading. In loaded solution, 5 m PZ has a 5–10 °C lower melting transition temperatures than 8 m PZ at the same CO_2 partial pressure. All the selected amines, except for 2E-4M-IMI, can lower the melting transition temperature of 5 m PZ by 3–7 °C, with a more significant effect at low CO_2 partial pressure.

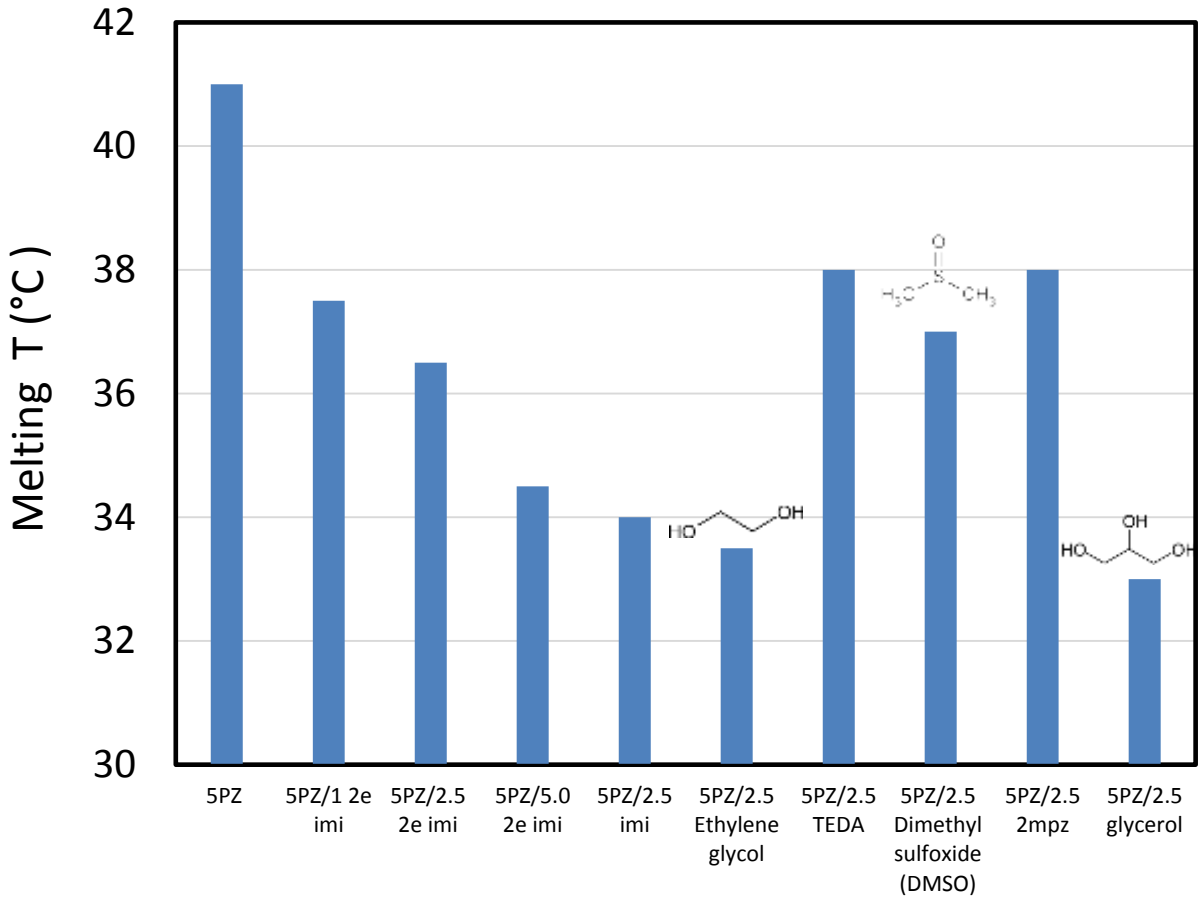

Figure 8: Melting transition temperature for unloaded 5 m PZ-based blends

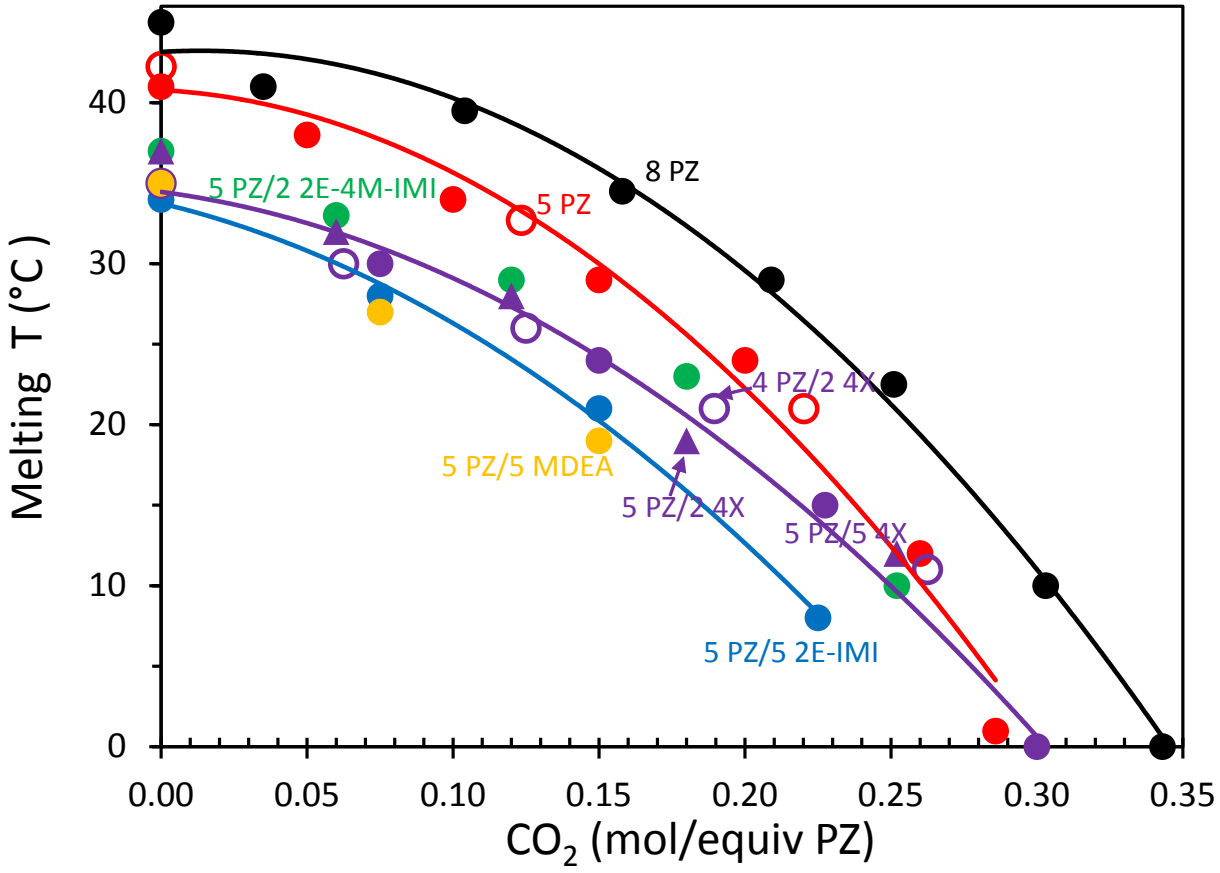

Figure 9: Melting transition temperature for loaded PZ-based blends over a range of CO_2 loading.

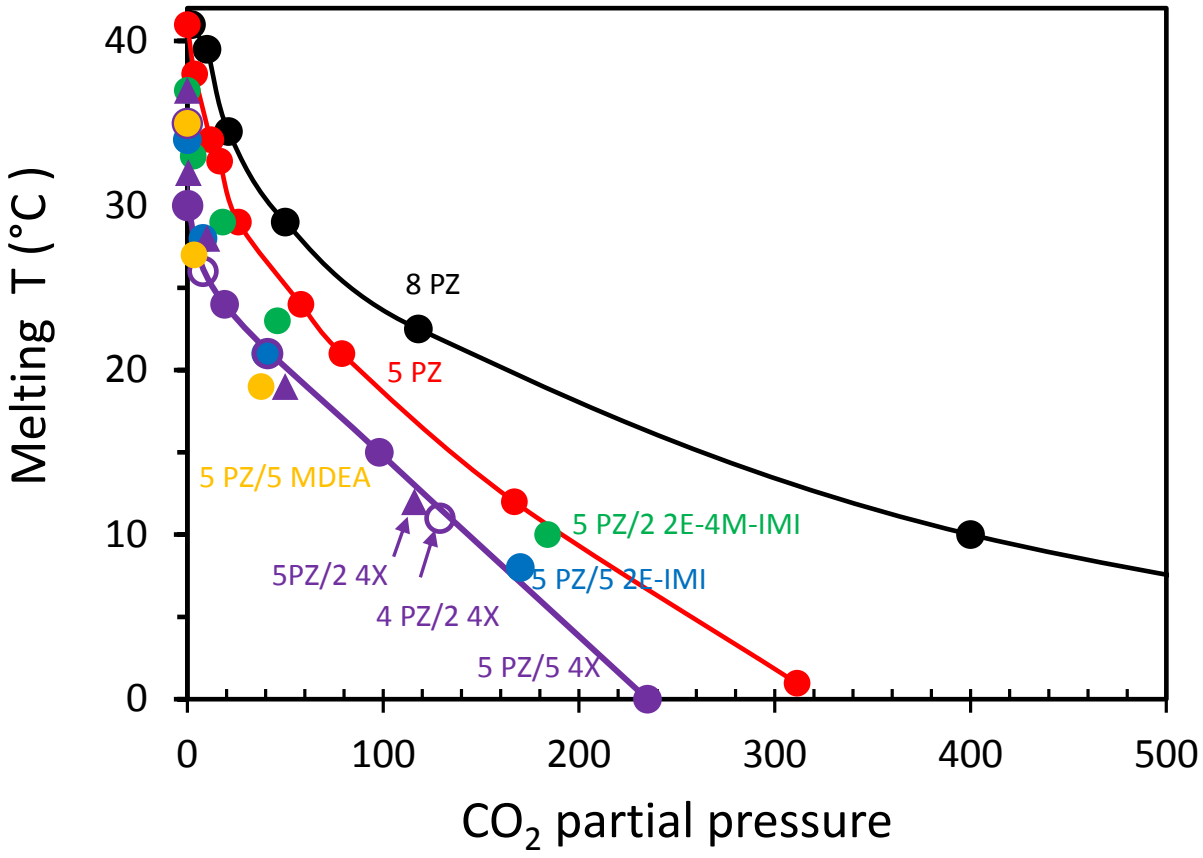

Figure 10a: Melting transition temperature for loaded PZ-based blends over a range of CO_2 partial pressure

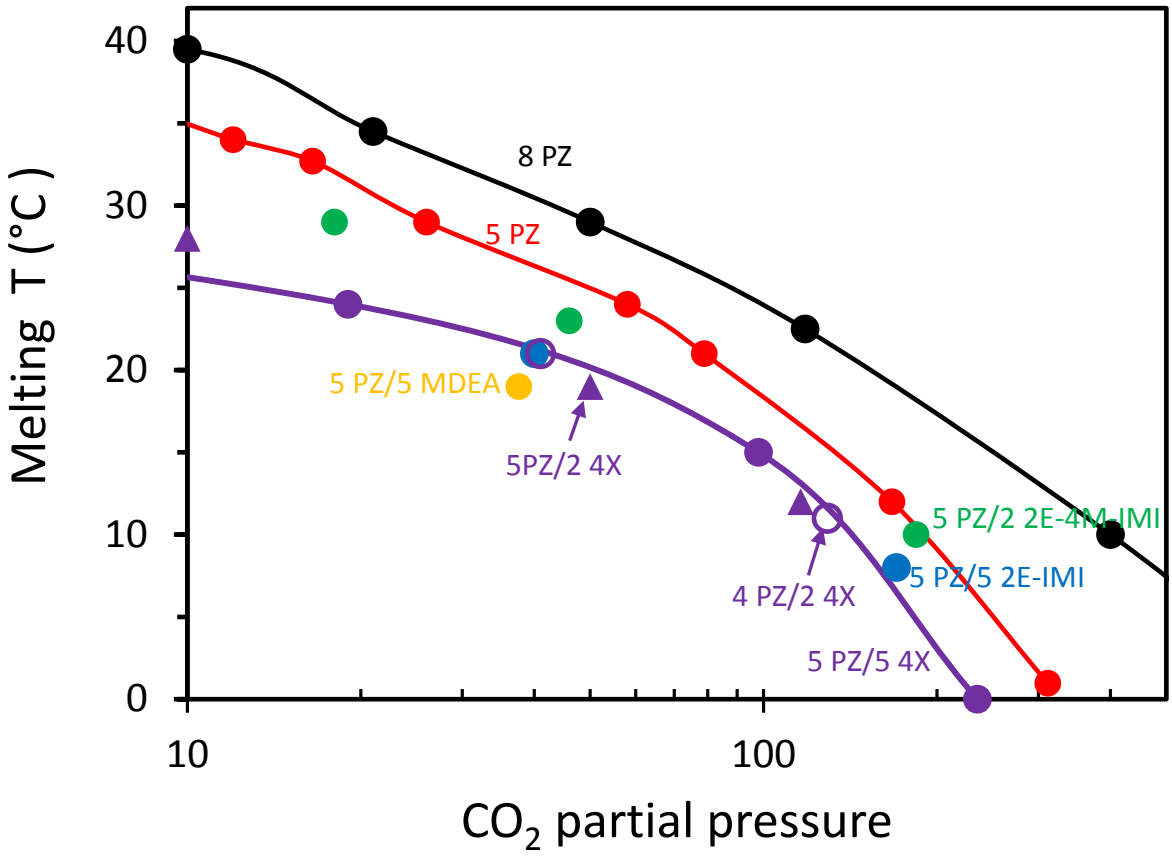

Figure 10b: Melting transition temperature for loaded PZ-based blends over a range of CO_2 partial pressure

Conclusions

1. IPAE, BMEA, 1,2-DM-IMI, and 2PDE have higher volatility than AMP.
2. IMI, 2E-IMI, and 4X have higher volatility than PZ but lower volatility than MEA.
3. Loaded 5 m PZ/5 m 2E-IMI has a similar amine partial pressure to 8 m PZ at 45 °C, but lower partial pressure at 65 °C.
4. Blending IMI decreases the CO_2 capacity of PZ. Blending 2M-IMI or 2E-IMI maintains the CO_2 capacity of PZ. Blending 4X increases the CO_2 capacity of PZ.
5. 5 m PZ/2.5 m 2E-IMI has almost the same CO_2 capacity as 5 m PZ/5 m 2E-IMI. However, 5 m PZ/5 m 4X has significantly higher CO_2 capacity than 5 m PZ/2 m 4X and 4 m PZ/2 m 4X.
6. Blending 5 m IMI or 5 m 2E-IMI with 5 m PZ maintains its high CO_2 absorption rate, while blending 5 m 4X with 5 m PZ decreases its CO_2 absorption rate by 30%, although the rate of the blend is still comparable to 8 m PZ, which is much higher than 7 m MEA.
7. Although 5 m PZ/2 m 2E-4M-IMI and 5 m PZ/2.5 m 2E-IMI have a lower absorption rate than 5 m PZ at low CO_2 partial pressure, their absorption rate at high CO_2 partial pressure is comparable to 5 m PZ. The CO_2 absorption rate of 5 m PZ/2 m 4X and 4 m PZ/2 m 4X is lower than 5 m PZ, but still higher than 8 m PZ.

8. Assuming that normalized capacity has the same effect as absorption rate on the overall CO_2 capture cost, 5 m PZ/5 m IMI, 5 m PZ/5 m 2E-IMI, 5 m PZ/2.5 m 2E-IMI, 5 m PZ/2 m 2E-4M-IMI, 5 m PZ/2 m 4X, and 4 m PZ/2 m 4X have similar CO_2 capture cost to 5 m PZ, but lower cost than 8 m PZ, 5 m PZ/5 m MDEA, or 5 m PZ/5 m 4X.
9. No precipitate was observed for the selected PZ-based blends at rich CO_2 loading. In loaded solution, 5 m PZ has 5–10 °C lower melting transition temperatures than 8 m PZ at the same CO_2 partial pressure. All the selected amines, except for 2E-4M-IMI, can lower the melting transition temperature of 5 m PZ by 3–7 °C, with more significant effect at low CO_2 partial pressure.
10. For unloaded 5 m PZ-based blends, different components have different abilities to solubilize PZ: glycerol > ethylene glycol > IMI > 2E-IMI > dimethyl sulfoxide > triethylenediamine = 2-methyl-piperazine.
11. 5 m PZ/2 m 4X, 4 m PZ/2 m 4X, 5 m PZ/5 m IMI, and 5 m PZ/2.5 m IMI are superior solvents for CO_2 capture from coal-fired flue gas, showing comparable CO_2 absorption performance, and solvent stability to 5 m PZ, but better solvent solubility.

Future Work

1. A thermodynamic model will be developed for PZ/4X in Aspen Plus®.
2. Thermal degradation of PZ/4X will be measured rigorously.
3. PZ/IMI and PZ/ethylene glycol will be evaluated next quarter.

References

Chen X. *Carbon dioxide thermodynamics, kinetics, and mass transfer in aqueous piperazine derivatives and other amines*. The University of Texas at Austin. Ph.D. Dissertation. 2011.

Freeman SA. *Thermal Degradation and Oxidation of Aqueous Piperazine for Carbon Dioxide Capture*. The University of Texas at Austin. Ph.D. Dissertation. 2011.

Li L, Voice AK, Li H, Namjoshi O, Nguyen T, Du Y, Rochelle GT. "Amine blends using concentrated piperazine." *Energy Proc.* 2013;37:353–369.

Shannon MS, Bara JE. "Properties of Alkylimidazoles as Solvents for CO_2Capture and Comparisons to Imidazolium-Based Ionic Liquids." *Ind. Eng. Chem. Res.* 2011;50:8665–8677.

Nguyen T. *Amine Volatility in CO_2 Capture*. The University of Texas at Austin. Ph.D. Dissertation. 2013.

Chapter 1: Introduction

The phenomenon of climate change is the main environmental issue facing our world today. The current world economy is mostly powered by energy stored in various types of fossil fuels. As fossil fuels are converted into usable energy, such as electricity, large amounts of CO_2 are generated as a byproduct and released into the atmosphere. The accumulation of the emitted CO_2 in the atmosphere is the cause of climate change. The current methods of extracting energy from fossil fuels (mostly combustion) must be adapted to minimize the impact of human activities on the environment. This need to reduce CO_2 emissions offers a potential market for new technologies and innovations.

The focus of this work is the amine scrubbing process, specifically in its application for CO_2 capture from coal-fired power plants. This chapter provides the relevant background for the application of this engineering research work. First, the reality of climate change and its main cause being the production of energy are discussed. A closer look at the energy and electric power sector in the U.S. demonstrates the significance of coal-fired power plants as a category for energy production and CO_2 emission. Next, the technology of carbon capture and sequestration (CCS) with amine scrubbing is discussed and proposed as the solution for CO_2 emission reduction from coal power plants. Last, the specific scope of this work, which examines the role of amine structure on the performance of the amine scrubbing process, will be presented.

1.1 BACKGROUND

1.1.1 Climate Change

Historically, the scientific community has demonstrated a clear consensus on the reality of climate change as the result of human activities (Oreskes 2004). The climate of the Earth is the result of the energy balance of the planet. The Earth receives energy from the sun in the form of solar radiation, which is at and near the wavelength of visible light. This energy is absorbed at the Earth surface and transformed into heat, which is reflected back into space at a much longer wavelength as far infrared thermal (IR) radiation. The atmosphere then acts as an insulation medium by selectively absorbing the long wavelength thermal radiation from the Earth before its release to space. The energy from the absorbed radiation is then partially re-emitted from the atmosphere back to the Earth surface. This regulatory role of the atmosphere is referred to as the greenhouse effect, and is responsible for maintaining the climate on Earth. Without the atmosphere, the temperature at the Earth surface would be much colder.

The components of the atmosphere which are responsible for the absorption of long wavelength radiation are referred to as greenhouse gases, which mainly include water vapor, carbon dioxide (CO_2), methane, and ozone. Significant change in the atmospheric concentration of CO_2 and other greenhouse gases will lead to a shift in the temperature on Earth and climate change (IPCC 1996).

Atmospheric CO_2 concentration has increased by approximately 38% in the last 160 years, from 280 ppm in the pre-1850 years (Etheridge 1998) to 385 ppm in 2008 (Keeling 2009).

Anthropological activities since the industrial era, mainly the combustion of fossil fuels for energy, are the causes for this drastic rise of CO_2 in the atmosphere.

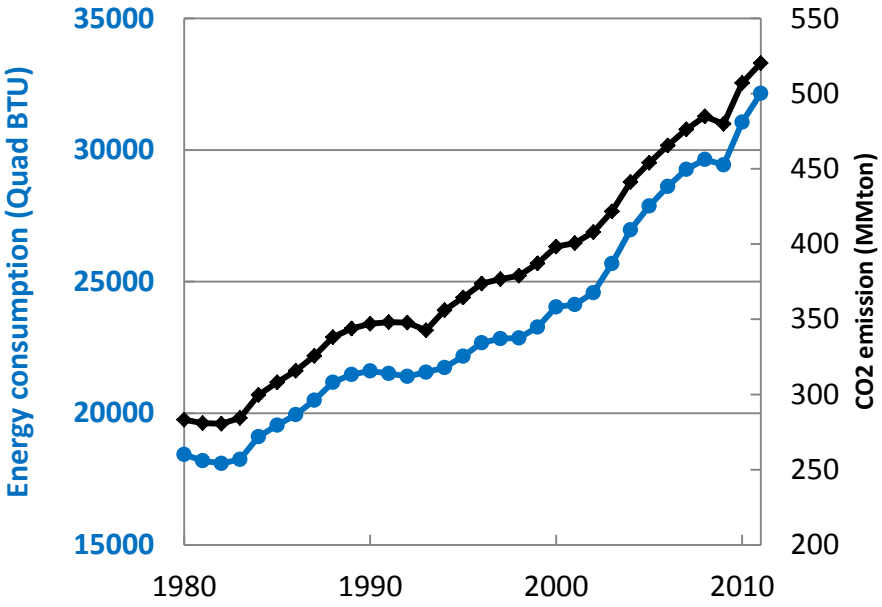

Figure 1.1: World energy consumption and CO_2 emission from 1980 to 2011 (EIA 2014a)

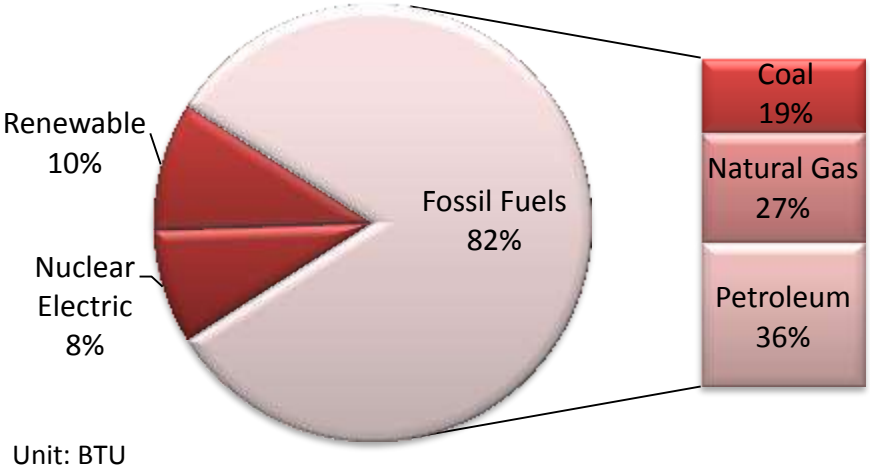

Figure 1.2: U.S. energy consumption in 2013 by fuel source (EIA 2014b)

The energy demand of the world has increased steadily for the past 30 years (Figure 1.1). While renewable energy technologies are currently growing at an exciting and rapid rate, the energy demand of the world is still largely supplied by fossil fuels. As shown in Figure 1.2, the energy consumed in the U.S. in 2013 was mostly met by fossil fuel sources (82% BTU). The increase in world energy consumption is directly related to a corresponding increase in CO_2

emission, as shown in Figure 1.1. As the world energy demand continues to grow, controlling the emission of CO_2 from the combustion of fossil fuels and meeting the associated economic costs are necessary in order to return the atmosphere to its natural composition and reduce climate change.

1.1.2 CO_2 Emission from Coal-Fired Power Plants

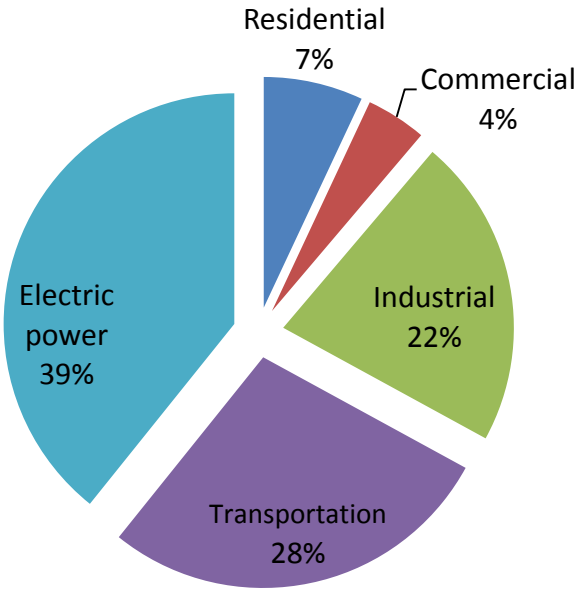

Figure 1.3: U.S. energy consumption from primary sources in 2013 by sector (EIA 2014b)

Currently, a major portion of the energy in the world is being used for the generation of electricity, which is then used to power other sectors of the economy. As Figure 1.3 shows, the electric power sector consumed nearly 40% of primary energy sources in 2013, leading both the transportation and industrial sector. At the same time, the electric power sector is the largest contributor of CO_2 emission. In the U.S., the electric power sector was responsible for close to 40% of the total CO_2 emitted in 2013 (Figure 1.4). Not only is the electricity sector an important target for the reduction of CO_2 emission, the industry has one characteristic which makes it convenient for the application of necessary technologies. Electric power plants are mostly large point sources of CO_2 emissions, generating large amounts of CO_2 continuously at set locations. Considering the economies of scale, which suggests the cost of industrial products is lower for larger process units, as the equipment cost of the plant is shared among a larger total number of products. Thus, the application of CO_2 emission control technologies to power plants is expected to be more cost effective compared to small moving sources (such as the transportation sector).

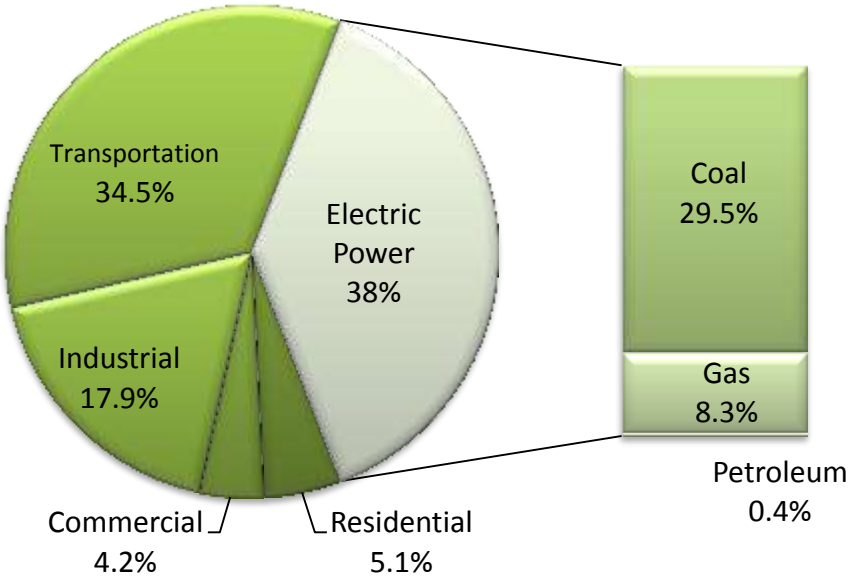

Figure 1.4: U.S. CO_2 emission (from primary fuel consumption) in 2013 by sector (EIA 2014b)

The generation of electricity in the world today is mostly through the combustion of fossil fuels. As Figure 1.5 shows, in the U.S., coal is the largest fuel source for the electric sector (39% kwhr), followed by natural gas (28%), leading both the renewable and nuclear fuel sources. While coal is the largest fuel source for the electric sector, it also produces more CO_2 than natural gas per unit of electricity generated (EIA). As a result, coal fired power plants are currently responsible for nearly 80 % of the CO_2 emitted by the electric sector in the U.S. (Figure 1.4). Moreover, compared to natural gas power plants, coal fired power plants generate flue gas with higher CO_2 content (approximately 4 times that of natural gas combined cycle power plants). As the Sherwood plot (Figure 1.6) suggests, the cost of separation decreases linearly with increase in the concentration of the material in the source stream. The application of CO_2 separation technologies would be cheaper for coal fired power plants compared to natural gas plants.

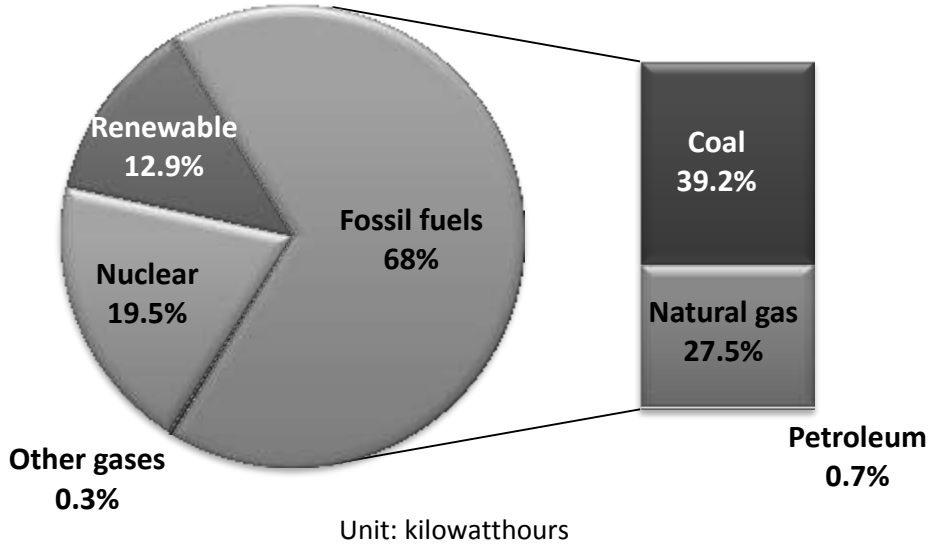

Figure 1.5: U.S. electricity generation in 2013 by fuel source (EIA 2014b)

It is essential for potential CO_2 emission regulations to target coal fired power plants, as the emission from these plants is significant relative to other sectors. It is also likely that regulation strategies will first focus on coal power plants, as it is expected to be cheaper and easier to remove the CO_2 from these sources than others (such as cars or natural gas power plants). Therefore, the main application of this work is the conventional coal fired power plants. The typical conditions of such a plant in the U.S. are used as the basis for the majority of the technical analysis.

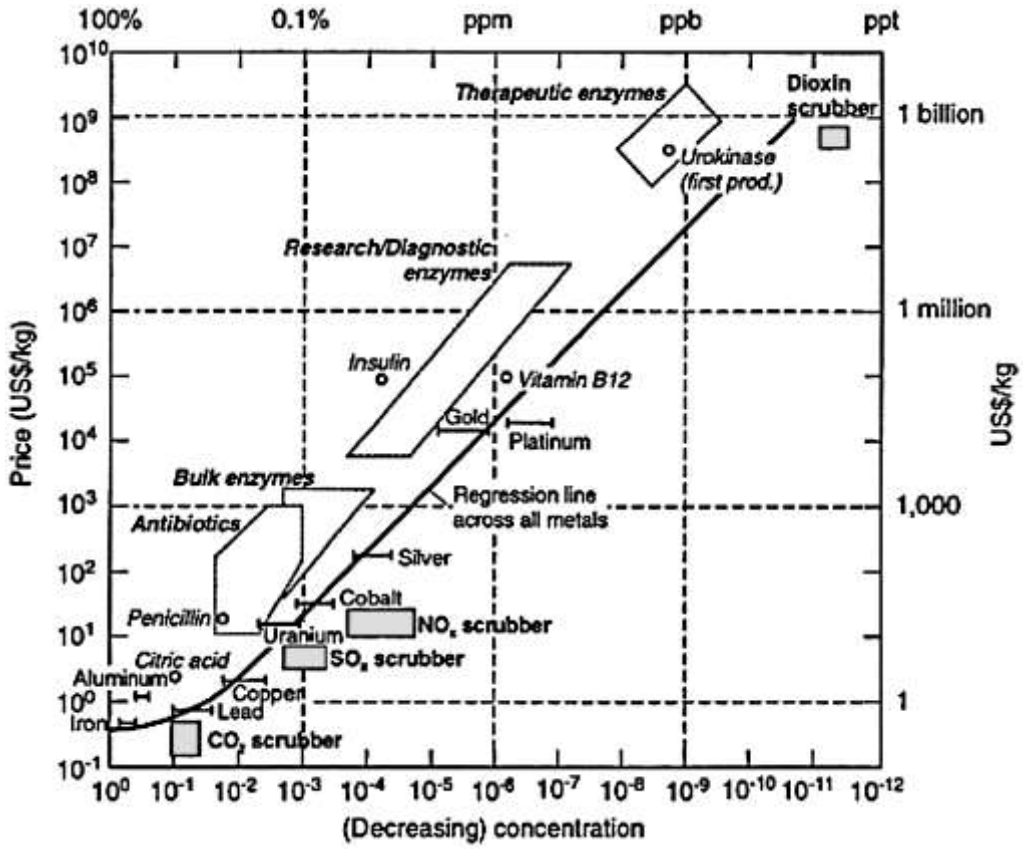

Figure 1.6: Sherwood plot of industrial separation processes cost dependence on concentration in the source stream (House et al. 2011)

1.1.3 Potential of CO_2 Regulation

With the reality of climate change confirmed by all scientific research on the topic, few action have been taken to address the issue and the world CO_2 emissions continue to rise (Figure 1.1). Without an effective policy either limiting or penalizing carbon emissions, there is no economic incentive for the power industry to reduce the production of CO_2 in the current world market.

The regulation of CO_2 emission for the purpose of mitigating climate change is challenging for two main reasons. First, while climate change is a global environmental issue, the emission of CO_2 is a matter of international economy as it is directly associated with the production of goods and energy. Each country contributes differently in their CO_2 emissions; at the same time the effect of climate change is likely to harm some countries more than others. It is difficult to form an agreement when each country has different degrees of, and sometimes conflicting, motivation and economic priorities with regard to climate change and emission control. To make matters worse, as the global trading of energy and goods increases, the economy of CO_2 becomes more complex. The countries producing the emissions are not usually the same as the countries consuming them, making assigning appropriate responsibilities even more difficult. The second challenge is the complexity of the solution itself. To achieve the

necessary CO_2 emission reduction, the policy solution is likely to involve all sectors of the world economy, as well as the deployment of many new technologies, and changing the way the world as a whole distributes and uses energy. Due to these challenges, effective regulation has yet to be implemented for the reduction of worldwide CO_2 emission.

History of International Climate Change Policies

The international discussion for a plan to mitigate climate change and reduce world CO_2 emission began over 30 years ago. The first official international collaboration was the formation of the Intergovernmental Panel on Climate Change (IPCC) in 1988. Formulated by the World Meteorological Organization (WMO) and the United Nations Environment Program (UNEP), the IPCC aimed to "prepare, based on available scientific information, assessments on all aspect of climate change and its impacts, with a view of formulating realistic response strategies" (IPCC 2014). With the Fifth Assessment Report (AR5) released recently, along with the previous reports and other activities, the IPCC provides comprehensive and publicly available scientific information on the issue of climate change. Even though the IPCC does not directly produce emission reduction policies, its reports and other work products laid the scientific foundation for the development of all future international policies and treaties.

Based on the results of IPCC, the United Nations Framework Convention on Climate Change (UNFCCC) was negotiated and signed in 1992. The objective of the UNFCCC treaty is to "stabilize greenhouse gas concentrations in the atmosphere at a level that would prevent dangerous anthropogenic interference with the climate system" (UN General Assembly 1994). Even though the UNFCCC has nearly universal membership, with participants including all United Nation member states, the European Union, and two other small countries, the treaty included no binding limits on greenhouse gases emissions for any individual member. Instead, the UNFCCC aimed to facilitate negotiations of subsequent emission binding treaties among its members with the convening of annual Conference of the Parties (COP) which began in 1995. The most significant outcome of the COPs is the signing of the Kyoto Protocol in 1997. The Kyoto Protocol established binding targets for a group of developed countries (Annex I) to collectively reduce CO_2 emission by 5% from 1990 emission levels during the first commitment period of 2008–2012. The Annex I group originally included the European Union and 42 other nations. Despite being a key member of the Annex I group to the Kyoto Protocol, the U.S. eventually refused to ratify the treaty under the Bush administration, as the treaty did not pass through the Senate. Prior to the targeted deadline of the first commitment period, Canada, Japan, and Russia also withdrew from the protocol. Even though the remaining Annex I countries ultimately met the adjusted collective emission reduction target, it can be argued the Kyoto Protocol achieved little in terms of global reduction of CO_2 emission (Helm 2008), mainly because of the failure of the United States and China to participate. Perhaps the most significant contribution of the Kyoto Protocol is the facilitation of an international discussion of climate policy, as well as the lessons learned through the experience (Böhringer 2003).

Post-Kyoto Climate Policies

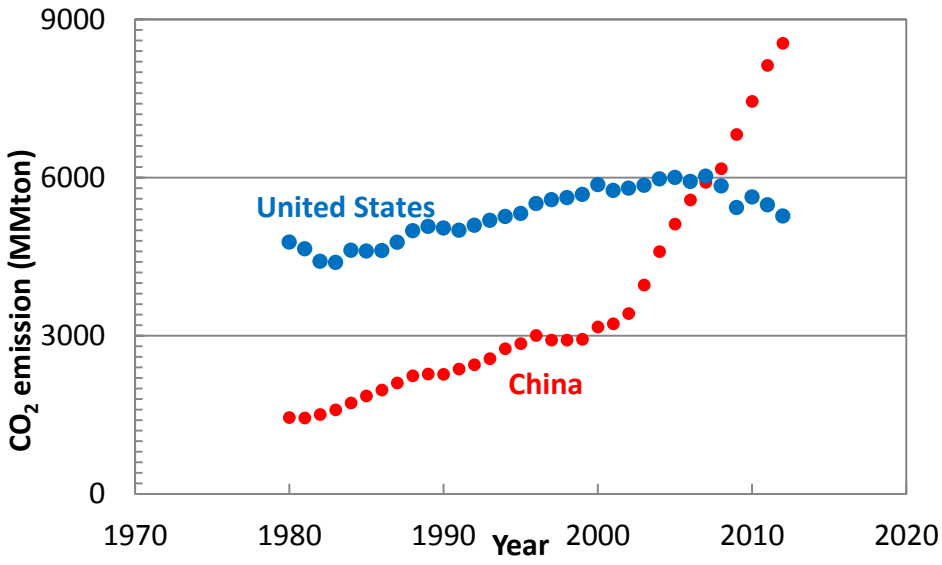

Figure 1.7: Total CO_2 emission by the U.S. and China from 1980 to 2013 (EIA 2014a)

Based on the experience of Kyoto, it is apparent that the involvement of U.S. and China are crucial to the effective regulation of global CO_2 emissions. As shown in Figure 1.7, the CO_2 emissions from China have increased rapidly since 2000; whereas the U.S. has historically produced large amounts of CO_2. Currently, U.S. and China are the largest energy consumers and CO_2 emitters in the world (Figure 1.8). Historically, both countries have held back from making international commitments with regards to the climate change. However, new promises have been made by the leaders of the two countries to reduce CO_2 emission. In June 2013, with his Climate Action Plan, President Obama re-affirmed the goal of 17 percent CO_2 emission reduction from 2015 level by 2020 (Executive Office of the President 2013). Specifically, the plan called for cutting carbon pollution from power plants, with clean coal technologies as part of the solution. Following this announcement, an unprecedented collaboration was formulated between the leaders of the U.S. and China. In November 2014, during the Asian Pacific Economic Cooperation summit, President Obama committed the U.S. to reduce 26 to 28 percent carbon by 2025 (relative to 2005). As part of the agreement, President Xi Jinping pledged for China to reach its carbon peak by 2030, with at least 20 percent of the energy produced to come from clean energy sources by the same time. However, the implementation of specific regulations to achieve these goals faces significant challenges, likely more so for the U.S. As the U.S. Congress is currently controlled by the Republican party which historically held anti-climate change views, and is expected to block any regulation for CO_2 emission (Landler 2014). Nonetheless, this agreement between U.S. and China provides significant motivation for the continuous research and development of technologies to achieve the goal (Buchele 2014).

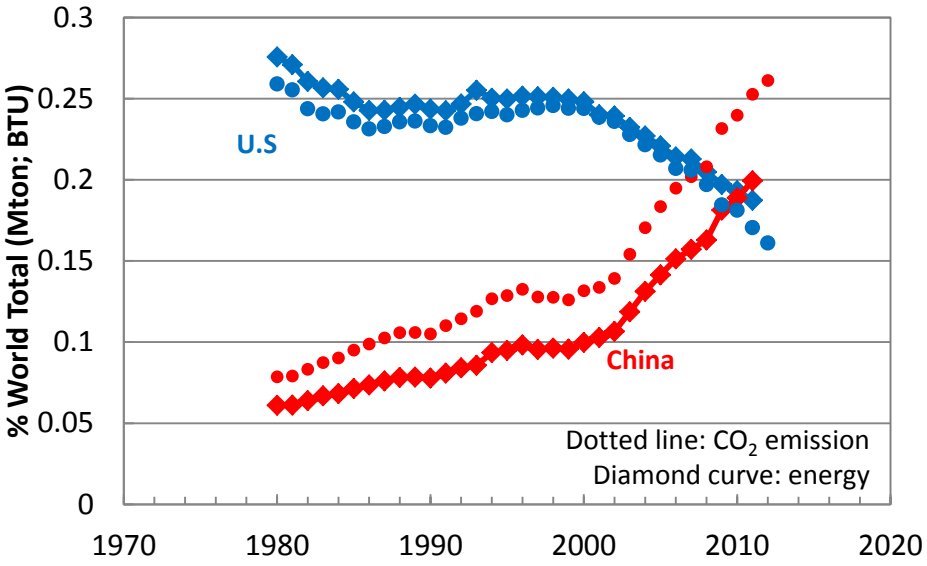

Figure 1.8: CO_2 emission and energy consumption in the U.S. and China as fraction of world total since 1980 (EIA 2014a).

1.2 Carbon Capture and Sequestration (CCS)

The technical solution to the reduction of CO_2 emission from power plants and other large point sources is carbon capture and sequestration (CCS), which involves first capturing the CO_2 from the emission source, followed by long term storage of the separated CO_2 at appropriate natural under-ground formations.

The process of CCS can be divided into three distinct steps: capture, transport, and storage. The first step, CO_2 capture, refers to the separation of CO_2 from other components of the fuel source (pre-combustion) or the flue gas (post-combustion), which typically include nitrogen, oxygen, and other particulates. As part of the capture step, the separated CO_2 is targeted to be produced at a high pressure (approximately 150 bar), which is necessary for the subsequent transport and storage steps. The transportation step involves the design and construction of pipelines from the emission source to the nearest source, as well as the flow assurance of pressurized (and supercritical) CO_2 that is being transported. The storage sites have mainly been targeted as under-ground geological formations that are appropriate for the long term trapping of CO_2. The storage step involves finding and testing of the storage site, the injection of pressurized CO_2 at the appropriate rate, and the long term monitoring of the area for leakage. Based on current estimates, the cost of transportation and storage is about $15 per metric ton of CO_2 (Dooley et al. 2008). The cost of capture varies depending on the technology used and the emission source. With coal fired power plants as the emission source, with a base case amine scrubbing capture technology, the cost of capture is currently about $50 per ton CO_2 (Rochelle 2009). Thus, CCS is dominated by the capture step, which contributes to at least two-thirds of the total process cost. Therefore, the capture step offers the greatest opportunity for potential improvement in process efficiency or cost reduction, which can ultimately affect the cost of the overall CCS process.

1.2.1 CO_2 Capture Technologies

Various types of separation technologies can be used for the capture of CO_2 in CCS. For coal fired power plants, the available capture technologies can be divided into pre-combustion and post-combustion technologies. Pre-combustion generally refers the separation of CO_2 from the power cycle prior to the combustion step. One promising example is the integrated gasification combined cycle (IGCC) process, which involves the gasification of coal and a chemical shift to produce H_2 and CO_2. After a high temperature separation step, the H_2 is then combusted in a gas turbine, and a pure stream of CO_2 is generated as byproduct. Also promising is the oxy-combustion process, which involves the combustion of coal with pure oxygen, generating a smaller flue gas stream with higher CO_2 content relative to conventional coal combustion using air. One important disadvantage of pre-combustion and oxy-combustion processes is that they require significant modification to the conventional power generation cycle, which will lead to high retrofitting cost and shut down time if applied to existing power plants. Alternatively, the pre-combustion technologies offer some potential as a low carbon option for future power generation plants, where retrofitting is a not an issue.

Existing power plants currently contribute to a major part of the electricity sector in the U.S. and the world. They are likely to continue to do so, as renewable energy technologies face capacity limiting challenges and are not expected to dominate the electricity market in the near future. Thus, the CO_2 emissions from the existing coal fired plants cannot be effectively eliminated through the deployment of renewables, instead these emissions requires cost-effective technologies that do not disrupt electric production. Post-combustion technologies are the most appropriate solution to existing power plants, as they separate CO_2 from the flue gas after the combustion and power generation stages of the process. Typical coal fired power plants generate flue gas with approximately 12 percent CO_2, and the balance mostly consists of N_2 with small amount of O_2 and trace amounts of other gases and particulates. Post-combustion CO_2 capture involves the separation of CO_2 from the rest of the flue gas and the subsequent compression of the separated CO_2 stream. Majority of current research efforts focuses on three types of separations technologies: absorption, adsorption, and membrane separation. Base on considerations of thermodynamic limitations and current cost of advanced membrane materials, it has been shown the absorption technology is the most efficient and cheapest option (Rochelle 2009). This work focuses on one absorption technology, aqueous amine scrubbing, for post-combustion capture.

1.2.2 Amine Scrubbing for CO_2 Capture

Currently, amine scrubbing is the choice post-combustion CO_2 capture technology for CCS. It is the most mature and technically ready for commercial deployment (Rochelle 2009). This chemical separation process (Figure 1.10) involves first directly contacting post-combustion flue gas with an aqueous solvent of amine and water, where CO_2 is separated from the gas into the liquid by chemically reacting with the amine molecules and mass transfer in to the liquid phase. The captured CO_2 is then released in a second step by heating the liquid solvent which reverses the CO_2 and amine reaction. The concentrated CO_2 gas is compressed and sent for sequestration, and the regenerated solvent is then recycled for continuous operation.

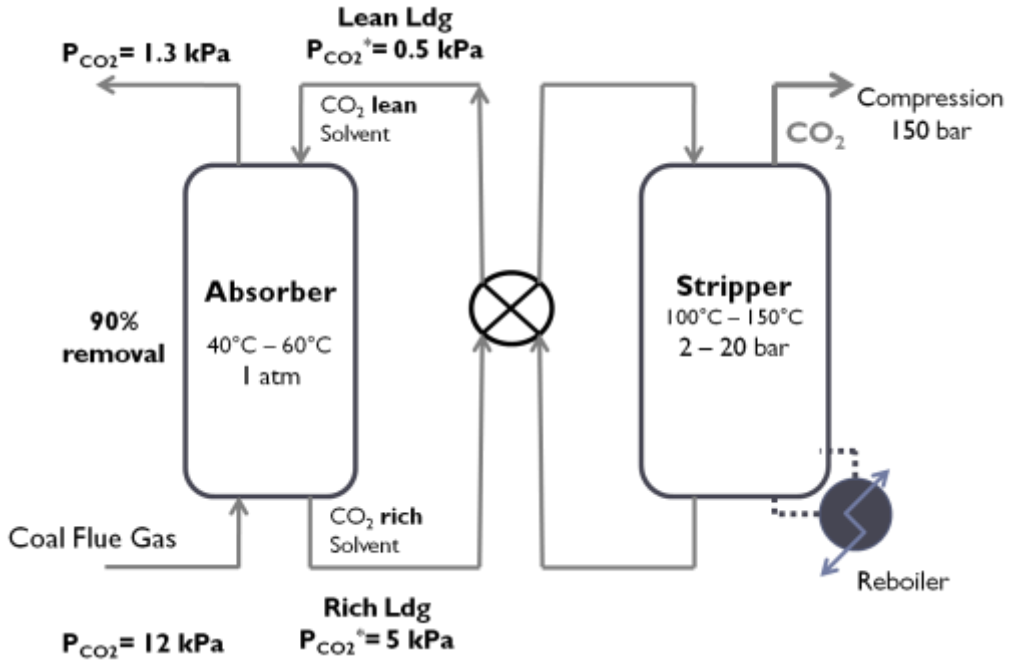

Figure 1.10: Simplified diagram of the amine scrubbing process

Critical process conditions

Without limitation of CO_2 concentration for power plant flue gas, in the analysis of CO_2 capture technologies a target of 90 percent CO_2 removal from the inlet concentration is largely assumed as a starting point for performance comparisons. In this work, the analysis of the performance of amine scrubbing process also uses 90 percent removal as the target for comparison.

Another main target of this process is the pressure of the CO_2 product stream: the separated CO_2 stream is set to be compressed to 150 bar. The compression of CO_2 is considered to be part of this amine scrubbing process and will be included in the overall cost analysis. The high pressure of the CO_2 product stream is required by the downstream CO_2 transport and sequestration steps. The value of 150 bars is assumed as a common basis for comparison. Including this compression step is crucial, as the cost of CO_2 compression will affect the optimum operating condition of the absorption/stripping process, and neglecting this effect can lead to misguided conclusions.

The temperature of the absorption column is set to be at 40 °C. The driving force for CO_2 mass transfer is higher at lower temperatures, and thus enhances the rate of separation. Considering typical temperatures for most populated areas in the world, 40 °C is set as the base case for analysis as it is the lowest achievable temperature without requiring refrigeration at an added cost. This temperature is used as the focus for all mass transfer experiments in this work to best represent real process conditions.

Current Technical Challenges

While amine scrubbing is currently the state of the art technology for post-combustion CO_2 capture, the cost of the application of this technology can still be further reduced. The energy cost of amine scrubbing is significant and consists of heat required to regenerate the solvent and compression work for the CO_2 product. The capital cost of the process is also significant. Currently, the base case capture process is expected to cost about 20–30% of total power plant output to remove 90% of CO_2 in the flue gas (Rochelle 2009). Degradation of the amine solvent, controlling and treatment of degradation products, and amine loss due to volatile emissions also add to the cost and affect performance. The improvement of amine scrubbing can be approached in three areas. First, finding new solvents with optimum chemical and physical properties at low costs can potentially reduce the energy requirement of the process as well as lowering the capital cost. Second, optimization of the process design and enhancing the heat integration and recovery can improve the efficiency of the process and reduce energy cost. Third, the potential environmental impact of the amine scrubbing process itself must be addressed. The degradation of the amine over time results in accumulation of potentially hazardous materials, as well as reduction in process performance. The potential emission of the amine and its degradation products through entrainment and aerosol formations in the absorber columns are relevant concerns about the safety of the process.

1.3 SOLVENT SCREENING FOR AMINE SCRUBBING

The search for new and better solvents has been a major part of the research and development efforts for amine scrubbing. Specifically, the mass transfer rate of CO_2 in the solvent is an important screening parameter, as it directly affects the absorber size and cost of the process. Also important is the CO_2 capacity of the solvent and other thermodynamic properties, as they affect the efficiency of the CO_2 stripping and compression which ultimately adds to the energy cost of the process.

Since the 1990s, numerous results of screening various amine structures for this process have been published. Many of the commercially available amine (and amine containing) structures, as well as many novel structures that are synthesized on a bench scale, have been tested. However, the screening measurements varied greatly in quality and many of the studies were not designed to best represent process conditions. The abundance of previous screening work still leaves room for continuous testing of both new and tested amine solvents with improved experimental designs and analysis. Amine blends using two or more different amine structures have shown promising performances as solvents for CO_2 capture. Since the number of combinations of available amines is large, the investigation of these blended systems offers much opportunity for further research.

1.3.1 Literature review

There are eight journal articles on the systematic screening of amine solvents for absorption rates and CO_2 carrying capacity in the application of post-combustion CO_2 capture (Table 1.1). With the exception of Chen (2010), the screening works are limited for several reasons. First, absorption rates were often measured with no CO_2 loading in the solvents. Optimized process design always requires amines solvents in the absorber to have some level of CO_2 loading (usually significant enough to drastically change the ionic and physical properties of

the solvent). Thus, the relative performance of CO_2 free amine solvent cannot be used to represent real process performance. Also, the gas sparging apparatus typically used provides hydrodynamic conditions very different from those of structured packings, which further confound the reported results. Moreover, the hydrodynamics of gas sparging experiments are typically inconsistent and cannot be accurately quantified. While data from this type of experiment suggests an apparent rate of absorption specific to the experimental conditions, it cannot provide fundamental mass transfer properties of the solvent and cannot be used to accurately predict rates at process conditions.

Table 1.1: Summary of published solvent rate screening results

Author	**Amines**	**Conc**	**CO_2 loading**	**T (°C)**	**Apparatus**	**Data type**
Hook, 1997	MEA, AMP, 6 amino acids	2.5 M	n/a	22 /26 /120	Stirred reactor	Total CO_2 absorbed as function of time
Ma'mun el al., 2007	8 (AEEA, MEA based structures)	30 wt%	yes	40	Gas sparging	Rate of CO_2 absorption (mol/L/s)
Singh, Niederer, & Versteeg, 2007	14 (unbranched, primary: alkanolamine, akylamine, di-amine	0.1-2.5 M	not quantified	~30	Stirred absorption screening apparatus	Total CO_2 absorbed as function of time
Singh, Niederer, & Versteeg, 2009	33 (various functional groups, cyclic structures)	0.5-2.5M	not quantified	~30	Stirred screening apparatus	Total CO_2 absorbed as function of time
Puxty et al., 2009	76 amines	< 30 wt%	no	40	Isothermal gravimetric analysis. Gas sparging	Initial rate of CO_2 absorption (mol/L/s)
Aronu et al., 2009	MEA, 5 amines and their mixtures	approx 30 wt%	yes	40/80	Gas sparging	Rate of CO_2 absorption (mol/L/s)
Chowdhury et al., 2009	11 amines (7 novel)	30 wt%	estimated	40/70	Gas sparging	Absorption rate / total CO_2 at 50% of saturated CO_2 loading
Chen, 2011	14 amines and blends	4.8 – 12 m	0.05-0.6	40-100	Wetted wall column	Liquid film mass transfer coefficient (k_g')

Dubois & Thomas, 2012	6 amines	5-50 wt%	no	25	Cable-bundle scrubber	Fraction of CO_2 absorbed, k_{app}
Brœder & Svendsen, 2012	amines and blends using 7 structures	4 - 8 M	0 – (0.2-0.8)	40 / 80	Gas sparging	Rate of CO_2 absorption/desorption (mol/L)
Song et al., 2012	16 amino acids, blends w/ PZ	1 M	no	40 / 80	Gas sparging	Initial absorption/desorption rate (mol/L/s)

Table 1.2: Summary of published CO_2 capacity screening results

Author	**Amines**	**T (°C)**	**Method**	**Result type**
Hook, 1997	MEA, AMP, 6 amino acids	100	Heated regeneration apparatus	CO_2 loading after 1 hour of heating
Ma'mun el al., 2007	2.9 M AEEA	40 / 120	VLE apparatus for atmospheric and medium pressures	Vapor-liquid equilibrium, capacity (mol/L solution)
Singh, Niederer, & Versteeg, 2007, 2009	47 amines	~ 30	Stirred absorption screening apparatus	Total capacity: maximum loading after absorption for a long time
Puxty et al., 2009	76 amines	40	Isothermal gravimetric analysis. Gas sparging.	Total CO_2 uptake at apparent equilibrium
Aronu et al., 2009	MEA, 5 amines and their mixtures	40 / 80	Absorption / desorption by gas sparging	Difference between maximum rich and minimum lean loading
Chowdhury et al., 2009	IPAE, IBAE, IPDEA, 1M-2PPE	40 / 120	Glass autoclave equilibrium cell	Vapor-liquid equilibrium
Chen, 2011	14 amines and blends	40-100	Wetted wall column	Vapor-liquid equilibrium
Porcheron et al., 2011	30 amines	40	High throughput screening equilibrium apparatus	Vapor-liquid equilibrium
Dubois &	6 amines	boiling	Temperature	Regeneration efficiency:

Thomas, 2012		point	controlled glass stirred regeneration device	$\left(\frac{\alpha_{rich} - \alpha_{lean}}{\alpha_{rich}}\right)$
Brœder & Svendsen, 2012	amines and blends using 7 structures	40 / 80	Absorption / desorption by gas sparging	Difference between maximum rich and minimum lean loading
Song et al., 2012	16 amino acids, blends w/ PZ	40	Gas sparging	Approximate degree of CO_2 saturation at 40 °C

Table 1.3: Previous absorption rate measurements by at the University of Texas in Austin using a wetted wall column

Category	Amine	Con (m)	T (°C)	CO_2 loading (mol/mol alk)	Author / Year
Primary monoamine	Monoethanolamine (MEA)	7-13	40-100	0.2-0.5	Dugas, 2009
	Diglycolamine (DGA®)	3.2, 17.7	25-60	0-0.45	Al-juaied, 2004
		3.8, 11.5	25-110	0.02-0.55	Pacheco 1998
		10	40-100	0.3-0.5	Chen 2011
Primary (mono-hindered)	2-amino-2methyl-1 propanol (AMP)	4.8	40-100	0.15-0.56	Chen 2011
Primary (diamine)	Ethylenediamine (EDA)	12	40-100	0.36-0.49	Zhou 2010 Chen 2011
	1,2-Diaminopropane (MEDA)	8	40-100	0.36-0.42	Chen 2011
	(Methylamino)propylamine (MAPA)	8	40-100	0.25-0.52	Chen 2011
Secondary (mono, non-cyclic)	Diethanolamine (DEA)	4.8	40-120	0.02-0.46	Mshewa 1995
Secondary (mono, cyclic)	2-piperidineethanol (2-PE)	8	40-100	0.21-0.7	Chen 2011
Secondary (di-amine, cyclic) *Piperazine and*	Piperazine (PZ)	2-12	40-100	0.2-0.5	Dugas 2009
	1-Methylpiperazine (1MPZ)	8	40-100	0.1-0.26	Chen 2011
	2-Methylpiperazine (2MPZ)	8	40-100	0.1-0.37	Chen 2011

derivatives	1-(2-Aminoethyl)piperazine (AEP)	6	40-100	0.1-0.36	Chen 2011
	N-(2-hydroxyethyl)piperazine (HEP)	8	40-100	0.06-0.28	Chen 2011
	2,5-trans-dimethylpiperazine (2,5DMPZ)	2	40-100	0.15-0.26	Chen 2011
Tertiary	Methyldiethanolamine (MDEA)	4.5, 8.4	25-110	0.02-0.55	Pacheco 1998
		8.4	40-120	0.02-0.46	Mshewa 1995
PZ based blend	MDEA/PZ	7.6/0.2-0.6	25-70	0-0.31	Bishnoi 2000
		7/2, 5/5	40-100	0.09-0.27 0.18-0.37	Chen 2011
	K+/PZ	0-6.2 / 0.6-3.6	25-110	0-0.45	Cullinane 2005
	MEA/PZ	7/2	40-100	0.2-0.5	Dugas 2009
	2MPZ/PZ	8	40-100	0.16-0.39	Chen 2011
	1,4-DMPZ/1MPZ/PZ	0.5/3.75/3.75	40-100	0.21-0.32	Chen 2011
Amine blend	DGA®/Morpholine	14/3.5	25-60	0-0.45	Al-Juaied 2004
	MDEA/DGA®	0.8/10.3	25-110	0.02-0.55	Pacheco 1998
	MDEA/DEA	7.6/1, 4.2/4.8	40-120	0.02-0.46	Mshewa 1995

Rigorous evaluation of solvent performance is often time consuming and experimentally demanding. At the University of Texas in Austin, a bench scale wetted wall column has been used by many researchers to perform rigorous CO_2 mass transfer experiments for different amine solvents. To assess the energy performance of each solvent, these works historically performed rigorous vapor-liquid-equilibrium measurements. The experimental results are then analyzed to develop sophisticated models of the system. Due to the amount of experimental work involved and the rigorousness of the analysis, typically each study only focuses on one amine solvent. The published works on solvent performance using this rigorous method are summarized in Table 1.3. Recent studies, by Dugas (2009) and Chen (2011), greatly improved the efficiency of the experimental work required for the mass transfer and VLE measurements. As a result, Chen was able to collect comprehensive mass transfer and VLE data for more than 10 amine systems.

1.3.2 Solvent screening research needs

The main objective of solvent screening research is always the search for and testing of new systems. Currently, many of the common amines have been tested and their performance

evaluated. However, opportunities are still available for the investigation of amine blends, novel amine containing molecules (such as amino acids and ionic liquids), and synthesized or uncommon amines.

A great number of previous screening works do not properly represent real process conditions. The experiments are often performed at temperatures and concentrations far from the operating condition of the process. Also, a significant portion of literature screening work does not fully address the effect of CO_2 loading on the performance of the solvent, which is an important parameter. These gaps found in literature offer room for future studies. A majority of the data collected in the screening studies lack significantly in quality, leaving more opportunities to be improved. Adopting rigorous experimental methods and designs can greatly improve the quality of the mass transfer and VLE measurements necessary to achieve accurate conclusions in solvent screening.

1.4 Objective and Scope of This Work

The objective to this work is to contribute to the improvement of amine scrubbing for CO_2 capture by studying the effect of solvent choice on the performance of the process. Specifically, this work aims to demonstrate the effect of amine choice on the rate of CO_2 mass transfer in the absorption process and the corresponding capital cost in the process. Also, the effect of solvent choice on the thermodynamics of the system and the related energy cost of the process is studied. Using data collected in this work and in literature, as well as fundamental mass transfer principles, this work will evaluate the role of amine chemistry and structure on the rate of CO_2 mass transfer in this reactive absorption process.

1.4.1 Experimental screening of aqueous amines

More than 20 aqueous amine, amine blend, and amino acid solvents are tested in this work. Each solvent was chosen for at least one of the following reasons: 1) one or more expected attractive properties in the amine scrubbing process; 2) suggested in the literature to be an attractive molecule or structure group; 3) systematic study of the effect of amine structure on absorption performance. All of the amines and amino acids tested in this work are currently commercially available and financially affordable (less than $1000 for 1 kg).

For many of the solvents included, this work is the first effort to evaluate their potential for CO_2 capture. Some solvents have been tested as solvents for CO_2 capture previously, with available results found in literature. In these cases, this work provides a more rigorous measurement of CO_2 mass transfer and capacity, such that the direct contribution to process cost can be inferred from the data.

In the screening process, this work also aims to collect fundamental CO_2 mass transfer and vapor-liquid equilibrium (VLE) data at (and around) process conditions for each of the solvents. These data are expected to be used in advanced process modeling activities for evaluation of various process configurations.

The CO_2 mass transfer and VLE data reported in this work is collected using a pre-existing experimental apparatus, with a mature operating method developed by previous researchers (Dugas 2009; Chen 2011). Little modification was made to the apparatus and method. However, the operating range of the experimental apparatus was widened to include

20 °C as part of this work. The error and reproducibility of the pre-existing method was also quantified.

1.4.2 Absorption rate generalization

The absorption rates of CO_2 into the liquid solvent determine the size of the absorption column and ultimately the capital cost of the capture process. Different amine solvents have different absorption rates, which are determined by the chemical properties of the amine and the physical properties of the solvent. Rate measurements collected in this work and found in literature are used to outline the general relationship between amine chemistry and the CO_2 absorption rate of the solvent. This generalized correlation is used to predict absorption rates of new solvents.

1.4.3 Estimate process performance

The experimental data collected are used to perform simple estimations of process performance and optimization. A spreadsheet absorber model is constructed to estimate the packing requirement by directly applying the mass transfer data measured by the wetted wall column. The energy performance of the solvent are also estimated in the spreadsheet model using only VLE data of the CO_2/amine/H_2O system.

1.5 REFERENCES

Al-Juaied, M. A. (2004). *Carbon Dioxide Removal from Natural Gas by Membranes in the Presence of Heavy Hydrocarbons and by Aqueous Diglycolamine®/Morpholine*. Department of Chemical Engineering, University of Texas at Austin. PhD dissertation.

Aronu, U. E., Svendsen, H. F., Hoff, K. A., & Juliussen, O. (2009). Solvent selection for carbon dioxide absorption. *Energy Procedia*, *1*(1), 1051–1057.

Bishnoi, S. (2000). *"Carbon Dioxide Absorption and Solution Equilibrium in Piperazine Activated Methyldiethanolamine."* Department of Chemical Engineering, The University of Texas at Austin. Ph.D. Dissertation.

Böhringer, C. (2003). The Kyoto Protocol: A Review and perspectives. Oxford Review of Ecomonics Policy, Vol 19 (3), 451-466.

Brœder, P., & Svendsen, H. F. (2012). Capacity and Kinetics of Solvents for Post-Combustion CO2 Capture. *Energy Procedia*, *23*(1876), 45–54. Buchele, M., (2014 November 12) Climate Deal Puts Spotlight on Carbon Capture Technology. *NPR State Impact*. Retrieved from http://stateimpact.npr.org/texas/2014/11/12/climate-deal-puts-spotlight-on-carbon-capture-technology/

Chen, X. (2011). *Carbon Dioxide Thermodynamics , Kinetics , and Mass Transfer in Aqueous Piperazine Derivatives and Other Amines*. Department of Chemical Engineering, University of Texas at Austin. Ph.D. Dissertation.

Chowdhury, F. A., Okabe, H., Shimizu, S., Onoda, M., & Fujioka, Y. (2009). Development of novel tertiary amine absorbents for CO2 capture. *Energy Procedia*, *1*(1), 1241–1248.

Cullinane, J. T. (2005). *"Thernodynamics and Kinetics of Aqueous Piperazine with Potassium Carbonate for Carbon Dioxide Absorption."* Department of Chemical Engineering, The University of Texas at Austin. Ph.D. Dissertation.

Dooley, J. J., Dahowski, R. T., & Davidson, C. L. (2008). "On the Long-Term Average Cost of CO_2 Transport and Storage – Prepared for the U.S. Department of Energy under Contract DE-AC05-76RL01830." Pacific Northwest National Laboratory. Richland, Washington.

Dubois, L., & Thomas, D. (2012). Screening of Aqueous Amine-Based Solvents for Postcombustion CO2 Capture by Chemical Absorption. *Chemical Engineering & Technology*, *35*(3), 513–524.

Dugas, R. E. (2009). *Carbon Dioxide Absorption , Desorption , and Diffusion in Aqueous Piperazine and Monoethanolamine*. Department of Chemical Engineering, University of Texas at Austin. Ph.D. Dissertation.

EIA (2014a). "International Energy Statistics" Retrieved December 15, 2014, from http://www.eia.gov/countries/data.cfm

EIA (2014b). " Monthly Energy Review December 2014" U.S. Energy Information Administration.

Etheridge, D. M., Steel, L. P., et al. (1998). Historical CO_2 record from the Law Dome DE08, DE08-2, and DSS ice cores. Aspendale, Victoria, Australia, Division of Atmospheric Research, CSIRO.

Executive Office of the President (2013). The President's Climate Action Plan. The White House, Washington D.C.

Helm, D. (2008). Climate-change policy: why has so little been achieved? *Oxford Review of Economic Policy*, Vol 24 (2), 211-238.

Hook, R. J. (1997). An Investigation of Some Sterically Hindered Amines as Potential Carbon Dioxide Scrubbing Compounds. *Industrial & Engineering Chemistry Process Design and Development*, *36*, 1779–1790.

House, K. Z., Baclig, A. C., Ranjan, M., van Nierop, E. A., Wilcox, J., & Herzog, H. J. (2011). Economic and energetic analysis of capturing CO_2 from ambient air. *Proceedings of National Academy of Science of USA*, 108 (51) 20428-20433.

IPCC (1996). "Climate Change 1995: The Science of Climate change (Contribution of Work Group I to the Second Assessment Report of Intergovernmental Panel on Climate Change). J.T. Houghton, L.G. Meira Filho, B.A. Callander, N. Harris, A. Kattenberg and K. Maskell (eds.)." Cambridge University Press, UK: 59.

IPCC (2014). "Organization: History." Retrieved December 20, 2014, from http://www.ipcc.ch/organization/organization_history.shtml

Keeling, R. F., Piper, S. C., et al. (2009). Atmospheric CO2 values (ppmv) derived from in situ air samples collected at Mauna Loa, Hawaii, USA. La Jolla, California USA, Carbon Dioxide Research Group, Scripps Institution of Oceanography (SIO), University of California.

Landler, M. (2014, November 12). U.S. and China Reach Climate Accord After Months of Talks. New York Times, p.A1.

Ma'mun, S., Svendsen, H. F., Hoff, K. A., & Juliussen, O. (2007). Selection of new absorbents for carbon dioxide capture. *Energy Conversion and Management*, *48*(1), 251–258.

Mshewa, M. M. (1995). "Carbon Dioxide Desorption/Absorption with Aqueous Mixtures of Methyldiethanolamine and Diethanolamine at 40 to 120 °C." Department of Chemical Engineering, University of Texas at Austin. Ph.D. Dissertation.

Oreskes, N. (2004). Essay on Climate Change. Science (New York, N.Y.), 306 (December), 1686.

Pacheco, M. A. (1998). "Mass Transfer, Kinetics and Rate-Based Modeling of Reactive Absorption." Department of Chemical Engineering, University of Texas at Austin. Ph.D. Dissertation.

Porcheron, F., Gibert, A., Jacquin, M., Mougin, P., Faraj, A., Goulon, A., & Raynal, L. (2011). High throughput screening of amine thermodynamic properties applied to post-combustion CO2 capture process evaluation. *Energy Procedia*, *4*, 15–22.

Puxty, G., Rowland, R., Allport, A., Yang, Q., Bown, M., Burns, R., & Attalla, M. (2009). Carbon dioxide postcombustion capture: a novel screening study of the carbon dioxide absorption performance of 76 amines. *Environmental Science & Technology*, *43*(16), 6427–33. Singh, P., Niederer, J. P. M., & Versteeg, G. F. (2007). Structure and activity relationships for amine based CO2 absorbents—I. *International Journal of Greenhouse Gas Control*, *1*(1), 5–10.

Singh, P., Niederer, J. P. M., & Versteeg, G. F. (2009). Structure and activity relationships for amine-based CO2 absorbents-II. *Chemical Engineering Research and Design*, *87*(2), 135–144.

Song, H.-J., Park, S., Kim, H., Gaur, A., Park, J.-W., & Lee, S.-J. (2012). Carbon dioxide absorption characteristics of aqueous amino acid salt solutions. *International Journal of Greenhouse Gas Control*, *11*, 64–72.

UN General Assembly (1994), *United Nations Framework Convention on Climate Change: resolution / adopted by the General Assembly*. A/RES/48/189. Retrieved December 20, 2014, from http://unfccc.int/files/essential_background/background_publications_htmlpdf/application/pdf/conveng.pdf

CO_2 absorption rate measurement of 5 m Piperazine

Quarterly Report for October 1 – December 31, 2014

by Ye Yuan

Supported by the Texas Carbon Management Program

McKetta Department of Chemical Engineering

The University of Texas at Austin

January 31, 2015

Abstract

In order to compare the CO_2 absorption rate of 5 m piperazine (PZ) with that of previously measured solvents, the Wetted Wall Column (WWC) repeatability was checked. Absorption rates were measured at three different loadings across the lean and rich operating range at a temperature of 40 ºC. The absorption rates (k_g') measured, together with new findings from Du under the same conditions, confirmed the k_g' measured by Dugas in 2009 with less than 10% difference. The k_g' of 5 m PZ was approximately 30% higher than that of 8 m PZ.

Introduction

The CO_2 absorption rate of 5 m PZ was repeated by WWC and compared with previous measurement by Dugas (2009). Absorption rates at CO_2 loading of 0.2, 0.3, and 0.35 and 40 ºC were measured and compared. Experimental data under the same conditions as Du was included in the comparison. All the k_g' results of 5 m PZ were plotted against those of 8 m PZ.

Experimental Methods

The absorption rates were measured using the wetted wall column. The method is identical to that used by Chen (2011).

Materials

The solvent was prepared by mixing chemicals gravimetrically. Initial chemical species are piperazine (98%, Sigma-Aldrich) and DDI water (100%, Millipore). To achieve each loading condition, CO_2 was added to the solvent by bubbling gaseous CO_2 (99.99%, Matheson Tri-Gas) into the solvent.

Table 1: Chemical species in 5 m PZ

	molecular weight (g/mol)	Mass (g)	Wt %
Piperazine (PZ)	86.14	516.8	30.10%
Water	18.02	1200	69.90%

Table 2: Chemical species in 5 m PZ

Chemical	purity	Source
Piperazine (PZ)	98.00%	Sigma-Aldrich
DDI water	100.00%	Millipore, Direct-Q
Carbon Dioxide	99.99%	Matheson Tri-Gas

Experimental Safety

One possible safety hazard of the experiment is getting PZ into the eyes. Contact with eyes may cause severe irritation, and possible eye burns. In case of contact, immediately flush eyes with water for at least 15 min, and contact emergency ophthalmologist immediately. Nearby emergency ophthalmologists are available at the Eye Institute of Austin (tel: 512.454.8744 or 512.860.2992).

Results and Discussion

The liquid film mass transfer coefficient (k_g') of 5 m PZ was measured at three loadings across the lean and rich loading range at 40 ºC. The experimental data is attached in the appendix. The k_g' is plotted against CO_2 equilibrium partial pressure (P*) in Figure 1 and was compared with data from Du (2014) and Dugas (2009). There are small differences among the three lines; however, they were within the error range of the WWC. Given the precision of the apparatus, this showed the experiment results were consistent. The repeatability enabled screening of new solvents using the WWC and comparison of the absorption rate property of the new solvents with previous screened solvents.

In Figure 1, the k_g' of 5 m PZ is compared with that of 8 m PZ. The 8 m PZ data were from Rochelle (2012) and Dugas (2009). 5 m PZ showed about 30% higher k_g' than 8 m PZ. This could be because 5 m PZ has lower viscosity. High solvent viscosity will significantly reduce the diffusivity of all species in solution.

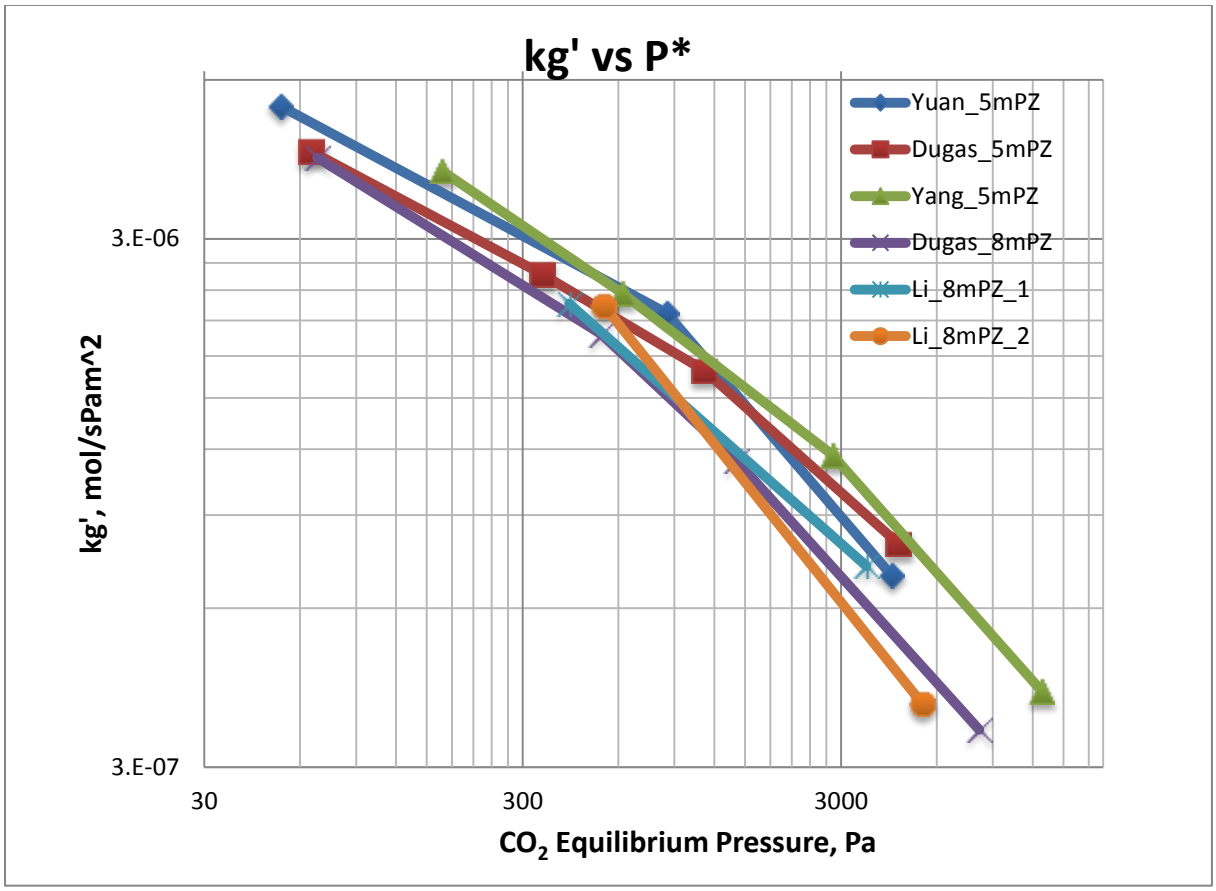

Figure 1: CO_2 absorption rate versus CO_2 equilibrium partial pressure

Conclusions

1. Additional rate measurement of 5 m PZ at 40 ºC in the WWC confirmed the earlier results of Dugas.
2. The k_g' of 5 m PZ is 30% greater than that of 8 m PZ.

Future Work

The liquid samples from each loading will be analyzed for CO_2 content and total alkalinity. Total Inorganic Carbon (TIC) will be used to measure the total moles of CO_2 per unit mass of liquid sample. Cation chromatography will be used to determine total alkalinity. New blends of PZ/tertiary or hindered amine will be measured in the WWC.

References

Dugas RE. *Carbon dioxide absorption, desorption, and diffusion in aqueous piperazine and monoethanolamine*. The University of Texas at Austin. Ph.D. Dissertation. 2009.

Chen X. *Carbon dioxide thermodynamics, kinetics, and mass transfer in aqueous piperazine derivatives and other amines*. The University of Texas at Austin. Ph.D. Dissertation. 2011.

Rochelle GT et al. "CO_2 Capture by Aqueous Absorption, First Quarterly Progress Report 2012." Luminant Carbon Management Program. The University of Texas at Austin. 2012.

Rochelle GT et al. "CO_2 Capture by Aqueous Absorption, Fourth Quarterly Progress Report 2012." Luminant Carbon Management Program. The University of Texas at Austin. 2013.

Appendix:

Table A: Detailed WWC data for 5 m PZ

PZ	CO_2 ldg	P^*_{CO2}	T	P	Gas_{dry}	Gas	$P_{CO2\ in\ dry}$	$P_{CO2\ in\ wet}$	$P_{CO2\ out\ dry}$	$P_{CO2\ out\ wet}$	CO_2 flux	K_G	kg	K_G/kg	kg'
m	mol/mol alk	Pa	C	psig	std l/min	std l/min	Pa	Pa	Pa	Pa	mol/s m^2	mol/s*Pa*m^2	mol/s* Pa*m^2		mol/s*Pa*m^2
5	~0.2	52	40	40	5.00	5.10	0	0	28.3	27.7	-7.24E-05	1.99E-06	2.87E-06	0.65	5.35E-06
							28.3	27.7	40.3	39.6	-3.09E-05	1.74E-06			
							89.7	88	70.9	69.5	4.83E-05	1.88E-06			
							189	185	120	117	1.77E-04	1.86E-06			
												1.87E-06			
5	~0.3	875	40	40	5.00	5.10	0	0	322	316	-8.25E-04	1.17E-06	2.87E-06	0.43	2.17E-06
							460	451	618	606	-4.05E-04	1.19E-06			
							932	914	915	898	4.25E-05	1.42E-06			
							1350	1320	1180	1160	4.18E-04	1.17E-06			
												1.24E-06			
5	~0.35	4320	40	40	5.00	5.10	0	0	841	824	-2.15E-03	5.53E-07	2.87E-06	0.19	6.92E-07
							3390	3320	3590	3520	-5.12E-04	5.69E-07			
							10300	10100	9180	9000	2.90E-03	5.55E-07			
							13300	13000	11600	11400	4.34E-03	5.53E-07			
												5.58E-07			

Absorber Intercooling Evaluation

Quarterly Report for October 1 – December 31, 2014

by Darshan Sachde

Supported by the Texas Carbon Management Program

McKetta Department of Chemical Engineering

The University of Texas at Austin

January 31, 2015

Abstract

In previous work, a shortcut method using an energy balance around the absorber was developed to predict the lean loading for each flue gas application where a temperature-related mass transfer pinch becomes limiting and intercooling is necessary to achieve maximum solvent capacity. The method only requires the use of a thermodynamic model for flash calculations and eliminates the need for the rigorous rate-based modeling to identify conditions for maximum intercooling benefit. The method was updated significantly to improve prediction accuracy by accounting explicitly for the solvent contributions to the energy balance (i.e., ability of the solvent to carry or "trap" heat in the column). The updated method provides estimates of the gas and solvent outlet temperatures, total heat capacity of each phase, maximum temperature in the column, and the transition lean loading. The new approach successfully predicted outlet temperatures and total heat capacity for all three applications. The maximum temperature and transition lean loading estimates were improved significantly over the previous method for coal and steel applications (within ~2% of actual values). The accuracy of the predictions for the NGCC application were not significantly improved, however. The energy balance for the NGCC application was particularly sensitive to assumptions made to eliminate the rate-based portion of the model (CO_2 removed at the bulge). A correction to represent the appropriate CO_2 removal at the bulge yielded a much better estimate of maximum temperature and lean loading (within 1% of actual values). Future work will focus on providing a simplified method of addressing the removal at the bulge to ensure the shortcut approach is robust for all applications.

Introduction

Previous work used the minimum solvent rate (or maximum rich loading) to evaluate potential benefits of intercooling for a wide range of lean loading for three CO_2 flue gas feed concentrations representative of potential capture applications (NGCC, coal-fired boiler, steel blast furnace). The analysis isolated conditions where intercooling could provide capacity (energy performance) benefits. In addition, a shortcut method was developed to estimate the operating condition (lean loading) where a capacity-limiting, temperature-related mass transfer pinch forms. The development of the simplified method allows a quick assessment of when intercooling is required for a given flue gas application and preferred lean loading operating condition. This method should eliminate the requirement of a rigorous rate-based model and the extensive number of cases required in the previous L_{MIN} analysis. However, the previous method over-estimated the transition loading by as much as 14%, somewhat limiting the general

applicability of the method and highlighting the potential for error in simplification used to develop the method. A new method was developed which incorporates a full-column energy balance and accounts for the contribution of the solvent carrying (trapping) heat in the column. This modification is consistent with the actual condition at pinch formation, where the heat carrying capacity is not dominated by a single phase.

Shortcut Method for Evaluating Solvent Capacity Benefits of Intercooling

In previous work, the minimum solvent flow rate (L_{MIN}) was used to assess potential benefits of intercooling configurations (Rochelle et al., 2014a). L_{MIN} for any absorption process can be defined as the solvent rate required to achieve a specific solute removal (or specific gas inlet and outlet compositions) for a given inlet solvent composition (loading) with infinite mass transfer area available. L_{MIN} also corresponds to the maximum rich loading (maximum solvent capacity) achievable and serves as a proxy for the best energy performance that can be achieved with the design and operating conditions of a given absorber

For each operating condition, an isothermal absorber represents the best possible performance (lowest L_{MIN}) and an adiabatic (no intercooling) absorber represents the worst case performance (highest L_{MIN}). Intercooled absorbers will fall between these limiting cases. The ratio of the adiabatic L_{MIN} to the isothermal L_{MIN} at each condition can serve as a screening tool for the conditions where intercooling will be beneficial for energy performance. High values of the preceding ratio indicate large potential benefits of intercooling. A ratio equal to (or approaching) unity indicates that the benefits of intercooling are negligible or non-existent. Figure 1 summarizes the L_{MIN} results for the coal-fired boiler case.

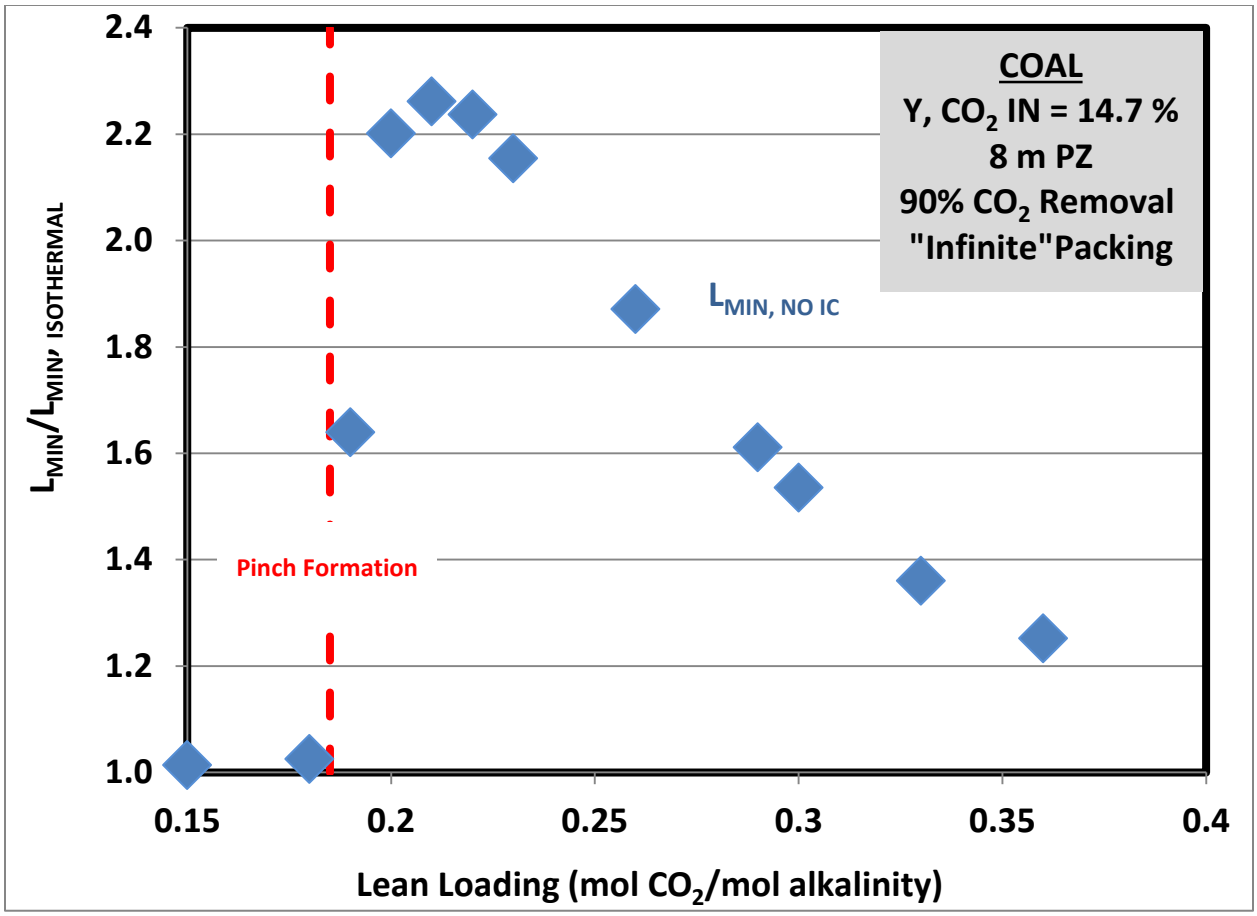

Figure 1: Ratio of the minimum solvent rate ("infinite" packing) for an adiabatic absorber (no intercooling) to an isothermal absorber (40 °C) for 90% CO_2 capture from a coal-fired boiler (13.5% CO_2) using 8 m PZ. The lean loading for the transition to a temperature-related pinch (- - -) is identified.

The figure also identifies the lean loading where a temperature-related pinch forms (~ 0.18 mol CO_2/mol alkalinity). The formation of the pinch was described in detail in previous work (Rochelle et al., 2014b) and is the focus of the modified shortcut method. The formation of a temperature-related pinch marks the onset of solvent capacity penalties if intercooling is not implemented in an absorber design. Therefore, if a loading in this range can be approximated for each flue gas application, a decision regarding intercooling implementation can be made quickly without performing the full analysis used to generate Figure 1.

The goal of the shortcut method is to estimate a lean loading to represent the transition region represented in Figure 1. The method requires a relationship between the lean loading and the conditions at the mass transfer pinch (temperature, loading, and gas composition at the pinch). Several observations during the L_{MIN} analysis allow assumptions to develop the relationship between the lean loading and pinch conditions.

First, the temperature-related mass transfer pinch, which signifies the transition in Figure 1, occurs at the maximum temperature in the column. Therefore, the first step in developing a shortcut method requires estimation of the maximum temperature. Figure 2 provides

information regarding inlet, outlet, and maximum temperatures in the column as a function of lean loading alongside the trend in the L_{MIN} ratio.

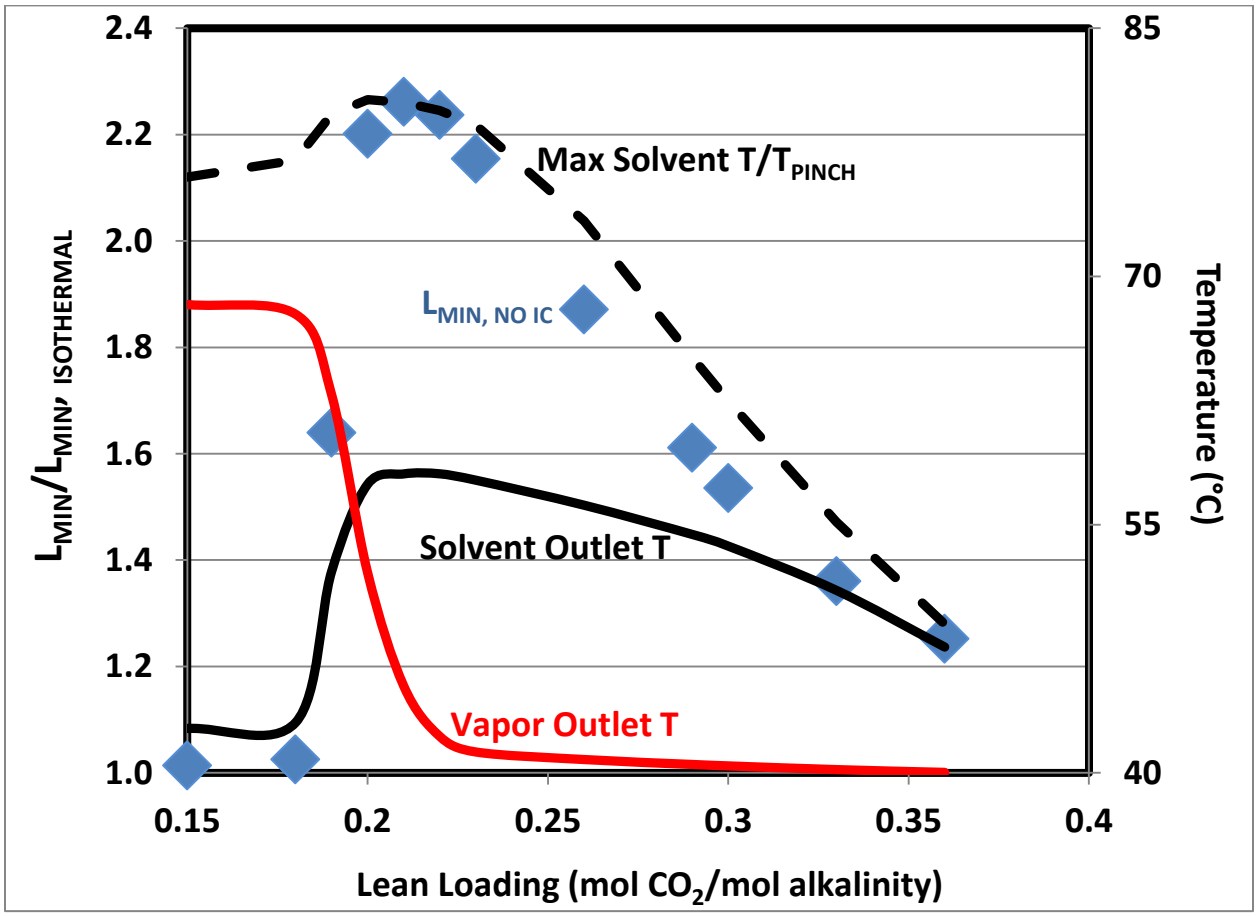

Figure 2: Ratio of the minimum solvent rate ("infinite" packing) for an adiabatic absorber (no intercooling) to an isothermal absorber (40 °C) for 90% CO_2 capture from a coal-fired boiler (13.5% CO_2) using 8 m PZ. Vapor outlet (solid red), solvent outlet (solid black), and maximum column temperature (dashed black) are shown to explain trends in the L_{MIN} ratio.

The temperature plot reveals that prior to the formation of a lean end temperature-related pinch (< 0.19 mol CO_2/mol alkalinity), the vapor temperature leaving the column is significantly higher than the solvent temperature leaving the column. In other words, the gas is carrying a majority of the heat generated by CO_2 absorption out of the top of the column. This is supported by the observation that the total gas heat capacity (including capacity to carry water) is much higher than the solvent heat capacity in this lean region (see Figure 3). As the lean end pinch forms, the solvent rate is increased significantly to overcome the pinch and achieve 90% CO_2 removal. This is reflected in the crossover of the solvent outlet and vapor outlet temperatures. This crossover also reflects a transition of the dominant heat carrying phase. Figure 3 presents the total heat capacity (includes mass flow rate) of each phase as a function of loading through this transition.

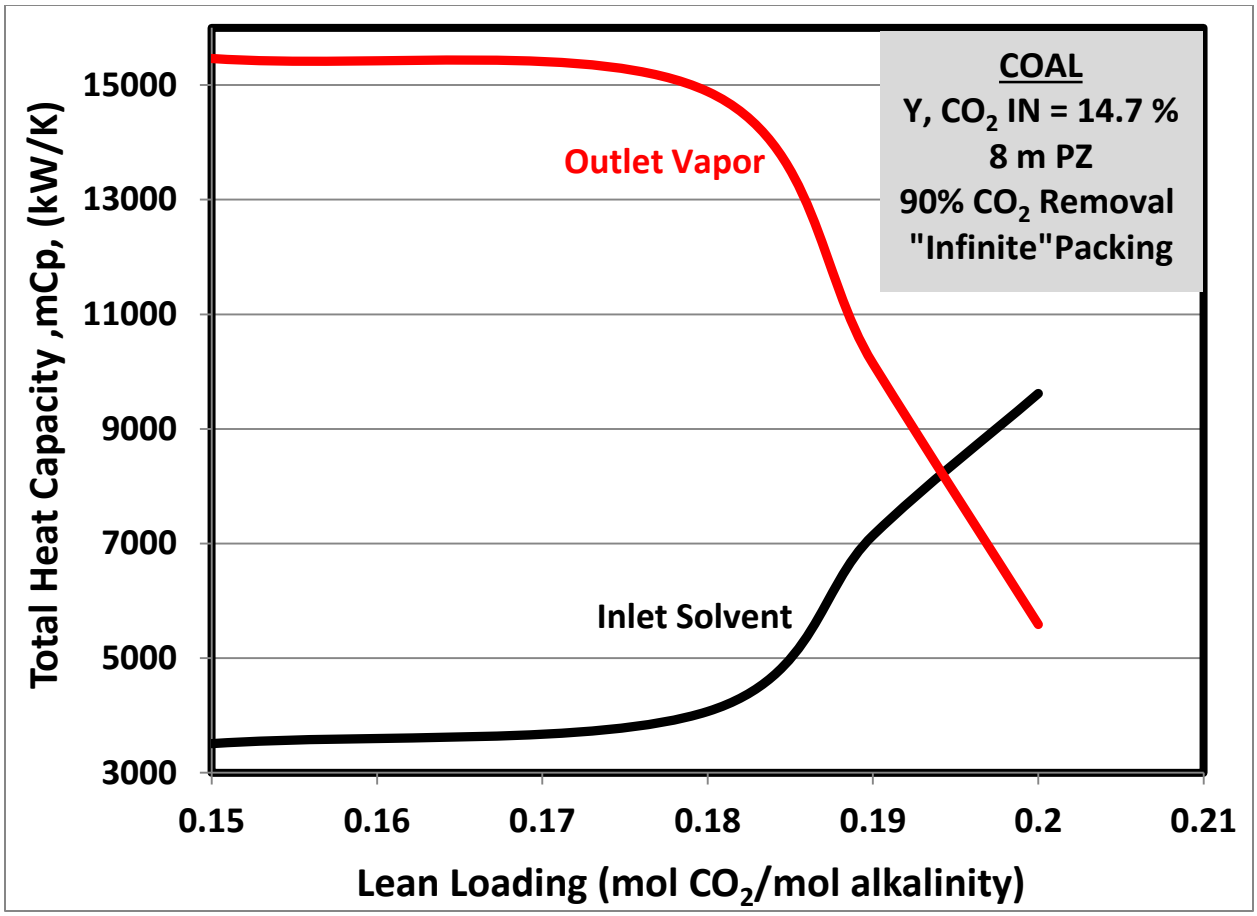

Figure 3: Total Heat Capacity (mass flow rate * specific heat capacity) of the Outlet Vapor and the Inlet Solvent for an adiabatic absorber (no intercooling) operating at the minimum solvent rate (L_{MIN}) for a given lean loading to achieve 90% CO_2 capture from a coal-fired boiler (13.5% CO_2) using 8 m PZ. The vapor heat capacity includes saturation of the gas to water to account for the ability of the gas to carry heat in the form of water vapor (latent heat contribution). (The crossover in total capacity (~ 0.195 mol CO_2/mol alkalinity) coincides with the formation of a temperature-related pinch.

As seen in Figure 3, the total heat capacity of the vapor and solvent are identical at approximately the same loading where the temperature-related pinch forms and the outlet temperatures of each phase are equal (Figure 2, ~ 0.19 mol CO_2/mol alkalinity). The total heat capacity of the vapor includes saturation of the vapor to water at the outlet temperature. This accounts for the ability of the gas to carry heat as water vapor (latent heat) in addition to the sensible heat contribution. Beyond this transition, the solvent carries an increasingly large portion of the heat and eventually begins to wash the heat out of the column and moderate the temperature effect.

In the previous shortcut method, a simplifying assumption was made that the gas carries all of the heat generated by CO_2 when operating near the lean loading where the temperature-related pinch forms (Rochelle et al., 2014c). This leads to the conclusion that the solvent leaves the column at the same temperature it enters (carries no heat from absorption). The solvent phase

can be eliminated from the energy balance and the maximum temperature can be estimated with vapor phase calculations.

However, as the preceding analysis depicts, this assumption does not reflect the conditions when the temperature-related pinch forms and resulted in the prediction error in the previous analysis (Rochelle et al., 2014c). A more rigorous assumption (total solvent and vapor heat capacities and outlet temperatures are equal) is applied in the updated approach. The heat carried by the solvent is now included in the energy balance and two steps are required to estimate the maximum temperature that occurs at the pinch:

1) Use a total column energy balance to find the vapor and solvent outlet temperatures (identical at the pinch). The solvent contribution to the energy balance can then be explicitly included in the calculation of a maximum temperature.
2) Use a partial energy balance around the pinch/temperature bulge in the column by defining a system from the temperature pinch down the column to the solvent outlet/vapor inlet. The maximum temperature or pinch conditions are represented by the top of the column in this system (solvent inlet/vapor outlet = maximum temperature). Using the solvent outlet condition from step 1, the maximum temperature at the bulge can be estimated after additional simplifying assumptions.

These two steps are described in detail in the following sections.

Step 1: Total Column Energy Balance: Estimate Outlet Temperatures

An energy balance (Equation 1) around an adiabatic absorber was used as the starting point to estimate the outlet temperatures when operating with a temperature-related pinch.

$$\begin{aligned} &N_{Gas,OUT}\widetilde{C}_{P,GAS,OUT}\left(T_{GAS,OUT}-T_{REF}\right)-N_{Gas,IN}\widetilde{C}_{P,GAS,IN}\left(T_{GAS,IN}-T_{REF}\right)\\ &\quad+\Delta N_{H2O,GAS}\Delta H_{VAP,T_{REF}}+\Delta N_{CO2,GAS}\Delta H_{ABS,T_{REF}}\\ &\quad=N_{Solvent,IN}\widetilde{C}_{P,Solvent,IN}\left(T_{Solvent,IN}-T_{REF}\right)\\ &\quad-N_{Solvent,OUT}\widetilde{C}_{P,Solvent,OUT}\left(T_{Solvent,OUT}-T_{REF}\right) \end{aligned} \tag{1}$$

where:

N = Molar flow rate of given phase (gas or solvent) (kmol/s);
C_P = Molar heat capacity of given phase (kJ/kmol-K);
T = Temperature of given phase (gas or solvent) (K);
T_{REF} = Reference temperature to allow integration sensible heat (K);
ΔH_{VAP} = Heat of vaporization of water at T_{REF} (kJ/kmol);
ΔH_{ABS} = Average heat of absorption of CO_2 at T_{REF} (kJ/kmol).

Several steps can be taken to simplify the energy balance based on the information in Figures 2 and 3:

1) Assign a reference temperature that is equal to the inlet temperatures of the gas and solvent ($T_{REFERENCE} = T_{SOLVENT,\,IN} = T_{GAS,\,IN}$ = 40 °C). This eliminates the inlet enthalpy contributions from the energy balance in Equation 1.
2) The heat of vaporization term for water can be merged with the heat capacity of the outlet gas to create a total heat carrying capacity of the gas (accounts for latent and sensible heat). This assumption is equivalent to calculating the heat capacity of the gas if saturated to water vapor at the outlet temperature and is consistent with the total heat capacity presented for the vapor in Figure 3.

3) Assume that the solvent and vapor outlet temperatures and total heat capacities are equivalent when the temperature-related pinch forms ($T_{SOLVENT,\ OUT} = T_{GAS,\ OUT} = T_{OUT}$; $N_{GAS\ OUT}\ C_{P,GAS\ OUT} = N_{SOLVENT\ OUT}\ C_{P,SOLVENT\ OUT}$). This assumption is supported by the data presented in Figures 2 and 3 indicating the temperature and total heat capacity crossover at temperature-induced pinch formation.

Equation 2 provides the simplified energy balance that results from applying the preceding assumptions and re-arranging terms.

$$(\boldsymbol{T_{OUT}} - \boldsymbol{T_{REF}}) = \frac{\Delta \boldsymbol{N_{CO2,GAS}} \Delta \boldsymbol{H_{ABS,T_{REF}}}}{\boldsymbol{2N\widetilde{C}_{P,OUT}}} \tag{2}$$

The CO_2 removed is 90% of the entering CO_2 when considering the full column energy balance. The unknowns (highlighted in red) are the outlet temperature and the total heat capacity of the outlet streams (reflecting the assumption that the outlet conditions for the vapor and solvent are identical). The heat capacity term is a function of the outlet temperature and can be estimated by calculating the total heat capacity via an adiabatic flash calculation for the vapor leaving the column (90% CO_2 removed, N_2/O_2 same as inlet, saturated to H_2O at T_{OUT}). The vapor phase is convenient for this calculation since the outlet composition is fixed by the specifications of the design. Since the outlet temperature is the only unknown, and it appears on both sides of Equation 2, an iterative calculation is performed until a single T_{OUT} is obtained. This temperature can be used in the following energy balance around the pinch in the column.

Step 2: Temperature Bulge Energy Balance: Estimate Maximum (Pinch) Temperature

The second part of the analysis consists of an energy balance around the portion of the column below the temperature bulge (maximum temperature occurs at the vapor outlet and liquid inlet). Equation 3 describes the balance around the bulge/pinch in the column.

$$\begin{aligned} &\boldsymbol{N_{Gas,Pinch}\widetilde{C}_{P,GAS,Pinch}(T_{MAX} - T_{REF}) - N_{Gas,IN}\widetilde{C}_{P,GAS,IN}(T_{GAS,IN} - T_{REF})} \\ &\quad + \Delta \boldsymbol{N_{H2O,GAS}} \Delta \boldsymbol{H_{VAP,T_{REF}}} + \Delta \boldsymbol{N_{CO2,GAS}} \Delta \boldsymbol{H_{ABS,T_{REF}}} \\ &\quad = \boldsymbol{N_{Solvent,Pinch}\widetilde{C}_{P,Solvent,Pinch}(T_{MAX} - T_{REF})} \\ &\quad - \boldsymbol{N_{Solvent,OUT}\widetilde{C}_{P,Solvent,OUT}(T_{Solvent,OUT} - T_{REF})} \end{aligned} \tag{3}$$

If a reference temperature of 40 °C is used in the analysis, the gas inlet term can be eliminated. The solvent outlet temperature and total heat capacity of the solvent outlet are known from the previous step (full column energy balance). The other solvent heat capacity term (NC_P at the pinch) is defined by assuming the total heat capacity of the solvent is constant over the column. This is supported by the observation that the specific heat capacity of the solvent is a weak function of the temperature and loading changes in the absorber and that the total mass flow rate of the solvent changes by a small amount in comparison to the gas. These simplifications result in Equation 4.

$$\begin{aligned} &\boldsymbol{N_{Gas,Pinch}\widetilde{C}_{P,GAS,Pinch}(T_{MAX} - T_{REF})} + \Delta \boldsymbol{N_{H2O,GAS}} \Delta \boldsymbol{H_{VAP,T_{REF}}} + \Delta \boldsymbol{N_{CO2,GAS}} \Delta \boldsymbol{H_{ABS,T_{REF}}} \\ &\quad = \boldsymbol{N_{Solvent}\widetilde{C}_{P,Solvent}(T_{MAX} - T_{Solvent,OUT})} \end{aligned} \tag{4}$$

The remaining terms are unknown, including T_{MAX}, the pinch temperature, which is a target prediction of the shortcut method. Further assumptions are required to solve the temperature-bulge energy balance.

First, for all three flue gas applications, the formation of the temperature-related pinch occurred near the lean end of the column. In other words, a majority of the CO_2 removal occurred below the pinch. Table 1 includes the lean loading where the temperature-related pinch forms for each application, the loading at the mass transfer pinch, and the removal above the pinch.

Table 1: Lean End Pinch Evaluation

Flue Gas Source	Lean Loading: Pinch Formation mol CO_2/mol alk.	Loading at Mass Transfer Pinch	Portion of CO_2 Removal Above Pinch
Natural Gas Combined Cycle (NGCC)	0.22	0.221	0.69%
Coal-Fired Boiler	0.19	0.194	3%
Steel Blast Furnace	0.18	0.187	5.3%

From the data in Table 1, it is apparent that the temperature-related end pinch occurs at the inlet loading of the column (minimal removal above pinch). The energy balance is simplified by assuming that all CO_2 removal (90% removal) has occurred below the pinch (defines the CO_2 absorption term in Equation 3). This is a major assumption since the actual CO_2 removal at the temperature pinch is strongly influenced by rate-based mass and heat transfer and cannot be predicted from a thermodynamic model alone. Future work will consider the sensitivity of minimum solvent rate to rate-based model parameters to determine the robustness of this assumption.

Finally, the CO_2 mass transfer pinch coincides with a mass transfer pinch for H_2O. By assuming the solvent is in equilibrium with water at the lean inlet conditions, the water balance component of the energy balance in Equation 4 can be approximated.

An iterative approach can now be implemented to estimate the temperature at the pinch and the loading at the pinch:

1) Guess a maximum temperature (pinch temperature) and assume 90% CO_2 removal ($T_{INITIAL}$).
2) Solve the energy balance in Equation 2 for the water transferred and estimate the water content in the exiting gas. The composition of the gas at the pinch is now completely specified.
3) Perform a bubble point calculation to estimate the lean loading required to achieve equilibrium to the water content in the exiting gas at the maximum temperature from step 1.
4) Perform a bubble point calculation to estimate a new maximum temperature (T_{FINAL}) required to achieve equilibrium to CO_2 in the exiting gas at the lean loading from step 3.
5) Use the new temperature estimate to repeat steps 1 through 4 until the $T_{INITIAL} = T_{FINAL}$.

Results

The process in the preceding section provides a prediction of the outlet solvent temperature and total heat capacity, maximum solvent temperature, and lean loading at the transition depicted in Figure 1. Figures 4–6 superimpose the loading estimates for the updated shortcut method and old shortcut method over the full L_{MIN} analysis for each of the three flue gas applications.

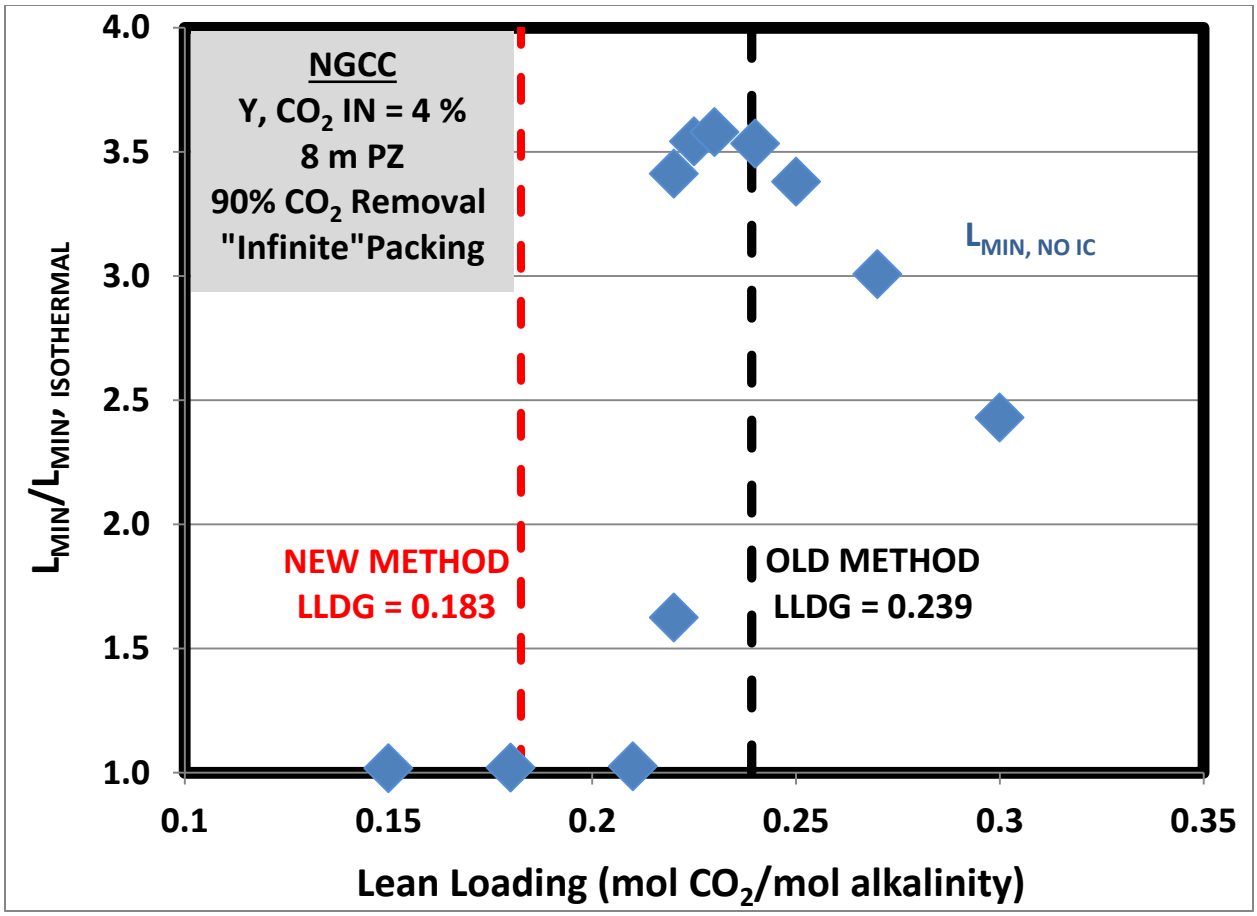

Figure 4: Ratio of the minimum solvent rate ("infinite" packing) for an adiabatic absorber (no intercooling) to an isothermal absorber (40 °C) for 90% CO_2 capture from a natural gas combined cycle turbine (4.1% CO_2) using 8 m PZ. The lean loading approximation for the transition to a temperature-related pinch is identified for the new shortcut method (- - -) and the old method (- - -).

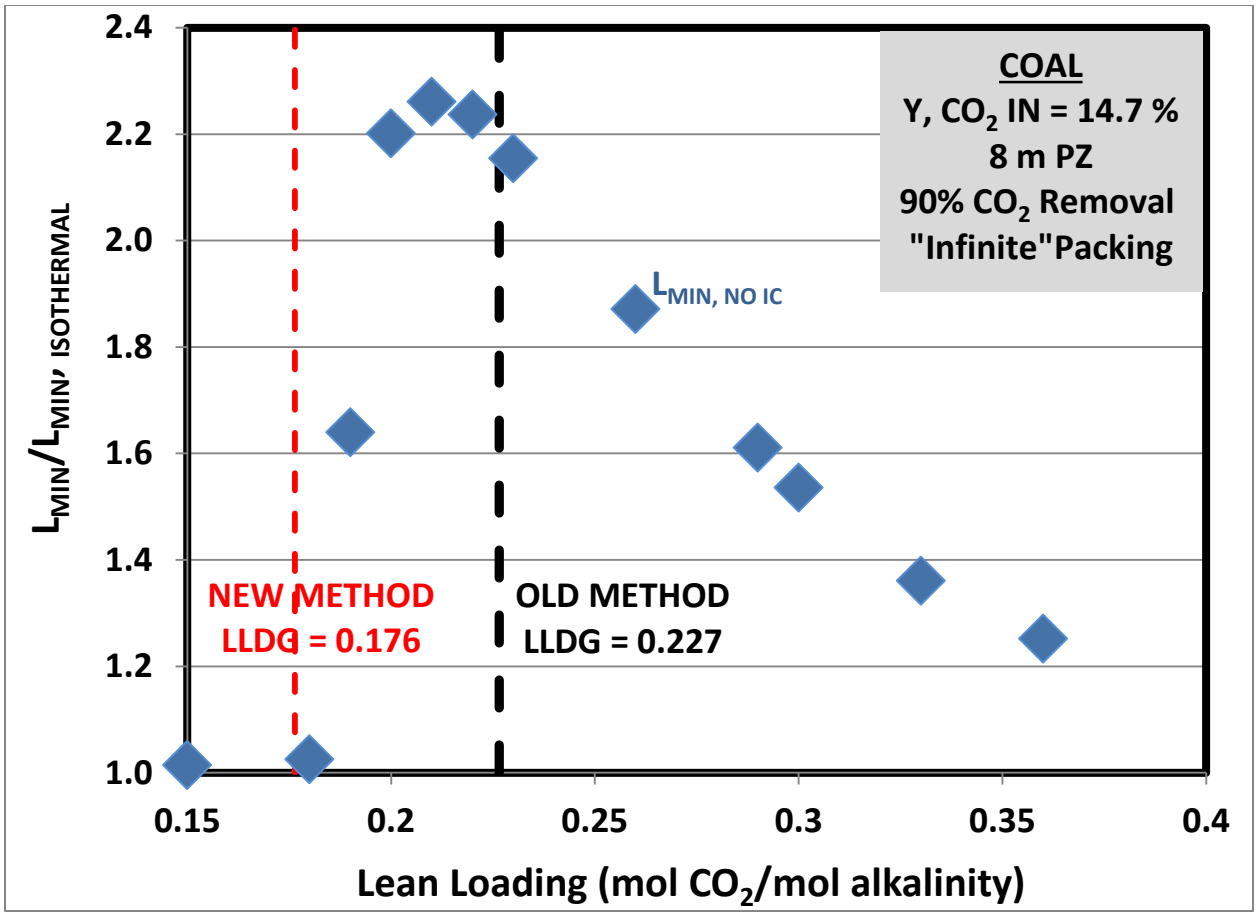

Figure 5: Ratio of the minimum solvent rate ("infinite" packing) for an adiabatic absorber (no intercooling) to an isothermal absorber (40 °C) for 90% CO_2 capture from a coal-fired boiler (13.5% CO_2) using 8 m PZ. The lean loading approximation for the transition to a temperature-related pinch is identified for the new shortcut method (- - -) and the old shortcut method (- - -).

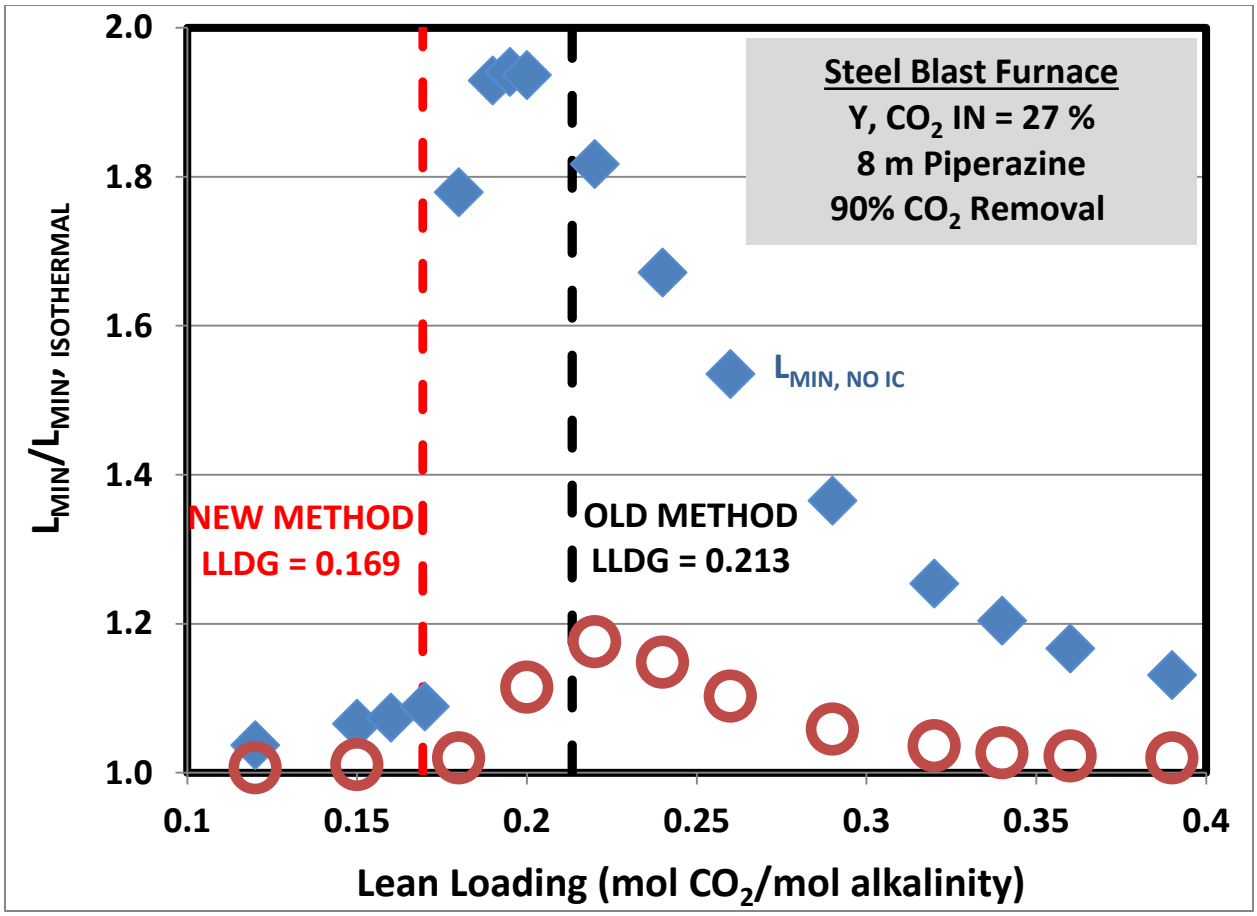

Figure 6: Ratio of the minimum solvent rate ("infinite" packing) for an adiabatic absorber (no intercooling) to an isothermal absorber (40 °C) for 90% CO_2 capture from a steel blast furnace (27% CO_2) using 8 m PZ. The lean loading approximation for the transition to a temperature-related pinch is identified for the new shortcut method (- - -) and the old method (- - -).

The new shortcut method provides a significantly improved estimate of the transition lean loading (pinch formation) for all but the NGCC case. The discrepancy in the NGCC case is discussed in the subsequent section. The old shortcut method consistently overestimates the transition lean loading due to the assumption that the maximum temperature can be estimated by letting the gas carry all of the heat out of the column. By incorporating the solvent contribution to the energy balance (Part 1), the new method provides a much better estimation of heat "trapped" in the column when the mass transfer pinch forms.

The predictions from the updated shortcut method are tabulated alongside the actual values from the rigorous rate-based simulation in Tables 2 and 3.

Table 2: Energy Balance Predictions for the Updated Shortcut Method (Part 1)

	Outlet T (°C) : Step 1 Result		Total Heat Capacity, mCp (kW/K) : Step 1 Result	
	Predicted	Actual	Predicted	Actual
NGCC	45.5	45–49 °C	8068	7900–8900
COAL	55.2	52–58 °C	7149	7140–9620
STEEL	62.0	51–62 °C	4966	4920–6840

As evident in Table 2, the results for step 1 of the method indicate that the total energy balance for the column (and associated simplifications) yields good estimates for the outlet temperature and total heat capacity for all three flue gas applications. This portion of the method did not require any assumptions regarding the rate-based model, and thus appears robust despite using only thermodynamic calculations to provide the estimates.

Table 3: Energy Balance Predictions for the Updated Shortcut Method (Part 2)

	Transition LLDG : Step 2 Result		TMAX (°C) : Step 2 Result	
	Predicted	Actual	Predicted	Actual
NGCC	0.183	0.21–0.22	65.5	60–64
COAL	0.176	0.18–0.20	80.4	80–81
STEEL	0.169	0.17–0.19	88.2	87–89

Table 3 indicates that the energy balance around the temperature bulge yields good estimates for the lean loading and maximum temperature for the coal and steel applications, although the lean loading is slightly underestimated. However, for the NGCC case, the lean loading is significantly underestimated and the maximum temperature is overestimated. This error is believed to be induced by the assumption that all CO_2 removal occurs below the pinch. The details of this issue are discussed for the NGCC case in the following section.

Error in NGCC Predication and Rate-Based Model Parameter Sensitivity

Two issues make the NGCC case most susceptible to error when applying the shortcut method. First, the maximum temperature (pinch temperature) is lower for the NGCC case than for coal and steel (due to lower CO_2 concentration). Therefore, the relative contribution of the sensible heat terms (temperature difference terms) compared to the latent heat terms (CO_2 and H_2O) in Equation 4 is the smallest for the NGCC case. Any error in the estimation of the latent heat terms lead to greater error in maximum temperature and lean loading estimates the NGCC case.

The primary assumption in the new shortcut method regarding the latent heat terms is that all CO_2 removal is occurring below the pinch. Table 1 indicates that the assumption appears to be most appropriate for the NGCC case (most removal does occur below the pinch at the transition loading). However, the NGCC case exhibits multiple steady state solutions for the transition loading (i.e., more than one solvent rate yields 90% CO_2 removal at the transition loading). This observation is evident in Figure 4 where two solvent rates are reported for the transition lean loading of 0.22 mol CO_2/mol alkalinity. The lower solvent rate corresponds to the removal reported in Table 1 (i.e., all removal below the pinch). If the higher solvent rate case is used, approximately 9% of total CO_2 removal occurs above the pinch. This discrepancy is significant in the NGCC case as confirmed by re-evaluating the shortcut method with the reduced CO_2 removal. The results of the new shortcut method, applying the actual CO_2 removal from the rigorous rate-based simulation in place of the previous assumption, are summarized in Figure 7.

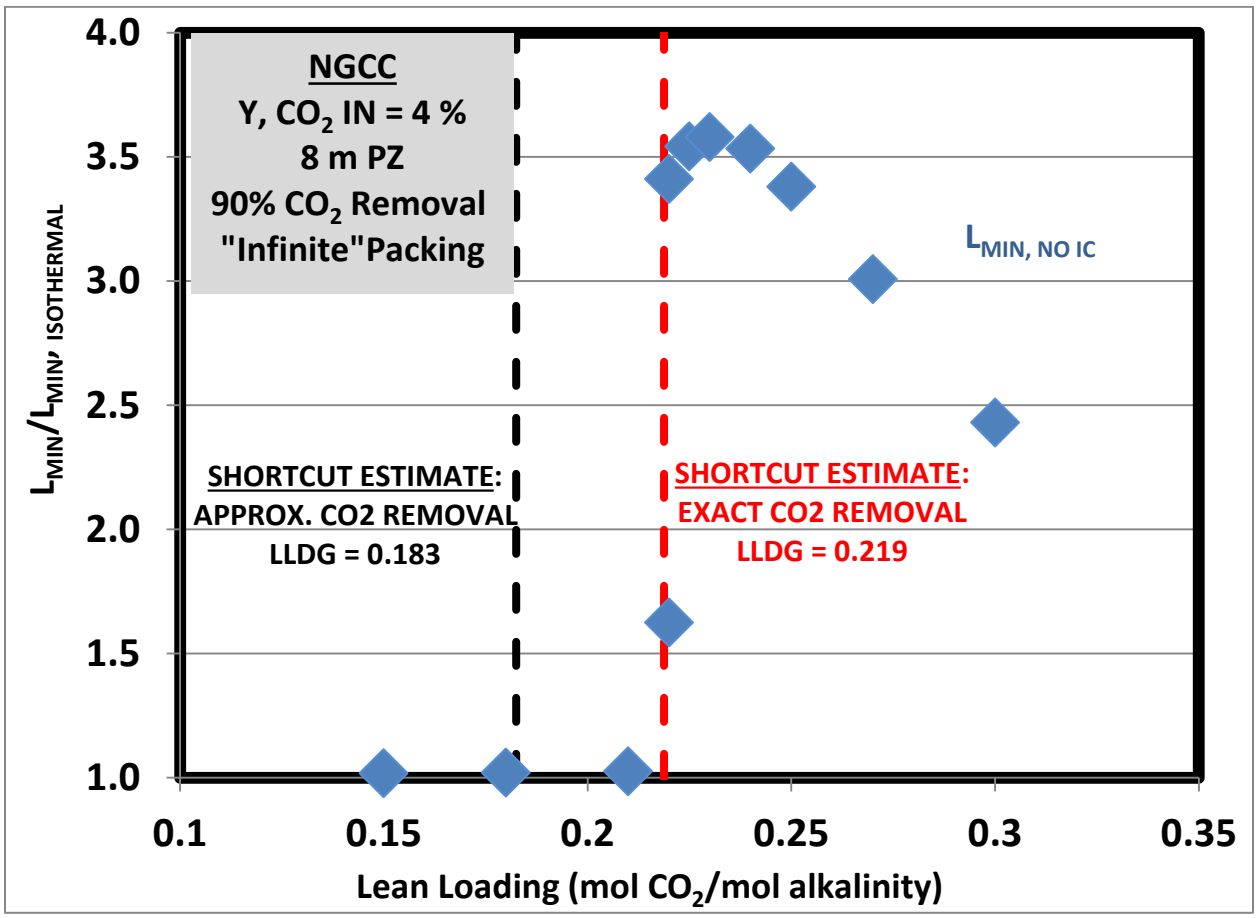

Figure 7: Ratio of the minimum solvent rate ("infinite" packing) for an adiabatic absorber (no intercooling) to an isothermal absorber (40 °C) for 90% CO_2 capture from a natural gas combined cycle turbine (4.1% CO_2) using 8 m PZ. The lean loading approximation for the transition to a temperature-related pinch is identified for the shortcut method using an approximation of all CO_2 removal occurring below the pinch (- - -) and using the exact removal at the pinch obtained from the rigorous rate-based simulation (- - -).

The figure shows the significantly improved estimate for the transition lean loading when the appropriate CO_2 removal is specified in the energy balance. Further investigation is required to understand the effect of multiple steady states and to develop a method to predict the removal at the bulge to ensure a robust shortcut method for other solvent systems or CO_2 concentrations.

Conclusions

An updated shortcut method was developed using a two-step energy balance around an adiabatic (no intercooling) absorber and several observations from rigorous rate-based modeling to estimate the transition lean loading for each flue gas application where a temperature-related pinch formed. The prediction of this transition loading allows identification of operating regions where intercooling is essential to maximize solvent capacity. The updated shortcut method incorporated the solvent contribution to the overall energy balance in the first step of the method and significantly improved the transition loading estimate for the coal and steel applications over

the previously developed method. However, the NGCC prediction significantly under-predicted the transition loading, and required specification of the CO_2 removal at the pinch (from rate-based calculations) to improve the estimate. The predicted loadings from the new shortcut method can be compared to the previous method prediction and the actual transition loading range for each flue gas application:

- NGCC: Actual = 0.21–0.22 vs. Predicted (NEW) = 0.219 vs. Predicted (OLD) = 0.239
- Coal: Actual = 0.18–0.20 vs. Predicted (NEW) = 0.176 vs. Predicted (OLD) = 0.227
- Steel: Actual = 0.17–0.19 vs. Predicted (NEW) = 0.169 vs. Predicted (OLD) = 0.213.

The new method is within 2% of the actual transition loading range for all applications whereas the error in the previous method was as large as 14%. As before, the estimates are developed by using only simple energy balances and flash calculations (thermodynamic model). Rate-based calculations were not required (as in the full L_{MIN} analysis), thus significantly simplifying calculation and providing a quick method to determine if intercooling is required for a selected lean loading. The final correction for the NGCC case introduced data from the rate-based calculations and requires further investigation to validate the robustness of the estimation method.

Future Work

The observations from the NGCC calculation in the shortcut method will form the starting point for detailed investigation of the role of rate-based parameters in the minimum solvent rate. The temperature-induced mass transfer pinch is not strictly a thermodynamic phenomenon and is strongly influenced by rate-based transfer of water, CO_2, and heat. Sensitivity analyses are underway to consider the effect of physical mass transfer coefficients and kinetic parameters on the minimum solvent rate for the cases evaluated previously. One goal of the analysis will be to generalize the rate-based effects on minimum solvent rate to improve predictions of pinch behavior for cases such as the NGCC application in the shortcut method. Furthermore, the sensitivity analysis will provide model validation for prediction of solvent capacity within the error of the rate-based parameters of the model.

Safety

One of the primary safety issues associated with the absorber unit operation in an amine scrubbing facility is exposure to the amine. One method for reducing the overall risk of amine exposure is to reduce overall solvent inventory in the system. This analysis continued the evaluation of potential solvent capacity benefits of intercooling in the absorber. At conditions where intercooling may significantly improve solvent capacity (reduce the solvent circulation rate), a secondary benefit is a potentially significant reduction of the overall solvent inventory in the system.

References

Rochelle GT et al. "CO_2 Capture by Aqueous Absorption, First Quarterly Progress Report 2014." Texas Carbon Management Program. The University of Texas at Austin. 2014a.

Rochelle GT et al. "CO_2 Capture by Aqueous Absorption, Fourth Quarterly Progress Report 2013." Texas Carbon Management Program. The University of Texas at Austin. 2014b.

Rochelle GT et al. "CO_2 Capture by Aqueous Absorption, Third Quarterly Progress Report 2014." Texas Carbon Management Program. The University of Texas at Austin. 2014c.

Modeling and Optimization of Advanced Stripper Configurations

Quarterly Report for October 1 – December 31, 2014

by Yu-Jeng Lin

Supported by the Texas Carbon Management Program

McKetta Department of Chemical Engineering

The University of Texas at Austin

January 31, 2015

Abstract

The lean/rich amine cross exchanger is one of the cost centers in the amine scrubbing process, and accounts for 20–30% of the capital cost. To reduce the cost, heat transfer performance can be enhanced by increasing pressure drop or reducing solvent viscosity.

A literature review on empirical correlations of heat transfer and pressure drop for plate-and-frame exchangers is presented in this report. The corrugation angle is the primary design geometry, which is typically designed at 30–60^{o}. The heat transfer coefficient at 60^{o} is almost double that at 30^{o}; however, the pressure drop at a large corrugation angle is also greater. The dependence of the pressure drop per unit length on the heat transfer coefficient is 0.35–0.40, which implies that the heat transfer coefficient will increase 30% by doubling the pressure drop per unit length.

The cost associated with the optimization of the cross exchanger has been developed as a function of the fluid velocity, the physical properties, the exponents of the empirical correlations and the pricing parameters. The dependence of viscosity on the exchanger cost is 0.3–0.4. A lower concentration of PZ, 5 m PZ, has been proposed to provide better solid solubility. Compared with 8 m PZ, the lower viscosity of 5 m PZ reduces the exchanger cost by around 30%, which nearly cancels out the increase in cost caused by the reduced capacity.

Introduction

In the amine scrubbing process, the lean/rich amine cross exchanger is used to recover the sensible heat from the hot lean solvent. The exchanger heat duty is 3 to 5 times the actual heat input. Since a large amount of heat is transferred, the capital cost of the cross exchanger is one of the cost centers, accounting for 20–30% of capital cost. To reduce the cross exchanger cost, the most important design parameter, the temperature driving force (LMTD), should be optimized. Furthermore, the heat transfer coefficient can be enhanced by increasing the pressure drop and using a less viscous solvent.

The plate-and-frame type heat exchanger (PHE) shown in Figure 1 is used as the cross exchanger. The hot and cold fluids flow through between plates where the heat transfer area is

provided. The ports on the plates serve as fluid collectors or distributors. Gaskets are used on the ports and frames to avoid fluid mixing and leakage.

As shown in Figure 2, the corrugated plates can enhance the heat transfer by generating turbulence. The turbulent flow can happen even at a low Reynolds number (Re). The corrugation angle, β, is the primary geometry variable, which can be designed between 0 and 90º. Both the heat transfer coefficient and the pressure drop increase with increasing β.

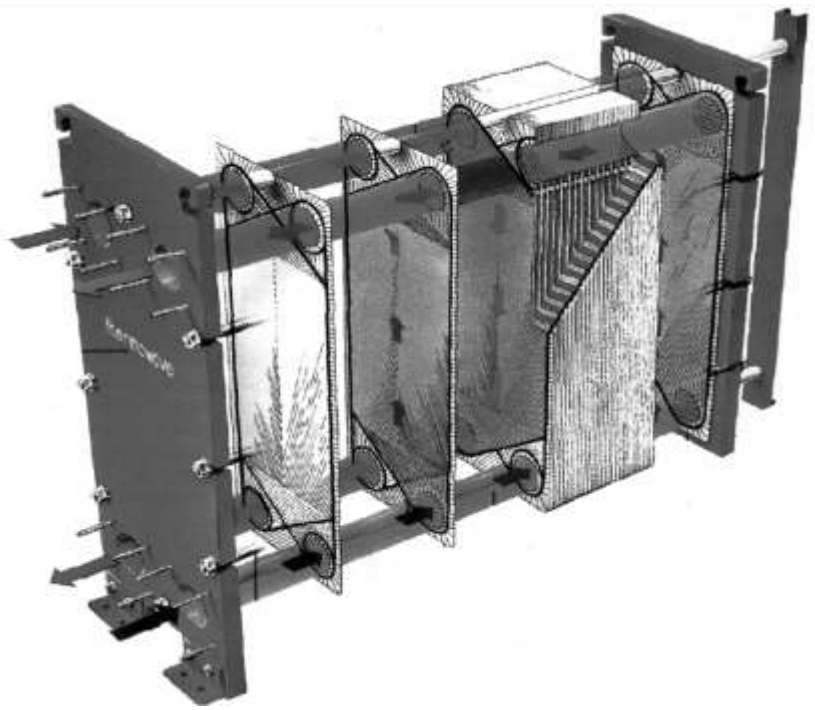

Figure 1: Plate–and-frame exchanger (Reppich, 1999)

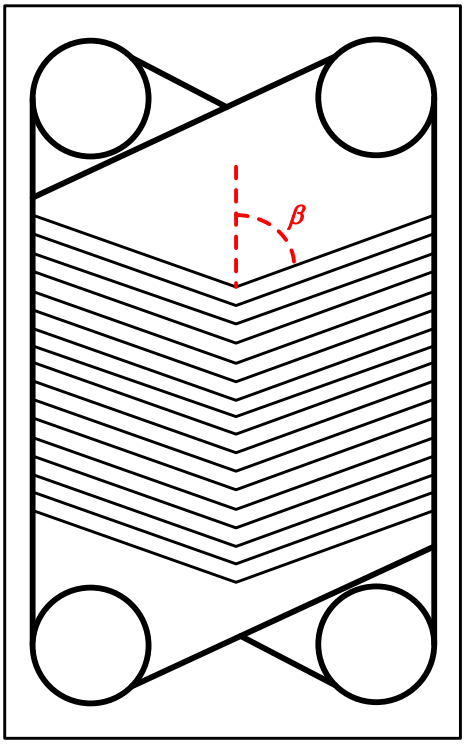

Figure 2: Corrugated plate and corrugation angle, β

Literature review

Empirical correlations will be used to estimate the heat transfer coefficient and the pressure drop. Table 1 shows the literature review of the heat transfer and the pressure drop correlations for PHE. Two dimensionless groups, Nusselt number, Nu, and Fanning friction factor, f, are used to calculate the heat transfer coefficient, h, and the total pressure drop, ΔP, respectively, as shown in Equations 1 and 2.

$$h = Nu\frac{D_e}{k} \tag{1}$$

$$\Delta P = \frac{2fL_T\rho u^2}{D_e} \tag{2}$$

Water was used as the working fluid in most experiments from the literature. By varying the fluid flow rate, Nu and f data were obtained with various Re. As shown in Equations 3 and 4, the Nusselt number is typically expressed as a function of Reynolds number and Prandtl number (Pr) using a power law. The friction factor is inversely proportional to the Reynolds number. In most of the literature, the exponent of the Prandtl number was fixed from 0.33–0.5, and the experimental data were regressed to determine the constants C_{Nu} and C_f, and the exponents, m and p. The most common corrugation angles tested were 30º and 60º.

$$Nu = C_{Nu}Re^{m}Pr^{n} \tag{3}$$

$$f = C_f Re^{-p} \tag{4}$$

Table 1: Empirical correlations of heat transfer and pressure drop for plate-and-frame exchanger

Year	Author	Fluid	Heat transfer correlation	Pressure drop correlation
1972	Okada	Water	$Nu = 0.327Re^{0.65}Pr^{0.4}\ (\beta = 60)$ $Nu = 0.157Re^{0.66}Pr^{0.4}\ (\beta = 30)$	
1975	Resenblad, Kullendroff	Water	$Nu = 0.289Re^{0.697}Pr^{0.33}$	
1975	Changal Vaie	Water	$Nu = 0.298(\phi)^{1-0.646}Re^{0.646}Pr^{0.316}$	$f = (36\phi Re^{-1} + 0.2)\phi$
1984	Kumar	Water	$Nu = 0.348Re^{0.663}Pr^{0.33}\left(\frac{\mu}{\mu_w}\right)^{0.17}\ (\beta = 60)$ $Nu = 0.108Re^{0.703}Pr^{0.33}\left(\frac{\mu}{\mu_w}\right)^{0.17}\ (\beta = 30)$	$f = 2.99Re^{-0.183}(\beta = 60)$ $f = 0.76Re^{-0.215}(\beta = 30)$
1993	Heavner, Wanniarachchi	Water	$Nu = 0.308Re^{0.667}Pr^{0.33}\left(\frac{\mu}{\mu_w}\right)^{0.17}\ (\beta_{avg} = 56.5)$ $Nu = 0.118Re^{0.720}Pr^{0.33}\left(\frac{\mu}{\mu_w}\right)^{0.17}\ (\beta_{avg} = 33.5)$	$f = 1.441Re^{-0.1353}(\beta_{avg} = 56.5)$ $f = 0.545Re^{-0.1555}(\beta_{avg} = 33.5)$
1994	Roetzel	Water	$Nu = 0.371Re^{0.703}Pr^{0.33}$	
1995	Thonon		$Nu = 0.2946Re^{0.7}Pr^{0.33}\ (\beta = 60)$ $Nu = 0.2267Re^{0.631}Pr^{0.33}\ (\beta = 30)$	$f = 0.37Re^{-0.172}(\beta = 60)$ $f = 0.572Re^{-0.217}(\beta = 30)$
1995	Talik, Swanson	Propylene glycol/water	$Nu = 0.2Re^{0.75}Pr^{0.4}(\beta = 60)$	$f = 48.26Re^{-0.74}(\beta = 60)$
1995	Muley, Manglik	Water	$Nu = 0.105Re^{0.755}Pr^{0.33}\left(\frac{\mu}{\mu_w}\right)^{0.14}\ (\beta = 45)$	$f = 1.274Re^{-0.15}(\beta = 45)$
1999	Muley, Manglik	Water	$Nu = C_1(\beta)C_2(\phi)Re^{a(\beta)}Pr^{0.33}\left(\frac{\mu}{\mu_w}\right)^{0.14}$	$f = C_3(\beta)C_4(\phi)Re^{-b(\beta)}$
2008	Warnakulasuriya, Worek	Salt solution	$Nu = 0.292Re^{0.725}Pr^{0.35}\left(\frac{\mu}{\mu_w}\right)^{0.14}\ (\beta = 60)$	$f = 23.8Re^{-0.205}(\beta = 60)$
2010	Khan, Ayub	Water	$Nu = 0.1368Re^{0.7424}Pr^{0.35}\left(\frac{\mu}{\mu_w}\right)^{0.14}\ \beta = 30$ $Nu = 0.1449Re^{0.8414}Pr^{0.35}\left(\frac{\mu}{\mu_w}\right)^{0.14}\ \beta = 60$	

The physical properties of 8 m PZ shown in Table 2 are used to demonstrate the empirical correlations found in literature. Since the temperature of the cross exchanger variesfrom 50 to 140 ºC, the physical properties were estimated at 90 ºC, around the average temperature of the cross exchanger. The Prandtl number for 8 m PZ is around 70, which is an order of magnitude higher than water. The plate spacing is assumed to be 2 mm.

Table 2: Physical properties of 8 m PZ at 90 ºC and 0.30 CO_2 loading

Viscosity (cP)	3
Thermal conductivity (W/m-K)	0.15
Heat capacity (kJ/kg-K)	3.5

The Nusselt number and the Fanning friction factor with varied Reynolds number are shown in Figure 3 and Figure 4, respectively. Two corrugation angles, 30º and 60º are shown in red and green, respectively. It is clear that the PHE with 60º provides higher heat transfer coefficient, which is about double that of 30º. At the same corrugation angle, the difference of the Nusselt number between correlations can vary more than 50%. The friction factors predicted from the correlations are more scattered, but generally the PHE at 60º has higher pressure drop. PHE with a greater corrugation angle can provide better heat transfer performance, and it causes higher pressure drop.

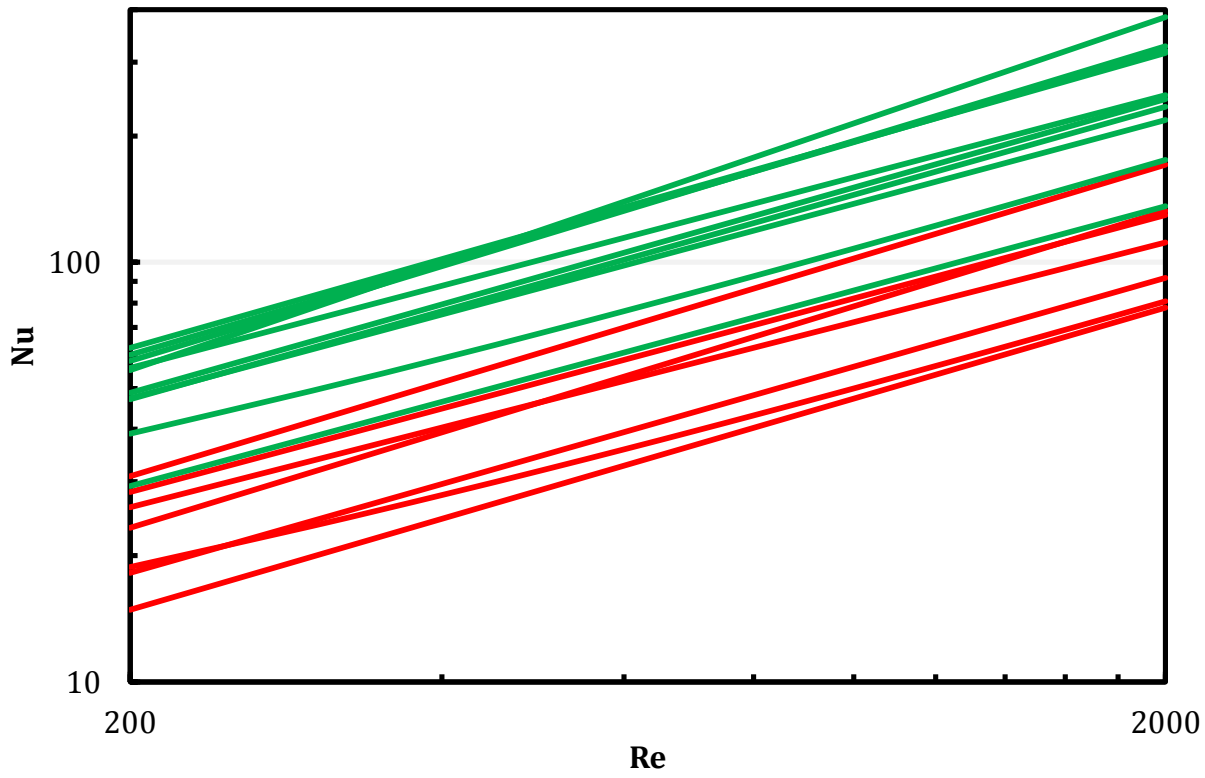

Figure 3: Nusselt number predicted by empirical correlations with varied Reynolds number; red lines: β = 30º; green lines: β = 60º

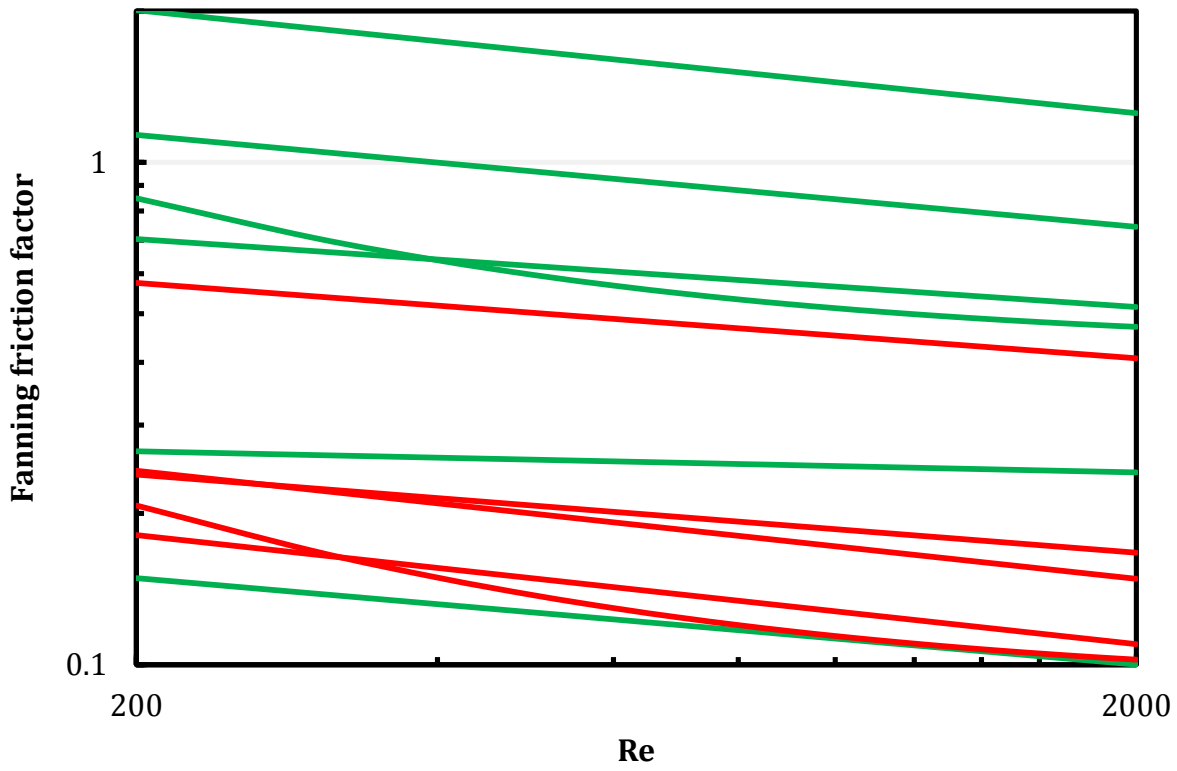

Figure 4: Fanning friction factor predicted by empirical correlations with varied Reynolds number; red lines: β = 30º; green lines: β = 60º

Optimization of cross exchanger

When the physical properties of fluids are given, the only degree of freedom that determines the heat transfer coefficient and the pressure drop is the fluid velocity. The optimum fluid velocity will balance between the enhanced heat transfer performance and the penalty caused by the pressure drop. The trade-offs are the capital cost of the cross exchanger and the cost associated with the pressure drop.

Figure 5 shows the flow pattern and the geometry of a single-pass PHE. The fluid velocity is determined by the cross-sectional area that is perpendicular to the flow direction. If the plate spacing, δ, is fixed, the fluid velocity can be varied by adjusting the total plate width, W_T. The total heat transfer area will be the product of W_T and total length of flow path, L_T.

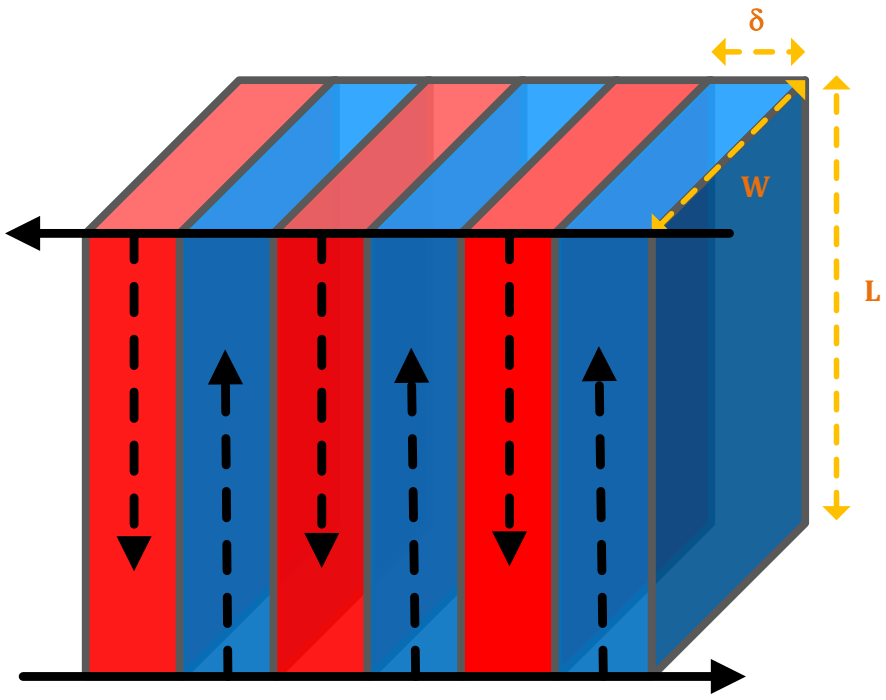

Figure 5: Flow patter and geometry of a single-pass plate-and-frame exchanger

If the correlations in Equations 3 and 4 are applied, the pressure drop per unit length will be proportional to the Reynolds number with exponent 2-p (Equation 5). Substituting the Reynolds number for pressure drop per unit length shows that the dependence of the pressure drop per unit length on Nusselt number is m/(2-p) (Equation 6).

$$\frac{\Delta P}{L} = \frac{2f\rho u^2}{D_e} \propto fRe^2 \propto Re^{2-p} \tag{5}$$

$$Nu \propto Re^m \propto \left(\frac{\Delta P}{L}\right)^{\frac{m}{2-p}} \tag{6}$$

Figure 6 shows the dependence of the pressure per unit length on the Nusselt number with varied corrugation angle. The dependence is around 0.35 to 0.40 as predicted by empirical correlations, which implies that if the pressure drop per unit length doubles, the heat transfer coefficient will increase around 30%.

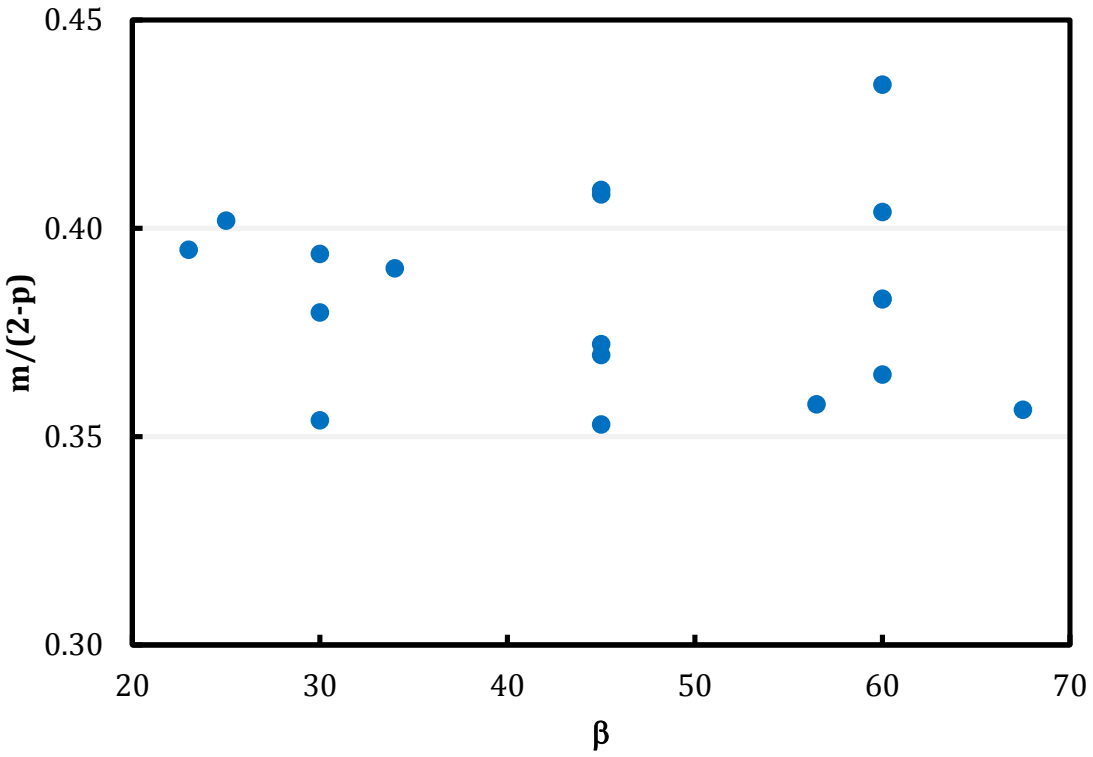

Figure 6: The dependence of pressure drop per unit length on Nusselt number predicted by empirical correlations with varied corrugation angle

To optimize the fluid velocity, u, the total cost associated with the cross exchanger is derived. All the dimensionless groups are taken apart and expressed as a function of the fluid velocity, the physical properties and the constants and exponents from the empirical correlations. Equation 7 and 8 show the expression of the heat transfer coefficient and the total pressure drop, respectively.

$$h = \frac{k}{D_e} C_{Nu} Re^m Pr^n = C_{Nu} \rho^m {D_e}^{m-1} k^{1-n} {C_p}^n u^m \mu^{n-m} \tag{7}$$

$$\Delta P = \frac{2 f_f L \rho u^2}{D_e} = 2 C_f \rho^{1-p} {D_e}^{-p-1} u^{2-p} \mu^p L \tag{8}$$

If the total width is used to determine the fluid velocity, the total length will be determined by the total heat transfer area, A. The total length can be related to the heat transfer area and the fluid velocity using Equation 9.

$$L_T = \frac{A}{W_T} = \frac{A}{\frac{\dot{V}}{\delta u}} \tag{9}$$

The overall heat transfer coefficient, U, is approximated as one half of the heat transfer coefficient on one side (Equation 10). Equation 11 is used to relate the heat transfer area and the overall heat transfer coefficient.

$$U \cong \left(\frac{1}{h}+\frac{1}{h}\right)^{-1} = \frac{h}{2} \tag{10}$$

$$A = W_T L = \frac{Q}{U\Delta T_{LM}} \tag{11}$$

By plugging Equations 9–10 into Equations 7 and 8, the heat transfer area and the total pressure drop can be calculated using Equations 12 and 13. The exchanger area is inversely proportional to the fluid velocity with a power of m, which is around 0.6–0.75 for PHE. The magnitude of m determines the enhancement of the heat transfer that caused by increasing the fluid velocity. The dependence of the fluid velocity on the total pressure drop is 3-m-p. The p affects the friction factor and the m indirectly determines the total length. A longer flow path length will cause more total pressure drop.

$$A = \frac{Q}{\Delta T_{LM}}\frac{2}{C_{Nu}}\rho^{-m}{D_e}^{1-m}k^{n-1}{C_p}^{-n}u^{-m}\mu^{m-n} \tag{12}$$

$$\Delta P = 4\frac{C_f}{C_{Nu}}\frac{\delta}{\dot{V}}\frac{Q}{\Delta T_{LM}}\rho^{1-m-p}{D_e}^{-m-p}k^{n-1}{C_p}^{-n}u^{3-m-p}\mu^{m-n+p} \tag{13}$$

The total cost associated with the cross exchanger optimization includes the pump work cost, the capital cost of the pump, and the exchanger. The pump work can be calculated using Equation 14. After adding the pricing parameters, Equation 15 shows the total cost associated with the cross exchanger, which should be minimized. In the cost optimization, once the m and p are known, the optimum fluid velocity is mainly driven by the equipment purchase cost of the exchanger and the pump, the scaling and the annualizing factor, α and β_A, and the cost of electricity, C_{COE}.

$$W_{pump} = \frac{\dot{V}\Delta P}{\eta_p} \tag{14}$$

$$Cost_{total} = \left(C_{COE} + \alpha\beta_A C_{PEC,p}\right)\frac{4C_f}{C_{Nu}}\frac{\delta}{\eta_p}\frac{Q}{\Delta T_{LM}}\rho^{1-m-p}{D_e}^{-m-p}k^{n-1}{C_p}^{-n}u^{3-m-p}\mu^{m-n+p}$$

$$+\alpha\beta_A C_{PEC,ex}\frac{Q}{\Delta T_{LM}}\frac{2}{C_{Nu}}\rho^{-m}{D_e}^{1-m}k^{n-1}{C_p}^{-n}u^{-m}\mu^{m-n} \tag{15}$$

Another approach to reducing the cost of the cross exchanger is to decrease the viscosity of the solvent. From Equation 15, both the pressure drop cost and the exchanger cost decrease with decreasing viscosity. Figure 6 shows the dependence of viscosity on the exchanger cost predicted by the empirical correlations with varied corrugation angle. Most of the viscosity

dependence is between 0.30 and 0.40, which means that reducing viscosity by 50% can save on cross exchanger cost by 20–25%.

It has been shown that the lower concentration of 5 m PZ provides a better solid solubility than 8 m PZ. Table 3 compares 5 m and 8 m PZ. The cross exchanger cost with varied amine concentration is mainly affected by the solvent capacity and the viscosity. The reduced capacity of 5 m PZ increases the exchanger duty by 35%, which results in a 35% increase in the exchanger cost according to Equation 15. However, the effect of lower viscosity can reduce the exchanger cost by 30%. Combining these two effects, the cross exchanger cost of 5 m PZ is expected to be comparable to that of 8 m PZ.

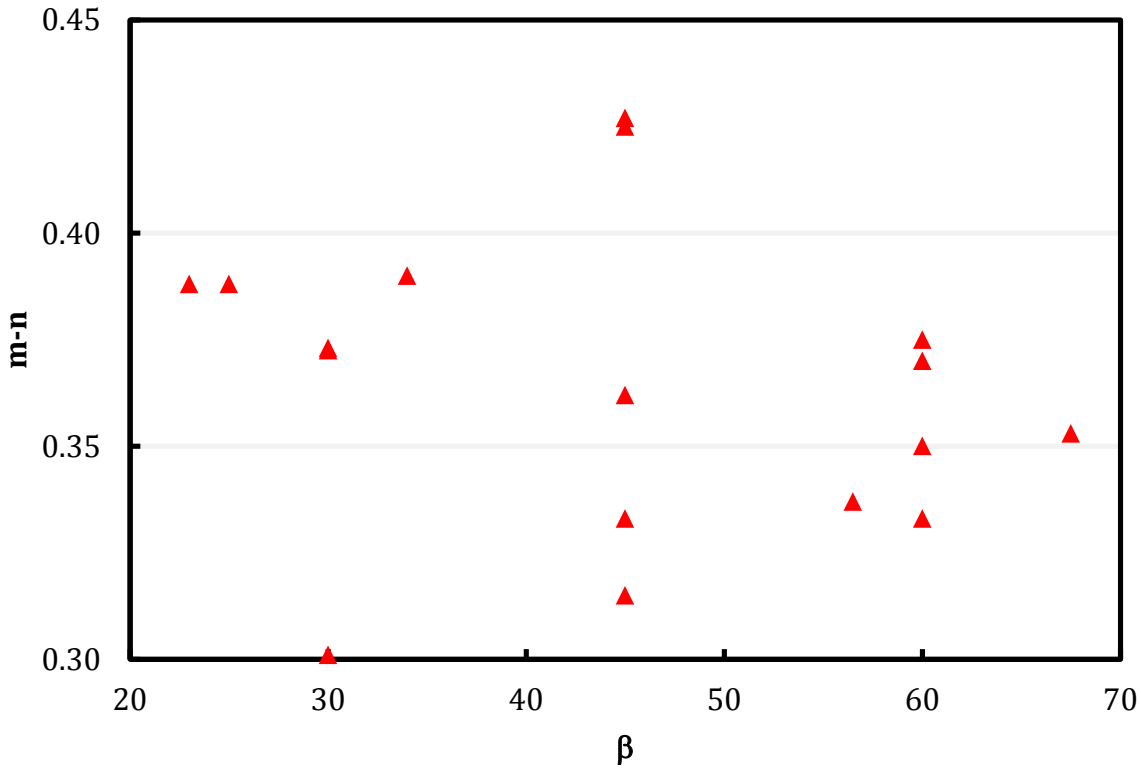

Figure 7: The dependence of viscosity on the exchanger cost predicted by empirical correlations with varied corrugation angle

Table 3: The comparison of 8 m and 5 m PZ

PZ concentration (m)	8	5
PZ concentration (mol PZ/kg solution)	4.7	3.5
Viscosity @90 ºC/0.30 Ldg (cP)	1.26	3.06

Conclusions

1. Literature on heat transfer coefficient and pressure drop of plate-and-frame exchangers has been reviewed.

2. The corrugation angle is the primary design variable, which produces turbulence and enhances heat transfer performance. The heat transfer coefficient at 60º corrugation angle is about double that at 30º

3. The heat transfer coefficient can be enhanced by increasing the pressure drop. The dependence of the pressure drop per unit length on the heat transfer coefficient is around 0.35–0.40.

4. Decreasing the fluid viscosity can reduce the pump cost and the exchanger cost. The dependence of the viscosity on the cross exchanger cost is around 0.35–0.40. Compared to 8 m PZ, the effect of lower viscosity of 5 m PZ can reduce the cross exchanger cost by 30%.

Future Work

1. Economics of the advanced flash stripper using 5 m PZ will be analyzed and compared to 8 m PZ.

2. Energy performance of natural gas and steel/iron plant applications will be evaluated.

Nomenclature

A	Cross exchanger area
C_{COE}	Cost of electricity
C_f	Constant in Equation (4)
C_{Nu}	Constant in Equation (3)
C_p	Heat capacity
$C_{PEC,ex}$	Purchased equipment cost of cross exchanger
$C_{PEC,p}$	Purchased equipment cost of pump
D_e	Equivalent diameter$(= 2\delta)$
f	Fanning friction factor
h	Heat transfer coefficient
k	Thermal conductivity
L_T	Total length of flow path
Nu	Nusselt number $(= hD_e/k)$
m	Exponent of Equation (3)
n	Exponent of Equation (3)
p	Exponent of Equation (4)

Q Cross exchanger heat duty

Re Reynolds number ($= \rho u D_e/\mu$)

U Overall heat transfer coefficient

$\dot{V}$ Solvent volume flow rate

u Thermal conductivity

W_T Total width of plates

Greek

α Scaling factor

β Corrugation angle

β_A Annualizing factor

ΔP Total pressure drop

ΔT_{LM} Log mean temperature difference

δ Plate spacing

η_p Pump efficiency

μ Solvent viscosity

ρ Solvent density

References

Rosenblad G, Kullendorff A. "Estimating heat transfer rates from mass transfer studies on plate heat exchanger surfaces." *Wärme-und Stoffübertragung*. 1975;8:187–191.

Focke WW, Zachariades J, Olivier I. "The effect of the corrugation inclination angle on the thermohydraulic performance of plate heat exchangers." *Int J Heat Mass Transf*. 1985;28(8):1469–1479.

Roetzel W, Das S, Luo X. "Measurement of the heat transfer coefficient in plate heat exchangers using a temperature oscillation technique." *Int J Heat Mass Transf*. 1994;37:325–331.

Martin H. "A theoretical approach to predict the performance of chevron-type plate heat exchangers." *Chem Eng Process*. 1996;35:301–310.

Manglik R, Ding J. "Laminar flow heat transfer to viscous powerlaw fluids in double-sine ducts." *Int J Heat Mass Transf*. 1997;40(6):1379–1390.

Muley A. "Enhanced heat transfer characteristics of viscous liquid flows in a chevron plate heat exchanger." *J Heat Transfer*. 1999;121:1011–1017.

Muley A, Manglik R. "Experimental study of turbulent flow heat transfer and pressure drop in plate heat exchanger with chevron plates." *J Heat Transfer*. 1999;121:110–117.

Reppich M. "Use of high performance plate heat exchangers in chemical and process industries." *Int J Therm Sci*. 1999;38(11):999–1008.

Ayub ZH. "Plate Heat Exchanger Literature Survey and New Heat Transfer and Pressure Drop Correlations for Refrigerant Evaporators." *Heat Transf Eng*. 2003;24(5):3–16.

Warnakulasuriya FSK, Worek WM. "Heat transfer and pressure drop properties of high viscous solutions in plate heat exchangers." *Int J Heat Mass Transf*. 2008;51:52–67.

Khan TS, Khan MS, Chyu M-C, Ayub ZH. "Experimental investigation of single phase convective heat transfer coefficient in a corrugated plate heat exchanger for multiple plate configurations." *Appl Therm Eng*. 2010;30:1058–1065.

Absorber performance in hybrid-separation process with 5 m PZ and 5 m MDEA/5 m PZ

Quarterly Report for October 1 – December 31, 2014

by Yue Zhang

Supported by the

Howard A. Halff Endowed Graduate Fellowship in Chemical Engineering

and the Texas Carbon Management Program

McKetta Department of Chemical Engineering

The University of Texas at Austin

January 31, 2015

Acknowledgement: This material is based on work supported in part by the Department of Energy under Award Number DE-FE0013188.

Abstract

In a hybrid-parallel process combining amine scrubbing with membrane technology, the CO_2 concentration in the flue gas is enriched to 23.4% and removal level is increased to 95% (Case 19). This work simulates absorber performance of Case 19 with the Independence model for 5 molal (m) PZ and 5 m MDEA/5 m PZ in Aspen Plus®. Different intercooling configurations and absorber operating conditions have been tested to achieve better absorber performance and minimize stripper energy use.

5 m MDEA/5 m PZ offers higher CO_2 capacity but a lower absorption rate than 5 m PZ. Compared to 5 m PZ, absorber costs increase by 50% and advanced flash stripper costs decrease by 47%. The total equipment costs go down by 13%.

Introduction

A hybrid system combining amine scrubbing with membrane technology has been proposed by Membrane Technology and Research, Inc.to reduce energy cost (Freeman et al., 2014). In the hybrid process, the CO_2 concentration in the flue gas may be enriched.

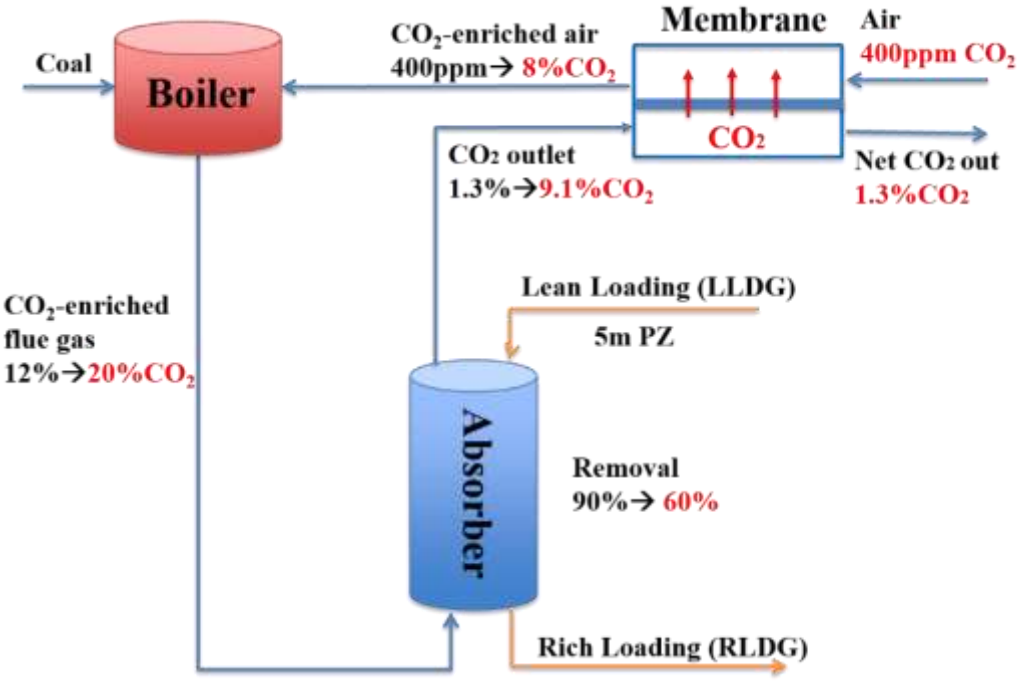

Figure 1: Hybrid-series system combining amine scrubbing with membrane technology

In the hybrid-series arrangement (Figure 1) (Freeman et al., 2014) the outlet CO_2 can be increased to 9.1% and removal can be reduced to 60%, which will result in smaller absorber packing height. With a larger driving force at the top and bottom of the absorber, higher lean loading can be used.

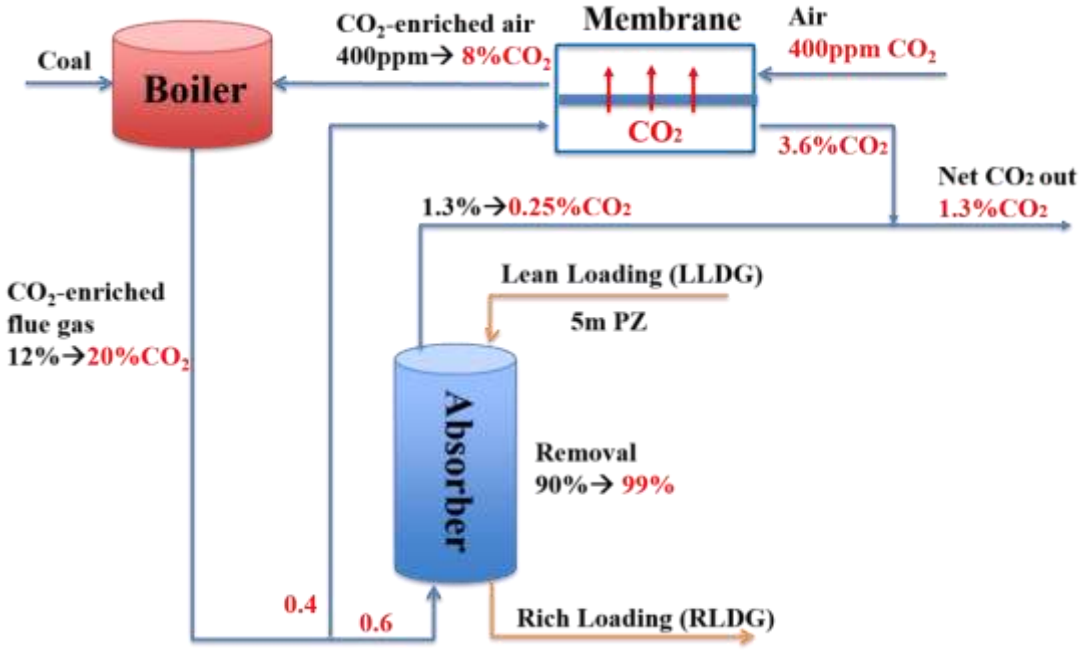

Figure 2: Hybrid-parallel system combining amine scrubbing with membrane technology

In hybrid-parallel arrangement (Figure 2), CO_2 removal can be increased to 99%. Both the absorber and the membrane will process less CO_2, which requires a smaller absorber diameter and smaller membrane area.

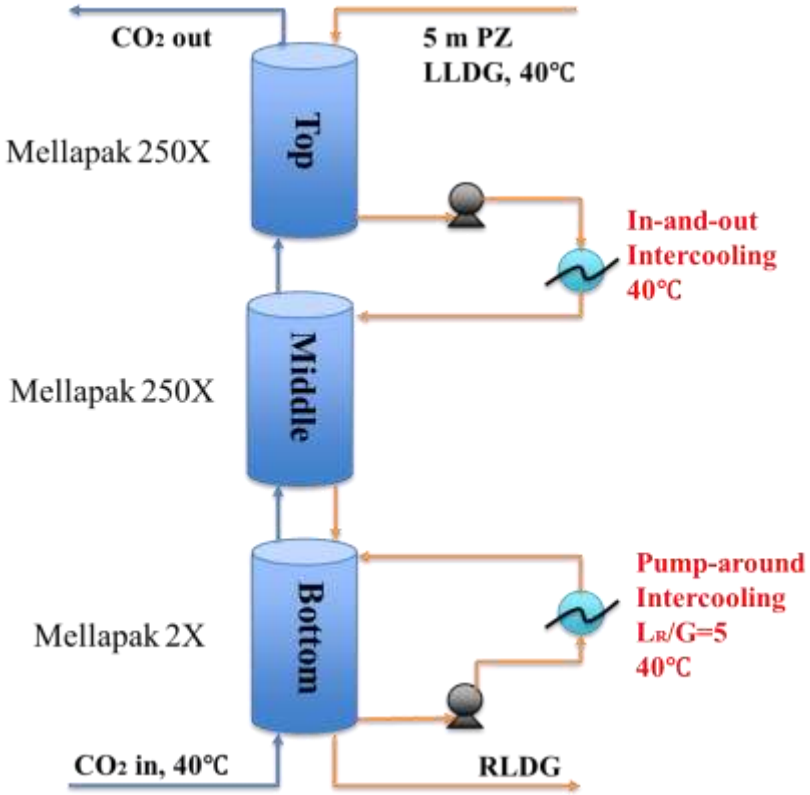

Figure 3: In-and-out and pump-around intercooling

Mellapak 2X was chosen for the bottom pump-around section and Mellapak 250X was chosen for the top and middle sections. In-and-out intercooling (I&O IC) in the middle of the absorber and pump-around intercooling (PA IC) around the bottom section were applied to the absorber (Figure 3). This absorber configuration was tested with four different cases: Cases 13 & 14 for hybrid-series arrangement and Cases 18 & 19 for hybrid-parallel arrangement. The corresponding purchased equipment costs for each case are listed in Table 1.

Table 1: Purchased equipment costs of hybrid-series and hybrid-parallel arrangement with I&O IC and PA IC with Mellapak 250X/250X/2X

Equipment Prices at 593 MWe		Series		Parallel	
		Case 13	Case 14	Case 18	Case 19
Operating conditions	% Removal	60%	60%	99%	95%
	Inlet CO_2	18%	18%	20%	20%
	LLDG	0.29 (over-stripping)	0.378 (normal)	0.227 (normal)	0.303 (normal)

	RLDG	0.404	0.415	0.398	0.408
	L/G	5	16	6	9
	Diameter (m)	19	22	16	17
	Height (m)	7	15	9	11
Purchased Equipment Costs	Absorber ($M)	16	26	13	13
	Rich/Lean Amine Exchanger ($M)	23	74	16	28
	Total costs ($M)	78	159	67	84

Table 1 shows that total purchased equipment cost for Cases 18 & 19 is less than that for Cases 13 & 14, suggesting that hybrid-parallel arrangement cases are better than hybrid-series arrangement cases. A new intercooling configuration, a solvent with larger capacity, and higher L/L_{min} were implemented to improve the absorber performance of Case 19. 5 m MDEA/5 m PZ offers higher CO_2 capacity but a lower absorption rate and higher viscosity compared with 5 m PZ, so it is expected to result in greater delta loading and lower stripper energy cost, but it may also result in a higher absorber packing height. This work simulates absorber performance of Case 19 with the Independence model (Frailie, 2014) for 5 m MDEA/5 m PZ in Aspen Plus® under different absorber packing types, intercooling configurations, and operating conditions. Economic analysis has also been included.

Absorber Performance of Case 19 with 5 m MDEA/5 m PZ

With simple pump-around intercooling

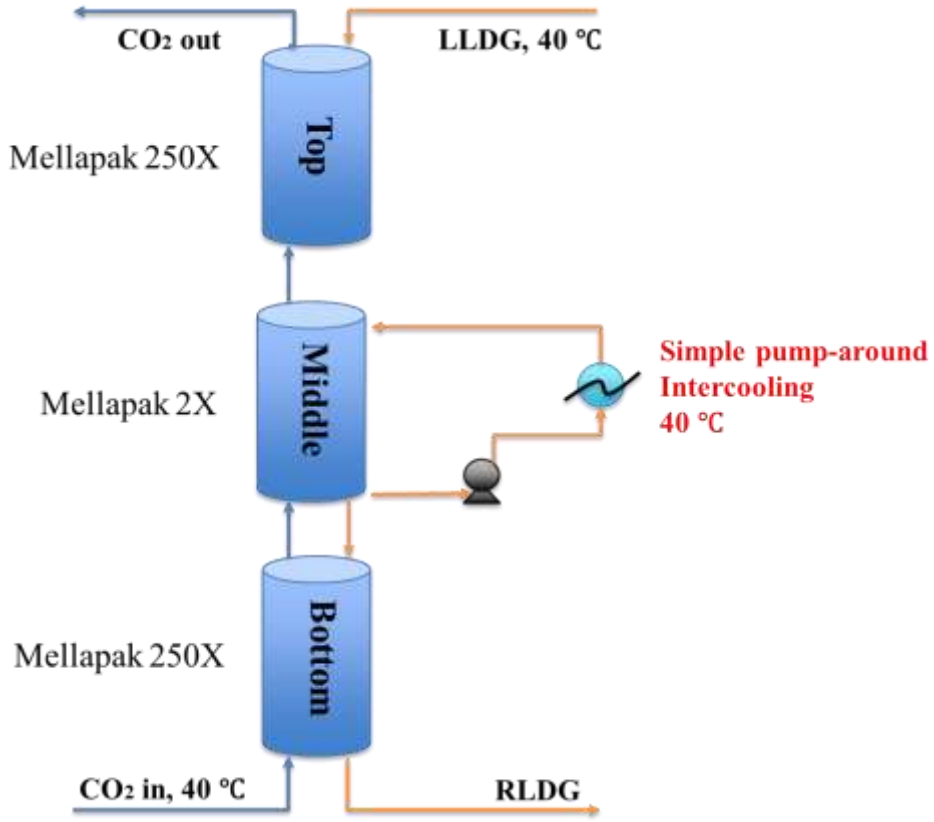

Figure 4: Simple pump-around intercooling

Based on Case 19 using 5 m PZ, Mellapak 2X was chosen for the pump-around section and Mellapak 250X was chosen for all the other sections. Simple pump-around intercooling around the middle section was first tested with 23.4% inlet CO_2, 95% removal, and 0.209 lean loading. For Case 19-1, liquid feed flow rate (L) was first set at $1.1*L_{min}$ and the pump-around intercooling L_R/G was set at 5 mol/mol. For Case 19-2, L was increased to $1.2*L_{min}$ and the pump-around intercooling L_R/G was kept at 5 mol/mol. Then L was kept at $1.2*L_{min}$ and the pump-around intercooling L_R/G was increased to 10 mol/mol, as Case 19-2(1). Aspen Plus®-calculated absorber results with optimized intercooling position are listed in Table 2. Figure 5 shows the liquid and vapor temperature as well as normalized flux along the column for Case 19-2(1).

Table 2: Absorber performance of Case 19 with simple pump-around intercooling with Mellapak 250X/2X/250X

Case	RLDG	L_R/G	L/L_{min}	Total Surface Area ($1000*m^2$)	Surface Area Fraction			Normalized Packing ($sec*m^2/mol$)
					Top	Mid	Bot	
19-1	0.368	5	1.1	1475.7	0.3	0.6	0.1	635
19-2	0.355	5	1.2	1316.8	0.3	0.6	0.1	567
19-2(1)	0.363	10	1.2	1072.8	0.4	0.5	0.2	462

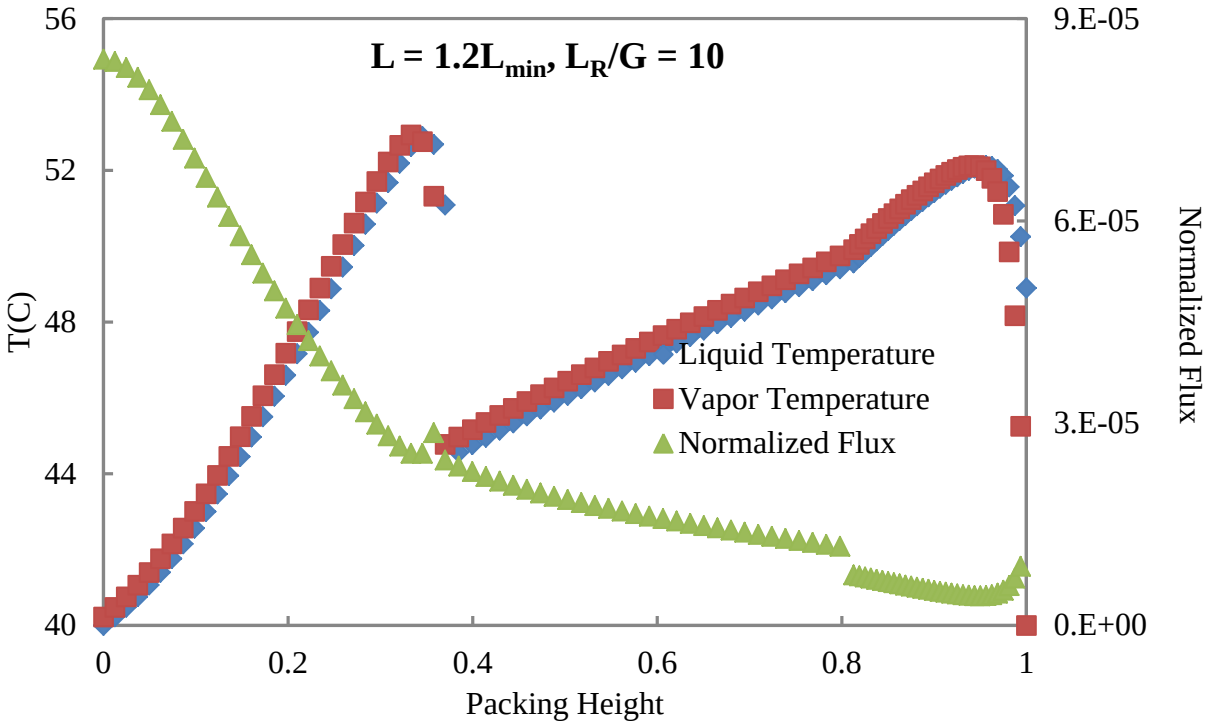

Figure 5: Normalized flux and temperature profile for Case 19-3

Table 2 shows that total surface area decreases in Case 19-2, suggesting that the absorber performs better at 1.2*L_{min}. When the pump-around recycle rate is increased, the total surface area is even lower (Case 19-3), suggesting that the absorber performs better at a higher lean solvent rate and a higher pump-around recycle rate. Figure 5 shows that the simple pump-around intercooling cannot cool the gas and liquid to 40 °C, and the temperature bulge in the bottom section limits the mass transfer rate. A more advanced intercooling configuration is required to cool down the hot gas and liquid.

Absorber performance of Case 19 with advanced pump-around intercooling

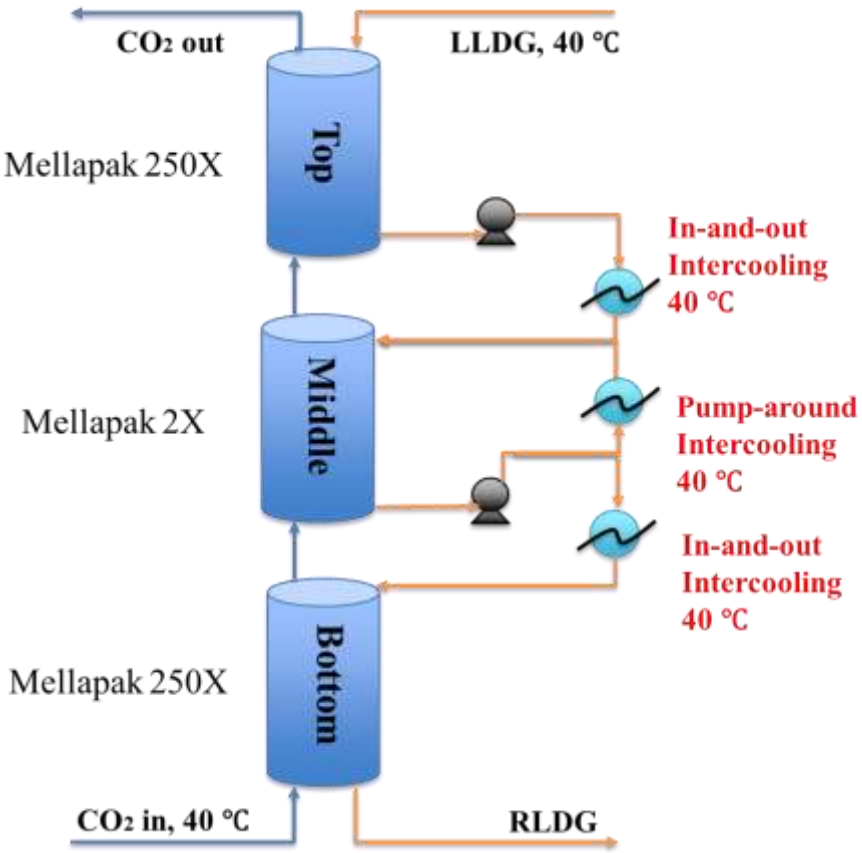

Figure 6: Advanced pump-around intercooling

Two in-and-out intercoolings are added above and below the pump-around intercooling, which is called advanced pump-around intercooling. L/L_{min} was first set at 1.2, and L_R/G was set at 10 mol/mol (Case 19-3) and 15 mol/mol (Case 19-3(1)). L_R/G was set at 10 mol/mol and L/L_{min} was increased to 1.3 (Case 19-4). Aspen Plus® was used to calculate absorber results with optimized intercooling position, as listed in Table 3. The absorber liquid/gas temperature profile and the normalized flux along the column of Case 19-3 are shown in Figure 7.

Table 3: Absorber performance with advanced pump-around intercooling with Mellapak 250X/2X/250X

Case	RLDG	L_R/G	L/L_{min}	Surface Area Fraction			Normalized Packing(sec*m^2/mol)
				Top	Mid	Bot	
19-3	0.404	10	1.2	0.30	0.54	0.21	670
19-3(1)	0.406	15	1.2	0.31	0.57	0.18	692
19-4	0.389	10	1.3	0.35	0.51	0.20	522

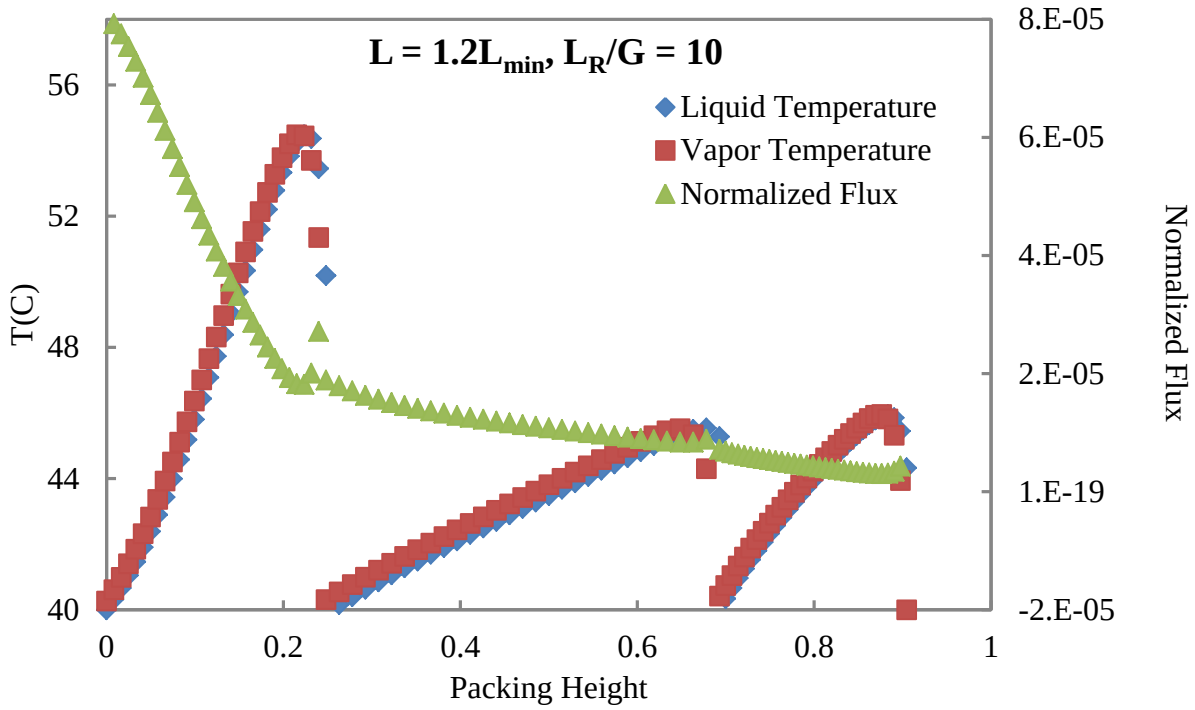

Figure 7: Normalized flux and temperature profile of Case 19-4

As shown in Table 3, rich loading of advanced pump-around intercooling cases is higher than that of simple pump-around cases, which results in better stripper energy performance. The absorber liquid/gas temperature profile suggests that the advanced pump-around intercooling can cool the gas and liquid to 40 °C before entering the next stage (Figure 7). Table 3 shows that for a fixed L_R/G, both the absorber normalized packing and RLDG decrease with L/L_{min}. Absorber capital costs can be saved but stripper energy performance is worse. Although increased solvent recycling improves the mass transfer rate, it is easier to cause flooding in the pump-around section, as a result of which the diameter becomes larger and normalized packing increases. When L/L_{min} increases from 1.2 to 1.3, both RLDG and normalized packing decrease, resulting in lower absorber capital costs and higher exchanger costs. Further economic analysis has been done to determine the best case.

Absorber economics of Case 19 with 5 m PZ and 5 m MDEA/5 m PZ

Calculation methods for absorber costing are based on Frailie (Frailie, 2014) Absorber operating conditions and corresponding total purchased equipment costs of Case 19-PZ and Case 19-4 are listed in Table 4.

Table 4: Absorber operating conditions and total purchased equipment costs of Case 19 with 5 m PZ and 5 m MDEA/5 m PZ

Equipment Prices at 593 MWe		Case 19-PZ	Case 19-4
Operating Conditions	Solvent	5 m PZ	5 m MDEA/5 m PZ
	L/L_{min}	1.1	1.3
	IC type	I&O IC and PA	Advanced PA IC

		IC	
	LLDG	0.303 (normal)	0.209 (normal)
	RLDG	0.411	0.389
	L/G	10	6
	Diameter (m)	16	15
	Height (m)	10	29
Total Purchased Equipment Costs	Absorber ($M)	13	22
	Rich/Lean Amine Exchanger ($M)	26	9
	Total costs ($M)	79	67

Table 4 shows that the delta loading of 5 m MDEA/5 m PZ increases by 66% due to the high CO_2 capacity, but packing height increases by 190% due to low absorption rate and high viscosity. The stripper benefits significantly from the greater delta loading and lower lean solvent flow rate, but the lower absorption rate results in higher absorber costs. Table 4 shows that absorber column costs increase by 69%, and total purchased equipment costs go down by 15%.

Future work

Cases with over-stripping LLDG will be tested to lower the absorber packing height.

Conclusions

1. The advanced pump-around intercooling (with two in-and-out intercoolings added above and below) is more efficient than the simple pump-around intercooling. It can sufficiently cool down the gas and liquid to 40 °C before entering the next stage.

2. The delta loading of 5 m MDEA/5 m PZ increases by 66% due to the high CO_2 capacity, but packing height increases by 190% due to low absorption rate and high viscosity.

3. With 5 m MDEA/5 m PZ, absorber column costs increase by 69%, and total purchased equipment costs go down by 15%.

References

Freeman B, Hao P, Baker R, Kniep J, Chen E, Ding J, Zhang Y, Rochelle GT. "Hybrid membrane-absorption CO_2 capture process". Presented at *GHGT-12*, Austin. October 5–9, 2014.

Frailie PT. *Modeling of Carbon Dioxide Absorption/Stripping by Aqueous Methyldiethanolamine/Piperazine*. The Univeristy of Texas at Austin. Ph.D. Dissertation. 2014.

Zhang Y, Rochelle GT. Absorber Performance with High CO_2. Presented at *GHGT-12*, Austin. October 59, 2014.

Stripper Performance and Equipment Costs Using 5 m PZ and MDEA/PZ

Quarterly Report for October 1 – December 31, 2014

by Junyuan Ding

Supported by Membrane Technology and Research, Inc.,

and the DOE cooperative agreement DE-FE0013188

McKetta Department of Chemical Engineering

The University of Texas at Austin

January 31, 2015

Abstract

In previous work, four cases whose inlet CO_2 concentration and CO_2 removal rate were given by MTR (Cases 13, 14, 18-1, and 19-1) were simulated using 5 m piperazine (PZ) based on absorber performance. Due to the outstanding energy properties of aqueous PZ, including high CO_2 capacity, high thermal stability, moderately high viscosity, oxidative degradation resistance, and low volatility in CO_2-loaded solutions, it is a superior solvent for CO_2 capture by amine scrubbing. 5 m PZ minimizes the precipitation problem that the more viscous 8 m PZ causes in the solvent loop.

Since 5 m MDEA/5 m PZ has a greater CO_2 capacity than 5 m PZ, Case 18-MDEA/PZ (Case 18-2) and Case 19-MDEA/PZ (Cases 19-2, 19-3, and 19-4) using 5 m MDEA/5 m PZ stripping at 120 °C were studied to reduce the heat duty compared with Case 18-1 (rich loading of 0.401 mol CO_2/mol N and lean loading of 0.227 mol CO_2/mol N) and Case 19-1 (rich loading of 0.411 mol CO_2/mol N and lean loading of 0.303 mol CO_2/mol N) using 5 m PZ. The base-case stripping configuration was the advanced flash with warm rich bypass and cold rich exchanger bypass. The Independence model for MDEA/PZ in Aspen Plus® was used to simulate the stripping performance. Equipment costs for Cases 18 and 19 using 5 m PZ and 5 m MDEA/5 m PZ were analyzed according to the economic part of the Frailie dissertation.

Previous work optimized stripping using 5 m PZ with rich loading from 0.37 to 0.43 mol CO_2/mol N. In this work, 5 m MDEA/5 m PZ with a wide range of rich loading stripping at 150 ℃ was studied to simulate the stripper energy performance of a similar tertiary amine.

1: Stripper Performance and Equipment Costs Using 5 m MDEA/5 m PZ

Introduction

Figure 1 shows the hybrid amine/membrane CO_2 capture process developed by combining a CO_2 membrane separator with the absorber/stripper. The membrane separator was developed by

Membrane Technology and Research, Inc. (MTR). The absorber and stripper performance is simulated using the Independence model for PZ in Aspen Plus®.

Due to the high CO_2 capacity of MDEA/PZ, less solvent is regenerated for the same amount of CO_2 product. Stripping energy will be reduced by substituting 5 m MDEA/5 m PZ for 5 m PZ. Equipment cost is also expected to decrease because of the smaller lean/rich amine exchanger although more stages of compressor are required. The lower CO_2 loading limit for 5 m MDEA/5 m PZ is also higher than 5 m PZ, which means it is not as effective as 5 m PZ for low CO_2 inlet concentration. The absorption rate of 5 m MDEA/5 m PZ is also lower than 5 m PZ. The capital cost of the absorber will increase since the required packing height increases.

If most of the gas were sent to the membrane unit, a large area of membrane would be needed to achieve efficient removal of the CO_2 into the air stream. This would be expensive, but would have the benefit that the concentration of CO_2 in the flue gas would increase to around 25%.

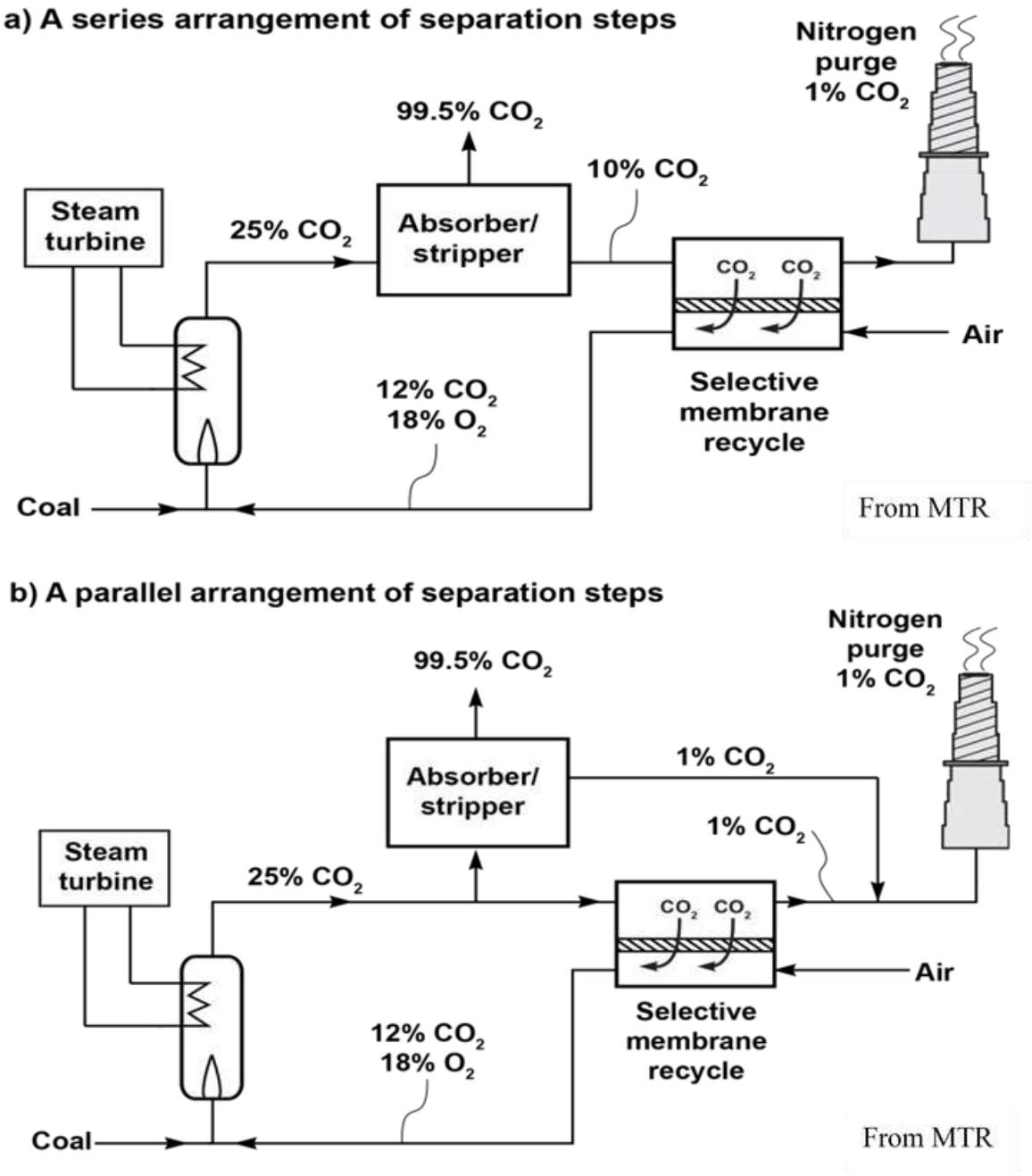

Figure 1: Two configurations of hybrid amine/membrane CO_2 capture model

Methods

Hybrid amine/membrane

The amine regeneration system for the hybrid amine/membrane process was simulated using the Independence model in Aspen Plus®. Figure 2 shows the advanced flash stripper configuration. All of these cases are simulated using 5 m MDEA/5 m PZ stripping at 120 °C, main exchanger

LMTD = 5 °C, top exchanger LMTD = 20 °C, lean solvent output at 40 °C, and 150 bar CO_2 product.

When CO_2 rich loading and lean loading of the advanced flash stripper are given, the overall equivalent work will vary with the cold rich bypass and warm rich bypass. There is an optimal point where the equivalent work is minimized. The corresponding cold rich bypass and warm rich bypass is the optimal bypass for this specific CO_2 rich and lean loading.

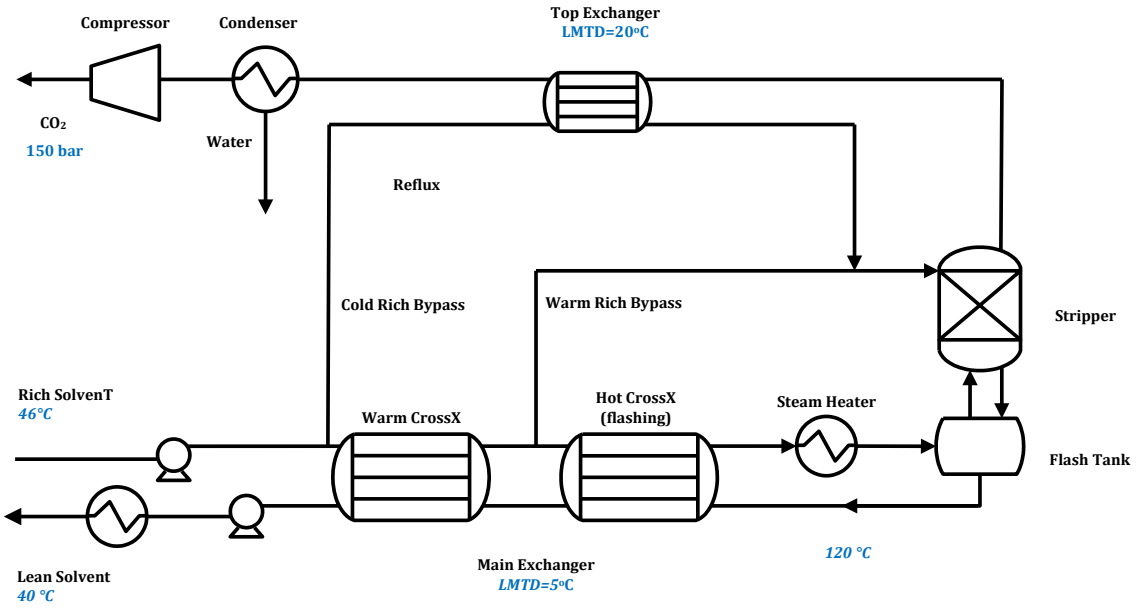

Figure 2: Stripping configuration using 5 m MDEA/5 m PZ

Equivalent Work Calculation

Equivalent work replaces heat duty as a more general metric of energy use than heat duty alone. It is defined as the sum of pump work, compression work, and heat work, as Equation 1 shows.

$$W_{eq}\ (\text{kJ/mol}\quad CO_2) = W_{heat} + W_{pump} + W_{comp} \tag{1}$$

Heating work can be generated from the heat duty of the reboiler using Equation 2. A typical value of 90% is used for the turbine efficiency (η) and T_{sink} is taken as 313K.

$$W_{heat}\ (\text{kJ/mol}\quad CO_2) = \eta\left(\frac{T_{source} + \Delta T - T_{sink}}{T_{source} + \Delta T}\right)Q_{reb} \tag{2}$$

Compression work can be approximated by Equation 3, which is typically assumed to be at a discharge pressure of 150 bar.

$$W_{comp}\ (\text{kJ/mol}\quad CO_2) = \begin{cases} 4.572\ \ln\left(\frac{150}{P_{in}}\right) - 4.096 & \cdots P_{in} \le 4.56\ bar \\ 4.023\ \ln\left(\frac{150}{P_{in}}\right) - 2.181 & \cdots P_{in} \ge 4.56\ bar \end{cases} \tag{3}$$

Process Safety

The stripper pressure should never exceed the pressure rating of the vessel. The stripper vessel will be equipped with a relief valve that will discharge the CO_2/amine mixture to a safe, low pressure point, probably the inlet to the absorber.

Results and Discussion

Stripper Performance Using 5 m MDEA/5 m PZ (Case 19-MDEA/PZ)

Table 1: Comparison of stripper performance using 5 m PZ and MDEA/PZ

Case	19-1	19-2	19-3	19-4
Solvent	5 m PZ	5 m MDEA/ 5 m PZ	5 m MDEA/ 5 m PZ	5 m MDEA/ 5 m PZ
L/Lmin	1.2	1.2	1.2	1.3
Packing Type	250X 2X 250X	250X 250X 250X	250X 2X 250X	250X 2X 250X
CO_2 rich loading (mol CO_2/mol N)	0.411	0.398	0.404	0.389
CO_2 lean loading (mol CO_2/mol N)	0.303	0.209	0.209	0.209
Pressure (bar)	8.69	2.80	2.81	2.80
Cold rich bypass (%)	4	8	8	9
Warm rich bypass (%)	10	30	30	24
Heat duty (kJ/mol CO_2)	93.32	94.60	93.83	95.78
Equivalent work (kJ/mol CO_2)	33.28	32.45	32.29	32.69

Table 1 compares the energy performance of Case 19 using 5 m PZ and 5 m MDEA/5 m PZ. Case 19-1 is the base case using 5 m PZ. Case 19-2 is the base case using 5 m PZ/5 m MDEA. Case 19-3 changed the second packing section of the absorber from 250 X to 2 X to reduce absorber capital cost. Case 19-4 uses 1.3 L_{min} for the absorber instead of 1.2 L_{min} to reduce required packing height. At the same CO_2 partial pressure, L/G and stripping pressure are much lower for the blended solvent. As a result, compression work is a little higher and pump work is much lower. The total equivalent work of 5 m MDEA/5 m PZ is lower than that of 5 m PZ.

Table 2: Purchased Equipment Cost of Case 19 using 5 m PZ and 5 m MDEA/5 m PZ at 593 MWe in Million dollars

Description	Case 19	Case 19-2	Case 19-3	Case 19-4
Inlet Gas Blower	2.84	2.84	2.84	2.84
Absorber	13.44	26.16	25.54	21.84
Absorber Intercooler	2.74	2.22	2.09	2.22
Absorber Intercooler Pump	2.22	2.48	1.71	1.77
Rich Amine Pump	0.97	0.54	0.50	0.53
Rich Amine Carbon Filter	0.17	0.12	0.11	0.12
Particulate Filter	0.14	0.14	0.14	0.14
Rich/Lean Amine	25.84	8.88	8.61	9.14

Exchanger				
Lean Solvent Cooler	1.31	0.78	0.65	0.78
Stripper	0.71	0.98	0.96	0.96
	1.01	0.69	0.67	0.71
Steam Heater	8.08	8.15	8.09	8.21
Overhead Condenser	0.52	0.78	0.78	0.78
Overhead Accumulator	0.03	0.03	0.03	0.03
Compressors	10.04	12.20	12.19	12.20
Multi-stage Centrifugal Pump	0.54	0.54	0.54	0.54
Makeup Amine Tank	0.35	0.35	0.35	0.35
Makeup Amine Pump	0.01	0.01	0.01	0.01
Water Tank	0.10	0.10	0.10	0.10
Water Pump	0.01	0.01	0.01	0.01
Surge Tank	0.93	0.63	0.62	0.65
Lean MEA Pump	0.60	0.33	0.31	0.33
Reclaimer	4.91	2.58	2.49	2.70
Dehydration Unit	1.97	1.97	1.97	1.97
Total	79.49	73.48	71.33	68.93
Capture	66.94	58.78	56.63	54.22
Compression	12.55	14.70	14.70	14.70

Table 2 shows the purchased equipment costs of Case 19 using 5 m PZ and 5 m MDEA/5 m PZ of 593 MWe based on Frailie (2014). For the stripper, the cost centers are the heat exchangers, steam heater, and compressors. Total equipment costs for the blended solvent are lower than those for 5 m PZ. The principle differences are in the main exchanger, compressor, and reclaimer, due to lower solvent flow rate caused by higher CO_2 capacity. Case 19-2 has an absorber capital cost about twice that of Case 19-1, and a higher compressor cost. The costs associated with the rich amine pump, main heat exchanger, lean solvent cooler, and reclaimer are considerably lower due to the lower solvent rate. The total capital cost of Case 19-2 is therefore 1/12 that of Case 19-1. The absorber cost of Case 19-3 decreased from Case 19-2 while stripper cost reduced just a little. The absorber cost of Case 19-4 is significantly less than that of Case 19-2 while the stripper cost increased slightly. Both cases using 5 m PZ and 5 m MDEA/5 m PZ are using main exchanger LMTD of 5 °C, which might not be their optimum LMTD. Energy performance and equipment costs will be different from these two tables when using their optimum LMTD.

Conclusions

1. The energy cost of using MDEA/PZ is lower than using 5 m PZ. For Case 19, equivalent work using 5 m MDEA/5 m PZ (32.69 kJ/mol CO_2) is less than using 5 m PZ (33.28 kJ/mol CO_2).

2. The capital cost of Case 19-4 using MDEA/PZ (MM$ 68.93) is less than using PZ (MM$79.49).

2: Stripper Performance using 5 m PZ/5 m MDEA

Introduction

This work focuses on simulating the energy performance of a tertiary amine/PZ blend, which has similar properties to MDEA/PZ. The simulations were performed with rich loading of 0.34 and 0.37 mol/equiv PZ in 5 m PZ/5 m MDEA.

Output CO_2 pressure, heat duty, compression work, pump work, and cold/warm rich bypass are recorded and calculated. For each CO_2 rich loading, there is an optimal lean loading, which requires the minimum equivalent work for CO_2 scrubbing. The absorber and stripper performance is simulated using the Independence model for PZ in Aspen Plus®.

Methods

The amine regeneration system for the hybrid amine/membrane process was simulated using the Independence model in Aspen Plus®. Figure 1 shows the advanced flash stripper configuration. All of these cases' energy performances are simulated using 5 m PZ/5 m MDEA stripping at 150 °C, main exchanger LMTD = 5 °C, top exchanger LMTD = 20 °C, lean solvent output at 40 °C, and 150 bar CO_2 product pressure.

When CO_2 rich loading and lean loading of the advanced flash stripper are given, the overall equivalent work will vary with the cold rich bypass and warm rich bypass. There is an optimal point where the equivalent work is minimized. The corresponding cold rich bypass and warm rich bypass will be the optimal bypass for this specific CO_2 rich and lean loading.

Lean loading as partial pressure of CO_2 at 40 °C in kPa is a surrogate for lean loading in mol CO_2/mol alkalinity to be plotted on the X axis to compare energy performance of 5 m MDEA/5 m PZ and 5 m PZ. The lean loading range is from 0.5 kPa to 1.28 kPa partial pressure of CO_2. 5 m PZ at a rich loading of 0.4 mol CO_2/mol alkalinity has 7.63 kPa partial pressure of CO_2. 5 m PZ/5 m MDEA rich loading of 0.34 mol CO_2/mol alkalinity has 5.1 kPa partial pressure of CO_2. 5 m PZ/5 m MDEA rich loading of 0.37 mol CO_2/mol alkalinity has 5.55 kPa partial pressure of CO_2.

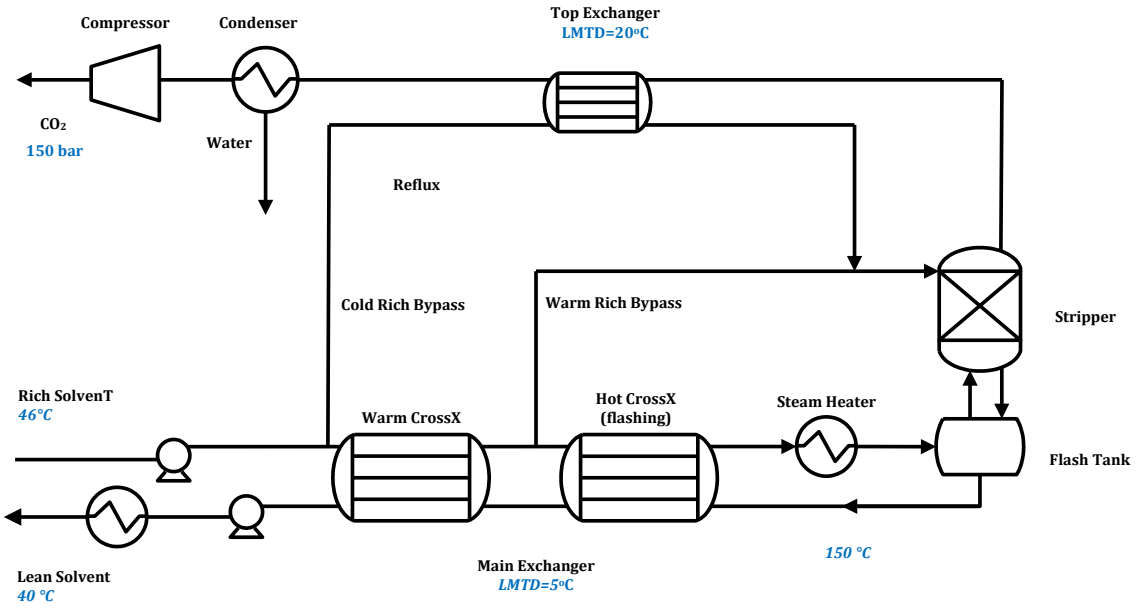

Figure 1: Stripping configuration using 5 m PZ/5 m MDEA and 5 m PZ

Equivalent Work Calculation

Equivalent work replaces heat duty as a more general metric of energy use than heat duty alone. It is defined as the sum of pump work, compression work, and heat work, as Equation 1 shows.

$$W_{eq}\ (\text{kJ/mol}\ \ CO_2) = W_{heat} + W_{pump} + W_{comp} \quad (1)$$

Heating work can be generated from the heat duty of the reboiler using Equation 2. A typical value of 90% is used for the turbine efficiency (η) and T_{sink} is taken as 313K.

$$W_{heat}\ (\text{kJ/mol}\ \ CO_2) = \eta\left(\frac{T_{source} + \Delta T - T_{sink}}{T_{source} + \Delta T}\right)Q_{reb} \quad (2)$$

Compression work can be approximated by Equation 3, which is typically assumed to be at a discharge pressure of 150 bar.

$$W_{comp}\ (\text{kJ/mol}\ \ CO_2) = \begin{cases} 4.572\ \ln\left(\frac{150}{P_{in}}\right) - 4.096 & \cdots P_{in} \le 4.56\ bar \\ 4.023\ \ln\left(\frac{150}{P_{in}}\right) - 2.181 & \cdots P_{in} \ge 4.56\ bar \end{cases} \quad (3)$$

Results and Discussion

Regression analysis over a wider range of rich loading

Table 1 shows the partial pressure and optimal lean loading at different CO_2 rich loading of 5 m PZ and 5 m MDEA/5 m PZ. Figure 2 compares the total equivalent work for variable CO_2 rich loading of 5 m PZ/5 m MDEA and 5 m PZ. As CO_2 rich loading increases, the total equivalent work requirement decreases for the same lean loading. Since CO_2 capacity becomes dominant at high lean loading, total equivalent work for all these rich loadings changes rapidly at high lean

loading values and becomes flat at the low lean loading end. 5 m PZ/5 m MDEA has lower energy consumption than 5 m PZ.

Table 1: Partial pressure and optimal lean loading at different CO_2 rich loading of 5 m PZ and 5 m MDEA/5 m PZ

Solvent	5 m PZ	5 m MDEA/5 m PZ	5 m MDEA/5 m PZ
CO_2 rich loading (mol CO_2/mol N)	0.40	0.34	0.37
Rich loading as partial pressure of CO_2 (kPa)	7.63	5.1	5.55
Optimum CO_2 lean loading (mol CO_2/mol N)	0.26	0.19	0.21
Optimum lean loading as partial pressure of CO_2 (kPa)	0.16	0.30	0.46

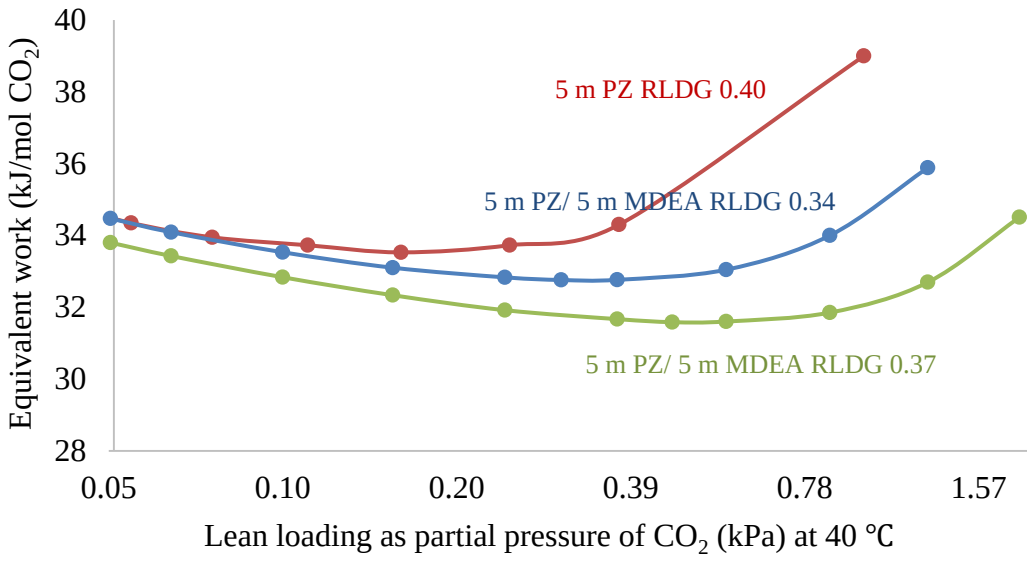

Figure 2: Equivalent work of different solvents at different rich and lean loadings

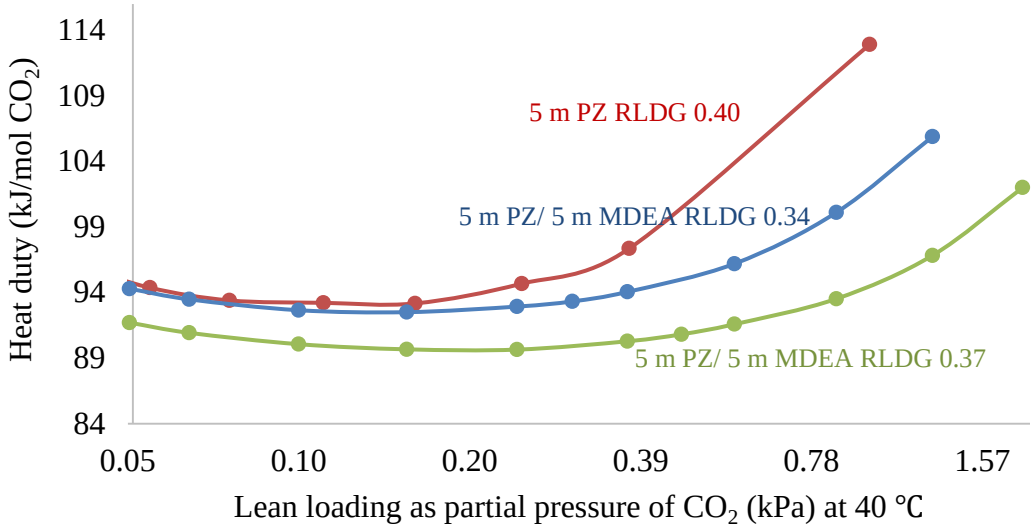

Figure 3: Heat duty of different solvents at different rich and lean loadings

Heat duty of the stream heater is composed of sensible heat requirement, latent heat requirement, and stripping steam heat requirement. Heat work accounts for about 70% of the total equivalent work. Figure 3 shows the comparison of heat duty for different solvents at different rich and lean loadings. Heat duty also has its minimum value at a CO_2 loading difference of 0.14 mol CO_2/mol PZ. The sensible heat requirement dominates at high lean loading (low capacity). The stripping steam requirement dominates at low lean loading. 5 m PZ has its optimum lean loading point at 0.26 mol CO_2/ mol alkalinity (0.16 kPa) lean loading with 0.4 mol CO_2/mol alkalinity (7.63 kPa) rich loading, which is the same as the optimum total equivalent work lean loading. 5 m PZ/5 m MDEA has its optimum lean loading point at 0.22 mol CO_2/ mol alkalinity (0.15 kPa) lean loading with 0.34 mol CO_2/mol alkalinity (5.1 kPa) rich loading, and 0.18 mol CO_2/mol alkalinity (0.24 kPa) lean loading with 0.37 mol CO_2/mol alkalinity (5.55 kPa) rich loading, which is lower than the optimum total equivalent work lean loading.

Thermodynamically, the stripping pressure at 150 °C (Figure 4) of 5 m PZ/5 m MDEA depends only on the lean loading. At the same stripping temperature and lean loading partial pressure of CO_2, 5 m PZ/5 m MDEA has a higher stripping pressure than 5 m PZ.

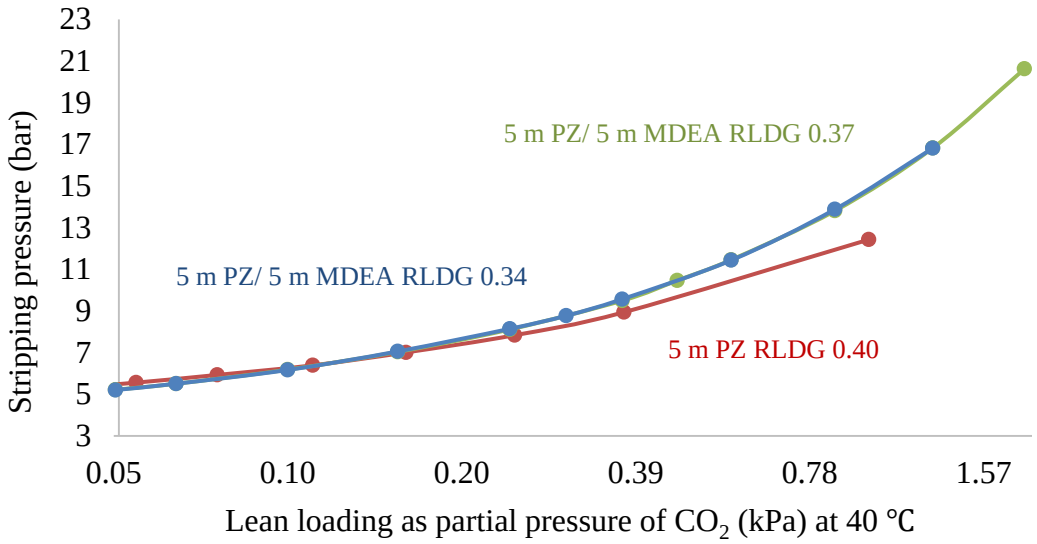

Figure 4: Stripping pressure of different solvents at different rich and lean loadings

Conclusions

As the 5 m PZ/5 m MDEA CO_2 rich loading varies from 0.34 to 0.37, the optimum lean loading increases from 0.19 to 0.21 mol/equivalent PZ CO_2, and the minimum total equivalent work decreases from 32.8 kJ/mol CO_2 to 31.6 kJ/mol CO_2., both lower than that of 5 m PZ.

Future Work

1. Compare MTR Case 18 results using 5 m PZ and 5 m MDEA/5 m PZ.
2. Optimize stripper performance using 5 m MDEA/5 m PZ.
3. Develop the ammonia purging model based on amine degradation rate and ammonia emission standard.
4. Simulate stripper energy performance using 5 m PZ for pilot plant.

References

Frailie PT. *Modeling of Carbon Dioxide Absorption/Stripping by Aqueous methyldiethanolamine/Piperazine.* The University of Texas at Austin. Ph.D. Dissertation. 2014.

Freeman B, Hao P, Baker R, Kniept J, Chen E, Ding J, Zhang Y, Rochelle GT. "Hybrid membrane-absorption CO_2 capture process." Presented at GHGT-12, Austin, United States, October 6, 2014.

Freeman SA. *Thermal Degradation and Oxidation of Aqueous Piperazine for Carbon Dioxide Capture.* The University of Texas at Austin. Ph.D. Dissertation. 2011.

Lin Y-J, Madan T, Rochelle GT. "Regeneration with Rich Bypass of Aqueous Piperazine and Monoethanolamine for CO_2 Capture." *IECR.* 2014;53:4067–4074.

Madan T. *Modeling of Stripper Configurations for CO_2 Capture using Aqueous Piperazine*. The University of Texas at Austin. M.S. Thesis. 2011.

Merkel TC, Lin H, Wei X. "Power plant post-combustion carbon dioxide capture: An

opportunity for membranes." *J Membr Sci.* 2010;359:115–125.

Rochelle GT et al. "CO_2 Capture by Aqueous Absorption, Second Quarterly Progress Report 2014." Texas Carbon Management Program. The University of Texas at Austin. 2014.

Van Wagener DH. *Stripper Modeling for CO_2 Removal Using Monoethanolamine and Piperazine Solvents.* The University of Texas at Austin. Ph.D. Dissertation. 2011.

Xu Q. *Thermodynamics of CO_2 Loaded Aqueous Amines.* The University of Texas at Austin. Ph.D. Dissertation. 2011.

Chapter 5: Mass Transfer Model Development

5.1 Area model

The effective mass transfer area model was developed based on the experimental data measured in this work. Table 5.1 lists the packings in the database along with their physical dimensions. The structured packings in the database were all stainless steel and manufactured by Sulzer ChemTech, GTC Technology, and Raschig. Every packing surface except those of Raschig SuperPak was perforated. The packing surface areas varied from 125 to 500 m^2/m^3 while the corrugation angles varied from 45 to 70 degrees. The channel dimensions (channel base B and crimp height h) in Table 5.1 are based on actual measurements. The channel dimensions and corrugation angle were used in the Mixing Points Density (M) calculation, which will be discussed in 5.2. Three random packings in the Raschig Super Ring family were also included in the database (Table 5.2).

Table 5.1 Structured packing information

Packing name	Surface area ($m^2/m3$)	Corrugation angle (deg)	Channel base, B (m)	Crimp height, h (m)
MP 125Y	125	45	0.0635	0.0254
RSP 200X	200	60	0.03175	0.004763
MP 2X	205	60	0.03175	0.014288
MP 250Y	250	45	0.03016	0.0111
MP 250X	250	60	0.0254	0.0111
RSP 250Y	250	60	0.03175	0.004763
GT-PAK^{TM} 350Y	350	45	0.0167	0.00754
GT-PAK^{TM} 350Z	350	70	0.0175	0.00794
A 350Y	350	45	0.0254	0.007938
B 350X	350	60	0.0175	0.009
GT-PAK^{TM} 500Y	500	45	0.0143	0.00635

Table 5.2. Random packing information

	Nominal size	Void fraction	Surface area
	mm	%	m^2/m^3
RSR#0.3	15	96	315
RSR#0.5	20	97	250
RSR#0.7	25	98	180

The effective mass transfer area model was developed based on Tsai's area model (2010). Tsai used dimensionless numbers to correlate the packing mass transfer area database. According to Tsai's experiments as well as effective area measurements conducted in this work, the effective area is assumed to be only a function of liquid flow rate, liquid density and surface tension, and considered to be independent of gas flow rate and liquid phase viscosity. This assumption is supported by the majority of experimental data, although at some conditions we do find the effective area slightly changes with gas flow rate. The effective mass transfer area model developed by Tsai is given in (5-1).

$$\frac{a_e}{a_P} = 1.34\,[(We_L)(Fr_L)^{-1/3}]^{0.116} \qquad (5\text{-}1)$$

Where,
We_L is the liquid phase Weber number, $\rho_L u_L^2 \delta_L/\sigma$;
Fr_L is the liquid phase Froude number, $u_L^2/g\delta_L$.

In the Tsai model, the liquid film thickness (δ_L) was used as the characteristic length. To calculate the liquid film thickness, the classic Nusselt film thickness assumption (Bird et al., 2002) was used:

$$\delta_{Nusslet} = \sqrt{\frac{3u_{film}\mu_L}{\rho_L g \sin\theta}} = \sqrt[3]{\frac{3\mu_L}{\rho_L g \sin\theta}\left(\frac{Q}{L_P}\right)} \qquad (5\text{-}2)$$

Thus, the dimensionless number group can be expressed by:

$$(We_L)(Fr_L)^{-1/3} = \left(\frac{\rho_L}{\sigma}\right) g^{1/3} \left(\frac{Q}{L_P}\right)^{4/3} \qquad (5\text{-}3)$$

Where,
Q is the volumetric liquid flow rate, (m^3/s);
L_P is the wetted perimeter, m.
For structured packings, the wetted perimeter can be calculated from channel dimensions:

$$L_P = A * \frac{4S}{Bh} \qquad (5\text{-}4)$$

Where,
A is the column cross section area, (m^2);
S is the packing channel side, (m);
B is the packing channel base, (m);
h is the packing crimp height, (m).

However, with a larger scope including random packings and hybrid packings such as Raschig Super-Pak family, the original Tsai model is not applicable. In those situations where channel dimensions are not known or hardly defined, using liquid superficial velocity over packing total area (u_L/a_P) instead of (Q/L_P) is a good alternative. The mass transfer area model in this work is developed based on Tsai model, utilizes u_L/a_P as the liquid flow rate per wetted perimeter. The experimental coefficient is changed from 1.34 to 1.41 which provides a better fit of the larger database.

$$\frac{a_e}{a_P} = 1.41\,[(\frac{\rho_L}{\sigma}) g^{1/3} (\frac{u_L}{a_P})^{4/3}]^{0.116} \qquad (5\text{-}5)$$

Figure 5.1a shows the comparison of the experimental data and the modified Tsai model. Figure 5.1b shows the fractional mass transfer area plotted over the dimensionless number group $(We_L)(Fr_L)^{-1/3}$. The database includes 14 packings measured in this work and contains a large scope of packing type (structured, random, and hybrid). The model shows a good fit with most data except for GT-PAK^{TM} 500Y, which shows a lower effective area than predicted. The average deviation of this area model is 10.5%, which is quite acceptable considering the broad scope of the packing type.

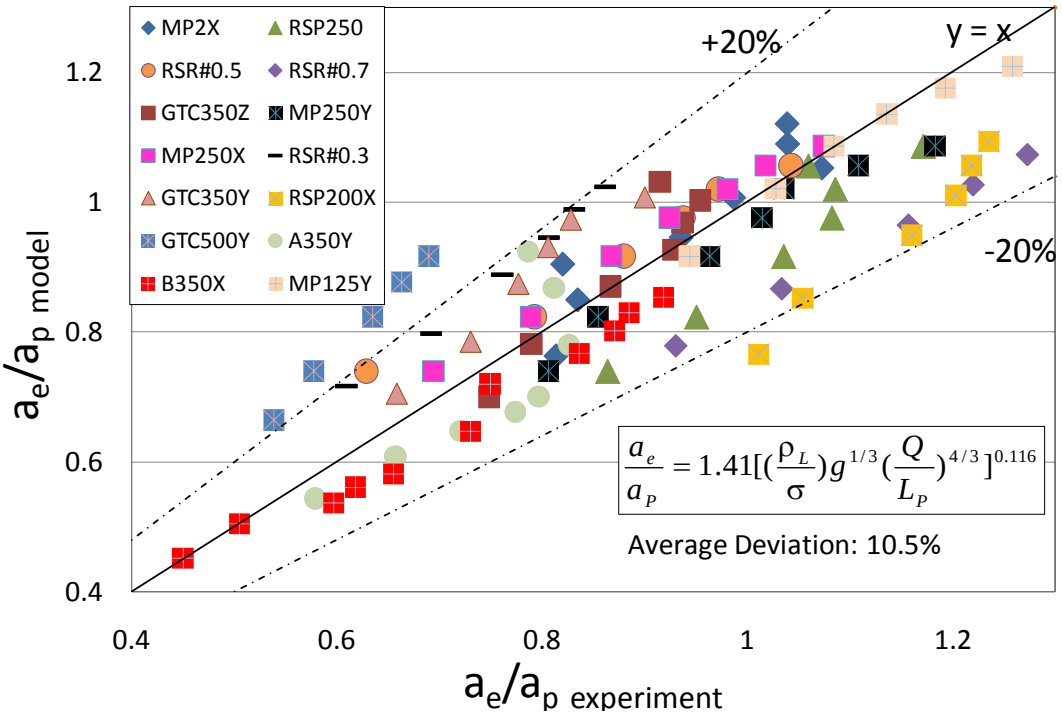

Figure 5.1a. Comparison of experimental data and modified Tsai model

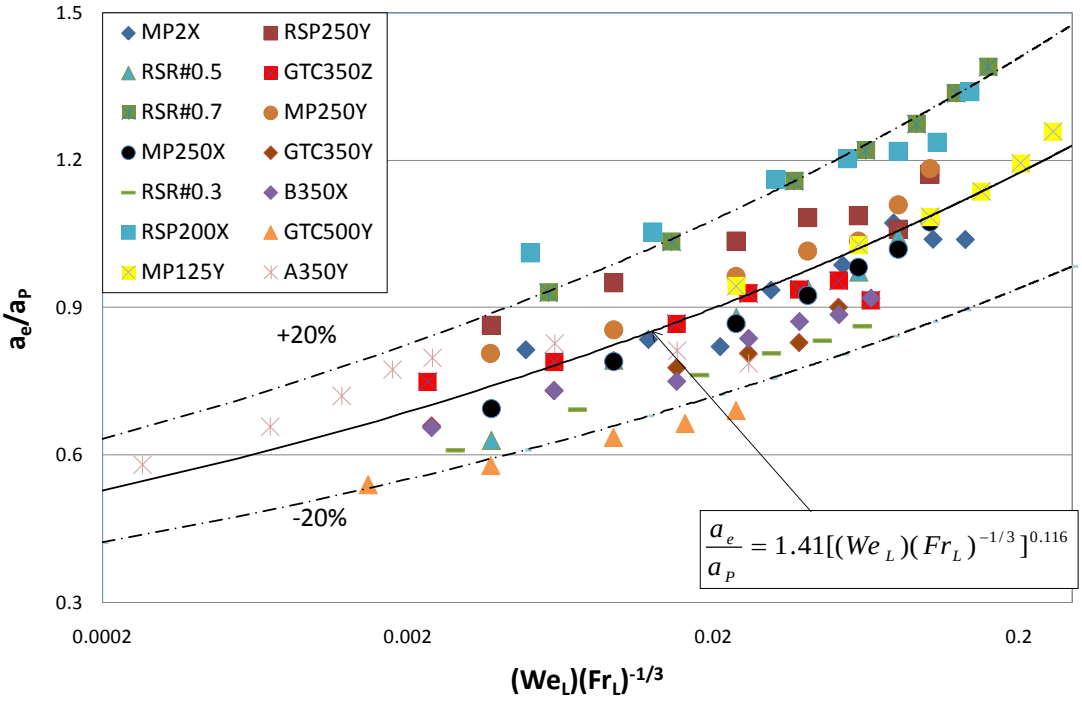

Figure 5.1b. Fractional mass transfer area shown in dimensionless group

5.2 Comparison with literature area models

Previous mass transfer models have been thoroughly discussed in Chapter 2. The mass transfer

area model developed in this work is compared with previous mass transfer area models. The experimental data are also displayed for reference. The correlations are reproduced from Chapter 2.

Onda et al. (1968):

$$\frac{a_e}{a_P} = 1 - \exp[\ -1.45\ (\frac{\sigma_C}{\sigma_L})^{0.75}\ \mathrm{Re}_L^{0.1}\ Fr_L^{-0.05} We_L^{0.2}\ ] \qquad (2\text{-}4)$$

Billet and Schultes (1993):

$$\frac{a_e}{a_P} = 1.5(a_P d_h)^{-0.5}(\frac{u_L d_h}{\nu_L})^{-0.2}(\frac{u_L^2 \rho_L d_h}{\sigma})^{0.75}(\frac{u_L^2}{g d_h})^{-0.45} \qquad (2\text{-}5a)$$

Bravo-Rocha-Fair (1985):

$$\frac{a_e}{a_P} = 0.498\ (\frac{\sigma^{0.5}}{Z^{0.4}})(Ca_L\ \mathrm{Re}_G)^{0.392} \qquad (2\text{-}11)$$

Rocha-Bravo-Fair (1996):

$$\frac{a_e}{a_P} = F_{SE}\ \frac{29.12\ u_L^{0.4} \nu_L^{0.2} S^{0.359}}{(1 - 0.93\cos\gamma)(\sin\alpha)^{0.3}\varepsilon^{0.6}}(\frac{\rho_L}{\sigma g})^{0.15} \qquad (2\text{-}14)$$

Delft (1999):

$$\frac{a_e}{a_P} = \frac{1 - \Omega}{1 + A / u_{Ls}^B} \qquad (2\text{-}19)$$

Besides the above literature area models, the area model used in Aspen Plus® developed by Hanley and Chen (2011) was compared:

$$\frac{a_m}{a_d} = 0.539\ \ \mathrm{Re}_V^{0.145}\ \mathrm{Re}_L^{-0.153}\ We_L^{0.2} Fr_L^{-0.2}(\frac{\rho_V}{\rho_L})^{-0.033}(\frac{\mu_V}{\mu_L})^{0.090}(\frac{\cos(\theta)}{\cos(\pi/4)})^{4.078} \qquad (5\text{-}6)$$

A preliminary mass transfer area model based directly on Linek (2011) measurements for Mellapak packing was chosen to compare with the model developed in this work:

$$\frac{a_e}{a_P} = 1.343\ u_L^{0.104} \qquad (5\text{-}7)$$

Figures 5.2 and 5.3 show the comparison between the area model developed in this work and the literature models. The differences between the model developed in this work and literature models are quite distinct. The differences are small for some recent literature models: 11% for Delft (1999), 13% for Linek (2011), 36% for Hanley (2011). The differences become large for models based on hydrocarbon systems or based mostly on random packing: 45% for Bravo (1992), 73% for Rocha (1996), 37% for Onda (1968), and 59% for Billet (1993).

The closest model was developed by Linek since it was based on a similar system (absorption of 1% CO_2 in air with 1 gmol/NaOH solution). The deviation is due to the larger gas phase resistance. It should be noted that the Delft model fail to predict the effect of liquid superficial velocity on mass transfer area with an exponent of 0.011, which is lower than the exponent predicted by all other models.

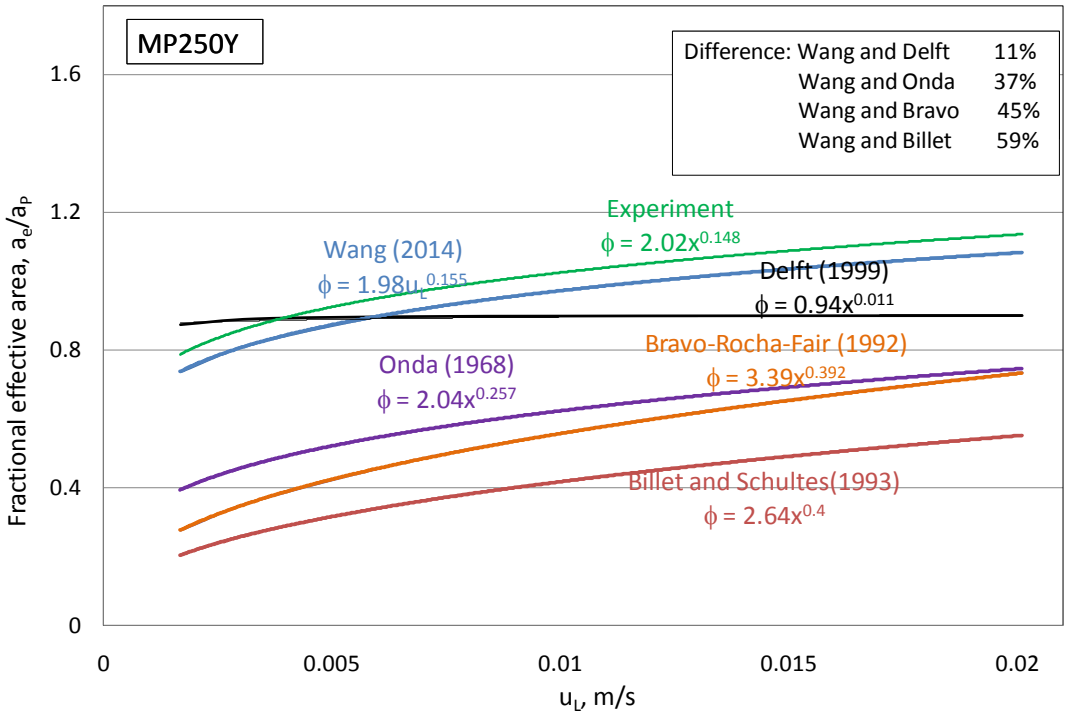

Figure 5.2. Comparison of literature area model (I) and model in this work

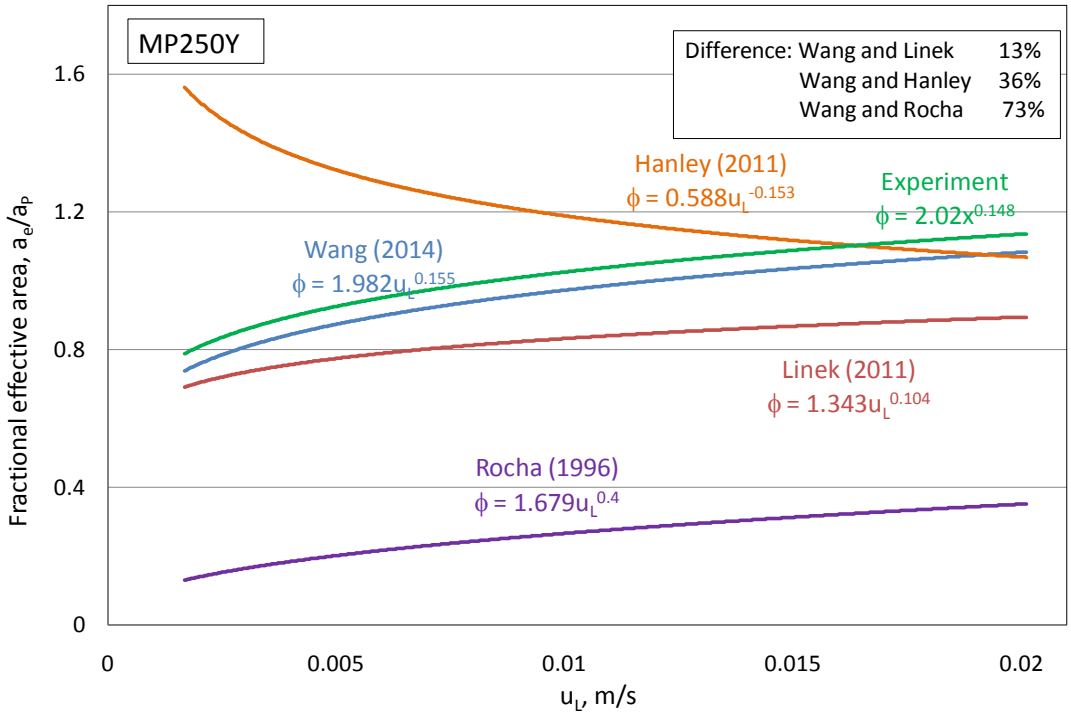

Figure 5.3. Comparison of literature area models (II) and the model of this work

5.3 Liquid film mass transfer coefficient

5.3.1 Mixing Point Density

In the previous chapter (Chapter 4), the effects of operating conditions and packing geometry on liquid and gas film mass transfer coefficients were explored. The liquid film mass transfer coefficient increases with packing surface area, and decreases with packing corrugation angle. In the model development, a new concept, Mixing Point Density (M), was introduced to account for the packing geometry effect on k_L and k_G.

Figure 5.4 shows the liquid flow mechanism inside structured packing (side view). Structured packing is composed of corrugated metal sheets. Liquid flows along these corrugated sheets. At the joint points of metal sheets (marked by circles in Figure 5.4), flows mix with each other, change directions, and create turbulence. Thus, these mixing points are believed to be the key points for mass transfer in structured packing. In packing with a lower corrugation angle or larger surface area, there will be more mixing points than packing with a higher corrugation angle at the same packed height, which means liquid and gas flows mix with each other more often, change directions more frequently, and create more turbulence. Therefore, the effect of surface area and corrugation angle on k_L and k_G can be quantified.

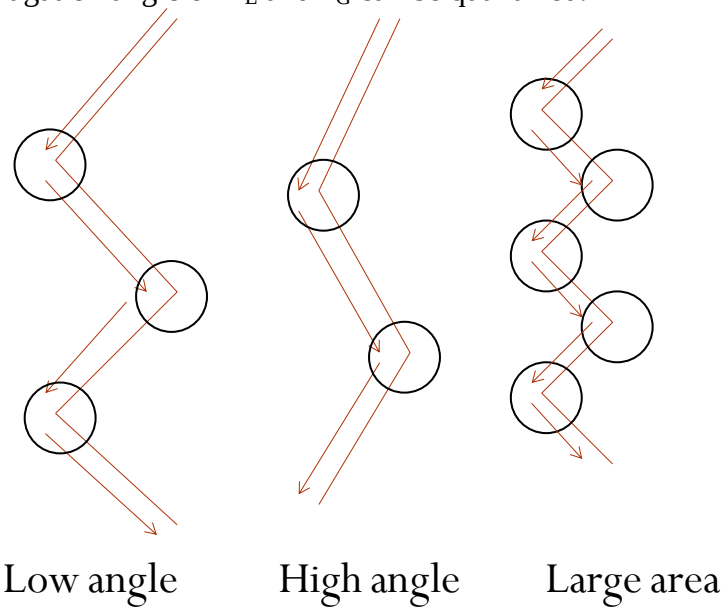

Figure 5.4. Liquid flow along corrugated metal sheets

To quantify the number of mixing points inside structured packing, their geometric structures were evaluated. Figure 5.5 shows the lateral view of a structured packing with a corrugation angle θ. From the lateral view, the corrugated metal sheets can be seen as bunches of parallel lines with a tilt angle θ to the horizontal line. In the structured packing, each corrugated metal sheet contacts with the one next to it. In the lateral view, it is expressed by the parallel lines crossing with another set of parallel lines in a reversed angle (π-θ). The crossed corrugated metal sheets form hundreds of square pyramids, which are the triangles in the lateral view. The mixing points are the vertices of the triangles, which are marked in black circles in the lateral view. The bottom of the triangle is the channel base B, and the height of the triangle is (B/2)*tanθ.

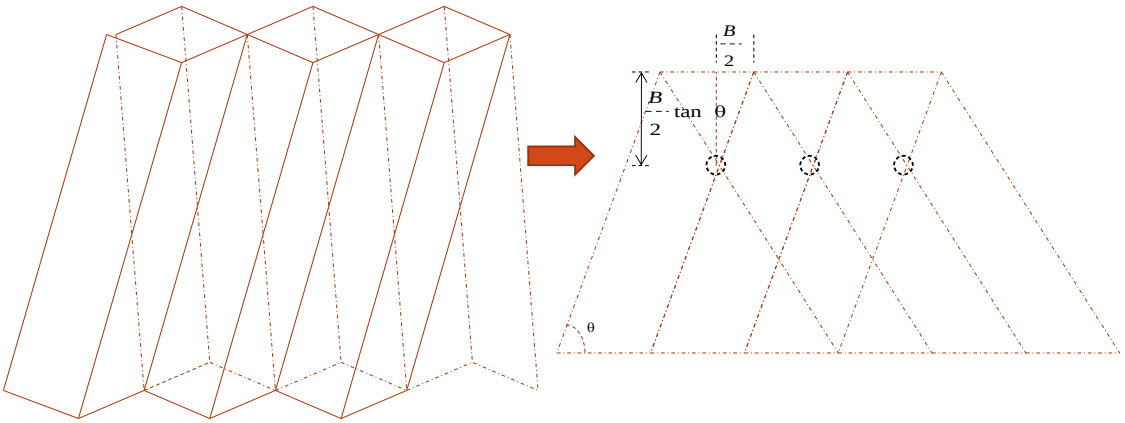

Figure 5.5. Lateral View of a Structured Packing with a Corrugation Angle θ

Structured packing is composed of those square pyramids formed by the crossed metal sheets. The pyramids can be better seen from the top view of the packing (Figure 5.6). The height of the square pyramid is (B/2)*tanθ, the bottom area of the pyramid is B*h. The volume of each square pyramid can be calculated:

$$V_{pyramid} = \frac{1}{3} * h * S_{bottom} = \frac{1}{6} B * h * B \tan \theta \qquad (5\text{-}8)$$

Where,
B is the packing channel base, (m);
h is the packing crimp height, (m);
θ is the packing corrugation angle.

Thus, the total amount of square pyramids per m^3 volume is:

$$N_{pyramid} = \frac{V_{total}}{V_{pyramid}} = \frac{6}{B * h * B \tan \theta} \qquad (5\text{-}9)$$

Each pyramid has five mixing points; however, each pyramid is also sharing mixing points with other four adjacent pyramids. Thus, the number of mixing points per pyramid is 5/5. Finally, the total number of mixing points per m^3 which is the Mixing Point Density can be calculated:

$$M = N_{pyramid} * mixing\ points\ per\ pyramid = \frac{6}{B * h * B \tan \theta} \qquad (5\text{-}10)$$

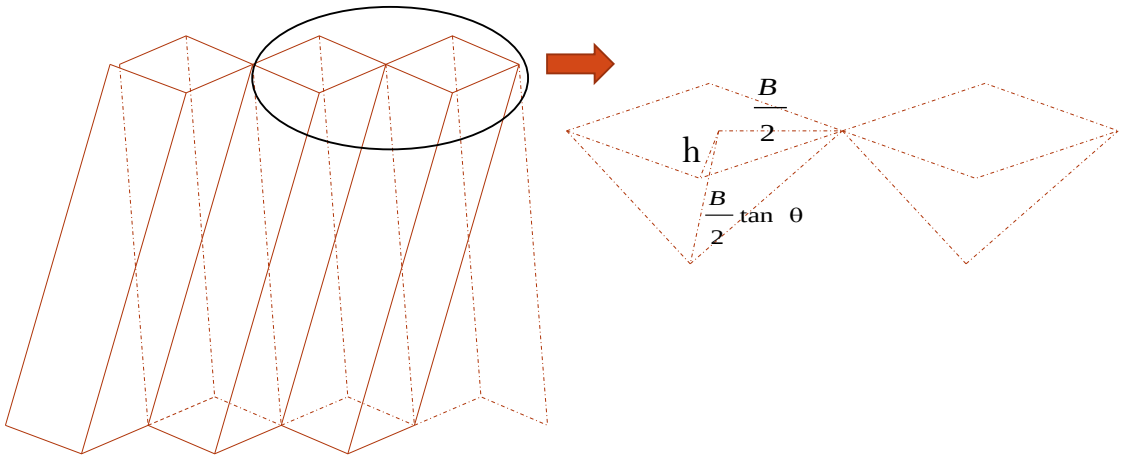

Figure 5.6. Top view of a Structured Packing with a Corrugation Angle θ □

5.3.2 Preliminary k_L and k_G models

In previous work, the effects of liquid or gas superficial velocity ($u_{L/G}$), the packing surface area (a_P), and the mixing point density (M) on k_L and k_G were explored. The preliminary k_L and k_G correlations include these three factors ($u_{L/G}$, a_P, M):

$$k_{L/G} = f(u_{L/G}, M, a_P) \qquad (5\text{-}11)$$

Taking a natural logarithm of both sides, Equation (5-11) can be written as:

$$\ln(k_{L/G}) = C + m\ln(u_{L/G}) + n\ln(M) + k\ln(a_P) \qquad (5\text{-}12)$$

Through data regression, the experimental constant C and the exponents for each factor can be calculated. Finally, the preliminary k_L and k_G models for structured packings are developed:

$$k_L = 3.08E-3 * u_L^{0.72} M^{0.42} a_P^{-1.15} \qquad (5\text{-}13)$$

$$k_G = 9.6E-3 * u_G^{0.54} M^{0.29} a_P^{-0.5} \qquad (5\text{-}14)$$

The comparison between experimental data and values predicted by preliminary k_L and k_G models are shown in Figure 5.7 and Figure 5.8. The deviation between experimental data and model value is 22% for k_L while the deviation between experimental data and model value is 13% for k_G.

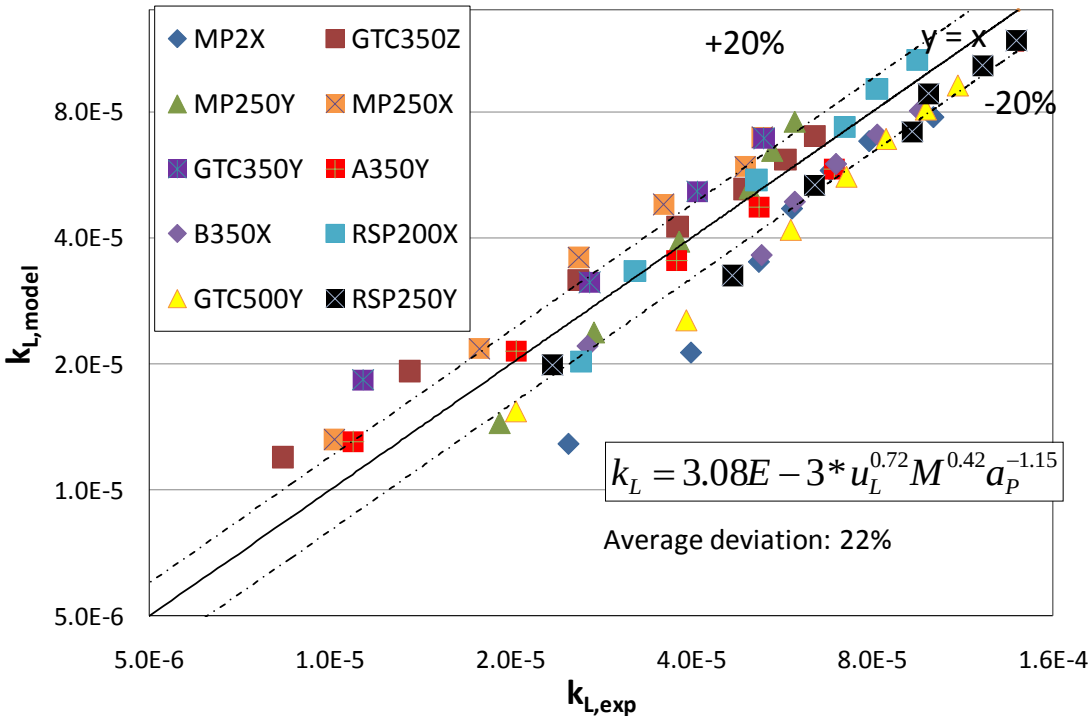

Figure 5.7. Comparison between experimental k_L and k_L predicted by preliminary model

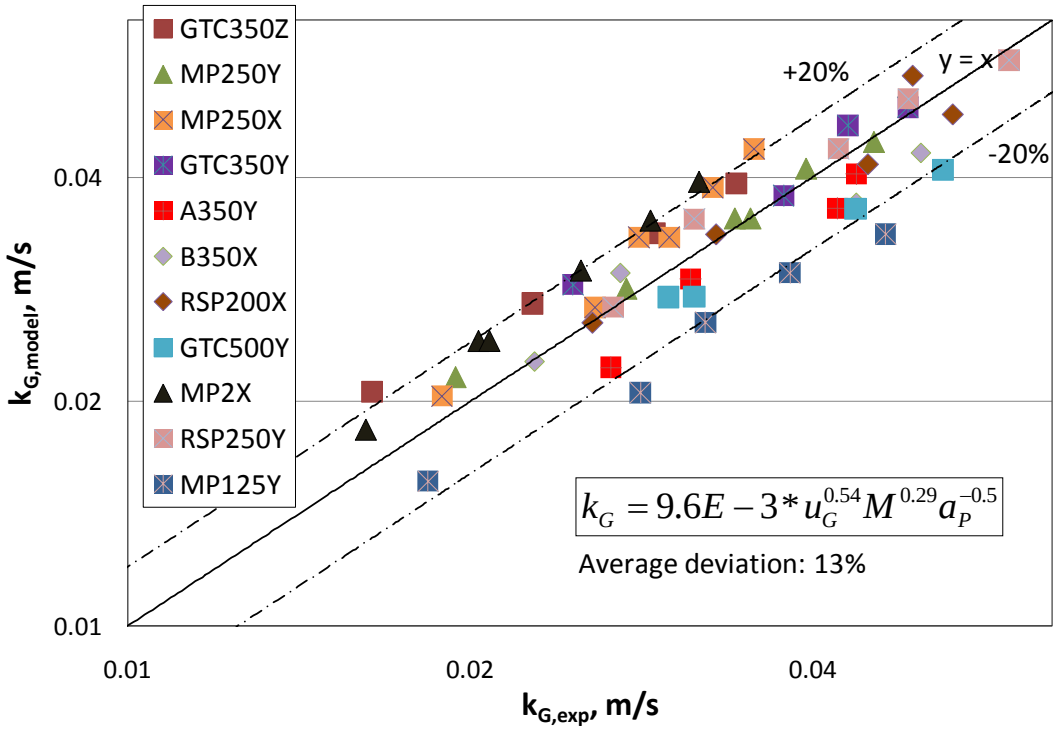

Figure 5.8. Comparison between experimental k_G and k_G predicted by preliminary model

5.3.2 Dimensionless k_L and k_G models

Fundamental models utilize the dimensionless form of velocity (Reynolds number, Re), the dimensionless form of liquid or gas phase physical properties (Schmidt number, Sc), and the dimensionless form of packing geometries (Mixing number, Mi) as the variables. The dimensionless form of k_L or k_G (Sherwood number, Sh) is used as the dependent variable. Thus, the model can be written as:

$$Sh_{L/G} = C * \mathrm{Re}_{L/G}^{m} Sc_{L/G}^{n} Mi^{p} \qquad (5\text{-}15)$$

Other researchers' conclusions are used for the effect of Schmidt number on Sherwood number since the Schmidt number influence is not yet explored in this work. For the gas phase, Mehta's conclusion (1966) is used in this model, which is that Sh_G depends on Sc_G to the power of 0.5. For the liquid phase, Mangers' conclusion (1980) is used with a dependence of Sh_L on Sc_L to the power of 0.5.

The dimensionless k_L and k_G models for structured packings are:

$$Sh_L = 4.24 * \mathrm{Re}_L^{0.72} Mi^{0.42} Sc_L^{0.5}, \; k_L = Sh_L a_P D_L \qquad (5\text{-}16)$$

$$Sh_G = 0.83 * \mathrm{Re}_G^{0.58} Mi^{0.3} Sc_G^{0.5}, \; k_G = Sh_G a_P D_G \qquad (5\text{-}17)$$

Where,

Mixing number Mi is the number of mixing points in a certain volume and can be calculated by:

$$Mi = M * l_{eq}^3 = \frac{M}{a_P^3} = \frac{6}{a_P^3 * B * h * B \tan\theta} \qquad (5\text{-}18)$$

The characteristic dimension here is the equivalent radius (r_{eq}) of the characteristic diamond formed by channel base B, channel side S, and crimp height h in regular structured packing, which is also the bottom area of pyramid mentioned in Figure 5.6.

$$l_{eq} = r_{eq} = \frac{Bh}{4S} = \frac{1}{a_P} \qquad (5\text{-}19)$$

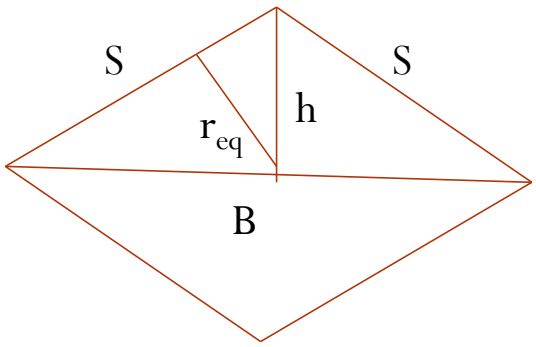

Figure 5.9. Characteristic diamond formed by B, S, h in regular structured packing

Sh, Re, and Sc are defined as:

$$Sh = \frac{k * l_{eq}}{D} = \frac{k}{D * a_p} \qquad (5\text{-}20)$$

$$\mathrm{Re} = \frac{\rho u l_{eq}}{\mu} = \frac{\rho u}{\mu a_p} \qquad (5\text{-}21)$$

$$Sc = \frac{\upsilon}{D} = \frac{\mu}{\rho D} \qquad (5\text{-}22)$$

Figure 5.10a shows the liquid phase Sherwood number (Sh_L) plotted over the dimensionless number group $(Re_L)(Mi)^{0.42/0.74}(Sc_L)^{0.5/0.74}$. Figure 5.11a shows the gas phase Sherwood number (Sh_G) plotted over the dimensionless number group $(Re_G)(Mi)^{0.42/0.74}(Sc_G)^{0.5/0.74}$. The dimensionless correlations for k_L and k_G can then be determined. The comparisons between experimental data and values predicted by dimensionless k_L and k_G models are shown in Figures 5.10b and 5.11b. The deviation between experimental data and model value is 22% for k_L while the deviation between experimental data and model value is 12% for k_G.

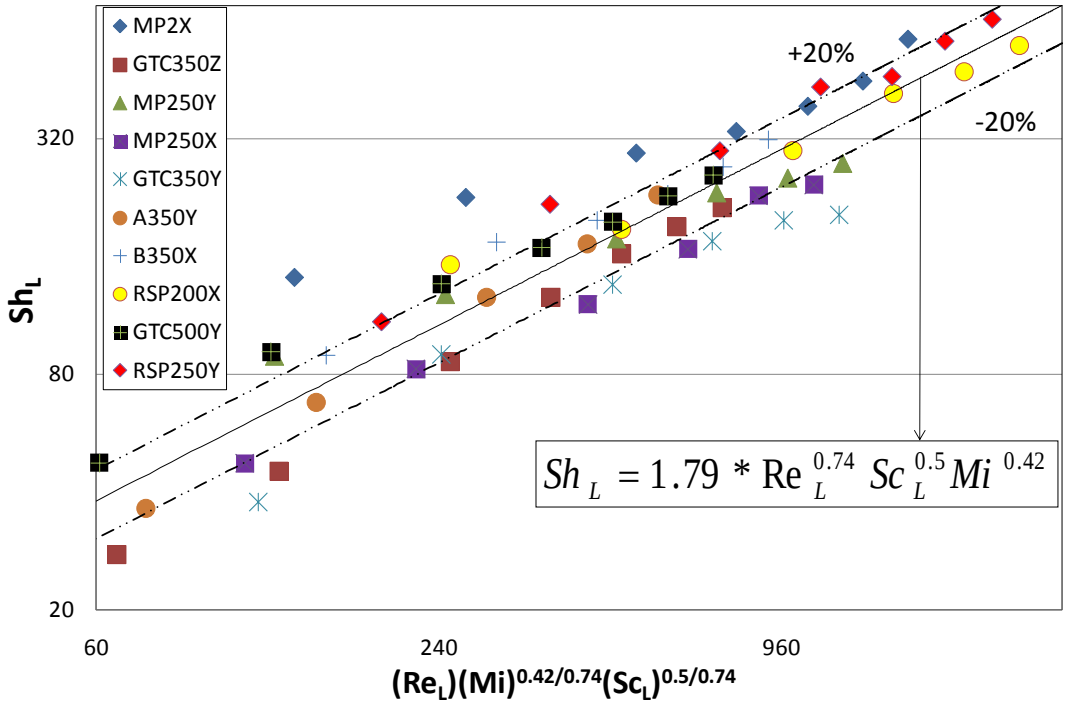

Figure 5.10a. Sh_L over dimensionless group $(Re_L)(Mi)^{0.42/0.74}(Sc_L)^{0.5/0.74}$

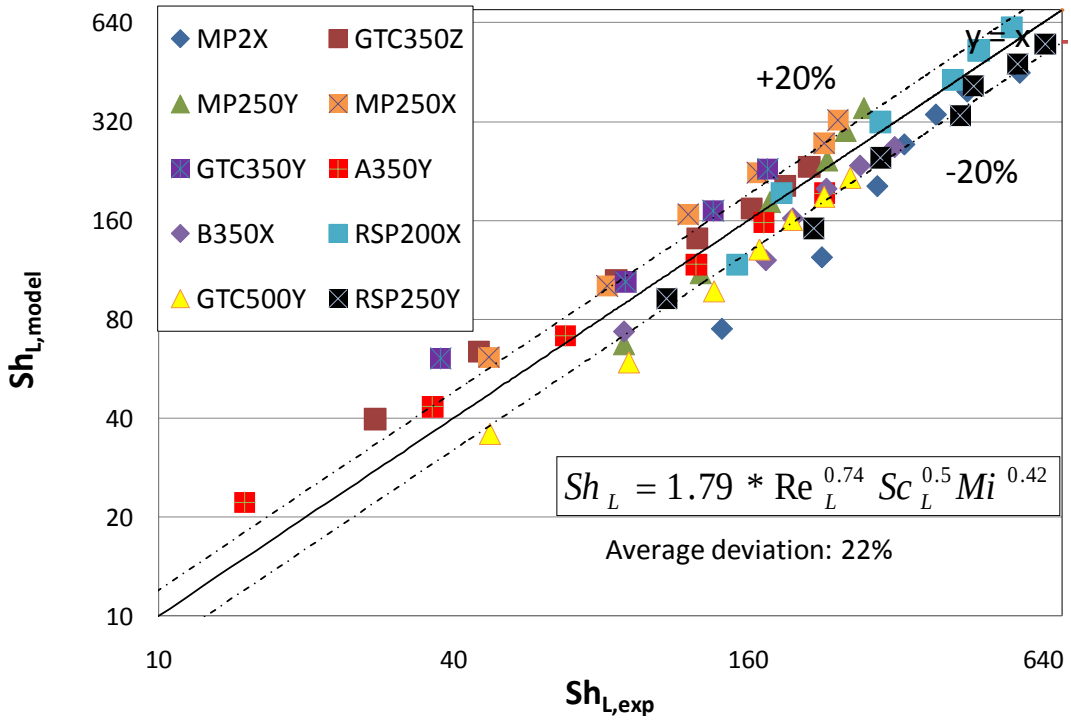

Figure 5.10b. Comparison between experimental Sh_L and Sh_L predicted by dimensionless model

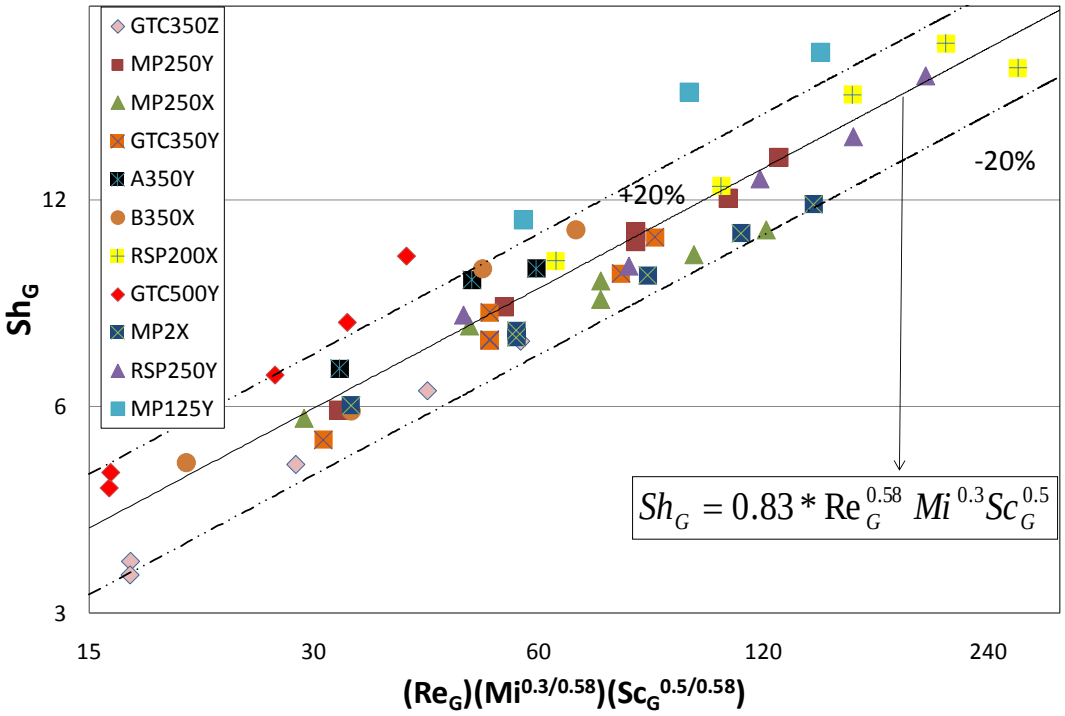

Figure 5.11a. Sh_G over dimensionless group $(Re_G)(Mi)^{0.3/0.58}(Sc_G)^{0.5/0.58}$

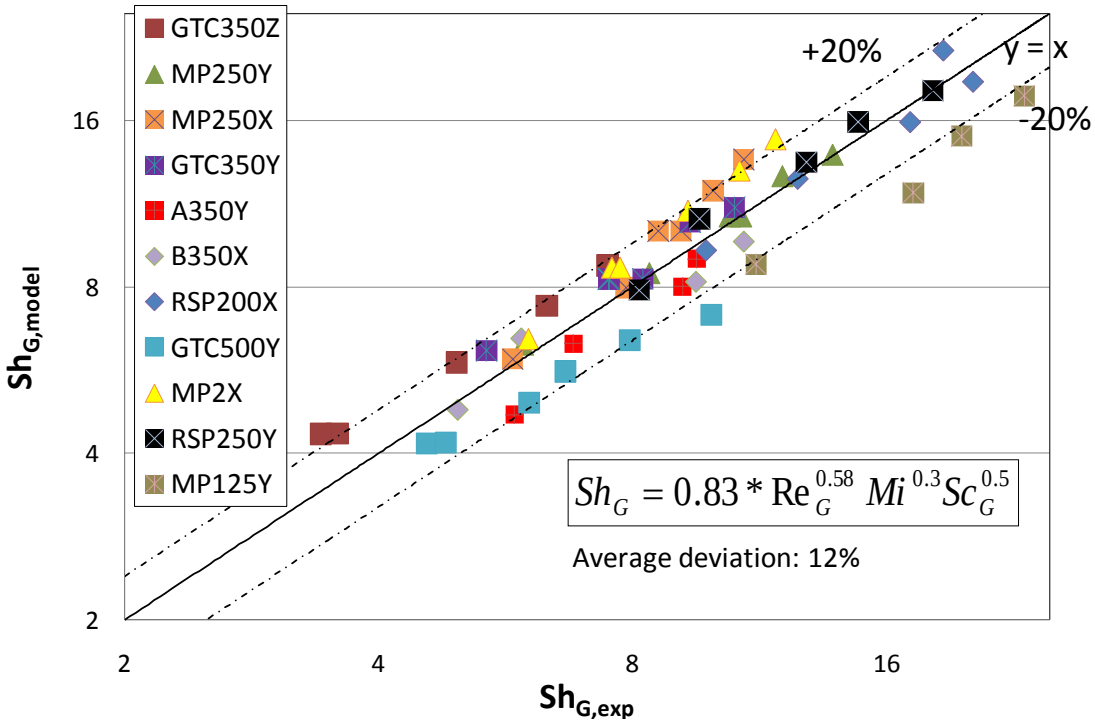

Figure 5.11b. Comparison between experimental Sh_G and Sh_G predicted by dimensionless model

5.4 Comparison with literature k_L and k_G models

Similar with the area model comparison, the liquid film and gas film mass transfer coefficient models developed in this work are compared with literature k_L and k_G models. The correlations are reproduced from Chapter 2.

Billet and Schultes (1993):

$$k_G = \frac{2}{\sqrt{\pi}} \sqrt{D_G \frac{u_G}{(\varepsilon - h_L) l_\pi}} \qquad (2\text{-}27)$$

$$k_L = \frac{2}{\sqrt{\pi}} \sqrt{D_L \frac{u_L}{h_L l_\pi}} \qquad (2\text{-}28)$$

Bravo-Rocha-Fair (1985):

$$\frac{k_G d_{eq}}{D_G} = 0.0328 \left[\frac{d_{eq} \rho_G (u_{G,eff} + u_{L,eff})}{\mu_G}\right]^{0.77} \left(\frac{\mu_G}{\rho_G D_G}\right)^{0.33} \qquad (2\text{-}9)$$

$$k_L = 2\sqrt{\frac{D_L u_{L,eff}}{\pi S}} \qquad (2\text{-}10)$$

Rocha-Bravo-Fair (1996):

$$\frac{k_G S}{D_G} = 0.054\ [\frac{\rho_G S(u_{Ge} + u_{Le})}{\mu_G}]^{0.8} (\frac{\mu_G}{D_G \rho_G})^{0.33} \qquad (2\text{-}12)$$

$$k_L = 2\sqrt{\frac{D_L C_E u_{Le}}{\pi S}} \qquad (2\text{-}13)$$

Delft (1999):

$$k_G = \sqrt{k_{G,lam}^2 + k_{G,turb}^2} \qquad (2\text{-}29)$$

$$Sh_{G,lam} = 0.664\ Sc_G^{1/3} \sqrt{\mathrm{Re}_{Grv} \frac{d_{hG}}{l_{G,pe}}} \qquad (2\text{-}31)$$

$$Sh_{G,turb} = \frac{\mathrm{Re}_{Grv}\ Sc_G \frac{\zeta_{GL}\varphi}{8}}{1 + 12.7\sqrt{\frac{\zeta_{GL}\varphi}{8}}(Sc_G^{2/3} - 1)} [1 + (\frac{d_{hG}}{l_{G,pe}})^{2/3}] \qquad (2\text{-}32)$$

$$k_L = 2\sqrt{\frac{D_L u_{Le}}{\pi 0.9 d_{hG}}} \qquad (2\text{-}54)$$

$$d_{hG} = \frac{\frac{(bh - 2\delta s)^2}{bh}}{[(\frac{bh - 2\delta s}{2h})^2 + (\frac{bh - 2\delta s}{b})^2]^{0.5} + \frac{bh - 2\delta s}{2h}} \qquad (2\text{-}55)$$

$$\delta = (\frac{3\mu_L u_{LS}}{\rho_L g a \sin\alpha})^{1/3} \qquad (2\text{-}56)$$

Besides the above literature k_G and k_L models, the k_G and k_L models used in Aspen Plus® developed by Hanley and Chen (2011) were also compared:

$$k_x = 0.33\ \mathrm{Re}_L^{1}\ Sc_L^{1/3} (\frac{c_L D_L}{d_e}) \qquad (5\text{-}23)$$

$$k_y = 0.0084\ \mathrm{Re}_V\ Sc_V^{1/3} (\frac{c_V D_V}{d_e})(\frac{\cos(\theta)}{\cos(\pi/4)})^{-7.15} \qquad (5\text{-}24)$$

The preliminary k_La model based directly on Linek (2011) measurements was compared with model developed in this work (k_Ga correlation was not developed):

$$k_L a = 0.562\ * u_L^{0.668} \qquad (5\text{-}25)$$

Figures 5.12-5.15 shows the comparison between literature k_La and k_Ga models with models developed in this work. Since most literature models were developed from measured k_La and k_Ga values with a theoretical assumption of area, the most reasonable comparison is with the respective ka.

In the k_La comparison, most literature models use the assumption of penetration theory (Higbie, 1935) with different expression of equivalent liquid velocity (u) and characteristic length (L).

The difference between the model developed in this work (absorption systems) and models from distillation systems (Bravo, Delft, Rocha) is from 30% to 40%. The difference becomes smaller (20% to 30%) when comparing with model developed from absorption system (Linek) or models developed from distillation system and absorption system (Billet and Schultes, Hanley and Chen).

In the k_Ga comparison, the model developed in this work is higher than literature models by 40 to 80%. One possible reason could be that all literature models are developed from distillation system where equilibrium is not fully established. For the system used in this work which is absorption of SO_2 with NaOH, equilibrium is not a concern since the reaction is instantaneous. Another possible reason could be the additional mass transfer caused by wall effects and end effects since this work used a short packed bed (20 to 40 inches), although careful end effect measurements have been conducted in this work to minimize this effect.

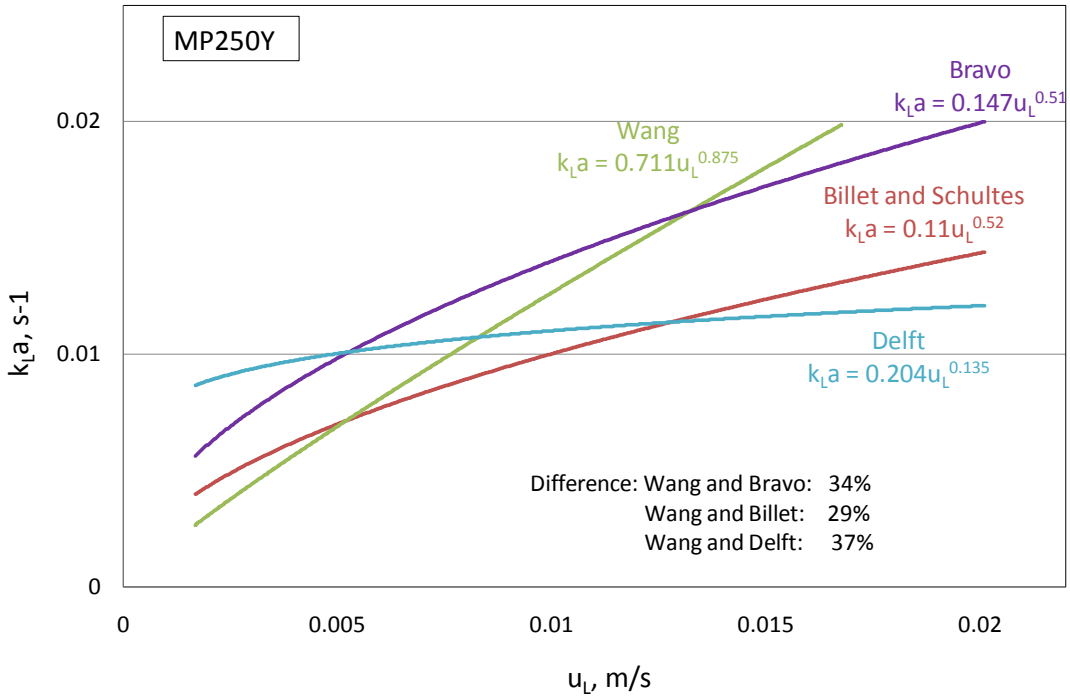

Figure 5.12. Comparison between literature k_La models and k_La model developed in this work (I)

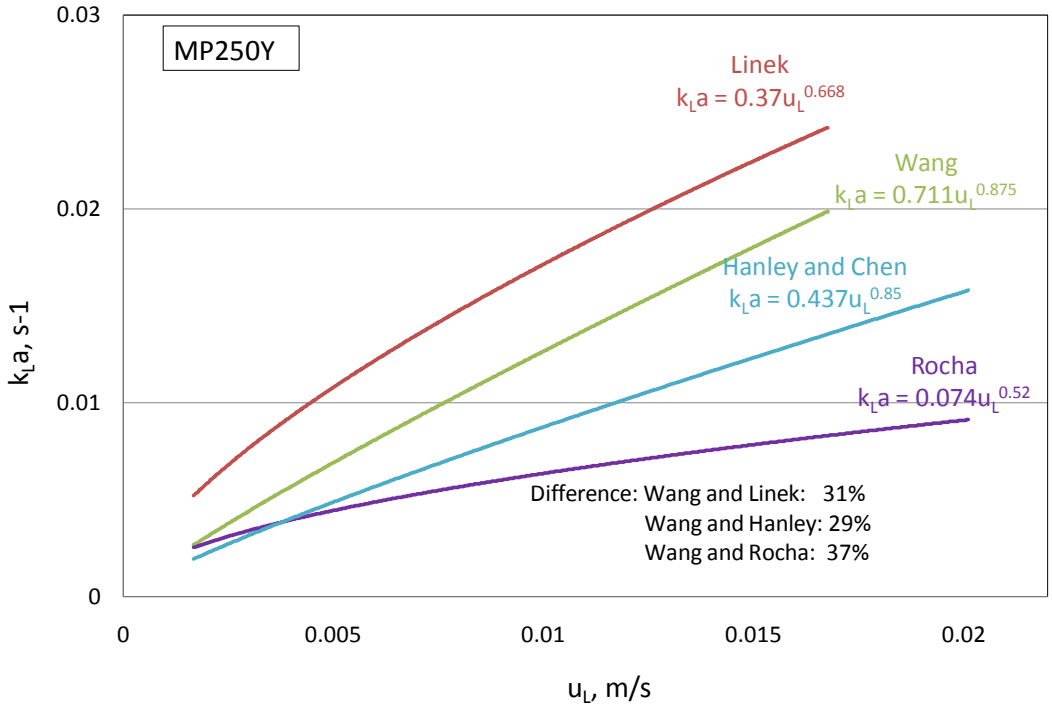

Figure 5.13. Comparison between literature k_La models and k_La model developed in this work (II)

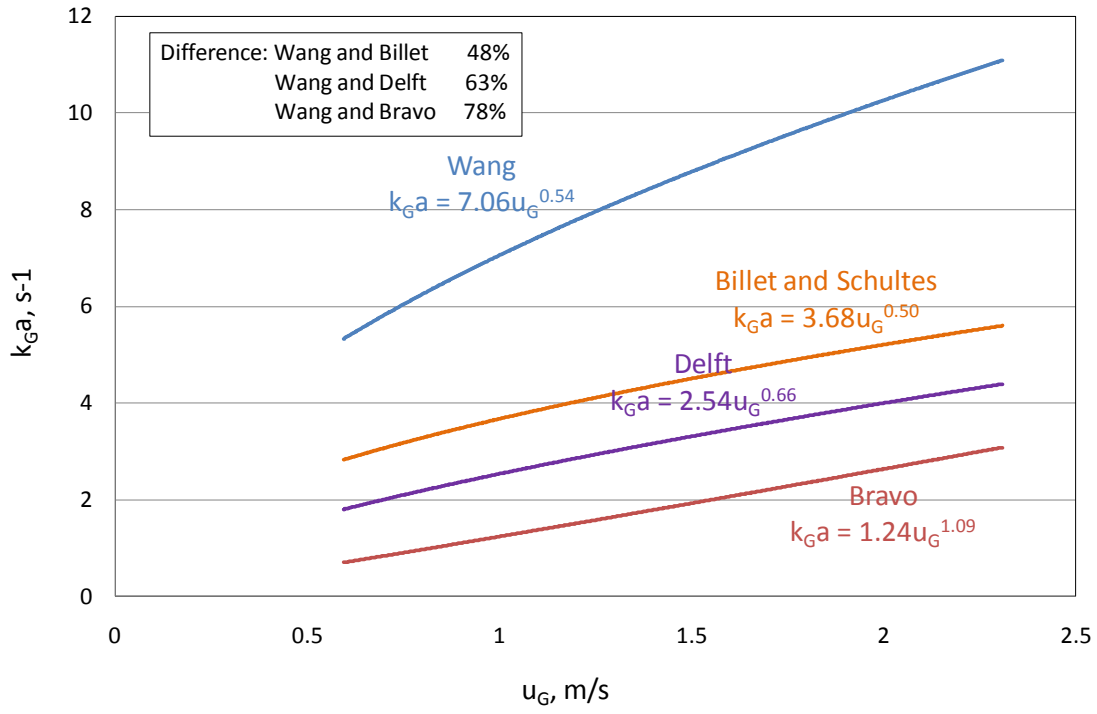

Figure 5.14. Comparison between literature k_Ga models and k_Ga model developed in this work (I)

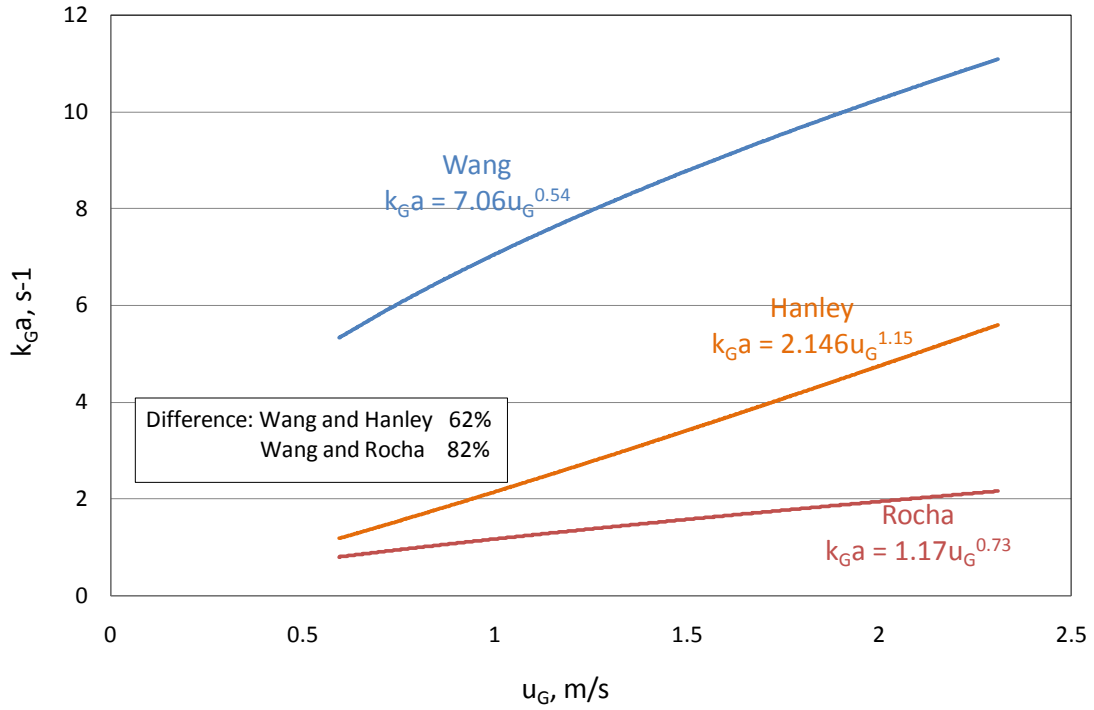

Figure 5.15. Comparison between literature k_Ga models and k_Ga model developed in this work (II)

5.5 k_L and k_G models for random packings

Another interest in this work is to extend the applied range of the k_L and k_G models to include random packings. In this work, three metal random packings from the Raschig Super Ring family (RSR#0.3, RSR#0.5, and RSR#0.7) were considered. The k_L and k_G correlations with mixing point density (Equation 5-13 and 5-14) are considered as mass transfer models for random packings. However, the mixing point density M needs to be defined and calculated from random packings when applying these models.

5.5.1 Calculated Mixing Point Density (M_{kL} and M_{kG}) for random packing

For structured packing, the mixing point density is defined as the number of contacting points between corrugated metal sheets per m^3. Mixing points divide structured packing into hundreds of small pyramids. The volume of each pyramid can be calculated by channel base B, crimp height h, and corrugation angle θ. Then the mixing point density can be calculated (Equation 5-10). For random packing whose structure is not as regular as structured packing, it is difficult to apply the same calculation. The calculated mixing point density (M_{kL} or M_{kG}) are used for random packings.

The calculated mixing point density (M_{kL}) means the value of M in the k_L model that can give the lowest deviation from experimental data. M_{kL} is back calculated from experimental data and Equation (5-13). Microsoft® Excel Solver program is used in the calculation. M_{kG} is calculated in the same way. The concept of M_{kL} and M_{kG} comes from the concept of packing factor F_P,

which is a characteristic constant used in packing pressure drop calculation and can be calculated from experimental data.

Table 5.3 lists the calculated M_{kL} and M_{kG} values for the random packings studied in this work. According to Table 5.3, the calculated mixing point density for k_L and k_G are close except for RSR#0.3, whose M_{kG} value is 1.8 times of M_{kL} value.

Table 5.3. Calculated Mixing Point Density for Random Packings

RSR#0.3		RSR#0.5		RSR#0.7	
M_{kL}	M_{kG}	M_{kL}	M_{kG}	M_{kL}	M_{kG}
2.44E6	4.33E6	0.47E6	0.56E6	0.73E6	0.39E6

5.5.2 Global mass transfer coefficient models for structured and random packings

Since the mixing point density for random packing can be calculated, Equations (5-13) and (5-14) can be used as global mass transfer coefficient models. For random packings, the M_{kL} and M_{kG} values back calculated from experimental data are used in the model. Figure 5.16 and 5.17 show the comparison between values predicted by global mass transfer k_L and k_G models and experimental data. For random packings, k_L and k_G correlations have good prediction. For k_L model, the average deviation is 3.8% for RSR#0.3, 2.9% for RSR#0.5, and 11.5% for RSR#0.7. For k_G model, the average deviation is 4.2% for RSR#0.3, 10% for RSR#0.5, and 3.4% for RSR#0.7.

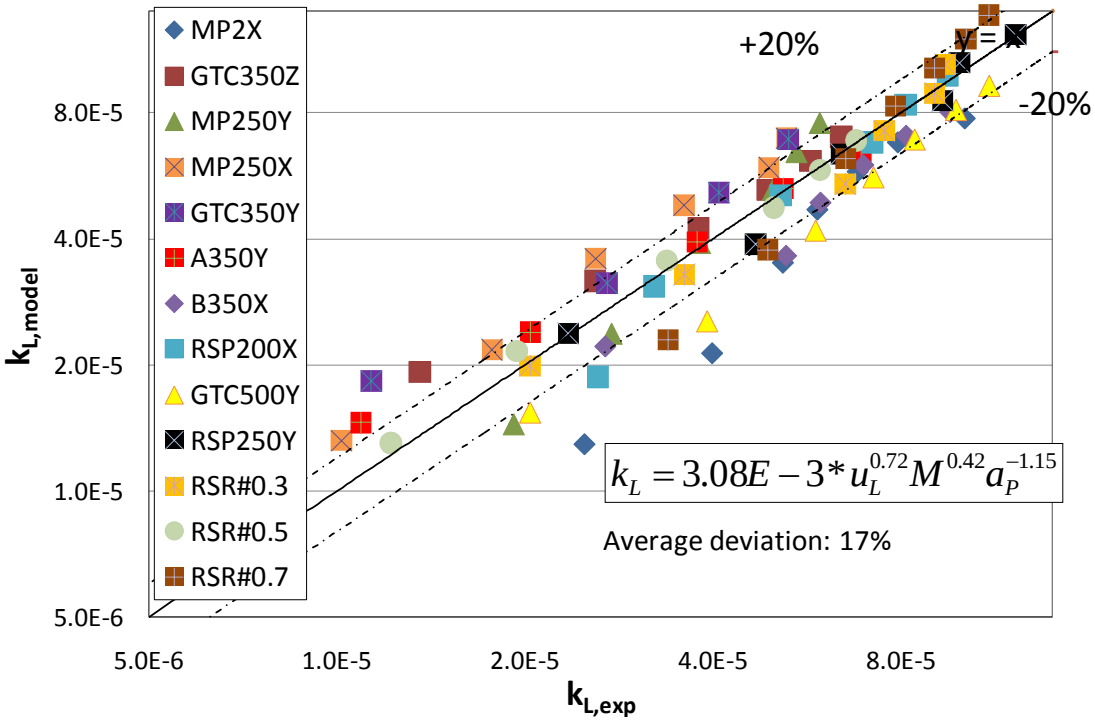

Figure 5.16. Comparison between global k_L model and experimental data

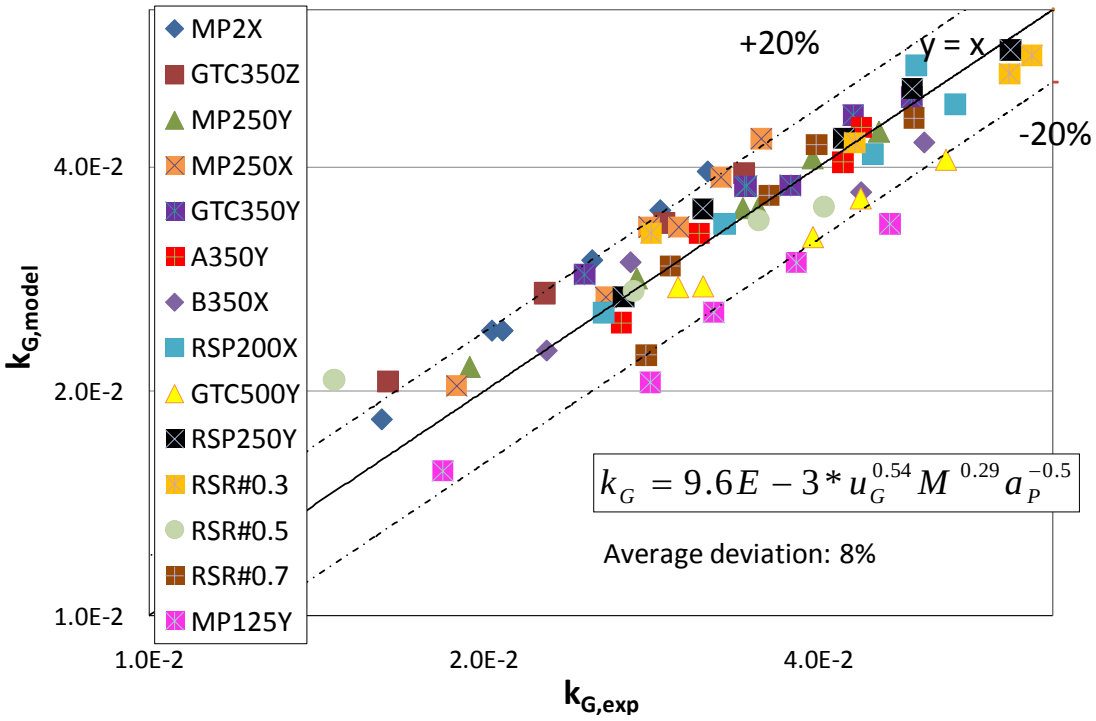

Figure 5.17. Comparison between global k_G model and experimental data

5.6 Mixing Point Density calculated from packing surface area (a_P) and corrugation angle (θ)

The mixing point density calculated by Equation (5-10) needs the specific structured packing geometry information: channel base B and crimp height h. However, this kind of information is not always available. To solve this problem, another way to calculate mixing point density using packing surface area (a_P) and corrugation angle (θ) instead of channel base and crimp height is explored. This method builds the relationship between B, S, h and a_P, θ. Then, B, S, h can be expressed by a_P and θ. Finally, Equation (5-10) can be expressed by a_P and θ.

For a given structured packing, the distance between channels is unique. Figure 5.18 shows the channel distance L. Like channel base B and crimp height h, the channel distance L is also a structured packing geometric characteristic. Figure 5.19 shows the lateral view of a structured packing channel. For regular structured packing, the two side surfaces of the packing channel are mutually perpendicular. In other words, the angle α between the two side planes equals to 90 degree. Thus, the cross section of the packing channel is an isosceles right triangle. The two right-angle sides are channel distance L. The hypotenuse equals to √2L, shown by dash line in Figure 5.18 and 5.19.

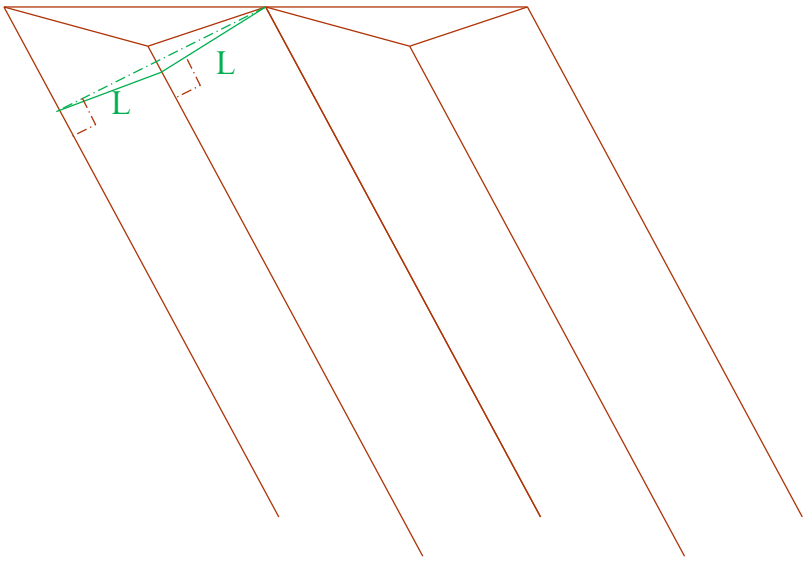

Figure 5.18. Structured packing with a channel distance L

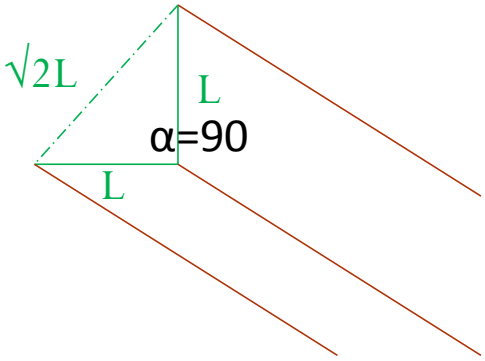

Figure 5.19. Lateral view of structured packing channel

The top surface of the packing channel is the triangle formed by channel base B and channel side S (details shown in Figure 9). The channel base B, hypotenuse of channel cross section √2L, and the ridge of packing channel D form a right angle triangle in the longitudinal section (Figure 5.20). In the right angle triangle, the angle between the packing channel base B and packing channel ridge D is the packing corrugation angle θ. Thus, channel base B can be expressed by L:

$$B = \frac{\sqrt{2}L}{\sin\theta} \qquad (5\text{-}26)$$

The other right-angle side (channel ridge D) can be expressed by L:

$$D = \frac{\sqrt{2}L}{\tan\theta} \qquad (5\text{-}27)$$

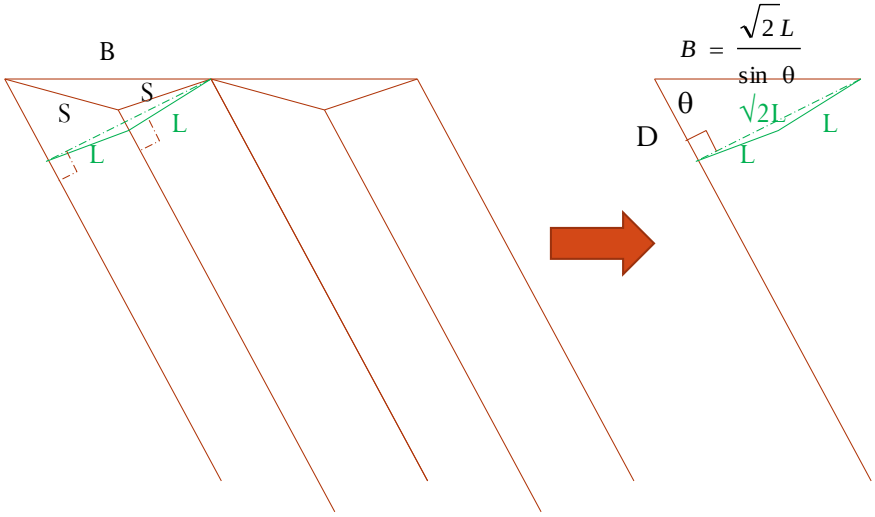

Figure 5.20. Longitudinal section of structured packing channel (I)

Figure 5.21 shows the relation between channel side S and channel ridge D. S is the hypotenuse in the right-angle triangle formed by S, L, and D/2. S can be expressed by L and D:

$$S^2 = (D/2)^2 + L^2 \qquad (5\text{-}28)$$

Combine (5-27) and (5-28), channel side S can be expressed by L:

$$S = \frac{\sqrt{2\tan^2\theta + 1}}{\sqrt{2}\tan\theta} L \qquad (5\text{-}29)$$

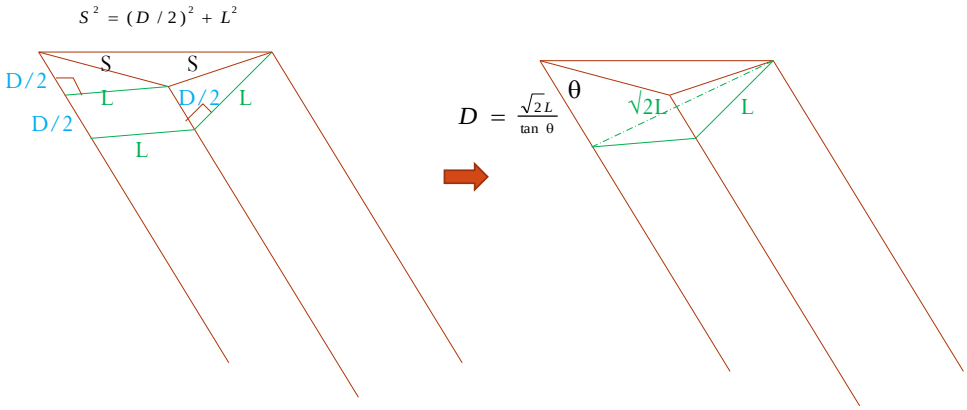

Figure 5.21. Longitudinal section of structured packing channel (II)

Since B and S are expressed by L, the crimp height h can then be expressed by L:

$$h = \sqrt{S^2 - (\frac{B}{2})^2} = \sqrt{\frac{(2\tan^2\theta + 1)L^2}{2\tan^2\theta} - \frac{L^2}{2\sin^2\theta}} = \frac{L}{\sqrt{2}} \qquad (5\text{-}30)$$

In structured packings, geometric characteristics B, S, h have the relation with packing surface area a_P:

$$\frac{Bh}{4S} = \frac{1}{a_P} \qquad (5\text{-}31)$$

Combine equations (5-26), (5-29), (5-30), (5-31), the channel distance L can then be calculated

by a_P and θ:

$$L = \frac{2\sqrt{2}\sqrt{\sin^2\theta + 1}}{a_P} \qquad (5\text{-}32)$$

Since B and h can be expressed by L, and L can be expressed by a_P and θ, finally the mixing point density can be calculated from packing surface area a_P and corrugation angle θ:

$$M = \frac{6}{BhB * \tan\theta} = \frac{3 * a_P^3 \sin\theta\cos\theta}{16(\sin^2\theta + 1)^{3/2}} \qquad (5\text{-}33)$$

The mixing point density calculated in this way is an alternative to the way calculated by B and h, especially in the cases when B and h values are not available. Table 5.4 shows the mixing point density (M′) calculated from a_P and θ compared with the mixing point density (M) calculated directly from B and h. The deviation between M′ and M is most likely due to bended packing channels (the packing channel angle α differs from 90 degree) in packing transportation, installment processes. Generally, the deviation is acceptable for most packings (around 20%), except for A350Y which surface area is believed to be less than 350 m^2/m^3.

Table 5.4. Comparison between mixing point density M calculated from B, h and M′ calculated from a_P, θ

	MP2X	GT-PAK™350Z	GT-PAK™350Y	MP250Y	MP250X
M	0.27E6	0.90E6	2.87E7	0.59E6	0.48E6
M′	0.30E6	0.99E6	2.19E7	0.79E6	0.55E6
Deviation	13%	11%	-23%	-34%	13%
M	A350Y	B350X	GT-PAK™500Y	RSP250Y	
M′	1.17E6	1.26E6	4.63E6	1.25E6	
Deviation	2.19E6	1.50E6	6.38E6	0.80E6	
	87%	20%	38%	-36%	

The k_L and k_G correlations were regressed using the mixing point density (M′) calculated in this way:

$$k_L = 0.05 * u_L^{0.72} M'^{0.6} a_P^{-2.07} \quad (5\text{-}34)$$

$$k_G = 0.024 * u_G^{0.55} M'^{0.53} a_P^{-1.26} \quad (5\text{-}35)$$

Figure 5.22 and 5.23 show the comparison between experimental data and k_L, k_G models using mixing point density calculated from a_P and θ. The k_L and k_G models from alternative mixing point density (M′ calculated from a_P and θ with the assumption of standard structured packing geometry) is not as perfect as the models from original mixing point density, but still have good comparison with experimental data. It provides an alternative way when packing characteristic lengths are not available.

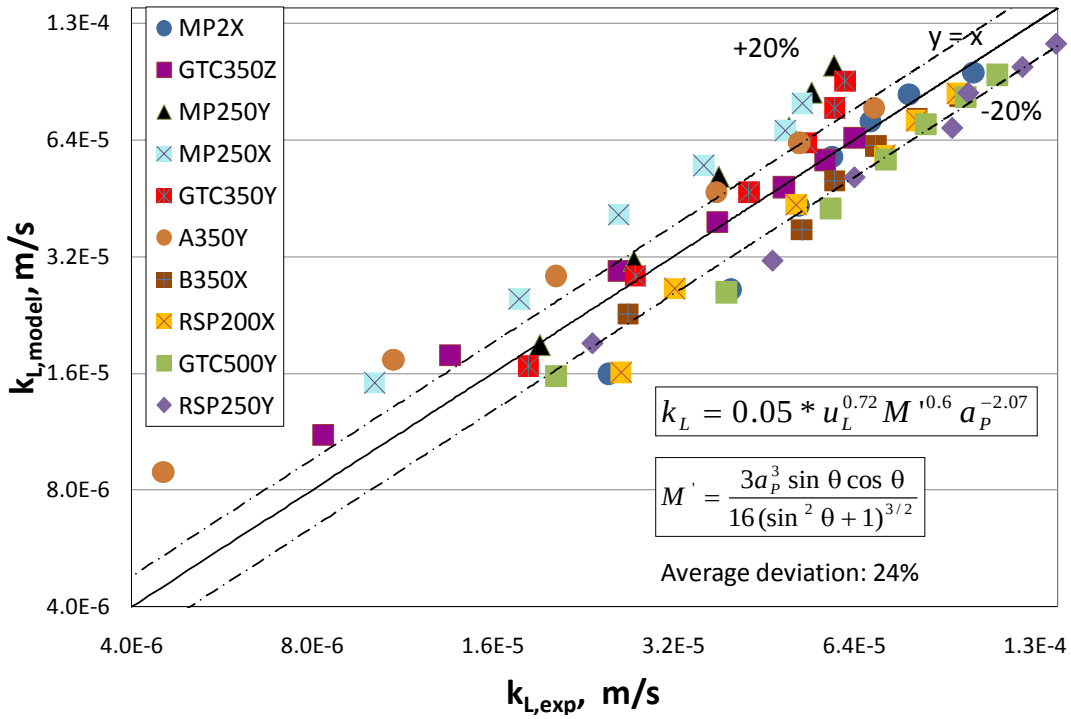

Figure 5.22. Comparison between experimental data and k_L models using mixing point density calculated from a_P and θ

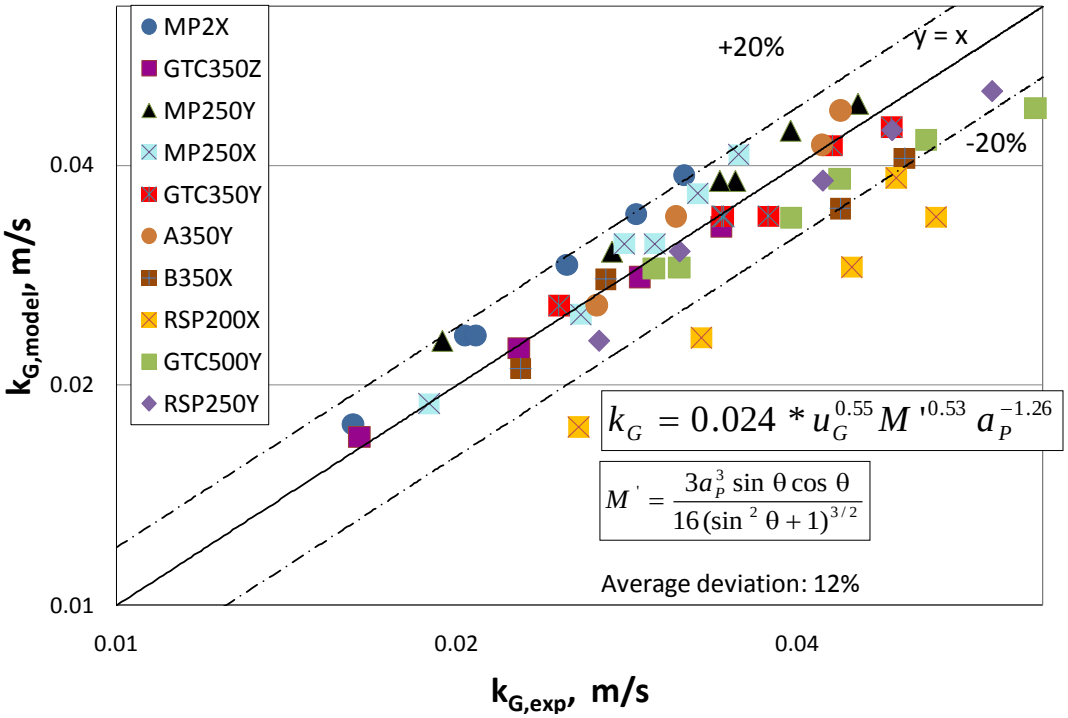

Figure 5.23. Comparison between experimental data and k_G models using mixing point density calculated from a_P and θ

5.7 Conclusions

In this chapter, three mass transfer models are developed. The database includes eleven structured packings with surface area ranging from 125 m^2/m^3 to 500 m^2/m^3 and corrugation angle from 45 degree to 70 degree, and three random packings from Raschig Super Ring family. The experimental systems use the absorption/desorption from aqueous solvents with liquid physical properties close to those of pure water.

The three mass transfer correlations developed in this work are:

$$\frac{a_e}{a_P} = 1.41\left[\left(\frac{\rho_L}{\sigma}\right) g^{1/3} \left(\frac{u_L}{a_P}\right)^{4/3}\right]^{0.116}$$

$$k_L = 3.08\ E-3 * u_L^{0.72} M^{0.42} a_P^{-1.15}$$

$$k_G = 9.6\ E-3 * u_G^{0.54} M^{0.29} a_P^{-0.5}$$

Where,

a_e is the effective mass transfer area, (m^2/m^3);

a_P is the total surface area, (m^2/m^3);

ρ_L is the liquid density, (kg/m^3);

σ is the liquid phase surface tension, (N/m);

g is the gravity constant, (9.8 m/s^2);

u_L is the superficial liquid velocity, (m/s);

k_L is the liquid film mass transfer coefficient, (m/s);

M is the mixing point density, (pts/m^3);

k_G is the gas film mass transfer coefficient, (m/s);

u_G is the superficial gas velocity, (m/s).

The dimensionless k_L and k_G models for structured packings are:

$$Sh_L = 4.24 * \mathrm{Re}_L^{0.72}\ Mi^{0.42} Sc_L^{0.5},\ k_L = Sh_L a_P D_L$$

$$Sh_G = 0.83 * \mathrm{Re}_G^{0.58}\ Mi^{0.3} Sc_G^{0.5},\ k_G = Sh_G a_P D_G$$

Where,

The dimensionless number Sh, Re, Mi, and Sc are defined in Equations (5-18) to (5-22).

The effective area model uses the basic form of the Tsai model (2010). Liquid superficial velocity over packing total area (u_L/a_P) is used as the liquid flow rate per wetted perimeter instead of (Q/L_P). Thus the applied range of this area model is extended to include hybrid packings and random packings. The experimental coefficient is changed from 1.34 to 1.41 which provides a better fit of the larger database. The wetted area varies with liquid rate to the 0.155 power and is independent of the corrugation angle and the mixing point density (Mi).

A new concept, Mixing Points Density (M), is introduced to represent the packing geometry

effect on k_L and k_G. For regular structured packing, M can be calculated from basic packing geometries (channel base B, crimp height h, and corrugation angle). If these characteristic lengths data are not available, an alternative method to calculate mixing point density from a_P and θ is provided (Equation 5-33). For random packing, calculated M (M_{kL} or M_{kG}) is used to fit mass transfer models. The average deviation for experimental data and k_L model is 17%, and for k_G model is 8%.

Mass transfer models developed in this work are compared with literature models. The models have good consistency with models developed from aqueous absorption systems. There are significant differences between models developed in this work and models developed from hydrocarbon systems (distillation systems).

References

Akita K, Yoshida F. "Gas holdup and volumetric mass transfer coefficient in bubble columns: effects of liquid properties." *Industrial & Engineering Chemistry Process Design and Development.* 1973;12(1):76-80.

Billet R, Mackowiak J. "Recent progress in distillation design." *5th International Congress in Scandinavia on Chemical Engineering.* Copenhagen, Denmark. 1980.

Billet R, Schultes M. "Predicting mass transfer in packed column." *Chem. Eng. Technol.* 1996;16: 1-9.

Bird RB, Stewart WE, Lightfoot EN. *Transport Phenomena.* New York, John Wiley & Sons, Inc.: 2002.

Bravo JL, et al. "Mass Transfer in Gauze Packings." *Hydrocarbon Processing.* 1985; 91-95.

Bravo JL, Rocha JA, Fair JR. "A comprehensive model for the performance of columns containing structured packings." *ICHEME Symp. Ser.* 1992;128: 489-507.

Brunazzi E, Paglianti A. "Liquid-Film Mass-Transfer Coefficient in a Column Equipped with Structured Packings." *Ind. Eng. Chem. Res.* 1997; 36: 3792-3799.

Bureau of Labor Statistics. CPI Detailed Report (complete text and tables). February 2014.

Danckwerts PV., Kennedy AM., Roberts D. "Kinetics of CO2 absorption in alkaline solutions—II: Absorption in a packed column and tests of surface-renewal models." Chem. Eng. Sci. 1963:18:63–72.

Danckwerts PV. Gas-Liquid Reactions. McGraw-Hill Book Company, New York. 1970.

Danckwerts PV., Sharma MM. "Absorption of carbon dioxide into solutions of alkalis and amines." Chem Engr. 1966; 202: 244-280.

Dugas RE. *Carbon Dioxide Absorption, Desorption and Diffusion in Aqueous Piperazine and Monoethanolamine.* The University of Texas at Austin. Ph.D. Dissertation. 2009.

EIA. *Electric Power Monthly Report.* U.S. Energy Information Administration. 2013.

El-Behlil MA, El-Gezawi SM, Adma SA. "Volatile Organic Chemicals Removal from Contaminated Water using Air Stripping Low Profile Sieve Tray Towers." *Sixteenth International Water Technology Conference,* Istanbul, Turkey, 2012.

Fujita S, Sakuma S. "Wetted area of Raschig rings in packed columns." *Chem. Eng. (Japan).* 1954;18: 64-67.

Fair JR, Seibert AF, Behrens M, Saraber PP, Olujic Z. Structured Packing Performance-Experimental Evaluation of Two Predictive Models. *Ind. Eng. Chem. Res.* 2000;39(6):1788-1796.

Frailie P. "Process Economics of Amine Scrubbing Systems." *PSTC Fall Meeting,* Austin. 2013.

Freeman SA et al. "Density and viscosity of aqueous (piperazine + carbon dioxide) solutions." *Journal of Chemical and Engineering Data.* 2011;56(3): 574-581.

Henriques de Brito, et al. "Effective Mass-Transfer Area in a Pilot Plant Column Equipped with Structured Packings and with Ceramic Rings." *Ind. Eng. Chem. Res.* 1994;33(3):647-656.

Higbie, R. "The rate of absorption of a pure gas into a still liquid during short periods of exposure." *Trans. Am. Inst. Chem. Engrs.* 1935;31:365-383.

Johnstone HF, and Pigford RL. "Distillation in wetted-wall column." *Trans. Am. Inst. Chem. Engrs.* 1942;38:25-50.

JPI. *Air Stripping of VOCs from Water.* Houston, Texas, Jaeger Products Inc (JPI). 1996.

Kunesh JG, et al. "Sieve Tray Performances for Steam Stripping Toluene from Water in a 4-ft Diameter Column." *Ind. Eng. Chem. Res.* 1996; 35: 2660-2671.

Lin YJ, Madan T, Rochelle GT. "Regeneration with Rich Bypass of Aqueous Piperazine and Monoethanolamine for CO_2 Capture." *Ind. Eng. Chem. Res.* 2014; 53: 4067−4074.

Linek V, Moucha T, Rejl FJ. "Hydraulic and mass transfer characteristics of packings for absorption and distillation columns. Rauschert-Metall-Sattel-Rings." Trans IChemE. 2001;79: 725-732.

Linek V, Petericek P. "Effective interfacial area and liquid side mass transfer coefficients in aborption columns packed with hydrophilised and untreated plastic packings." *Chem Eng Res Des.* 1984;62:13-21.

Mangers RJ, Ponter AB. "Effect of viscosity on liquid film resistance to mass transfer in a packed column." *Ind. Eng. Chem. Process Des. Dev.* 1980;19: 530-537.

Mehta VD, Sharma MM. "Effect of diffusivity on gas-side mass transfer coefficient." *Chemical Engineering Science.* 1966;21: 361-365.

Mouch T, Linek V, Prokopová E. "Effect of packing geometrical details influence of free tips on volumetric mass transfer coefficients of Intalox saddles." *Chem. Eng. Res. Des.* 2005;83:88-92.

Olujic Z, Kamerbeek AB, de Graauw J. "A Corrugation Geometry Based Model for Efficiency of Structured Distillation Packing." *Chem. Eng. Process.* 1999;38: 683-695.

Olujic Z, Seibert AF, Fair JR. Influence of corrugation geometry on the performance of structured packings: an experimental study. *Chem. Eng. Process* 2000;39(4):335-342.

Onda K, Sada E. "Liquid-side mass transfer coefficient packed towers." *AIChE Journal.* 1959;5:235-239.

Onda K, Takeuchi H, Okumoto Y. "Mass transfer coefficients between gas and liquid phases in packed columns." *Journal of Chemical Engineering of Japan.* 1968;1(1): 56-62.

Peters MS, Timmerhaus KD. *Plant Design and Economics for Chemical Engineers.* New York, McGraw-Hill, Inc.: 1991.

Pilling M. (Sulzer Chemtech USA, Inc., Tulsa, OK). Personal Communication to Chao Wang. 2014.

Razi N et al. "Cost and energy sensitivity analysis of absorber design in CO2 capture with MEA." *International Journal of Greenhouse Gas Control.* 2013;19: 331-339.

Rochelle GT, Fisher KS, Beitler C, Rueter C, Searcy K, Jassim M. "Integrating MEA Regeneration with CO_2 Compression and Peaking to Reduce CO_2 Capture Costs." Final

Report for Trimeric Corp. (Subcontract of DOE Contract DE-FG02-04ER84111). June, 2005.

Rocha JA, Bravo JL, Fair JR. "Distillation Columns Containing Structured Packings: A Comprehensive Model for Their Performance. 1. Hydraulic Models." *Ind. Eng.Chem. Res.* 1993;32(4):641-651.

Rocha, JA, Bravo JL, Fair JR. "Distillation Columns Containing Structured Packings: A Comprehensive Model for Their Performance. 2. Mass-Transfer Models." *Ind. Eng. Chem. Res.* 1996; 35:1660.

Sahay BN, Sharma MM. "Effective interfacial area and liquid and gas side mass transfer coefficients in a packed column." *Chemical Engineering Science.* 1973;28:41-47.

Sharma MM, Danckwerts PV. "Chemical methods of measuring interfacial area and mass transfer coefficients in two-fluid systems." *British Chemical Engineering.* 1970;15(4): 522-528.

Sherwood, TK. et al., *Mass transfer*. McGraw-Hill, New York, 1975.

Shi MG, Mersmann A. "Effective Interfacial Area in Packed Columns." *Ger. Chem. Eng.*1985;8:87-96.

Song D, Seibert AF, Rochelle GT. "Effect of liquid viscosity on the liquid phase mass transfer coefficient of packing. " Energy Procedia.

Tsai R., Schultheiss P., et al. “Influence of Surface Tension on Effective Packing Area”. Ind. Eng. Chem. Res. 2008;47:1253-1260.

Tsai R. "Mass Transfer Area of Structured Packing". The University of Texas at Austin. Ph.D Dissertation. 2010.

Yaici W., Laurent A. "Determination of gas-side mass transfer coefficients in trickle-bed reactors in the presence of an aqueous or an organic liquid phase." International Chemical Engineering. 1988;28(2):299-305.

Wang C et al. "Packing characterization: Mass Transfer Properties. " *Energy Procedia.* 2012;23: 23-32.

Wang C et al. "Characterization of novel structured packing for CO2 capture." *Energy Procedia.* 2013;37: 2145-2153.

Xu Q. "Total pressure and CO_2 solubility at high temperature in aqueous amines." *Energy Procedia.* 2011;4: 117-124.

Effect of liquid viscosity on the liquid film mass transfer coefficient in packed columns

Quarterly Report for October 1 – December 31, 2014

by Di Song

Supported by the Texas Carbon Management Program

and the

Process Science and Technology Center

McKetta Department of Chemical Engineering

The University of Texas at Austin

January 31, 2015

Abstract

In this quarter, the reaction kinetics (k_g') of CO_2/NaOH/H_2O/glycerol was measured in the wetted wall column (WWC) with elevated NaOH concentration (0.3 M). The trend of k_g' as a function of glycerol concentration follows exactly that for the cases with 0.1 M NaOH. Models of the overall reaction rate constant (k_{Alk}) and surface alkalinity depletion were modified based on the new k_g' data. A detailed research plan for experiment in the pilot-scale air/water column was proposed.

Introduction

Packed columns are important for separation processes including post-combustion CO_2 capture. Since the amine solvent used for CO_2 scrubbing may have a viscosity significantly greater than water, it is important to know how μ_L affects k_L in the column. Few of the existing k_L (k_La) correlations provide satisfactory predictions for the influence of μ_L (Rochelle et al., 2013). This project aims to build a reliable k_L correlation to predict the effect of μ_L on k_L. The overall plan and experimental methods for the project are summarized in previous reports (Rochelle et al., 2014a, 2014b).

Results

The k_g' of CO_2/NaOH/H_2O/glycerol for the normal (0.1 M) and elevated (0.3 M) caustic concentration is summarized in Figures 1 and 2. The trend of k_g' as a function of glycerol concentration for the two caustic concentrations is almost identical, which proves the reproducibility of the WWC measurement. Depletion of surface alkalinity was corrected by a modified model using effective diffusivity of the ions (Geankoplis, 2003). k_{Alk} can be determined from empirical k_g' by Equation 6, based on which models have been built (Equations 1–6) to calculate k_{Alk}. Parameters of the model are summarized in Table 1. Calculated k_{Alk} and k_{Alk} determined from empirical k_g' are shown in Figure 3.

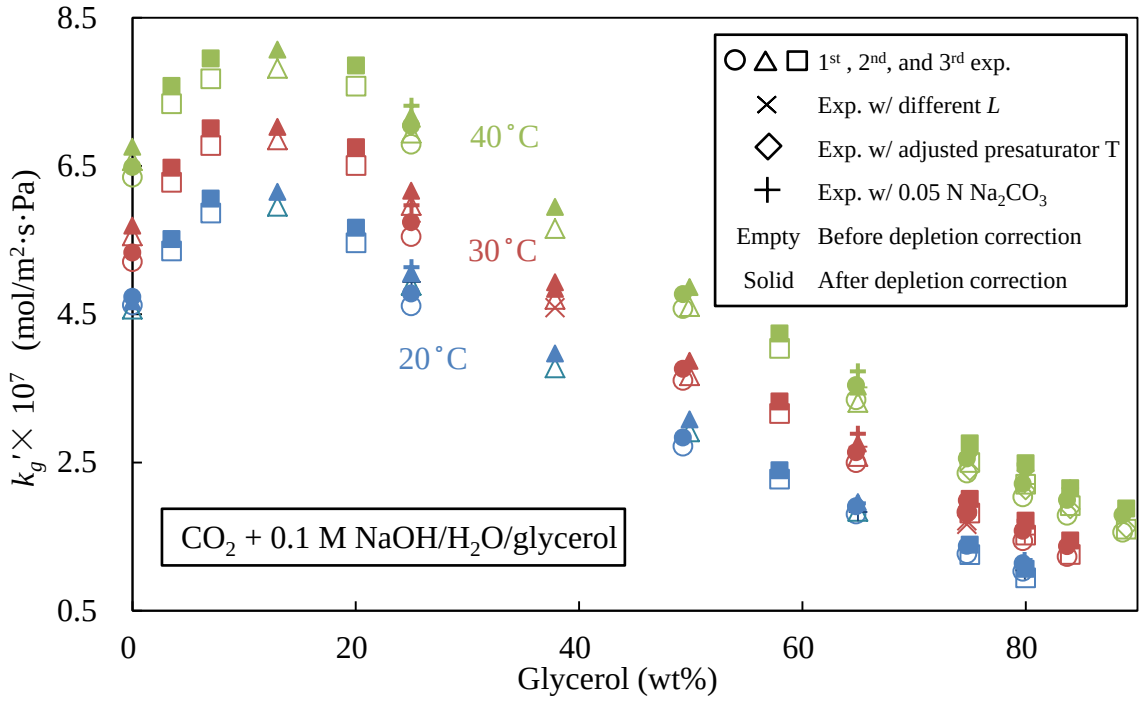

Figure 1: k_g' of CO_2/NaOH/H_2O/glycerol (nominally 0.1 M NaOH)

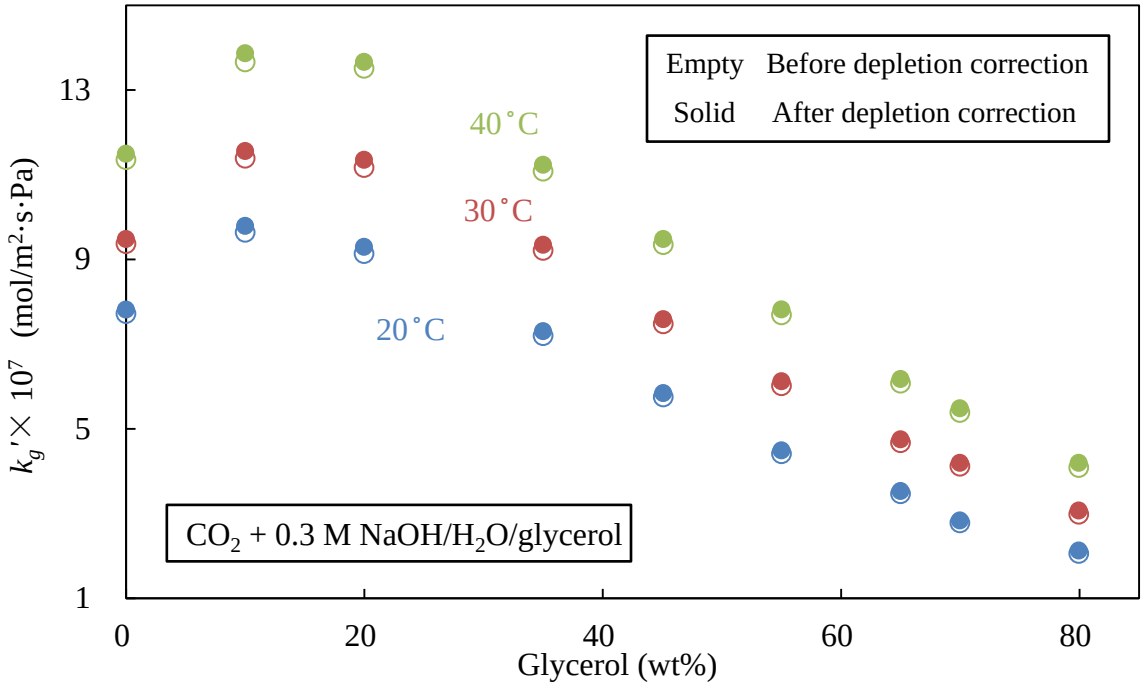

Figure 2: k_g' of CO_2/NaOH/H_2O/glycerol (nominally 0.3 M NaOH)

$$K_T = A_1 + exp\left(B_1 - \frac{C_1}{T}\right) \quad (1)$$

$$k_{OH^-} = 10^{\left(A_2 - \frac{B_2}{T} + C_2 I - 3\right)} \quad (2)$$

$$k_{gly^-} = exp\left(A_3 - \frac{B_3}{T}\right) \quad (3)$$

$$k_{Alk} = \frac{[OH^-]}{[Alk]} k_{OH^-} + \frac{[Gly^-]}{[Alk]} k_{gly^-} \quad (4)$$

$$[Gly^-]^2 - \left\{[Gly]_T + \frac{1}{K_T} + [Alk]\right\}[Gly^-] + [Alk][Gly]_T = 0 \quad (5)$$

$$[OH^-] = [Alk] - [Gly^-] \quad (6)$$

Table 1: Parameters in Equations 1–6

Subscript	A	B	C
1	0.25	-81.04	0
2	12.46	2477.0	-0.082
3	19.90	4582.9	-

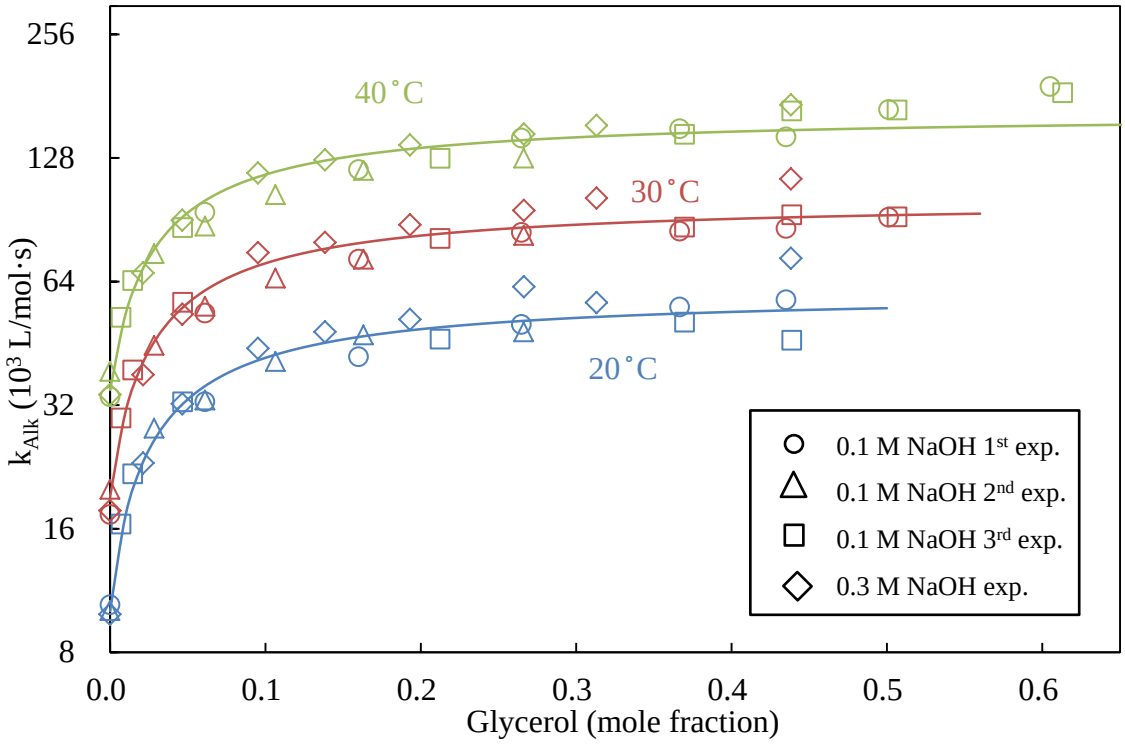

Figure 3: Calculated k_{Alk} and k_{Alk} determined from empirical k_g'

Detailed research plan for a_e and k_L measurement in the air/water column

Research Objective

Systematically investigate the effect of liquid viscosity on effective mass transfer area and liquid-phase mass transfer coefficient for structured packings.

Equipment

The pilot-scale PVC column to be used is located in the outdoor area of the Separation Research Program (SRP) facility at Pickle Research Campus of The University of Texas at Austin. It has an outside diameter of 0.46 m (18 in.), an inner diameter of 0.427 m (16.8 in), and a total height of approximately 7.62 m (25 ft.). A pressurized fractal liquid distributor with 432 drip points/m^2 (40 points/ft^2, i.e., F40) is installed at the top of the column. A Trutna collector was installed above the distributor to prevent liquid entrainment. The configuration is shown in Figure 4.

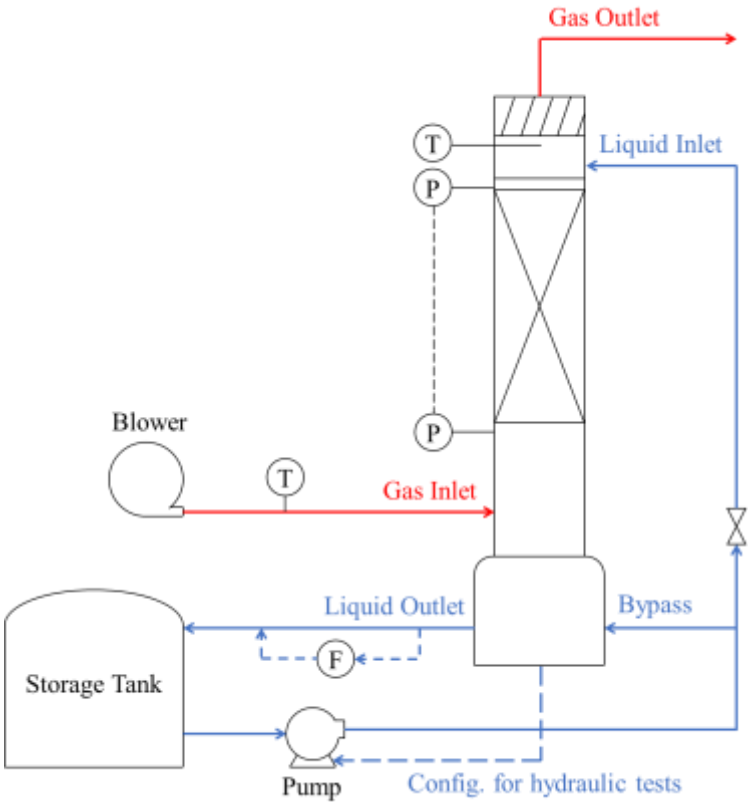

Figure 4: Configuration of pilot packed column

(F: filter, P: pressure transmitter, T: thermocouple)

A 30 kw (40 hp) blower will be used to supply ambient air into the column, with the gas flow rate monitored by an Annubar flow meter. A centrifugal pump will be used for liquid flow from a 1.3 m^3 (350 gal) storage tank to the top of the column. The liquid flow rate will be measured by a micromotion coriolis meter. A level transmitter is installed at the column sump to estimate the liquid inventory in the system. Pressure drop through the packing will be determined by a

pair of differential pressure transmitters. The temperatures of the inlet and outlet gas will be measured by thermocouples, and the temperature of the liquid will be measured by the micromotion meter. Approximately 3 m (10 ft) of packing will be used for both a_e and k_L measurements. DeltaV software developed by Emerson is used for system control.

During the experiment, depletion of bulk alkalinity will be monitored by mass balance of CO_2. Between each experiment, Total Inorganic Carbon (TIC) analysis will be conducted to verify the carbonate concentration for the next experiment. The goniometer apparatus owned by the Freeman research group at the University of Texas at Austin will be used to measure the contact angle and surface tension of the liquids. The cone-plate viscometer maintained by Dr. Keith Friedman will be used for viscosity measurement of liquid samples. The densitometer owned by the Rochelle research group will be used for measurement of liquid density, based on which the total glycerol concentration in the liquid can be determined. The pH and total alkalinity of liquid samples will be measured by acid titration with a titrator owned by the Rochelle group. A Horiba infrared carbon dioxide analyzer will be used to measure the inlet and outlet CO_2 concentration in the gas phase. A gas chromatograph will be used for analysis of toluene concentration in the liquid samples.

Chemicals

NaOH pellets will be purchased from PHARMCO-AAPER or EMD Chemicals Inc. The titration HCl and phenolphthalein solution will be purchased Ricca Chemical Company. The concentrated HCl solution for neutralization will be purchased from J.T. Baker. The N_2 and 450 ppm_V CO_2 cylinders will be purchased from Praxair. (Toluene source unclear yet.)

The price and source of glycerol are still uncertain. Many companies provide glycerol in quantity (Bulk Apothecary, Jedwards Int. Inc., Parchem, etc.) The price for one batch (approximately 2000 lbs) of pure glycerol will be about $1,400 (Bulk Apothecary). The actual price is expected to be lower because: 1. the glycerol provided on the website is USP 99.7% palm-based vegetable glycerol, which is an overqualified product for the experiments; 2. according to the sales assistant, an extra discount will be given for a bulk order; 3. glycerol will be diluted by water for experiments. Since the minimum shelf life of glycerol is 12 months unopened in a cool (65–75 °F) environment, glycerol can be purchased in large quantities in advance of experiments.

Proposed packings

Structured packings: MP250X (Y), MP125Y, GT-PAK350Y (Z), RSP250Y

Hybrid: RSP250Y

MP250X will be tested first as a standard for structured packings. Packings with different corrugation angle and specific area will be tested to incorporate the combined influence of these factors and μ_L change on a_e and k_L. If time allows, a few random packings (RSR#0.5, IMTP#25, etc.) will also be measured.

Experimental Methods

The basic method and procedure for the experiments follow those of Tsai (Tsai, 2010) and Wang (Wang, Perry, Rochelle, & Seibert, 2012; Wang, Perry, Seibert, & Rochelle, 2012). Different concentrations of glycerol (0, 60, 85 wt %) will be added into the liquid as a viscosity enhancer

to reach the proposed μ_L range 1–100 cP. Hydraulic studies will be done prior to a_e and k_L measurement using liquid without caustic to determine pressure drop and liquid hold-up.

Experiment Protocols

Hydraulic tests

In a hydraulic run, the storage tank will be filled with liquid, which will be pumped to the column sump without return. The liquid line will be configured to circulate liquid between the sump and column. The pneumatic valve controlling flow to the column will be closed, but the pump will be left operating to keep the liquid lines as primed as possible. The blower will be turned on, and the liquid level in the sump will be allowed to stabilize for 5–10 minutes to establish a baseline liquid-level reading. The pneumatic valve will then be opened. A constant liquid load will be set, and the air flow rate will be incremented until flooding conditions (2 in H_2O/ft). The liquid hold-up and pressure drop will be measured at the same time. Hold-up will be determined from the difference between the current and baseline liquid levels.

Mass transfer experiments

In consideration of the availability of the column and the price of glycerol, a_e and k_L measurement will be conducted simultaneously. The storage tank will be charged with certain amount of water, after which NaOH pellets will be added. After 10–15 minutes circulation of the solution between the storage tank and column sump, glycerol will be added to reach the desired μ_L and make the total volume 0.75 m^3 (200 gallons). Two liters of toluene will then be added into the liquid. Toluene will be metered continuously into the sump tank to maintain a constant toluene concentration in the solution. The solution will be circulated through the loop shown in Figure 1. The packing will be pre-wetted at a relatively high liquid load for at least 5 minutes. Samples will be taken before experiments to verify μ_L and the concentrations of NaOH and toluene. Because of the possible increase in liquid hold-up for viscous liquids, the blower duty will be adjusted according to the results of hydraulic tests to avoid flooding. At the same time that CO_2 concentration is measured by CO_2 analyzer, liquid samples will be taken for toluene concentration. For each condition, at least 10 minutes will be given for the system to reach steady state. After taking a satisfactory number of points for different liquid loads, the gas rate will be changed to a different value in the pre-loading zone.

During both hydraulic tests and mass transfer experiments, a portion of the flow from the storage tank will be diverted and recycled back to the tank in a bypass line, in order to operate in a more favorable drive-speed region of the pump.

Procedure flow charts

Two different experimental procedures are proposed: one changes packing at a particular glycerol concentration, the other changes glycerol concentration at the same packing. The two procedure flow charts are shown in Figures 5 and 6.

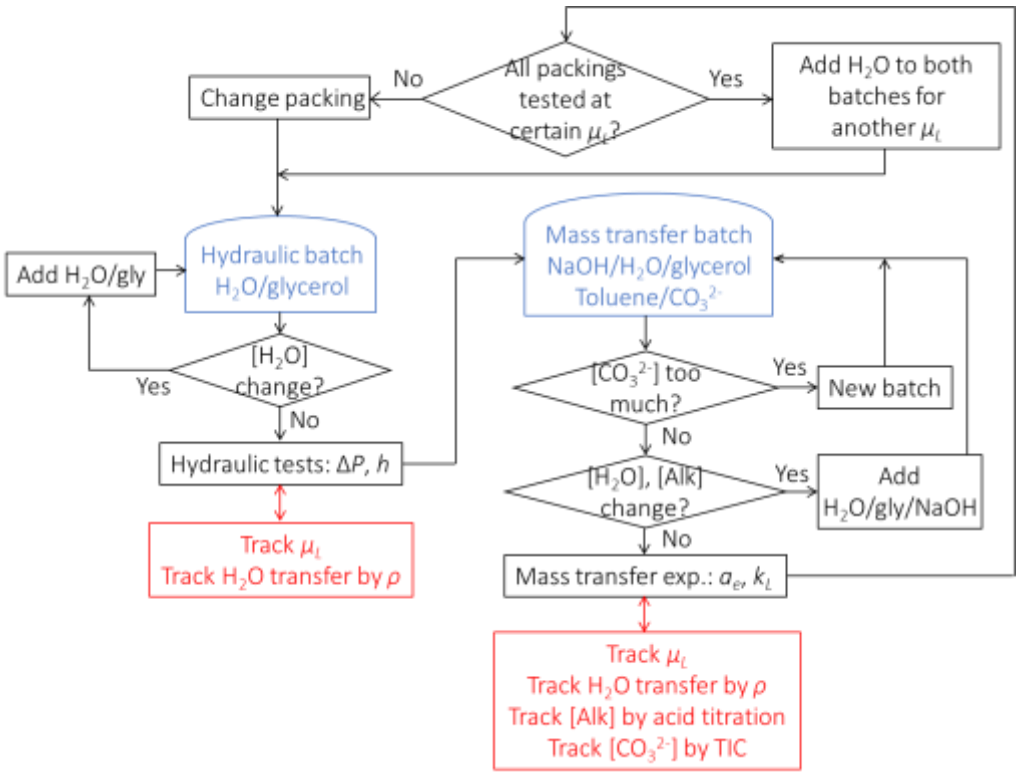

Figure 5: Procedure flow chart (one glycerol concentration for different packings)

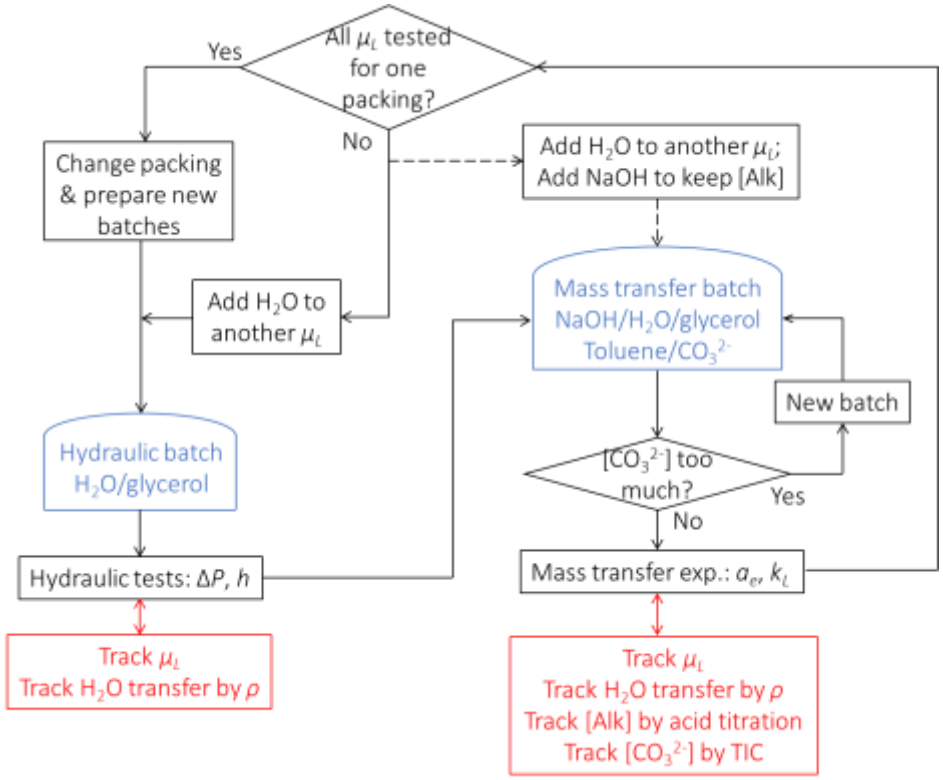

Figure 6: Procedure flow chart (one packing for different glycerol concentrations)

The procedure that changes packing at constant glycerol concentration (Figure 5) saves money in solution preparation. However, the other procedure (Figure 6) is more likely to be used considering that less time and labor is required, as well as less damage done to the packing during packing changing.

Experimental Concerns

Hydraulic tests and mass transfer experiments of aqueous solutions without glycerol will be conducted first for at least one structured packing with a_e and k_L measured simultaneously. There are two purposes for this preliminary experiment: 1. to make sure that the results agree with those of Tsai and Wang; 2. to check if there is any difference between the experimental methods of separate and simultaneous measurement of a_e and k_L. If significant difference is observed, separate measurement of a_e and k_L will be made to see whether the difference comes from the method of simultaneous measurement or from the systematic/personal difference between the current experiments and those of Tsai and Wang. Since different packing heights were used for previous measurement of a_e (10 ft.) and k_L (6 ft.), an intermediate packing height (8 ft.) will be used in the simultaneous measurement.

For economic reason, glycerol-rich solution will be reused for multiple measurements. Between experiments, solution will be preserved in a closed tank in a cool place for future use. Because of the no-caustic policy for hydraulic tests, two batches of solution will be prepared for hydraulic tests and mass transfer experiments, respectively. Since there will be no significant physical property change other than mass transfer of water during the hydraulic tests, the hydraulic batch is expected to last much longer than the mass transfer batch. For the mass transfer batch, because the accumulation of carbonate might change the reaction kinetics and lead to inaccuracy in a_e data, liquid samples will be taken after each experiment to measure the total active alkalinity and TIC in order to make sure that the carbonate concentration remains in an acceptable range. According to preliminary WWC experiments, no significant change in k_g' was observed for solutions at a concentration of 0.05 M carbonate (equivalent to 50% consumption of bulk alkalinity). If necessary, further WWC experiments will be done to find out the maximum acceptable concentration of carbonate in solutions with unaffected k_g'. Whenever the accumulation of carbonate starts to have a noticeable effect on k_g', a new batch for mass transfer experiments needs to be prepared. The accumulation of carbonate might not be as big a problem as it seems because: 1. the partial pressure of CO_2 is relatively low (atmospheric concentration); 2. for solutions with high glycerol concentration, the absorption rate of CO_2 is much lower than purely aqueous solution; 3. For solutions with low glycerol concentration, the price for one batch will decrease at the same time that absorption rate increases. Because of the 2nd reason above, it is recommended to start mass transfer experiments with higher glycerol concentration, and then decrease the concentration by adding water. Extra liquid samples (besides those taken for toluene concentration determination) will be taken before, during, and after each experiment at both liquid inlet and outlet to measure the total bulk active alkalinity and density in order to determine the amount of extra NaOH and water needed to compensate for the bulk alkalinity depletion and water vaporization. TIC and μ_L of those samples should also be measured to monitor the accumulation of carbonate and the change of μ_L as a function of column heights and experiment times.

When preparing the solutions, water should be first added into the tank, and should be circulated between tank and sump to dissolve NaOH pellets. Glycerol should be gradually added into the

tank after all NaOH pellets have dissolved to avoid lengthy NaOH dissolution and liquid dead zones of pure glycerol with extremely high μ_L (> 1000 cP). After that, enough time should be given for the solution to circulate to reach homogeneity before adding toluene.

In terms of solution preservation, the shelf life of glycerol in proper storage condition could be at least 12 months at 25 °C, and the highest temperature for storage at ambient condition is 52 °C (P&G Chemicals). Though a preliminary bench-scale sterilization experiment in the lab environment has shown that no biocide is needed for glycerol-rich solutions in open containers because no significant physical property change was observed other than mass transfer of water in 45 days (Rochelle et al., 2014b), special care should still be taken to monitor the appearance and physical properties of the solutions as a function of time.

Since the liquid hold-up at constant liquid load is expected to increase significantly at high glycerol concentration, gas flowrate and liquid load will need to be lowered in order to keep the operation at pre-loading zone. Therefore, data from hydraulic tests are necessary before any mass transfer experiments at the same glycerol concentration are performed. Smaller interval and range of gas flow rate and liquid load should be used in hydraulic tests to avoid unexpected flooding.

During the hydraulic test, care should be taken to ensure minimal condensation or entrainment of liquid in the pressure transmitter lines especially at high liquid loads or around the flood point. The transmitter tubing should be routinely checked and purged to solve this problem.

Three glycerol concentrations (0, 60, 85 wt %) will be tested to represent conditions of low, medium, and high μ_L (0.9, 8.9 and 80.2 cP at 25 °C, respectively). The actual concentration may be adjusted due to the effect of ambient temperature on μ_L. The order of experiments should be from high to low glycerol concentration to slow down the carbonate accumulation. However, experiments with 60 wt % glycerol solution will be conducted first for the initial packings for the following reasons: 1. the 60 wt % batch is relatively cheap compared to higher concentration solutions, which enables a greater tolerance for unexpected experiment failure; 2. the μ_L for 60 wt % glycerol solution is not drastically different from that of water, which lowers the possibility and damage of any unexpected problem for viscous liquid. After experience for the viscous system is obtained from the 60 wt % glycerol solutions, experiments will be done in order of decreasing glycerol concentration.

Surface depletion of alkalinity is not believed to be a problem, but this needs to be verified when the k_L data is obtained. According to the calculation based on the method of Pigford (Bird, Stewart, & Lightfoot, 2002; Pigford, 1942) for WWC data, surface depletion is within 10% of bulk alkalinity for most of the cases at approximate P_{CO2} of 500 ppm. This result is based on the worst case scenario assumption that all alkalinity is in the form of glycerol anion rather than hydroxide, which has an approximately ten times greater diffusivity than the former. The P_{CO2} and N_{CO2} in the packed column experiment are also expected to be lower than similar WWC cases (500 ppm and 6e-9 mol/s·cm^2 as the lowest WWC case compare to 400 ppm and 6e-10 mol/s·cm^2 as a typical packed column case), which help ameliorate the surface depletion. The dependence of k_g' on alkalinity concentration is 0.5 instead of 1, which will further decrease the apparent effect of surface depletion. Therefore, surface depletion of alkalinity is not believed to be a problem for packed column experiments.

Mass transfer of water will not have an immediate effect on k_g' according to the WWC data with different presaturator temperatures (20–40 °C). However, lengthy exposure to counter-current

air might change the bulk concentration of water in the long run, especially when the solutions are to be reused. The mass transfer direction of water could be either way, depending on the glycerol concentration as well as the temperature and relative humidity of the ambient air. For solutions with lower glycerol concentrations, water is more likely to evaporate from the solution to air, while for solutions with higher glycerol concentration, the reverse will probably occur. The change in bulk water concentration for one experiment is not believed to be significant and will be corrected by taking the average value of water concentration (determined by density measurement) before and after the experiment. Immediately prior to each experiment, a specific amount of water (or glycerol) and NaOH will be added to the solution to reach the desired μ_L and NaOH concentration.

The compatibility of NaOH/H_2O/glycerol/toluene with the current chromatography technique for toluene concentration measurement will be checked before mass transfer experiments. The solubility of glycerol in n-heptane is lower than 0.7 mmol/L over the temperature range 20–100 °C (Staveley & Milward, 1957). This agrees with the qualitative analysis that solubility of NaOH and glycerol in n-heptane should be very low because of the high hydrophilicity. However, an empirical check of standard samples with known toluene concentration at different glycerol concentrations is the safest way to avoid any inaccuracy.

Figure 4 shows that, though the infinite dilution activity coefficient of toluene decreases rapidly with increasing glycerol, the value will still be well above 100 at the highest proposed glycerol concentration, which will result in a high Henry's constant and ensure a liquid-phase dominated mass transfer system. The appearance of NaOH and carbonate ions are also believed to increase the activity coefficient and make the system more controlled by liquid-phase resistance. Moreover, as μL increases, the decrease in kL will compensate partly for the decrease in activity coefficient.

According to Tsai (2010), the temperature used in the calculation of kg' will be an average of gas and liquid temperature, with the liquid weighted more heavily (i.e., gas temperatures first averaged, then averaged with the liquid). This practice was based purely on experience and was found to be more accurate in reconciling the mass transfer area data at ambient temperature extremes (i.e., summer and winter) than simply using the liquid temperature. The "corrected" temperature was on average within 3 °C of the liquid temperature according to Tsai, so the applied correction was not extreme.

The k_g' for pure aqueous NaOH solutions measured by the WWC is systematically higher than the values calculated by Pohorecki and Moniuk (1988) by an average of 48.6%. This is also true for k_g' data measured by Tsai. In order to conform to previous SRP data of a_e, the Pohorecki & Moniuk model will still be used for solutions without glycerol. However, for solutions with glycerol, a slightly modified model of k_{OH^-} (Equation 5) will be used to calculate the overall rate constant, k_{Alk}, for better agreement with the WWC data.

Figure 1 shows that the k_g' for CO_2/NaOH/H_2O/glycerol at the three proposed glycerol concentrations ranges from 0.25 to 0.95 times the k_g' for pure aqueous NaOH solutions. Such k_g' will translate to a HTU_{OG} for typical 250Y packing of about 10–100 ft., and outlet CO_2 concentration in the gas phase of about 140–360 ppm (assuming 400 ppm inlet concentration) if a_e and u_g are kept constant. For the 360 ppm case, the gas flow rate should be kept low to avoid flooding and ensure a statistically adequate removal of CO_2. For k_L experiments, assuming -0.5 dependence of k_L on μ_L, the k_L could be as low as 0.1 times that for pure aqueous NaOH

solutions, which will result in HTU_{OL} for typical 250Y packing of about 30–50 ft. and subsequent outlet toluene concentration of about 120 ppm at 10 ft. packing (assuming 250 ppm inlet concentration).

Since 8 ft. of packing will be used in the mass transfer experiment, the end effect is considered to be unimportant. For the first few experiments, CO_2 concentration in the gas may be measured at both the gas inlet duct and the point right below the packing support to verify this assumption. It is unlikely, but if necessary, different packing height (e.g., 10 ft. and 8 ft.) could be used to quantify the end effect.

Safety

1. Hard hats are required for experiments outside the control room.
2. Alkaline solvents (NaOH) should be neutralized to pH 6–10 before disposal.
3. A gas mask with respirator is required when handling volatile and toxic chemicals.
4. Steel reinforced gloves are required when handling sheet metal structured packing.
5. During WWC experiments, special caution should be taken to keep the reaction chamber pressure constant by adjusting the gas flow rate and needle valve. A too high pressure may cause leakage or failure of glass tubes.

Conclusions

k_g' for CO_2/H_2O/NaOH/glycerol with elevated NaOH concentration (0.3 M) has been measured at 20, 30, and 40 °C. k_g' initially increases about 25% when glycerol increases to 15 wt % because of the catalytic effect of glycerol, and then decreases about 70% when glycerol increases to 80 wt % because of the impeding effect of elevated μ_L on mass transfer. The overall trends of k_g' are the same for at concentrations of 0.1 M and 0.3 M NaOH. Model parameters of surface alkalinity depletion, k_{Alk}, and k_g' have been updated based on the new data.

a_e and k_L will be measured simultaneously at three glycerol concentrations (0, 60, and 85 wt %), which correspond to three μ_L at 20 °C: 1.0, 10.9, and 110.8 cP, respectively. It is proposed that the glycerol-rich solutions will be reused for experiments at one specific packing. The following packings will be tested: MP125Y, MP250X, MP250Y, RSP 250Y. Possible challenges for the viscous system have been discussed.

Future Work

Refine experiment plan for the air/water column. Write the SOP for experiments in the air/water column with elevated liquid viscosity. Add a bypass line of the air/water column to install online viscometer and conductivity sensor.

References

Bird, R. Byron, Stewart, Warren E., & Lightfoot, Edwin N. (2002). *Transport Phenomena* (2 ed.). New York: John Wiley & Sons.

Geankoplis, C.J. (2003). *Transport Processes and Separation Process Principles: Includes Unit Operations*: Prentice Hall Professional Technical Reference.

Pigford, Robert L. (1942). *Counter-diffusion in a wetted wall column.* (Ph.D.), The University of Illinois at Urbana Champaign, USA. Available from http://worldcat.org /z-wcorg/ database.

Pohorecki, Ryszard, & Moniuk, Wladyslaw. (1988). Kinetics of reaction between carbon dioxide and hydroxyl ions in aqueous electrolyte solutions. *chemical Engineering Science, 43*(7), 1677–1684.

Rochelle, Gary T., Du, Yang, Fine, Nathan, Frailie, Peter, Fulk, Steven, Li, Le, . . . Wang, Chao. (2013). CO_2 Capture by Aqueous Absorption, Third Quarterly Progress Report 2013, *Texas Carbon Management Program*.

Rochelle, Gary T., Du, Yang, Fine, Nathan, Frailie, Peter, Fulk, Steven, Li, Le, . . . Wang, Chao. (2014a). CO_2 Capture by Aqueous Absorption, First Quarterly Progress Report 2014, *Texas Carbon Management Program*.

Rochelle, Gary T., Du, Yang, Fine, Nathan, Frailie, Peter, Fulk, Steven, Li, Le, . . . Wang, Chao. (2014b). CO_2 Capture by Aqueous Absorption, Second Quarterly Progress Report 2014, *Texas Carbon Management Program*.

Staveley, L. A. K., & Milward, G. L. (1957). Solutions of alcohols in nonpolar solvents. IV. Thermodynamic properties of glycol in benzene, heptane, and cyclohexane. *J. Chem. Soc.*, 4369-4375. doi: 10.1039/jr9570004369

Tsai, Robert E. (2010). *Mass Transfer Area of Structured Packing.* (Ph.D.), The University of Texas at Austin, USA.

Wang, Chao, Perry, Micah, Rochelle, Gary T., & Seibert, A. Frank. (2012). Packing Characterization: Mass Transfer Properties. *Energy Procedia, 23*(0), 23–32. doi: 10.1016/j.egypro.2012.06.037

Wang, Chao, Perry, Micah, Seibert, A. Frank, & Rochelle, Gary T. (2012). *Characterization of novel structured packings for CO_2 Capture*. Paper presented at the GHGT-11, Kyoto.

Heat Exchanger Economics and 2PE Thermodynamic Model

Quarterly Report for October 1 – December 31, 2014

by Brent Sherman

Supported by the Carbon Capture Simulation Initiative through

DOE 373-DOE-FE-13118-UTEXAS

McKetta Department of Chemical Engineering

The University of Texas at Austin

January 31, 2015

Abstract

Three different projects addressed generic modeling methods, the effect of viscosity, and economics. A rigorous plate-and-frame heat exchanger economic tool was coded in Aspen Plus® using a calculator block. This brings the previous offline rigor online, enabling optimization of the exchangers. The online and offline calculations agree on average within 2% with a maximum deviation of 10%. A 2-piperadineethanol thermodynamic model was constructed using analogs from the AMP eNRTL Aspen Plus® model. This is the first step in proving the hypothesis that hindered amines enhance the rate of CO_2 absorption through increasing the solubility of CO_2 in solution. The 2PE model was used as an opportunity to investigate ways to correlate viscosity. This investigation showed that the best method is the semi-empirical modified Weiland equation rather than the internal correlations that are available in Aspen Plus®.

Introduction

This work has four goals: rigorous thermodynamic and kinetic models; a generic amine modeling method; viscosity process effects; and economic evaluation. Developing more rigorous models enables the creation of a generic amine modeling method. The aim of the method is to streamline model development, shortening the time to a process model. Process performance will be evaluated from an economic standpoint with special interest paid to viscosity effects.

Work this quarter concerned the last three goals and was split into three projects: a heat exchanger and economic calculation tool, a thermodynamic model of 2-piperadineethanol (2PE), and viscosity regression methods. The heat exchanger tool can be used to better understand viscosity process effects through economic evaluation, while the thermodynamic model of 2PE uses a generic method by adapting the 2-amino-1-propanol (AMP) model. The 2PE model was used as an opportunity to explore novel viscosity regression methods.

Heat Exchanger Economics: History and Rationale

The economics of the heat exchanger includes the flashing and non-flashing plate-and-frame heat exchangers as well as the rich and lean pumps. The pumps are included as the pressure drop in the heat exchangers impacts the pump economics.

Modeling the heat exchanger rigorously in Aspen Plus® without adding to the already difficult problem of convergence has been a group goal for at least two years. The first efforts consisted of taking simulation results and doing manual offline calculations (Frailie, 2014). This has the advantage of being very simple, having no impact on convergence, and showing all intermediate values. This method has the major disadvantage of making optimization prohibitively time consuming, as each iteration requires manual action.

Moving to online calculations would enable rapid optimization by eliminating manual action. The first effort to move online was by Sherman (Rochelle et al., 2013). He overloaded the user heat transfer subroutine of the HEATX block to size a non-flashing heat exchanger. The subroutine had insufficient input/output control to eliminate manual action and obfuscated the intermediate values.

The next effort involved a USER2 block, but again overcoming input control proved difficult (i.e., pulling in arbitrary stream properties for streams not connect to the USER2 block). Aspen Plus® help revealed a bug in the calculator block that was preventing access to necessary stream variables. The bug was resolved, and so a calculator block instead of a USER2 block could be used. This calculator block approach is taken here.

2PE Thermodynamics

A 2PE thermodynamic model is of interest only as a stepping stone to a kinetic model for proving the following enhanced solubility hypothesis. The hypothesis for hindered amines having a faster rate of CO_2 absorption than tertiary amines is the formation, diffusion, and subsequent hydrolysis of carbamate to form bicarbonate, the major product. This process enhances the effective solubility of CO_2, which accelerates the absorption of CO_2.

To prove this hypothesis, the hindered 2PE system and the AMP system must be modeled. While the amount of carbamate formed in AMP was found to have no effect on the thermodynamics, the carbamate reaction was significant for matching k_g' behavior. Similar effects are expected in the 2PE system. However, unlike for AMP there is debate over whether 2PE forms a carbamate (Ciftja et al., 2014; Fernandes et al., 2012; Xu et al., 1993).

2PE Viscosity

The viscosity in all Rochelle group process models is calculated using a semi-empirical correlation in a subroutine. Using an external subroutine introduces additional complexity, and so it is desirable to eliminate subroutines. Aspen Plus® has built many amine scrubbing models for acid gas treating that use internal viscosity correlations, indicating that a physically representative model ought to be possible without resorting to semi-empirical viscosity correlations. This was attempted earlier with AMP, but without success (Rochelle et al., 2014b).

CCSI Update

The uncertainty quantification (UQ) focus of the Carbon Capture Simulation Initiative (CCSI) has shifted from the volatility of 2-methylpiperazine (2MPZ) to the kinetics of 2MPZ. As part of this effort, the kinetic modeling procedure is being automated. This will enable running a large number of cases to determine the importance of each parameter. This work is in progress.

Three separate product manuals were written: one for a process model of 2MPZ, one for a process model of 2MPZ/piperazine (PZ), and one for a non-flashing plate-and-frame heat exchanger. These are in the Appendix.

Modeling Methods

Heat Exchanger Economics

As discussed in the introduction, a calculator block is used to size and cost flashing and non-flashing plate-and-frame heat exchangers. Using a calculator block allows for convergence separate from the flowsheet. As the calculation is done online, optimization of the economics is convenient. The equations are based on the previous work of Lin, who has documented the correlations used and the economic assumptions made (Rochelle et al., 2014a).

Two different versions of the calculator block were made. A simple version that only models a non-flashing plate-and-frame heat exchanger was designed for CCSI and is documented in §3 of the Appendix. A more advanced version that handles non-flashing and flashing exchangers along with the pumps and economics is documented in §4 of the Appendix.

2PE Thermodynamics

As this is not intended to be a process model, the thermodynamic model must only support the kinetic model. For this reason, amine volatility is negligible and the heat of absorption is less important. The model is constructed in Aspen Plus® using the eNRTL activity coefficient framework. The little data available is summarized in Table 1.

Table 1: 2PE Thermodynamic data

System	Type	# of data	T (°C)	Loading (mol CO_2/mol alk)	C_{Am}	Source
2PE	C_p	11	30–80	—	100 wt. %	(Chiu et al., 2010)
		44			0.2–0.8 mol frac.	
2PE+H_2O	pKa	5	15–60		<0.1 M	(Xu et al., 1992)
2PE+H_2O+CO_2	VLE	14	40–100	0.205–0.635	8 m	(Chen, 2011)

To model the system in Aspen Plus®, the components were defined using AMP analogs. The aqueous Gibbs free energy of formation ΔG°_{aq} and the aqueous enthalpy of formation ΔH°_{aq} for the ions, $2PECOO^-$ and $2PEH^+$, and the Gibbs free energy of formation ΔG° and the aqueous enthalpy of formation ΔH° for the molecule 2PE were taken from $AMPCOO^-$, $AMPH^+$, and AMP. The molecular weight and charge were also defined. (There is a bug that causes Aspen Plus® to appear to define CHARGE from the molecular structure without actually doing it. The ionic charge must be entered manually.)

Equations 2–4 show the model chemistry used. The equilibrium constants are calculated from the ΔG and ΔH of each species, not from a polynomial expression. To match the pKa data (Xu et al., 1992), ΔG°_{aq} and ΔH°_{aq} for $2PEH^+$ were manually changed. Once the pKa was matched, the fourteen VLE data were regressed using the Data Regression System (DRS) (Chen, 2011). The temperature independent parameter $C_{i,j}$ of the binary interaction term $\tau_{i,j}$ of Equation 1 was regressed for the interactions between ($2PEH^+$, CO_3^{2-}), H_2O, ($2PEH^+$, HCO_3^-), H_2O, and ($2PEH^+$, HCO_3^-), 2PE.

$$\tau_{i,j} = C_{i,j} + \frac{D_{i,j}}{T} \tag{1}$$

$$2\ 2PE + CO_2 \leftrightarrow 2PECOO^- + 2PEH^+ \tag{2}$$

$$2PE + CO_2 + H_2O \leftrightarrow 2PEH^+ + HCO_3^- \tag{3}$$

$$2PE + HCO_3^- \leftrightarrow 2PEH^+ + CO_3^{2-} \tag{4}$$

2PE Viscosity

In an attempt to eliminate the viscosity subroutine, the correlations of Aspen Plus® were used. For the pure component viscosity of 2PE the Andrade Equation (5) was used.

$$\ln \mu = \mathrm{A} + \frac{B}{T} + C\ln T \tag{5}$$

where μ is viscosity and *A*, *B*, and *C* are parameters. The modified Andrade Equation (Equation 6) is used for mixtures.

$$\ln \mu = \sum_i f_i ln\mu_i + \sum_i \sum_j \left(k_{ij} f_i f_j + m_{ij} f_i^2 f_j^2\right) \tag{6}$$

where μ is the mixture viscosity, f_i (f_j) is the mole fraction of component i (j), μ_i is the pure viscosity of component i, $k_{ij} = a_{ij} + \frac{b_{ij}}{T}$, and $m_{ij} = c_{ij} + \frac{d_{ij}}{T}$. a_{ij}, b_{ij}, c_{ij}, and d_{ij} are parameters. The viscosity data sets of Chen (2011) and Xu et al. (1992) described in Table 2 were regressed together using the DRS. *A* and *B* of Equation 5 were regressed along with k_{ij} and m_{ij} of (2PE, H_2O) and (HCO_3^-, $2PEH^+$) for a maximum of ten parameters.

Table 2: 2PE hydraulic data

System	Type	# of data	T (°C)	Loading (mol CO_2/mol alk)	C_{Am}	Source
2PE+H_2O	ρ	60	15–60	—	5-30 wt %	(Paul et al., 2006)
	μ	60			5-30 wt %	
	ρ	30	25–84.2		10–100 wt %	(Xu et al., 1992)
	μ	35	25–85.2		10–100 wt %	
2PE+H_2O+CO_2	μ	4	40	0.205–0.684	8 m	(Chen, 2011)

Results and Discussion

Heat Exchanger Economics

To confirm the accuracy of the online calculations, the results were compared to the offline spreadsheet calculation. The test case was 5 m PZ with a lean loading of 0.22 mol CO_2/mol alk and a rich loading of 0.40 mol CO_2/mol alk in the advanced flash stripper (AFS) configuration. This configuration has a non-flashing and a flashing heat exchanger. Table 3 shows that the two calculations agree on average within 2% with a maximum relative difference of 10.8%. While the equations are all exactly the same, the implementation of floating point operations in Microsoft Excel and Aspen Plus® leads to disagreement.

Table 3: Heat exchanger economics comparison of the offline, online, and percent relative difference as calculated by $\frac{offline-online}{offline}$.

	Non-flashing			Flashing			Total		
Calculation	Offline	Online	Rel. D.	Offline	Online	Rel. D.	Offline	Online	Rel. D.
Exchanger CAPEX ($/tonne CO_2)	3.61	3.62	–0.5%	1.66	1.71	–3.0	5.26	5.33	–1.3%
Rich pump OPEX ($/tonne CO_2)	0.302	0.297	1.8%	0.187	0.185	0.9%	0.489	0.482	1.5%
Lean pump OPEX ($/tonne CO_2)							0.371	0.355	4.4%
Rich pump CAPEX ($/tonne CO_2)	0.158	0.155	1.8%	0.098	0.097	0.9%	0.257	0.252	1.5%
Lean pump CAPEX ($/tonne CO_2)							0.202	0.193	4.4%
TAC ($/tonne CO_2)							6.58	6.61	–0.5%
Area (m^2)	3.50E+04	3.52E+04	–0.5%	1.61E+04	1.66E+04	–3.0%	5.11E+04	5.18E+04	–1.3%
LMTD (K)	4.97	4.95	0.4%	5.50	5.04	0.3%	5.00	4.98	0.3%
Duty (W)	3.66E+08	3.66E+08	0.0%	1.95E+08	1.95E+08	0.0%	5.61E+08	5.61E+08	0.0%
Plate length (m)	17.84	17.78	0.3%	7.01	6.81	2.9%	24.85	24.59	1.0%
ΔP_{rich} (Pa)	4.18E+05	4.10E+05	1.8%	4.09E+05	4.05E+05	0.9%	8.27E+05	8.16E+05	1.4%
ΔP_{lean} (Pa)	4.42E+05	4.34E+05	1.8%	1.14E+05	1.01E+05	10.8%	5.56E+05	5.36E+05	3.6%

2PE Thermodynamics

The fit of pKa is shown in Figure 1. The two parameters used to fit five data points are $\Delta G^{\circ}_{aq} = -1.77 \times 10^{8}$ and $\Delta H^{\circ}_{aq} = -4.02 \times 10^{8}$ of $2PEH^{+}$. The fit is good with an R^2 of 0.992 and a mean squared error of 1.58E–03.

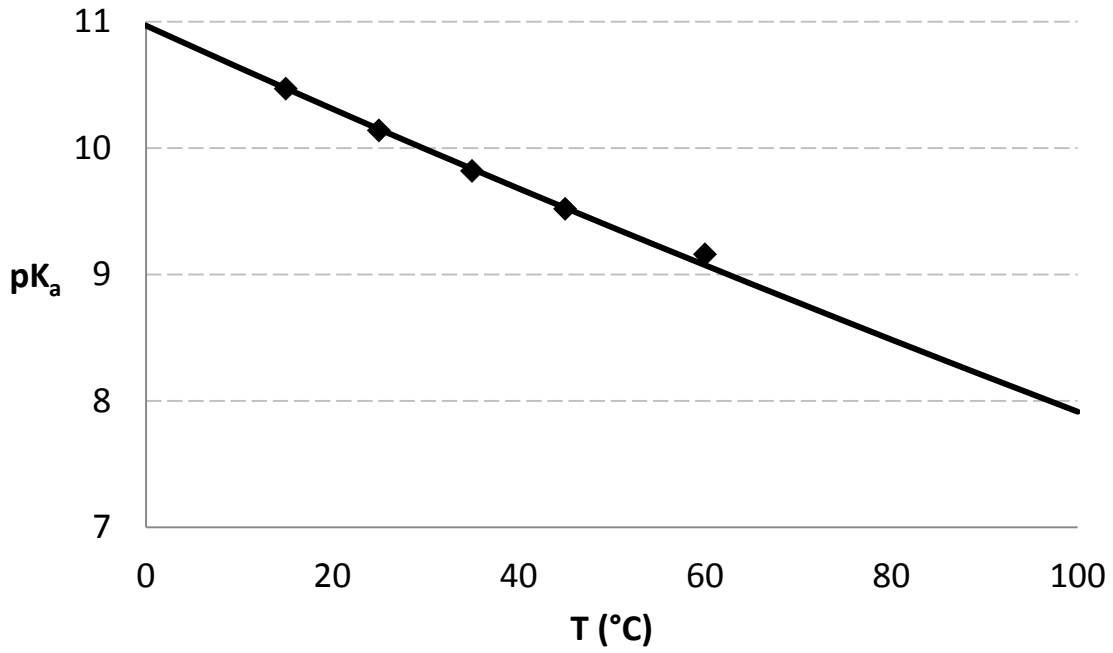

Figure 1: 2PE pKa model fit with data from Xu et al. (1992)

The results of fitting VLE are shown in Figure 2, while the parameters used are shown in Table 3. Table 4 shows that the parameters are not strongly correlated. The VLE fit is weak at the rich end, but this fit is sufficient to model the kinetics.

The heat of absorption is predicted from the VLE using the Lewis and Randall equation shown in Figure 3 along with the results. Close to loadings of 0 and 1 mol CO_2/mol alk, ΔH_{abs} is ill behaved. While across the loading range for coal-fired capture 0.37 to 0.68 mol CO_2/mol alk the prediction is better behaved, it shows a very strong temperature dependence.

Table 4: 8 m 2PE thermodynamic adjusted parameters

i	j	Default	Value	σ^2
($2PEH^{+}$,CO_3^{-2})	H_2O	–4	–5.01	0.22
($2PEH^{+}$, HCO_3^{-})	H_2O	–4	–3.68	0.01
($2PEH^{+}$, HCO_3^{-})	2PE	–2	–4.08	0.11

Table 5: Correlation matrix of 8 m 2PE thermodynamic parameters

Parameter	($2PEH^+$,CO_3^{-2}), H_2O	($2PEH^+$, HCO_3^-), H_2O	($2PEH^+$, HCO_3^-), 2PE
($2PEH^+$,CO_3^{-2}), H_2O	1		
($2PEH^+$, HCO_3^-), H_2O	0.73	1	
($2PEH^+$, HCO_3^-), 2PE	–0.48	–0.36	1

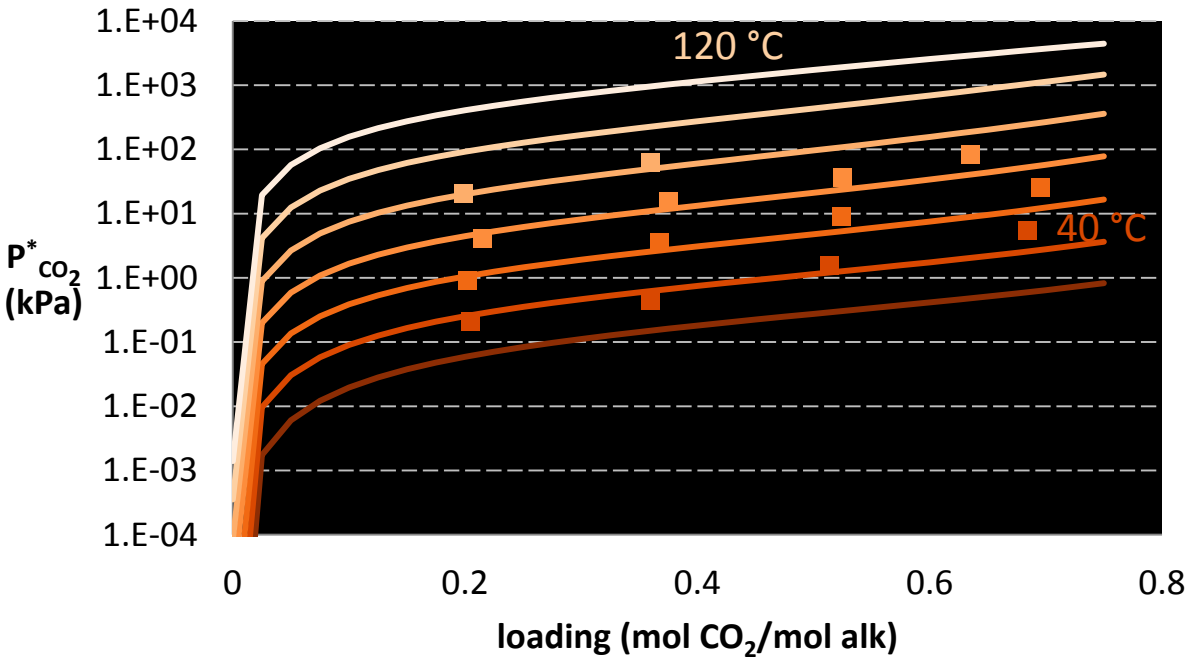

Figure 2: 8 m 2PE VLE fit with model curves at 20 °C increments and data from Chen (2011)

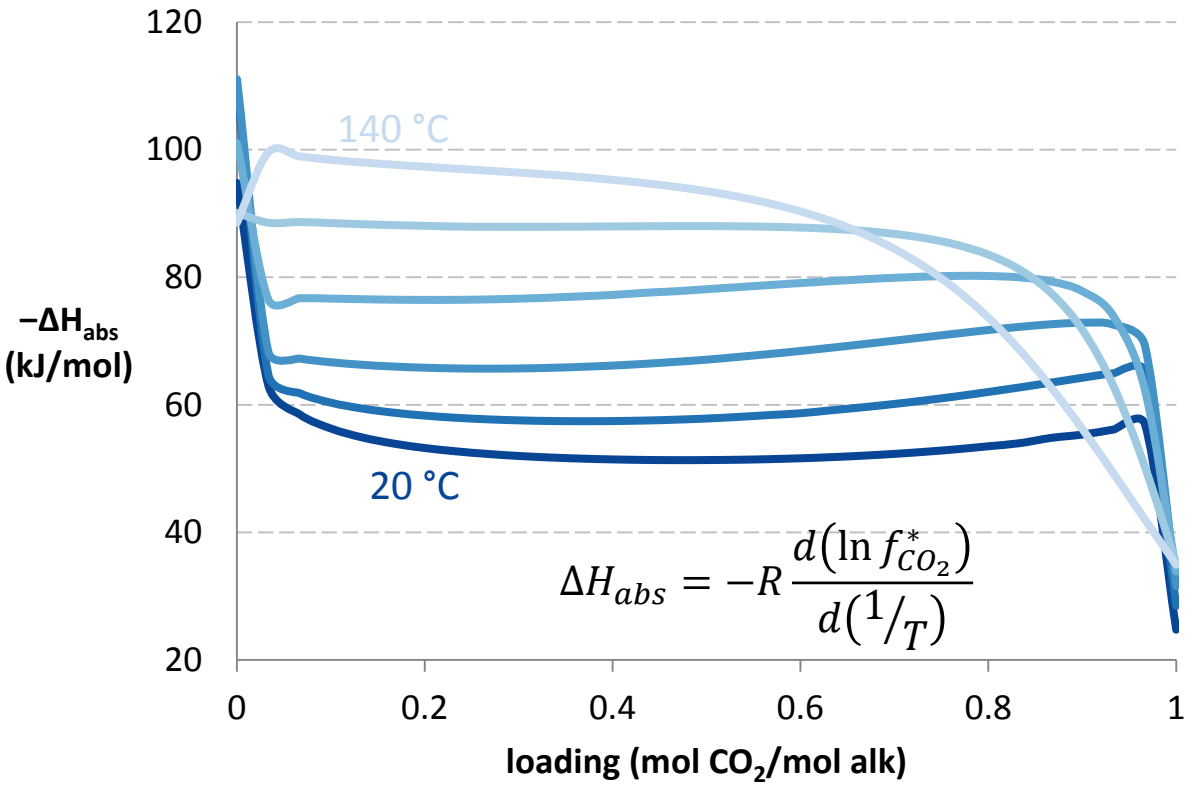

Figure 3: 8 m 2PE ΔH_{abs} prediction at 20 °C increments using the shown equation

The speciation predicted by the model is shown in Figure 4 and replotted on a log scale to better show the carbamate concentration in Figure 5. As shown, the primary product is bicarbonate, with a small amount of carbamate present. This is similar to the AMP system, as expected as that system was used as an analog (Rochelle et al., 2014c).

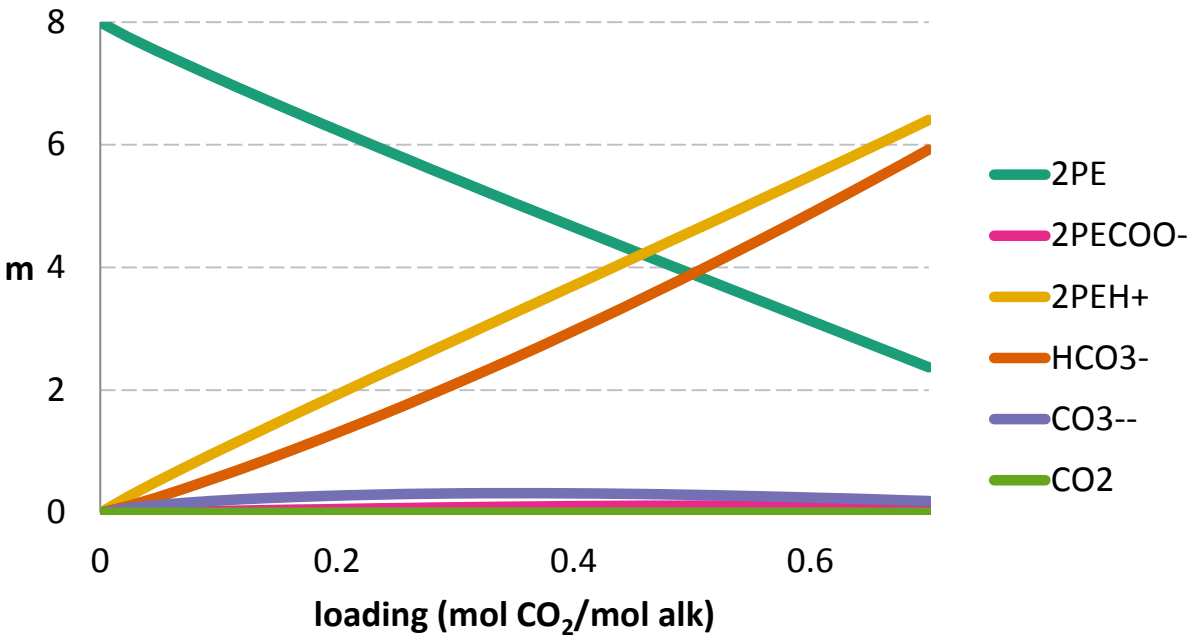

Figure 4: 8 m 2PE speciation prediction at 40 °C

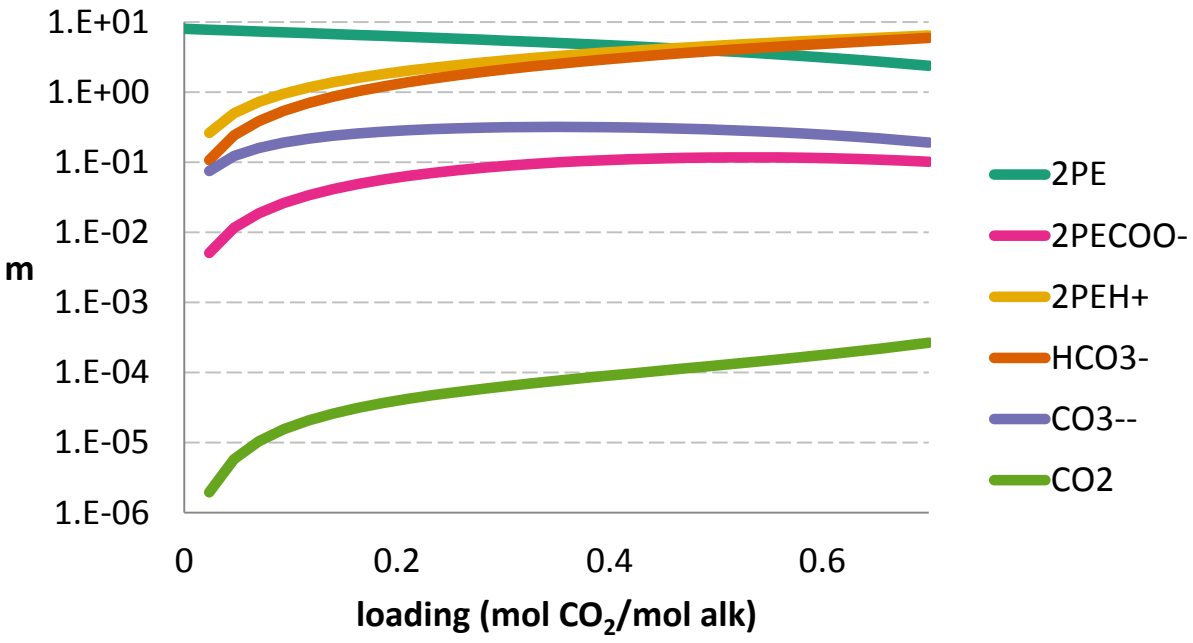

Figure 5: 8 m 2PE speciation prediction on log scale at 40 °C

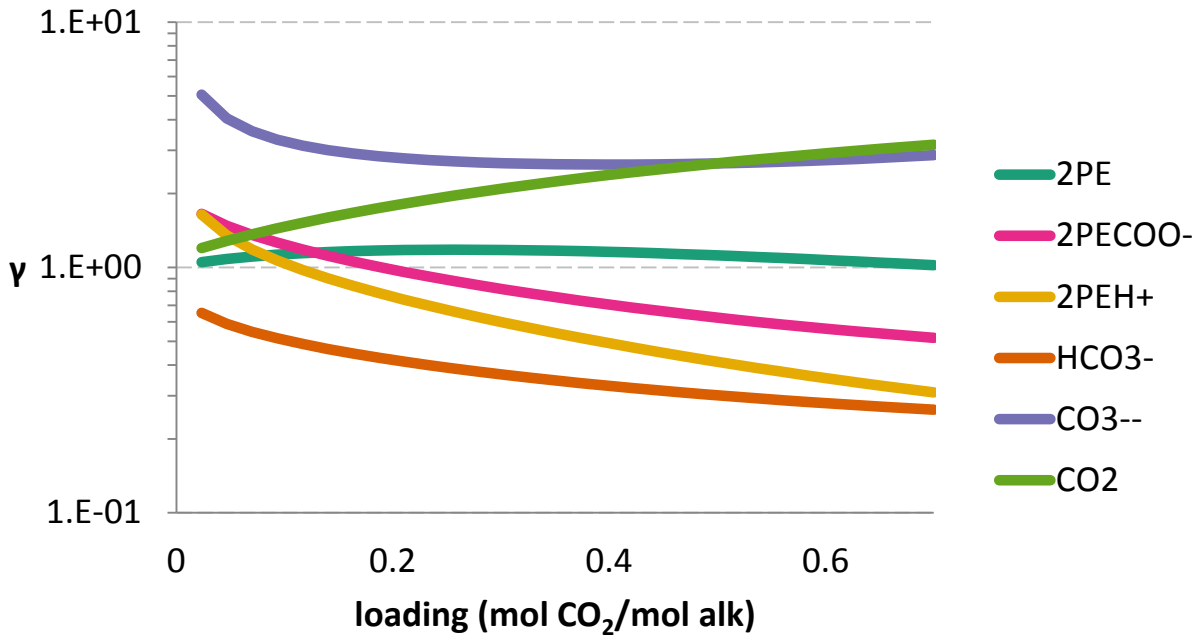

Figure 6: 8 m 2PE activity coefficient prediction at 40 °C

The species activity coefficients are shown in Figure 6, where the behavior of carbonate is extreme at a loading outside the range of interest. The increasing activity coefficient of CO_2 is significant for physical absorption of CO_2, which should only be a minor kinetic mechanism except at very high loading.

2PE Viscosity

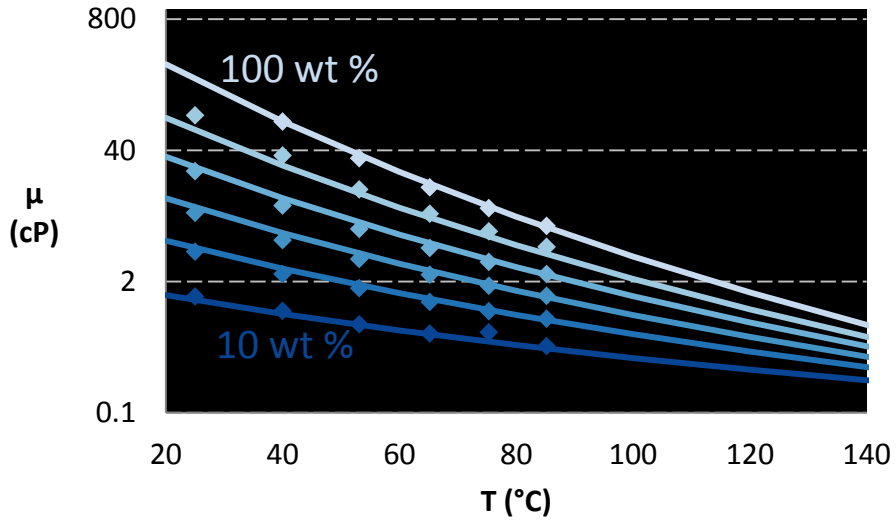

Figure 7: Aqueous and pure 2PE viscosity predicted by the model at 10, 30, 45, 60, 75, and 100 wt % 2PE compared to data (Xu et al., 1992)

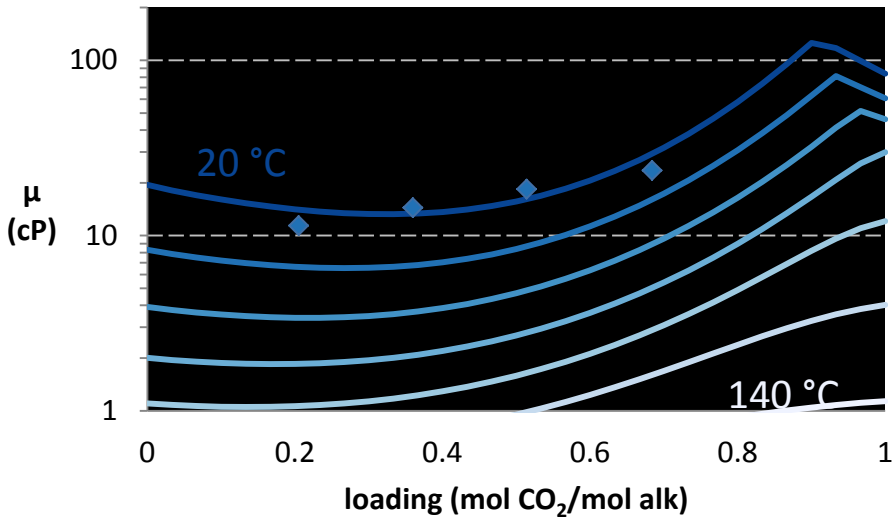

Figure 8: 8 m 2PE predicted viscosity at 20 °C increments with 40 °C data (Chen, 2011)

Table 6: Viscosity parameters for Equations 5 and 6, where $\sigma^2 = 0$ indicates a boundary

Parameter	Component i	Component j	Value	σ^2
A	2PE		−22.49	1.949
B	2PE		6248.22	651.935
a	2PE	H_2O	−9.294	1.199
b	2PE	H_2O	10000	0
c	2PE	H_2O	−81.06	6.975
d	2PE	H_2O	10000	0
a	HCO_3^-	$2PEH^+$	10000	0
b	HCO_3^-	$2PEH^+$	10000	0
c	HCO_3^-	$2PEH^+$	10000	0
d	HCO_3^-	$2PEH^+$	10000	0

Figures 7 and 8 were produced using the parameters of Table 6. As Figure 7 shows, the model represents a wide range of unloaded 2PE viscosity. At higher temperatures, the curves crossed until *A* and *B* of Equation 5 were simultaneously regressed with k_{ij} and m_{ij} of Equation 6 for 2PE and H_2O. The modified Andrade equation needs six parameters to correlate the unloaded data, whereas the modified Weiland equation needs only four to correlate the data.

The loaded predictions of Figure 8 show that the correlation has failed to represent the data. Despite using three more parameters than would be needed in the modified Weiland equation, the model predictions are nonsensical.

The regression may have failed due to the very limited loaded data, which has no variation in amine concentration or temperature. This is why the temperature dependent parameters, *b* and *d*, are at their regression bounds.

In order to rule out this data problem, the Aspen Plus® AMP model was considered. The model documentation shows in Figure 9 that viscosity decreases with loading, contrary to reality (Aspen Technology, 2013). Nevertheless, the predictions do not seem to be as poorly behaved as in Figure 8, whose predictions are non-monotonic with a peak. However, replotting the data for 30 wt % AMP on proper axes in Figure 10 shows poor correlation behavior similar to Figure 8. This model used the Jones-Dole electrolyte correlation to calculate mixture viscosity instead of the modified Andrade equation.

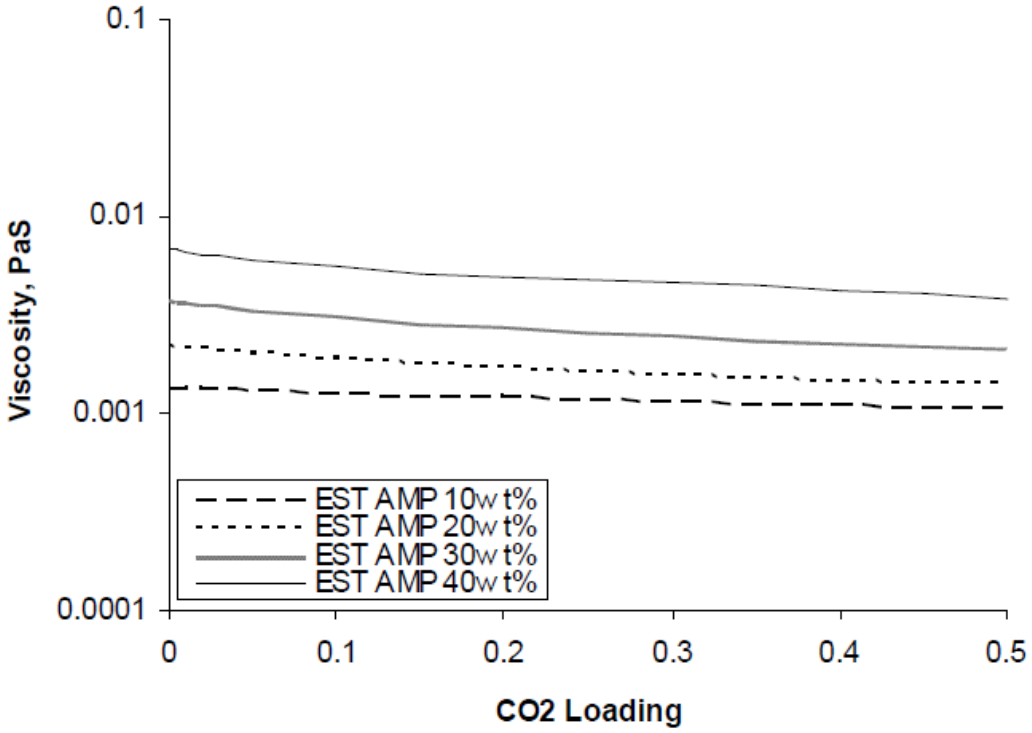

Figure 9: AMP viscosity predictions at 25 °C from the built in model

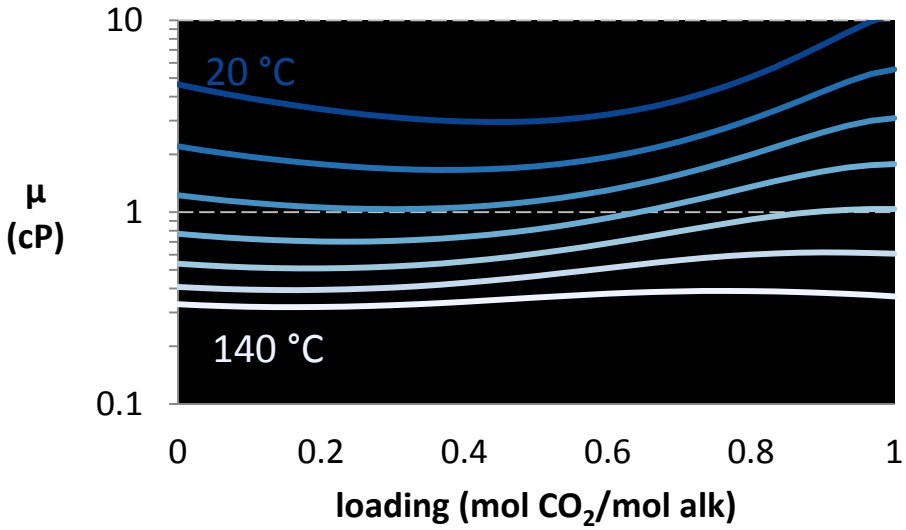

Figure 10: Viscosity of 30 wt % AMP predicted by built in model at 20 °C increments

Conclusions

1. Neither the modified Andrade equation nor the Jones-Dole electrolyte correlation represents loaded amine viscosity.
2. Online calculations of flashing and non-flashing plate-and-frame heat exchanger economics agree on average within 2% of offline calculations.

Future Work

- 2PE C^{13} NMR will be run to determine whether carbamate forms.
- The hydraulics of 2PE will be regressed in MATLAB using the modified Weiland equation to obtain standard deviations for the parameters.
- The uncertainty of the kinetic parameters for 2MPZ will be quantified.
- The heat exchanger economics tool will be generalized and streamlined.
- The heat exchanger economics tool will be used to understand the effect of viscosity on process economics.

References

Aspen Technology. "Rate-Based Model of the CO_2 Capture Process by AMP using Aspen Plus." 2013.

Chen X. *Carbon Dioxide Thermodynamics, Kinetics, and Mass Transfer in Aqueous Piperazine Derivatives and Other Amines*. The University of Texas at Austin. Ph.D. Dissertation. 2011.

Chiu L, Liu H, Li M. "Heat Capacity of Alkanolamines by Differential Scanning." *J Chem Eng Data*. 2010;631–636.

Ciftja AF, Hartono A, Svendsen HF. "Experimental study on carbamate formation in the AMP–CO_2–H_2O system at different temperatures." *Chem Eng Sci.* 2014;107:317–327.

Fernandes D, Conway W, Burns R, Lawrance G, Maeder M, Puxty G. "Investigations of primary and secondary amine carbamate stability by 1H NMR spectroscopy for post combustion capture of carbon dioxide." *J Chem Thermo*. 2012;54:183–191.

Frailie PT. *Modeling of Carbon Dioxide Absorption/Stripping by Aqueous Methyldiethanolamine/Piperazine*. The University of Texas at Austin. Ph.D. Dissertation. 2014.

Paul S, Mandal B. "Density and viscosity of aqueous solutions of 2-piperidineethanol, (2-piperidineethanol+monoethanolamine), and (2-piperidineethanol+diethanolamine) from (288 to 333) K." *J Chem Eng Data*. 2006;51:1406–1410.

Rochelle GT et al. "CO_2 Capture by Aqueous Absorption, Third Quarterly Progress Report 2013." Texas Carbon Management Program. The University of Texas at Austin. 2013.

Rochelle GT et al. "CO_2 Capture by Aqueous Absorption, First Quarterly Progress Reports 2014." Texas Carbon Management Program. The University of Texas at Austin. 2014a.

Rochelle GT et al. "CO_2 Capture by Aqueous Absorption, Fourth Quarterly Progress Reports 2013." Texas Carbon Management Program. The University of Texas at Austin. 2014b.

Rochelle GT et al. "CO_2 Capture by Aqueous Absorption, Third Quarterly Progress Reports 2014." Texas Carbon Management Program. The University of Texas at Austin. 2014c.

Xu S, Wang Y, Otto FD, Mather AE. "Physicochemical properties of 2-piperidineethanol and its aqueous solutions." *J Chem Eng Data*. 1992;37:407–411.

Xu S, Wang Y, Otto FD, Mather AE. "Kinetics of the reaction of carbon dioxide with aqueous 2-piperidineethanol solutions." *AIChE J*. 1993;39:1721−1725.

1 2MPZ Product Manual

2MPZ CO_2 Capture Simulation User Manual

Version 2014.10.0

October 31, 2014

Revision Log

Version Number	Release Date	Description
Version 2014.10.0	10/31/2014	The Aspen Plus® model is the same. The documentation has been updated for V8.4.

Table of Contents

List of Figures

List of Tables

To obtain support for this package, please send an email to
ccsi-support@acceleratecarboncapture.org.

1. INTRODUCTION

This document describes a 2-methylpiperazine (2MPZ) CO_2 capture system process simulation. The amine scrubbing system is divided into separate absorber and stripper simulations. The model consists of ThunderMoon.bkp with supporting subroutines full.dll and 2mpzloc.opt. This manual was written using Aspen Plus® V7.3.

1.1.Predicting CO_2 Solubility

Knowing the solubility of CO_2 enables the user to select a loading range as well as a stripper temperature and pressure. In this five minute example, a property analysis block is used to generate a series of isotherms for a fixed amine concentration and variable loading.

1. Open ThunderMoon.bkp, press F8 to open the Data Browser, and then under Setup change the Run type to Property Analysis.
2. In the left panel, navigate to Properties→Analysis. Click "New…" to create a new analysis block. Enter its ID as "82MPZVLE" and then select the type as generic. Change the system basis to Mass and then set H2O to 1000 kg/sec.
3. On the Variable tab, change Temperature to Vapor Fraction and then set it to 1e-05. Create three variables: (1) Temperature, (2) Mole Flow 2MPZ, and (3) Mole Flow CO2. Select these variables and then click "Range/List" at the bottom of the window to define them.
    a. Temperature is a list: 293.15, 313.15, 333.15, 353.15, 373.15
    b. Mole Flow 2MPZ is a list: 8
    c. Mole Flow CO2 is a range: Lower=0, Upper=8, Points=20.
4. On the Tabulate tab, select PPCO2-KP for the partial pressure of CO_2 in kilopascals.
5. Run the simulation. A popup displays, "Table generation completed with warnings. Results are present. Display Run-Status results form?" Click "Cancel".
6. To view the results, navigate to Properties→Analysis→82MPZVLE→Results. Some of the results are shown in Table 1. Using additional graphing software, the user can plot results as shown in Figure 1.

Table 1: Excerpt of 2MPZ VLE Results

Temp	Mole Flow 2MPZ	Mole Flow CO2	Vapor PPMX CO2
K	kmol/sec	kmol/sec	kPa
293.15	8	0	0
293.15	8	0.4	0.000101
293.15	8	0.8	0.000312
293.15	8	1.2	0.000629
293.15	8	1.6	0.001112
293.15	8	2	0.001886
293.15	8	2.4	0.003193

Temp	Mole Flow 2MPZ	Mole Flow CO2	Vapor PPMX CO2
K	kmol/sec	kmol/sec	kPa
293.15	8	2.8	0.005527
293.15	8	3.2	0.009976
293.15	8	3.6	0.019235
293.15	8	4	0.040809
293.15	8	4.4	0.097194
293.15	8	4.8	0.249722
293.15	8	5.2	0.607471
293.15	8	5.6	1.256137
293.15	8	6	2.213122
293.15	8	6.4	3.523392
293.15	8	6.8	5.433286
293.15	8	7.2	8.835594
293.15	8	7.6	18.2461
293.15	8	8	188.3118

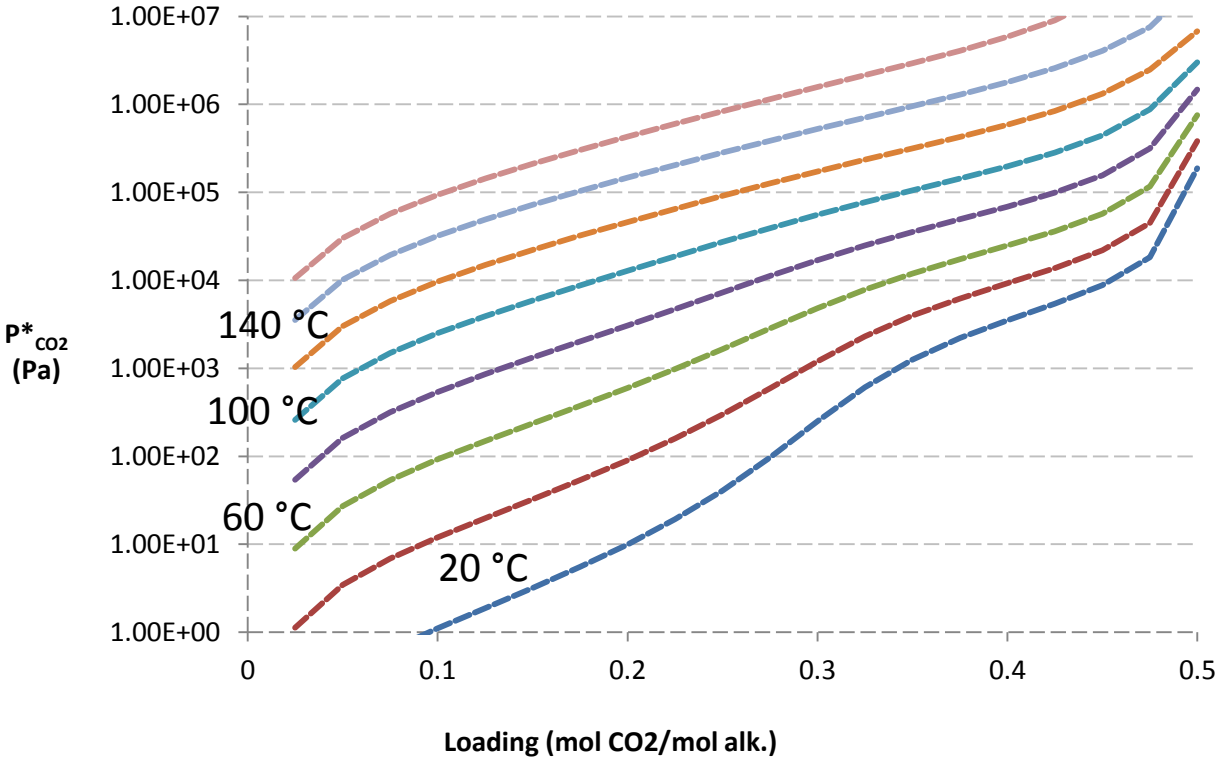

Figure 1: CO_2 solubility in 8 m 2MPZ.

Using Property Analysis blocks, the user can explore many other properties of the solvent, such as vapor pressure or viscosity.

1.2.Features list

This product is a thermodynamic and kinetic model of 2MPZ for amine scrubbing; therefore, it represents the CO_2 solubility, speciation, amine vapor pressure, heat capacity, pKa, heat of absorption, density, and viscosity for 2MPZ. While the model can extrapolate over a range of amine concentration, loading, and temperature, it is based on data collected primarily at 8 m 2MPZ with loadings ranging from 0 to 0.4 mol CO_2/mol alkalinity.

2. TUTORIAL

This tutorial assumes basic knowledge of Aspen Plus® software. Consult the Aspen Plus® documentation, "Getting Started Building and Running a Process Model", for additional information.

2.1.Absorber Simulation

Description

This example describes how to simulate a rate-based absorber. It includes tips on converging simulations, using design specifications to meet process criteria, and determining the proper discretization to be used for rate-based calculations.

Examples

Setup

1. Build the flowsheetof Figure 2, using an ABSBR1 RadFrac column. In the model library panel at the bottom of the window, navigate to Columns→RadFrac→ABSBR1. (If the model library is not visible, press F10.) Place the block on the flowsheet and name it "ABSORBER". If a prompt to name the flowsheet does not display, right-click on it and then select "Rename Block".

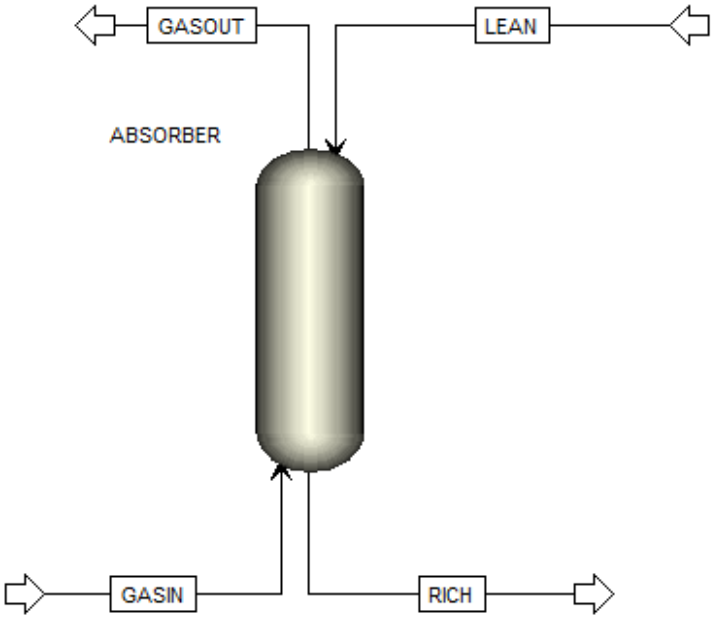

Figure 2: A Simple Absorber.

2. Select "Material STREAMS" in the model library. Create GASIN by clicking on the arrow on the left of the block (the feed) and then clicking elsewhere. Create RICH by clicking on the arrow at the bottom (the bottoms). Create GASOUT by clicking on the arrow at the top (the vapor distillate). Lastly, create LEAN by clicking on the now blue arrow on the left (the feed).
3. Double-click on GASIN to configure it as follows:
    a. Temperature: 40 C
    b. Pressure: 1 atm
    c. Total flow: 5 kmol/sec
    d. Composition: Mole-Frac
        i. H2O: 7.3
        ii. CO2: 12
        iii. N2: 80.7

    Note: Aspen normalizes the mole fractions to one.
4. Select LEAN from the left panel and configure it as follows:
    a. Temperature: 40 C
    b. Pressure: 1 atm
    c. Total flow: 20 kmol/sec
    d. Composition: Mole-Frac
        i. H2O: 55.556
        ii. CO2: 4.32
        iii. 2MPZ: 8

5. In the left panel, navigate to Blocks→ABSORBER and configure its Setup as follows:
    a. On the configuration tab
        i. Calculation type: Rate-Based
        ii. Number of stages: 30
        iii. Condenser: none
        iv. Reboiler: none
    b. On the Streams tab
        i. GASIN On-Stage 30
        ii. LEAN On-Stage 1
    c. On the Pressure tab set the Top stage pressure to 1 atm.
6. Configure the absorber Reactions with two sections
    a. One starts on stage 1 and ends on stage 3 with Reaction ID ZERO.
    b. The other starts on stage 4 and ends on stage 30 with Reaction ID ZERO.

    Note: This reaction set is used to ease convergence of the simulation. It is the 2MPZ reaction set with all activation energies and reaction pre-exponentials set to 0.
7. Create a new pack rating section 1. Configure its Specifications as follows:
    a. Starting stage: 1
    b. Ending stage: 30
    c. Type: MELLAPAK
    d. Vendor: SULZER
    e. Material: STANDARD
    f. Dimension: 250X
    g. Section diameter: 8 meter
    h. Section packed height: 15 meter

    Note: As the column is packed, the number of stages does not represent trays. It is purely a computational construct. The more stages, the more finely discretized the column. However, this results in more computation time. As a very rough approximation, one stage for every half meter of packing is recommended. Use more stages for greater temperature and mass transfer gradients.
    i. Navigate to Rate-based from the panel at the left (Pack Rating→1→Rate-based). Configure it as follows:
        i. Select the Rate-based calculations check box.
        ii. Flow model: Countercurrent
        iii. Film resistance
            1. Liquid phase: Discrxn
            2. Vapor phase: Film
    j. On the Holdups tab, set the Holdup Method Correlation to Percent-Data and set the Liquid Phase to Correlation with % of free volume set to 5.
    k. On the Design tab, select the Design mode check box to calculate column diameter with Base Stage as 30.
    l. On the Optional tab, set the Additional discretization points to the 32 shown in Table 2.

Table 2: Boundary Layer Discretization

Point	Liquid film	Point	Liquid film
1	6.40E-05	17	0.0106
2	7.68E-05	18	0.0127
3	0.000159	19	0.0152
4	0.000229	20	0.0182
5	0.00033	21	0.0219
6	0.000476	22	0.0263
7	0.000571	23	0.0315
8	0.0007	24	0.0378
9	0.000986	25	0.0454
10	0.00118	26	0.059
11	0.00142	27	0.0826
12	0.00187	28	0.124
13	0.0027	29	0.198
14	0.00389	30	0.317
15	0.0056	31	0.507
16	0.00806	32	0.862

8. Under Flowsheeting, navigate to Options→Calculator and then create a new Calculator named, C-RM. This block calculates the fraction of CO_2 captured.
    a. On the Define tab, create three variables:

Variable	Information flow	Definition
REMOVE	Export	Parameter Parameter no.=2
CO2IN	Import	Mole-Flow Stream=GASIN Substream=MIXED Component=CO2 Units=kmol/sec
CO2OUT	Import	Mole-flow Stream=GASOUT Substream=MIXED Component=CO2 Units=kmol/sec

    b. On the Calculate tab, type "F REMOVE=(CO2IN-CO2OUT)/CO2IN"
Note: Between "F" and "REMOVE" there are 5 spaces.

9. Create a Design Spec named REMOVAL
    a. On the Define tab, create a variable REMOVE and assign it to parameter 2.
    b. On the Spec tab
        i. Spec: REMOVE
        ii. Target: 0.90
        iii. Tolerance: 0.000001
    c. On the Vary tab
        i. Type: Stream-Var
        ii. Stream: LEAN
        iii. Variable: MOLE-FLOW
        iv. Lower: 5
        v. Upper: 300

Running the Simulation

1. Deactivate the design spec by right-clicking on it and selecting "Deactivate".
2. Run the simulation, which provides Aspen a good initial guess.
3. Change the absorber Reactions to R-1 from ZERO for stages one to three. Run the simulation.
4. Chang th absorber Reactions to R-1 from ZERO for the remaining stages. Run the simulation.
5. Increase the section packed height under the pack rating to 12 m, and then run the simulation.
6. Review the C-RM calculator block results (Flowsheeting Options→Calculator→C-RM→Results on the Define Variable tab) to determine if the fractional CO_2 removal is approximately 0.51.
    a. Increase the LEAN stream total flow in 10 kmol/sec increments until the percent removal is within 0.10 of 0.90. Be sure to run the simulation after each increment.
7. Once approximately 90% removal has been achieved, activate the Design Spec REMOVAL by right-clicking on Design Spec→Removal and selecting Activate. Run the simulation.
8. The converged absorber should now be removing 90% of the incoming CO_2. Results should be similar to those shown in Figures 3-5 below. View them by selecting Results Summary→Streams, Flowsheeting Options→Design Spec→Removal→Results, and Blocks→ABSORBER→Pack Rating→1→Results.

Display: Streams Format: ELEC_M Stream Table

	GASIN	LEAN	RICH	GASOUT
Temperature K	313.1	313.1	323.7	313.3
Pressure N/sqm	101325	101325	101325	101325
Vapor Frac	1	0	0	1
Solid Frac	0	0	0	0
Mole Flow kmol/sec	5	35.173	35.244	4.39
Mass Flow kg/sec	146.016	1102.58	1127.61	120.987
Volume Flow cum/sec	128.34	1.005	1.017	112.784
Enthalpy Gcal/hr	-277.175	-8733.42	-8930.62	-79.991
Mole Flow kmol/sec				
H2O	0.365	30.541	30.275	0.295
CO2	0.6	< 0.001	< 0.001	0.06
N2	4.035		< 0.001	4.035
HCO3-		0.136	0.482	
CO3--		0.069	0.059	
H+				
OH-				
2MPZ		0.407	0.15	< 0.001
2MPZCOO		1.463	1.18	
H2MPZCOO		0.527	0.995	trace
2MPZCOO2		0.098	0.107	
2MPZH+		1.933	1.995	
Mole Frac				
H2O	0.073	0.868	0.859	0.067
CO2	0.12	1 PPM	9 PPM	0.014
N2	0.807		3 PPM	0.919
HCO3-		0.004	0.014	
CO3--		0.002	0.002	
H+				

Figure 3: Excerpt of stream results.

Variable	Initial value	Final value	Units
MANIPULATED	37.4542	35.1733	KMOL/SEC
REMOVE	0.917333	0.9	

Figure 4: Design specification REMOVAL results.

Packed column rating results

Section starting stage:	1	
Section ending stage:	30	
Column diameter:	8.77634	meter
Maximum fractional capacity:	0.827013	
Maximum capacity factor:	0.0735589	m/sec
Section pressure drop:	2301.54	N/sqm
Average pressure drop / Height:	153.436	N/cum
Maximum stage liquid holdup:	5.25548	cum
Max liquid superficial velocity:	0.0170312	m/sec
Surface area:	256	sqm/cum
Void fraction:	0.987	
1st Stichlmair constant:	1	
2nd Stichlmair constant:	1	
3rd Stichlmair constant:	0.32	

Figure 5: Packed Column Rating Results.

2.2.Stripper Simulation

Description

This example is a guide to simulating a simple stripper and a heat exchanger.

Examples

Setup

1. Open ThunderMoon.bkp.
2. Construct the flowsheet shown in Figure 6. From Columns in the Model Library, select RadFrac→STRIP1 for the stripper. From Heat Exchangers, select Heater for CX-COLD, CX-HOT, and HX-TRIM. From Pressure Changers, select pump for LEANPUMP. Create the streams using the “Material STREAMS” button.

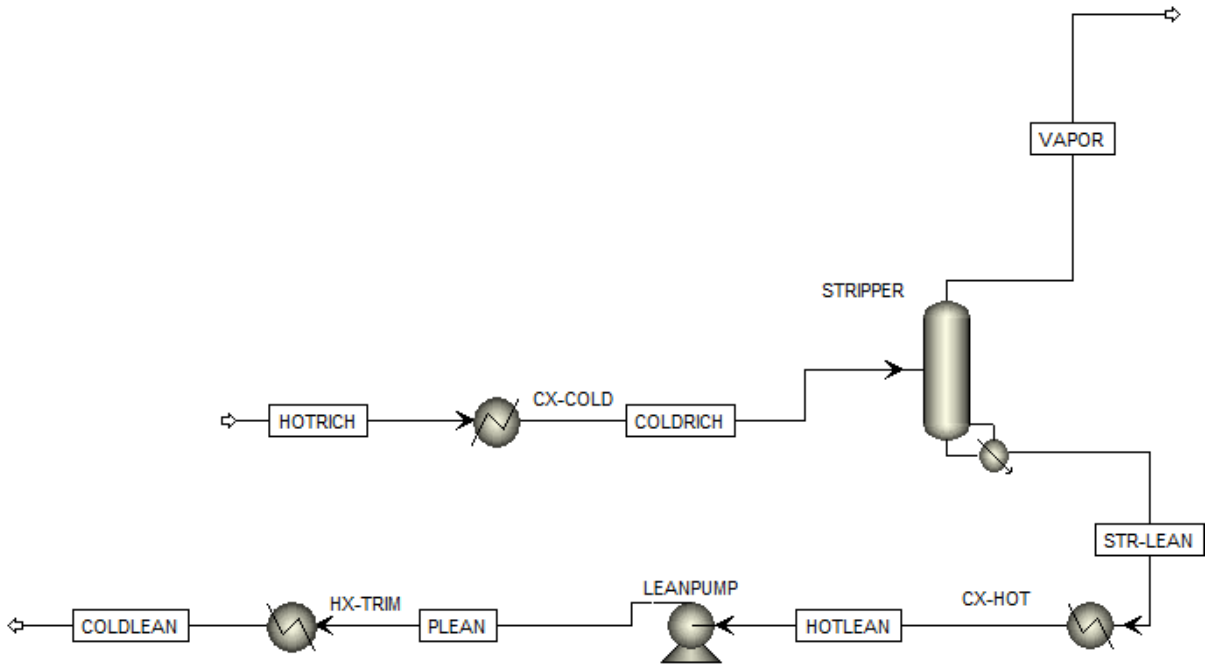

Figure 6: Stripper Simulation Flowsheet

3. Set HOTRICH to the values from the absorber example.
    a. Temperature: 323.7 K
    b. Pressure: 11 bar
    c. Total flow: 35.244 kmol/sec
    d. Composition: Mole-Frac
        i. H2O 55.556
        ii. CO2 5.29
        iii. 2MPZ 8

    Note: The pressure is set as if coming from a pump. This pump is neglected for simplicity.
4. Set CX-COLD
    a. Pressure: 0 N/sqm
    b. Temperature: 85 C
    c. Valid phases: Liquid-Only

    Note: Pressure drop is neglected.
5. Configure STRIPPER Setup as follows:
    a. On the Configuration tab
        i. Calculation Type: Rate-Based
        ii. Number of Stages: 15
        iii. Condenser: None
        iv. Reboiler: Kettle
        v. Reboiler Duty: 225 MW

   b. On the Streams tab, feed COLDRICH to stage 1 as liquid.
   c. On the Pressure tab, set the top stage pressure to 3 bar.
6. Set reactions in the stripper to stages 1-15 using Chemistry ID REDUCED
7. Create a new Pack Rating for the stripper and configure it as follows:
   a. Under Setup, stages 1-14 use MELLAPAK, SULZER, STANDARD, 250X with a diameter of 5 m and a section packed height of 2 m.
   b. Under Rate-Based, select the Rate-based calculations check box with Film Resistance set to Film for liquid and vapor phases. On the Design tab, select the "Design mode check box to calculate column diameter" and set the base stage to 14.
8. Configure CX-HOT
   a. Temperature: 50 C
   b. Pressure: 0 N/sqm
9. Configure LEANPUMP
   a. Discharge pressure: 250 kPa
10. Configure HX-TRIM
    a. Temperature: 40 C
    b. Pressure: 0 N/sqm

    Note: This flowsheet takes the rich stream from the previous absorber tutorial, passes it through a cross-exchanger, and then to the stripper. CX-COLD and CX-HOT are used to simulate the cross exchanger. HX-TRIM is the trim cooler to lower the lean solvent down to 40°C prior to entering the absorber.
11. Create a LOADINGS calculator.
    a. Define the variables as shown in Table 3.
    b. The Fortran code is

```
F      LLDG=(LCO2+LCO3+LHCO3+L2MPZCOO+2*L2MPZC2+LH2MPZC)/
F      (2*(L2MPZ+L2MPZH+L2MPZCOO+L2MPZC2+LH2MPZC))

F      RLDG=(RCO2+RCO3+RHCO3+R2MPZCOO+2*R2MPZC2+RH2MPZC)/
F      (2*(R2MPZ+R2MPZH+R2MPZCOO+R2MPZC2+RH2MPZC))
```

Table 3: Variables for the LOADINGS Calculator

Variable Name	Information Flow	Definition
RLDG	Export	Parameter Parameter no.=3
LLDG	Export	Parameter Parameter no.=4
LCO2	Import	Mole-Frac Stream=STR-LEAN Substream=MIXED Component=CO2
L2MPZ	Import	Mole-Frac Stream=STR-LEAN Substream=MIXED Component=2MPZ
L2MPZH	Import	Mole-Frac Stream=STR-LEAN Substream=MIXED Component=2MPZH+
L2MPZCOO	Import	Mole-Frac Stream=STR-LEAN Substream=MIXED Component=2MPZCOO
L2MPZC2	Import	Mole-Frac Stream=STR-LEAN Substream=MIXED Component=2MPZCOO2
LH2MPZC	Import	Mole-Frac Stream=STR-LEAN Substream=MIXED Component=H2MPZCOO
LHCO3	Import	Mole-Frac Stream=STR-LEAN Substream=MIXED Component=HCO3-
LCO3	Import	Mole-Frac Stream=STR-LEAN Substream=MIXED Component=CO3--
R2MPZ	Import	Mole-Frac Stream=HOTRICH Substream=MIXED Component=2MPZ
R2MPZH	Import	Mole-Frac Stream=HOTRICH Substream=MIXED Component=2MPZH+
R2MPZCOO	Import	Mole-Frac Stream=HOTRICH Substream=MIXED Component=2MPZCOO
R2MPZC2	Import	Mole-Frac Stream=HOTRICH Substream=MIXED Component=2MPZCOO2
RH2MPZC	Import	Mole-Frac Stream=HOTRICH Substream=MIXED Component=H2MPZCOO
RHCO3	Import	Mole-Frac Stream=HOTRICH Substream=MIXED Component=HCO3-
RCO3	Import	Mole-Frac Stream=HOTRICH Substream=MIXED Component=CO3--

12. Make a Design Spec named SETLEAN.
    a. Define LLDG as Parameter 4
    b. Spec LLDG to 0.27 with a tolerance of 0.001.
    c. On the Vary tab under Manipulated variable limits, Lower: 0 and Upper: 5.5E8 Watts. Now, under Manipulated variable set the following:
        i. Type: Block-Var
        ii. Block: STRIPPER
        iii. Variable: QN

13. Make a Design Spec named SETTEMP.
    a. Define TEMP as Stream-Var Stream=STR-LEAN Substream=MIXED Variable=TEMP Units=K
    b. Spec TEMP to 423.15 K with a tolerance of 0.01.
    c. On the Vary tab, set the manipulated variable limits to 300000 to 1500000N/sqm. Under Manipulated variable set the following:
        i. Type: Block-Var
        ii. Block: STRIPPER
        iii. Variable: STAGE-PRES
        iv. ID1: 1

Running the Simulation

1. Deactivate both design specs.
2. Run the simulation.
3. Review the lean loading (LLDG) in the LOADINGS calculator block by navigating to the Define Variable tab of Results. Decrease the stripper reboiler duty in 25 MW increments until the lean loading is close to the desired value of 0.27. Run the simulation after each decrement.
4. Activate the SETLEAN design spec and then run the simulation.
5. Activate the SETTEMP design spec and then run the simulation.
6. Create a heat stream from CX-HOT to CX-COLD named Q-XC. To clear the temperature specification of CX-COLD, double-click on the block, right-click on temperature under flash specifications, and then select “Clear”.
7. Run the simulation. Results similar to those in Figures 7-9 should be displayed. To view these results, navigate to Results Summary→Streams, Flowsheeting Options→Design Spec→SETLEAN→Results, Flowsheeting Options→Design Spec→SETTEMP→Results, and Blocks→STRIPPER→Pack Rating→1→Results.

	COLDLEAN	COLDRICH	HOTLEAN	HOTRICH	PLEAN	STR-LEAN	VAPOR
Temperature K	313.1	425.2	323.1	323.7	323.1	423.2	424.9
Pressure N/sqm	250000	1.11458e+06	1.072e+06	1.11458e+06	250000	1.072e+06	1.072e+06
Vapor Frac	0	0	0	0	0	0	1
Solid Frac	0	0	0	0	0	0	0
Mole Flow kmol/sec	31.949	32.455	31.949	32.423	31.949	31.962	1.085
Mass Flow kg/sec	1007.89	1043.53	1007.89	1043.53	1007.89	1007.89	35.634
Volume Flow cum/sec	0.915	1.009	0.919	0.937	0.92	0.992	3.459
Enthalpy Gcal/hr	-7937.29	-7980.07	-7909.64	-8261.79	-7910.2	-7627.91	-300.81
Mole Flow kmol/sec							
H2O	27.683	27.419	27.645	27.743	27.646	27.36	0.472
CO2	< 0.001	0.032	< 0.001	< 0.001	< 0.001	0.013	0.611
N2							
HCO3-	0.125	0.917	0.163	0.546	0.163	0.503	
CO3--	0.063	0.006	0.061	0.053	0.061	0.008	
H+							
OH-							
2MPZ	0.369	0.324	0.404	0.11	0.404	0.676	0.002
2MPZCOO	1.347	0.951	1.322	0.997	1.322	1.186	
H2MPZCOO	0.496	0.894	0.501	1.024	0.501	0.477	trace
2MPZCOO2	0.09	0.011	0.081	0.101	0.081	0.012	
2MPZH+	1.777	1.901	1.77	1.85	1.77	1.728	
Mole Frac							
H2O	0.866	0.845	0.865	0.856	0.865	0.856	0.435
CO2	1 PPM	976 PPM	2 PPM	12 PPM	2 PPM	411 PPM	0.563
N2							
HCO3-	0.004	0.028	0.005	0.017	0.005	0.016	
CO3--	0.002	177 PPM	0.002	0.002	0.002	245 PPM	

Figure 7: Excerpt of Stream Results.

Variable	Initial value	Final value	Units
MANIPULATED	5.97279e+07	5.97279e+07	WATT
LLDG	0.269967	0.269967	

Variable	Initial value	Final value	Units
MANIPULATED	1.08314e+06	1.072e+06	N/SQM
TEMP	423.408	423.151	K

Figure 8: The Design Specification Results.

Packed column rating results

Section starting stage:	1	
Section ending stage:	14	
Column diameter:	4.1165	meter
Maximum fractional capacity:	0.832963	
Maximum capacity factor:	0.0258591	m/sec
Section pressure drop:	984.922	N/sqm
Average pressure drop / Height:	492.461	N/cum
Maximum stage liquid holdup:	0.438715	cum
Max liquid superficial velocity:	0.0757641	m/sec
Surface area:	256	sqm/cum
Void fraction:	0.987	
1st Stichlmair constant:	1	
2nd Stichlmair constant:	1	
3rd Stichlmair constant:	0.32	

Figure 9: Excerpt from Packed Column Rating Results.

3. USAGE INFORMATION

3.1. Environment/Prerequisites

This product requires Aspen Plus® V7.3 or newer with an Aspen Rate-Based Distillation license. As such, the supported environments are limited to:

- Windows XP SP3
- Windows Vista Business SP2
- Windows Vista Ultimate SP2
- Windows 7 Ultimate (32 and 64 Bit)
- Windows 7 Professional (32 and 64 Bit)

3.2. Support

Support can be obtained from ccsi-support@acceleratecarboncapture.org or by filling out the "Submit Feedback/Request Support" form available on the product distribution page.

3.3. Restrictions

The model is centered at an amine concentration of 8 m. Extrapolating far from this concentration should be done with care.

3.4.Next Steps

The next release will include a heat exchanger model that predicts area as a function of pressure drop and solvent viscosity and a model for $k_l a$ in the absorber and stripper as a function of viscosity.

4. DEBUGGING

The model is running correctly if it is converging for the above tutorials with similar results. If it is not, see the next section, "How to Debug".

4.1.How to Debug

Always run the simulation with the control panel visible. It is the only output available during computation, and it notifies the user whether or not the simulation will converge. This enables the user to avoid wasting time on fruitless computation. Furthermore, it alerts the user to any problems encountered during computation.

Subroutine Errors

If the following error message displays:

```
*** SEVERE ERROR
    COULD NOT RESOLVE USER OR IN-LINE FORTRAN SUBROUTINE(S):
```

the simulation will not run. The possible causes and solutions are:

1. The .bkp file and the .dll and .opt files are not located in the same directory. Move them all into the same directory to resolve this.
2. The linker is not specified in the run settings. Set the linker to 2mpzloc.opt.

Simulation Problems

- If warnings are displayed regarding unusual liquid molefrac profile or unusual component production profile, follow the suggested instructions in the error message.
- If a warning is displayed stating that the water liquid viscosity model MULH2O is violated due to the temperature being lower than the minimum temperature limit, something is not specified correctly. Review the inputs and re-run.
- Ignore flooding errors (`TPSAR MESSAGE: XXX.XX% FLOOD IN COLUMN EXCEEDS 80%`) unless it displays in the final step.

Aiding Convergence

- Only reinitialize when absolutely necessary.
- Make small changes in a converged model.
- Converge an initial, simple case before enabling reactions and design specifications. It is recommended that only small changes are made; therefore, only turn on one of these at a time.
- Before enabling the design specification, the variable should be close to the desired value.

4.2.Known Issues

- Flash errors can occur if the solvent goes above 0.5 mol CO_2/ mol alk.
- Multiple warnings display regarding property data while processing input specifications that follow this pattern, "PARAMETER XXX DATA SET 1 FOR COMPONENT 2MPZ HAS BEEN ENTERED MORE THAN ONCE. THE LAST ENTRY WILL BE USED.", where XXX is the parameter name.
- In running the tutorials, warnings display that the mole fractions are normalized to unity.
- Warnings display that IONRDL is missing for 2MPZCOO, 2MPZCOO2, and 2MPZH+.
- Using design mode to calculate column diameter for the absorber can lead to inconsistent results. With the absorber tutorial, the model may converge with a diameter of 4.58 m.

4.3.Reporting Issues

To report an issue, please send an email to ccsi-support@acceleratecarboncapture.org.

5. MODEL HISTORY

This section details the creation of Thunder Moon, including the data used in the regressions.

5.1.Thermodynamic Model

Thunder Moon is based on previous work using the electrolyte NRTL model (Chen, 2011). The model is focused on the operating conditions for capture from a coal-fired power plant, meaning a loading range from 0.27 to 0.37 mol CO_2/mol alkalinity. The thermodynamic framework was modified slightly in that the default chemistry used had proton and hydroxide ions removed to enhance convergence. The equilibrium chemistry is shown in Table 4.

Table 4: The Thunder Moon Chemistry Block

Model Chemistry
2 2MPZ + CO_2 ↔ 2MPZCOO$^-$ + 2MPZH$^+$
2 2MPZCOO$^-$ + CO_2 ↔ 2MPZCOO2 + H2MPZCOO
2MPZCOO$^-$ + CO_2 + H2O ↔ HCO_3^- + H2MPZCOO
2MPZ + H2MPZCOO ↔ 2MPZH$^+$ + 2MPZCOO$^-$
2MPZCOO$^-$ + HCO_3^- ↔ CO_3^{--} + H2MPZCOO$^-$

Changing the chemistry reaction set did not significantly effect the thermodynamic model; therefore, all fits are the same as in (Chen, 2011). In the process of verifying all fits, a discrepancy between the calorimetric and thermodynamic methods for calculating heat of absorption was uncovered.

$$\Delta H_{abs} = -R\frac{d\left(\ln f^{*}_{CO_2}\right)}{d\left(1/T\right)} \quad (1)$$

$$\Delta H_{abs} = \frac{Q}{\dot{n}_{CO_2}} \quad (2)$$

where Q is the net-duty of the flash block, and $\dot{n}_{CO_2}$ is the molar flow rate of gaseous CO_2. The heat of absorption is calculated by sending a loaded solvent stream and a gaseous CO_2 stream to a flash block for a bubble point calculation.

The latter method using Equation 1 is shown in Figure 10; while the former using Equation 2 is shown in Figure 11. (The process model uses the calorimetric heat of absorption.) The disagreement between the two methods occurs above a loading of 0.25, as shown in Figure 12. It is suspected that the deviation above a loading of 0.25 mol CO_2/mol alk. is due to the zwitterion becoming a significant species.

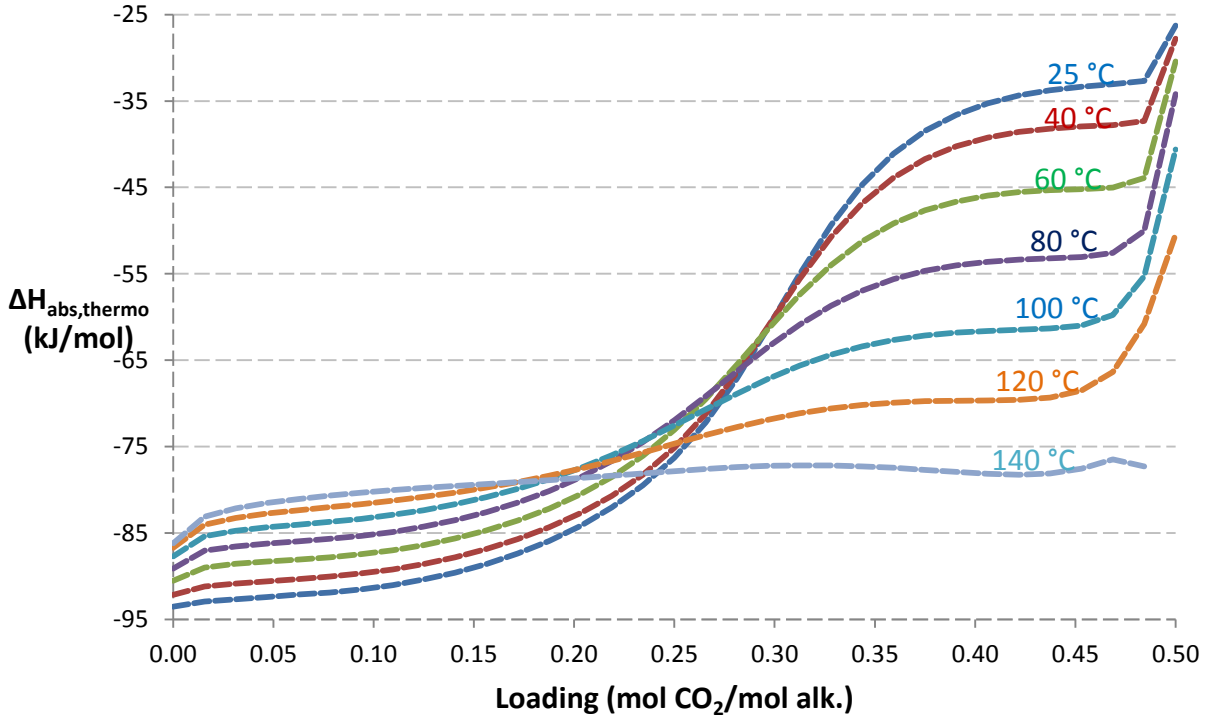

Figure 10: Thermodynamic heat of absorption of 8 m 2MPZ calculated from Equation 1.

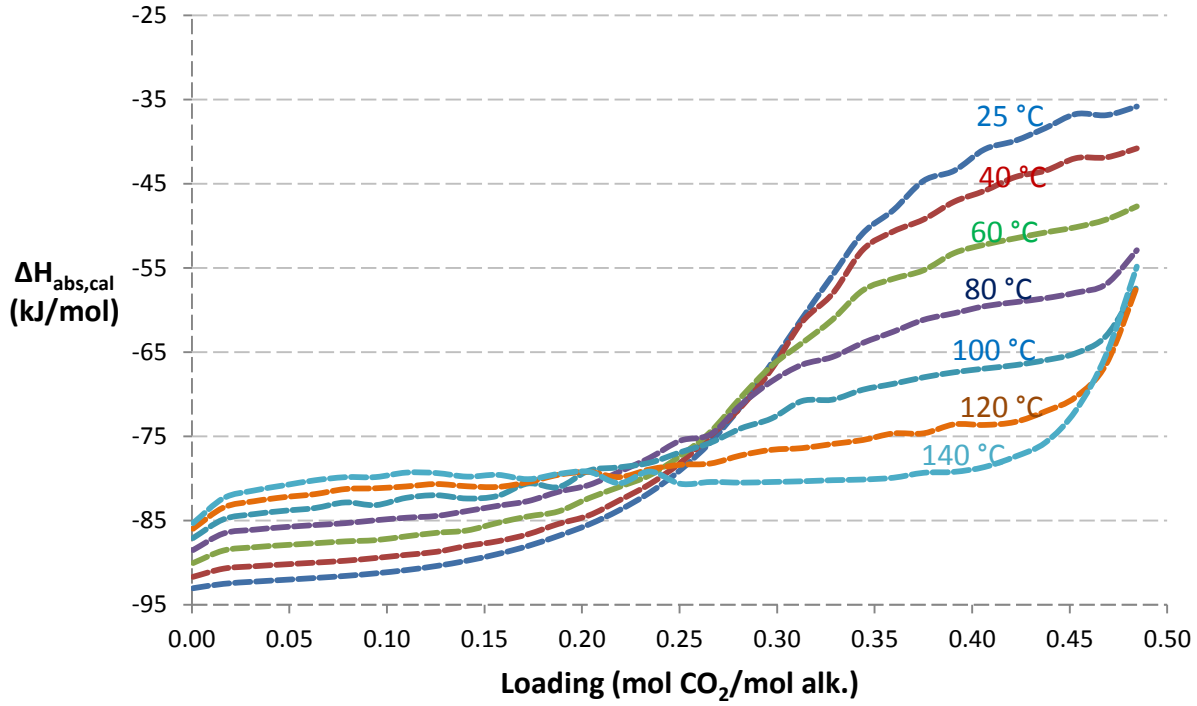

Figure 11: Calorimetric heat of absorption of 8 m 2MPZ calculated from Equation 2.

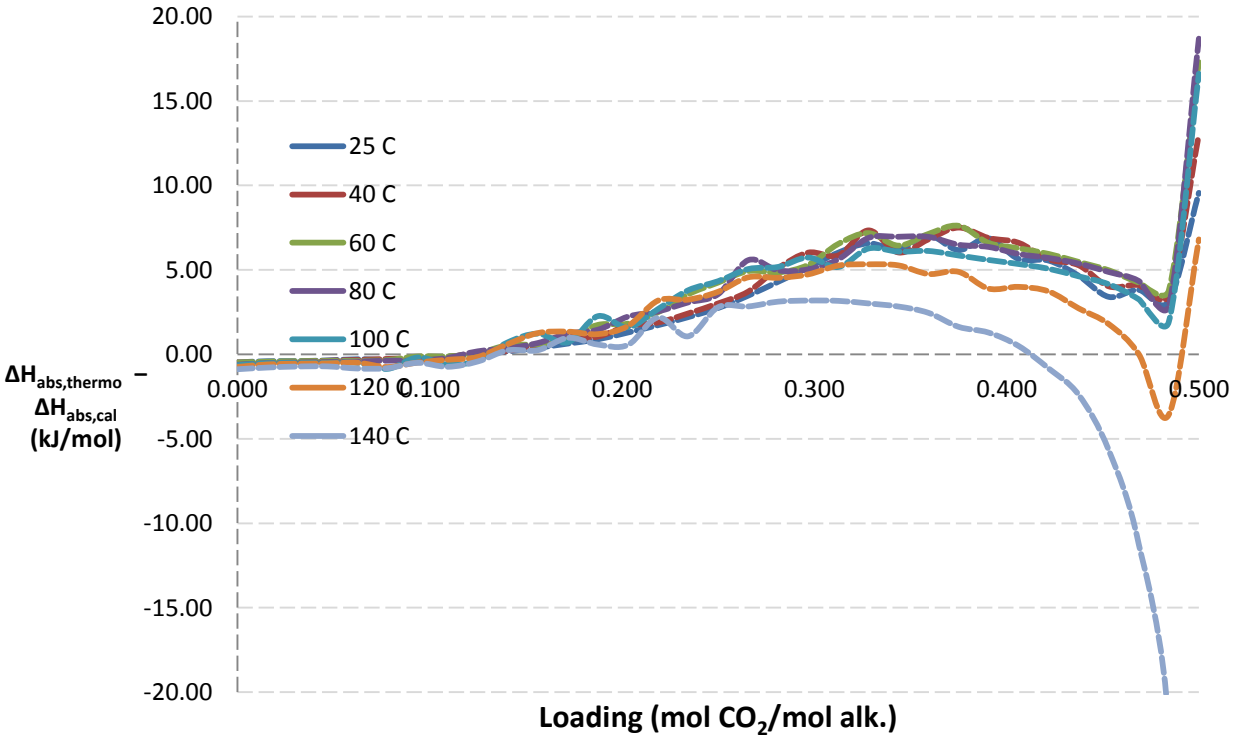

Figure 12: The absolute differences between the two heat of absorption calculations, which agree well until a loading of 0.25 mol CO_2/mol alk., where the zwitterion becomes significant.

In conclusion, the thermodynamic model represents amine volatility, CO_2 solubility, pK_a, speciation, density, and viscosity data (Chen, 2011).

5.2. Kinetic Model

The kinetics were regressed using a wetted wall column (WWC) Aspen Plus® simulation to adjust reaction rate constants, activation energies, and diffusion parameters to match experimental flux values within 20% (Plaza, 2011; Rochelle et al., 2012). Activity-based kinetics are used as in (Chen, 2011). The process flow diagram is shown in Figure 13.

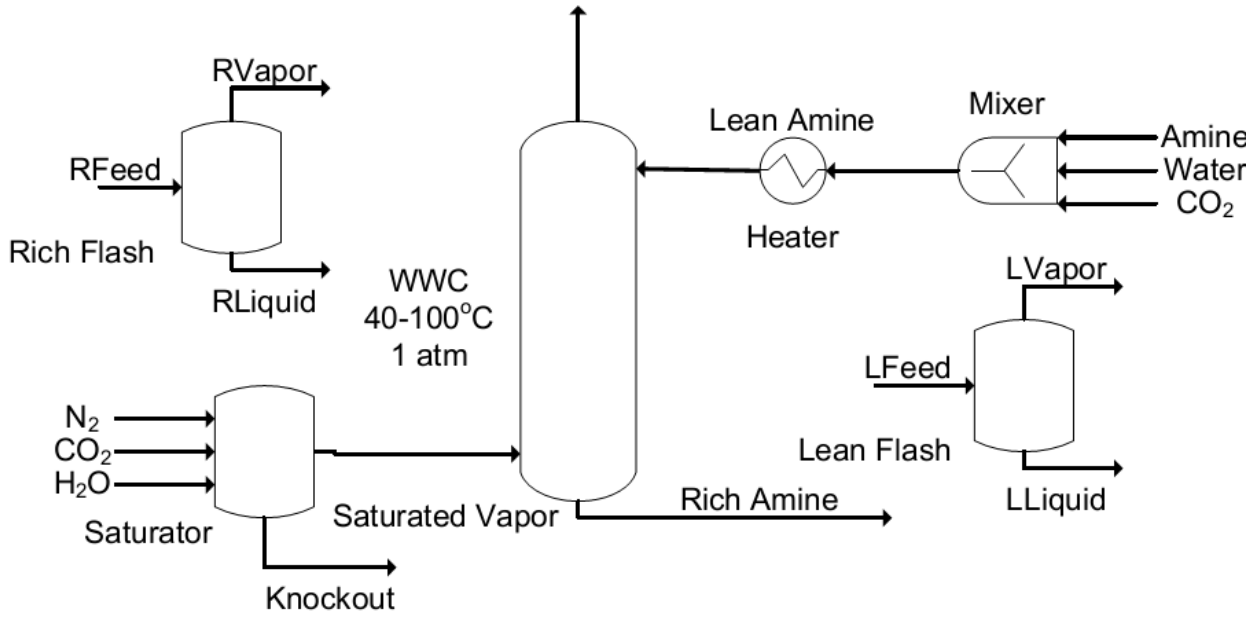

Figure 13: WWC process flow diagram for Aspen Plus®.

The solvent is fed as three separate streams of amine, water, and CO_2. When mixed, the solvent heats up due to heat of mixing and speciation; therefore, a heater is used to return it to the desired temperature for isothermal operation. The entire WWC is operated isothermally to mimic laboratory conditions. The gas is fed to a flash vessel, which saturates it with water. The gas and solvent are contacted in the WWC, which has the same height as the real life apparatus (9.1 cm) but a diameter that is 100x larger (0.44 cm x100). The rich and lean flash vessels flash the rich and lean amine streams after the heater to calculate the equilibrium partial pressure of CO_2.

Aspen Plus® discretizes the boundary layer to perform its mass transfer calculation for the reactions. The previous discretization used fifty − the maximum number of points possible − which means it requires the most computation time (Chen, 2011). Based on prior studies (Kucka et al., 2003) and looking at previous modeling work (Plaza, 2011), the number of discretization points was reduced without any loss of accuracy. The old and new discretizations are compared in Figure 14.

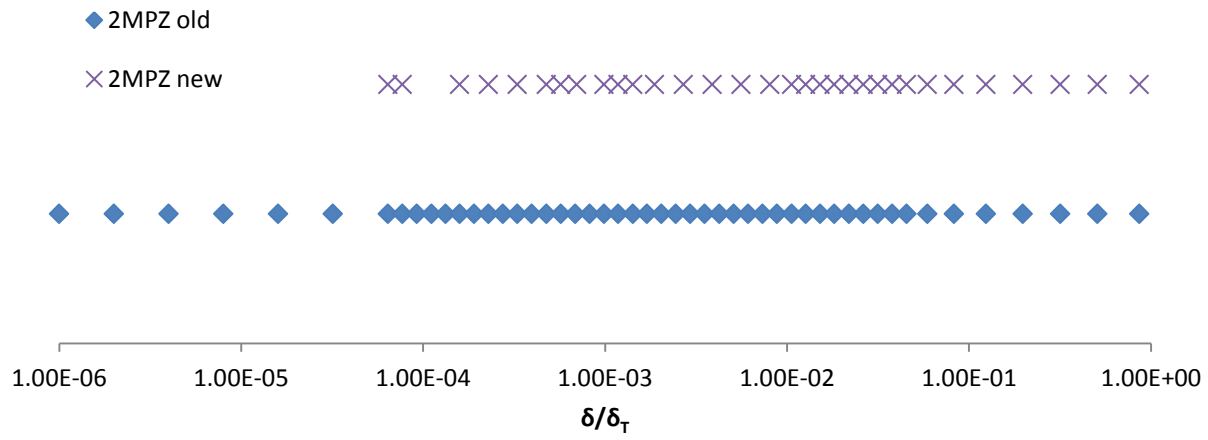

Figure 14: Boundary layer discretization. The x-axis is fraction through the boundary layer with the gas-liquid interface at left and the bulk liquid at right.

The complete reaction set used is shown in Table 5. The forward and reverse kinetic reactions are represented separately in Aspen Plus® using a powerlaw form shown in Equation 3.

$$k = k_o \exp\left[-\frac{E_A}{R}\left(\frac{1}{T}-\frac{1}{T_o}\right)\right] \tag{3}$$

The forward reaction rates are calculated, and then the reverse rates are back-calculated using the reaction equilibrium constant. The bicarbonate-forming reaction was fixed using values from literature (Ko & Li, 2000), while the dicarbamate-forming reaction was ratioed to the carbamate-forming reaction by assuming the Brønsted plot of PZ holds ($k_{carbamate} = 0.88k_{dicarbamate}$). This plot is shown in Figure 15. Thus, only the carbamate-forming reaction was regressed.

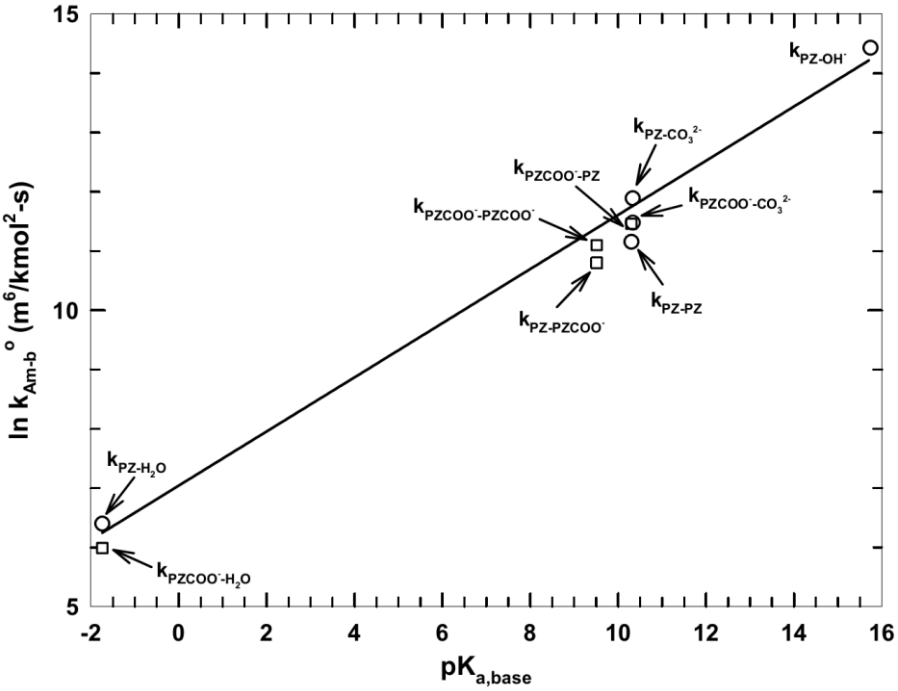

Figure 15: Brønsted plot showing the reaction rate constant (k_{Am-b}) vs the pKa of a base for an amine catalyzed by a base, $k_{Am-base}$.

To calculate k_o and E_A, two points were chosen at different loadings: one where the bicarbonate reaction is insignificant and a second, higher one where the bicarbonate is significant. At each of these points, the 40°C and 60°C fluxes were examined. Using a fixed set of kinetic parameters, the loading was adjusted to ensure that at zero driving force there is zero flux. This adjustment was made until the ratio of predicted flux to actual flux for the absorption and desorption points were within 1% of each other, or until the loading had been adjusted up to 10% of the operational loading range. Therefore, the maximum loading adjustment was ±0.01 mol CO_2/mol alk.

Once this loading adjustment was completed, a design specification was used to match the flux exactly by varying the k_o of one reaction. This is tested at two different temperatures to produce a coherent set of k_o and E_A for all reactions. The diffusivity parameters of Equation 4 were also adjusted. The diffusivity adjustments were made to fit the higher temperature data points primarily.

$$D = D_o\left(\frac{T}{T_{ref}}\right)^{\beta}\left(\frac{\mu}{0.0465}\right)^{\alpha} \tag{4}$$

With all parameters fixed, the WWC flux cases were all simulated. The power-law parameters, the loading, and the diffusivity parameters were adjusted. The flux cases were again simulated and this process was repeated until a satisfactory fit emerged.

Using a very small reaction set, most of the data were matched within 20%. There were nine predicted fluxes not within 20% of the experimental fluxes. The kinetic fit is displayed in Figure 16 and Figure 17. As seen in Figure 16**Figure** 16, the predictions worsen at higher temperatures as experimental error is expected to increase and as the mechanism shifts to diffusion-dominated. In addition to increasing scatter with increasing temperature, there is a linear systematic bias. Efforts to correct for this bias by changing the reference temperature for diffusivity were unsuccessful. Figure 17 shows no systematic trend with loading and the scatter with temperature remains approximately constant.

Table 5 shows the power-law parameters, and Table 6 shows diffusivity parameters. While the dependence of diffusivity on viscosity is reasonable, its dependence on temperature is probably indicative not of a physical effect, but of the diffusivity being distorted to fit temperature dependence effects.

Table 5: Reaction Set for 2MPZ with Forward Reactions above the Rule

Reaction	k_o (kmol/s-m^3)	E_A (kJ/mol)
$2MPZCOO^- + H_2O + CO_2 \rightarrow H2MPZCOO + HCO_3^-$	2.62E6	98.0
$2\ 2MPZ + CO_2 \rightarrow 2MPZH^+ + 2MPZCOO^-$	1.45E10	21.9
$2\ 2MPZCOO^- + CO_2 \rightarrow 2MPZ(COO^-)_2 + H2MPZCOO$	1.28E10	21.9
$H2MPZCOO + HCO_3^- \rightarrow 2MPZCOO^- + H_2O + CO_2$	3.67E5	174
$2MPZH^+ + 2MPZCOO \rightarrow 2\ 2MPZ + CO_2$	3.96E4	97.8
$2MPZ(COO^-)_2 + H2MPZCOO \rightarrow 2\ 2MPZCOO^- + CO_2$	2.71E8	129

Table 6: Diffusivity Parameter Values

Diffusivity Parameter	8 m 2MPZ value
D_o	4.4E-11 m^2/s
α	-1.50
β	-11.5
T_{ref}	373.15 K

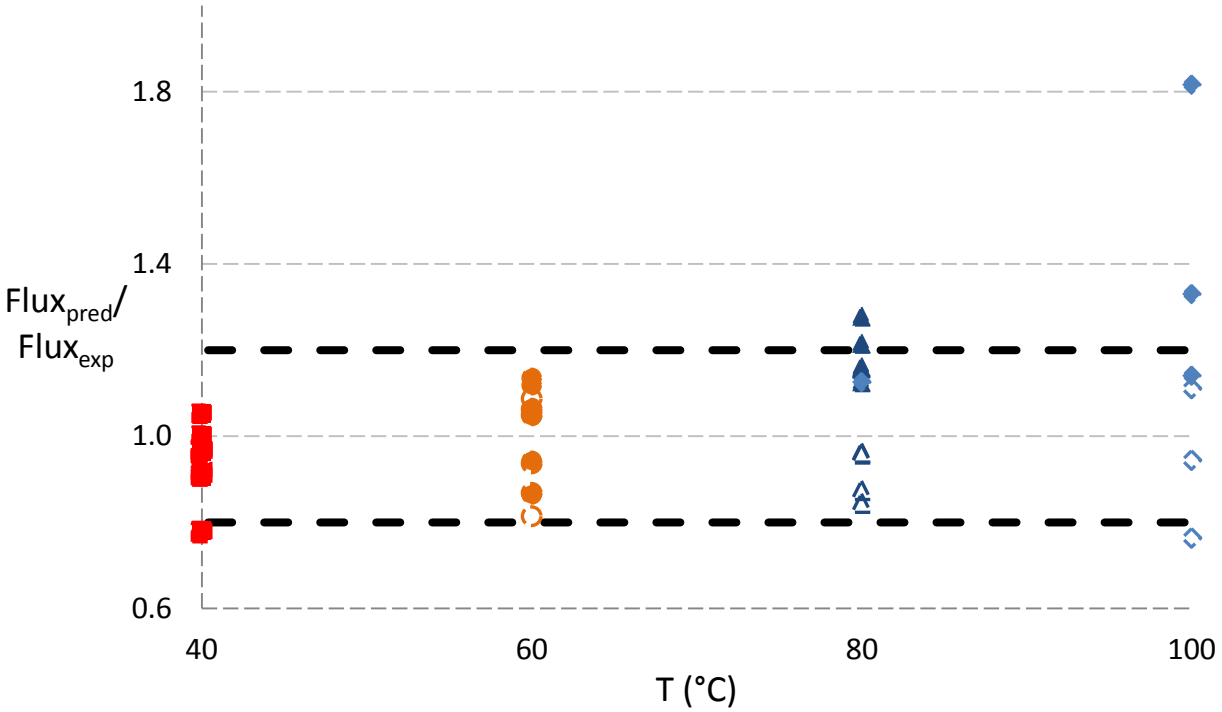

Figure 16: 8 m 2MPZ kinetic fit. There is a linear bias with temperature. Filled points represent absorption, open points desorption. Dashed lines delineate the target range ±20%.

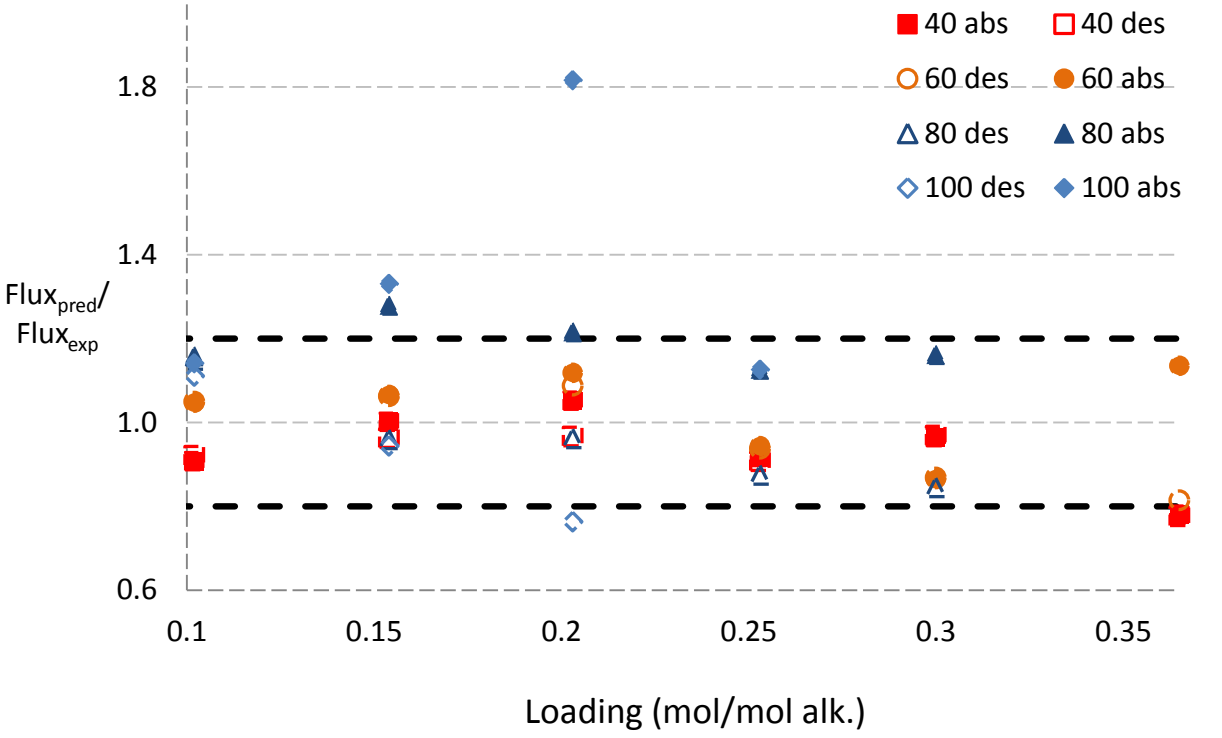

Figure 17: 8 m 2MPZ kinetic fit. Model flux ratioed to experimental flux shows no clear trend with loading. Filled points represent absorption, open points desorption. The dashed lines delineate the target range ±20%.

6. REFERENCES

Chen, X., "Carbon Dioxide Thermodynamics, Kinetics, and Mass Transfer in Aqueous Piperazine Derivatives and Other Amines," The University of Texas at Austin, PhD Dissertation, 2011.

Frailie, P., Plaza, J., Van Wagener, D., and Rochelle, G.T., "Modeling Piperazine Thermodynamics," *Energy Procedia*, 4, 35–42, 2011.

Freeman, S.A., "Thermal Degradation and Oxidation of Aqueous Piperazine for Carbon Dioxide Capture," The University of Texas at Austin, PhD Dissertation, 2011.

Hilliard, M.D., "A Predictive Thermodynamic Model for an Aqueous Blend of Potassium Carbonate, Piperazine, and Monoethanolamine for Carbon Dioxide," The University of Texas at Austin, PhD Dissertation, 2008.

Ko, J., and Li, M., "Kinetics of Absorption of Carbon Dioxide into Solutions of N-Methyldiethanolamine + Water," *Chem Eng Sci*., 55:4139–4147, 2008.

Plaza, J.M., "Modeling of Carbon Dioxide Absorption using Aqueous Monoethanolamine, Piperazine and Promoted Potassium Carbonate," The University of Texas at Austin, PhD Dissertation, 2011.

Rochelle, G.T., Xi, C., Li, L., Namjoshi, O., Xu, Q., Nguyen, T., Frailie, P., Van Wagener, D., Plaza, J. M., Wang, C., Chen, E., Ziaii, S., Dunia, R., Cohen, S., Closmann, F., Freeman, S., Voice, A., Ashouripashaki, M., Fulk, S., Rafique, H. A., "CO_2 Capture by Aqueous Absorption**,** First Quarterly Progress Report 2011." Luminant Carbon Management Program, The University of Texas at Austin, 2011.

Rochelle, G.T., Li, L., Nguyen, T., Li, H., Du, Y., Frailie, P., Chen, E., Sachde, D., Wang, C., Madan, T., Sherman, B., Walters, M., Ziaii, S., Cohen, S., Namjoshi, O., Voice, A., Fulk, S., Nielsen, P., Fine, N., Ashouripashaki, M., "CO_2 Capture by Aqueous Absorption**,** Second Quarterly Progress Report 2012," Luminant Carbon Management Program, The University of Texas at Austin, 2012.

Rochelle, G.T., Li, L., Du, Y., Frailie, P., Chen, E., Sachde, D., Lin, Y., Wang, C., Madan, T., Sherman, B., Walters, M., Namjoshi, O., Voice, A., Fulk, S., Nielsen, P., Fine, N., "CO_2 Capture by Aqueous Absorption**,** Fourth Quarterly Progress Report 2012," Luminant Carbon Management Program, The University of Texas at Austin, 2013.

Weiland, R.H., Dingman, J.C., Cronin, D.B., Browning, G.J., "Density and Viscosity of Some Partially Carbonated Aqueous Alkanolamine Solutions and Their Blends," *J. Chem. Eng. Data*, *9568*(1985), 378–382, 1998.

Xu, Q., "Thermodynamics of CO_2 Loaded Aqueous Amines," University of Texas at Austin, PhD Dissertation, 2011.

2 2MPZ/PZ Product Manual

2MPZ/PZ CO_2 Capture Simulation USER MANUAL

Version 2014.0.0
October 31, 2014

Revision Log

Version Number	Release Date	Description
Version 2014.0.0	10/31/2014	Initial version.

Table of Contents

List of Figures

List of Tables

To obtain support for this package, please send an email to
ccsi-support@acceleratecarboncapture.org.

1. INTRODUCTION

This document describes a 2-methylpiperazine (2MPZ)/ piperazine (PZ) CO_2 capture system process simulation. The amine scrubbing system is divided into separate absorber and stripper simulations. The model consists of 2MPZ+PZ.bkp with supporting files 2mpzpz.dll and sub.opt. This manual was written using Aspen Plus® V8.4 and is compatible with V8.4 and higher. The first example takes five minutes to complete, while the later two examples require thirty minutes each.

1.1.Predicting CO_2 Solubility

The solubility of CO_2 dictates the operational loading range as well as a stripper temperature and pressure. In this five minute example, a property analysis block is used to generate a series of isotherms for a fixed amine concentration and variable loading.

1. Open 2MPZ+PZ.bkp. When prompted to update databanks, decline.
2. In the Navigation Pane, select Properties and navigate to Analysis. Click "New…" to create a new analysis block. Enter its ID as "VLE" and select the type as generic. Change the system basis to Mass and set H2O to 1000 kg/sec.
3. On the Variable tab, change Temperature to Vapor Fraction and set it to 1e-05. Then, create four variables: (1) temperature, (2) mole flow 2MPZ, (3) mole flow PZ, and (4) mole flow CO2. Select each variable and define them by clicking the "Range/List" button.
   a. Temperature is a range: Lower=293.15, Upper=413.15, Increments=20
   b. Mole flow 2MPZ is a list: 4
   c. Mole flow PZ is a list: 4
   d. Mole flow CO2 is a range: Lower=0.001, Upper=8, Points=20.
4. On the Tabulate tab, select PPCO2-KP for the partial pressure of CO_2 in kilopascals.
5. To view the results, navigate to Properties→Analysis→VLE→Results. Some of the results are shown in Table 1. Using additional graphing software, they are plotted in Figure 1.

Table 1. Excerpt of 2MPZ VLE results.

TEMP	MOLEFLOW 2MPZ	MOLEFLOW PZ	MOLEFLOW CO2	VAPOR PPMX CO2
K	kmol/sec	kmol/sec	kmol/sec	kPa
293.15	4	4	0.001	4.8958e-09
293.15	4	4	0.40095	0.00024589
293.15	4	4	0.8009	0.00057192
293.15	4	4	1.20085	0.00087059
293.15	4	4	1.6008	0.00116965
293.15	4	4	2.00075	0.00153542
293.15	4	4	2.4007	0.00208361
293.15	4	4	2.80065	0.00305492
293.15	4	4	3.2006	0.00503915

293.15	4	4	3.60055	0.00954838
293.15	4	4	4.0005	0.01963430
293.15	4	4	4.40045	0.03794060
293.15	4	4	4.8004	0.06619960
293.15	4	4	5.20035	0.11772041
293.15	4	4	5.6003	0.23658341
293.15	4	4	6.00025	0.55188993
293.15	4	4	6.4002	1.58184108
293.15	4	4	6.80015	6.73970432
293.15	4	4	7.2001	45.7599422
293.15	4	4	7.60005	234.716411
293.15	4	4	8	975.058646

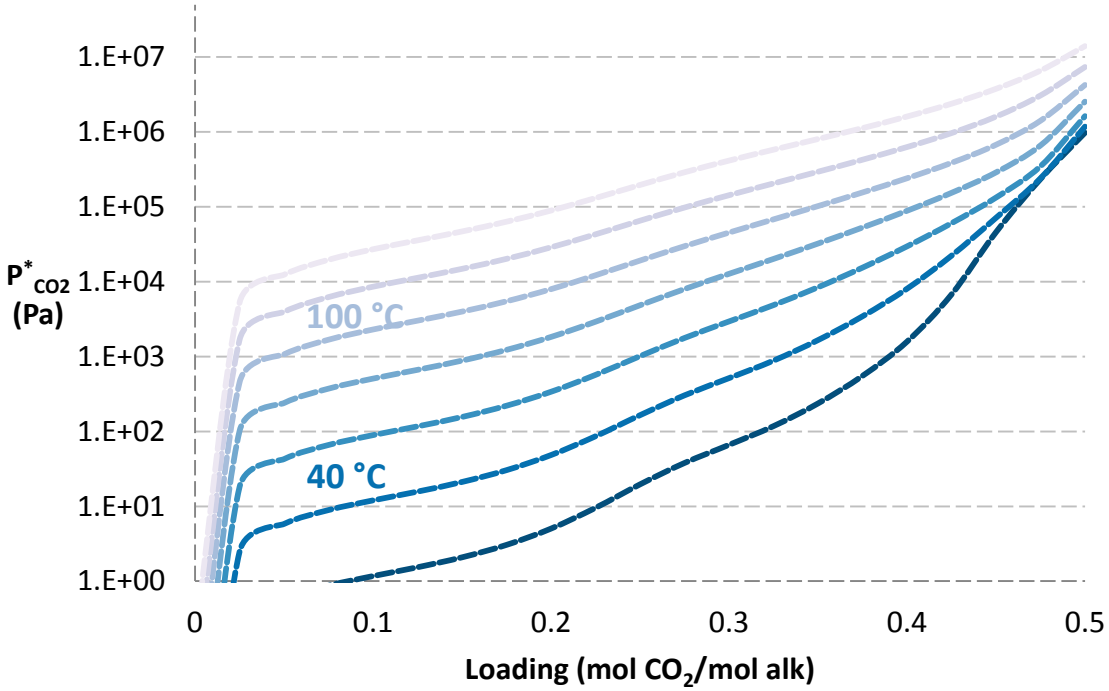

Figure 1. CO_2 solubility in 4 m 2MPZ/4 m PZ. Curves are spaced 20 °C apart.

Other property analysis blocks can be made to give properties such as speciation and volatility.

1.2.Features list

This product is a thermodynamic and kinetic model of 4 m 2MPZ/4 m PZ for amine scrubbing process modeling. It is focused on capture from coal-fired power plant flue gas; therefore, it represents the CO_2 solubility, speciation, amine vapor pressure, heat capacity, pKa, heat of absorption, density, and viscosity. While the model can extrapolate over a range of amine concentration, loading, and temperature, it is based on data collected primarily at 4 m 2MPZ/4 m PZ with loading from 0.15 to 0.4 mol CO_2/mol alkalinity.

2. TUTORIAL

2.1.Absorber Simulation

Description

This example describes how to simulate a rate-based absorber. It includes tips on: convergance, the use of design specifications to meet process criteria, and the proper boundary-layer discretization.

Setup

1. Build the flowsheet of Figure 2 using an ABSBR1 RadFrac column. In the Model Palette at the bottom of the window, select Columns→RadFrac→ABSBR1. (If you do not see the model library, press F10.) Place the block on the flowsheet and name it "ABSORBER".

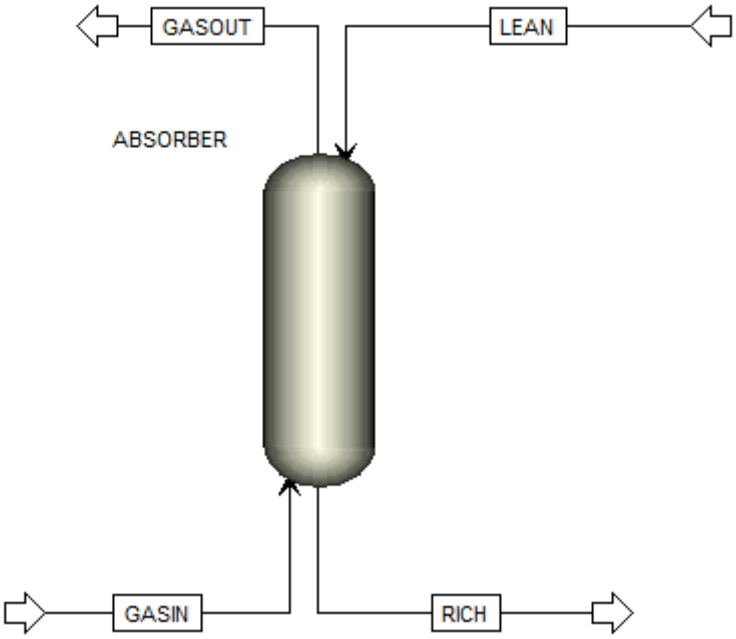

Figure 2. Simple Absorber Flowsheet.

2. Then select "Material" at the left of the Model Palette. Create GASIN by clicking on the arrow on the left of the block (the feed) and then clicking elsewhere. Create RICH by clicking on the arrow at the bottom (the bottoms). Create GASOUT by clicking on the arrow at the top (the vapor distillate). Lastly, create LEAN by clicking on the now blue arrow on the left (the feed).
3. Double click on GASIN to configure it as follows:
    a. Temperature: 40 C
    b. Pressure: 1 atm
    c. Total flow: 5 kmol/sec
    d. Composition: Mole-Frac
        i. H2O: 7.3
        ii. CO2: 12
        iii. N2: 80.7

Note: Aspen will normalize the mole fractions to one.

4. Select LEAN from the Navigation Pane and configure it as follows:
    a. Temperature: 40 C
    b. Pressure: 1 atm
    c. Total flow: 20 kmol/sec
    d. Composition: Mole-Frac
        i. H2O: 55.556
        ii. CO2: 4.8
        iii. 2MPZ: 4
        iv. PZ: 4
5. Navigate to Blocks→ABSORBER and configure its Setup as follows:
    a. On the configuration tab
        i. Calculation type: Rate-Based
        ii. Number of stages: 50
        iii. Condenser: none
        iv. Reboiler: none
    b. On the Streams tab
        i. GASIN On-Stage 50
        ii. LEAN On-Stage 1
    c. On the Pressure tab set the Top stage pressure to 1 atm.
6. Navigate to Specifications→Reactions. Make two reaction blocks.
    a. Starting stage=1; ending stage=3; Reaction ID=Z-PZ2MPZ.
    b. starting stage=4; ending stage=50;Reaction ID=Z-PZ2MPZ.
7. Navigat to Sizing and Rating→Packing Rating and click "New…" Name the section "1", and configure its Specification as follows:
    a. Starting stage: 1
    b. Ending stage: 50
    c. Type: MELLAPAK
    d. Vendor: SULZER
    e. Material: STANDARD
    f. Dimension: 250X
    g. Section diameter: 8.5 meter
    h. Section packed height: 8 meter

Note: As the column is packed, the number of stages does not represent trays. As a very rough approximation, one stage for every half meter of packing is recommended. Use more stages for greater temperature and mass transfer gradients.

    i. Navigate to Pack Rating→1→Rate-based and configure it as follows:
        i. Select the Rate-based calculations check box.
        ii. Flow model: Countercurrent
        iii. Film resistance
            1. Liquid phase: Discrxn
            2. Vapor phase: Film
    j. On the Optional tab, set the Additional discretization points to the 32 shown in Table 2.

Table 2. Boundary layer discretization.

Point	Liquid film	Point	Liquid film

1	6.40E-05	17	0.0106
2	7.68E-05	18	0.0127
3	0.000159	19	0.0152
4	0.000229	20	0.0182
5	0.00033	21	0.0219
6	0.000476	22	0.0263
7	0.000571	23	0.0315
8	0.0007	24	0.0378
9	0.000986	25	0.0454
10	0.00118	26	0.059
11	0.00142	27	0.0826
12	0.00187	28	0.124
13	0.0027	29	0.198
14	0.00389	30	0.317
15	0.0056	31	0.507
16	0.00806	32	0.862

8. Navigate to Flowsheeting Options→Calculator and create a new Calculator named C-RM. This block will calculate the fraction of CO_2 captured.
    a. On the Define tab, create three variables:

Variable	Information flow	Definition
REMOVE	Export	Parameter Parameter no.=2
CO2IN	Import	Mole-Flow Stream=GASIN Substream=MIXED Component=CO2 Units=kmol/sec
CO2OUT	Import	Mole-flow Stream=GASOUT Substream=MIXED Component=CO2 Units=kmol/sec

    b. On the Calculate tab, beginning in column 7 write "REMOVE=(CO2IN-CO2OUT)/CO2IN"
9. Still under Flowsheeting options, navigate to Design Specs. Click New and name it D-RM
    a. On the Define tab, create a variable REMOVE and assign it to parameter 2.
    b. On the Spec tab
        i. Spec: REMOVE
        ii. Target: 0.90
        iii. Tolerance: 0.000001
    c. On the Vary tab
        i. Type: Stream-Var
        ii. Stream: LEAN
        iii. Variable: MOLE-FLOW
        iv. Lower: 5
        v. Upper: 300

Running the Simulation

1. Deactivate the design spec by right-clicking on it and selecting "Deactivate".
2. Run the simulation. This provides an initial guess.
    a. You may see warnings about unusual liquid mole fraction and component production profiles. These can be ignored.

3. Change the absorber Reactions for stages 1 to 3 to R-PZ2MPZ from Z-PZ2MPZ. Run the simulation.
    a. You may see warnings about unusual liquid mole fraction and component production profiles. Again, these can be ignored.
4. Change the absorber Reactions for stages 4 to 50 to R-PZ2MPZ from Z-PZ2MPZ. Run the simulation.
5. Navigate to Flowsheeting Options→Calculator→C-RM→Results and on the Define Variable tab, the fractional CO_2 removal is displayed. It should be ~57%.
6. Increase the LEAN stream total flow in 5 kmol/sec increments until the percent removal is within 0.10 of 0.90. Be sure to run the simulation after each increment.
    a. At 25 kmol/sec, removal is ~67%.
    b. At 30 kmol/sec, ~78%.
    c. At 35 kmol/sec, ~91%.
7. Now, activate the Design Spec D-RM by right-clicking on it and selecting Activate. Run the simulation.
8. The absorber is now removing 90% of the inlet CO_2. Results should be similar to those in Table 3, Figure 3, and Figure 4. View them by navigating to Results Summary→Streams, Flowsheeting Options→Design Spec→D-RM→Results, and Blocks→ABSORBER→Pack Rating→1→Results.

Table 3. Stream results.

	GASIN	GASOUT	LEAN	RICH
Temperature K	313.1	314	313.1	325
Pressure N/sqm	101325	101325	101325	101325
Vapor Frac	1	1	0	0
Solid Frac	0	0	0	0
Mole Flow kmol/sec	5	4.397	32.215	32.279
Mass Flow kg/sec	146.016	121.109	992.102	1017.012
Volume Flow cum/sec	128.34	113.192	0.89	0.901
Enthalpy Gcal/hr	-277.174	-81.332	-8097.725	-8293.59
Mole Flow kmol/sec				
H2O	0.365	0.302	28.034	27.937
CO2	0.6	0.06	0	0
HCO3-	0	0	0.092	0.272
CO3--	0	0	0.034	0.014
H+	0	0	0	0
OH-	0	0	0	0
PZ	0	0	0.078	0.029
PZCOO-2	0	0	0.153	0.244
PZCOO-	0	0	0.824	0.592
PZH+	0	0	0.756	0.65
HPZCOO	0	0	0.216	0.514
N2	4.035	4.035	0	0
O2	0	0	0	0
2MPZ	0	0	0.116	0.031

2MPZCOO	0	0	0.394	0.151
H2MPZCOO	0	0	0.521	0.899
2MPZCOO2	0	0	0.022	0.022
2MPZH+	0	0	0.974	0.924

Variable	Initial value	Final value	Units
MANIPULATED	32.5423	32.2149	KMOL/SEC
REMOVE	0.908827	0.9	

Figure 3. Design spec results.

Packed column rating results

Section starting stage:	1	
Section ending stage:	50	
Column diameter:	8.5	meter
Maximum fractional capacity:	0.756228	
Maximum capacity factor:	0.0789936	m/sec
Section pressure drop:	1127.72	N/sqm
Average pressure drop / Height:	140.965	N/cum
Maximum stage liquid holdup:	0.648773	cum
Max liquid superficial velocity:	0.0160911	m/sec
Surface area:	256	sqm/cum
Void fraction:	0.987	
1st Stichlmair constant:	1	
2nd Stichlmair constant:	1	
3rd Stichlmair constant:	0.32	

Figure 4. Column pack rating results.

2.2.Stripper Simulation

Description

This example describes simulating a simple stripper and cross exchanger.

Setup

1. Construct the flowsheet of Figure 5. From Columns in the Model Palette, select RadFrac→STRIP1 for the stripper. From Exchangers, select Heater for CX-COLD, CX-

HOT, and HX-TRIM. From Pressure Changers, select Pump for LEANPUMP. Create the streams using the "Material" button.

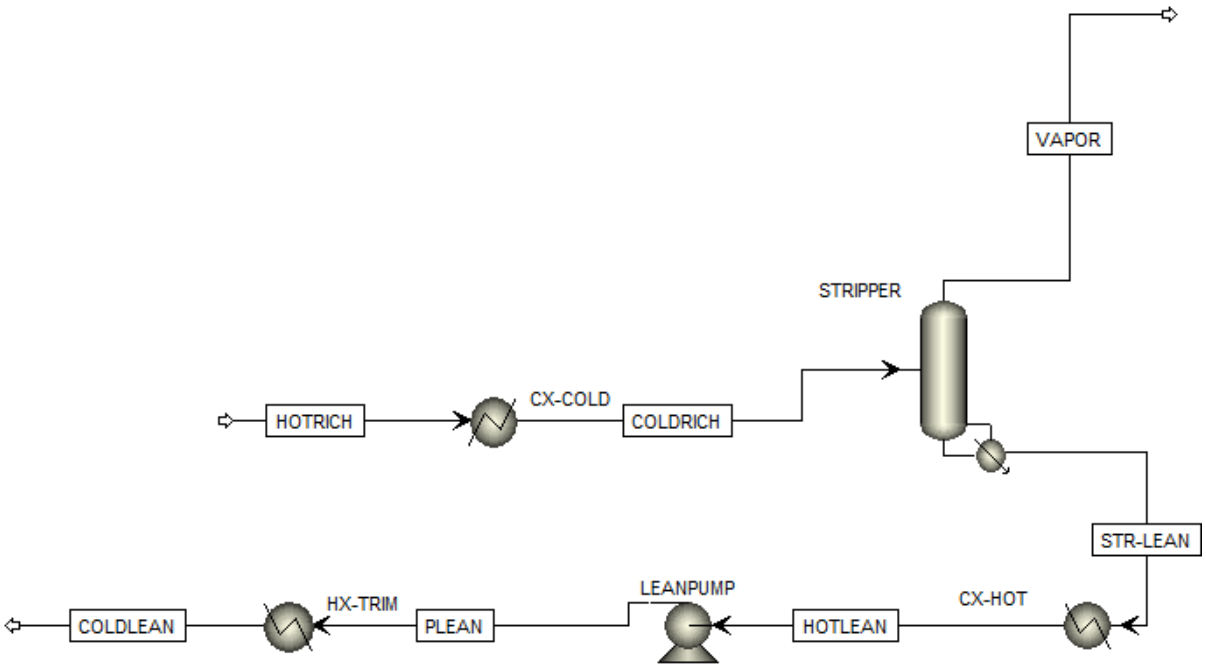

Figure 5. Simple Stripper Flow Sheet

2. Set HOTRICH to the values from the absorber example.
    a. Temperature: 325 K
    b. Pressure: 12 bar
    c. Total flow: 32.22 kmol/sec
    d. Composition: Mole-Frac
        i. H2O 55.556
        ii. CO2 5.87
        iii. 2MPZ 4
        iv. PZ 4

Note: The pressure is set as if coming from a pump, which is omitted.

3. Set CX-COLD
    a. Pressure: 0 N/sqm
    b. Temperature: 85 C
    c. Valid phases: Liquid-Only

Note: Pressure drop is neglected.

4. Configure STRIPPER Setup as follows:
    a. On the Configuration tab
        i. Calculation Type: Rate-Based
        ii. Number of Stages: 15
        iii. Condenser: None
        iv. Reboiler: Kettle
        v. Reboiler Duty: 200 MW

   b. On the Streams tab, feed COLDRICH to stage 1 as liquid.
   c. On the Pressure tab, set the top stage pressure to 3 bar.
5. Navigate to Stripper→Specifications→Reactions, select starting stage as 1, ending stage as 15, and Chemistry ID as REDUCED.
6. Navigate to Sizing and Rating→Packing Rating and create a new Pack Rating for the stripper by clicking "New." Let it be called 1, and configure it as follows:
   a. Under Setup, stages 1-14 use MELLAPAK, SULZER, STANDARD, 250X with a diameter of 4 m and a section packed height of 2 m.
   b. Under Rate-Based, check Rate-based calculations with Film Resistance set to Film for liquid and vapor phases.
7. Configure CX-HOT
   a. Temperature: 50 C
   b. Pressure: 0 N/sqm
8. Configure LEANPUMP
   a. Discharge pressure: 250 kPa
9. Configure HX-TRIM
   a. Temperature: 40 C
   b. Pressure: 0 N/sqm

Note: This flow sheet takes the rich stream from the previous absorber tutorial, passes it through a cross-exchanger, and then to the stripper. CX-COLD and CX-HOT will be used to simulate the cross exchanger. HX-TRIM is the trim cooler to lower the lean solvent down to 40 ℃ prior to entering the absorber.

10. Create a LOADINGS calculator.
    a. Define the variables as shown below.
    b. The Fortran code is

```
LLDG=(LCO2+LHCO3+LCO3+L2MPZC+2*L2MPZC2+LH2MPZC
.               +LPZCOO+2*LPZCOO2+LHPZCOO)
LLDG=LLDG/(2*(L2MPZ+LH2MPZ+L2MPZC+L2MPZC2+LH2MPZC
.             +LPZ+LHPZ+LPZCOO+LPZCOO2+LHPZCOO))

RLDG=(RCO2+RHCO3+RCO3+R2MPZC+2*R2MPZC2+RH2MPZC
.               +RPZCOO+2*RPZCOO2+RHPZCOO)
RLDG=RLDG/(2*(R2MPZ+RH2MPZ+R2MPZC+R2MPZC2+RH2MPZC
.             +RPZ+RHPZ+RPZCOO+RPZCOO2+RHPZCOO))
```

Variable name	Info. flow	Definition
RLDG	Export	Parameter Parameter no.=3
LLDG	Export	Parameter Parameter no.=4
		Mole-Frac Stream=STR-LEAN Substream=MIXED
LCO2	Import	Component=CO2
		Mole-Frac Stream=STR-LEAN Substream=MIXED
L2MPZ	Import	Component=2MPZ
		Mole-Frac Stream=STR-LEAN Substream=MIXED
LH2MPZ	Import	Component=2MPZH+
		Mole-Frac Stream=STR-LEAN Substream=MIXED
L2MPZC	Import	Component=2MPZCOO
L2MPZC2	Import	Mole-Frac Stream=STR-LEAN Substream=MIXED

		Component=2MPZCOO2
		Mole-Frac Stream=STR-LEAN Substream=MIXED
LH2MPZC	Import	Component=H2MPZCOO
		Mole-Frac Stream=STR-LEAN Substream=MIXED
LPZ	Import	Component=PZ
		Mole-Frac Stream=STR-LEAN Substream=MIXED
LHPZ	Import	Component=PZH+
		Mole-Frac Stream=STR-LEAN Substream=MIXED
LPZCOO	Import	Component=PZCOO-
		Mole-Frac Stream=STR-LEAN Substream=MIXED
LPZCOO2	Import	Component=PZCOO-2
		Mole-Frac Stream=STR-LEAN Substream=MIXED
LHPZCOO	Import	Component=HPZCOO
		Mole-Frac Stream=STR-LEAN Substream=MIXED
LHCO3	Import	Component=HCO3-
		Mole-Frac Stream=STR-LEAN Substream=MIXED
LCO3	Import	Component=CO3--
		Mole-Frac Stream=HOTRICH Substream=MIXED
R2MPZ	Import	Component=2MPZ
		Mole-Frac Stream=HOTRICH Substream=MIXED
R2MPZH	Import	Component=2MPZH+
		Mole-Frac Stream=HOTRICH Substream=MIXED
R2MPZC	Import	Component=2MPZCOO
		Mole-Frac Stream=HOTRICH Substream=MIXED
R2MPZC2	Import	Component=2MPZCOO2
		Mole-Frac Stream=HOTRICH Substream=MIXED
RH2MPZC	Import	Component=H2MPZCOO
		Mole-Frac Stream=HOTRICH Substream=MIXED
RPZ	Import	Component=PZ
		Mole-Frac Stream=HOTRICH Substream=MIXED
RPZH	Import	Component=PZH+
		Mole-Frac Stream=HOTRICH Substream=MIXED
RPZCOO	Import	Component=PZCOO-
		Mole-Frac Stream=HOTRICH Substream=MIXED
RPZCOO2	Import	Component=PZCOO-2
		Mole-Frac Stream=HOTRICH Substream=MIXED
RHPZCOO	Import	Component=HPZCOO
		Mole-Frac Stream=HOTRICH Substream=MIXED
RHCO3	Import	Component=HCO3-
		Mole-Frac Stream=HOTRICH Substream=MIXED
RCO3	Import	Component=CO3--

11. Make a Design Spec named D-LEAN.
    a. Define LLDG as Parameter 4
    b. Spec LLDG to 0.30 with a tolerance of 0.01.

c. On the Vary tab under Manipulated variable limits, Lower: 0 and Upper: 5.5E8 Watts. Now, under Manipulated variable set the following:
   i. Type: Block-Var
   ii. Block: STRIPPER
   iii. Variable: QN

12. Make a Design Spec named D-T.
    a. Define TEMP as Stream-Var Stream=STR-LEAN Substream=MIXED Variable=TEMP Units=K
    b. Spec TEMP to 423.15 K with a tolerance of 0.01.
    c. On the Vary tab, set the manipulated variable limits to 900,000 to 1,800,000 N/sqm. Now, under Manipulated variable set the following:
       i. Type: Block-Var
       ii. Block: STRIPPER
       iii. Variable: STAGE-PRES
       iv. ID1: 1

Running the Simulation

1. Deactivate both design specs.
2. Run the simulation.
    a. Ignore warnings about excess flood.
3. Review the lean loading (LLDG) in the LOADINGS calculator block by navigating to the Define Variable tab of Results. Decrease the stripper reboiler duty in 50 MW increments until the lean loading is close to the desired value of 0.30. Run the simulation after each decrement.
    a. At 200 MW, lean loading is 0.24 mol CO_2/mol alk.
    b. At 150 MW, 0.29 mol CO_2/mol alk.
4. Activate the D-LEAN design spec and run the simulation.
    a. Converges to 141 Megawatts at a loading of 0.30 mol CO_2/mol alk.
    b. Again, ignore flood warnings.
5. Activate the D-T design spec and run the simulation.
6. Create a heat stream from CX-HOT to CX-COLD by clicking on the arrow next to "Material" in the Model Palette and clicking on Heat from the pulldown menu. Call it Q-XC. To clear the temperature specification of CX-COLD, double-click on the block, right-click on temperature under flash specifications, and then select "Clear".
7. Run the simulation. The results are similar to those of Tables 4–7. To view them, look at Results Summary→Streams, Flowsheeting Options→Design Spec→D-LEAN→Results, Flowsheeting Options→Design Spec→D-T→Results, and Blocks→STRIPPER→Pack Rating→1→Results.

Table 4. Stream results excerpt.

	COLDLEAN	COLDRICH	HOTLEAN	HOTRICH	P-LEAN	STR-LEAN	VAPOR
Temperature K	313.1	358.1	323.1	325	323.1	423.2	358.3
Pressure N/sqm	250000	1200000	1156840	1200000	250000	1156840	1156840
Vapor Frac	0	0	0	0	0	0	1
Solid Frac	0	0	0	0	0	0	0
Mole Flow kmol/sec	29.471	29.498	29.471	29.496	29.471	29.49	0.492

Mass Flow kg/sec	909.215	930.222	909.215	930.22	909.215	909.215	21.008
Volume Flow cum/sec	0.815	0.841	0.819	0.824	0.819	0.885	1.221
Enthalpy Gcal/hr	-7419.91	-7491.28	-7394.04	-7579.92	-7394.59	-7123.45	-162.478
Mole Flow kmol/sec							
H2O	25.642	25.235	25.601	25.522	25.601	25.311	0.024
CO2	< 0.001	0.002	< 0.001	< 0.001	< 0.001	0.018	0.467
HCO3-	0.087	0.529	0.125	0.248	0.125	0.438	
CO3--	0.029	0.019	0.033	0.012	0.033	0.009	
H+							
OH-							
PZ	0.068	0.035	0.07	0.027	0.07	0.113	trace
PZCOO-2	0.149	0.088	0.12	0.226	0.12	0.008	
PZCOO-	0.751	0.555	0.756	0.553	0.756	0.468	
PZH+	0.683	0.644	0.683	0.585	0.683	0.735	
HPZCOO	0.205	0.534	0.228	0.466	0.227	0.533	trace
N2							
O2							
2MPZ	0.098	0.053	0.104	0.027	0.104	0.286	trace
2MPZCOO	0.342	0.226	0.351	0.135	0.351	0.58	
H2MPZCOO	0.506	0.655	0.482	0.84	0.482	0.175	trace
2MPZCOO2	0.019	0.013	0.021	0.009	0.021	0.009	
2MPZH+	0.892	0.908	0.898	0.845	0.898	0.805	

Table 5. D-LEAN results.

Variable	Initial value	Final value	Units
MANIPULATED	150000000	238821041	WATT
LLDG	0.400532081	0.303942513	

Table 6. D-T results.

Variable	Initial value	Final value	Units
MANIPULATED	942368.33	1156836.73	N/SQM
TEMP	420.985072	423.150108	K

Table 7. Pack Rating results.

Variable	Value	Unit
Section starting stage:	1	
Section ending stage:	14	
Column diameter:	4	meter
Maximum fractional capacity:	0.649040471	
Maximum capacity factor:	0.019789443	m/sec

Section pressure drop:	366.525406	N/sqm
Average pressure drop / Height:	183.262703	N/cum
Maximum stage liquid holdup:	0.426064232	cum
Max liquid superficial velocity:	0.067558708	m/sec
Surface area:	256	sqm/cum
Void fraction:	0.987	
1st Stichlmair constant:	1	
2nd Stichlmair constant:	1	
3rd Stichlmair constant:	0.32	

3. USAGE INFORMATION

3.1. Environment/Prerequisites

This product requires Aspen Plus® V8.4 or newer with an Aspen Rate-Based Distillation license. As such, the supported environments are limited to:

- Windows XP SP3
- Windows Vista Business SP2
- Windows Vista Ultimate SP2
- Windows 7 Ultimate (32 and 64 Bit)
- Windows 7 Professional (32 and 64 Bit)

3.2. Support

Support can be obtained from ccsi-support@acceleratecarboncapture.org or by filling out the "Submit Feedback/Request Support" form available on the product distribution page.

3.3. Restrictions

The model is centered at an amine concentration of 4 m 2MPZ/4 m PZ. Extrapolating far from this concentration should be done with care. The model is best between 40 and 160 °C and 0.15 and 0.4 mol CO_2/mol alk. Kinetic modeling should be kept to 20−60 °C.

3.4. Next Steps

Future releases will refine the kinetic fit.

4. DEBUGGING

The model is running correctly if it is converging for the above tutorials with similar results. If it is not, see the next section.

4.1. How to Debug

Always run the simulation with the control panel visible. It is the only output available during computation, and it will tell you whether or not the simulation will converge. This will allow you to avoid wasting time on fruitless computation. Furthermore, it will alert you to any problems

encountered during computation. Additional debugging information is available in the history file, which can be viewed by selecting History from the ribbon in the Summary section of the Home tab.

Subroutine Errors

If you see,

```
*** SEVERE ERROR
    COULD NOT RESOLVE USER OR IN-LINE FORTRAN SUBROUTINE(S):
```

the simulation will not run. The possible causes and solutions are,

1. The .bkp file and the .dll and .opt files are not located in the same directory. Move them all into the same directory to resolve this.
2. The linker is not specified in the run settings. Press Ctrl+F7 and under linker options type "sub.opt."

Simulation Problems

- If you see a warning stating that the water liquid viscosity model MULH2O is violated due to the temperature being lower than the minimum temperature limit, the simulation is trapped in a non-physical solution. Check your inputs and re-run.
- Ignore flooding errors (`TPSAR MESSAGE: XXX.XX% FLOOD IN COLUMN EXCEEDS 80%`) unless it is your final step, in which case adjust column diameter for desired flood.

Aiding Convergence

- Only reinitialize when large changes have been made, such as adding or removing a flowsheet block.
- Make small changes in a converged model.
- Converge an initial, simple case before increasing complexity.
- Before enabling the design specification, the variable should be close to the desired value.
- Mass transfer models affect convergence and results substantially, so be sure to choose the appropriate model for the packing used.

4.2.Known Issues

- The activity coefficient of H2MPZCOO is ill-behaved with loading and temperature. For this reason, two reactions involving it were removed to allow convergence of the absorber. This reduces the physical significance of this model.
- Flash errors can occur if the solvent goes above 0.5 mol CO_2/ mol alk, particularly at elevated temperatures.
- You will see multiple warnings about property data while processing input specifications that follow this pattern, "PARAMETER XXX DATA SET 1 FOR COMPONENT 2MPZ HAS BEEN ENTERED MORE THAN ONCE. THE LAST ENTRY WILL BE USED." where XXX is the parameter name. This is not a problem.
- In running the tutorials, you will see warnings that the mole fractions are normalized to unity.
- You will see warnings that IONRDL is missing for 2MPZCOO, 2MPZCOO2, and 2MPZH+.

4.3.Reporting Issues

To report an issue please send an email to ccsi-support@acceleratecarboncapture.org.

5. MODEL HISTORY

The model is detailed in: Sherman, B., Frailie, P. T., Le, L., Salta, N., & Rochelle, G. T. (2014). Thermodynamic and Kinetic Modeling of Piperazine/2-Methylpiperazine. *Energy Procedia*, *in press*. A pre-print is available at this link.

After publication, the model was modified to account for an unreasonable activity coefficient of the 2MPZ zwitterion. This was done by removing the two kinetic reactions of Table 8.

Table 8. Removed reactions from 4 m 2MPZ/4 m PZ kinetic model.

Stoichiometry	Reaction
$PZCOO^- + 2MPZCOO^- + CO_2 \leftrightarrow PZ(COO^-)_2 + H2MPZCOO$	5
$2\ 2MPZCOO^- + CO_2 \leftrightarrow 2MPZ(COO^-)_2 + H2MPZCOO$	10

The reason this was necessary is due to the departure of the forward-reverse power-law reaction equilibria from the true thermodynamic reaction equilibria. Ideally, the following relationship holds true.

$$K_{eq,j} = \frac{\Delta G_j^0}{RT} = \frac{k_f}{k_r} \tag{5}$$

In practice, the second equality of Equation 5 only holds from 40 to 60 °C. This is because $\frac{k_f}{k_r}$ does not account for the temperature dependence of the activity coefficients. Figure 7 shows the activity coefficients of the species involved in the 2MPZ zwitterion reactions at 40 °C. $\gamma_{H2MPZCOO}$ is two orders of magnitude below the analogous PZ species. In addition, $\gamma_{H2MPZCOO}$ exhibits a minima and stronger loading dependence than γ_{HPZCOO}.

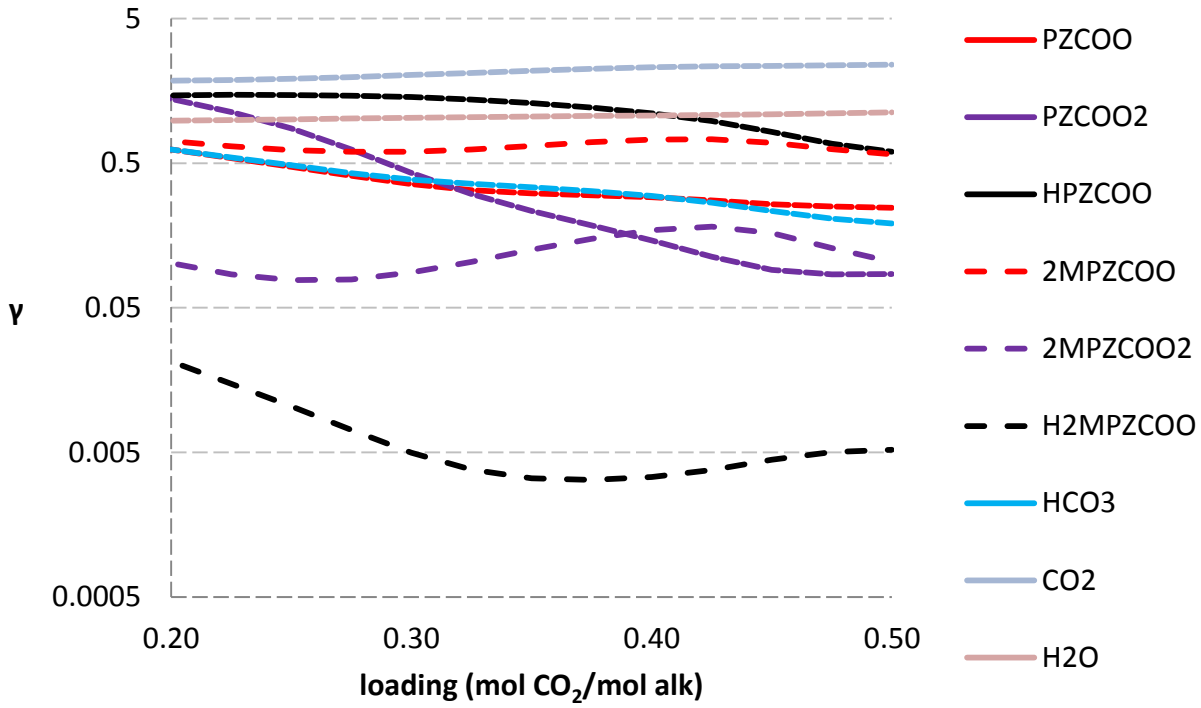

Figure 6. Activity coefficients at 40 °C for species of reactions 2, 5, and 10.

Therefore, to converge the absorber process model reactions 5 and 10 were deleted. All kinetic and diffusivity parameters were left at the previous values, resulting in the kinetic fit of Figures 8 and 9.

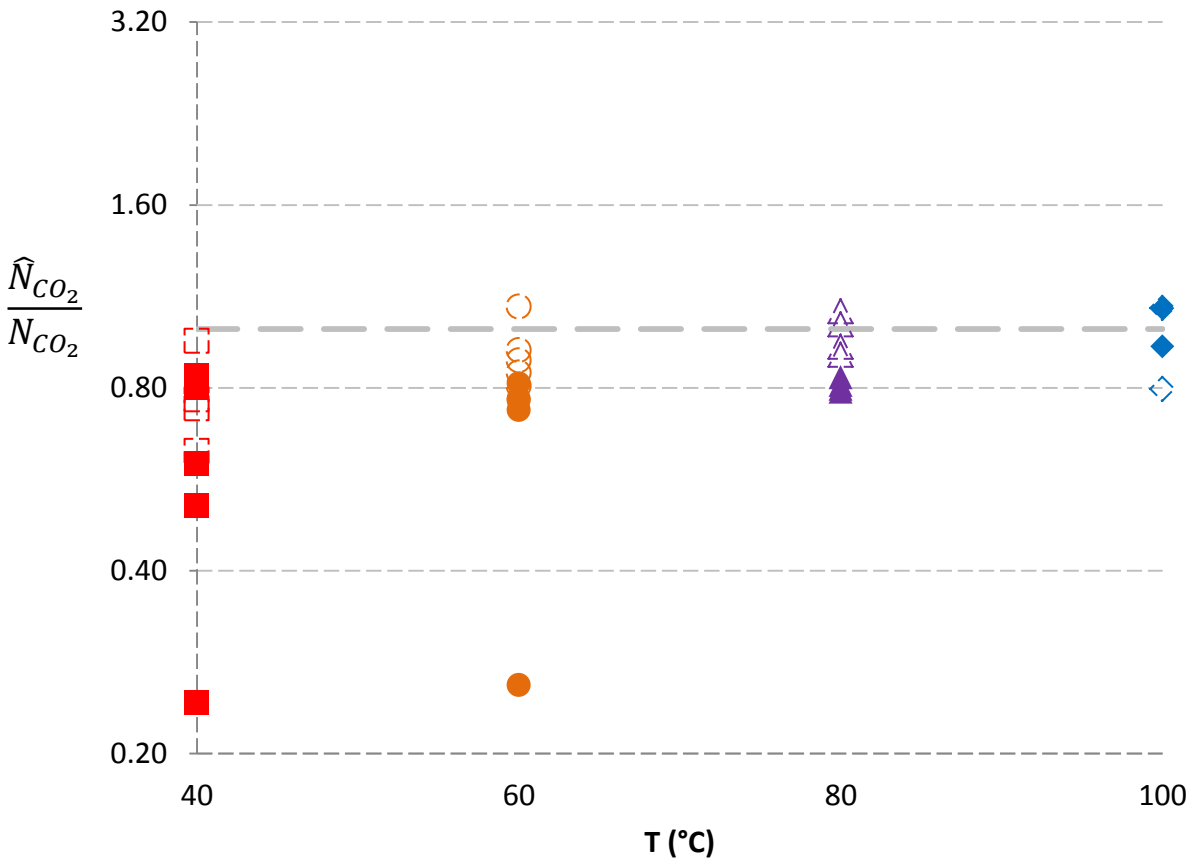

Figure 7. 4 m 2MPZ/4 m PZ kinetic fit less reactions 5 and 10. Data are from Chen (2011).

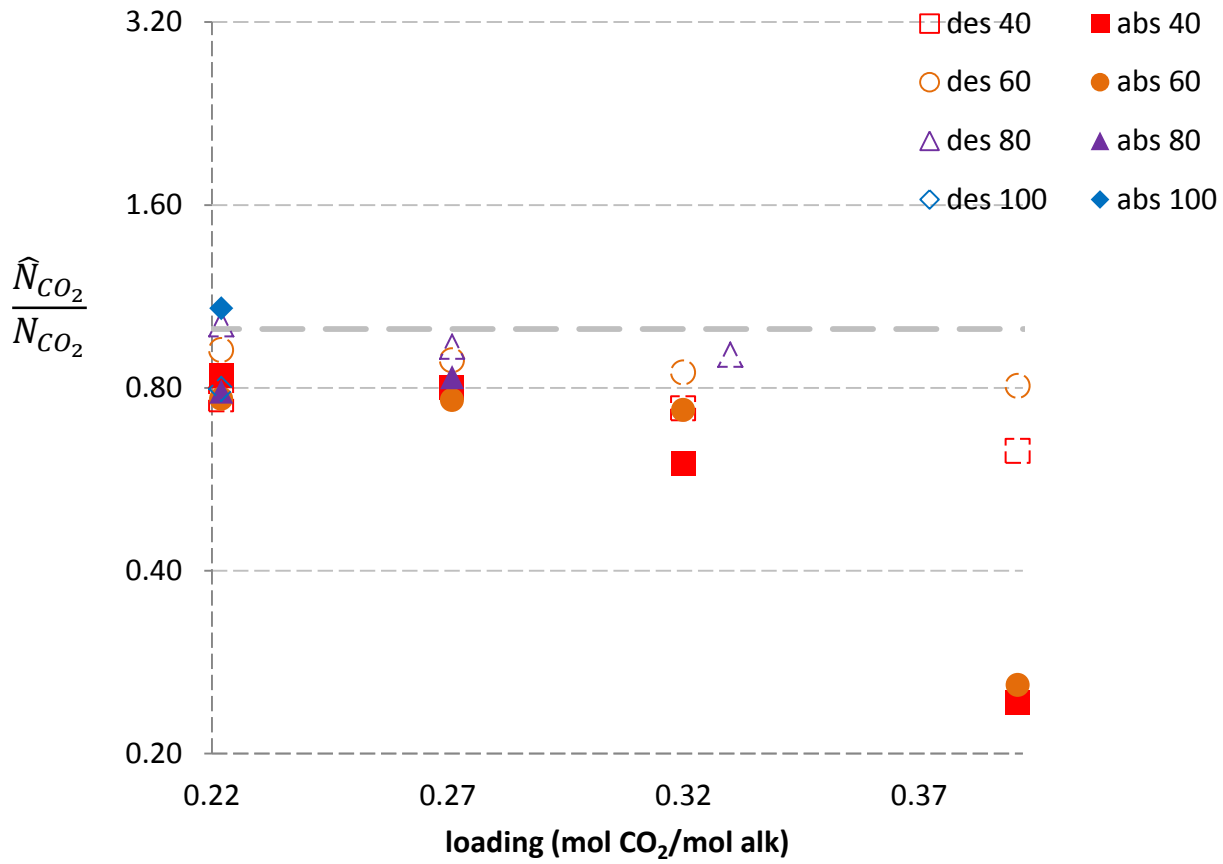

Figure 8. 4 m 2MPZ/4 m PZ kinetic fit less reactions 5 and 10. Data are from Chen (2011).

As expected, the model now tends to underpredict. There is a pronounced trend towards underprediction with increasing loading, and at 40 °C the model always underpredicts as compared with prior model results (Sherman, Frailie, Le, Salta, & Rochelle, 2014).

References

Chen, X. (2011). *Carbon Dioxide Thermodynamics, Kinetics, and Mass Transfer in Aqueous Piperazine Derivatives and Other Amines*. The University of Texas at Austin.

Sherman, B., Frailie, P. T., Le, L., Salta, N., & Rochelle, G. T. (2014). Thermodynamic and Kinetic Modeling of Piperazine/2-Methylpiperazine. *Energy Procedia, in press*.

3 CCSI Heat Exchanger Product Manual

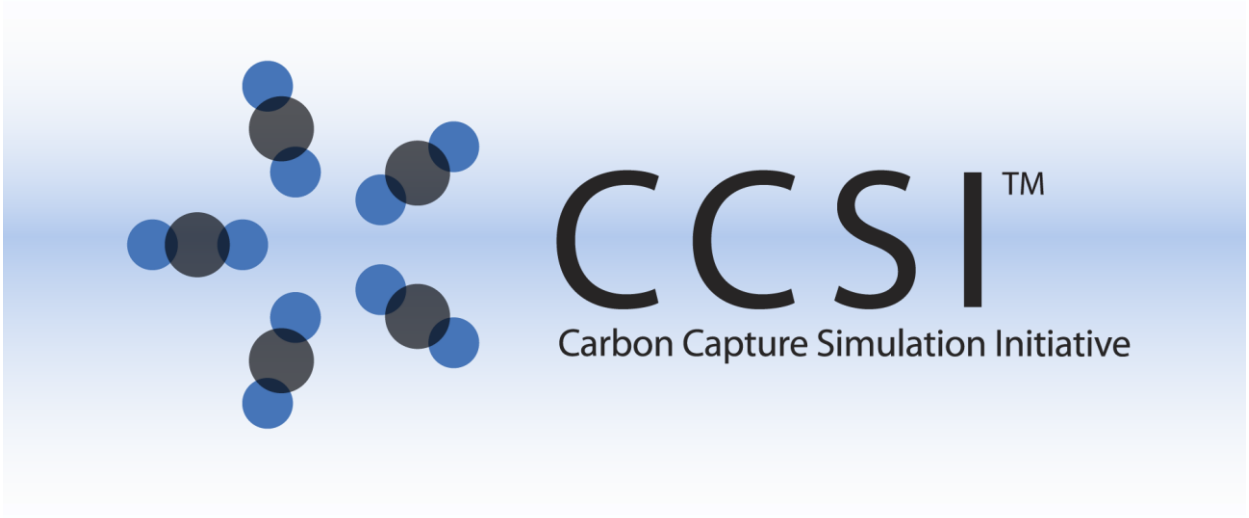

Heat Exchanger Model
User Manual

Version 2014.10.0

October 31, 2014

Revision Log

Version Number	Release Date	Description
Version 2014.10.0	10/31/2014	Initial release.

Table of Contents

List of Figures

List of Tables

To obtain support for this package, please send an email to
ccsi-support@acceleratecarboncapture.org.

1. Installation Requirements

This product requires Aspen Plus® V8.4 or newer. As such, the supported environments are limited to:

- Windows XP SP3
- Windows Vista Business SP2
- Windows Vista Ultimate SP2
- Windows 7 Ultimate (32 and 64 Bit)
- Windows 7 Professional (32 and 64 Bit)
- Windows 8

2. INTRODUCTION

The heat exchanger model can be used to optimize the size of the heat exchangers and their log-mean temperature difference (LMTD) to minimize capital and operating expenses. The model consists of HeatCalc.bkp. This manual was written using Aspen Plus® V8.4.

2.1. Features list

This product sizes a non-flashing plate and frame heat exchanger for amine scrubbing with aqueous piperazine. As this product consists of a calculator block and an optimization block, it does not interfere with convergence of the flowsheet. In addition to exchanger size, many other quantities of interest are reported, such as pressure drop, flow length, and velocity.

3. TUTORIAL

This tutorial assumes basic knowledge of Aspen Plus® software. Consult the Aspen Plus® documentation "Getting Started Building and Running a Process Model" for additional information.

The provided file is a template. This tutorial will explain how to cut and paste the necessary components into an existing process simulation, herein referred to as the destination file.

3.1. Setup: Property Sets

The heat exchanger calculator block depends on property sets. These need to be verified as present with the correct units.

1. Open HeatCalc.bkp.
2. In the Navigation Pane, navigate to **Analysis | EXPROP| Results**. The results should be like Table 1.
3. Confirm that the units match for the property sets by navigating to **Property Sets**, clicking each property set, and checking the value in the Units column.
4. Due to a bug, copying and pasting is overly involved. In the destination file, navigate to **Property Sets**. If there are no property sets, create one with any name.
5. Select a property set and click "Copy". This enables the "Paste" button.
6. In HeatCalc.bkp navigate to **Property Sets** and select all.

7. Click “Copy”.
8. Return to the destination file and click “Paste”.

Table 1. EXPROP Results

TEMP	MOLEFLOW MEA	MOLEFLOW CO2	LIQUID KMX	LIQUID CPMX	LIQUID MUMX	LIQUID RHOMX	VAPOR RHOMX	LIQUID SIGMAMX
K	kmol/sec	kmol/sec	Watt/m-K	J/kg-K	Pa-sec	kg/cum	kg/cum	N/m
313	7	3.15	5.54E-01	3.11E+03	1.57E-03	1.10E+03	4.96E-02	7.07E-02
313	7	3.85	6.02E-01	3.01E+03	1.62E-03	1.13E+03	2.98E-01	7.43E-02
323	7	3.15	5.61E-01	3.12E+03	1.29E-03	1.10E+03	8.30E-02	6.90E-02
323	7	3.85	6.07E-01	3.03E+03	1.33E-03	1.12E+03	5.45E-01	7.24E-02
333	7	3.15	5.66E-01	3.13E+03	1.09E-03	1.09E+03	1.36E-01	6.73E-02
333	7	3.85	6.09E-01	3.04E+03	1.12E-03	1.12E+03	9.70E-01	7.06E-02
343	7	3.15	5.69E-01	3.14E+03	9.27E-04	1.08E+03	2.23E-01	6.56E-02
343	7	3.85	6.07E-01	3.05E+03	9.59E-04	1.11E+03	1.69E+00	6.87E-02
353	7	3.15	5.71E-01	3.16E+03	8.02E-04	1.07E+03	3.64E-01	6.39E-02
353	7	3.85	5.99E-01	3.07E+03	8.30E-04	1.10E+03	2.85E+00	6.68E-02
363	7	3.15	5.71E-01	3.18E+03	7.04E-04	1.06E+03	6.02E-01	6.22E-02
363	7	3.85	5.84E-01	3.09E+03	7.27E-04	1.09E+03	4.67E+00	6.50E-02
373	7	3.15	5.68E-01	3.20E+03	6.24E-04	1.06E+03	1.01E+00	6.05E-02
373	7	3.85	5.63E-01	3.11E+03	6.43E-04	1.08E+03	7.41E+00	6.30E-02
383	7	3.15	5.62E-01	3.22E+03	5.60E-04	1.05E+03	1.72E+00	5.87E-02
383	7	3.85	5.36E-01	3.14E+03	5.73E-04	1.07E+03	1.13E+01	6.11E-02
393	7	3.15	5.50E-01	3.24E+03	5.06E-04	1.04E+03	2.95E+00	5.70E-02
393	7	3.85	5.04E-01	3.17E+03	5.14E-04	1.05E+03	1.67E+01	5.91E-02
403	7	3.15	5.33E-01	3.28E+03	4.60E-04	1.03E+03	5.04E+00	5.52E-02
403	7	3.85	4.69E-01	3.20E+03	4.63E-04	1.04E+03	2.37E+01	5.70E-02
413	7	3.15	5.08E-01	3.31E+03	4.20E-04	1.02E+03	8.41E+00	5.33E-02
413	7	3.85	4.34E-01	3.24E+03	4.18E-04	1.03E+03	3.23E+01	5.49E-02
423	7	3.15	4.75E-01	3.36E+03	3.85E-04	1.00E+03	1.35E+01	5.14E-02
423	7	3.85	3.99E-01	3.29E+03	3.79E-04	1.01E+03	4.27E+01	5.28E-02

Table 2. Property Sets

Name	Physical properties	Units	Qualifiers
CONDUC-L	KMX	Watt/m-K	Phase=Liquid
CPMX	CPMX	J/kg-K	Phase=Liquid
MDOT-V	MASSFLMX	kg/sec	Phase=Vapor
MU-L	MUMX	Pa-sec	Phase=Liquid
MU-V	MUMX	Pa-sec	Phase=Vapor
RHO-L	RHOMX	kg/cum	Phase=Liquid
RHO-V	RHOMX	kg/cum	Phase=Vapor
SURFT	SIGMAMX	N/m	Phase=Liquid

3.2. Setup: Flowsheet

Before moving the calculator blocks, the template streams must be renamed to the destination stream names.

1. Click the Main Flowsheet tab at the top to view the flowsheet of Figure 1.

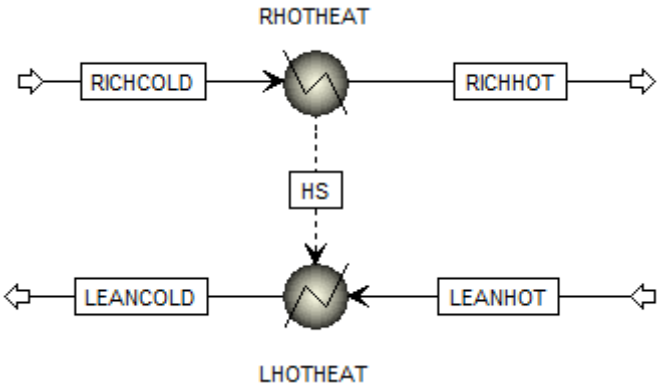

Figure 1. Linked heater blocks

1. Rename the heat and material streams to match the corresponding stream names of the destination flowsheet.
2. Navigate to **Flowsheeting Options | Calculator | C-HX | Results** and select the **Define Variable** tab. Verify that the results are close to those of Table 3. If they are not, check the property set units.

Table 3. C-HX results

Variable	Value written	Description	Units
EXCAP	4.38E-01	exchanger CAPEX	\$/tonne CO_2
RPUMPOP	6.83E-02	rich pump CAPEX	\$/tonne CO_2
RPUMPCAP	3.58E-02	rich pump OPEX	\$/tonne CO_2
TAC	5.42E-01	total annualized capital	\$/tonne CO_2
AREA	4.25E+03	exchanger area	m^2
LMTD	1.52E+01	log mean temperature difference	K
U	5.17E+03	overall heat transfer coefficient	W/K–m^2
DPRICH	9.43E+04	rich-side pressure drop	Pa
DPLEAN	9.17E+04	lean-side pressure drop	Pa
LPLATE	2.80E+00	plate length	m
VRICH	4.43E-01	rich-side fluid velocity	m/sec
VLEAN	4.72E-01	lean-side fluid velocity	m/sec

3.3. Setup: Calculator Blocks

Now that the property sets exist and the stream names agree, the calculator blocks can be imported.

1. Navigate to **Flowsheeting Options | Calculator** in the destination file.
2. If there are no calculator blocks, create one by clicking "New". Name it anything.
3. Select any calculator block and click "Copy". This enables the "Paste" button.
4. Return to HeatCalc.bkp, navigate to **Flowsheeting Options | Calculator**, and select C-HX. Click "Copy".
5. In the destination file click "Paste".

3.4. Setup: Optimization Block

This block functions similarly to Solver in Excel®. The provided optimization block minimizes the total annualized capital of the exchanger and the rich pump by varying the total width (NW) of the exchanger.

1. Navigate to **Model Analysis Tools | Optimization** in the destination file.
2. If there are no optimization blocks, create one by clicking "New". Name it anything.
3. Select any optimization block and click "Copy". This enables the "Paste" button.
4. Return to HeatCalc.bkp, navigate to **Model Analysis Tools | Optimization**, and select O-TAC. Click "Copy".
5. In the destination file click "Paste".

3.5. Running the Simulation

Aspen Plus® will sequence the calculator and optimization blocks after the flowsheet calculations, meaning the heat exchanger model has no impact on flowsheet convergence. Running the simulation is no different from running the simulation before adding in the heat exchanger model.

4. USAGE INFORMATION

4.1. Support

Support can be obtained from ccsi-support@acceleratecarboncapture.org or by filling out the "Submit Feedback/Request Support" form available on the product distribution page.

4.2. Restrictions

This model works with any non-flashing solvent in a plate and frame heat exchanger. Note that the heat transfer coefficient assumes turbulence and 45° herringbone plates. Additional restricting assumptions include

- a plate spacing of 2 mm
- a plate thickness of 6 mm
- plate material of 304 stainless steel
- assumptions on capital and electricity cost

4.3. Known Issues

- The exchanger and pump sizing is continuous, while in reality it is discrete.

5. DEBUGGING

- If the provided file does not yield similar results to those described here, then
  - check the property set units
  - check that the streams are properly named
  - use the four provided debugging outputs to troubleshoot

5.1. How to Debug

Always run the simulation with the control panel visible. The output will notify the user about potential problems and errors. For problems specific to C-HX, the four debugging output parameters (OUT1, OUT2, OUT3, and OUT4) can be used to check intermediate values.

5.2. Reporting Issues

To report an issue, please send an email to ccsi-support@acceleratecarboncapture.org.

6. MODEL HISTORY

6.1. Block Descriptions

C-HX

This block sizes and costs a non-flashing plate and frame heat exchanger.

Variables

The variables defined are listed in Table 4. As variable names are limited to seven characters, the following shorthand is used

- CR=cold, rich
- HR=hot, rich
- HL=hot, lean
- CL=cold, lean.

Table 4. C-HX Variable Definitions

Variable	Information flow	Definition
EXCAP	Export variable	Parameter Parameter no.=311
RPUMPOP	Export variable	Parameter Parameter no.=312
RPUMPCAP	Export variable	Parameter Parameter no.=313
TAC	Export variable	Parameter Parameter no.=315
AREA	Export variable	Parameter Parameter no.=310
LMTD	Export variable	Parameter Parameter no.=314
U	Export variable	Parameter Parameter no.=319
DPRICH	Export variable	Parameter Parameter no.=316
DPLEAN	Export variable	Parameter Parameter no.=317
LPLATE	Export variable	Parameter Parameter no.=318
VRICH	Export variable	Parameter Parameter no.=320
VLEAN	Export variable	Parameter Parameter no.=321

OUT1	Export variable	Parameter Parameter no.=300
OUT2	Export variable	Parameter Parameter no.=301
OUT3	Export variable	Parameter Parameter no.=303
OUT4	Export variable	Parameter Parameter no.=304
TCR	Import variable	Stream-Var Stream=RICHCOLD Substream=MIXED Variable=TEMP Units=K
THL	Import variable	Stream-Var Stream=LEANWRM Substream=MIXED Variable=TEMP Units=K
THR	Import variable	Stream-Var Stream=RICHWRM1 Substream=MIXED Variable=TEMP Units=K
TCL	Import variable	Stream-Var Stream=LEANCOLD Substream=MIXED Variable=TEMP Units=K
MCR	Import variable	Stream-Var Stream=RICHCOLD Substream=MIXED Variable=MASS-FLOW Units=kg/sec
MHL	Import variable	Stream-Var Stream=LEANWRM Substream=MIXED Variable=MASS-FLOW Units=kg/sec
MHR	Import variable	Stream-Var Stream=RICHWRM1 Substream=MIXED Variable=MASS-FLOW Units=kg/sec
MCL	Import variable	Stream-Var Stream=LEANCOLD Substream=MIXED Variable=MASS-FLOW Units=kg/sec
MUCR	Import variable	Stream-Prop Stream=RICHCOLD Prop-Set=MU-L Units=Pa-sec
MUHL	Import variable	Stream-Prop Stream=LEANWRM Prop-Set=MU-L Units=Pa-sec
MUHR	Import variable	Stream-Prop Stream=RICHWRM1 Prop-Set=MU-L Units=Pa-sec
MUCL	Import variable	Stream-Prop Stream=LEANCOLD Prop-Set=MU-L Units=Pa-sec
RHOCR	Import variable	Stream-Prop Stream=RICHCOLD Prop-Set=RHO-L Units=kg/cum
RHOHL	Import variable	Stream-Prop Stream=LEANWRM Prop-Set=RHO-L Units=kg/cum
RHOHR	Import variable	Stream-Prop Stream=RICHWRM1 Prop-Set=RHO-L Units=kg/cum
RHOCL	Import variable	Stream-Prop Stream=LEANCOLD Prop-Set=RHO-L Units=kg/cum
CPCR	Import variable	Stream-Prop Stream=RICHCOLD Prop-Set=CPMX Units=J/kg-K
CPHL	Import variable	Stream-Prop Stream=LEANWRM Prop-Set=CPMX Units=J/kg-K
CPHR	Import variable	Stream-Prop Stream=RICHWRM1 Prop-Set=CPMX Units=J/kg-K
CPCL	Import variable	Stream-Prop Stream=LEANCOLD Prop-Set=CPMX Units=J/kg-K
KCR	Import variable	Stream-Prop Stream=RICHCOLD Prop-Set=CONDUC-L Units=Watt/m-K

KHL	Import variable	Stream-Prop Stream=LEANWRM Prop-Set=CONDUC-L Units=Watt/m-K
KHR	Import variable	Stream-Prop Stream=RICHWRM1 Prop-Set=CONDUC-L Units=Watt/m-K
KCL	Import variable	Stream-Prop Stream=LEANCOLD Prop-Set=CONDUC-L Units=Watt/m-K
DUTY	Import variable	Heat-Duty Stream=WRMHS Units=Watt
CO2RM	Import variable	Mole-Flow Stream=PRODUCT1 Substream=MIXED Component=CO2 Units=kmol/sec
NW	Import variable	Parameter Parameter no.=366 Initial value=1962.13

All of the variables defined in the "Define" tab of the calculator block input are included in Table 5 in addition to all the variables defined in the "Calculate" tab.

Table 5. C-HX Variable Description

Variable	I/O	Description	Units
EXCAP	O	annualized exchanger CAPEX	\$/tonne CO_2
AREA	O	exchanger area	m^2
RPUMPOP	O	annualized rich pump OPEX	\$/tonne CO_2
RPUMPCAP	O	annualized rich pump CAPEX	\$/tonne CO_2
TAC	O	total annualized capital cost of exchanger and rich pump	\$/tonne CO_2
LMTD	O	LMTD of warm exchanger	K
U	O	overall heat transfer coefficient	W/K-m^2
DPRICH	O	pressure drop of rich stream	Pa
DPLEAN	O	pressure drop of lean stream	Pa
LPLATE	O	plate length	m
VRICH	O	velocity of rich stream	m/sec
VLEAN	O	velocity of lean stream	m/sec
OUT1	O	debugging output	arbitrary
OUT2	O	debugging output	arbitrary
OUT3	O	debugging output	arbitrary
OUT4	O	debugging output	arbitrary
TCR	I	temperature of CR	K
THL	I	temperature of HL	K
THR	I	temperature of HR	K
TCL	I	temperature of CL	K
MCR	I	mass flow of CR	kg/sec
MHL	I	mass flow of HL	kg/sec
MHR	I	mass flow of HR	kg/sec
MCL	I	mass flow of CL	kg/sec
MUCR	I	liquid viscosity of CR	Pa–sec
MUHL	I	liquid viscosity of HL	Pa–sec

MUHR	I	liquid viscosity of HR	Pa-sec
MUCL	I	liquid viscosity of CL	Pa-sec
RHOCR	I	liquid density of CR	kg/m^3
RHOHL	I	liquid density of HL	kg/m^3
RHOHR	I	liquid density of HR	kg/m^3
RHOCL	I	liquid density of CL	kg/m^3
CPCR	I	liquid heat capacity of CR	J/kg–K
CPHL	I	liquid heat capacity of HL	J/kg–K
CPHR	I	liquid heat capacity of HR	J/kg–K
CPCL	I	liquid heat capacity of CL	J/kg–K
KCR	I	liquid thermal conductivity of CR	W/m–K
KHL	I	liquid thermal conductivity of HL	W/m–K
KHR	I	liquid thermal conductivity of HR	W/m–K
KCL	I	liquid thermal conductivity of CL	W/m–K
DUTY	I	heat duty	W
CO2RM	I	mole flow of CO_2 in stripper overhead	kmol/sec
VCLW	O	volumetric flowrate of CL	m^3/sec
NW	I	total exchanger width	m
PLATESPACE	I	plate spacing	m
GRICH	O	mass flux of rich stream	kg/m^2–sec
GLEAN	O	mass flux of lean stream	kg/m^2–sec
VELCR	O	velocity of CR	m/sec
VELCL	O	velocity of CL	m/sec
VELHR	O	velocity of HR	m/sec
VELHL	O	velocity of HL	m/sec
DIAM	I	equivalent diameter	m
RECR	O	Reynolds number of CR	—
RECL	O	Reynolds number of CL	—
REHR	O	Reynolds number of HR	—
REHL	O	Reynolds number of HL	—
PRCR	O	Prandtl number of CR	—
PRCL	O	Prandtl number of CL	—
PRHR	O	Prandtl number of HR	—
PRHL	O	Prandtl number of HL	—
HCR	O	heat transfer coefficient of CR	W/m^2–K
HCL	O	heat transfer coefficient of CL	W/m^2–K
HHR	O	heat transfer coefficient of HR	W/m^2–K
HHL	O	heat transfer coefficient of HL	W/m^2–K
KPLATE	I	plate thermal conductivity	W/m^2–K
PLATETHICK	I	plate thickness	m
HPLATE	O	plate heat transfer coefficient	W/m^2–K
UCOLD	O	cold side overall heat transfer coefficient	W/m^2–K

UHOT	O	hot side overall heat transfer coefficient	$W/m^2–K$
DELTC	O	cold side temperature approach	K
DELTH	O	cold side temperature approach	K
FCR	O	Fanning friction factor of CR	—
FCL	O	Fanning friction factor of CL	—
FHR	O	Fanning friction factor of HR	—
FHL	O	Fanning friction factor of HL	—
DPCR	O	pressure drop per length of CR	Pa/m
DPCL	O	pressure drop per length of CL	Pa/m
DPHR	O	pressure drop per length of HR	Pa/m
DPHL	O	pressure drop per length of HL	Pa/m
ACOST	I	CAPEX of exchanger area	$\$/m^2$
ECOST	I	cost of electricity	$/MWh
ALPHA	I	converts PEC to total capital requirement	—
BETA	I	Lang factor (annualizes cost)	—
CFACTOR	I	capacity factor	—
PETA	I	pump efficiency	—
PCOST	I	pump CAPEX	$/W
CO2RMA	O	CO_2 removed per annum	tonne/annum
VCR	O	volumetric flowrate of CR	m^3/sec

Fortran Code

The first part of the code calculates and maps all necessary properties for the model calculations. The next part calculates the exchanger size. The last part calculates the economics and formats miscellaneous outputs.

If a comment line ends with a number in parentheses, eg (1), then there is a comment in this documentation. The comment shows the equation in a more readable format, explains all variables, and elucidates the equation origin.

```
C Brent Sherman
C 2014-11-17
C PURPOSE: Size a non-flashing plate and frame heat exchanger
C                    and cost it and the rich pump.
C Numbers in parentheses refer to comments in documentation.

C --- Calculations begin ---
C Set plate spacing (m).
      PSPACE=0.002
C Calculate mass flux (kg/sec-m2). (1)
      GRICH=MCR/(PSPACE*NW)
      GLEAN=MHL/(PSPACE*NW)
```

```
C Calculate stream velocity (m/sec). (2)
      VELCR=GRICH/(RHOCR)
      VELCL=GLEAN/(RHOCL)
      VELHR=GRICH/(RHOHR)
      VELHL=GLEAN/(RHOHL)
C Output velocities of rich and lean sides.
      VRICH=VELCR
      VLEAN=VELHR
C Calculate the Reynolds number. (3)
      DIAM=2*PSPACE
      RECR=GRICH*DIAM/MUCR
      RECL=GLEAN*DIAM/MUCL
      REHR=GRICH*DIAM/MUHR
      REHL=GLEAN*DIAM/MUHL

C Calculate the Prandtl number. (4)
      PRCR=(CPCR*MUCR)/KCR
      PRCL=(CPCL*MUCL)/KCL
      PRHR=(CPHR*MUHR)/KHR
      PRHL=(CPHL*MUHL)/KHL
C Calculate the heat transfer coefficient (W/m2-K). (5)
C h=Nu*ki/D
      HCR=(0.3*KCR/DIAM)*(PRCR**0.333)*(RECR**0.663)
      HCL=(0.3*KCL/DIAM)*(PRCL**0.333)*(RECL**0.663)
      HHR=(0.3*KHR/DIAM)*(PRHR**0.333)*(REHR**0.663)
      HHL=(0.3*KHL/DIAM)*(PRHL**0.333)*(REHL**0.663)
C Set wall thermal conductivity (W/m-K)
      KPLATE=16
C Set Plate thickness in m.
      PTHK=0.0006
C Calculate the plate heat transfer coefficient (W/m2-K).
      HPLATE=KPLATE/PTHK
C Calculate the overall heat transfer coefficients (W/m2-K). (6)
      UCOLD=(1/HCR)+(1/HCL)+(1/HPLATE)
      UCOLD=1/UCOLD
      UHOT=(1/HHR)+(1/HHL)+(1/HPLATE)
      UHOT=1/UHOT
C Calculate the temperature approaches (K).
      DELTC=TCL-TCR
      DELTH=THL-THR
C Calculate the area (m2). (7)
      AREA=-DUTY/((UHOT*DELTC-UCOLD*DELTH)
     .           /DLOG((UHOT*DELTC)/(UCOLD*DELTH)))

C LMTD (K)
      LMTD=(DELTC-DELTH)/DLOG(DELTC/DELTH)
C Overall heat transfer coefficient (W/K-m2) (8)
```

```
      U=-DUTY/(AREA*LMTD)

C --- Economic Calculations Begin ---
C Calculate plate length (m).
      LPLATE=AREA/NW
C Calculate Fanning friction factor for turbulent flow. (9)
      FCR=1.441*RECR**-0.206
      FCL=1.441*RECL**-0.206
      FHR=1.441*REHR**-0.206
      FHL=1.441*REHL**-0.206
C Calculate the pressure drop per length (Pa/m). (10)
      DPCR=(2*FCR*GRICH**2)/(RHOCR*DIAM)
      DPCL=(2*FCL*GLEAN**2)/(RHOCL*DIAM)
      DPHR=(2*FHR*GRICH**2)/(RHOHR*DIAM)
      DPHL=(2*FHL*GLEAN**2)/(RHOHL*DIAM)
C Calculate the rich-, and lean-side pressure drop (Pa). (11)
      DPRICH=((DPCR+DPHR)/2)*LPLATE
      DPLEAN=((DPCL+DPHL)/2)*LPLATE
C Economic parameters.
      ACOST=231.61
      ECOST=100
      ALPHA=5
      BETA=0.2
      CFACTOR=0.90
      PETA=0.65
      PCOST=0.4135

C Exchanger CAPEX ($/tonne CO2)
C Convert CO2 removed from kmol/sec to tonne/sec. (12)
      CO2RMA=CO2RM*44/1D3
      EXCAP=(AREA*ACOST*ALPHA*BETA)
     .                /(CO2RMA*3600*24*365*CFACTOR)

C Calcupalte pump CAPEX ($/tonne CO2). (13)
      VCR=MCR/RHOCR
      RPUMPCAP=(DPRICH*VCR/PETA)
     .         *PCOST*ALPHA*BETA
     .          /(CO2RMA*3600*24*365*CFACTOR)

C Calculate pump OPEX ($/tonne CO2). (14)
      RPUMPOP=(DPRICH*VCR/PETA)
     .                      *ECOST/(3600*1D6)/CO2RMA

C Calculate Total annualized capital ($/tonne CO2). (15)
      TAC=EXCAP+RPUMPOP+RPUMPCAP

C Debugging outputs (16)
```

```
OUT1= FCR
OUT2= DPCR
OUT3= DPHR
OUT4= LPLATE
```

Code Comments

1. The mass flux is calculated using Equation 1,

$$G = \frac{\dot{m}}{\delta \times nW} \tag{1}$$

where G is mass flux (kg/m^2–sec), $\dot{m}$ is mass flow rate (kg/sec), δ is plate spacing (m), n is number of plates, and W is plate width (m).

2. The velocity is calculated from the mass flux using Equation 2,

$$v = \frac{G}{\rho} \tag{2}$$

where v is velocity (m/sec) and ρ is liquid density (kg/m^3).

3. The Reynolds number Re is calculated using Equation 3,

$$Re = \frac{G}{\mu D} \tag{3}$$

where μ is the liquid viscosity (Pa−sec), and D is the equivalent diameter (m), which is twice the plate spacing.

4. The Prandtl number Pr is calculated in Equation 4,

$$Pr = \frac{C_p \mu}{k} \tag{4}$$

where C_p is the liquid heat capacity (J/kg−K), and k is the liquid thermal conductivity (W/m−K).

5. The heat transfer coefficient h (W/m^2−K) is calculated using Equation 5,

$$h = \frac{Nu * k}{D} = 0.3 \frac{k}{D} Pr^{0.333} Re^{0.663} \tag{5}$$

where Nu is the Nusselt number. This assumes herringbone plates with 45° corrugation angle (Ayub, 2003).

6. The overall heat transfer coefficient U_i of the hot or cold side (W/m^2–K) is calculated using Equation 6,

$$\frac{1}{U_i} = \frac{1}{h_1} + \frac{1}{h_2} + \frac{1}{h_{plate}} \tag{6}$$

where h_1 is the heat transfer coefficient of the rich stream (W/m^2–K), h_2 is the heat transfer coefficient of the lean stream (W/m^2–K), and h_{plate} is the heat transfer coefficient of the plate (W/m^2–K) equal to the plate thermal conductivity divided by plate thickness.

7. The exchanger area A (m^2) is calculated using Equation 7,

$$A = \frac{Q}{\frac{U_{hot}\Delta T_{cold} - U_{cold}\Delta T_{hot}}{\ln\left(\frac{U_{hot}\Delta T_{cold}}{U_{cold}\Delta T_{hot}}\right)}} \quad (7)$$

where Q is the duty (W), U_{hot} (U_{cold}) is the overall heat transfer coefficient of the hot (cold) side (W/m^2–K), and ΔT_{hot} (ΔT_{cold}) is the hot- (cold-) side temperature approach (K).

8. The overall heat transfer coefficient U (W/m^2–K) is calculated using Equation 8.

$$U = \frac{Q}{A\Delta T_{LMTD}} \quad (8)$$

9. The Fanning friction factor f_f is calculated using Equation 9.

$$f_f = 1.441Re^{-0.206} \quad (9)$$

10. The pressure drop per length $\Delta P/L$ (Pa/m) is calculated using Equation 10,

$$\frac{\Delta P}{L} = \frac{2f_f G^2}{\rho D} \quad (10)$$

where L is the length (m). This is calculated for each stream.

11. The pressure drop of the rich and lean sides ΔP (Pa) is calculated using Equation 11.

$$\Delta P_{rich} = \frac{\left(\frac{\Delta P}{L}\right)_{CR} + \left(\frac{\Delta P}{L}\right)_{HR}}{2} \times L \quad (11)$$

The equivalent equation is used for the lean side pressure drop.

12. The exchanger CAPEX *EXCAP* ($/tonne CO$_2$) is calculated using Equation 12,

$$EXCAP = \frac{A \times \$A \times \alpha\beta}{\dot{m}_{CO_2} \times 3600 \times 24 \times 365 \times C} \quad (12)$$

where *$A* is the cost per unit area ($/m^2), α is the conversion of PEC to total capital requirement, β is the Lang factor, $\dot{m}_{CO_2}$ is the mass flowrate of CO$_2$ leaving the stripper overhead (tonne/sec), and C is the capacity factor, which accounts for 10% plant downtime. The purchased equipment cost (PEC) came from vendor quotes. It is assumed to vary linearly with area.

13. The rich pump CAPEX *RPUMPCAP* ($/tonne CO$_2$) is calculated using Equation 13,

$$RPUMPCAP = \frac{\left(\frac{\Delta P_{rich} \times Q_{CR}}{\eta}\right) \times \$P \times \alpha\beta}{\dot{m}_{CO_2} \times 3600 \times 24 \times 365 \times C} \quad (13)$$

where Q_{CR} is the volumetric flowrate of the cold, rich stream (m^3/sec, η is the pump efficiency, and *$P* is the cost of the pump ($/W).

14. The rich pump operating cost RPUMPOP ($/tonne CO$_2$) is calculated using Equation 14,

$$RPUMPOP = \frac{\left(\frac{\Delta P_{rich} \times Q_{CR}}{\eta}\right) \times COE}{\dot{m}_{CO_2} \times 3600 \times 10^5} \quad (14)$$

where *COE* is the cost of electricity ($/MWh).

15. The total annualized capital *TAC* ($/tonne CO$_2$) is calculated using Equation 15,

$$TAC = EXCAP + RPUMPOP + RPUMPCAP \quad (15)$$

16. The following four outputs were used for debugging. They are available for displaying intermediate values. Change the variable on the right side of the equal sign to the variable or expression to display.

7. REFERENCES

Ayub, Z. H. Plate Heat Exchanger Literature Survey and New Heat Transfer and Pressure Drop Correlations for Refrigerant Evaporators. *Heat Transf Eng* **2003**, *24*, 3–16.

4 TxCMP Heat Exchanger Product Manual

Heat Exchanger Model
User Manual

Version 2014.10.0

November 11, 2014

Table of Contents

List of Figures

List of Tables

1. Installation Requirements

This product requires Aspen Plus® V8.4 or newer. As such, the supported environments are limited to:

- Windows XP SP3
- Windows Vista Business SP2
- Windows Vista Ultimate SP2
- Windows 7 Ultimate (32 and 64 Bit)
- Windows 7 Professional (32 and 64 Bit)
- Windows 8

2. INTRODUCTION

The heat exchanger model can be used to optimize the size of the heat exchangers and their log-mean temperature difference (LMTD) to minimize capital and operating expenses. The model consists of HeatCalc.bkp. This manual was written using Aspen Plus® V8.4.

2.1.Features list

This product sizes and costs plate and frame heat exchangers for amine scrubbing with aqueous piperazine. It can handle both flashing (two-phase) and non-flashing (single phase) exchangers. As this product consists of a calculator block and an optimization block, it does not interfere with convergence of the flowsheet. In addition to exchanger CAPEX and OPEX, the economics of the pumps are also calculated. Many other quantities of interest are reported, such as exchanger size, pressure drop, flow length, velocity, etc.

3. TUTORIAL

This tutorial assumes basic knowledge of Aspen Plus® software. Consult the Aspen Plus® documentation "Getting Started Building and Running a Process Model" for additional information.

The provided file is to be used as a template. The following tutorial will explain how to cut and paste the necessary components into an existing process simulation.

3.1.Setup: Property Sets

The heat exchanger calculator blocks depends on property sets. These need to be verified.

1. Open AFS HeatCalc V2.bkp.
2. In the Navigation Pane, navigate to **Analysis | EXPROP | Results**. The results should be like Table 1.
3. Confirm that the units match for the property sets by navigating to **Property Sets**, clicking each property set listed in Table 2, and checking the value in the Units column.
4. Due to a bug, copying and pasting is overly involved. In the destination file, navigate to **Property Sets**. If there are no property sets, create one with any name.
5. Select a property set and click "Copy". This enables the "Paste" button.

6. In AFS HeatCalc V2.bkp navigate to **Property Sets** and select all.
7. Click “Copy”.
8. Return to the destination file and click “Paste”.

Table 1. EXPROP results

TEMP	MOLEFLOW	MOLEFLOW	LIQUID	LIQUID	LIQUID	LIQUID	VAPOR	LIQUID
	PZ	CO2	KMX	CPMX	MUMX	RHOMX	RHOMX	SIGMAMX
K	kmol/sec	kmol/sec	Watt/m-K	J/kg-K	Pa-sec	kg/cum	kg/cum	N/m
313	8	4.8	2.36E-01	3.23E+03	9.86E-03	1.12E+03	4.90E-02	7.07E-02
313	8	6.4	1.77E-01	3.16E+03	1.11E-02	1.15E+03	1.29E-01	6.81E-02
323	8	4.8	2.25E-01	3.27E+03	7.42E-03	1.12E+03	8.46E-02	6.87E-02
323	8	6.4	1.71E-01	3.20E+03	8.30E-03	1.14E+03	2.43E-01	6.62E-02
333	8	4.8	2.14E-01	3.32E+03	5.72E-03	1.11E+03	1.43E-01	6.68E-02
333	8	6.4	1.65E-01	3.24E+03	6.34E-03	1.14E+03	4.45E-01	6.44E-02
343	8	4.8	2.05E-01	3.35E+03	4.51E-03	1.10E+03	2.39E-01	6.48E-02
343	8	6.4	1.59E-01	3.29E+03	4.95E-03	1.13E+03	7.93E-01	6.26E-02
353	8	4.8	1.96E-01	3.40E+03	3.62E-03	1.10E+03	3.91E-01	6.29E-02
353	8	6.4	1.54E-01	3.33E+03	3.94E-03	1.13E+03	1.38E+00	6.08E-02
363	8	4.8	1.87E-01	3.45E+03	2.95E-03	1.09E+03	6.32E-01	6.10E-02
363	8	6.4	1.48E-01	3.38E+03	3.18E-03	1.12E+03	2.33E+00	5.90E-02
373	8	4.8	1.79E-01	3.50E+03	2.44E-03	1.08E+03	1.00E+00	5.91E-02
373	8	6.4	1.42E-01	3.43E+03	2.61E-03	1.11E+03	3.82E+00	5.73E-02
383	8	4.8	1.71E-01	3.54E+03	2.04E-03	1.07E+03	1.57E+00	5.72E-02
383	8	6.4	1.37E-01	3.47E+03	2.18E-03	1.11E+03	6.11E+00	5.55E-02
393	8	4.8	1.63E-01	3.59E+03	1.73E-03	1.07E+03	2.41E+00	5.52E-02
393	8	6.4	1.31E-01	3.53E+03	1.83E-03	1.10E+03	9.52E+00	5.37E-02
403	8	4.8	1.55E-01	3.65E+03	1.48E-03	1.06E+03	3.64E+00	5.33E-02
403	8	6.4	1.26E-01	3.58E+03	1.56E-03	1.09E+03	1.45E+01	5.19E-02
413	8	4.8	1.48E-01	3.70E+03	1.28E-03	1.05E+03	5.40E+00	5.13E-02
413	8	6.4	1.20E-01	3.64E+03	1.34E-03	1.08E+03	2.14E+01	5.00E-02
423	8	4.8	1.40E-01	3.76E+03	1.12E-03	1.04E+03	7.88E+00	4.93E-02
423	8	6.4	1.15E-01	3.70E+03	1.17E-03	1.07E+03	3.10E+01	4.81E-02

Table 2. Property Sets

Name	Physical properties	Units	Qualifiers
CONDUC-L	KMX	Watt/m-K	Phase=Liquid
CPMX	CPMX	J/kg-K	Phase=Liquid
MDOT-V	MASSFLMX	kg/sec	Phase=Vapor
MU-L	MUMX	Pa-sec	Phase=Liquid
MU-V	MUMX	Pa-sec	Phase=Vapor
RHO-L	RHOMX	kg/cum	Phase=Liquid
RHO-V	RHOMX	kg/cum	Phase=Vapor
SURFT	SIGMAMX	N/m	Phase=Liquid

3.2.Setup: Flowsheet

Before moving the calculator blocks, the streams must be renamed.

1. Click the Main Flowsheet tab at the top to view the flowsheet of Figure 1. (If the tab is not visible, navigate to Simulation in the Navigation pane.)

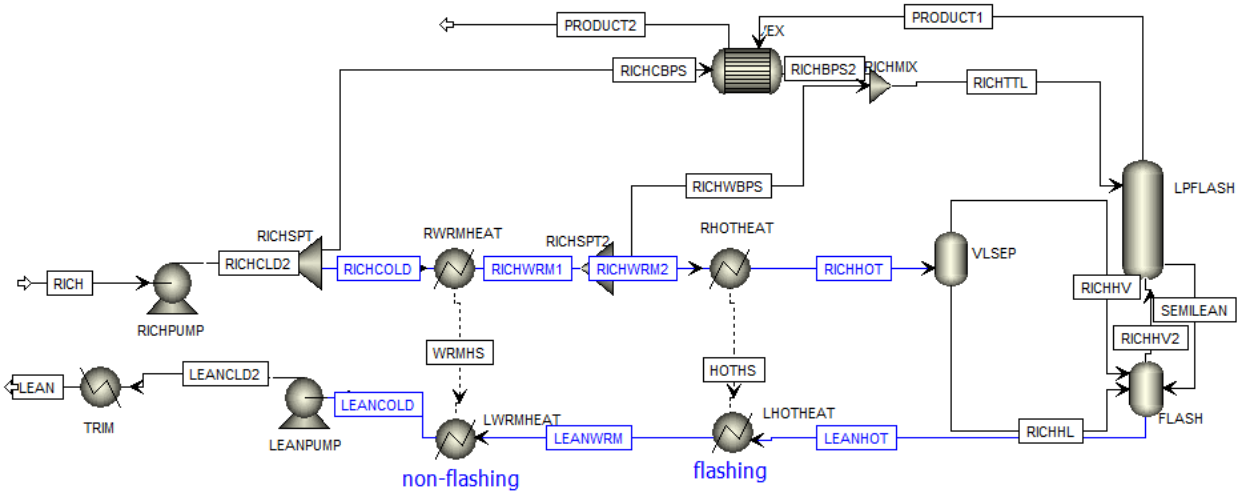

Figure 1. Advanced Flash Stripper flowsheet

1. Rename the blue streams to match the corresponding stream names of the destination flowsheet.
2. Navigate to **Flowsheeting Options | Calculator | C-HXWARM | Results** and select the **Define Variable** tab. Verify that the top results are close to those of Table 3. If they are not, check the property set units.

Table 3. C-HXWARM results

Variable	Value written	Description	Units
EXCAP	3.62	exchanger CAPEX	$/tonne CO_2
RPUMPOP	0.297	rich pump CAPEX	$/tonne CO_2
RPUMPCAP	0.156	rich pump OPEX	$/tonne CO_2
TAC	4.075	total annualized capital	$/tonne CO_2
AREA	3.51E+4	exchanger area	m^2
WRMLMTD	4.95	log mean temperature difference	K
U	2.10E+3	overall heat transfer coefficient	W/K–m^2
DPRICH	4.11E+5	rich-side pressure drop	Pa
DPLEAN	4.35E5	lean-side pressure drop	Pa
LPLATE	17.8	plate length	m
VRICH	0.339	rich-side fluid velocity	m/sec
VLEAN	0.352	lean-side fluid velocity	m/sec

3. Navigate to **Flowsheeting Options | Calculator | C-HXHOT | Results** and select the **Define Variable** tab. Verify that the top results are close to those of Table 4.

Table 4. C-HXHOT results

Variable	Value written	Description	Units
EXCAP	1.69	exchanger CAPEX	\$/tonne CO_2
RPUMPOP	0.192	rich pump CAPEX	\$/tonne CO_2
RPUMPCAP	0.101	rich pump OPEX	\$/tonne CO_2
TAC	6.61	total annualized capital	\$/tonne CO_2
AREA	1.64E+4	exchanger area	m^2
WRMLMTD	4.95	log mean temperature difference	K
HOTLMTD	5.04	overall heat transfer coefficient	K
TOTLMTD	4.98	rich-side pressure drop	K
U	2.40E+3	lean-side pressure drop	$W/K–m^2$
DPRICH	4.20E+5	plate length	Pa
DPLEAN	1.05E+5	rich-side fluid velocity	Pa
LPLATE	6.86	lean-side fluid velocity	m
VRICH	0.177		m/sec
VLEAN	0.187	exchanger CAPEX	m/sec
LPUMPCAP	0.195	lean pump CAPEX	\$/tonne CO_2
LPUMPOP	0.359	lean pump OPEX	\$/tonne CO_2

3.3. Setup: Calculator Blocks

Now that the property sets exist and the stream names agree, the calculator blocks can be imported.

1. Navigate to **Flowsheeting Options | Calculator** in the destination file.
2. If there are no calculator blocks, create one by clicking “New”. Name it anything.
3. Select any calculator block and click “Copy”. This enables the “Paste” button.
4. Return to AFS HeatCalc V2.bkp, navigate to **Flowsheeting Options | Calculator**, and select C-HXWARM and C-HXHOT. Click “Copy”.
5. In the destination file click “Paste”.

3.4.Setup: Optimization Block

This block functions similarly to the solver in Excel®. The provided optimization block minimizes the total annualized capital by varying the total width (NW) of the two exchangers.

1. Navigate to **Model Analysis Tools | Optimization** in the destination file.
2. If there are no optimization blocks, create one by clicking “New”. Name it anything.
3. Select any optimization block and click “Copy”. This enables the “Paste” button.
4. Return to AFS HeatCalc V2.bkp, navigate to **Model Analysis Tools | Optimization**, and select O-TAC. Click “Copy”.
5. In the destination file click “Paste”.

3.5. Running the Simulation

Aspen Plus® will sequence the calculator and optimization blocks after the flowsheet calculations, meaning the heat exchanger model has no impact on flowsheet convergence.

Running the simulation is no different from running the simulation before adding in the heat exchanger model.

4. USAGE INFORMATION

4.1.Restrictions

- The model is for 5 m PZ. There are a couple of solvent specific equations. If a different solvent is used, those equations must be redone.
- The heat transfer coefficient assumes turbulence and 45° herringbone plates.
- Additional assumptions include
  - a plate spacing of 2 mm
  - a plate thickness of 6 mm
  - plate material of 304 stainless steel
  - assumptions on capital and electricity cost

4.2. Known Issues

- The exchanger and pump sizing is continuous, while in reality it is discrete.

4.3.Next Steps

The next version will be only one block, such that non-flashing is a special case of a general model. It will also generalize for more solvents and concentrations.

5. DEBUGGING

- If the provided file does not yield similar results to those described here, then
  - check the property set units
  - check that the streams are properly named
  - use the four provided debugging outputs to troubleshoot

5.1.How to Debug

Always run the simulation with the control panel visible. The output will notify the user about potential problems and errors. For problems specific to C-HXWARM or C-HXHOT, the four debugging output parameters (OUT1, OUT2, OUT3, and OUT4) can be used to check intermediate values.

5.2.Known Issues

- The exchanger and pump sizing is continuous, while in reality it is discrete.

6. MODEL HISTORY

This work started as an attempt to simply move Yu-Jeng Lin’s offline spreadsheet caclulations online (Rochelle et al., 2014).

6.1. Block Descriptions

C-HXWARM

This block sizes and costs a non-flashing plate and frame heat exchanger.

Variables

The variables defined are listed in Table 5. As variable names are limited to seven characters, the following shorthand is used

- CR=cold, rich
- HR=hot, rich
- HL=hot, lean
- CL=cold, lean

Table 5. C-HXWARM Variable Definitions

Variable	Information flow	Definition
EXCAP	Export variable	Parameter Parameter no.=311
RPUMPOP	Export variable	Parameter Parameter no.=312
RPUMPCAP	Export variable	Parameter Parameter no.=313
TAC	Export variable	Parameter Parameter no.=315
AREA	Export variable	Parameter Parameter no.=310
WRMLMTD	Export variable	Parameter Parameter no.=314
U	Export variable	Parameter Parameter no.=319
DPRICH	Export variable	Parameter Parameter no.=316
DPLEAN	Export variable	Parameter Parameter no.=317
LPLATE	Export variable	Parameter Parameter no.=318
VRICH	Export variable	Parameter Parameter no.=320
VLEAN	Export variable	Parameter Parameter no.=321
OUT1	Export variable	Parameter Parameter no.=300
OUT2	Export variable	Parameter Parameter no.=301
OUT3	Export variable	Parameter Parameter no.=303
OUT4	Export variable	Parameter Parameter no.=304
TCR	Import variable	Stream-Var Stream=RICHCOLD Substream=MIXED Variable=TEMP Units=K
THL	Import variable	Stream-Var Stream=LEANWRM Substream=MIXED Variable=TEMP Units=K
THR	Import variable	Stream-Var Stream=RICHWRM1 Substream=MIXED Variable=TEMP Units=K
TCL	Import variable	Stream-Var Stream=LEANCOLD Substream=MIXED Variable=TEMP Units=K
MCR	Import variable	Stream-Var Stream=RICHCOLD Substream=MIXED Variable=MASS-FLOW Units=kg/sec
MHL	Import variable	Stream-Var Stream=LEANWRM Substream=MIXED Variable=MASS-FLOW Units=kg/sec
MHR	Import variable	Stream-Var Stream=RICHWRM1 Substream=MIXED

		Variable=MASS-FLOW Units=kg/sec
MCL	Import variable	Stream-Var Stream=LEANCOLD Substream=MIXED Variable=MASS-FLOW Units=kg/sec
MUCR	Import variable	Stream-Prop Stream=RICHCOLD Prop-Set=MU-L Units=Pa-sec
MUHL	Import variable	Stream-Prop Stream=LEANWRM Prop-Set=MU-L Units=Pa-sec
MUHR	Import variable	Stream-Prop Stream=RICHWRM1 Prop-Set=MU-L Units=Pa-sec
MUCL	Import variable	Stream-Prop Stream=LEANCOLD Prop-Set=MU-L Units=Pa-sec
RHOCR	Import variable	Stream-Prop Stream=RICHCOLD Prop-Set=RHO-L Units=kg/cum
RHOHL	Import variable	Stream-Prop Stream=LEANWRM Prop-Set=RHO-L Units=kg/cum
RHOHR	Import variable	Stream-Prop Stream=RICHWRM1 Prop-Set=RHO-L Units=kg/cum
RHOCL	Import variable	Stream-Prop Stream=LEANCOLD Prop-Set=RHO-L Units=kg/cum
CPCR	Import variable	Stream-Prop Stream=RICHCOLD Prop-Set=CPMX Units=J/kg-K
CPHL	Import variable	Stream-Prop Stream=LEANWRM Prop-Set=CPMX Units=J/kg-K
CPHR	Import variable	Stream-Prop Stream=RICHWRM1 Prop-Set=CPMX Units=J/kg-K
CPCL	Import variable	Stream-Prop Stream=LEANCOLD Prop-Set=CPMX Units=J/kg-K
KCR	Import variable	Stream-Prop Stream=RICHCOLD Prop-Set=CONDUC-L Units=Watt/m-K
KHL	Import variable	Stream-Prop Stream=LEANWRM Prop-Set=CONDUC-L Units=Watt/m-K
KHR	Import variable	Stream-Prop Stream=RICHWRM1 Prop-Set=CONDUC-L Units=Watt/m-K
KCL	Import variable	Stream-Prop Stream=LEANCOLD Prop-Set=CONDUC-L Units=Watt/m-K
DUTY	Import variable	Heat-Duty Stream=WRMHS Units=Watt
CO2RM	Import variable	Mole-Flow Stream=PRODUCT1 Substream=MIXED Component=CO2 Units=kmol/sec
VCLW	Export variable	Parameter Parameter no.=322
NW	Import variable	Parameter Parameter no.=366 Initial value=1962.13

All of the variables defined in the “Define” tab of the calculator block input are included in Table 6 in addition to all the variables defined in the “Calculate” tab.

Table 6. C-WRMHX Variable Description

Variable	I/O	Description	Units
EXCAP	O	annualized exchanger CAPEX	\$/tonne CO_2
RPUMPOP	O	annualized rich pump OPEX	\$/tonne CO_2
RPUMPCAP	O	annualized rich pump CAPEX	\$/tonne CO_2
TAC	O	total annualized capital cost of warm exchanger and rich pump	\$/tonne CO_2
AREA	O	exchanger area	m^2
WRMLMTD	O	LMTD of warm exchanger	K
U	O	overall heat transfer coefficient	W/K-m^2
DPRICH	O	pressure drop of rich stream	Pa
DPLEAN	O	pressure drop of lean stream	Pa
LPLATE	O	plate length	m
VRICH	O	velocity of rich stream	m/sec
VLEAN	O	velocity of lean stream	m/sec
OUT1	O	debugging output	arbitrary
OUT2	O	debugging output	arbitrary
OUT3	O	debugging output	arbitrary
OUT4	O	debugging output	arbitrary
TCR	I	temperature of CR	K
THL	I	temperature of HL	K
THR	I	temperature of HR	K
TCL	I	temperature of CL	K
MCR	I	mass flow of CR	kg/sec
MHL	I	mass flow of HL	kg/sec
MHR	I	mass flow of HR	kg/sec
MCL	I	mass flow of CL	kg/sec
MUCR	I	liquid viscosity of CR	Pa–sec
MUHL	I	liquid viscosity of HL	Pa–sec
MUHR	I	liquid viscosity of HR	Pa-sec
MUCL	I	liquid viscosity of CL	Pa-sec
RHOCR	I	liquid density of CR	kg/m^3
RHOHL	I	liquid density of HL	kg/m^3
RHOHR	I	liquid density of HR	kg/m^3
RHOCL	I	liquid density of CL	kg/m^3
CPCR	I	liquid heat capacity of CR	J/kg–K
CPHL	I	liquid heat capacity of HL	J/kg–K
CPHR	I	liquid heat capacity of HR	J/kg–K
CPCL	I	liquid heat capacity of CL	J/kg–K
KCR	I	liquid thermal conductivity of CR	W/m–K
KHL	I	liquid thermal conductivity of HL	W/m–K
KHR	I	liquid thermal conductivity of HR	W/m–K
KCL	I	liquid thermal conductivity of CL	W/m–K
DUTY	I	heat duty	W

CO2RM	I	mole flow of CO_2 in stripper overhead	kmol/sec
VCLW	O	volumetric flowrate of CL	m^3/sec
NW	I	total exchanger width	m
PSPACE	I	plate spacing	m
GRICH	O	mass flux of rich stream	kg/m^2–sec
GLEAN	O	mass flux of lean stream	kg/m^2–sec
VELCR	O	velocity of CR	m/sec
VELCL	O	velocity of CL	m/sec
VELHR	O	velocity of HR	m/sec
VELHL	O	velocity of HL	m/sec
DIAM	I	equivalent diameter	m
RECR	O	Reynolds number of CR	—
RECL	O	Reynolds number of CL	—
REHR	O	Reynolds number of HR	—
REHL	O	Reynolds number of HL	—
PRCR	O	Prandtl number of CR	—
PRCL	O	Prandtl number of CL	—
PRHR	O	Prandtl number of HR	—
PRHL	O	Prandtl number of HL	—
HCR	O	heat transfer coefficient of CR	W/m^2–K
HCL	O	heat transfer coefficient of CL	W/m^2–K
HHR	O	heat transfer coefficient of HR	W/m^2–K
HHL	O	heat transfer coefficient of HL	W/m^2–K
KPLATE	I	plate thermal conductivity	W/m^2–K
PHICK	I	plate thickness	m
HPLATE	O	plate heat transfer coefficient	W/m^2–K
UCOLD	O	cold side overall heat transfer coefficient	W/m^2–K
UHOT	O	hot side overall heat transfer coefficient	W/m^2–K
DELTC	O	cold side temperature approach	K
DELTH	O	cold side temperature approach	K
FCR	O	Fanning friction factor of CR	—
FCL	O	Fanning friction factor of CL	—
FHR	O	Fanning friction factor of HR	—
FHL	O	Fanning friction factor of HL	—
DPCR	O	pressure drop per length of CR	Pa/m
DPCL	O	pressure drop per length of CL	Pa/m
DPHR	O	pressure drop per length of HR	Pa/m
DPHL	O	pressure drop per length of HL	Pa/m
ACOST	I	CAPEX of exchanger area	$/$m^2$
ECOST	I	cost of electricity	$/MWh
ALPHA	I	converts PEC to total capital	—

		requirement	
BETA	I	Lang factor (annualizes cost)	—
CFACTOR	I	capacity factor	—
PETA	I	pump efficiency	—
PCOST	I	pump CAPEX	$/W
CO2RMA	O	CO_2 removed per annum	tonne/annum
VCR	O	volumetric flowrate of CR	m^3/sec
VCLW	O	volumetric flowrate of CL of warm	m^3/sec

Fortran Code

The first part of the code calculates and maps all necessary properties for the model calculations. The next part calculates the exchanger size. The last part calculates the economics and formats miscellaneous outputs.

If a comment line ends with a number in parentheses, eg (1), then there is a comment in this documentation. The comment shows the equation in a more readable format, explains all variables, and elucidates the equation origin.

```
C Brent Sherman
C 2014-10-24
C PURPOSE: Calculate plate and frame heat exchanger
C                    non-flashing properties.
C Numbers in parentheses refer to comments in documentation.
C This calculator assumes these units:
C  density                          (kg/m3)
C  heat capacity               (J/kg-m3)
C  viscosity                          (Pa-sec)
C  thermal conductivity (W/m-K)
C  temperature                 (K)
C  mass flow                    (kg/sec)
C  CO2 removed              (kmol/sec)
C --- Calculations begin ---
C Calculate mass flux (kg/sec-m2). (1)
C NW=total width (m); PSPACE=plate spacing (m).
c      NW=1962.13
       PSPACE=0.002
       GRICH=MCR/(PSPACE*NW)
       GLEAN=MHL/(PSPACE*NW)

C Calculate the velocity (m/sec). (2)
       VELCR=GRICH/(RHOCR)
       VELCL=GLEAN/(RHOCL)
       VELHR=GRICH/(RHOHR)
       VELHL=GLEAN/(RHOHL)
C Output velocities of rich and lean sides.
       VRICH=VELCR
       VLEAN=VELHR
C Calculate the Reynolds number. (3)
       DIAM=2*PSPACE
       RECR=GRICH*DIAM/MUCR
       RECL=GLEAN*DIAM/MUCL
       REHR=GRICH*DIAM/MUHR
       REHL=GLEAN*DIAM/MUHL

C Calculate the Prandtl number. (4)
       PRCR=(CPCR*MUCR)/KCR
       PRCL=(CPCL*MUCL)/KCL
       PRHR=(CPHR*MUHR)/KHR
       PRHL=(CPHL*MUHL)/KHL
C Calculate the heat transfer coefficient (W/m2-K). (5)
C h=Nu*ki/D
       HCR=(0.3*KCR/DIAM)*(PRCR**0.333)*(RECR**0.663)
       HCL=(0.3*KCL/DIAM)*(PRCL**0.333)*(RECL**0.663)
       HHR=(0.3*KHR/DIAM)*(PRHR**0.333)*(REHR**0.663)
       HHL=(0.3*KHL/DIAM)*(PRHL**0.333)*(REHL**0.663)
```

```
C Calculate the thermal conductivity of the wall.
C (w/m-K)
C Plate thickness in m.
      KPLATE=16
      PTHICK=0.0006
      HPLATE=KPLATE/PTHICK
C Calculate the overall heat transfer coefficients (W/m2-K). (6)
      UCOLD=(1/HCR)+(1/HCL)+(1/HPLATE)
      UCOLD=1/UCOLD
      UHOT=(1/HHR)+(1/HHL)+(1/HPLATE)
      UHOT=1/UHOT
C Calculate the temperature approaches (K).
      DELTC=TCL-TCR
      DELTH=THL-THR
C Calculate the area (m2). (7)
      AREA=-DUTY/((UHOT*DELTC-UCOLD*DELTH)
     .           /DLOG((UHOT*DELTC)/(UCOLD*DELTH)))

C Warm LMTD (K)
      WRMLMTD=(DELTC-DELTH)/LOG(DELTC/DELTH)
C Overall heat transfer coefficient (W/K-m2) (8)
      U=-DUTY/(AREA*WRMLMTD)
C --- Economic Calculations Begin ---
C Calculate length from Eq. 5
      LPLATE=AREA/NW
C Calculate Fanning frIction factor for turbulent flow. (9)
      FCR=1.441*RECR**-0.206
      FCL=1.441*RECL**-0.206
      FHR=1.441*REHR**-0.206
      FHL=1.441*REHL**-0.206
C Calculate the pressure drop per length (Pa/m). (10)
      DPCR=(2*FCR*GRICH**2)/(RHOCR*DIAM)
      DPCL=(2*FCL*GLEAN**2)/(RHOCL*DIAM)
      DPHR=(2*FHR*GRICH**2)/(RHOHR*DIAM)
      DPHL=(2*FHL*GLEAN**2)/(RHOHL*DIAM)
C Calculate the rich-, and lean-side pressure drop (Pa). (11)
      DPRICH=((DPCR+DPHR)/2)*LPLATE
      DPLEAN=((DPCL+DPHL)/2)*LPLATE
C Economic parameters.
      ACOST=231.61
      ECOST=100
      ALPHA=5
      BETA=0.2
      CFACTOR=0.90
      PETA=0.65
      PCOST=0.4135
```

```
C Exchanger CAPEX ($/tonne CO2)
C Convert CO2 removed from kmol/sec to tonne/sec. (12)
      CO2RMA=CO2RM*44/1D3
      EXCAP=(AREA*ACOST*ALPHA*BETA)
     .                /(CO2RMA*3600*24*365*CFACTOR)
C Pumping CAPEX in $/tonne CO2. (13)
      VCR=MCR/RHOCR
      RPUMPCAP=(DPRICH*VCR/PETA)
     .         *PCOST*ALPHA*BETA
     .          /(CO2RMA*3600*24*365*CFACTOR)

C Pumping OPEX in $/tonne CO2. (14)
      RPUMPOP=(DPRICH*VCR/PETA)
     .                       *ECOST/(3600*1D6)/CO2RMA

C Total annualized capital (15)
      TAC=EXCAP+RPUMPOP+RPUMPCAP
      VCLW=MCL/RHOCL
C Debugging outputs (16)
      OUT1= FCR
      OUT2= DPCR
      OUT3= DPHR
      OUT4= LPLATE
```

Code Comments

1. The mass flux is calculated using Equation 1,

$$G = \frac{\dot{m}}{\delta \times nW} \tag{1}$$

where G is mass flux (kg/m²–sec), $\dot{m}$ is mass flow rate (kg/sec), δ is plate spacing (m), n is number of plates, and W is plate width (m).

2. The velocity is calculated from the mass flux using Equation 2,

$$v = \frac{G}{\rho} \tag{2}$$

where v is velocity (m/sec) and ρ is liquid density (kg/m^3).

3. The Reynolds number Re is calculated using Equation 3,

$$Re = \frac{G}{\mu D} \tag{3}$$

where μ is the liquid viscosity (Pa–sec), and D is the equivalent diameter (m), which is twice the plate spacing.

4. The Prandtl number Pr is calculated in Equation 4,

$$Pr = \frac{C_p \mu}{k} \tag{4}$$

where C_p is the liquid heat capacity (J/kg–K), and k is the liquid thermal conductivity (W/m–K).

5. The heat transfer coefficient h (W/m^2–K) is calculated using Equation 5,

$$h = \frac{Nu * k}{D} = 0.3 \frac{k}{D} Pr^{0.333} Re^{0.663} \tag{5}$$

where Nu is the Nusselt number. This assumes herringbone plates with 45° corrugation angle (Ayub, 2003).

6. The overall heat transfer coefficient U_i of the hot or cold side (W/m^2–K) is calculated using Equation 6,

$$\frac{1}{U_i} = \frac{1}{h_1} + \frac{1}{h_2} + \frac{1}{h_{plate}} \tag{6}$$

where h_1 is the heat transfer coefficient of the rich stream (W/m^2–K), h_2 is the heat transfer coefficient of the lean stream (W/m^2–K), and h_{plate} is the heat transfer coefficient of the plate (W/m^2–K) equal to the plate thermal conductivity divided by plate thickness.

7. The exchanger area A (m^2) is calculated using Equation 7,

$$A = \frac{Q}{\frac{U_{hot}\Delta T_{cold} - U_{cold}\Delta T_{hot}}{\ln\left(\frac{U_{hot}\Delta T_{cold}}{U_{cold}\Delta T_{hot}}\right)}} \tag{7}$$

where Q is the duty (W), U_{hot} (U_{cold}) is the overall heat transfer coefficient of the hot (cold) side (W/m^2–K), and ΔT_{hot} (ΔT_{cold}) is the hot- (cold-) side temperature approach (K).

8. The overall heat transfer coefficient U (W/m^2–K) is calculated using Equation 8.

$$U = \frac{Q}{A\Delta T_{LMTD}} \tag{8}$$

9. The Fanning friction factor f_f is calculated using Equation 9.

$$f_f = 1.441 Re^{-0.206} \tag{9}$$

10. The pressure drop per length $\Delta P/L$ (Pa/m) is calculated using Equation 10,

$$\frac{\Delta P}{L} = \frac{2 f_f G^2}{\rho D} \tag{10}$$

where L is the length (m). This is calculated for each stream.

11. The pressure drop of the rich and lean sides ΔP (Pa) is calculated using Equation 11.

$$\Delta P_{rich} = \frac{\left(\frac{\Delta P}{L}\right)_{CR} + \left(\frac{\Delta P}{L}\right)_{HR}}{2} \times L \tag{11}$$

The equivalent equation is used for the lean side pressure drop.

12. The exchanger CAPEX $EXCAP$ ($/tonne CO_2) is calculated using Equation 12,

$$EXCAP = \frac{A \times \$A \times \alpha\beta}{\dot{m}_{CO_2} \times 3600 \times 24 \times 365 \times C} \tag{12}$$

where *$A* is the cost per unit area ($/m^2), α is the conversion of PEC to total capital requirement, β is the Lang factor, $\dot{m}_{CO_2}$ is the mass flowrate of CO_2 leaving the stripper overhead (tonne/sec), and *C* is the capacity factor, which accounts for 10% plant downtime. The purchased equipment cost (PEC) came from vendor quotes. It is assumed to vary linearly with area.

13. The rich pump CAPEX *RPUMPCAP* ($/tonne CO_2) is calculated using Equation 13,

$$RPUMPCAP = \frac{\left(\frac{\Delta P_{rich} \times Q_{CR}}{\eta}\right) \times \$P \times \alpha\beta}{\dot{m}_{CO_2} \times 3600 \times 24 \times 365 \times C} \quad (13)$$

where Q_{CR} is the volumetric flowrate of the cold, rich stream (m^3/sec, η is the pump efficiency, and *$P* is the cost of the pump ($/W).

14. The rich pump operating cost RPUMPOP ($/tonne CO_2) is calculated using Equation 14,

$$RPUMPOP = \frac{\left(\frac{\Delta P_{rich} \times Q_{CR}}{\eta}\right) \times COE}{\dot{m}_{CO_2} \times 3600 \times 10^5} \quad (14)$$

where *COE* is the cost of electricity ($/MWh).

15. The total annualized capital *TAC* ($/tonne CO_2) is calculated using Equation 15,

$$TAC = EXCAP + RPUMPOP + RPUMPCAP \quad (15)$$

16. The following four outputs were used for debugging. They are available for displaying intermediate values. Change the variable on the right side of the equal sign to the variable or expression to display.

C-HXHOT

This block sizes and costs a flashing plate and frame heat exchanger along with the economic calculations for the whole cross exchanger.

Variables

The variables defined are listed in Table 7.

Table 7. C-HXHOT Variable Definitions

Variable	Information flow	Definition
EXCAP	Export variable	Parameter Parameter no.=341
RPUMPOP	Export variable	Parameter Parameter no.=342
RPUMPCAP	Export variable	Parameter Parameter no.=343
TAC	Export variable	Parameter Parameter no.=345
AREA	Export variable	Parameter Parameter no.=310
WRMLMTD	Export variable	Parameter Parameter no.=314
HOTLMTD	Export variable	Parameter Parameter no.=361
TOTLMTD	Export variable	Parameter Parameter no.=362
U	Export variable	Parameter Parameter no.=319
DPRICH	Export variable	Parameter Parameter no.=316
DPLEAN	Export variable	Parameter Parameter no.=347

LPLATE	Export variable	Parameter Parameter no.=318
VRICH	Export variable	Parameter Parameter no.=320
VLEAN	Export variable	Parameter Parameter no.=321
LPUMPCAP	Export variable	Parameter Parameter no.=355
LPUMPOP	Export variable	Parameter Parameter no.=354
OUT1	Export variable	Parameter Parameter no.=330
OUT2	Export variable	Parameter Parameter no.=331
OUT3	Export variable	Parameter Parameter no.=333
OUT4	Export variable	Parameter Parameter no.=334
TCR	Import variable	Stream-Var Stream=RICHWRM2 Substream=MIXED Variable=TEMP Units=K
THL	Import variable	Stream-Var Stream=LEANHOT Substream=MIXED Variable=TEMP Units=K
THR	Import variable	Stream-Var Stream=RICHHOT Substream=MIXED Variable=TEMP Units=K
TCL	Import variable	Stream-Var Stream=LEANWRM Substream=MIXED Variable=TEMP Units=K
MCR	Import variable	Stream-Var Stream=RICHWRM2 Substream=MIXED Variable=MASS-FLOW Units=kg/sec
MHL	Import variable	Stream-Var Stream=LEANHOT Substream=MIXED Variable=MASS-FLOW Units=kg/sec
MHR	Import variable	Stream-Var Stream=RICHHOT Substream=MIXED Variable=MASS-FLOW Units=kg/sec
MCL	Import variable	Stream-Var Stream=LEANWRM Substream=MIXED Variable=MASS-FLOW Units=kg/sec
MUCR	Import variable	Stream-Prop Stream=RICHWRM2 Prop-Set=MU-L Units=Pa-sec
MUHL	Import variable	Stream-Prop Stream=LEANHOT Prop-Set=MU-L Units=Pa-sec
MUHR	Import variable	Stream-Prop Stream=RICHHOT Prop-Set=MU-L Units=Pa-sec
MUCL	Import variable	Stream-Prop Stream=LEANWRM Prop-Set=MU-L Units=Pa-sec
RHOCR	Import variable	Stream-Prop Stream=RICHWRM2 Prop-Set=RHO-L Units=kg/cum
RHOHL	Import variable	Stream-Prop Stream=LEANHOT Prop-Set=RHO-L Units=kg/cum
RHOHR	Import variable	Stream-Prop Stream=RICHHOT Prop-Set=RHO-L Units=kg/cum
RHOCL	Import variable	Stream-Prop Stream=LEANWRM Prop-Set=RHO-L Units=kg/cum
CPCR	Import variable	Stream-Prop Stream=RICHWRM2 Prop-Set=CPMX Units=J/kg-K
CPHL	Import variable	Stream-Prop Stream=LEANHOT Prop-Set=CPMX Units=J/kg-K
CPHR	Import variable	Stream-Prop Stream=RICHHOT Prop-Set=CPMX Units=J/kg-K
CPCL	Import variable	Stream-Prop Stream=LEANWRM Prop-Set=CPMX Units=J/kg-K
KCR	Import variable	Stream-Prop Stream=RICHWRM2 Prop-Set=CONDUC-L Units=Watt/m-K
KHL	Import variable	Stream-Prop Stream=LEANHOT Prop-Set=CONDUC-L Units=Watt/m-K
KHR	Import variable	Stream-Prop Stream=RICHHOT Prop-Set=CONDUC-L Units=Watt/m-K

KCL	Import variable	Stream-Prop Stream=LEANWRM Prop-Set=CONDUC-L Units=Watt/m-K
DUTY	Import variable	Heat-Duty Stream=HOTHS Units=Watt
DUTYW	Import variable	Heat-Duty Stream=WRMHS Units=Watt
CO2RM	Import variable	Mole-Flow Stream=PRODUCT1 Substream=MIXED Component=CO2 Units=kmol/sec
HRLDG	Import variable	Parameter Parameter no.=888
SIGHR	Import variable	Stream-Prop Stream=RICHHOT Prop-Set=SURFT Units=N/m
RHOV	Import variable	Stream-Prop Stream=RICHHOT Prop-Set=RHO-V Units=kg/cum
PHR	Import variable	Stream-Var Stream=RICHHOT Substream=MIXED Variable=PRES Units=N/sqm
MVAP	Import variable	Stream-Prop Stream=RICHHOT Prop-Set=MDOT-V Units=kg/sec
MUV	Import variable	Stream-Prop Stream=RICHHOT Prop-Set=MU-V Units=Pa-sec
PSTRIP	Import variable	Block-Var Block=LPFLASH Variable=PRES Sentence=PROFILE ID1=1 Units=N/sqm
DPLEANW	Import variable	Parameter Parameter no.=317
VCLW	Import variable	Parameter Parameter no.=322
EXCAPW	Import variable	Parameter Parameter no.=311
RPCAPW	Import variable	Parameter Parameter no.=313
RPOPW	Import variable	Parameter Parameter no.=312
NW	Import variable	Parameter Parameter no.=360 Initial value=2293.41

Table 8. C-HXHOT Variable Description

Variable	I/O	Description	Units
EXCAP	O	annualized exchanger CAPEX	\$/tonne CO_2
RPUMPOP	O	annualized rich pump OPEX	\$/tonne CO_2
RPUMPCAP	O	annualized rich pump CAPEX	\$/tonne CO_2
TAC	O	total annualized capital cost of cross exchanger and pumps	\$/tonne CO_2
AREA	O	exchanger area	m^2
WRMLMTD	O	LMTD of warm exchanger	K
HOTLMTD	O	LMTD of hot exchanger	K
TOTLMTD	O	LMTD of cross exchanger	K
U	O	overall hot heat transfer coefficient	$W/K\text{-}m^2$
DPRICH	O	pressure drop of rich stream	Pa
DPLEAN	O	pressure drop of lean stream	Pa
LPLATE	O	plate length	m
VRICH	O	velocity of rich stream	m/sec
VLEAN	O	velocity of lean stream	m/sec
LPUMPCAP	O	lean pump CAPEX	\$/tonne $_{CO2}$

LPUMPOP	O	lean pump OPEX	\$/tonne CO_2
OUT1	O	debugging output	arbitrary
OUT2	O	debugging output	arbitrary
OUT3	O	debugging output	arbitrary
OUT4	O	debugging output	arbitrary
TCR	I	temperature of CR	K
THL	I	temperature of HL	K
THR	I	temperature of HR	K
TCL	I	temperature of CL	K
MCR	I	mass flow of CR	kg/sec
MHL	I	mass flow of HL	kg/sec
MHR	I	mass flow of HR	kg/sec
MCL	I	mass flow of CL	kg/sec
MUCR	I	liquid viscosity of CR	Pa–sec
MUHL	I	liquid viscosity of HL	Pa–sec
MUHR	I	liquid viscosity of HR	Pa-sec
MUCL	I	liquid viscosity of CL	Pa-sec
RHOCR	I	liquid density of CR	kg/m^3
RHOHL	I	liquid density of HL	kg/m^3
RHOHR	I	liquid density of HR	kg/m^3
RHOCL	I	liquid density of CL	kg/m^3
CPCR	I	liquid heat capacity of CR	J/kg–K
CPHL	I	liquid heat capacity of HL	J/kg–K
CPHR	I	liquid heat capacity of HR	J/kg–K
CPCL	I	liquid heat capacity of CL	J/kg–K
KCR	I	liquid thermal conductivity of CR	W/m–K
KHL	I	liquid thermal conductivity of HL	W/m–K
KHR	I	liquid thermal conductivity of HR	W/m–K
KCL	I	liquid thermal conductivity of CL	W/m–K
DUTY	I	heat duty of hot exchanger	W
DUTYW	I	heat duty of warm exchanger	W
CO2RM	I	mole flow of CO_2 in stripper overhead	kmol/sec
HRLDG	I	loading of HR	mol CO_2/mol alk
SIGHR	I	liquid surface tension of HR	N/m
RHOV	I	vapor density of HR	kg/m^3
PHR	I	pressure of HR	N/m^2
MVAP	I	vapor mass flow rate of HR	kg/sec
MUV	I	vapor viscosity of HR	Pa–sec
PSTRIP	I	stripper pressure	N/m^2
DPLEANW	I	lean-side pressure drop of warm	N/m^2

		exchanger	
VCLW	I	volumetric flowrate of warm CL	m^3/sec
EXCAPW	I	annualized exchanger CAPEX of warm exchanger	\$/tonne CO_2
RPCAPW	I	annualized rich pump OPEX of warm exchanger	\$/tonne CO_2
RPOPW	I	annualized rich pump CAPEX of warm exchanger	\$/tonne CO_2
NW	I	total exchanger width	m
PLATESPACE	I	plate spacing	m
GCR	O	mass flux of CR	kg/m^2–sec
GHR	O	mass flux of HR	kg/m^2–sec
GLEAN	O	mass flux of lean stream	kg/m^2–sec
VELCR	O	velocity of CR	m/sec
VELCL	O	velocity of CL	m/sec
VELHR	O	velocity of HR	m/sec
VELHL	O	velocity of HL	m/sec
VRICH	O	rich velocity	m/sec
VLEAN	O	lean velocity	m/sec
DIAM	O	equivalent diameter	m
RECR	O	Reynolds number of CR	—
RECL	O	Reynolds number of CL	—
REHR	O	Reynolds number of HR	—
REHL	O	Reynolds number of HL	—
PRCR	O	Prandtl number of CR	—
PRCL	O	Prandtl number of CL	—
PRHR	O	Prandtl number of HR	—
PRHL	O	Prandtl number of HL	—
HCR	O	heat transfer coefficient of CR	W/m^2–K
HCL	O	heat transfer coefficient of CL	W/m^2–K
HHR	O	heat transfer coefficient of HR	W/m^2–K
HHL	O	heat transfer coefficient of HL	W/m^2–K
PSAT	O	saturation pressure at T_{wall}	N/m^2
DHVAP	O	vaporization enthalpy	J/kg
HNUC	O	heat transfer for nucleate boiling	W/m^2–K
VFRAC	O	vapor fraction of HR	—
XTT	O	Lockhart-Martinelli parameter	—
PHI2	O	two-phase multiplier	—
FXTT	O	effective turbulence factor	—
REV	O	Reynolds number of vapor phase	—
S	O	suppresion factor	K

HV	O	two-phase heat transfer coefficient	$W/m^2–K$
KPLATE	I	plate thermal conductivity	$W/m^2–K$
PLATETHICK	I	plate thickness	m
HPLATE	I	plate heat transfer coefficient	$W/m^2–K$
UCOLD	I	cold side overall heat transfer coefficient	$W/m^2–K$
UHOT	I	hot side overall heat transfer coefficient	$W/m^2–K$
DELTC	I	cold side temperature approach	K
DELTH	I	cold side temperature approach	K
TOTDUTY	O	cross exchanger duty	W
UAHOT	O	hot exchanger UA	W–m/K
UAWARM	O	warm exchanger UA	W–m/K
TOTUA	O	cross exchanger UA	W–m/K
FCR	O	Fanning friction factor of CR	—
FCL	O	Fanning friction factor of CL	—
FHR	O	Fanning friction factor of HR	—
FHL	O	Fanning friction factor of HL	—
DPCR	O	pressure drop per length of CR	Pa/m
DPCL	O	pressure drop per length of CL	Pa/m
DPHR	O	pressure drop per length of HR	Pa/m
DPHL	O	pressure drop per length of HL	Pa/m
DPV	O	pressure drop per length of HR due to flashing	Pa/m
ACOST	I	CAPEX of exchanger area	$\$/m^2$
ECOST	I	cost of electricity	$/MWh
ALPHA	I	converts PEC to total capital requirement	—
BETA	I	Lang factor (annualizes cost)	—
CFACTOR	I	capacity factor	—
PETA	I	pump efficiency	—
PCOST	O	pump CAPEX	$/W
CO2RMA	O	CO_2 removed per annum	tonne/annum
VHL	O	volumetric flow fo HL	m^3/sec
DPOTHER	I	pressure drop due to trim cooler and static head to absorber	Pa
PAVAIL	O	available pressure from stripper	Pa

Fortran Code

This code expands on the warm exchanger code structure. This code maps the input variables, accounts for flashing when sizing the exchanger, then performs economics for all the flashing and non-flashing exchanger along with the rich and lean pumps.

If a comment line ends in with a number in parthenses, eg (1), then there is a comment in this documentation. The comment shows the equation in a more readable format, explains all variables, and elucidates the equation origin.

```
C Brent Sherman
C 2014-10-24
C Calculate plate and frame heat exchanger non-flashing
      properties.
C This calculator assumes these units:
C  density                          (kg/m3)
C  heat capacity                (J/kg-m3)
C  viscosity                        (Pa-sec)
C  thermal conductivity (W/m-K)
C  temperature                 (K)
C  mass flow                    (kg/sec)
C  CO2 removed              (kmol/sec)
C --- Calculations begin ---
C Calculate mass flux (kg/sec-m2). (1)
C The total width of the exchanger (m) and plate spacing (m).
C      NW=2293.41
       PSPACE=0.002
       GCR=MCR/(PSPACE*NW)
       GHR=MHR/(PSPACE*NW)
       GLEAN=MHL/(PSPACE*NW)

C Calculate the velocity (m/sec). (2)
       VELCR=GCR/(RHOCR)
       VELCL=GLEAN/(RHOCL)
       VELHR=GHR/(RHOHR)
       VELHL=GLEAN/(RHOHL)
C Output velocities of rich and lean sides. (3)
       VRICH=VELCR
       VLEAN=VELHR
C Calculate the Reynolds number. (4)
       DIAM=2*PSPACE
       RECR=GCR*DIAM/MUCR
       RECL=GLEAN*DIAM/MUCL
       REHR=GHR*DIAM/MUHR
       REHL=GLEAN*DIAM/MUHL

C Calculate the Prandtl number. (5)
       PRCR=(CPCR*MUCR)/KCR
       PRCL=(CPCL*MUCL)/KCL
       PRHR=(CPHR*MUHR)/KHR
       PRHL=(CPHL*MUHL)/KHL
C Calculate the heat transfer coefficient (W/m2-K). (6)
C h=Nu*ki/D
       HCR=(0.3*KCR/DIAM)*(PRCR**0.333)*(RECR**0.663)
       HCL=(0.3*KCL/DIAM)*(PRCL**0.333)*(RECL**0.663)
       HHR=(0.3*KHR/DIAM)*(PRHR**0.333)*(REHR**0.663)
       HHL=(0.3*KHL/DIAM)*(PRHL**0.333)*(REHL**0.663)
```

```
C Calculate Psat (Pa) and dHvap (J/kg). (7)
C This is a polynomial of the loading correlated by Yu-Jeng Lin.
      PSAT=1391787263.9*HRLDG**4-1362139706.7*HRLDG**3
     .          +519440146.3*HRLDG**2-88035723.6*HRLDG+6060677.3
      DHVAP=(1000/18*40+HRLDG*700)*1000
     .                 /(1+HRLDG*0.44+0.43)

C Calculate the nucleate boiling h (W/m2-K) (8)
      HNUC=1.22D-3*(KHR**0.79*CPHR**0.45*RHOHR**0.49
     .              *(THL-THR)**0.24*(PSAT-PHR)**0.75)
     .
      /(SIGHR**0.5*MUHR**0.29*DHVAP**0.24*RHOV**0.24)
C      HNUC=(SIGHR**0.5*MUHR**0.29*DHVAP**0.24*RHOV**0.24)
C Two phase calculations. (9)
C Vapor fraction (kg/kg).
      VFRAC=MVAP/MHR
      XTT=((1-VFRAC)/VFRAC)**((2-0.25)/2)
     .           *(RHOV/RHOHR)**0.5*(MUHR/MUV)**0.1
      PHI2=1+20/XTT+(1/XTT)**2
      IF (XTT .LT. 10) THEN
           FXTT=2.35*(1/XTT+0.213)**0.736
           ELSE
           FXTT=1
      END IF
C Two-phase Reynolds number. (10)
      REV=REHR*FXTT**1.25
      S=1/(1+2.35D-6*REV**1.17)
C Calculate two-phase heat transfer coeff. (W/K-m2). (11)
      HV=S*HNUC+FXTT*HHR
C PTHICK=plate thickness in m.
      KPLATE=16
      PTHICK=0.0006
      HPLATE=KPLATE/PTHICK
C Calculate the overall heat transfer coefficients (W/m2-K).
      (12)
      UCOLD=(1/HCR)+(1/HCL)+(1/HPLATE)
      UCOLD=1/UCOLD
      UHOT=(1/HV)+(1/HHL)+(1/HPLATE)
      UHOT=1/UHOT
C Calculate the temperature approaches (K).
      DELTC=TCL-TCR
      DELTH=THL-THR
C Calculate the area (m2). (13)
      AREA=-DUTY/((UHOT*DELTC-UCOLD*DELTH)
     .           /DLOG((UHOT*DELTC)/(UCOLD*DELTH)))
```

```
C Hot LMTD (K)
      HOTLMTD=(DELTC-DELTH)/DLOG(DELTC/DELTH)

C Overall LMTD (K) (14)
      TOTDUTY=DUTY+DUTYW
      UAHOT=DUTY/HOTLMTD
      UAWARM=DUTYW/WRMLMTD
      TOTUA=UAHOT+UAWARM
      TOTLMTD=TOTDUTY/TOTUA

C Overall heat transfer coefficient (W/K-m2) (15)
      U=-DUTY/(AREA*HOTLMTD)
C --- Economic Calculations Begin ---
C Calculate length from Eq. 5
      LPLATE=AREA/NW
C Calculate Fanning friction factor for turbulent flow. (16)
      FCR=1.441*RECR**-0.206
      FCL=1.441*RECL**-0.206
      FHR=1.441*REHR**-0.206
      FHL=1.441*REHL**-0.206
C Calculate the pressure drop per length (Pa/m). (17)
      DPCR=(2*FCR*GCR**2)/(RHOCR*DIAM)
      DPCL=(2*FCL*GLEAN**2)/(RHOCL*DIAM)
      DPHR=(2*FHR*GHR**2)/(RHOHR*DIAM)
      DPHL=(2*FHL*GLEAN**2)/(RHOHL*DIAM)
      DPV=PHI2*DPHR
C Calculate the rich-, and lean-side pressure drop (Pa). (18)
      DPRICH=((DPCR+DPV)/2)*LPLATE
      DPLEAN=((DPCL+DPHL)/2)*LPLATE
C Economic parameters.
      ACOST=231.61
      ECOST=100
      ALPHA=5
      BETA=0.2
      CFACTOR=0.90
      PETA=0.65
      PCOST=0.4135

C Exchanger CAPEX ($/tonne CO2)
C Convert CO2 removed from kmol/sec to tonne/sec (19)
      CO2RMA=CO2RM*44/1D3
C      AREA=16086.41
      EXCAP=(AREA*ACOST*ALPHA*BETA)
     .                /(CO2RMA*3600*24*365*CFACTOR)
C Pumping CAPEX in $/tonne CO2 (20)
      VCR=MCR/RHOCR
      RPUMPCAP=(DPRICH*VCR/PETA)
```

```
     .          *PCOST*ALPHA*BETA
     .           /(CO2RMA*3600*24*365*CFACTOR)

C Pumping OPEX in $/tonne CO2 (21)
      RPUMPOP=(DPRICH*VCR/PETA)
     .                      *ECOST/(3600*1D6)/CO2RMA

C Calculate lean pump CAPEX and OPEX. (22)
C Calculate available pressure to see if pump needed.
C W suffix denotes variables from the warm exchanger.
      VHL=MHL/RHOHL
      DPOTHER=5D5
      PAVAIL=PSTRIP-DPOTHER
      IF (DPLEAN + DPLEANW .GT. PAVAIL) THEN
      LPUMPCAP=((DPLEAN+DPLEANW-PAVAIL)*(VHL/PETA))
     .                         *PCOST*ALPHA*BETA
     .                          /(CO2RMA*3600*24*365*CFACTOR)
      LPUMPOP=((DPLEAN+DPLEANW-PAVAIL)*((VCLW+VHL)/(2*PETA)))
     .                       *(ECOST/(36D2*1D6*CO2RMA))
      ELSE
      LPUMPCAP=0
      LPUMPOP=0
      END IF
C Total annualized capital (23)
      TAC=EXCAP+RPUMPOP+RPUMPCAP
     .         + EXCAPW+RPOPW+RPCAPW
     .         + LPUMPCAP+LPUMPOP
C Debugging outputs (24)
      OUT1= LPUMPOP
      OUT2= FOO+FOO2
      OUT3= FOO2
      OUT4= EXP(OUT2)
```

Code Comments

1. The mass flux is calculated using Equation 1,

$$G = \frac{\dot{m}}{\delta \times nW} \tag{1}$$

   where G is mass flux (kg/m²–sec), $\dot{m}$ is mass flow rate (kg/sec), δ is plate spacing (m), n is number of plates, and W is plate width (m).
2. The velocity is calculated from the mass flux using Equation 2,

$$v = \frac{G}{\rho} \tag{2}$$

   where v is velocity (m/sec) and ρ is liquid density (kg/m^3).
3. These two statements reformat the velocity for output.
4. The Reynolds number is calculated using the equivalent diameter in Equation 4,

$$Re = \frac{G}{\mu D} \tag{4}$$

where *Re* is the Reynolds number, μ is the liquid viscosity (Pa−sec), and *D* is the equivalent diameter (m), which is twice the plate spacing.

5. The Prandtl number is calculated in Equation 5,

$$Pr = \frac{C_p \mu}{k} \tag{5}$$

where *Pr* is the Prandtl number, C_p is the liquid heat capacity (J/kg−K), and *k* is the liquid thermal conductivity (W/m−K).

6. The heat transfer coefficient *h* (W/m^2−K) is calculated using Equation 6,

$$h = \frac{Nu * k}{D} = 0.3 \frac{k}{D} Pr^{0.333} Re^{0.663} \tag{6}$$

where *Nu* is the Nusselt number. This assumes herringbone plates with 45° corrugation angle (Ayub, 2003).

7. The saturation vapor pressure for 5 m PZ P_{sat} (Pa) at the wall temperature (5 K more than the stripper, so 155 °C) is calculated using the polynomial of Equation 7,

$$\begin{aligned} P_{sat} = {} & 1391787263.9\alpha_{HR}^4 - 1362139706.7\alpha_{HR}^3 \\ & + 519440146.3\alpha_{HR}^2 - 88035723.6\alpha_{HR} \\ & + 6060677.3 \end{aligned} \tag{7}$$

where α_{HR} is the loading of the hot, rich stream, (mol CO_2/mol alk). This was fit to data generated by Aspen. A property analysis block varying loading and temperature was run with an output of total pressure (property set PRES).

The latent heat of vaporization λ (J/kg) for 5 m PZ is calculated using the polynomial of Equation 8,

$$\lambda = \frac{1{,}000 \frac{J}{kJ} \left(\Delta H_{H_2O} m_{H_2O} + \Delta H_{CO_2} m_{CO_2} \right)}{1\ kg\ H_2O + kg\ CO_2 + 5\ kg\ PZ} \tag{8}$$

where ΔH_{H_2O} is the latent heat of water (40 kJ/mol), m_{H_2O} is the number of moles of water in 1 kg of solvent, ΔH_{CO_2} is the heat of desorption of CO_2 (70 kJ/mol), m_{CO_2} is the number of moles of CO_2 in one kg of solvent.

8. The heat transfer coefficient for nucleate boiling h_{nuc} (W/m^2−K) is calculated using Equation 9,

$$h_{nuc} = 0.00122 \frac{{k_L}^{0.79} {C_{pL}}^{0.45} {\rho_L}^{0.49} \Delta {T_e}^{0.24} \Delta {P_{sat}}^{0.75}}{\sigma^{0.5} {\mu_L}^{0.29} \lambda^{0.24} {\rho_V}^{0.24}} \tag{9}$$

where $\Delta T_e(K) = T_{HL} - T_{HR}$, $\Delta P_{sat}(Pa) = P_{sat} - P_{HR}$, $\sigma(\frac{N}{m})$ is surface tension of HR, $k_L \left(\frac{W}{m \cdot k}\right)$ is liquid thermal conductivity of HR, $C_{pL} \left(\frac{J}{kgK}\right)$ is liquid heat capacity of HR, $\rho_L \left(\frac{kg}{m^3}\right)$ is the vapor density, $\mu_L \left(\frac{kg}{m \cdot s}\right)$ is liquid viscosity of HR, $\lambda \left(\frac{J}{kg}\right)$ is latent heat of vaporization. This equation is for nucleate boiling on horizontal tubes (Forster and Zuber, 1955).

9. The two-phase heat transfer calculations involve a few steps. First, the Lockhart-Martinelli parameter X_{tt} is calculated. X_{tt} is the ratio of pressure drop of the liquid phase to the vapor phase, where $_{tt}$ means turbulent vapor and liquid. using Equation 10,

$$X_{tt} = \left[\frac{\left(\frac{\Delta P}{L}\right)_L}{\left(\frac{\Delta P}{L}\right)_V}\right]^{0.5} = \left(\frac{1-x}{x}\right)^{(2-n)/2}\left(\frac{\rho_V}{\rho_L}\right)^{0.5}\left(\frac{\mu_L}{\mu_V}\right)^{0.1} \quad (10)$$

where $\left(\frac{\Delta P}{L}\right)_L$ is the liquid phase pressure drop per length (Pa/m), $\left(\frac{\Delta P}{L}\right)_V$ is the vapor phase pressure drop per length (Pa/m), x is the vapor mass fraction, n depends on the tubing and is here taken as 0.25, and ρ_L (ρ_V) is the density of the HR liquid (vapor) (kg/m^3), and μ_L (μ_V) is the viscosity of HR liquid (vapor) (Pa−sec).

The two-phase multiplier ϕ_L^2 is caclculated using Equation 11,

$$\phi_L^2 = \frac{\left(\frac{\Delta P}{L}\right)_{TF}}{\left(\frac{\Delta P}{L}\right)_L} = 1 + \frac{20}{X_{tt}} + \frac{1}{X_{tt}^2} \quad (11)$$

where $\left(\frac{\Delta P}{L}\right)_{TF}$ is the two-phase flow pressure drop per length (Pa/m), and $\left(\frac{\Delta P}{L}\right)_L$ is the liquid only pressure drop per length (Pa/m).

The effective turbulence factor F is calculated using Equation 12,

$$F = \left(\frac{Re}{Re_L}\right)^{0.8} = \begin{cases} 2.35\left(\frac{1}{X_{tt}} + 0.213\right)^{0.736} & (X_{tt} < 10) \\ 1 & (X_{tt} > 10) \end{cases} \quad (12)$$

where $\left(\frac{\Delta P}{L}\right)_{TF}$ is the two-phase flow pressure drop per length (Pa/m), and $\left(\frac{\Delta P}{L}\right)_L$ is the liquid only pressure drop per length (Pa/m).

10. The vapor phase Reynolds number Re_V is calculated using Equation 13,

$$Re_V = Re_L F^{1.25} \quad (13)$$

where Re_L is the liquid Reynolds number of HR.
The suppresion factor S is calculated using Equation 14,

$$S = \frac{1}{1 + 2.53 \times 10^{-6} Re_V^{1.17}} \quad (14)$$

where Re_L is the liquid Reynolds number of HR.

11. The heat transfer coefficient h (W/K-m^2) is calculated using Equation 15,

$$h = Sh_{nuc} + Fh_L \quad (15)$$

where S is the suppresion factor, defined as $S = \frac{\text{effective } (T_w - T_{sat})}{\text{Overall } (T_w - T_{sat})}$, and h_L is the convective heat transfer coefficient of liquid only. F, S, and h are from Chen's correlation (Chen, 1966). This correlation assumes that the covnective and nucleate boiling heat

transfer coefficients are additive with convection suppressing nucleate boiling. When the flow rate increases, the effective temperature difference decreases.

12. The overall heat transfer coefficient for the hot and cold sides is calculated using Equation 16,

$$\frac{1}{U_i} = \frac{1}{h_1} + \frac{1}{h_2} + \frac{1}{h_{plate}} \tag{16}$$

where U_i is the overall heat transfer coefficient of the hot or cold side (W/m^2–K), h_1 is the heat transfer coefficient of the rich stream (W/m^2–K), h_2 is the heat transfer coefficient of the lean stream(W/m^2–K), and h_{plate} is the heat transfer coefficient of the plate (W/m^2–K) equal to the plate thermal conductivity divided by the plate thickness.

13. The exchanger area (m^2) is calculated using Equation 17,

$$A = \frac{Q}{\frac{U_{hot}\Delta T_{cold} - U_{cold}\Delta T_{hot}}{\log\left(\frac{U_{hot}\Delta T_{cold}}{U_{cold}\Delta T_{hot}}\right)}} \tag{17}$$

where Q is the duty (W), U_{hot} (U_{cold}) is the overall heat transfer coefficient of the hot (cold) side (W/m^2–K), h_1 is the heat transfer coefficient of the rich stream (W/m^2–K), h_2 is the heat transfer coefficient of the lean stream(W/m^2–K), and ΔT_{hot} (ΔT_{cold})is the heat transfer coefficient of the plate (W/m^2–K) equal to the plate thermal conductivity divided by the plate thickness.

14. The overall LMTD $\Delta T_{LM,OV}$ (K) is calculated using Equation 17,

$$\Delta T_{LM,OV} = \frac{Q_{OV}}{UA_{OV}} \tag{17}$$

where Q_{OV} is the overall duty (W), UA_{ov} is the overall heat transfer coefficient times area of the cross exchanger (W−m/K).

15. The overall heat transfer coefficient is calculated using Equation 18.

$$U = \frac{Q}{A\Delta T_{LMTD}} \tag{18}$$

16. The Fanning friction factor f_f is calculated using Equation 19.

$$f_f = 1.441 Re^{-0.206} \tag{19}$$

17. The pressure drop per length $\Delta P/L$ (Pa/m) for liquid is calculated using Equation 20,

$$\frac{\Delta P}{L} = \frac{2 f_f G^2}{\rho D} \tag{20}$$

where L is the length (m).

For vapor Equation 21 is used,

$$\frac{\Delta P}{L} = \phi_L^2 \left(\frac{\Delta P}{L}\right)_{HR} \tag{20}$$

18. The pressure drop of the rich and lean sides ΔP (Pa) is calculated using Equation 21.

$$\Delta P_{rich} = \frac{\left(\frac{\Delta P}{L}\right)_{CR} + \left(\frac{\Delta P}{L}\right)_{HR}}{2} \times L \tag{21}$$

The equivalent equation is used for the lean side pressure drop.

19. The exchanger CAPEX *EXCAP* ($/tonne CO_2) is calculated using Equation 22,

$$EXCAP = \frac{A \times \$A \times \alpha\beta}{\dot{m}_{CO_2} \times 3600 \times 24 \times 365 \times C} \tag{22}$$

where *$A* is the cost per unit area ($/m^2), α is the conversion of PEC to total capital requirement, β is the Lang factor, $\dot{m}_{CO_2}$ is the mass flowrate of CO_2 leaving the stripper overhead (tonne/annum), and *C* is the capacity factor, which accounts for 10% plant downtime. The purchased equipment cost (PEC) came from vendor quotes. It assumed to vary linearly with area.

20. The rich pump CAPEX *RPUMPCAP* ($/tonne CO_2) is calculated using Equation 23,

$$RPUMPCAP = \frac{\left(\frac{\Delta P_{rich} \times Q_{CR}}{\eta}\right) \times \$P \times \alpha\beta}{\dot{m}_{CO_2} \times 3600 \times 24 \times 365 \times C} \tag{23}$$

where Q_{CR} is the volumetric flowrate of the cold, rich stream (m^3/sec, η is the pump efficiency, and *$P* is the cost of the pump ($/W).

21. The rich pump operating cost RPUMPOP ($/tonne CO_2) is calculated using Equation 24,

$$RPUMPOP = \frac{\left(\frac{\Delta P_{rich} \times Q_{CR}}{\eta}\right) \times COE}{\dot{m}_{CO_2} \times 3600 \times 10^5} \tag{24}$$

where *COE* is the cost of electricity ($/MWh).

22. The lean pump CAPEX *LPUMPCAP* and OPEX *LPUMPOP* ($/tonne CO_2) is calculated using Equation 25 and 26,

$$LPUMPCAP = \frac{\left(\frac{\Delta P_{lean,ov} \times Q_{HL}}{\eta}\right) \times \$P \times \alpha\beta}{\dot{m}_{CO_2} \times 3600 \times 24 \times 365 \times C} \tag{25}$$

where $\Delta P_{lean,ov}$ is defined by Equation 26,

$$\Delta P_{lean,ov} = \Delta P_{lean,hot} + \Delta P_{lean,warm} - \Delta P_{avail} \tag{26}$$

where ΔP_{avail} (Pa) is the available pressure defined as the stripper pressure (PSTRIP) less the expected pressure drop in the trim cooler and the static head of the absorber (DPOTHER). The other undefined term of Equation 25 is Q_{HL}, the volumetric flowrate of HL.

$$LPUMPOP = \frac{\left(\frac{\Delta P_{lean,ov} \times \left(Q_{CL,warm} + Q_{HL}\right)}{\eta}\right) \times COE}{\dot{m}_{CO_2} \times 3600 \times 10^5} \tag{26}$$

The if switch determines if a lean pump is needed or not, meaning if the stripper pressure is sufficient to overcome the pressure drop of the trim cooler and absorber static head. If the lean pump is not needed, then these costs are 0.

23. The total annualized capital *TAC* for the cross exchanger, rich pump, and lean pump ($/tonne CO_2) is calculated using Equation 25,

$$TAC = EXCAP + RPUMPOP + RPUMPCAP + EXCAPW + RPOPW + RPCAPW + LPUMPCAP + LPUMPOP \quad (25)$$

24. The following four outputs were used for debugging. They are available for displaying intermediate values. Change the variable on the right side of the equal sign to the variable or expression to display.

O-TAC

This block optimizes the total annualized capital cost of the exchanger, rich pump, and lean pump (TAC, $/tonne CO_2) by varying the total width (NW, m) of both the warm and hot exchanger.

Variables

The variables are defined on both the **Define** and **Vary** tab.

Variable	Definition	Description	Units	Lower limit	Upper limit
TAC	Parameter Parameter no.=345	TAC of exchanger	$/tonne CO_2	N/A	N/A
1	Parameter Parameter no.=360	NW of hot exchanger	m	900	9000
2	Parameter Parameter no.=366	NW of warm exchanger	m	900	9000

Objective Function

The objective function is the minimization of TAC.

Constraints

No constraints are used.

7. REFERENCES

Ayub, Z. H. Plate Heat Exchanger Literature Survey and New Heat Transfer and Pressure Drop Correlations for Refrigerant Evaporators. *Heat Transf Eng* **2003**, *24*, 3–16.

Chen, J. Correlation for Boiling Heat Transfer to Saturated Fluids in Convective Flow. *Ind Eng Chem Process Des Dev* **1966**, *5*, 322–329.

Forster, H.; Zuber, N. Dynamics of Vapor Bubbles and Boiling Heat Transfer. *AIChE J* **1955**, *1*, 531–535.

Rochelle GT et al. "CO_2 Capture by Aqueous Absorption, First Quarterly Progress Reports." Texas Carbon Management Program. The University of Texas at Austin. 2014.

An Effective Multiloop Control Strategy for an Advanced Amine Scrubbing Process Configuration

Quarterly Report for October 1 – December 31, 2014

by Matthew S. Walters

Supported by the Texas Carbon Management Program

McKetta Department of Chemical Engineering

The University of Texas at Austin

January 31, 2015

Abstract

Proportional (P) and proportional integral (PI) controllers were demonstrated to be effective in regulating a low-fidelity model of an advanced amine scrubbing process configuration to the desired set point. P controllers were used for level control, and PI controllers were used for temperature and concentration control. The primary objective of the control strategy is to maintain a constant delivery rate of CO_2 to the compressor, in contrast to previous work which controlled the CO_2 removal rate in the absorber. The water balance is maintained by controlling the top temperature of the water wash and allowing for water makeup or bleed from the water wash recycle loop. A desired L/G ratio in the absorber is used to set the solvent circulation flowrate. This simple feedback control structure produces a slow, stable response but is not optimal. It is difficult to tune the bypass ratios around the main cross exchanger, because there is significant loop interaction and energy recovery. The bypass ratios were set to constant values in this work to avoid instability from the competing control loops. The concentration controller is also difficult to tune because of the slow nature of the response. The current tuning is too aggressive and resulted in oscillations in the amine concentration.

Introduction

Several challenges exist to developing an effective control strategy for post-combustion CO_2 capture with amine scrubbing. The amine plant is highly integrated with the upstream power plant and downstream CO_2 compression and storage. Significant solvent recycling and energy recovery is utilized to reduce capital and operating costs in the plant, leading to control loop interactions and time scale multiplicity in the process variables (Walters et al., 2014). The large energy penalty of capturing CO_2 requires that the process remain approximately optimized, including in off-design conditions. These challenges are summarized in Figure 1.

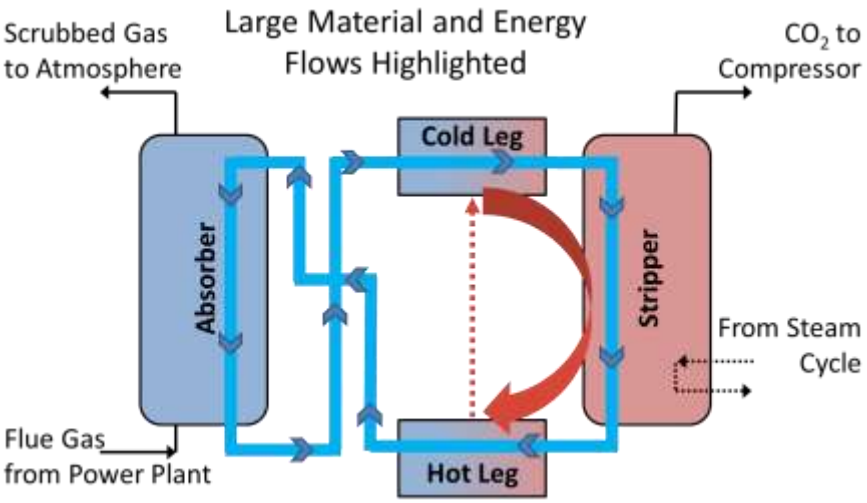

Figure 1: A simplified process flow diagram is shown here. The amine plant is integrated with the upstream power plant and downstream CO_2 compressor. Significant material and energy recycling is occurring within the amine plant. The process is energy intensive, with the steam for stripping and power for compression accounting for an energy penalty of ~20% on the power plant.

There are limited examples of plantwide control strategies proposed in the literature for post-combustion amine scrubbing. All works discussed here have used a multiloop PID control scheme. Ziaii (2012) concluded that controlling CO_2 capture rate led to unacceptable oscillations in process variables and instead suggested alternative process variables to control using real-time optimization. This strategy will only give the desired capture rate when there is no plant-model mismatch. Ceccarelli et al. (2014) showed that the controlled capture rate floated when a disturbance was introduced, which could possibly be due to non-aggressive controller tuning or a very large solvent inventory. The authors suggest that feedforward or advanced control strategies may be required to tightly control capture rate.

The previous works have considered a simple absorber and simple stripper with the first generation solvent MEA. High temperature/high pressure stripping using piperazine (PZ) solvent and advanced process configurations has been shown to reduce the total equivalent work of the process (Lin et al., 2014). The configuration used in this work is the in-and-out intercooled absorber and advanced flash stripper with PZ solvent. Including the water wash section of the absorber to represent the water balance and multiple bypass flows to increase energy recovery adds complexity compared to the base case designs used in previous work.

In all current or planned commercial amine scrubbing plants, the captured CO_2 will be used for enhanced oil recovery (EOR), meaning that there will be a customer expecting an agreed upon delivery rate of compressed CO_2 (Stéphenne, 2014; Spence et al., 2014; Knox, 2014). Even in the case of geological sequestration without EOR, there will be pipeline requirements that the capture plant must meet. By contrast, the sole customer on the absorber side of the process is Mother Earth; it is therefore only necessary to tightly control emissions out of the absorber if regulations set a strict and inflexible limit on the allowable CO_2 concentration being released. The control paradigm in previous works has been to maintain a desired capture rate (usually

90%) around the absorber. In this work, we propose maintaining a constant *delivery rate* of CO_2 to the pipeline, which is more in line with the objectives of the process.

Dynamic Simulation

The equations for a low fidelity model of the amine scrubbing plant with an advanced flash stripper were described in Walters et al. (2014). An in-and-out intercooled absorber with a water wash section has been added to this work. The equations for each unit operation have been implemented as MATLAB® S-functions and the process was simulated using Simulink®. The solver is ode15s with a relative error tolerance of 10^{-6}. The P&ID for the simulated system is given in Figure 2.

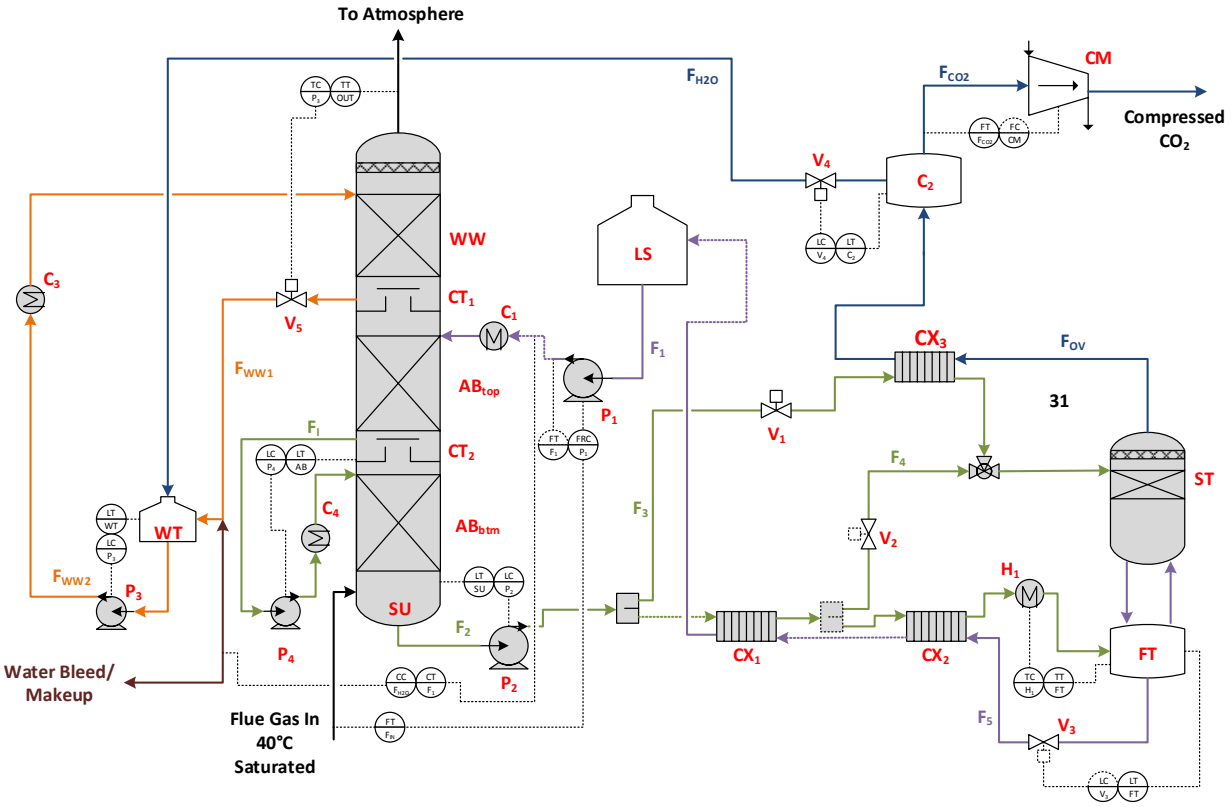

Figure 2: P&ID of the simulated process

Proportional (P) and proportional integral (PI) controllers were used to control the process. The controllers were simulated using the Discrete PID block from the Simulink® library. The sampling time is assumed to be one second. All controllers were given a lower saturation limit of zero and an upper saturation of 150% the steady state value. The lower limit is physically significant (for example a valve is completely closed). The upper limit was arbitrarily selected and will be based on design specifications in future work (for example the maximum flow when a valve is 100% open). The built-in back-calculation anti-windup method was used for the PI controllers. The P and PI control laws are given in Equations 1 and 2, respectively:

$$u(t) = u_{ss} + K_P e(t) \tag{1}$$

$$u(t) = u_{ss} + K_P e(t) + K_I \int_0^t e(t)dt \tag{2}$$

where:

$$e(t) \equiv x_{sp} - x$$

The continuous cycling method was used to tune the controllers. For the P controllers, the ultimate gain was multiplied by 0.1 to determine the proportional gain. Tyreus-Luyben tuning rules were used to calculate the proportional and integral gains for the PI controllers. Table 1 provides a summary of the controller parameters used in the simulation.

Table 1: Controller Parameters

Controlled Variable	Manipulated Variable	Controller Type	Set Point	K_P	K_I
l_{CT2}	F_I	P	1.0 m	-1.95 X 10^6	-
l_{SU}	F_2	P	3.0 m	-1.95 X 10^6	-
l_{FT}	F_5	P	9.8 m	-5.40 X 10^5	-
l_{WT}	F_{WW2}	P	6.0 m	-2.95 X 10^5	-
l_{C2}	F_{H2OR}	P	2.0 m	-3.50 X 10^4	-
T_{FT}^L	Q	PI	150 °C	1.81 X 10^6	7.98 X 10^5
$T_{WW,k=1}^V$	F_{WW1}	PI	42.4 °C	4.03 X 10^5	4.67 X 10^4
$C_{PZ,lean}$	F_{H2O}	PI	5 molal	-1.00 X 10^3	-100

The P and PI controllers from Table 1 are used to control levels, temperatures, and concentration. Levels in the system must be regulated for stable operation. The level set points for the sump, flash tank, condensate tank, and water tank were determined by requiring a 5-minute residence time at design conditions. The lean storage tank is designed to be a buffer tank so fluctuations in level are allowed. The temperature set point of the flash tank is set to the maximum degradation temperature of the PZ solvent, which is favorable for total energy requirements. In order to maintain the water balance around the absorber, the temperature of the vapor exiting the water wash is controlled. It is assumed that there is a mechanism to add or remove water from the water storage tank to control the water balance of the entire system, which is represented by molality of the lean solvent. It is also assumed that a concentration measurement is available online, which in practice could be inferred from a viscometer.

The compressor speed will be manipulated to control the CO_2 delivery flowrate. In this work, the compressor is not modeled and the CO_2 molar flowrate is set to a constant value, which in practice would be the set point to the compressor flow controller. This assumes that the compressor has been adequately designed to handle any flowrate set point. Removal rate around the absorber is not tightly controlled, leaving the solvent circulation rate (F_1 in Figure 2) as an available degree of freedom. The ratio of F_1 to the inlet flue gas flowrate will be set to a constant ratio, which will allow the absorber to operate near optimum conditions.

Results

The system was simulated using coal plant flue gas specified by Case 9 of NETL (2010). The control system was tested by introducing a 10% step change in the CO_2 delivery rate after one minute of steady state operation. The initial delivery rate corresponds to 50% capture. The step change and the dynamic response of the capture rate in the absorber are graphed in Figure 3. Figure 4 shows the response of the lean and rich loadings. The results of the variables that are under PI control are given in Figures 5–7.

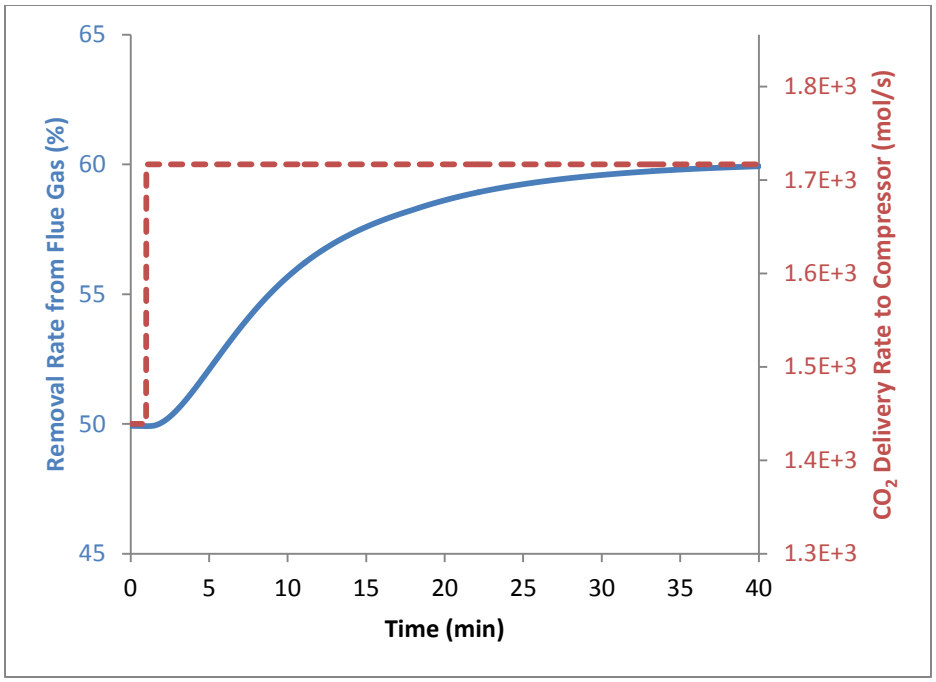

Figure 3: Slow response of the removal rate from the absorber in response to a 10% step change increase in CO_2 delivery rate at t = 1 min

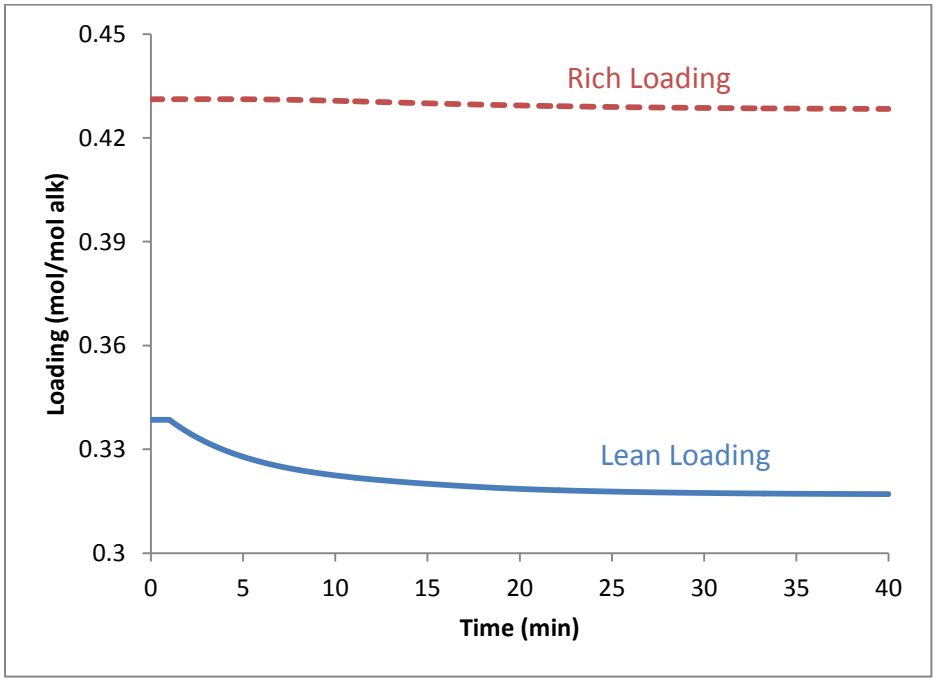

Figure 4: Slow response of loading in response to a 10% step change increase in CO_2 delivery rate at t = 1 min

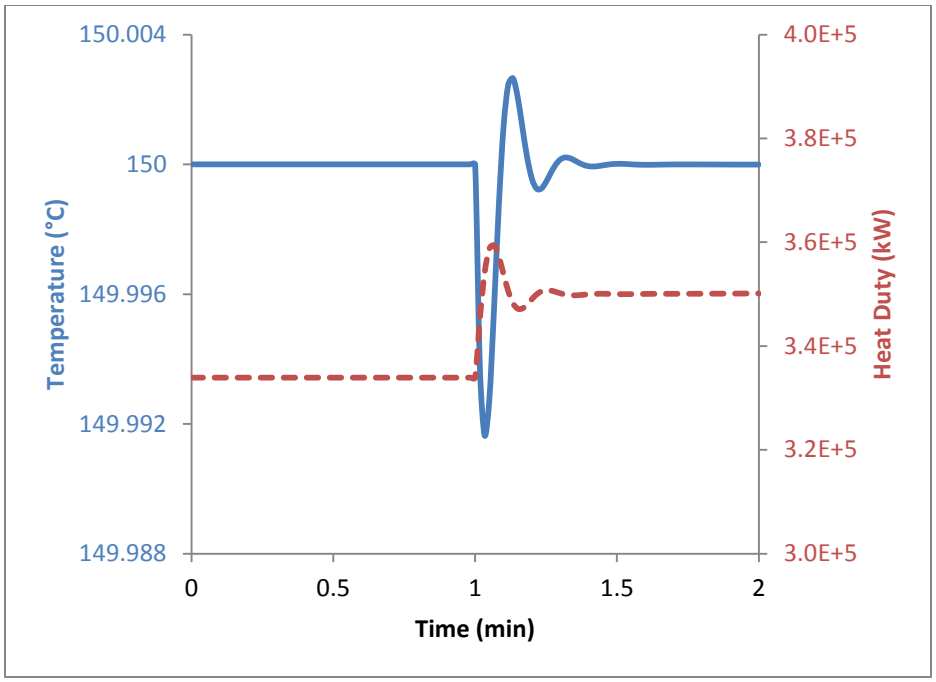

Figure 5: Closed loop flash tank temperature response to a 10% step change increase in CO_2 delivery rate at t = 1 min

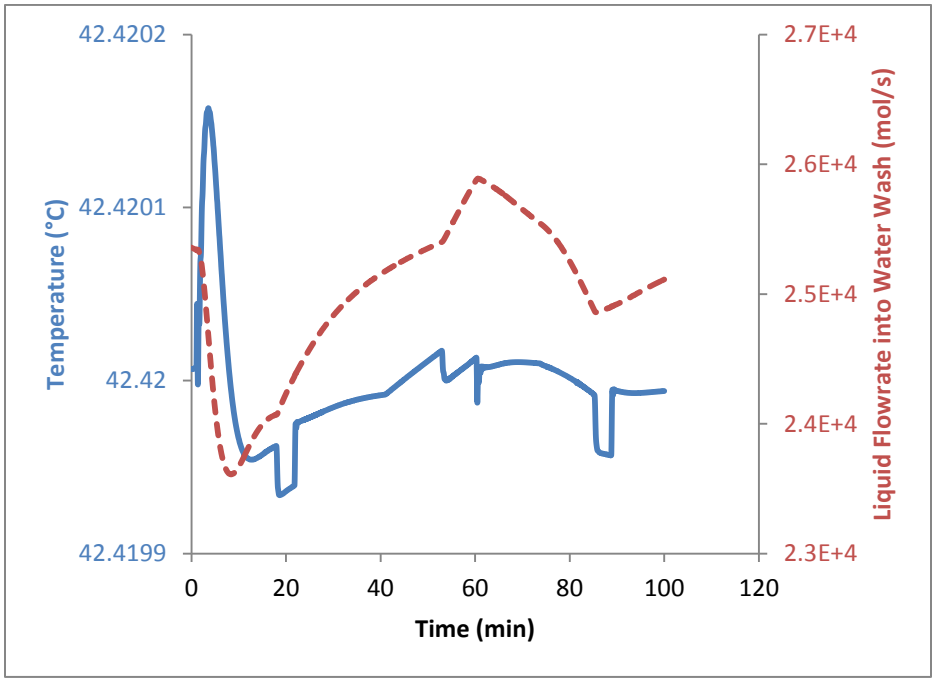

Figure 6: Closed loop water wash vapor exit temperature response to a 10% step change increase in CO_2 delivery rate at t = 1 min

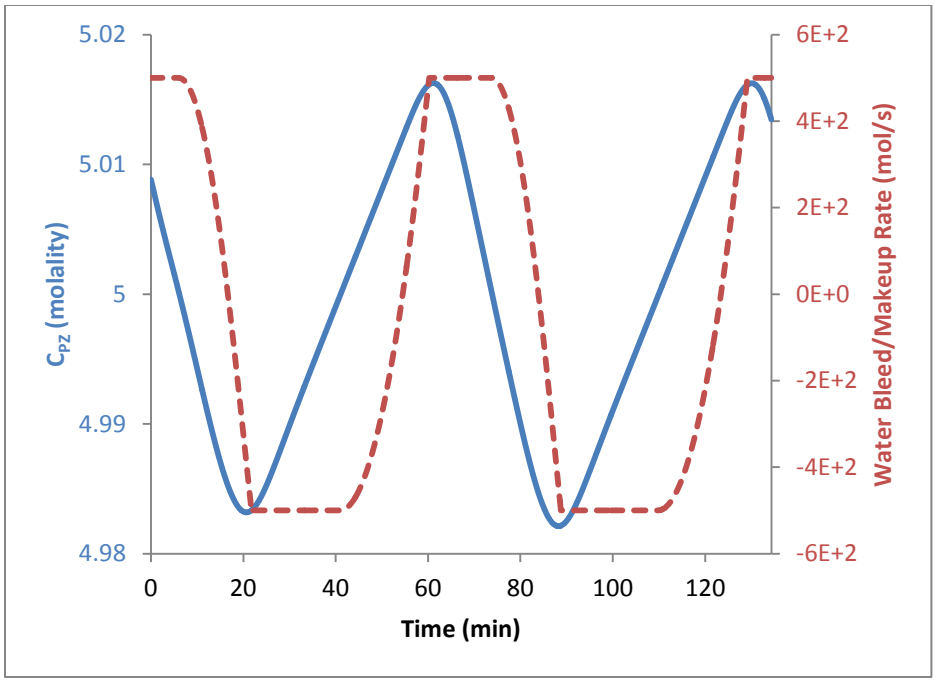

Figure 7: Closed loop PZ concentration response to a 10% step change increase in CO_2 delivery rate at t = 1 min

Discussion

There are three ways to quantify the rate of CO_2 removal, summarized in Figure 8: the difference between the inlet and outlet flue gas composition, the rich and lean loading, and the CO_2 flowrate in the flue gas to the absorber and the CO_2 flowrate to the compressor. Only one of these quantities can be independently controlled. As explained in the introduction, the CO_2 flowrate to the compressor is controlled in this work because it is desirable to maintain a constant flowrate to the pipeline. Previous research showed that controlling the other options leads to unacceptable oscillations in the process variables (Ziaii, 2012). The strategy used here gives a slow first-order response in loading to a step change in flowrate to the compressor, demonstrated in Figures 3 and 4.

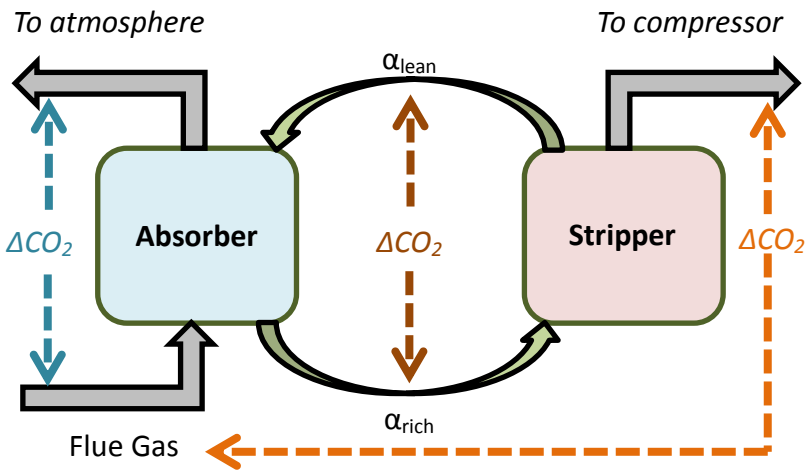

Figure 8: Alternative methods to quantify the removal rate of CO_2 for process control purposes

This strategy is stable but not optimal, because the plant spends a significant amount of time reaching steady state. Figure 9 shows the total equivalent work (excluding pump work) of the plant in response to a change in CO_2 delivery rate. The steam equivalent work calculation assumes a steam temperature of 160 °C, a sink temperature of 40 °C, and a turbine efficiency of 90%. The compressor work is calculated using the Van Wagener equation (Van Wagener, 2011). The absolute value of the work requirement is higher than expected, because no flashing is allowed in the cross exchanger. The observed trends should be the same after accounting for flashing. An advanced control strategy, such as model predictive control, could be used to bring the process to steady state faster and reduce the energy requirement.

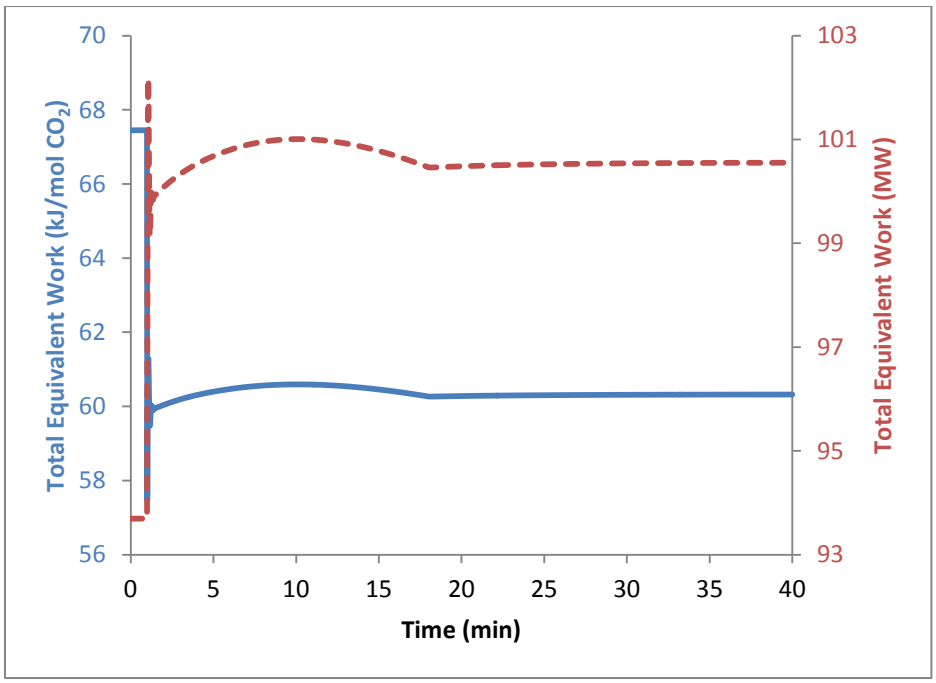

Figure 9: Total equivalent work response to a 10% step change increase in CO_2 delivery rate at t = 1 min

Flow control on the compressor could create operational challenges. An upset in process conditions may create a situation where increasing compressor speed cannot generate enough head to maintain the desired flowrate, leading to compressor surge. This is undesirable and creates a process safety issue. It is assumed the compressor is equipped with effective anti-surge control to avoid entering the surge region.

The bypass ratios remain constant at 9% and 35% for the cold and warm rich bypass flows, respectively. There is no guarantee that these ratios will be optimal in the presence of disturbances or set point changes. Attempting to control the hot side exit temperatures from CX1 and CX3 by manipulating the bypass ratios resulted in oscillations and was abandoned in this work. From an energy standpoint it is important to control these exit temperatures, because they represent work lost across the trim cooler and overhead condenser, respectively. Better tuning or an advanced control strategy is required to stably control these temperatures to their desired set point.

Conclusions

- P and PI controllers can effectively control the in-and-out intercooled absorber with advanced flash stripper when the CO_2 delivery rate to the compressor is specified.
- The total equivalent work of the plant is slow to reach its steady state in this feedback control strategy, and bypass ratios have not been optimized.
- The amine concentration controller is difficult to tune because concentration has a very slow response time.
- Using the bypass ratios to control temperatures around the cross exchangers caused instability.

Future Work

- Tune the concentration controller and attempt to eliminate the oscillations.
- Implement the bypass ratio controllers.
- Introduce noise into the measured outputs to determine the effectiveness of the control strategy under more realistic conditions.
- Test a model predictive controller that minimizes the total equivalent work of the process.

Notation

C	Concentration [mol/kg H_2O]
e	Error [varies]
F	Mole flowrate [mol/s]
K_I	Integral gain [varies]
K_P	Proportional gain [varies]
l	Level [m]
Q	Heat duty [kW]
T	Temperature [K]
x	Process variable [varies]

u	Manipulated variable [varies]
Subscripts	
sp	Set point
ss	Steady state
Superscripts	
L	Liquid phase
V	Vapor phase

References

Ceccarelli N, van Leeuwen M, Wolf T, van Leeuwen P, van der Vaart R, Maas W, Ramos A. "Flexibility of Low-CO_2 Gas Power Plants: Integration of CO_2 Capture Unit with CCGT Operation." *Energy Proc*. 2014;63:1703–1726.

Knox D. *WA Parish CO_2 Capture Project*. NRG Energy. 2014.

Lin Y-J, Madan T, Rochelle GT. "Regeneration with Rich Bypass of Aqueous Piperazine and Monoethanolamine for CO_2 Capture." *Ind Eng Chem Res*. 2014;53:4067–4074.

NETL. *Cost and Performance Baseline for Fossil Energy Plants, Volume 1: Bituminous Coal and Natural Gas to Electricity Rev. 2*. National Energy Technology Laboratory (NETL). 2010.

Spence B, Horan D, Tucker O. "The Peterhead-Goldeneye Gas Post-Combustion CCS Project." *Energy Proc*. 2014;63:6258–6266.

Stéphenne K. "Start-up of World's First Commercial Post-Combustion Coal Fired CCS Project: Contribution of Shell Cansolv to SaskPower Boundary Dam ICCS Project." *Energy Proc*. 2014;63:6106–6110.

Van Wagener DH. *Stripper Modeling for CO_2 Removal Using Monoethanolamine and Piperazine Solvents*. The University of Texas at Austin. Ph.D. Dissertation. 2011.

Walters MS, Edgar TF, Rochelle GT. "Dynamic Modeling, Validation, and Time Scale Decomposition of an Advanced Post-Combustion Amine Scrubbing Process." *Energy Proc*. 2014;63:1296–1307.

Ziaii SF. *Dynamic Modeling, Optimization, and Control of Monoethanolamine Scrubbing for CO_2 Capture*. The University of Texas at Austin. Ph.D. Dissertation. 2012.

Chapter 5: Modeling of Piperazine (PZ)-Promoted Methyldiethanolamine (MDEA) Degradation

5.1 INTRODUCTION & SCOPE

In Chapter 4, the degradation of tertiary amines in the presence of CO_2 was presented. The data presented in Chapter 4 are helpful in understanding the effects of CO_2 loading, amine concentration, and especially the amine structure on the rate of degradation on a practical level; however, they do not explicitly account for amine speciation as a function of degradation. Because of this limitation, the data presented in Chapter 4 cannot be effectively used to model and predict the rate of degradation as amine concentration, lean loading, and amine speciation are varied.

The degradation of PZ-promoted MDEA in the presence of H^+ is presented in this chapter and is modeled as a function of protonated and free amine species. Prior thermal degradation studies in the literature have not explicitly accounted for the presence of protonated species in degradation. This is representative of the initial degradation rate of PZ-promoted MDEA as it is initiated by a free amine attacking a protonated amine. A degradation pathway is proposed based on the product degradation slate and validated using rate measurements and fitting kinetic parameters to proposed rate laws. Degradation under acidified conditions is then compared to degradation in the presence of CO_2 and finally used to model degradation based on the design initial concentration and lean CO_2 loading from a process design perspective.

5.2 ACIDIFIED SOLVENT DEGRADATION OVERVIEW

Degrading solvents in the presence of H^+ instead of CO_2 can help in understanding the role that CO_2 plays in the degradation mechanism and can be used to

model the initial rate of degradation if the degradation is initiated by a free amine species attacking a protonated amine species.

Sulfuric acid is used to protonate the amines. Other strong acid alternatives, such as hydrochloric acid and nitric acid, were not used. The chloride in HCl can cause stress-corrosion cracking of the stainless steel degradation cylinders, and HNO_3 is an oxidizer and would generate degradation products that are not representative of thermal degradation.

Closmann (2011) degraded solutions of PZ-promoted MDEA under acidified conditions using methylsulfonic acid. This work established diethanolamine (DEA) and methypiperazine (1-MPZ) as major byproducts of thermal degradation of PZ-promoted MDEA.

Based on these data, Closmann proposed two different degradation pathways for PZ-promoted MDEA, which are shown in Figures 5.1 through 5.3.

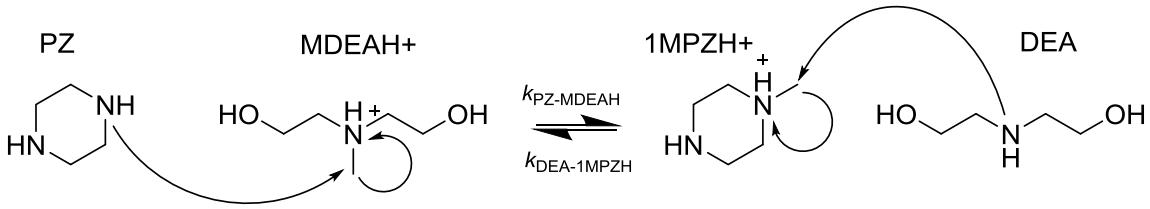

Figure 5.1: Proposed degradation mechanism of PZ-promoted MDEA to form DEA and 1-MPZ

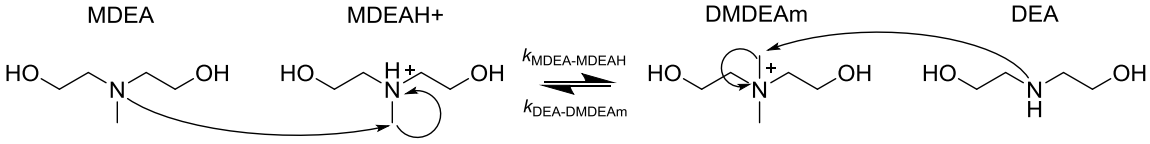

Figure 5.2: Proposed degradation mechanism of MDEA to form DEA and DMDEAm

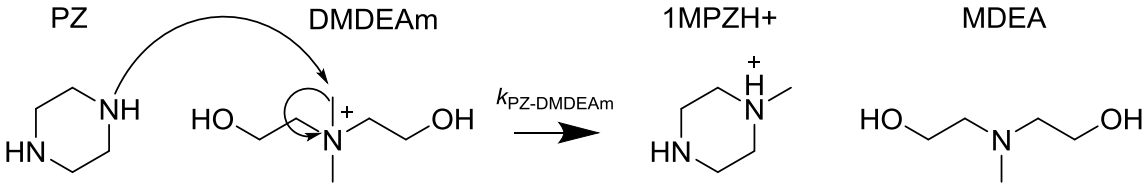

Figure 5.3: Attack of DMDEAm by PZ to form 1-MPZ and regenerate MDEA

In the first pathway, shown in Figure 5.1, free PZ can attack protonated MDEA (MDEAH+), forming DEA and 1-MPZ. In the second pathway, shown in Figure 5.2, free MDEA can attack MDEAH+ to form DEA and dimethyldiethanolammonium (DMDEAm), a quaternary amine. DMDEAm can then rapidly react with free PZ to form 1-MPZ and regenerate MDEA, shown in Figure 5.3. Both reaction mechanisms are supported by the product slate seen and by observations by Bedell that quaternary amines are present in the degradation of tertiary amines (Bedell, 2010)

5.3 PRODUCTS OBSERVED IN DEGRADATION

5.3.1 Products Seen in PZ-Promoted MDEA

The degradation products of both PZ-promoted MDEA and MDEA are shown in Tables 5.1 through 5.3, and the evolution of degradation products is shown in Figures 5.3 and 5.4.

Table 5.1: Products Observed in Degradation of PZ-Promoted MDEA

Structure	Name Abbreviation	Molecular Weight	Quantification^ & Identification
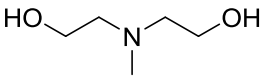	Methyldiethanolamine MDEA	119.2	Quantified – IC
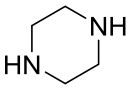	Piperazine PZ	86.1	Quantified – IC
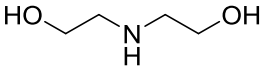	Diethanolamine DEA	105.1	Quantified – IC
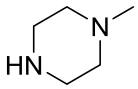	1-Methylpiperazine 1-MPZ	100.2	Quantified – IC
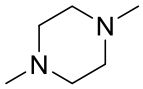	1,4-Dimethylpiperazine 1,4-DMPZ	114.2	Quantified – IC
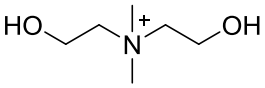	Dimethyldiethanolammonium DMDEAm	134.2	Quantified – IC*
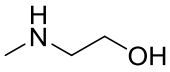	Methylaminoethanol MAE	75.1	Identified – IC
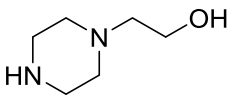	1-Hydroxyethylpiperazine 1-HePZ	131.2	Identified – IC
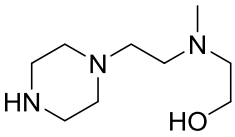	2-(methyl(2-(piperazin-1-yl)ethyl)amino)ethan-1-ol (HeMAEtPZ)	187	Estimated – IC Suspected – LCMS and based on IC elution times
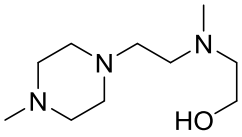	2-(methyl(2-(4-methylpiperazin-1-yl)ethyl)amino)ethan-1-ol (HeMAEtMPZ)	201	Estimated – IC* Suspected based on IC elution times

^All quantified products were also detected using LCMS.
*Only quantified for 7 m MDEA / 0.75 m PZ. Other experiments did not show quantifiable amounts of these compounds

Table 5.2: Mass Balance, PZ-Promoted MDEA, initially at 2.5 m PZ / 2.5 m MDEA and 0.14 mol H+/mol alkalinity at 150 °C after 865 hours

Amine	Concentration formed (lost) mol/kg	Mol/kg N	Mol/kg C
Parent Amines			
MDEA	(0.41)	(0.41)	(2.05)
PZ	(0.40)	(0.8)	(1.60)
Total Lost		(1.21)	(3.65)
Major Degradation Products			
DEA	0.41	0.41	1.64
1-MPZ	0.32	0.64	1.60
Total from Major Degradation Products		1.05 87%	3.24 89%
Other Degradation Products			
1,4-DMPZ	0.02	0.04	0.12
HeMAEtPZ	0.03	0.09	0.21
Total Material Balance		1.18 98%	3.57 98%

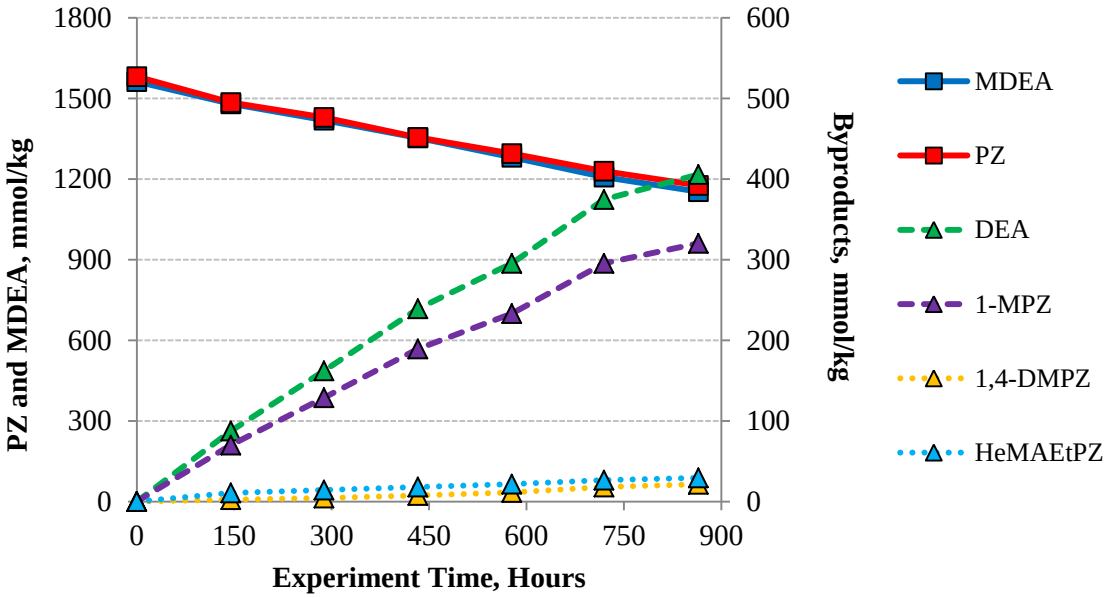

Figure 5.3: Degradation Products and Parent Amines of PZ-Promoted MDEA initially at 2.5 m PZ / 2.5 m MDEA and 0.14 mol H+/mol alkalinity at 150 °C.

Table 5.3: Mass Balance, PZ-Promoted MDEA, initially at 0.75 m PZ / 7 m MDEA and 0.11 mol H+/mol alkalinity at 165 °C after 187 hours

Amine Name	Concentration formed (lost) mol/kg	Mol/kg N	Mol/kg C
Parent Amines			
MDEA	(0.50)	(0.50)	(2.48)
PZ	(0.33)	(0.66)	(1.31)
Total Lost		(1.16)	(3.79)
Major Degradation Products			
DEA	0.42	0.42	1.66
1-MPZ	0.13	0.27	0.67
Total from Major Degradation Products		0.69 59%	2.33 61%
Other Degradation Products			
DMDEAm	0.01	0.01	0.04
1,4-DMPZ	0.07	0.14	0.41
HeMAEtPZ	0.05	0.15	0.34
HeMAEtMPZ	0.03	0.08	0.22
Total Material Balance		1.07 92%	3.34 88%

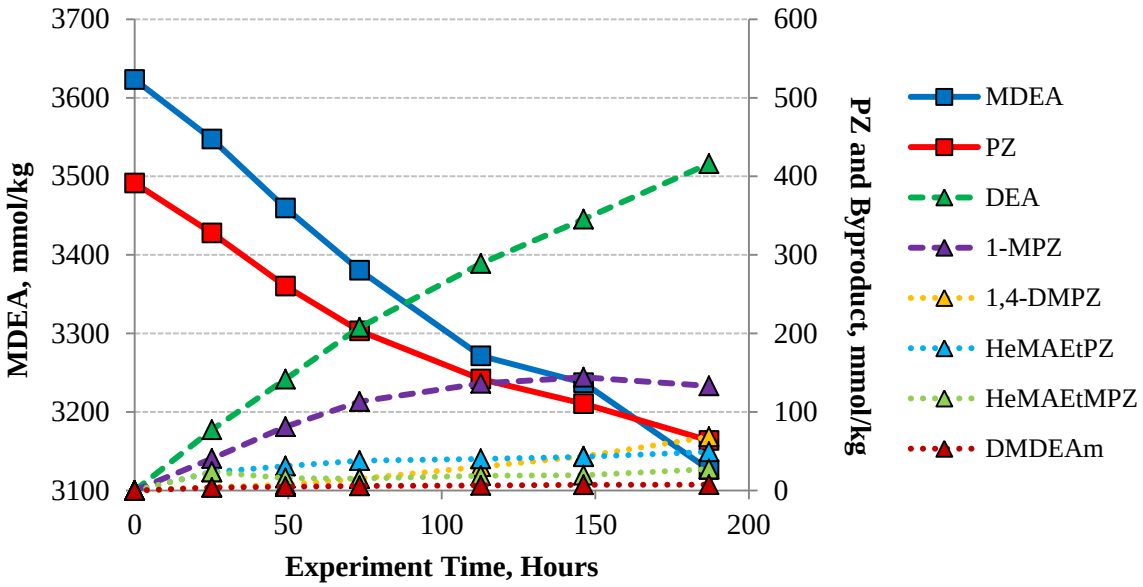

Figure 5.4: Degradation Products and Parent Amines of 0.75 m PZ / 7 m MDEA and 0.11 mol H+/mol alkalinity at 150 °C

The data from this study confirm Closmann's findings that DEA and 1-MPZ are the dominant degradation products of acidified PZ-promoted MDEA. These data strongly suggest that the interaction between the PZ and methyl groups on the tertiary amine is dominant. Additionally, the interaction between PZ and the carbon alpha to the hydroxyl group is minor. The quaternary amine was only able to be detected using MS and quantified using cation chromatography in experiments with an initial molar ratio of MDEA to PZ greater than 9. Other minor degradation products, such as dimethylpiperazine (1,4-DMPZ), were detected using cation chromatography and MS in the small quantities quantified. Minor PZ derivatives, such as 2-(methyl(2-(piperazin-1-yl)ethyl)amino)ethan-1-ol (MAHeEtPZ) were detected using MS and their concentrations were estimated based on their elution times using cation chromatography (IC) and the calibration curve of PZ. The formation of these products is consistent with free PZ attacking a carbon alpha to the hydroxyl function of MDEA. Their relative rates of reaction are slower than the formation of DEA and 1-MPZ, likely due to the poor leaving group ability of –OH compared to protonated amines (Carey 2010). An analog of MAHEtPZ, 2-(methyl(2-(4-methylpiperazin-1-yl)ethyl)amino)ethan-1-ol, or MAHEtMPZ, was suspected to be present in solution. The method to quantify MAHEtPZ is similar to the one used by Davis to estimate the concentration of byproducts for which standards are unavailable (Davis, 2009).

Closmann (2011) discussed the possibility of PZ attacking the hydroxyethyl group of MDEAH+ to form 1-hydroxyethylpiperazine (1-HePZ) and methylaminoethanol (MAE). Both of these compounds were detected using cation chromatography and MS, but their concentrations were too low to be quantified. 1-HePZ had a concentration less than 0.01 mol/kg in degraded PZ-promoted MDEA initially at 2.5 m PZ / 2.5 m MDEA and 0.14 mol H+/mol alkalinity after 650 hours at 150 °C. The peak area ratio between

DEA and MAE was approximately 34:1 in the same experiment. These results strongly suggest that the rate at which bulkier substituent groups are attacked by nucleophiles is significantly less than methyl groups. These observations have been suggested in the literature (Lichtfers, 2005; Anslyn, 2006) and will be expanded upon in Chapter 6.

The identified and quantified degradation products account for 98% of the lost amine in PZ-promoted MDEA at 2.5 m PZ / 2.5 m MDEA and 0.14 mol H+/mol alkalinity at 150 °C and for 90% in PZ-promoted MDEA at 0.75 m PZ / 7 m MDEA and 0.11 mol H+/mol alkalinity at 165 °C. The exclusion of MAE and 1-HePZ, other minor degradation products such as higher polyamines formed by S_N2 substitution with the –OH group, as well as inaccuracies in the quantification of MHEtPZ and MHEtMPZ might represent the loss of nitrogen and carbon that was unable to be quantified.

5.3.2 Products of MDEA Degradation

Tables 5.4 and 5.5 summarize the degradation products and material balance with in acidified MDEA degradation; these data are plotted in Figure 5.5. DEA and DMDEAm were the dominant degradation products and appeared to reach a thermodynamic equilibrium after about 500 hours of experiment time. Several other tertiary amines and their associated quaternary amines were detected using mass spectrometry and cation chromatography. The elution times of the tertiary amines were nearly the same as MDEA and thus could not be accurately quantified. The peak area ratio between DEA and MAE was 60:1, and the peak area ratio between MDEA and DMAE was 200:1. Low resolution MS indicated that the relative abundance of TEA and THeMAm was an order of magnitude less than DMAE and choline. Additional products whose elution times were consistent with diamines were detected using cation

chromatography, suggesting that MDEA and/or its degradation products participated in amine attack on carbons alpha to hydroxyl groups to form diamines.

Table 5.1: Products observed in MDEA Degradation

Structure	Name Abbreviation	Molecular Weight	Quantification & Identification
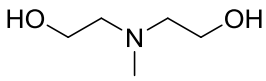	Methyldiethanolamine MDEA	119.2	Quantified – IC
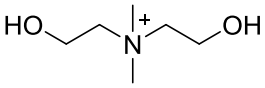	Dimethyldiethanolammonium DMDEAm	134.2	Quantified – IC
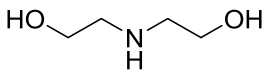	Diethanolamine DEA	105.1	Quantified – IC
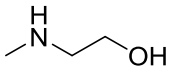	Methylaminoethanol MAE	75.1	Identified – IC
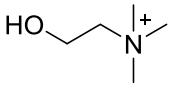	Choline TMHeAm	104.2	Identified – IC
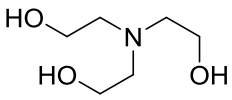	Triethanolamine TEA	149.1	Suspected – LCMS
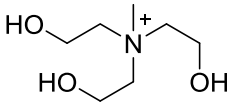	Tris(hydroxyethyl)methylammonium THeMAm	164	Suspected – LCMS
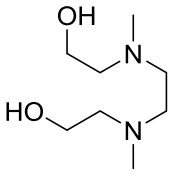	2,2'-(ethane-1,2-diylbis(methylazanediyl))-bis(ethan-1-ol) HeMAEtAHeM	176	Suspected – LCMS
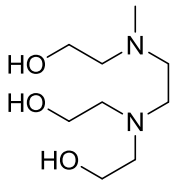	2,2'-((2-((2-hydroxyethyl)(methyl)amino)ethyl)-azanediyl)bis(ethan-1-ol) HeMAEtADHe	206	Suspected – LCMS

Table 5.5: Mass Balance, MDEA, initially at 5 m MDEA and 0.20 mol H+/mol alkalinity at 150 °C

	After 143 hours			After 647 hours		
Amine Name	Concentration formed (lost) mol/kg	Mol/kg N	Mol/kg C	Concentration formed (lost) mol/kg	Mol/kg N	Mol/kg C
Parent Amines						
MDEA	(0.18)	(0.18)	(0.90)	(0.40)	(0.40)	(2.00)
Total Lost		(0.18)	(0.90)		(0.40)	(2.00)
Major Degradation Products						
DEA	0.08	0.08	0.32	0.12	0.12	0.49
DMDEAm	0.08	0.08	0.46	0.15	0.15	0.87
Total from Major Degradation Products		0.15 88%	0.78 87%		0.27 68%	1.36 68%

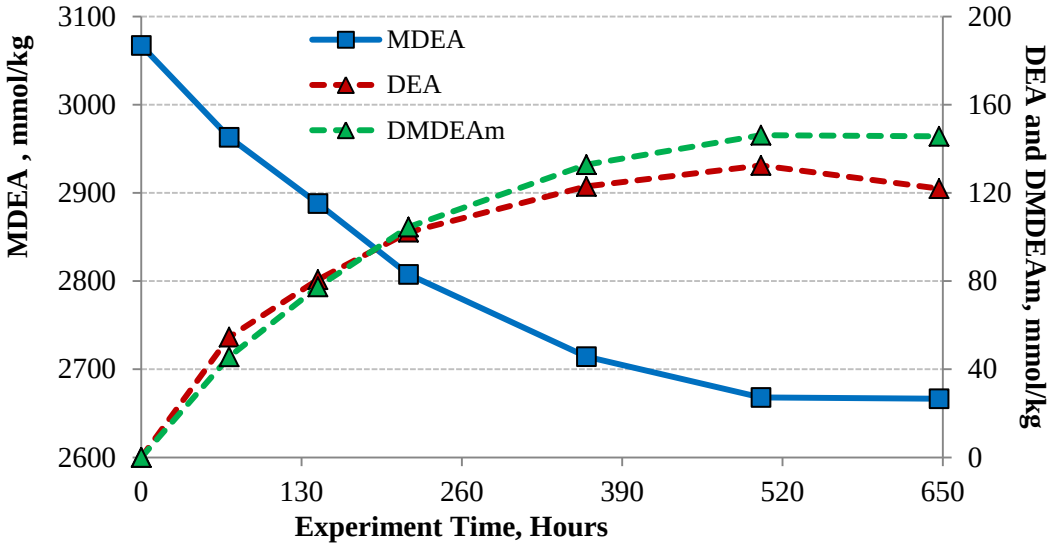

Figure 5.5: Parent Amine and Degradation Products of MDEA initially at 5 m MDEA and 0.2 mol H+/mol alkalinity at 150 °C

DMDEAm was proposed as an intermediate degradation product by Chakma (Chakma, 1988) but was unable to be found in degraded solutions by both Chakma and Lepaumier (Lepaumier, 2010). Ethylene glycol, a product that Lepaumier and Chakma both identified in MDEA degradation, was not detected using mass spectrometry in this

study. Lepaumier and Chakma both used a gas chromatograph to analyze for degradation compounds. Quaternary amines with at least one hydroxyl group will, upon boiling, decompose to form a tertiary amine and the corresponding glycol from the hydroxyl group (Mathews 1916). If DMDEAm were to be boiled, DMAE and ethylene glycol will be formed, and it is likely that this is what was observed in previous studies of MDEA degradation.

5.4 MODELING KINETICS OF PZ-PROMOTED MDEA AND MDEA DEGRADATION

5.4.1 Methodology

Amine degradation is modeled using the mechanisms shown in Figures 5.1 through 5.3, all of which involve reactions between free and charged amine species. A pKa model was developed in Matlab R2013a to determine the ratio between protonated amine species and free amine species based on the concentration of total measured on the IC and the concentration of acid measured gravimetrically. This model assumes that the species form an ideal solution with an activity coefficient equal to 1.

pKa data were readily available for MDEA, PZ, DEA, 1-MPZ, and 1,4-DMPZ; the data were regressed and extrapolated from 135 to 165 °C to match experimental conditions (Khalili 2009, Simond 2012). pKa data were not readily available for MHEtPZ and MHEtMPZ; the pKa of these species were estimated computationally using MarvinSketch (ChemAxon). Only the first pKa and the first and second pKa values were used to estimate protonated amine concentration for diamines and triamines, respectively, as the solution pH is sufficiently high that the diprotonated diamines and triprotonated triamines are negligible. This assumption has been made in numerous thermodynamic models (Frailie 2014, Aspen Technology 2011) that model CO_2 absorption processes. The regressed values of the pKa are shown in Table 5.6.

Table 5.6: Regressed pKa values used to estimate concentrations of free and protonated amine species

Structure Abbreviation	pKa 25 °C	pKa 135 °C	pKa 150 °C	pKa 165 °C
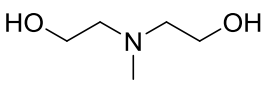 MDEA	8.53	6.9	6.74	6.59
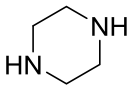 PZ	pKa1: 9.73 pKa2: 5.35	7.73	7.54	7.36
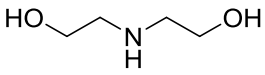 DEA	8.88	6.89	6.70	6.53
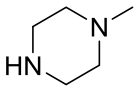 1-MPZ	pKa1: 9.14 pKa2: 4.63	7.43	7.27	7.11
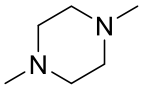 1,4-DMPZ	pKa1: 8.38 pKa2: 3.81	6.51	6.33	6.16
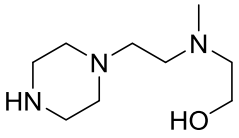 HeMAEtPZ	pKa1: 9.44 pKa2: 8.62 pKa3: 1.50	pKa1: 7.44 pKa2: 6.98	pKa1: 7.25 pKa2: 6.82	pKa1: 7.07 pKa2: 6.68
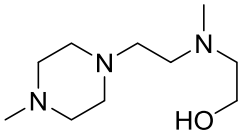 HeMAEtMPZ	pKa1: 9.02 pKa2: 8.00 pKa3: 0.03	pKa1: 7.38 pKa2: 6.29	pKa1: 7.22 pKa2: 6.13	pKa1: 7.07 pKa2: 5.97

Note: pKa1 and pKa2 for HeMAEtPZ were assumed to vary the same as PZ and MDEA, respectively, and pKa1 and pKa2 for HeMAEtMPZ were assumed to vary the same as MDEA and 1-MPZ, respectively, as data were extrapolated to higher temperatures.

The rate loss of total amine was numerically estimated using a finite difference method (Fogler 2005). This allowed rate constants and activation energies to be estimated by regressing the rate data with the concentration data using a nonlinear regression solver. The XLSTAT nonlinear solver package (AddInSoft, 2014) was used to regress the kinetic parameters.

The following equations were used to model the degradation of PZ-promoted MDEA and MDEA. The units of each amine species is in mol/kg.

$$\frac{d[\mathrm{PZ}_{\mathrm{total}}]}{dt} = -k_{\mathrm{PZ-MDEAH}} * [\mathrm{PZ}_{\mathrm{free}}] * [\mathrm{MDEAH}^{+}] .. + k_{\mathrm{DEA-1MPZH}} * [\mathrm{DEA}_{\mathrm{free}}] * [\mathrm{1MPZH}^{+}] .. - k_{\mathrm{PZ-DMDEAm}} * [\mathrm{PZ}_{\mathrm{free}}] \quad \text{Eq. 5.1}$$

$$\frac{d[\mathrm{MDEA}_{\mathrm{total}}]}{dt} = -k_{\mathrm{PZ-MDEAH}} * [\mathrm{PZ}_{\mathrm{free}}] * [\mathrm{MDEAH}^{+}] .. - k_{\mathrm{MDEA-MDEAH}} * [\mathrm{MDEA}_{\mathrm{free}}] * [\mathit{MDEAH}^{+}] + k_{\mathrm{DEA-1MPZH}} * [\mathrm{DEA}_{\mathrm{free}}] * [\mathrm{1MPZH}^{+}] .. + k_{\mathrm{MDEA-DMDEAm}} * [\mathrm{DMDEAm}] * [\mathrm{DEA}_{\mathrm{free}}] + k_{\mathrm{PZ-DMDEAm}} * [\mathrm{PZ}_{\mathrm{free}}] \quad \text{Eq. 5.2}$$

Each rate is assumed to follow Arrhenius behavior, which is shown in Eq. 5.3.

$$k = A * \exp\left(\frac{-E_A}{R * T}\right) \quad \text{Eq. 5.3}$$

In Eq. 5.1, $k_{\mathrm{PZ\text{-}MDEAH}}$ and $k_{\mathrm{DEA\text{-}1MPZH}}$are the forward and reverse rates of PZ attacking protonated MDEA, which is depicted in Figure 5.1. $k_{\mathrm{PZ\text{-}DMDEAm}}$ is the pseudo first-order rate constant where free PZ attacks DMDEAm. The inability to quantify DMDEAm in the majority of the degraded PZ-promoted MDEA solutions does not preclude its presence in small quantities.

Eq. 5.2 is the same as Eq.5.1 with the addition of two additional terms: $k_{MDEA\text{-}MDEAH}$ and $k_{DEA\text{-}DMDEAm}$ are the forward and reverse rates of free MDEA attacking a protonated MDEA, which is depicted in Figure 5.2. $k_{PZ\text{-}DMDEAm}$ is the pseudo first-order rate constant in which free PZ attacks DMDEAm and is positive because it leads to MDEA formation. $k_{PZ\text{-}MDEAH}$, k $k_{DEA\text{-}1MPZH}$, and $k_{PZ\text{-}DMDEAm}$ will be equal to zero in Eq. 5.2 in the absence of PZ.

In Eq. 5.3, A is the pre-exponential factor, E_A is the activation energy in J/mol, R is the gas constant and is equal to 8.314 J/(mol*K), and T is the temperature in Kelvin. The model regressed A and E_A for each rate. The model rate constants were evaluated using Eq. 5.3.

Interactions between free and protonated PZ and free and protonated 1-MPZ were neglected. Data from Freeman (Freeman, 2011) indicated that concentrated PZ as well as a blend of 1-MPZ / PZ were found to be an order of magnitude more stable than PZ-promoted MDEA in the presence of CO_2; as a result, any S_N2 interactions between the two species will be significantly slower than the interactions between PZ and MDEA.

5.4.2 Modeling Results: PZ-Promoted MDEA Degradation

Table 5.7 shows the regressed values of the kinetic rate constants from the model. Data from three different regression cases are presented. In Case A, only $k_{PZ\text{-}MDEAH}$ was considered and only for experiments whose initial PZ concentration was equal to the MDEA concentration. Cases B and C used data from all PZ-promoted MDEA experiments. Case B only considered the forward rates $k_{PZ\text{-}MDEAH}$ and $k_{MDEA\text{-}MDEAH}$, whereas Case C considered all forward and reverse rates. The regression results from Case C are shown in Figure 5.8 as a parity plot.

The acid loading of each experiment was chosen to approximate the operational lean loading from plants designed to remove CO_2 from coal-derived flue gas, and total parent amine degradation was kept to a maximum of 25% loss to ensure that the initial degradation rate would be modeled with reasonable accuracy.

Table 5.7: Regressed Kinetic Parameters for PZ-Promoted MDEA

	Case A	Case B	Case C
Conditions:	1.6 mol/kg PZ 1.6 mol/kg MDEA 0.14 mol H+/mol alk 135 °C – 165 °C	0.4 - 1.6 mol/kg PZ 1.6 – 3.6 mol/kg MDEA 0.09 - 0.14 mol H+/mol alk 135 °C – 165 °C	
Data Points	15	35	
Second-Order Rate Constant at 150 °C kg mol^{-1} s^{-1}*10^6			
$k_{PZ\text{-}MDEAH}$	1.64	1.48	1.48
$k_{MDEA\text{-}MDEAH}$	--	0.12	0.12
$k_{DEA\text{-}1MPZH}$	--	--	0
$k_{MDEA\text{-}DMDEAm}$	--	--	0
$k_{PZ\text{-}DMDEAm}$ (s^{-1})	--	--	0.02
Activation Energy kJ mol^{-1}			
$E_{APZ\text{-}MDEAH}$	131	143	141
$E_{AMDEA\text{-}MDEAH}$	--	124	128
$E_{ADEA\text{-}1MPZH}$	--	--	n/a
$E_{AMDEA\text{-}DMDEAm}$	--	--	n/a
$E_{APZ\text{-}DMDEAm}$	--	--	128
Correlation Coefficient	0.95	0.71	0.72

The regression results suggest that free PZ attacking a protonated MDEA is the dominant degradation route in PZ-promoted MDEA degradation. The MDEA-MDEA degradation pathway is not as dominant and is an order of magnitude slower than the PZ pathway. Addition of the reverse reactions does not appreciably change the forward rate constants at the conditions of the experiment; $k_{PZ\text{-}MDEAH}$ and $k_{MDEA\text{-}MDEAH}$ vary by about

15% as additional rate parameters and experimental conditions are added to the model, and the correlation coefficient of the model improves only slightly. The model overpredicts the degradation of PZ at low ratios of PZ / MDEA and is likely due to the estimation and extrapolation of the concentration and pKa of the triamine products, which comprised 20% of the degradation product balance at an initial concentration of 0.4 mol/kg PZ and 1.6 mol/kg MDEA. The reverse reactions are inconsequential in determining reaction rates at all experimental conditions.

The ratio between $k_{PZ\text{-}MDEAH}$ and $k_{MDEA\text{-}MDEAH}$ was found to be between 12 and 13. Bedell (2010) investigated the rate of tetramethylammonium chloride (TMACl) disappearance using PZ and MDEA as nucleophiles; Bedell found that the ratio of the second-order rate constants between PZ and TMACl and MDEA and TMACl was 14 and is close to the ratio observed in this study.

The regression results from Case C were used to estimate the rate of another experiment whose data set was not used to regress the parameters of the kinetic model. The experiment was run at an initial condition of 2.5 m PZ / 2.5 m MDEA and 0.14 mol H+/mol alk at 165 °C. The data are shown in Figure 5.9. Data for another experiment at an initial condition of 2.5 m PZ / 2.5 m MDEA and 0.15 mol H+/mol alk added as hydrochloric acid, a monovalent strong acid, instead of sulfuric acid as the proton source is shown in Figure 5.10. The model prediction assumes that only DEA and 1-MPZ are present as byproducts.

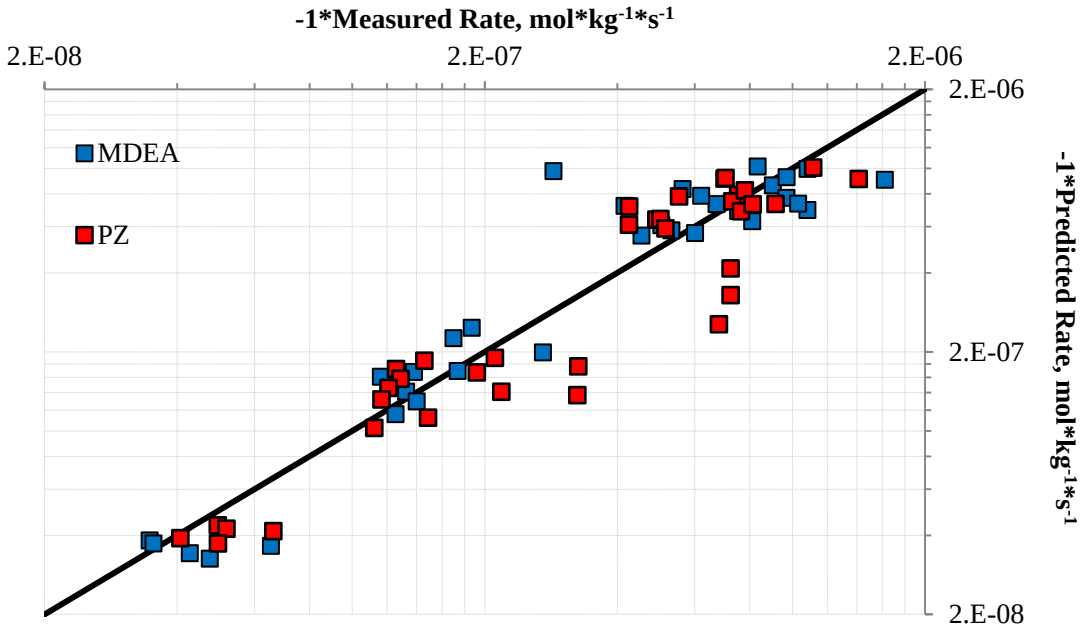

Figure 5.8: Parity Plot Showing Regression Results for Case C

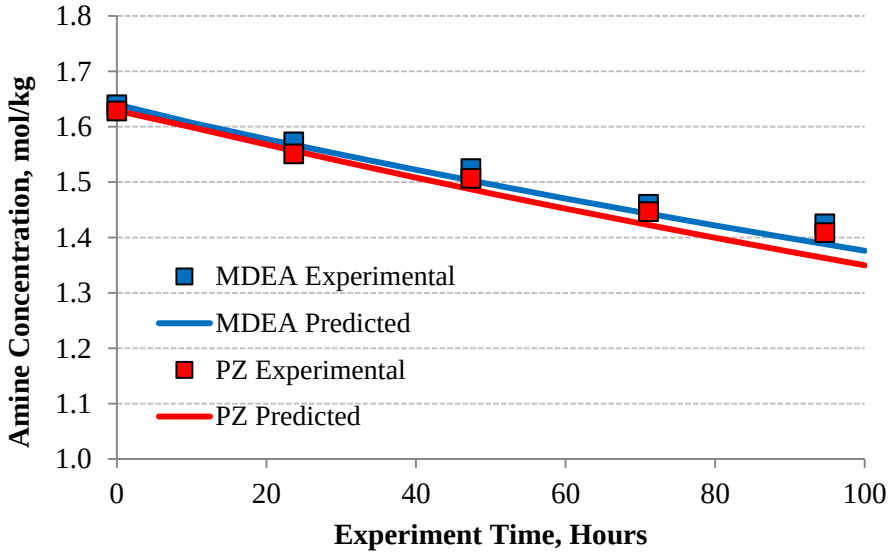

Figure 5.9: Model Prediction and experimental data for the degradation of 2.5 m PZ / 2.5 m MDEA with 0.14 mol H+/mol alk as H_2SO_4 at 165 °C

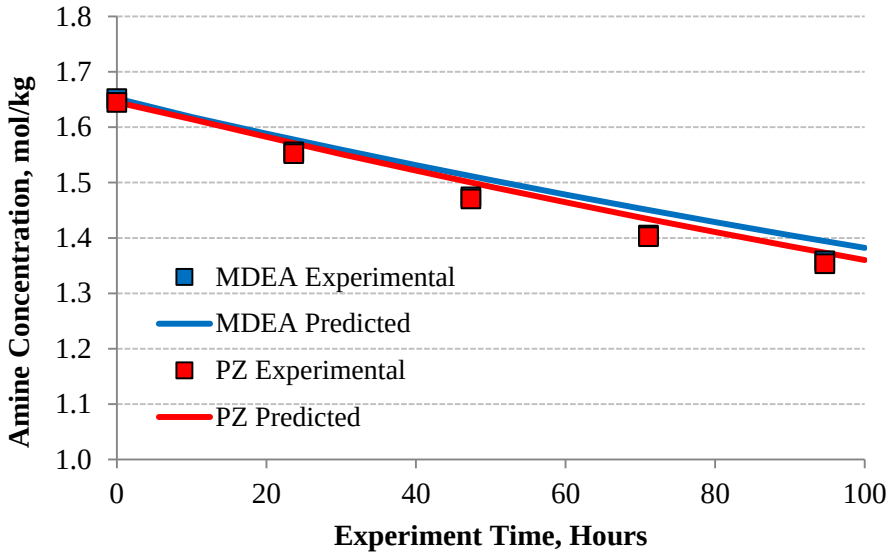

Figure 5.10: Model Prediction and experimental data for the degradation of 2.5 m PZ / 2.5 m MDEA with 0.14 mol H+/mol alk as HCl at 165 °C

The kinetic model overpredicts the degradation rate for 2.5 m PZ / 2.5 m MDEA and 0.14 mol H+/mol alkalinity at 165 °C by about 20% and underpredicts degradation for 2.5 m PZ / 2.5 m MDEA and 0.15 mol H+/mol alkalinity added as hydrochloric acid at 165 °C by about 25%. The measured concentration of PZ and MDEA is within 5% of the predicted model values for both sets of data. The model begins to deviate from the experimental results as the total degradation increases and is likely due to the omission of minor degradation products present in solution in the model and the exclusion of other interactions between PZ, MDEA, and other degradation products. The model prediction also indicates that the acid counterion does not appreciably change the solution activity to affect rate.

5.4.3 Modeling Results: MDEA Degradation

Table 5.9 shows the rate constants of the regressed data set for MDEA degradation. Eq. 5.2 was used to regress kinetic parameters for these experiments. Figure 5.11 shows the results as a parity plot.

Table 5.9: Regressed Kinetic Parameters for MDEA

Conditions:	3.0 mol/kg MDEA 0.20 mol H+/mol alk 135 °C – 165 °C
Data Points	15
Second-Order Rate Constant at 150 °C kg mol^{-1} s^{-1}*10^{6}	
$k_{\text{MDEA-MDEAH}}$	0.30
$k_{\text{MDEA-DMDEAm}}$	12
Activation Energy kJ mol^{-1}	
E_{A1}	117
E_{A2}	121
Correlation Coefficient	0.93

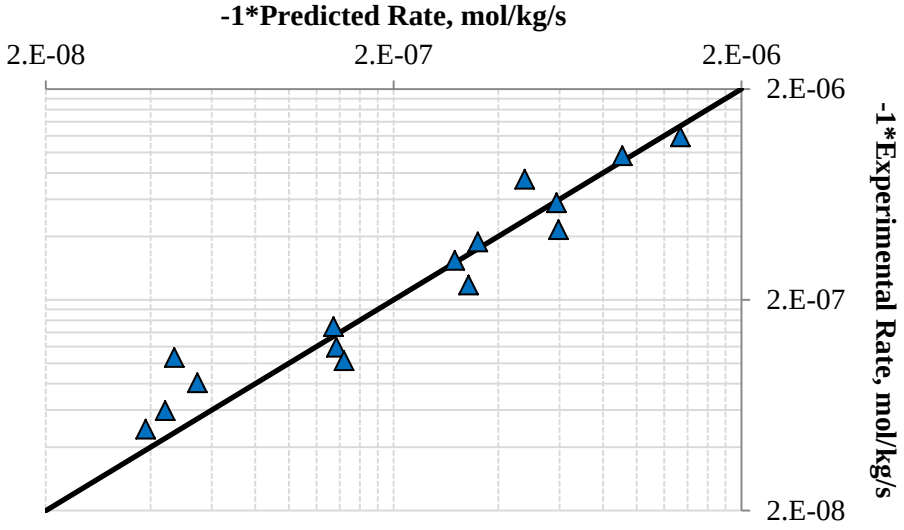

Figure 5.11: Parity Plot of MDEA Degradation Results

The forward rate parameter $k_{MDEA\text{-}MDEAH}$ is about two and a half times greater in MDEA solutions than the parameter regressed with the PZ-promoted MDEA experiments. The MDEA degradation experiments were run at a higher acid loading (0.2 mol H+/mol alkalinity) than the PZ-promoted MDEA experiments. It is possible that the higher solvent loading, lower concentration of free amino groups, and lack of PZ made the MDEA solvent more aprotic than PZ-promoted MDEA at experimental conditions; increased solvent aproticity can lead to greater S_N2 reaction rate. The reverse rate parameter $k_{DEA\text{-}DMDEAm}$ is about 40 times as fast as $k_{MDEA\text{-}MDEAH}$. DEA is known to be a weaker nucleophile than PZ due to its lower pKa value, and the high ratio of $k_{DEA\text{-}DMDEAm}$ to $k_{MDEA\text{-}MDEAH}$ indicates that the quaternary amine is a better leaving group than protonated tertiary amines.

5.4.4 Comparison of Initial Rates of PZ-Promoted MDEA Degradation in H+ Loaded Solutions and CO_2-Loaded Solutions

The acid-loaded experiments are useful in validating the initial degradation pathway of PZ-promoted MDEA and understanding the degradation rate as a function of amine speciation. However, the data need to be compared and reconciled against degradation of CO_2-loaded PZ-promoted MDEA to be used to model thermal degradation from a process design perspective.

Table 5.9 lists the activation energy of thermal degradation of PZ-promoted MDEA loaded either with H+ or CO_2 at conditions approximating operating lean loading.

Table 5.9: Activation Energy of Thermal Degradation of PZ-Promoted MDEA Solvents at Lean Loading

Solvent Composition	E_A PZ kJ/mol	E_A MDEA kJ/mol
0.75 – 2.5 m PZ 2.5 – 7 m MDEA 0.11 – 0.14 mol H+/mol alk	141 (Case C, E_{A1})	
2 m PZ 7 m MDEA 0.12 mol CO_2/mol alk	147	140
5 m PZ 5 m MDEA 0.24 mol CO_2/mol alk	139	140

The data indicate that the model activation energy is generally similar to the activation energies seen in CO_2-loaded degradation and shows good agreement with the value predicted by the kinetic model.

Table 5.10 shows the speciation of major species present in CO_2-loaded PZ-promoted MDEA solvents at the temperature encountered in the amine desorber. The "Independence" (Frailie, 2014) thermodynamic framework, regressed using AspenPlus 7.3 (AspenTech, 2011), was used to determine the concentration and quantity of free amine, protonated amine, and amine carbamate at the given solvent loading. The speciation data from the model are presented in Table 5.10.

Table 5.10: Concentration (mol/kg) of Species Present in Loaded CO_2 Solutions at 150 °C with a Lean Loading Corresponding to 500 Pa CO_2 at 40 °C

Structure	Name	7 m MDEA 2 m PZ	5 m MDEA 5 m PZ
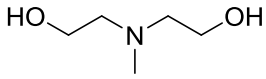	MDEA	3.15	2.02
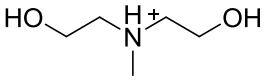	MDEAH+	0.23	0.28
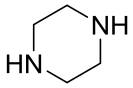	PZ	0.62	0.56
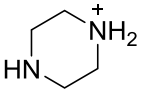	PZH+	0.19	0.53
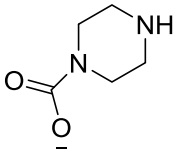	PZ Carbamate	0.20	0.54
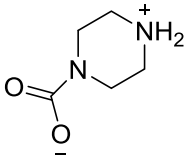	PZ Zwitterion	0.27	0.64
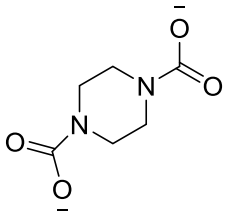	PZ Dicarbamate	0.01	0.02
HCO_3^-	Bicarbonate	0.19	0.21
CO_3^{2-}	Carbonate	0.01	0.01
CO_2	Physically Absorbed CO_2	0.03	0.03

The speciation data indicate that, in addition to free PZ, protonated PZ, and PZ-carbamate, the dicarbamate salt as well as the PZ zwitterion is present. This suggests that the PZ carbamate salt can function as a nucleophile and thus participate in the degradation pathway. The pKa of the PZ carbamate was found by Bishnoi (Bishnoi, 2000) to be about 9.14. This value is between that of PZ and morpholine, which has a pKa of about 8.50 (Haynes, Ed., 2014). Davis (Davis, 2009) found that morpholine functioned as a strong nucleophile and has a similar degradation rate to PZ in the degradation of CO_2-loaded monoethanolamine (MEA) blended either with PZ or morpholine.

Both of the mechanisms shown in Figures 5.1 and 5.2 include DEA as a degradation product. DEA can form a carbamate and then form an oxazolidinone via the carbamate polymerization pathway. The oxazolidinone can then react with PZ. Data shown in Chapter 4 indicate that DEA concentration is nearly constant in CO_2-loaded degradation and behaves as a reactive steady-state intermediate. Data shown in Section 5.4.3 indicate that the quaternary amine salt is much more reactive than other protonated amine species, and thus it too can behave as a steady state intermediate.

The initial acid rate measurements need to consider these phenomena to properly account for the initial degradation rate in systems loaded with CO_2. The free PZ concentration in Eq. 5.1 and Eq. 5.2 can been modified to reflect the sum of PZ and PZ carbamate. The initial rate of PZ degradation can be assumed to be twice as fast as MDEA degradation because one equivalent of MDEA can, if byproducts are accounted for, react with two equivalents of PZ. Initial rate measurements of PZ-promoted MDEA under CO_2-loaded conditions indicated that this ratio was 1.85. Thus, the initial rate of PZ-promoted MDEA degradation can be corrected using the following two terms:

$$\frac{d[\mathrm{MDEA}_{\ \mathrm{total}}]}{dt} = -k_{\mathrm{PZ-MDEAH}} * [\mathrm{PZ}_{\ \mathrm{free}} + \mathrm{PZCOO}^{\ -}] * [\mathrm{MDEAH}^{\ +}] .. \\ -k_{\mathrm{MDEA-MDEAH}} * [\mathrm{MDEA}_{\ \mathrm{free}}] * [MDEAH^{\ +}] \quad \text{Eq. 5.4}$$

$$\frac{d[\mathrm{PZ}_{\ \mathrm{total}}]}{dt} = 2 * \frac{d[\mathrm{MDEA}_{\ \mathrm{total}}]}{dt} \quad \text{Eq. 5.5}$$

Data directly comparing the CO_2-loaded experimental rates approximated using 0^{th} order kinetics whose average rate was taken over 100-120 hours with the initial rates predicted by the kinetic model at 150 °C is shown in Table 5.11.

Table 5.11: Comparison of Corrected Model Results to Experimental CO_2-Loaded Degradation Data at 150 °C

Solvent Composition	PZ loss mol/kg/h*10^{-3} Model	PZ loss mol/kg/h*10^{-3} Experimental	MDEA loss mol/kg/h*10^{-3} Model	MDEA loss mol/kg/h*10^{-3} Experimental
2 m PZ 7 m MDEA 0.12 mol CO_2/mol alk	2.2	2.3±0.2	1.1	1.4±0.6
5 m PZ 5 m MDEA 0.24 mol CO_2/mol alk	3.6	3.0±1	1.8	2.2±1

With the corrections added, the kinetic model does a reasonable job predicting the initial loss rate of both MDEA and PZ to ±20%. The predicted values are within the 95% confidence limit of the regressed 0^{th} order rate.

5.5 PROCESS DESIGN MODELING

If the corrections presented section 5.4.4 are incorporated into the kinetic model, the data from the model can be extended and used in process design problems to predict the thermal degradation rate as a function of design lean loading, design starting amine

concentration, and design stripping temperature. These predictions are helpful in setting process envelopes, such as the maximum stripping temperature, based on the plant design specifications for all CO_2 capture and removal processes. Oxidative degradation will have to be taken into account to understand the net overall degradation rate for CO_2 removal from sources with oxygen present such as the flue gas from power plants. The thermal degradation rate, however, can serve as a representative overall degradation rate for processes that remove CO_2 and H_2S from high pressure streams, such as liquefied natural gas and synthesis gas treating, due to the absence of other dominating degradation pathways from these sources.

The "Independence" framework was used to determine the concentration of free amine, protonated amine, and PZ carbamate as a function of lean loading, starting concentration, and stripping temperature. The process design specifications used for the model in this study are presented in Table 5.12.

Table 5.12: Process Design Specifications Used in Model

Parameter	Value
Lean Loading	100 Pa CO_2 500 Pa CO_2 (at 40 °C)
Rich Loading	5000 Pa CO_2 (at 40 °C)
Residence Time	30 minutes
Residence Time in Sump (treated as CSTR)	10 minutes
Stripping Temperature	105 °C, 120 °C, 135 °C
Weight Percent Amine in solvent, CO_2-free basis	45%

Figure 5.12 shows the predicted total degradation rate in grams amine/tonne CO_2 captured as a function of PZ weight fraction of total amine, temperature, and lean loading, CO_2 capacity at a lean loading of 100 and 500 Pa CO_2, and CO_2 capacity corrected for viscosity at 500 Pa CO_2. The model predictions are compared to estimated degradation rate data extracted from the maximum stripping temperature analysis presented in Chapter 4.

Overall, the model is able to predict the degradation rate to within 20% of amine lost from experimental data. Because the MST analysis takes into account the rate throughout the entire degradation and not just the initial rate, it is possible that the initial rate is underpredicted relative to the model. The CO_2-loaded experiments also might have different slightly different solution activities and solvation properties that might slow down the S_N2 reactions in the CO_2-loaded solution compared to the acid-loaded solution. The model also uses a stoichometric factor of 2 to predict PZ loss as opposed to the slightly lower values seen in experimental results.

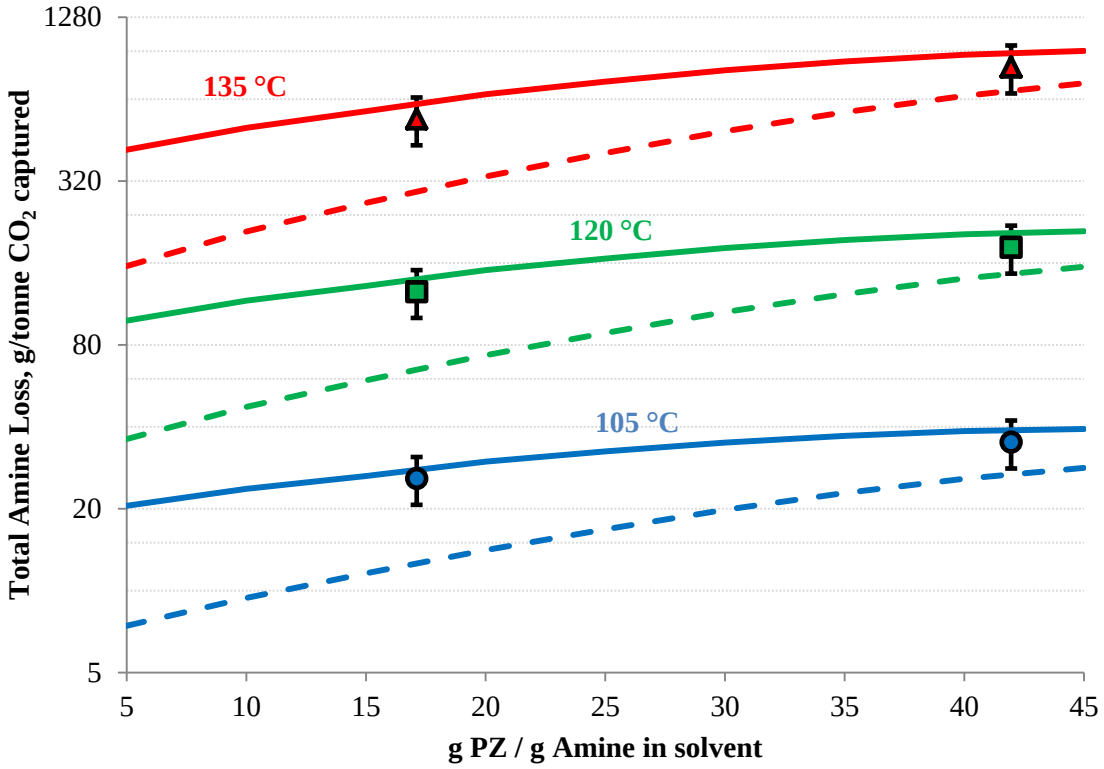

Figure 5.12: Process Design Model for Predicting Degradation Losses. Solid lines represent amine loss at a lean loading of 500 Pa CO_2. Thick dashed lines represent amine loss at a lean loading of 100 Pa CO_2. Points represent predictions from experimental data based on the MST analysis presented in Chapter 4; error bars denote ±20% deviation from measurements.

The degradation rate as predicted by the model is significantly less with a lean loading of 100 Pa CO_2 and low PZ concentration than at higher lean loading and higher PZconcentration. As PZ concentration increases, the amount of CO_2 in solution increases to maintain the equilibrium CO_2 partial pressure and, as a result, the concentration of protonated MDEA also increases to a point where the net initial forward rate at a lean loading of 100 Pa CO_2 is greater than at a lean loading of 500 Pa CO_2. These data are shown in Figure 5.13. The overall degradation rate, however, is reduced due to the higher intrinsic capacity of running a solvent with lower lean loading. In real systems,

however, the intrinsic degradation rate will likely be somewhat less than the predicted rate at a lean loading of 100 Pa CO_2. At lower loading, the relative amount of DEA complexed with CO_2 will be less than at richer loading, reducing the stoichometric factor between MDEA and PZ and thus the overall degradation rate.

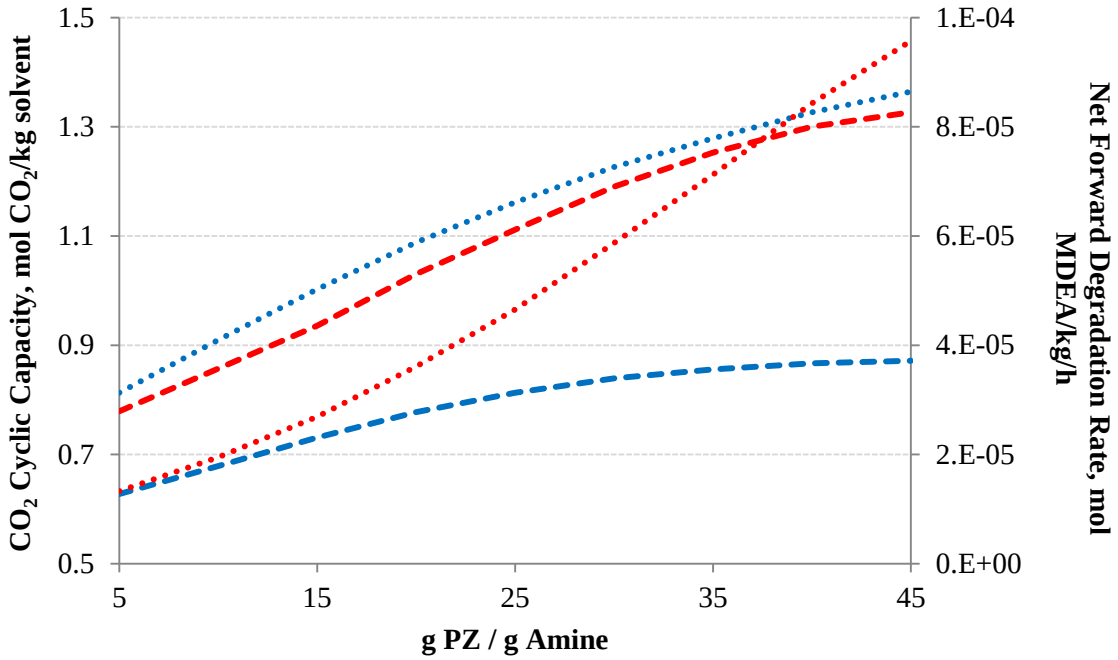

Figure 5.13: Intrinsic predicted MDEA loss (red lines) and CO_2 cyclic capacity (blue lines) at lean loadings of 100 Pa CO_2 (dotted lines) and 500 Pa CO_2 (dashed lines) at a concentration of 45 wt% amine and 120 °C.

Based on these data, it is possible to consider running at a lower lean loading and higher stripping temperature. A higher stripping temperature increases the desorption pressure of CO_2 in the stripper, reducing CO_2 compression costs, and can also serve to control the steady-state concentration of nitrosamine, which is a carcinogenic byproduct formed from the reaction of NOx in the flue gas with secondary amines, in solution (Fine, 2013). A lower lean loading will also increase the driving forces in the absorber,

reducing its size, and will also require smaller heat exchange equipment throughout the plant due to the lower circulation rate, reducing capital costs of the plant.

Assuming a price of $3/kg for the amine, an average of $0.2 can be saved per tonne of CO_2 captured at a lean loading of 100 Pa CO_2 versus 500 Pa CO_2 at 120 °C. At 135 °C, an average of $0.9 can be saved from running at the leaner loading. Regardless of temperature, the costs from the expected additional energy required to strip the solvent to a lean loading to 100 Pa CO_2 instead of 500 Pa CO_2 is about $1.1 per tonne of CO_2 if an electricity price of $100/MW*h is used (Lin, 2014). Therefore, it is not cost effective to run at a lower lean loading strictly from the viewpoint of thermal degradation and plant efficiency.

5.6 CONCLUSIONS

- Degradation of PZ-promoted MDEA is initiated by a S_N2 substitution involving free and protonated amine.
- The dominant initial degradation pathway involves free PZ attacking the methyl group of protonated MDEA, forming 1-MPZ and DEA. These happen to be the dominant degradation products in PZ-promoted MDEA and can account at least 60% of the mass lost by PZ and MDEA.
- MAE and 1-HePZ were observed in PZ-promoted MDEA degradation; however, their estimated concentrations were more than an order of magnitude less than DEA and 1-MPZ and indicate that attack on a hydroxyethyl chain is not favored.
- Minor degradation products include 1,4-DMPZ and triamines whose structures suggest PZ attacking carbons alpha to the hydroxyl function of the MDEA and can account from 10 to 30% of the mass lost.

- The less dominant pathway involves MDEA attacking protonated MDEA, forming the quaternary amine salt DMDEAm and DEA. This pathway is the principal degradation pathway for MDEA degradation in the absence of PZ.
- DEA and DMDEAm can account for about 90% of the amine loss initially and eventually begin to approach equilibrium in MDEA degradation.
- Other tertiary amines, such as DMAE and TEA, and quaternary amine salts, such as THEMAm and choline, were detected on MS but were not quantified using the IC. Diamines consistent with MDEA attack on the carbon alpha to the hydroxyl were observed on MS in MDEA degradation experiments.
- The second-order rate constants predicted by the kinetic model indicate that the rate constant of PZ attacking MDEAH+ is $1.5*10^{-6}$ kg/mol/s at 150 °C and MDEA attacking MDEAH+ is $0.12*10^{-6}$ kg/mol/s in the presence of PZ. The rate of the reverse reactions to regenerate MDEA and PZ is not a significant contributor to modeling the amine losses initially.
- In the absence of PZ, the rate constant of MDEA attacking MDEAH+ is about $0.3*10^{-6}$ kg/mol/s and the reverse rate reaction to regenerate MDEA from DEA and DMDEAm is 40 times as fast as the forward reaction.
- The kinetic model is able to predict initial rates within 20% of the experimental CO_2 amine loss rates after making corrections to the kinetic model to account for additional PZ loss in the presence of CO_2 and the reactivity of the PZ carbamate. The activation energy of degradation predicted by the model is about 140 kJ/mol and is similar to the activation energy of degradation observed in CO_2-loaded experiments which ranged from 140-147 kJ/mol.

- The kinetic model, when applied to process design conditions, is able to predict initial degradation rates that match reasonably (within 20%) to the results predicted by the T_{MAX} analysis presented in Chapter 4 as initial starting conditions and concentrations are varied.
- At lower lean loading, net overall degradation is reduced due to the significantly higher working capacity of the solvent (as predicted by the model). The additional energy cost to strip to a lean loading of 100 Pa CO_2 incurs a cost penalty 5.5 times greater than the savings from achieving a reduced degradation rate at 120 °C.

Thermal Degradation of Sterically Hindered Amines Blended with Piperazine

Quarterly Report for October 1 – December 31, 2014

by Daniel Hatchell

Supported by the Texas Carbon Management Program

McKetta Department of Chemical Engineering

The University of Texas at Austin

January 31, 2015

Abstract

This report presents thermal degradation data for six sterically hindered amine (SHA) blends with piperazine (PZ): 1-amino-2-methyl-1-propanol (AMP), 2-amino-2-methyl-1,3-propanediol (AMPD), 2-amino-2-(hydroxymethyl)-1,3-propanediol (TRIS), 2-(*tert*-butylamino)ethanol (tBuAE), 2-piperadinemethanol (PM), and 2-piperadineethanol (PE). The SHA/PZ blends were prepared with 3.2 m SHA/1.6 m PZ and loaded 0.22 mol CO_2/mol alkalinity. These solutions were degraded at 135 ºC, 150 ºC, and 165 ºC. Concentrations of both species over time were plotted to determine degradation rate constants and reaction activation energies. 4 m AMP/2 m PZ with the same CO_2-loading was degraded under the three temperatures to test the effect of concentration on degradation rate. 3.2 m AMP/1.6 m PZ was loaded with acid instead of CO_2 and degraded at 165 ºC to determine the role of CO_2.

AMP/PZ and tBuAE/PZ are the most stable blends, followed by AMPD/PZ, then TRIS/PZ and PE/PZ, and finally PM/PZ. These degradation reactions follow first-order rate kinetics. Concentration does not affect degradation rate at lower temperature but appears to at 165 ºC. Acid-loaded AMP/PZ undergoes significantly less degradation than CO_2-loaded AMP/PZ.

Introduction

Significant work exists in literature investigating the properties of amines for potential use as CO_2 scrubbing solvents. Amines with complementing characteristics have been studied together in blends with some success. One notable example is solvents featuring sterically hindered amines (SHAs). A SHA is defined as a compound with an amino group that is sterically hindered by a branch on the alpha-carbon. These amines demonstrate good performance in conjunction with primary or secondary amines, especially with piperazine (PZ) (Sartori, 1983). SHA/PZ blends are interesting solvents because of their high capacity and fast rate of reaction with CO_2.

SHAs follow a different reaction pathway to absorb CO_2. An ordinary primary or secondary amine absorbs CO_2 by reacting to form a carbamate. This process requires two amino groups: one forms a N-C bond with the CO_2, and the other accepts a hydrogen and protonates (Davis, 2009). SHAs, on the other hand, are too hindered around the amino group to form stable carbamates. These compounds instead react with CO_2 to form a bicarbonate ion and a

protonated amine (Sartori, 1983). The former reaction is fast, but has a theoretical absorption limit of 0.5 mol CO_2/mol alkalinity because it requires two amino groups. The latter reaction is usually slow, but only occupies one amino group and therefore has a higher capacity of 1 mol CO_2/mol alkalinity. A SHA/PZ blend takes advantage of both beneficial characteristics: the presence of PZ enables a fast absorption of CO_2, and the SHA increases overall solvent capacity.

Experimental Methods

This study investigates the hindered amines given in Table 1.

Table 1: Amines Tested

Name	Structure
PZ **Piperazine**	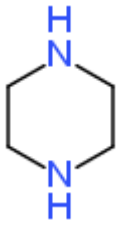
AMP **1-amino-2-methyl-1-propanol**	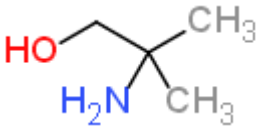
AMPD **2-amino-2-methyl-1,3-propanediol**	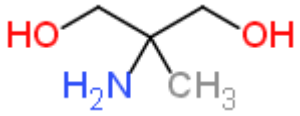
TRIS **2-amino-2-(hydroxymethyl)-1,3-propanediol**	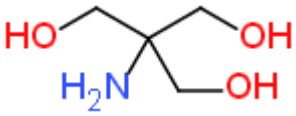
tBuAE **2-(*tert*-butylamino)ethanol**	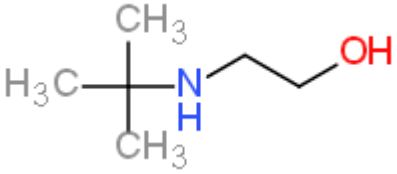
PM **2-Piperadinemethanol**	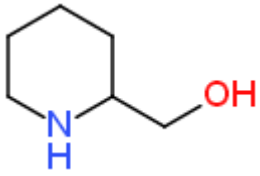
PE **2-Piperadineethanol**	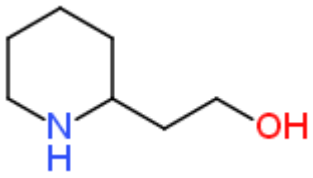

Amines were prepared gravimetrically with distilled, deionized water (DDI). Solvents were mixed on a 2 to 1 SHA to PZ molality basis that depended on the particular experiment series. The amines were loaded by bubbling CO_2 through a glass cylinder. CO_2 accumulation was measured by the increase in solvent weight. Samples used in acid-loaded experiments were prepared gravimetrically with sulfuric acid. All six SHAs were degraded at 135 ºC, 150 ºC, or 165 ºC at 3.2 m SHA/1.6 m PZ and 0.22 mol CO_2/mol alkalinity, the "base case" conditions. This concentration was chosen because it is the upper limit for tBuAE/PZ to remain soluble. AMP/PZ was additionally degraded at the same temperature and loading at 4 m AMP/2 m PZ. A third acid-loaded experiment degraded 3.2 m AMP/1.6 m PZ at 165 ºC with 0.22 mol H^+/mol alkalinity.

Completed amines were distributed into 3/8" Swagelok® stainless steel cylinders. Each cylinder has a volume of 4.5 ml and was filled with 4.3 ml of solvent. The number of cylinders devoted to a particular experiment series varied based on experimental conditions. The filled cylinders were sealed and placed into convective ovens at 135 ºC, 150 ºC, or 165 ºC. The samples were removed periodically over the following weeks to give a range of elapsed reaction times. Once removed from the oven and cooled, the contents were extracted and diluted for analysis by cation chromatography (Dionex ICS-2100). The dissolved products in the diluted samples were separated in a Dionex CS17 column and the relative quantities of each were plotted in a chromatograph. This method clearly isolated SHA and PZ responses from the degradation products. Comparison to a known standard converted the measured chromatograph responses into molal concentrations.

Safety

Proper PPE was worn at all times when handling sulfuric acid for preparation of the acid-loaded samples. The stainless steel cylinders used for experiments discussed in this report can pressurize under high temperatures. Standard operating procedures are in place to ensure safe cylinder handling.

Results and Discussion

Figures 1–8 plot thermal degradation data for all six SHA/PZ blends at 135 ºC, 150 ºC, and 165 ºC under the base case conditions of 3.2 m SHA/1.6 m PZ and CO_2 α = 0.22. PM/PZ concentrations are plotted separately because the compound degrades more rapidly than the others.

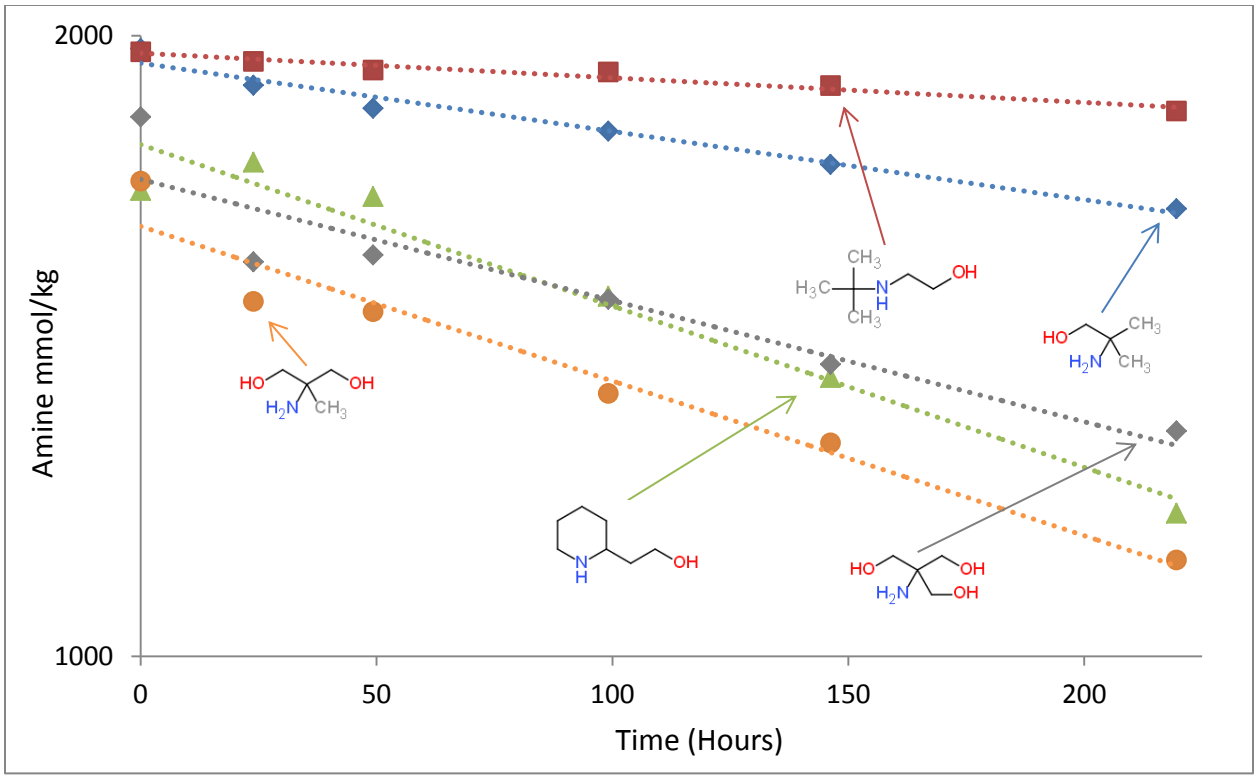

Figure 1: Degradation of SHAs in 3.2 m SHA/1.6 m PZ at 165 °C and CO_2 α = 0.22

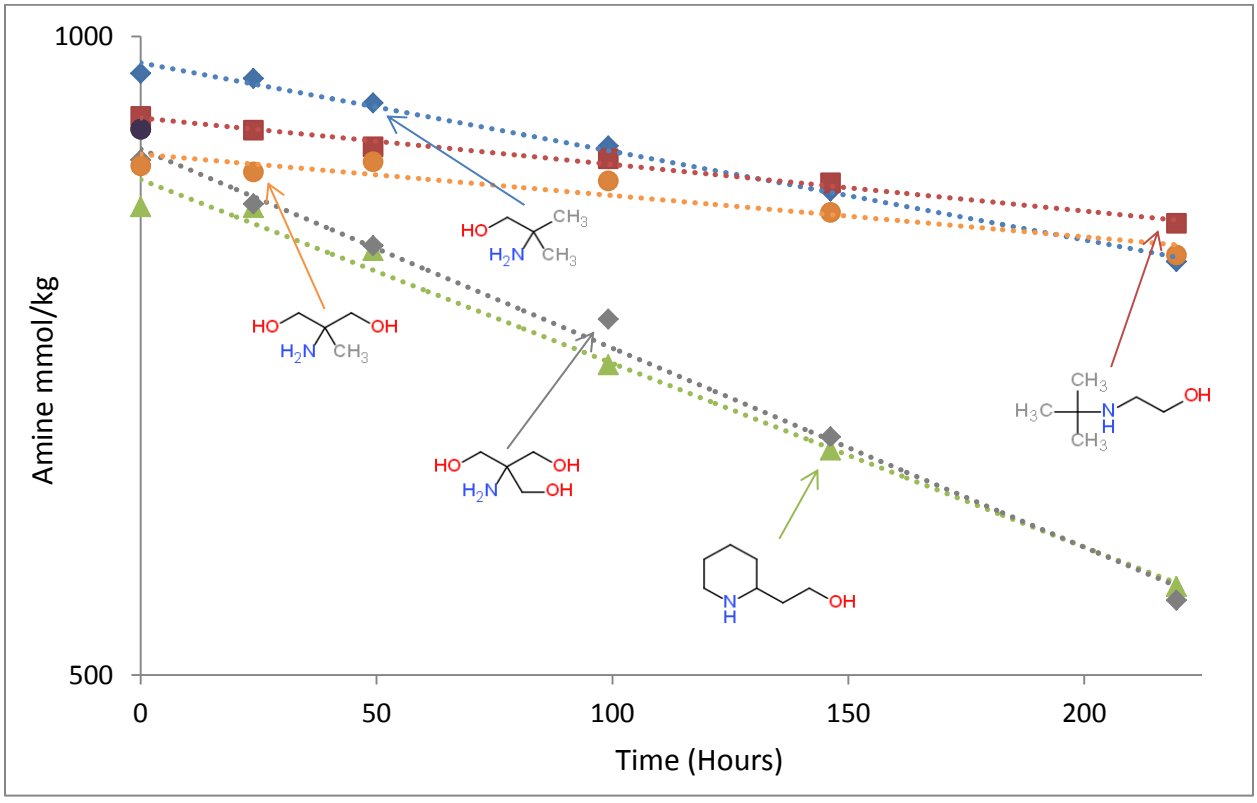

Figure 2: Degradation of PZ in 3.2 m SHA/1.6 m PZ at 165 °C and CO_2 α = 0.22

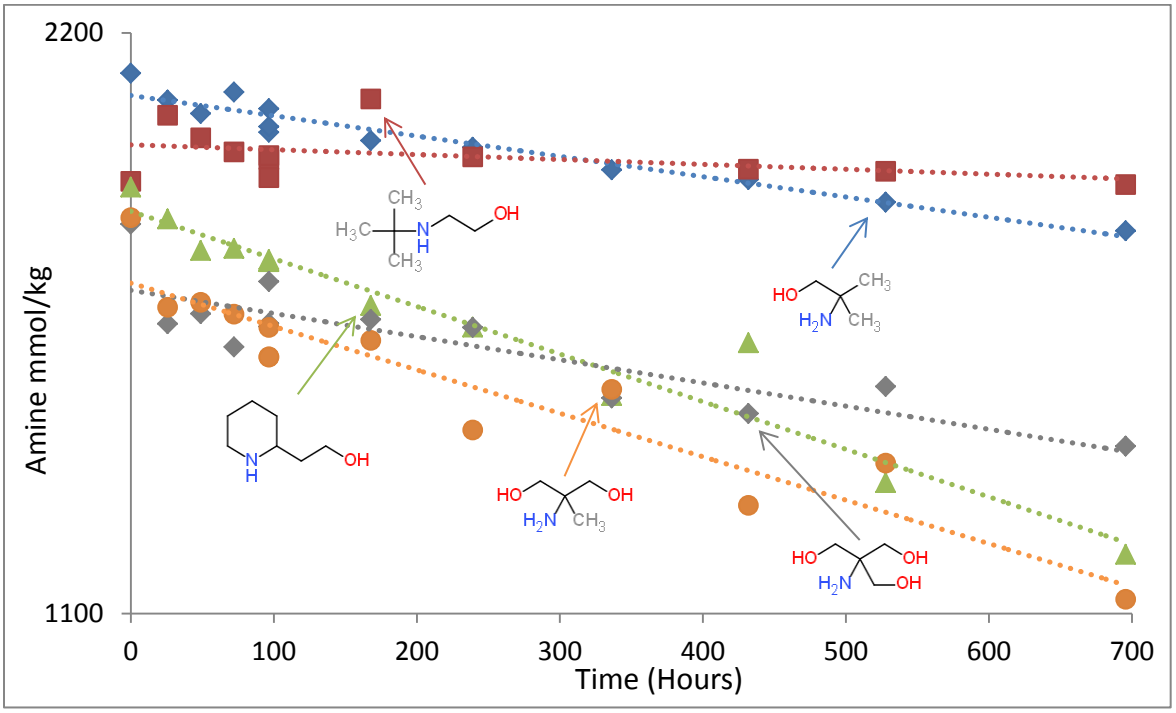

Figure 3: Degradation of SHAs in 3.2 m SHA/1.6 m PZ at 150 °C and CO_2 α = 0.22

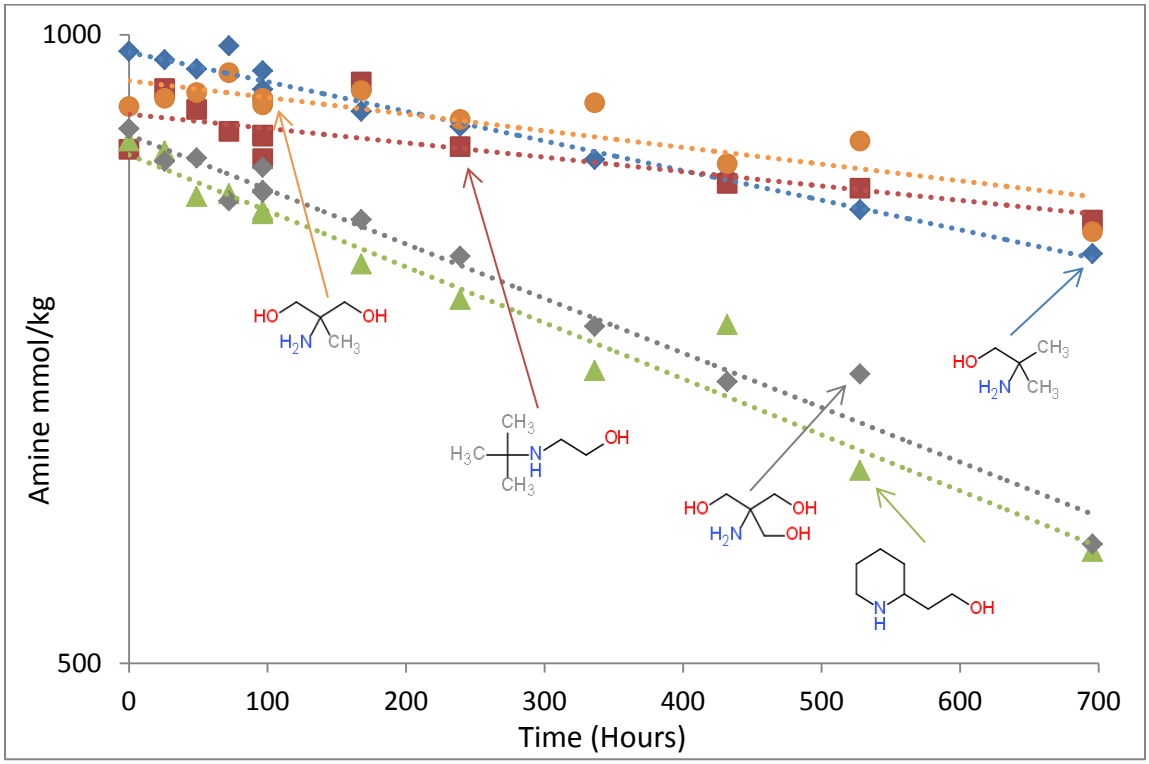

Figure 4: Degradation of PZ in 3.2 m SHA/1.6 m PZ at 150 °C and CO_2 α = 0.22

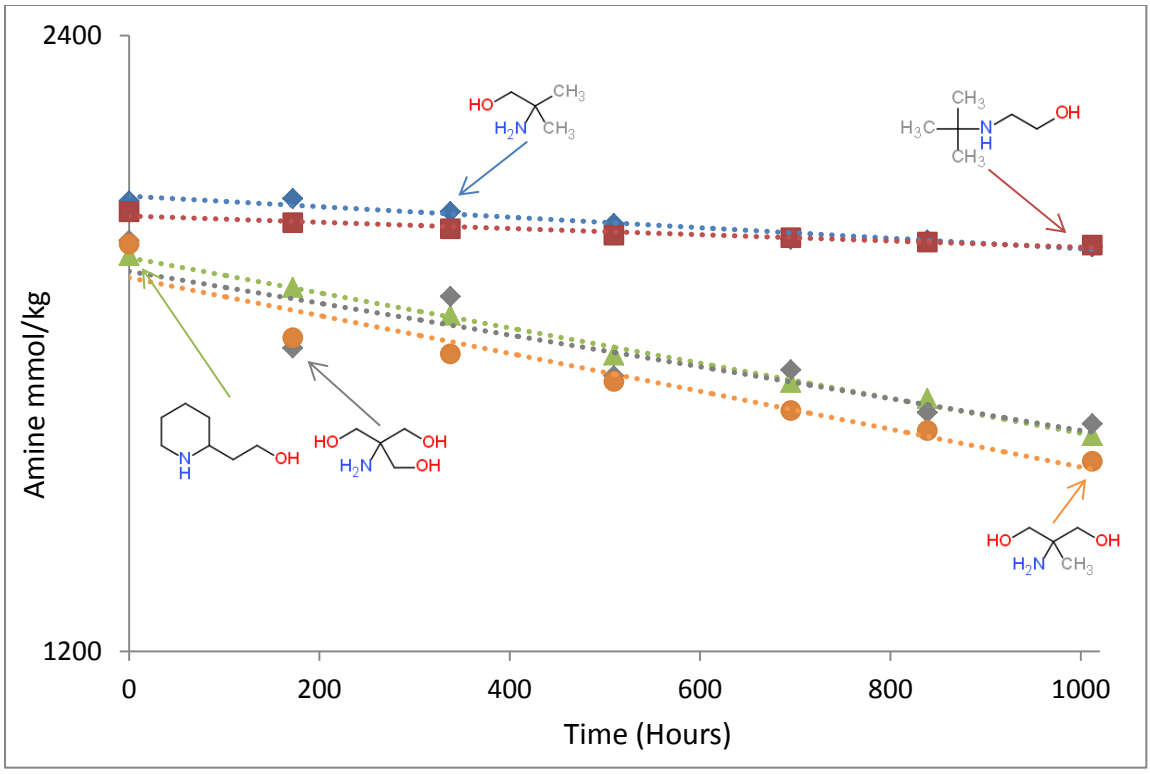

Figure 5: Degradation of SHAs in 3.2 m SHA/1.6 m PZ at 135 °C and CO_2 α = 0.22

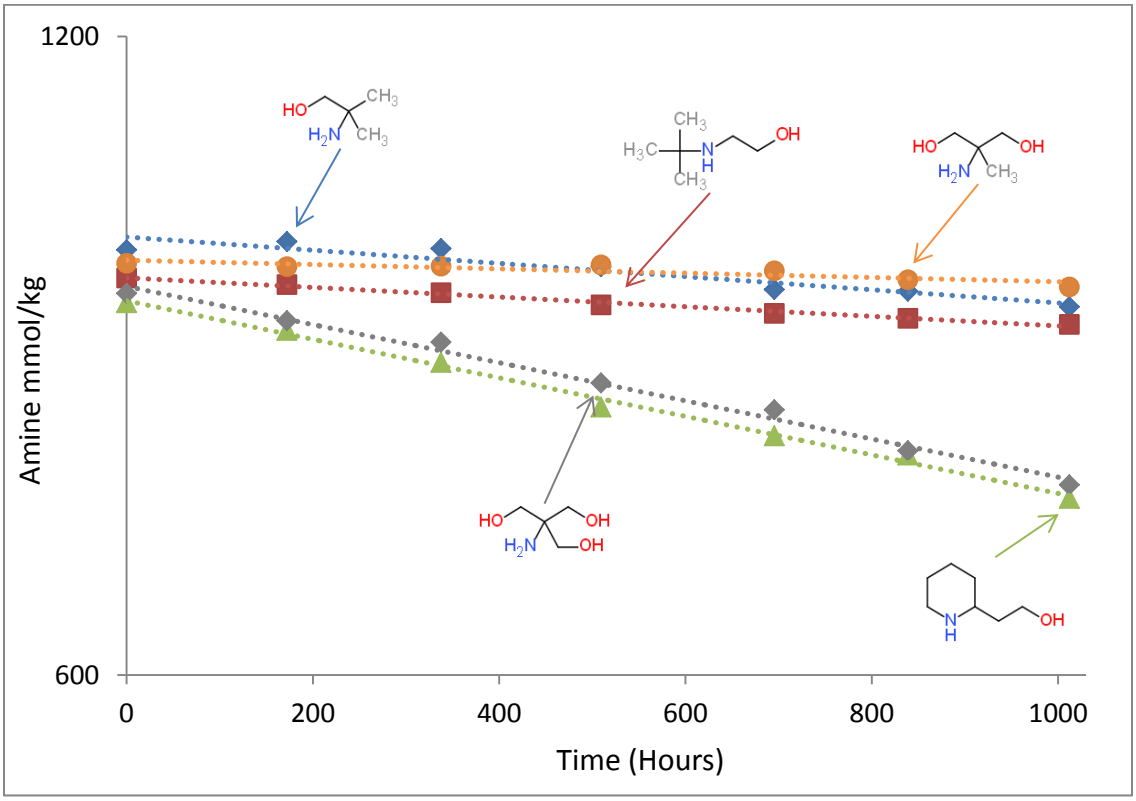

Figure 6: Degradation of PZ in 3.2 m SHA/1.6 m PZ at 135 °C and CO_2 α = 0.22.

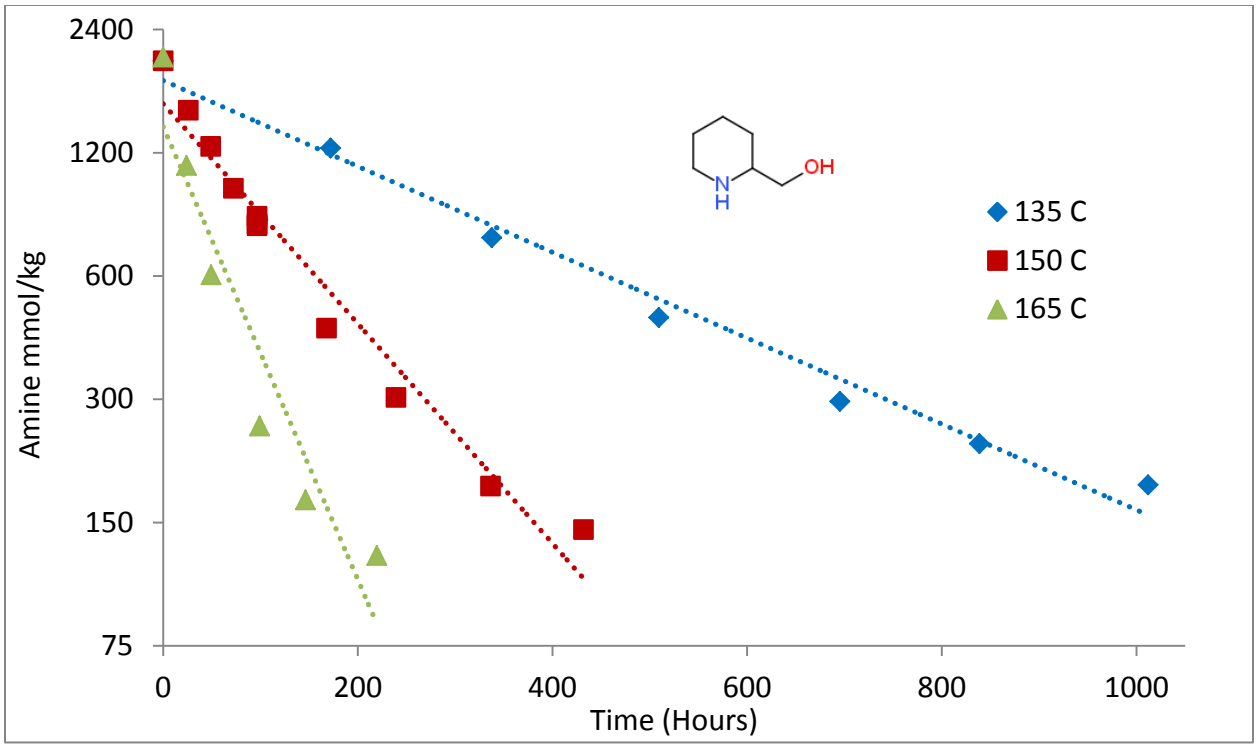

Figure 7: Degradation of PM in 3.2 m PM/1.6 m PZ at CO_2 α = 0.22

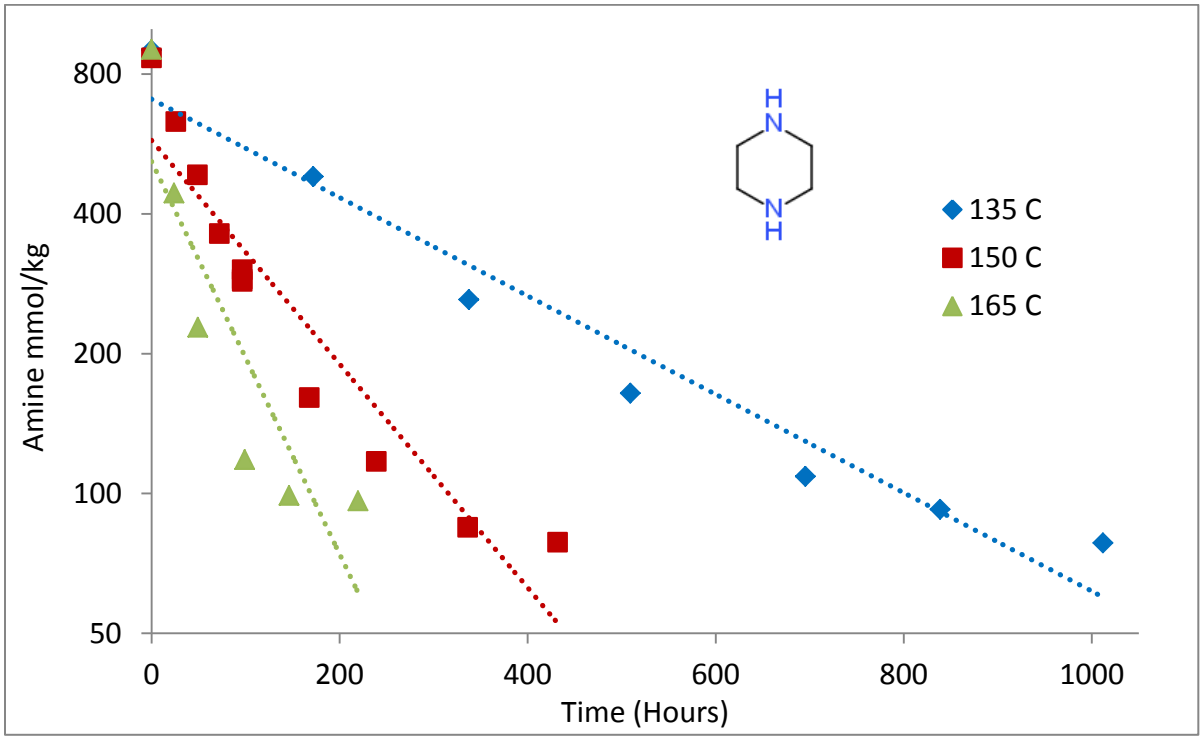

Figure 8: Degradation of PZ in 3.2 m PM/1.6 m PZ at CO_2 α = 0.22

The degradation plots are linear on a log scale, indicative of first-order rate kinetics. The exception is degradation in PM/PZ, which demonstrates first-order kinetics at higher concentrations but appears to significantly slow over time. This behavior suggests that PM/PZ is reaching chemical equilibrium with the degradation products.

The amines sort themselves into three distinct levels of stability. The least stable solvent is PM/PZ, the moderately stable solvents are PE/PZ and TRIS/PZ, and the most stable solvents are AMP/PZ and tBuAE/PZ. AMPD/PZ behaves differently; while AMPD degrades at rates similar to the moderately stable amines PE/PZ and TRIS/PZ, the PZ degrades at rates similar to the most stable amines AMP/PZ and tBuAE/PZ. Rate constants of these degradation plots are listed below in Table 2.

Figures 9 and 10 demonstrate the effect of concentration on AMP/PZ degradation. The first plot compares the degradation of AMP in 3.2 m AMP/1.6 m PZ, taken from the figures above, with that of AMP in a 4 m AMP/2 m PZ, keeping CO_2-loading constant. The second plot demonstrates the same effect of concentration on PZ degradation.

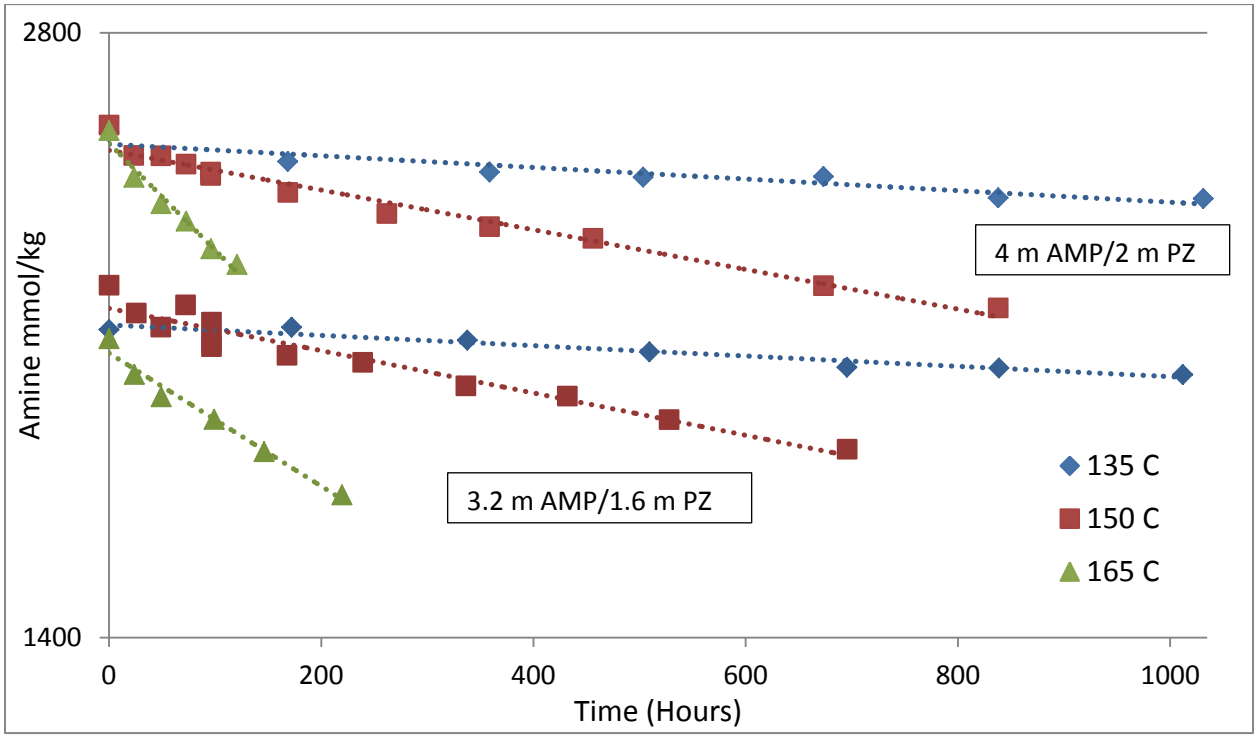

Figure 9: Degradation of AMP in AMP/PZ at variable temperature and concentration and CO_2 α = 0.22. 4 m AMP/2 m PZ is at the top of plot; 3.2 m AMP/1.6 m PZ is at the bottom.

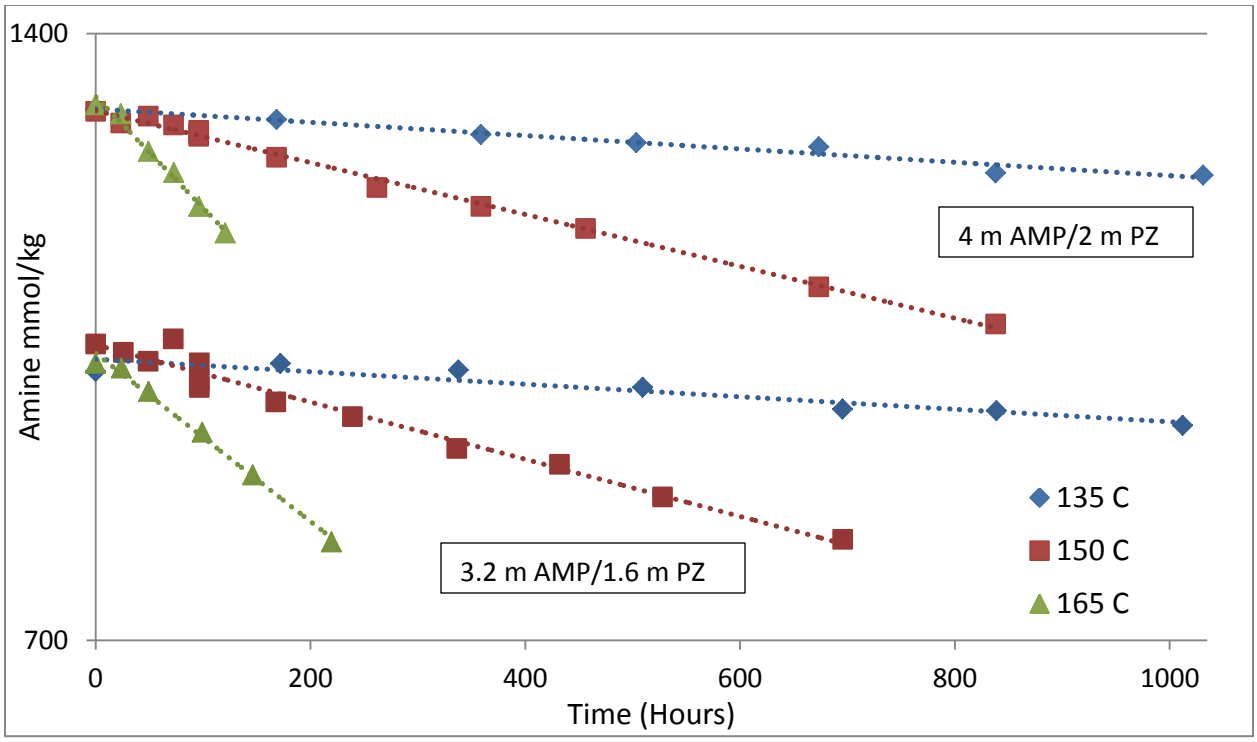

Figure 10: Degradation of PZ an AMP/PZ at variable temperature and concentration and CO_2 α = 0.22. 4 m AMP/2 m PZ is at the top of plot; 3.2 m AMP/1.6 m PZ is at the bottom.

AMP in the 3.2 m blend and 4 m blend degrades with a reaction rate of 5.9e-5 hr^{-1} and 6.7e-5 hr^{-1}, respectively, at 135 ºC; 2.42e-4 hr^{-1} and 2.27e-4 hr^{-1} at 150 ºC; and 7.63e-4 hr^{-1} and 1.224e-3 hr^{-1} at 165 ºC. PZ degrades with reaction rates of 7.2e-5 hr^{-1} and 7.6e-5 hr^{-1} for the 3.2 m and 4 m blend at 135 ºC; 3.26e-4 hr^{-1} and 2.96e-4 hr^{-1} at 150 ºC; and 9.61e-4 hr^{-1} and 1.272e-3 hr^{-1} at 165 ºC. Reaction rates at 135 ºC and 150 ºC are very similar across both concentrations for both species; reaction rates at 165 ºC appear to be higher for 4 m AMP/2 m PZ.

Table 2 lists the reaction rates in hr^{-1} of both species in all six blends at the three different temperatures studied, as well as reaction rates of species in the 4 m AMP/2 m PZ blend, taken from the previous eight figures.

Table 2: List of reaction rates in hr^{-1} and activation energies in kJ/mol. Rates and activation energies are presented for the SHA (at the top of the table) and for PZ (at the bottom of the table, in bold) for each blend at 135 ºC, 150 ºC and 165 ºC. CO_2 α = 0.22. Unless otherwise specified, concentrations are in 3.2 m SHA/1.6 m PZ.

Amine	135 ºC (hr^{-1}*e5)	150 ºC (hr^{-1}*e5)	165 ºC (hr^{-1}*e5)	Activation Energy (kJ/mol)
AMP	5.9	24.2	76.3	130
4 m AMP	6.7	22.7	122.4	140
AMPD	21.3	51.8	172.7	100
TRIS	17.9	27.7	135.4	100
PM	294.4	926.3	2486.5	110

PE	21.3	56.8	180.2	110
tBuAE	3.5	5.8	27.5	100
AMP	7.2	32.6	96.1	130
4 m AMP	7.6	29.6	127.2	140
AMPD	2.3	18.4	44.9	150
TRIS	20.7	60.1	216	120
PM	366.2	1115.6	2795.1	100
PE	20.9	61.8	199.4	110
tBuAE	5.2	15.8	50.5	110

The activation energies listed in Table 2 were calculated based on the change of degradation rate constant across the three temperatures.

Figure 11 demonstrates the effect of CO_2 loading and acid loading on AMP and PZ degradation in 3.2 m AMP/1.6 m PZ.

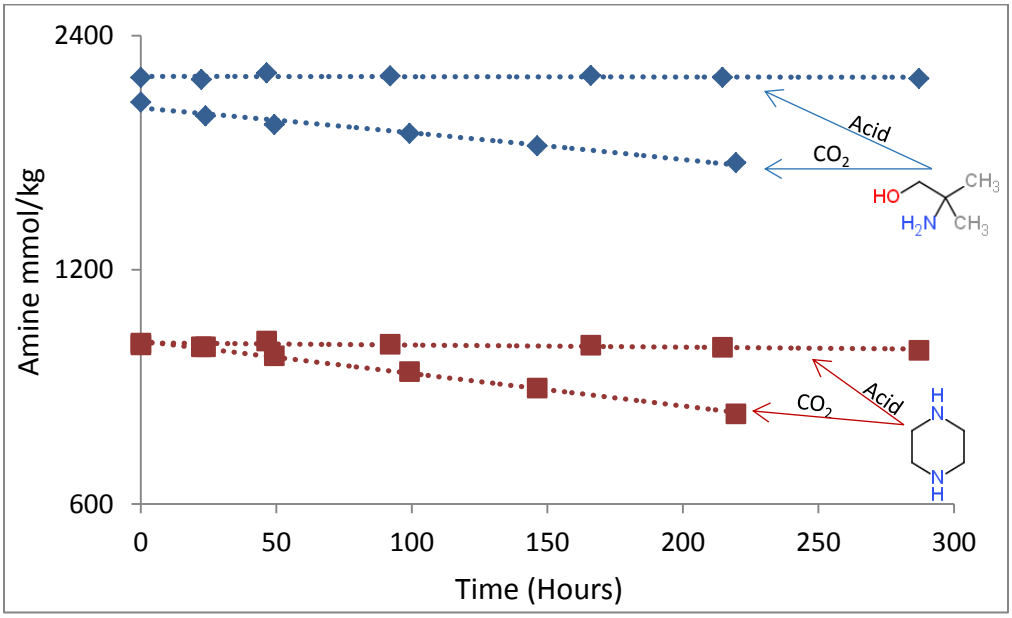

Figure 11: Degradation of AMP and PZ in a 3.2 m AMP/1.6 m PZ blend at 165 °C under CO_2 α = 0.22 or H^+ α = 0.22. The acid-loaded samples do not appreciably degrade.

The acid-loaded samples of AMP/PZ do not appreciably degrade at 165 °C. AMP degrades with a reaction rate of 1.0e-5 hr^{-1} under these acidified conditions, compared to 76.3e-4 hr^{-1} under CO_2-loaded conditions. PZ degrades with a reaction rate of 6.3e-5 hr^{-1} under acidified conditions, compared to 9.61e-4 hr^{-1} under CO_2-loaded conditions. This sharp drop in degradation rates from CO_2-loaded conditions to acid-loaded conditions suggests that the degradation mechanism requires and incorporates CO_2.

Conclusions

1. AMP/PZ and tBuAE/PZ are the most stable blends, followed by AMPD/PZ, then TRIS/PZ and PE/PZ, and finally PM/PZ. The following activation energies were calculated in kJ/mol: 130 for AMP and 130 for PZ of the 3.2 m AMP/1.6 m PZ blend; 140 and 140 for the 4 m AMP/2 m PZ blend; 100 and 150 for AMPD/PZ; 100 and 120 for TRIS/PZ; 110 and 100 for PM/PZ; 110 and 110 for PE/PZ; and 100 and 110 for tBuAE/PZ.
2. AMP in a 3.2 m AMP/1.6 m PZ blend degrades with a rate constant of 5.9e-5 hr^{-1}, 2.42e-4 hr^{-1} and 7.63e-4 hr^{-1} at 135 ºC, 150 ºC and 165 ºC, respectively; AMP in a 4 m AMP/2 m PZ blend degrades with a rate constants of 6.7e-4 hr^{-1}, 2.27e-4 hr^{-1} and 1.224e-3 hr^{-1}; PZ in a 3.2 m AMP/1.6 m PZ blend degrades with a rate constants of 7.2e-5 hr^{-1}, 3.26e-4 hr^{-1} and 9.61e-4 hr^{-1}; PZ in a 4 m AMP/2 m PZ blend degrades with a rate constants of 7.6e-5 hr^{-1}, 2.96e-4 hr^{-1} and 1.272e-3 hr^{-1}. The reaction rate of AMP/PZ degradation is concentration independent at lower temperatures, although this is less certain for the 165 ºC experiments.
3. The AMP/PZ blend degraded with reaction rates of 1.0e-5 hr^{-1} and 6.3e-5 hr^{-1} under the acidified conditions, significantly less than the corresponding CO_2-loaded rates of 7.63e-4 hr^{-1} and 9.61e-4 hr^{-1}.

Future Work

The degraded samples produced from these experiments will be measured with ICP-OES for metals concentrations to indicate the corrosivity of the different blends. The samples will also be examined with Total Inorganic Carbon analysis and titration to determine if the loss of compound corresponds with an equivalent loss in alkalinity, an important step in ascertaining the degradation mechanism. Select samples will be studied under mass spectroscopy to help identify byproducts.

References

Sartori G, Savage DW. "Sterically Hindered Amines for CO_2 Removal from Gases." *Ind Eng Chem Fundam.* 1983;22;249–258.

Davis JD. *Thermal Degradation of Aqueous Amines Used for Carbon Dioxide Capture.* The University of Texas at Austin. Ph.D. Dissertation, 2009.

Oxidative Degradation of Amines

Quarterly Report for October 1 – December 31, 2014

by Hanbi Liu

Supported by the Texas Carbon Management Program

McKetta Department of Chemical Engineering

The University of Texas at Austin

January 31, 2015

Abstract

The oxidative degradation of diamines in a stirred reactor was measured at 70 °C, 98 kPa O_2, and 2 kPa CO_2. Diethanolamine (DEA) and methylaminoethanol (MAE) at an initial concentration of 5 m, 10 m ethanolamine (MEA), and a 5 m MEA/2.5 m propylenediamine (PDA), at initial loading of 0.4 mol CO_2/mol alkalinity and initial metals concentration of 0.4 mM Fe, 0.2 mM Mn, 0.1 mM Ni, and 0.05 mM Cr, were oxidatively degraded. The purpose of these experiments was to study the structural effect of amines on their degradation rates.

Approximately 78% of MEA, 69% of DEA, and 63% of MAE were lost after 300 hours run time. DEA degradation follows second order kinetics with a rate constant of $3*10^{-6}$ 1/(mmol/kg-hr. MAE degradation follows second order kinetics with a rate constant of $1*10^{-6}$ 1/(mmol/kg-hr). MEA degradation follows first order kinetics with a rate constant of 0.015 1/(mmol/kg-hr).

Experimental Methods

Solutions were prepared gravimetrically. The solvents were made by first mixing amine with water in a glass bottle using a digital scale. CO_2 was bubbled through a gas washing bottle containing the amine solvent. Target amine concentration was 5 m and target CO_2 loading was 0.4 mol CO_2/mol alkalinity.

A schematic of the low gas flow apparatus is shown below. Carbon dioxide and oxygen from their respective gas cylinders were passed through two calibrated mass flow controls to maintain a reactor pressure of 98 kPa O_2 and 2 kPa CO_2, and the jacketed glass reactor was charged with approximately 350 ml of amine solution. The reactor head was sealed with a Teflon® cap. The O_2/CO_2 mixture was saturated with water before being fed to the reactor through the Teflon® cap. The reactor was agitated at 1400 rpm and maintained at 70 ^oC. The apparatus is identical to the LGF reactor used by Voice (2013).

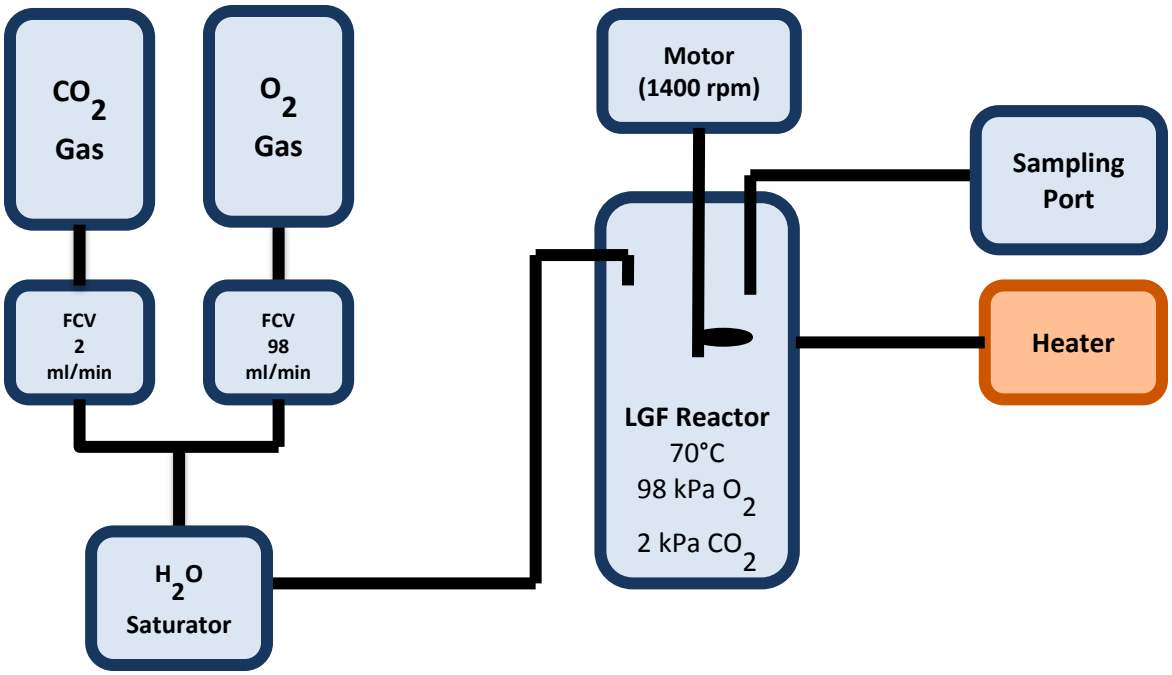

Figure 1: Low gas flow oxidation apparatus used in the experiment

The water balance was maintained each time a sample was removed to make up for water loss through evaporation. Table 1 lists a sampling schedule that was generally followed for each experiment.

Table 1: General sampling schedule of oxidation experiments

Sample number	Time since start of experiment
1	At starting time
2	1 day
3	2 day
4	3 days
5	4~5 days
6	6~7 days
7	9~10 days
8	13~14 days

Table 2: Amines tested this quarter in the LGF

Amine Name	Abbreviation	Structure
Diethanolamine	DEA	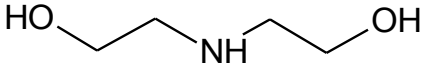

methylaminoethanol	MAE	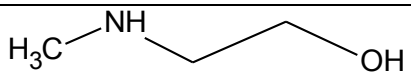
Ethanolamine	MEA	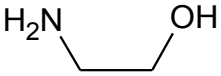
1,3-diaminopropane	PDA	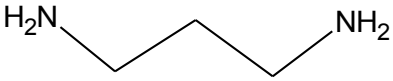

Cation chromatography was used to analyze for parent amine concentrations and degradation by-product concentrations; samples were diluted by a factor of 10000, and the separation was carried out using a Dionex CS17 column. Anion chromatography was used to qualitatively analyze for formate salts and nitrite. Samples were first hydrolyzed using concentrated sodium hydroxide and then diluted by a factor of 100. The separation was carried out using a Dionex AS15 column. The analytical methods are identical to those of Voice (2013).

Safety

Amine solutions were prepared in the fume hood as several of the amines were volatile, and the oxidation experiment was also conducted in the fume hood to vent any volatile degradation products away from the lab.

Results

Figure 2 shows the degradation of DEA. The amine concentrations are calculated based on cation chromatography results. The first five points were used to construct a fit and later points after degradation reached equilibrium were excluded. The degradation of DEA follows second order rate law with rate constant $3*10^{-6}$ $(mmol/kg\text{-}hr)^{-1}$ and 69% of the amine was lost by the end of the experiment.

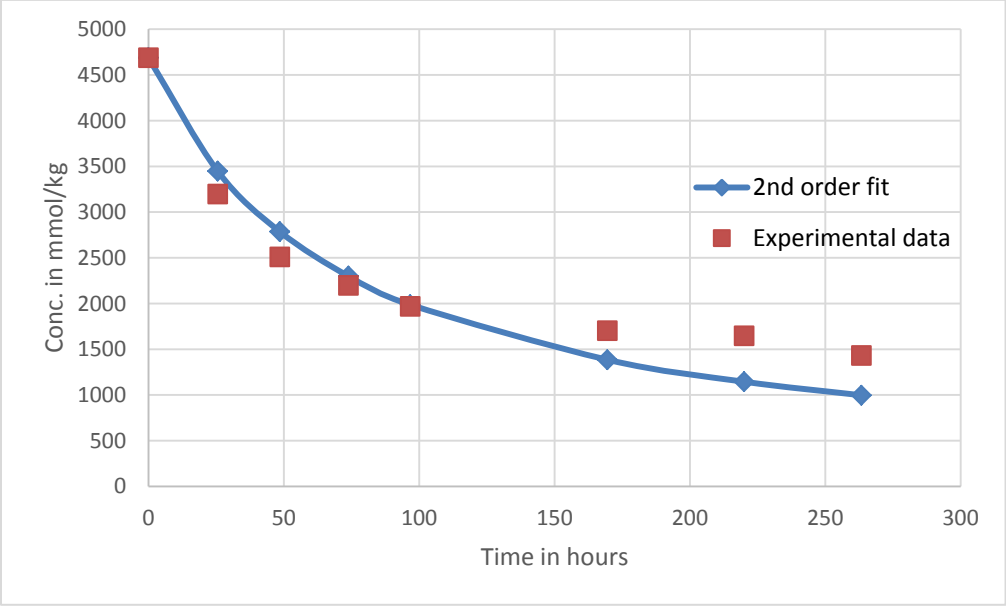

Figure 2. Oxidation of 5 m DEA. 70 ^{o}C, 98 kPa O_2, 2 kPa CO_2, 100 ml/min gas flow, 1400 rpm, 0.4 mM Fe, 0.2 mM Mn, 0.1 mM Ni, 0.05 mM Cr.

The degradation of MAE follows second order rate law with rate constant $1*10^{-6}$ $(mmol/kg\text{-}hr)^{-1}$. About 63% of the amine was lost by the end of the experimental period.

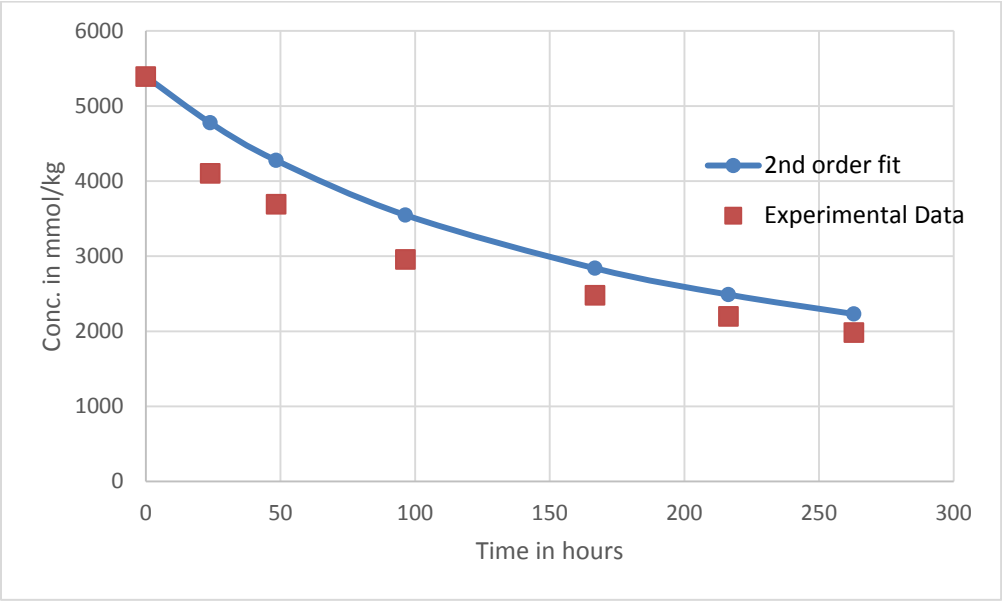

Figure 3: Oxidation of 5 m MAE. Conditions: 70 °C, 98 kPa O_2, 2 kPa CO_2, 100 ml/min gas flow, 1400 rpm, 0.4 mM Fe, 0.2 mM Mn, 0.1 mM Ni, 0.05 mM Cr.

MEA shows significant initial degradation that follows first order kinetics and then reaches equilibrium after roughly 120 hours. The rate constant is 0.015 1/hr and about 78% of the amine was lost by the end of the experiment. Only the first four data points are used to fit first-order rate law.

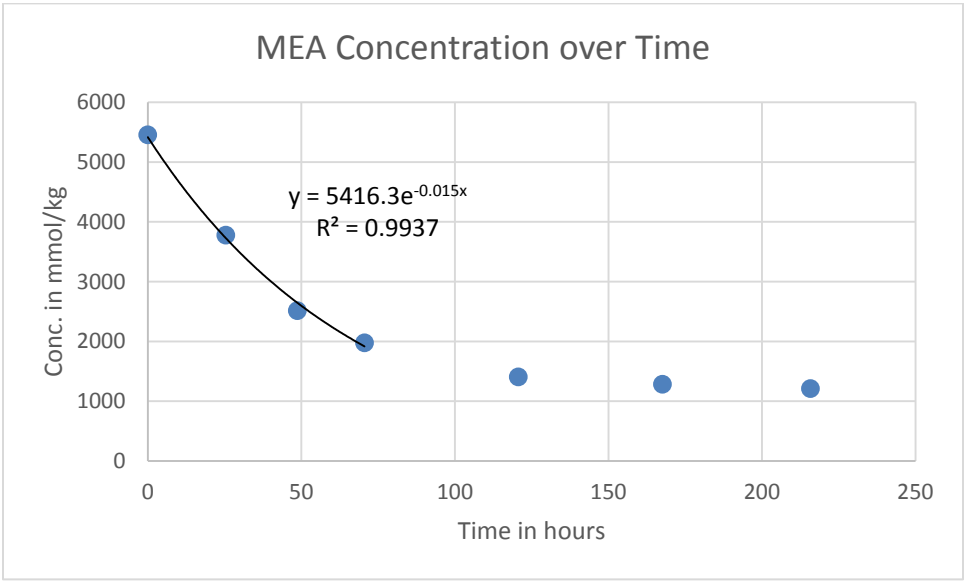

Figure 4: Oxidation of 5 m MEA. 70 °C, 98 kPa O_2, 2 kPa CO_2, 100 ml/min gas flow, 1400 rpm.

The degradation rate of MAE and DEA supports the hypothesis that amines with 2 carbons between the amino and neighboring functional group tend to show significant degradation.

Data on two major oxidation products, formate and oxalate, have been presented for selected amines tested in previous quarters. In this quarter, the concentration of another major product, nitrite, was analyzed for most of the amines tested. Primary amines with an even number of carbons between the amino and the next oxygen-containing functional group (ether or hydroxyl) produce the most nitrite over time. Examples of such amines include MEA, Jeffamine®, and DGA®. This trend is followed by primary diamines with an even number of carbons, such as HMDA and DAB. Secondary amines with even number of carbons between the amino and neighboring functional groups such as MAE and DEA did not produce as much nitrite as the primary amines.

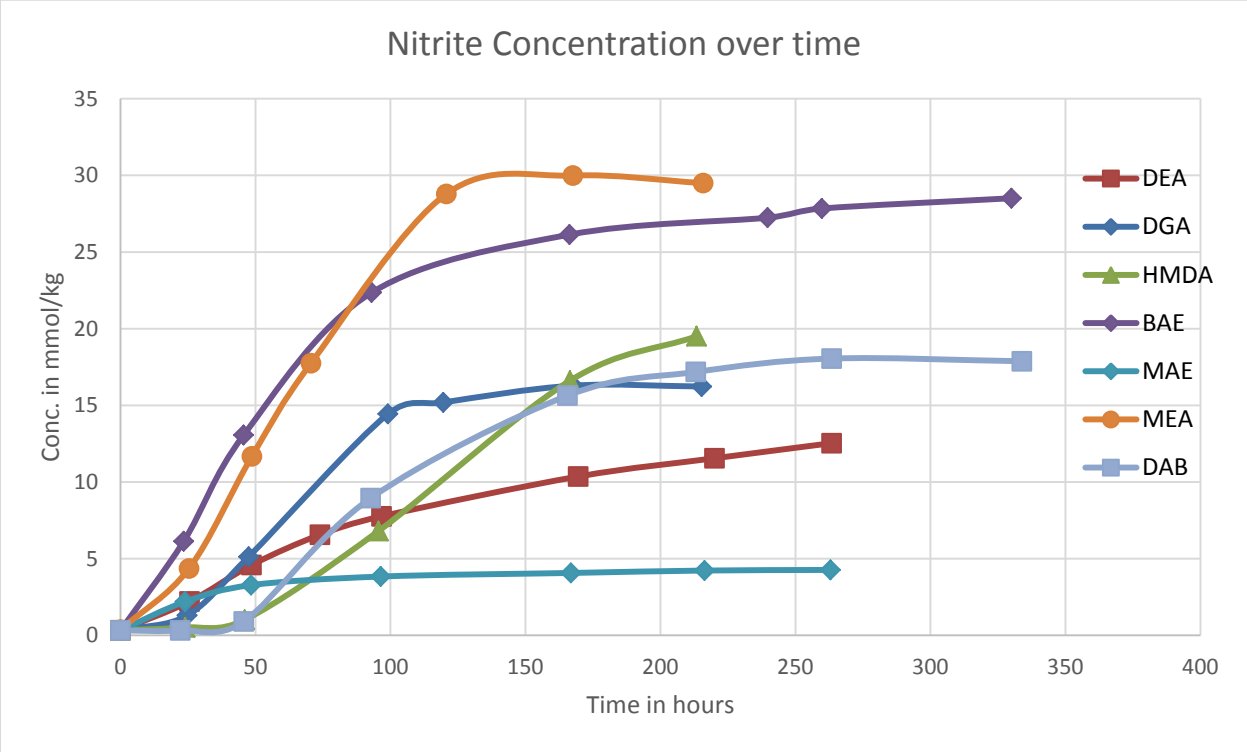

Figure 5: Total Nitrite. Conditions: 70 °C, 98 kPa O_2, 2 kPa CO_2, 100 ml/min gas flow, 1400 rpm.

Figure 5 shows nitrite formation as a function of amine loss. Figure 6 shows nitrite formation as a function of amino group loss. Diamines produce more nitrite per amine loss because every diamine degraded has two amino groups. Primary amine degradation produces nitrite at a faster rate than secondary amines in most cases. Secondary amines are more inert to nitrite formation, but DEA forms more nitrite than MAE per amine loss.

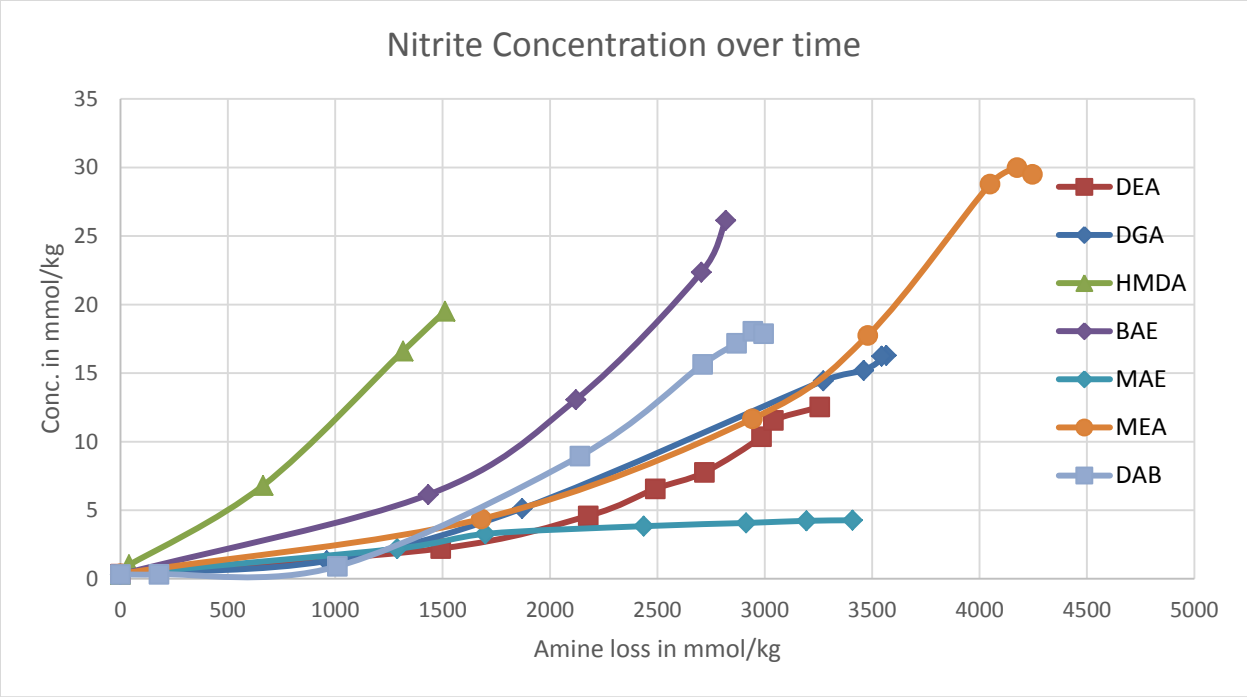

Figure 6: Total Nitrite vs. Amine Loss. Conditions: 70 ^{o}C, 98 kPa O_2, 2 kPa CO_2, 100 ml/min gas flow, 1400 rpm.

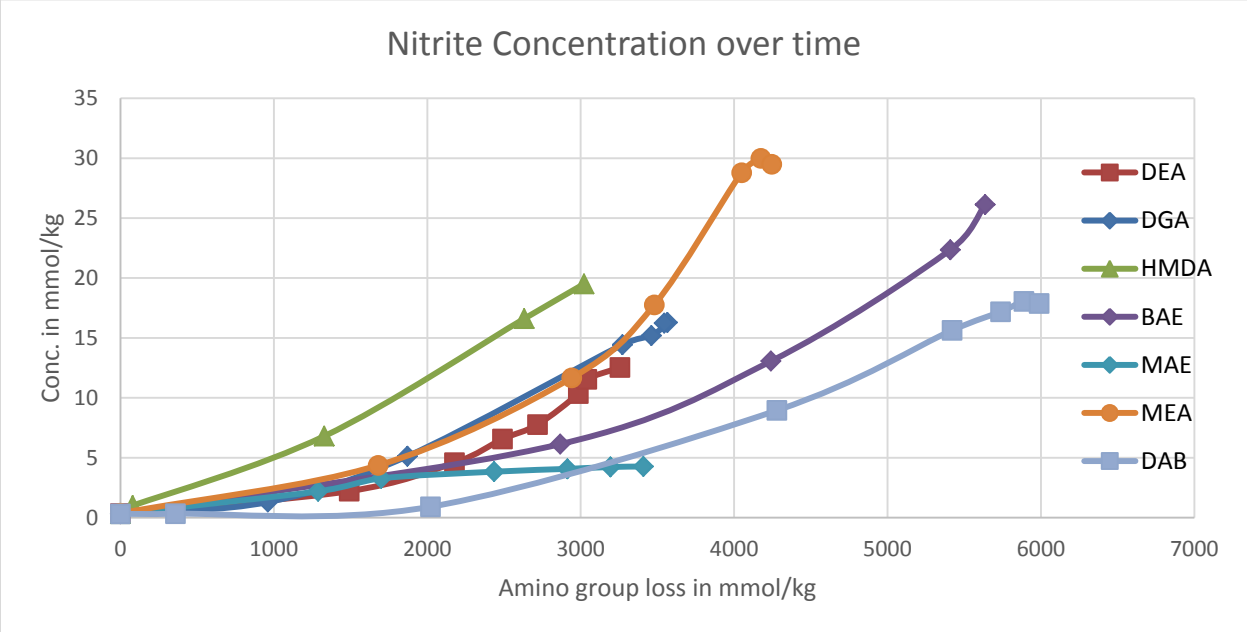

Figure 7: Total Nitrite vs. Amino Group Loss. Conditions: 70 ^{o}C, 98 kPa O_2, 2 kPa CO_2, 100 ml/min gas flow, 1400 rpm.

Conclusions

1. MEA degrades by first order rate law with k = 0.015 1/hr at 70 ^{o}C, 98 kPa O_2, 2 kPa CO_2 with 0.4 mM Fe, 0.2 mM Mn, 0.1 mM Ni, and 0.05 mM Cr. 78% of the amine was lost by the end of the experiment.
2. DEA degrades by second order rate law with k = $3*10^{-6}$ $(mmol/kg\text{-}hr)^{-1}$ at 70 ^{o}C, 98 kPa O_2, 2 kPa CO_2 with 0.4 mM Fe, 0.2 mM Mn, 0.1 mM Ni, and 0.05 mM Cr. 69% of the amine was lost by the end of the experiment.
3. MAE degrades by second order rate law with k = $3*10^{-6}$ $(mmol/kg\text{-}hr)^{-1}$ at 70 ^{o}C, 98 kPa O_2, 2 kPa CO_2 with 0.4 mM Fe, 0.2 mM Mn, 0.1 mM Ni, and 0.05 mM Cr. 63% of the amine was lost by the end of the experiment.
4. Nitrite concentration in degradation samples suggest the following rough order of cumulative nitrite production:
    a. Primary amines with 2 carbons between the amino group and the neighboring group that is either an ether or hydroxyl, as seen in MEA, BAE, and DGA®.
    b. Primary diamines with an even number of carbons between the two amino groups, as seen in HMDA and DAB.
    c. Secondary amines with 2 carbons between the amino group and neighboring functional groups, as seen in DEA and MAE.

Future Work

Oxidation of MAPA should offer insight on whether amines that have three carbons between the amino group and the neighboring functional group show resistance to oxidation. This hypothesis was true for primary amines such as MPA and PDA, and MAPA will test whether this hypothesis is true for secondary amines.

References

Goff GS. *Oxidative Degradation of Aqueous Monoethanolamine in CO_2 Capture Processes: Iron and Copper Catalysis, Inhibition, and O_2 Mass Transfer*. The University of Texas at Austin. Ph.D. Dissertation. 2005.

Sexton AJ. *Amine Oxidation in CO_2 Capture Processes*. The University of Texas at Austin. Ph.D. Dissertation. 2008.

Voice AK, *Amine Oxidation in Carbon Dioxide Capture by Aqueous Scrubbing*. The University of Texas at Austin. Ph.D. Dissertation. 2013.

Aerosol Observation and Separation in Amine-Based CO_2 Capture

Quarterly Report for October 1 – December 31, 2014

by Matt Beaudry

Supported by the Texas Carbon Management Program

McKetta Department of Chemical Engineering

The University of Texas at Austin

January 31, 2015

Abstract

Amine emissions in aerosol form are a significant problem for amine-based CO_2 capture plants. Unarrested soot and condensed hydrolyzed SO_3 travel through the absorber while collecting water and amine. Conventional water wash columns are ineffective at removing the amine once it is captured in the aerosols. While Brownian diffusion units have proven to be fairly effective at reducing amine emissions, cyclonic separators offer the potential for improved capture performance with a simpler system at a lower cost. A swirl tube cyclonic separator has been designed and will be implemented in both the Aerosol Growth Column and the PRC Pilot Plant. The flexibility of the design will allow for capture of aerosols at controllable sizes. Another aerosol sampling system has been designed to utilize centrifugal forces to control the size of particles sampled by FTIR analysis. It is hoped that this will provide similar data to the PDI with more robust and less expensive equipment.

Introduction

Aerosols and Emissions

The emission of volatile compounds is a major concern at CO_2 capture facilities utilizing amine scrubbing. Amine solvent lost through the overhead of absorber columns not only represents an environmental and safety hazard, but also has undesirable economic implications. Amine losses can occur via three different processes: through the gas phase as a function of vapor pressure in the absorber column; liquid entrainment as the gas velocity increases; and as a mist composed of aerosols. Losses through the gas phase can be mitigated with the use of a water wash. Liquid entrainment can be reduced by designing the column to use a gas velocity that prevents the entrainment of liquid droplets.

Aerosol formation in absorber columns occurs when SO_3 is present in the incoming flue gas. The SO_3 hydrolyzes to H_2SO_4 in the humid atmosphere of the absorber. From there, aerosols in absorber columns can grow via two different mechanisms: heterogeneous or homogeneous nucleation. Heterogeneous nucleation occurs in the presence of soot or fly ash particulate. Growth occurs as the aerosol collects sulfuric acid, water, and amine. This is the dominant aerosol growth mechanism in most industrial processes (Mertens, 2013), especially for strong

acids besides H_2SO_4 (Schaber, 1995). Khakharia et al. (2013) reported that amine emissions were heavily influenced by soot concentrations at lower soot and SO_3 concentrations, but increasing the SO_3 concentration relative to the soot content more significantly increased the amine emissions.

Homogeneous nucleation of aerosols occurs exclusively between molecules of the condensable components (Mertens, 2013). This is a very rapid process, occurring within a second of the sulfuric acid hydrolyzation (Wix, 2010). As the SO_3 content in the flue gas increases, this becomes the more dominant mechanism for aerosol growth. Khakharia (2013) found absorber outlet MEA emissions up to 72 ppmv with 10^6 particles per soot per cm^3, and up to almost 400 ppmv with 10^8 particles of H_2SO_4 per cm^3.

Mertens et al. (2014) found that most incoming aerosols entering the absorber column measured less than 0.2 μm in diameter. On entering the absorber, the aerosols grow in size due to the high water saturation and coagulation with other aerosols. It was noted that most amine is lost through aerosols between 0.5 and 2.0 μm in diameter for this particular pilot plant (Mertens, 2014).

Aerosol Collection

Research this quarter focused on the use of cyclonic separators for aerosol removal. Cyclonic separators operate by using centrifugal forces to separate particles from a gas stream, due to the difference in density between the aerosol droplets and the gas. This technology was outlined in the last two quarterly reports (Rochelle, 2014a and b). These devices are frequently used in agricultural and coal processing industries and are relatively easy to implement, thanks to their simple design and absence of moving parts.

Two important parameters in designing cyclonic separators are the cut size and the steepness of the cut curve. These parameters are most heavily influenced by the velocity of the gas inside the separator, and the diameter of the gas outlet. The cut size refers to the cutoff collection size for the separator. If a cyclonic separator has a cutoff size of 1 μm, this means that particles 1 μm and larger will be collected, while smaller particles will pass through the system. The steepness of the cut curve determines the effectiveness of the separator. A sharp cut curve indicates that the separator collects almost all particles above the designed cut size, while a soft cut curve is more lenient on the collection of larger particles. For these experiments, a sharper cut curve is preferred.

Safety

Much of the electricity-using equipment in this lab's bench and pilot scale research is fabricated in house. Electrical work can be dangerous, and taking the proper precautions is absolutely necessary. Electrically powered devices must be shut off and unplugged prior to having maintenance performed. Care must be taken to ensure conduits and plugs are not exposed to moisture. Proper design of electricity distribution systems, and the grounding of equipment, will help mitigate many of the risks associated with electric devices.

Experimental Methods

Aerosol Collection

An aerosol collection system has been designed for use with both the Aerosol Growth Column (AGC) and the PRC Pilot Plant. Flexibility of the design is of utmost importance. As outlined in last quarter's report, a swirl tube type cyclonic separator will be utilized. This is presented in Figure 1.

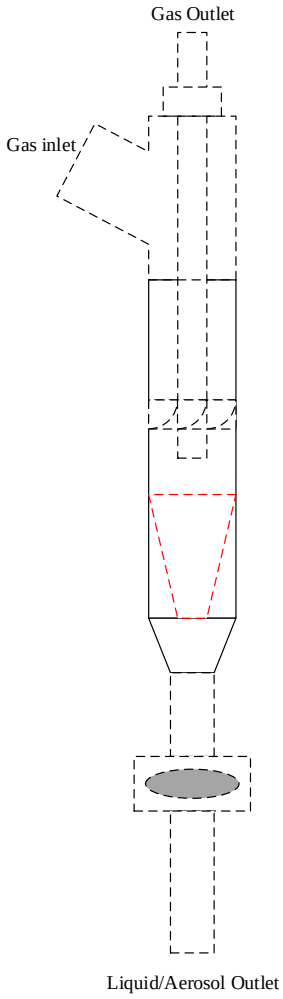

Figure 1: Side view of swirl tube apparatus

The swirl tube itself has an outer diameter of approximately 5.72 cm and a total length of 130 cm. The long length is to allow for flow stabilization before entering the vaned section of the tube, and for the variation of cyclone length. The outer shell of the swirl tube will be constructed from transparent acrylic, to allow visual confirmation of the cyclonic separator performance. The vanes will have an entry angle in line with the flow and the tube body, and an exit angle of 30°.

The system will be capable of collecting aerosols of varying sizes. One of the key parameters for determining cut size in this design is the diameter of the vortex finder, or the gas outlet. This

system is designed to use ¼", ½", ¾", and 1" steel piping. Combined with varying the total gas flow rate, this will allow for the collection of particles at any cut size between 0.3 and 5 µm.

Efforts this past quarter have focused on finalizing the design for the swirl tube apparatus and ordering the components necessary for its manufacture. Most of the parts have now been ordered, and the building of this device will begin next quarter. It is hoped that the swirl tube apparatus will be ready by the beginning of the pilot plant campaign on February 16th.

Aerosol Observation

The effectiveness of the swirl tubes will be evaluated with a Fourier Transform Infrared Spectrometer (FTIR) and a Phase Doppler Interferometer (PDI). The PDI operates by intersecting two lasers at an angle through a small, well-defined volume. A particle that passes through this volume scatters light that is collected by an optical receiver, which uses a phase-Doppler type analysis to determine particle sizes and number concentration. The FTIR will be used to quantify the amount of amine that is captured in the aerosols at varying points in the system. Obtaining FTIR samples before and after the swirl tube will determine how successful the swirl tube is at capturing the amine-laden aerosols. An FTIR probe will be placed at the same location as the PDI window downstream of the absorber column. By placing a valved bypass around the swirl tube, the concentrations of the components both entering and leaving the aerosol removal devices can be determined. If sufficiently precise data from the FTIR is captured, a mass balance can be calculated across the aerosol removal device to potentially determine the exact composition of the aerosols.

Phase Doppler Interferometers are very expensive and fragile pieces of equipment, an unfortunate combination. A device is required that can perform a similar analysis without the risks of an expensive breakdown. The goal is to develop a piece of equipment that utilizes varying centrifugal force to remove aerosols of different sizes. This can be coupled with FTIR analysis, along with precise knowledge of the aerosol composition, to determine the size range of aerosols produced in a given process. An outline of the design is presented in Figure 2. It is based on a device described by Prado, who used similar equipment to study the effect of liquid entrainment through sieve trays in distillation columns (Prado, 1986).

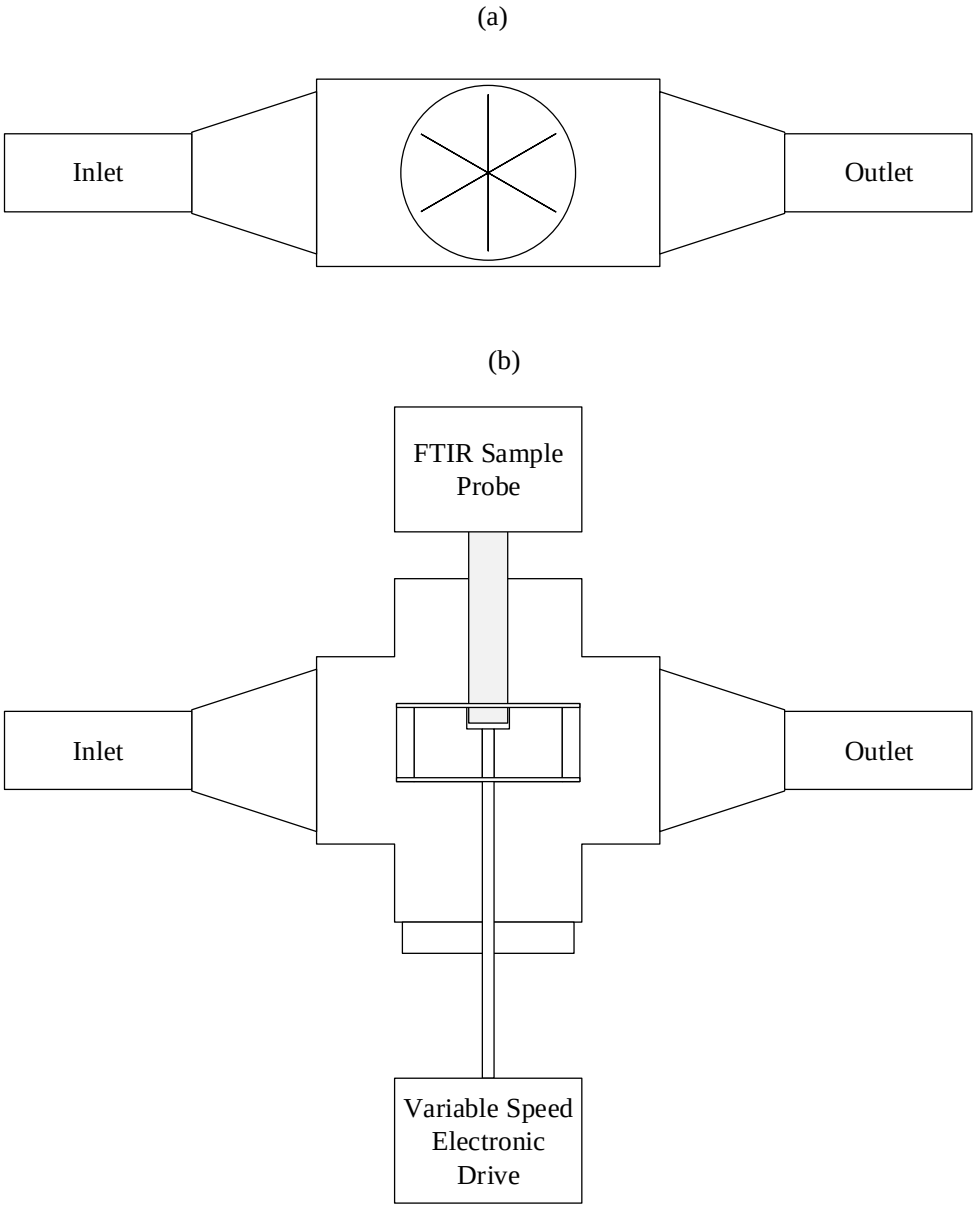

Figure 2: Schematic of (a) side view and (b) top view of centrifugal sampling device

The device will be placed downstream of the absorber column and can be alternated with the swirl tube apparatus. A piping cross forms the shell of the device, with the aerosol-laden vapor entering and leaving through the inlet and outlet, as labeled in Figure 2. An FTIR sample probe will enter the cross perpendicular to the fluid flow, directly across from a variable speed electronic drive coupled to a paddle wheel-type fan. Fluid will enter the sample probe tip at a location inside the paddle wheel. By varying the speed of rotation of the paddle wheel, the size of aerosols sampled can be varied. At slower speeds, small and large aerosols are both allowed to enter the FTIR probe tip. As the speed increases, the larger aerosols are contacted by the paddle wheel and blocked from entering the probe tip due to their greater momentum compared to the smaller aerosols. It is hoped to link a rotational speed to the cutoff size of aerosols

blocked from entering the probe. These data will be coupled with FTIR analysis to eliminate the PDI system and its associated expenses.

The components necessary for this apparatus have been obtained and the building of the device has commenced. Figures 3 and 4 present side and top views of the paddle wheel fan.

Figure 3: Angled side view of paddle wheel fan

Figure 4: Top view of paddle wheel fan

The current paddle wheel fan is constructed of Teflon blades and plexiglass sides. The plexiglass will be replaced with machined stainless steel early next quarter. The FTIR probe tip is designed to fit inside the hole, (inside the red circles) shown in both Figures 3 and 4.

Figure 5 shows the paddle wheel affixed to the drive shaft. A variable speed drive will connect to the drive shaft and control the rotational speed of the fan. This drive shaft passes through a pump shaft seal to inhibit the release of the aerosol-laden process stream. The shaft seal is attached to a bushing for easy connection to the piping cross.

Figure 5: Paddle wheel fan with drive shaft and shaft seal

Figures 6 and 7 show the sampling device in its entirety and a zoomed in view of the piping cross itself, respectively. The FTIR probe tip fits precisely into the paddle wheel. In these views the process stream inlet is entering the plane of the figure, at the inlet of the piping cross, and exiting out the other side.

Figure 6: Paddle wheel fan sampler and FTIR probe

Figure 7: Zoomed in view of paddle wheel fan sampler and FTIR probe

Once the replacement sides for the paddle wheel are delivered, this device will be ready for implementation. It will be used during the upcoming pilot plant campaign.

Discussion

Effective aerosol collection from absorber outlet streams should be possible with the use of swirl tubes. Minimal pressure drop is expected across these cyclonic separators. The magnitude of the pressure drop is dependent on the aerosol concentration, and varying the amount of aerosol produced in the Aerosol Growth Column or the pilot plant may result in an increased pressure drop across the swirl tube. Current calculations indicate that pressure drop should not be severe enough to negatively affect performance of the Aerosol Growth Column or the PRC Pilot Plant. It is believed that combining this technique with FTIR analysis will be a cost effective method for capturing and characterizing aerosols.

A simpler and more robust aerosol size sampling system is preferable, due to the high costs and low durability of the PDI. A centrifugal sampling system has been designed, and will be

constructed and tested next quarter. If a strong correlation can be made between the PDI results and the results from this device, the PDI may no longer be necessary.

Future Work

The goal of this project is to determine the effectiveness of cyclonic separators, or more specifically swirl tubes, and other capture devices for removing and measuring aerosols from the outlet stream of an amine-based CO_2 capture plant. Next quarter, construction of the swirl tube itself will be completed and device testing will begin. The centrifugal sampling device will also be implemented and tested in comparison to the PDI.

Planning will continue on the eventual upgrades to the Aerosol Growth Column. A water wash column will be added to the current configuration, and an increased number of FTIR and PDI sample locations will be added.

Research will also be conducted on the viability of using a Condensation Particle Counter (CPC) to aid in aerosol observation. CPCs are less expensive and more reliable than PDIs, and may prove to be a more cost-effective aerosol measurement technique if used in conjunction with cyclonic separators.

References

Khakharia P, Brachert L, Mertens J, Huizinga A, Schallert B, Schaber K, Vlugt T, Goetheer E. "Investigation of aerosol based emission of MEA due to sulphuric acid aerosol and soot in a Post Combustion CO_2 Capture process." *Int J Greenhouse Gas Control*. 2013;19:138–144.

Mertens J, Lepaumier H, Desagher D, Theilens ML. "Understanding ethanolamine (MEA) and ammonia emissions from amine based post combustion carbon capture: Lessons learned from field tests" *Int J Greenhouse Gas Control*. 2013;13:72–77.

Mertens J, Brachert L, Desagher D, Theilens ML, Khakharia P, Goetheer E, Schaber K. "ELPI$^+$ measurements of aerosol growth in an amine absorption column" *Int J Greenhouse Gas Control*. 2014;23:44–50.

Prado M., "The Bubble-to-Spray Transition on Sieve Trays: Mechanisms of the Phase Inversion". Ph.D. Dissertation, Austin, The University of Texas at Austin, 1986.

Rochelle GT et al. "CO_2 Capture by Aqueous Absorption, Second Quarterly Progress Report 2014." Texas Carbon Management Program. The University of Texas at Austin. 2014.

Rochelle GT et al. "CO_2 Capture by Aqueous Absorption, Third Quarterly Progress Report 2014." Texas Carbon Management Program. The University of Texas at Austin. 2014.

Schaber K. "Aerosol formation in absorption processes" *Chem Eng Sci*. 1995;50:1347–1360.

Wix A, Brachert L, Sinanis S, Schaber K. "A simulation tool for aerosol formation during sulphuric acid absorption in a gas cleaning process" *J Aerosol Sci*. 2010;41:1066–1079.

Piperazine Oxidation in Pilot Plants

Quarterly Report for October 1 – December 31, 2014

by Paul T. Nielsen

Supported by the Texas Carbon Management Program

McKetta Department of Chemical Engineering

The University of Texas at Austin

January 31, 2015

Abstract

PZ was oxidized by reaction with hydrogen peroxide at absorber conditions in the HGF apparatus. An initial rate of 0.03 moles ammonia was observed per mole of peroxide added regardless of PZ concentration, dissolved metal concentration, or the presence of the free radical scavenger Inhibitor A (Inh A). However, PZ solvent without Inh A and with high metal concentration had a greater rate of ammonia generation after some oxidation had already occurred. Formate accumulation was also reduced by a factor of 3 in solvent containing Inh A. Ammonia was produced at a lower rate than formate in peroxide oxidation compared to previous experiments in the HTOR cyclic oxidation apparatus. Oxidation at high temperature may produce a relatively greater amount of ammonia per mole of amine oxidized. N_2O was also observed from peroxide oxidation. This species has not been previously quantified as an oxidation product in cyclic oxidation experiments.

A simplified correlation for the effect of heat stable salts on MEA and PZ viscosity was developed. Sulfate, formate, and acetate are expected to have the greatest effect on solvent viscosity in a carbon capture facility, with nitrate having a much lesser effect. Therefore, limiting amine oxidation, scrubbing SO_x before the absorber, and solvent reclaiming will be the most important strategies to control solvent viscosity in a capture plant.

Introduction

Amine solvents used in post-combustion CO_2 capture degrade via a combination of thermal degradation in the stripper and oxidation by the flue gas in the absorber, which typically contains between 5 and 12 vol % O_2. Dissolved oxygen can react to form peroxides and free radical carriers, which can be carried over to the heated stripper to further oxidize the amine. The most representative method of determining the rate of amine loss and types of products formed is a cyclic system combining the effects of both oxidation and high-temperature thermal degradation. This can only be accomplished in a bench-scale cyclic degradation apparatus or in a pilot plant.

Experimental Methods

High Gas Flow Apparatus (HGF)

The HGF oxidizes amines at absorber conditions in a 1 L glass reactor loaded with 350 mL of amine continuously sparged with 7.5 L/min of air and 0.5–2% CO_2. The gas leaving the reactor is analyzed by FTIR for ammonia and other volatile oxidation products, and liquid samples can be taken periodically and analyzed to quantify the accumulation of liquid phase oxidation products. A complete description of the apparatus can be found in Sexton (2008).

Analytical Methods

A complete description of analytical methods used can be found in previous quarterly reports (Rochelle et al., 2014) and Freeman (2011).

Results and Discussion

Amine Oxidation via Peroxide Addition in HGF

Hydrogen peroxide was reacted with PZ solvent in the HGF reactor to determine if peroxide produces similar degradation products to amine oxidation in typical absorber conditions. Two solvents were tested: 5 m PZ with 0.4 mM Fe^{2+} and 0.1 mM Mn^{2+} added, and 8 m PZ from the SRP pilot plant. The SRP PZ contains 1 wt % Inhibitor A (Inh A) and less than 0.1 mM dissolved metal ions, as well as minimal amounts of degradation products (Nielsen, 2012).

2.5 mL of 30 wt % hydrogen peroxide in water was injected into the solvent using a 3 mL syringe. Vigorous foaming was observed for up to 15 minutes after peroxide injection, probably caused mainly by the peroxide reacting with itself to produce molecular oxygen and water. Figure 1 shows ammonia peaks produced by addition of hydrogen peroxide. Ammonia reached a maximum 30 minutes after the injection of peroxide and returned to baseline in 8 hours.

N_2O was also observed in a smaller but much sharper peak of less than 20 minutes. Trace amounts of N_2O had been observed in previous oxidation experiments, but in concentrations too low to allow for accurate quantification (Voice, 2013). Based on the rapid return to baseline of the N_2O peak and slower return of the ammonia peak, it is hypothesized that oxidation occurs rapidly, within the first 20 minutes of peroxide injection, producing liquid-phase ammonia and ammonium, which is then stripped out over time by air sparging in the HGF. N_2O is not very soluble and is stripped out immediately upon production.

NO, NO_2, EDA, PZ, methylamine, and 1-MPZ were also analyzed by FTIR but showed no change over baseline. These species may still be produced but in amounts lower than the detection limit of the FTIR.

An injection of 5 times the peroxide (12.5 mL) produced 5 times the ammonia and N_2O. Surprisingly, a third injection of the initial amount of 2.5 mL peroxide still produced 5 times the ammonia. Possibly, accumulation of liquid phase products from the first two injections helped catalyze additional oxidation on the third injection.

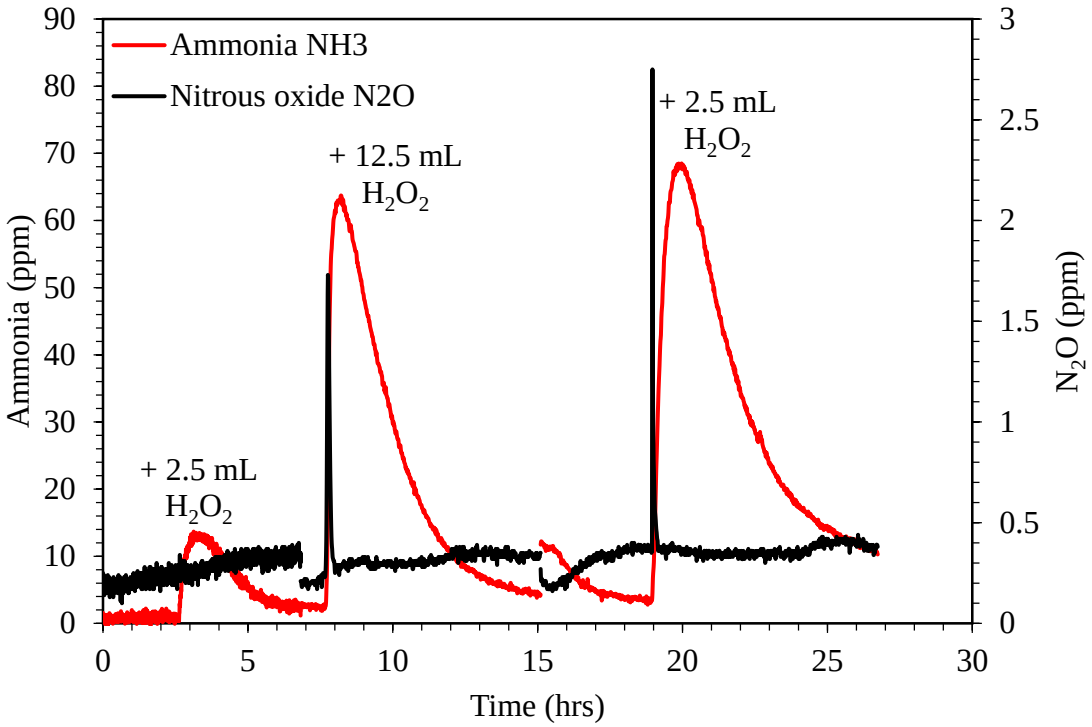

Figure 1: Ammonia and N_2O production from the oxidation of 5 m PZ via hydrogen peroxide (30 wt %) in HGF (350 mL solvent, 7.5 L/min air + 0.5% CO_2, 0.4 mM Fe^{2+}, 0.1 mM Mn^{2+})

Figure 2 shows the FTIR results of the second experiment with SRP PZ. Peroxide was added more slowly, in 2.5 mL increments, to see if the rate of ammonia generation increased with the amount of cumulative oxidation. However, the amount of ammonia produced per mole of peroxide added was constant throughout the experiment. At the end of the experiment, 7.5 mL of peroxide was added, which produced three times the normal amount of ammonia. N_2O was observed with every addition of peroxide, at a ratio of approximately 2–3 orders of magnitude less than ammonia.

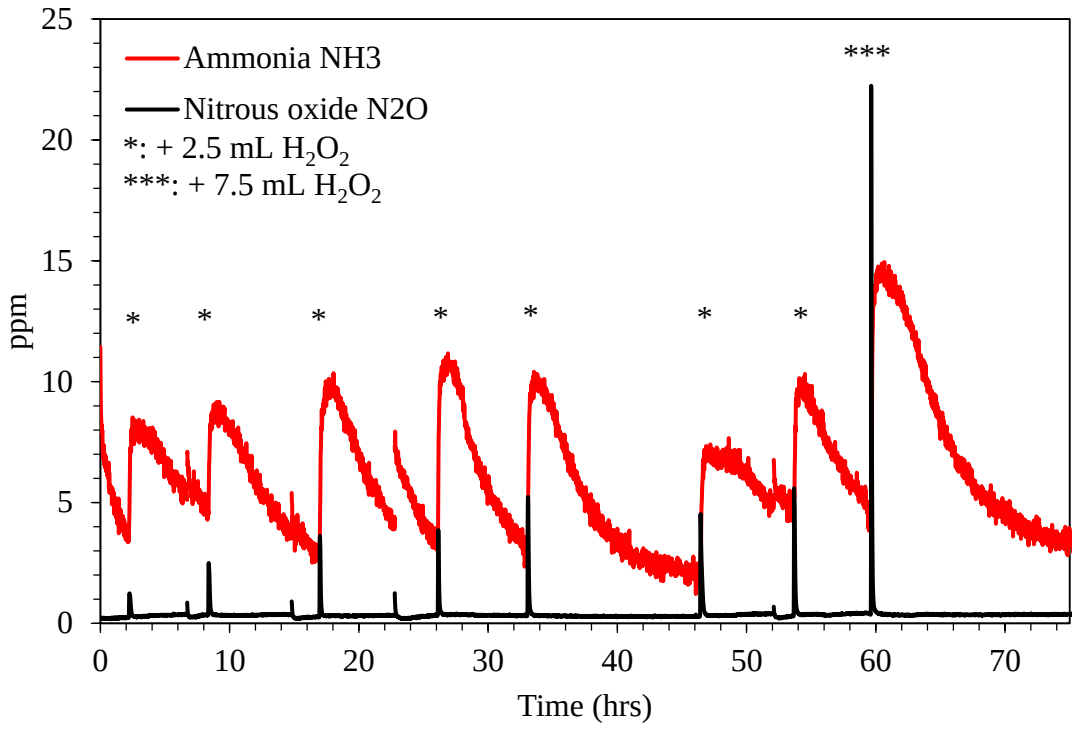

Figure 2: Ammonia and N_2O production from the oxidation of SRP PZ (8 m, 1 wt % Inh A, <0.1 mM Fe^{2+}) via hydrogen peroxide (30 wt %) in HGF

At the end of the second experiment, 7.5 mL of acetaldehyde was added to the solvent to determine if an increase in aldehydes would result in an increase in ammonia production on peroxide injection, as observed at the end of Experiment 1 (Figure 3). The addition of acetaldehyde resulted a sharp peak in both ammonia and N_2O, which quickly returned to baseline, possibly due to the aldehyde oxidizing the amine and increased foaming affecting the mass transfer of ammonia to the gas phase. Excessive foaming caused by the acetaldehyde resulted in the planned addition of peroxide being aborted. A thick stable foam built up in the reaction vessel above tolerable levels. If peroxide were added, the additional vigorous foaming could potentially flood the vessel and damage the FTIR.

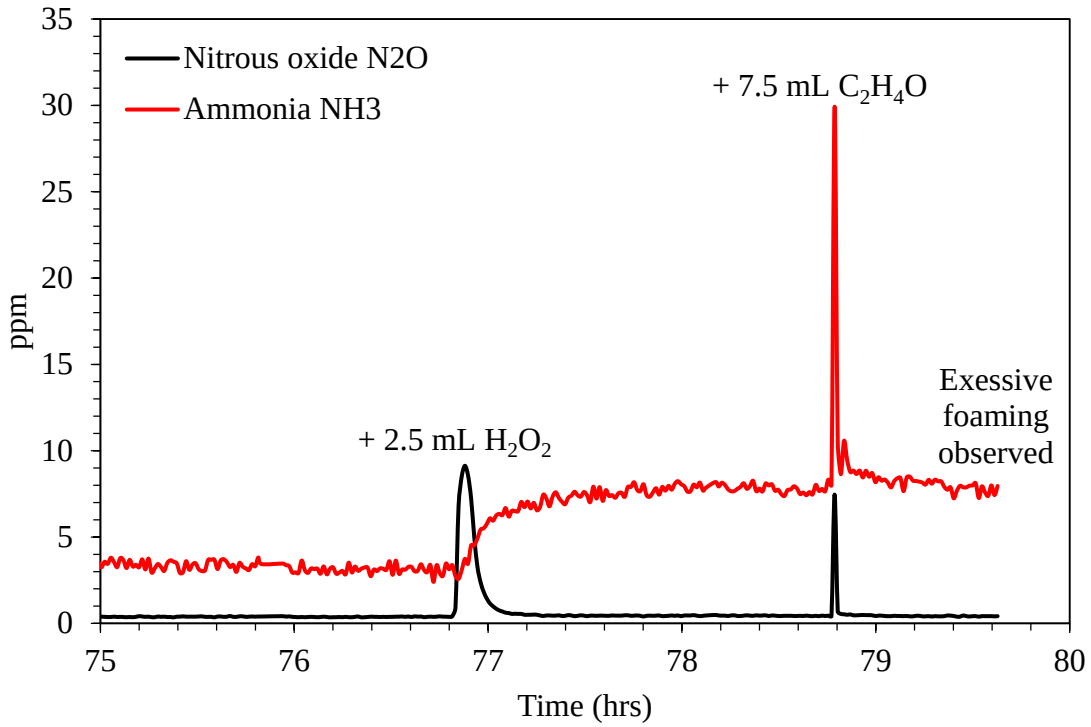

Figure 3: Ammonia and N_2O production from the oxidation of SRP PZ (8 m, 1 wt % Inh A, <0.1 mM Fe^{2+}) via hydrogen peroxide (30 wt %) and acetaldehyde (>97%) in HGF

When the ammonia returned to baseline after each injection of peroxide, a liquid sample was taken and analyzed for total heat stable salts for both experiments. Figure 4 shows cumulative ammonia emitted and total formate accumulated in the solvent as a function of total peroxide added for the two experiments. Ammonia was initially produced at a rate of 0.03 moles per mole of peroxide added for both experiments. Experiment 1 had high metals and no inhibitor while Experiment 2 had low metals and Inh A, indicating that the presence of metals or free radical scavengers does not influence the initial rate of ammonia production via peroxide oxidation. However, Experiment 2 did not see an increase in ammonia production rate later in the experiment, unlike Experiment 1. Also, total formate accumulated at one third the rate in Experiment 2 compared to Experiment 1. Acetate, oxalate, and nitrate were observed in lower molar concentrations than formate.

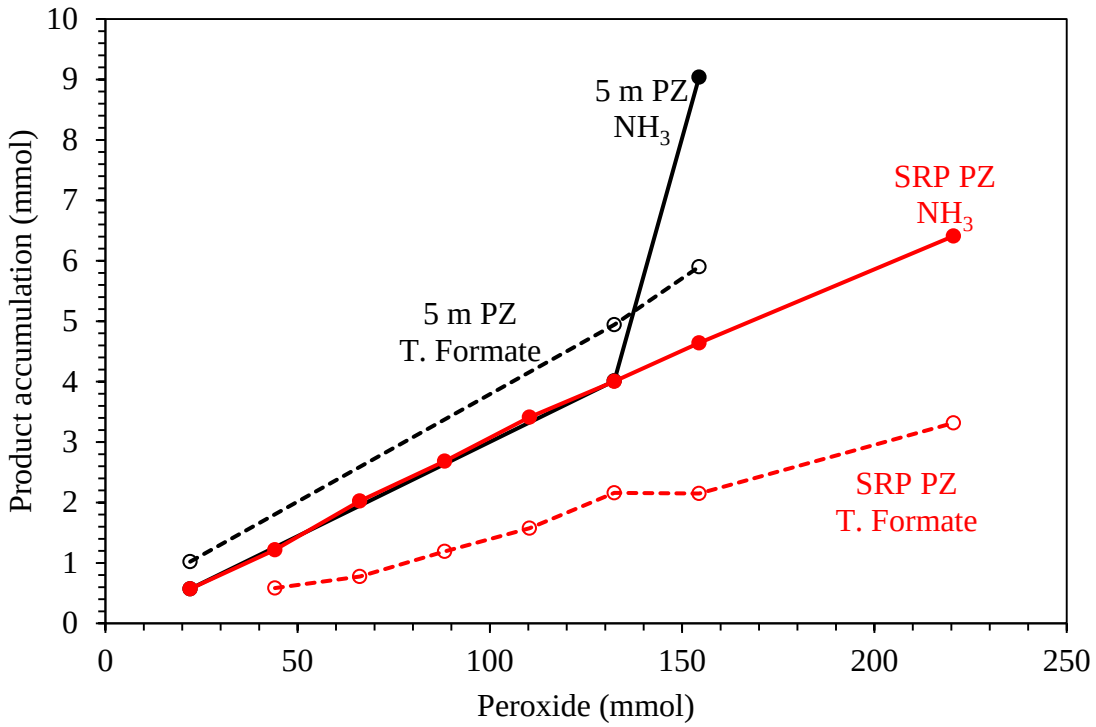

Figure 4: Cumulative production of ammonia and total formate from the oxidation of 5 m PZ and SRP PZ via hydrogen peroxide in HGF

Ethylenediamine (EDA) was observed to accumulate in the liquid phase of both solvents during the experiments. EDA is a stable intermediary degradation product produced as PZ is oxidized to ammonia. While EDA is more volatile than PZ, the amount produced in the experiment was too little to be quantified in the gas phase by FTIR. Figure 5 shows the total EDA accumulation for both experiments.

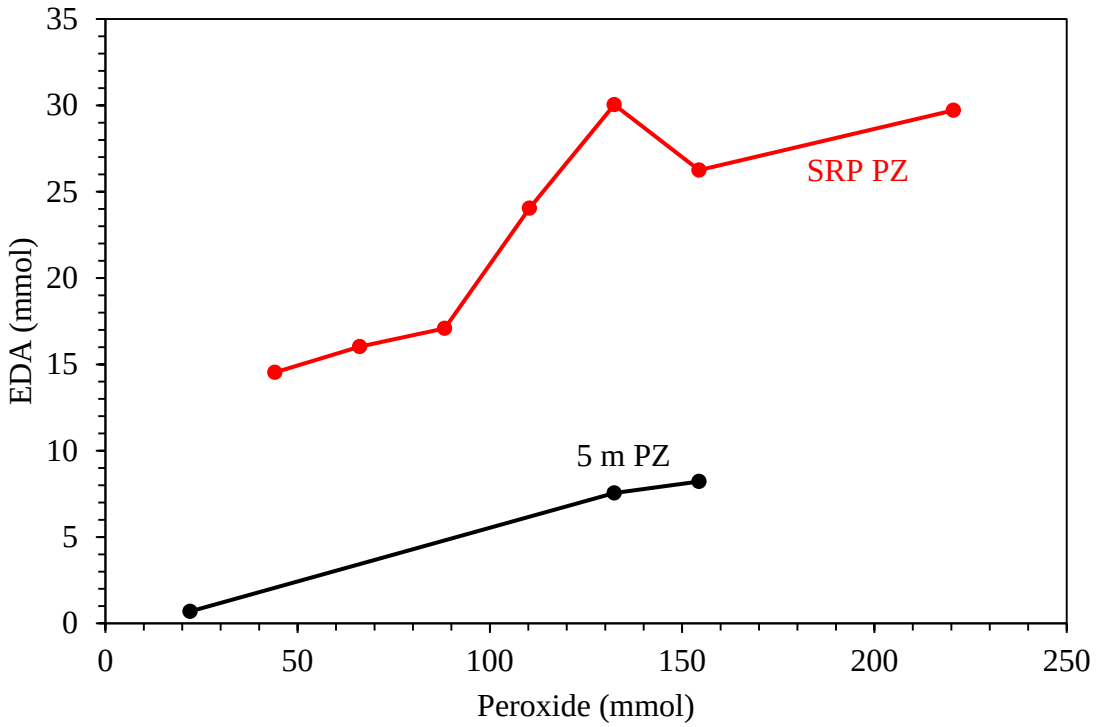

Figure 5: Cumulative production of EDA in the liquid phase from the oxidation of 5 m PZ and SRP PZ via hydrogen peroxide in HGF

In both experiments, the total amount of ammonia, formate, and EDA produced was relatively similar in relative magnitude of molar amounts, at 0.015 to 0.04 moles produced per mole of peroxide added. This is significantly different from previous observations of the oxidation of amines in pilot plants and cyclic degradation apparatuses. 1 mole of ammonia is typically observed per mole of PZ oxidized in these systems, while only 0.1 to 0.2 moles of formate and EDA are accumulated (Voice, 2014). It is possible that cycling the solvent from absorber to stripper conditions produces relatively more ammonia than peroxide oxidation at absorber conditions.

Effect of Heat Stable Salt on Solvent Viscosity

The effect of sulfate and formate accumulation on solvent viscosity was presented in a previous quarterly report (Rochelle et al., 2014). Accumulation of 10 wt % heat stable salts can double solvent viscosity. An expansion of the correlation used by Freeman for the viscosity of PZ was used to model the data collected (Freeman, 2011). The resulting model (Equations 1 and 2) fit the data to less than 5% error but was analytically cumbersome, with 13 regressed coefficients. In the equations, μ is viscosity, T is temperature in K, C_i is the molar concentration of species I, and values a through g_i are the regressed coefficients:

$$\ln\left(\frac{\mu}{\mu_{H2O}}\right) = a + \varphi_1 + \frac{\varphi_2}{T\,[K]} \quad (1)$$

$$\varphi_i = b_i C_{CO2} + c_i C_{amine} + d_i C_{CO2} C_{amine} + e_i C_{salt} + f_i C_{CO2} C_{salt} + g_i C_{salt} C_{amine} \quad (2)$$

A simpler model could be constructed if it is assumed the increase in viscosity as a result of heat stable salt accumulation is solely a function of the concentration of the salt and is not affected by temperature or the concentration of alkaline amine and CO_2. Also, it can be assumed that the presence of salt does not affect the coefficients previously regressed for clean solvent. This reduces the correlation to the Freeman model with a single additional term eC_{salt}:

$$\ln\left(\frac{\mu}{\mu_{H2O}}\right) = a + \varphi_1 + \frac{\varphi_2}{T\,[K]} + eC_{salt} \quad (3)$$

$$\varphi_i = b_i C_{CO2} + c_i C_{amine} + d_i C_{CO2} C_{amine} \quad (4)$$

This can further be reduced to Equation 5, where μ_0 is the predicted solvent viscosity at an equivalent alkalinity, loading, and temperature without salt accumulation:

$$\ln\left(\frac{\mu}{\mu_0}\right) = eC_{salt} \quad (5)$$

The value of e can be regressed linearly from the natural log of the measured viscosity over predicted clean solvent viscosity at equivalent alkalinity, loading, and temperature as a function of salt molar concentration. The results of this regression for sulfate in 7 m MEA and 8 m PZ are shown in Figures 6 and 7. The viscosity of clean MEA was modeled using the Weiland correlation (Weiland, 1998), while the viscosity of clean PZ was modeled using the Freeman correlation (Freeman, 2011).

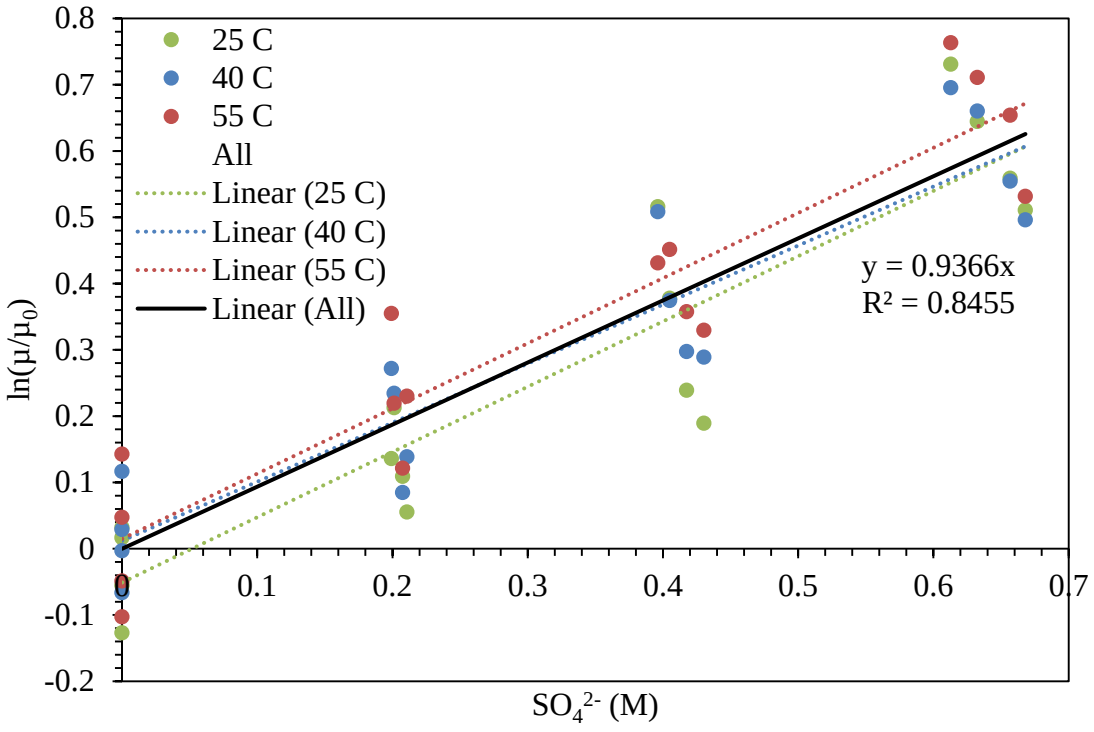

Figure 6: Effect of $[MEA^+]_2[SO_4^{2-}]$ on viscosity of 7 m MEA at 0 to 0.52 mol CO_2/mol alkalinity at 25, 40, and 55 °C

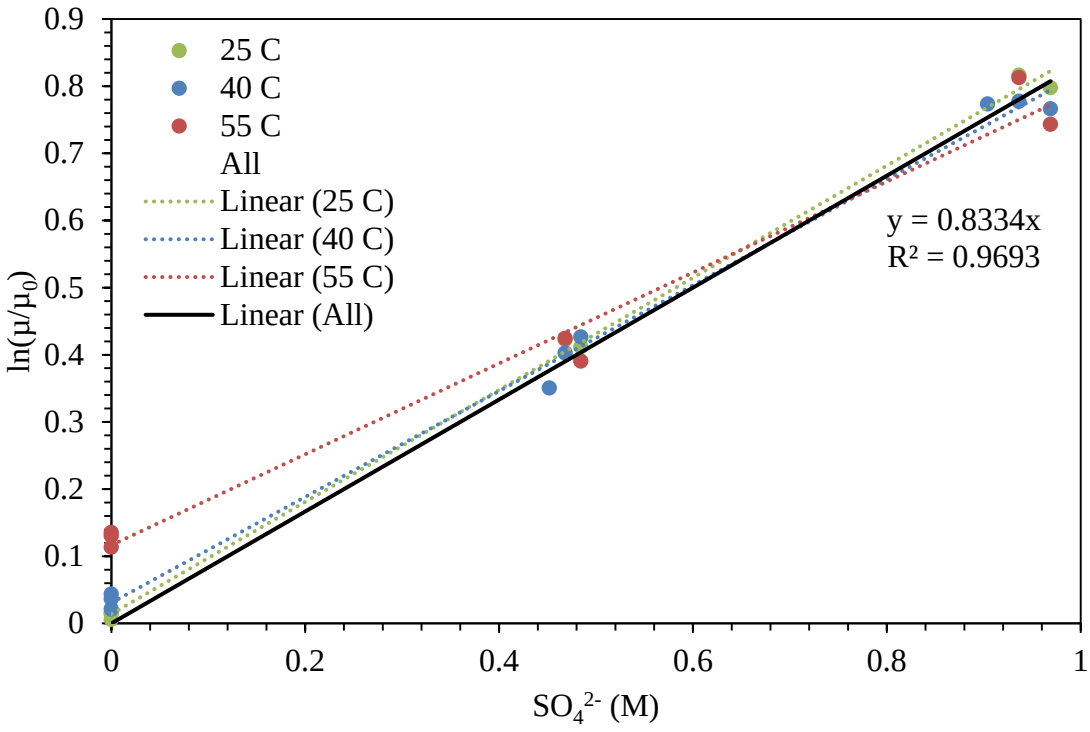

Figure 7: Effect of $[PZ^{2+}][SO_4^{2-}]$ on viscosity of 8 m PZ at 0.3 to 0.45 mol CO_2/mol alkalinity at 25, 40, and 55 °C

Table 1 shows the regressed values of the coefficient e for sulfate in 7 m MEA using subsets of the collected data at either constant temperature or constant CO_2 loading. Temperature had no significant effect on the regression, varying by 10% with no observable trend. Loading had a stronger effect, increasing 15% from unloaded to saturated solution. However, this may be an artifact of variability observed between measured viscosity and the Weiland correlation used to predict clean solvent viscosity. The observed viscosity was consistently lower than predicted for low loading and higher than predicted at high loading regardless of salt concentration, producing the spread in the data in Figure 6. This may be due to a methodological error made in the measurements, or an error in the correlation. The data for PZ shows no such trend relative to loading, though measurements were made over a smaller loading range of 0.25 to 0.45 mol CO_2/mol alkalinity.

Table 1: Regressed value of parameter e for 7 m MEA + MEA-Sulfate from data at constant temperature or CO_2 loading

Data subset:	Value of e:
25 °C	0.98
40 °C	0.89
55 °C	0.98
0 mol CO_2/mol alk.	0.9
0.18 mol CO_2/mol alk	0.94
0.34 mol CO_2/mol alk	1.00
0.52 mol CO_2/mol alk	1.05
All data	0.94

Table 2 shows the regressed values for the coefficient e for multiple heat stable salts for 7 m MEA and 8 m PZ. The viscosity of each solvent was measured at salt concentrations up to 10 wt % at 25, 40, and 55 °C and constant alkalinity. Alkalinity was maintained by adding the salts in acid form and adding additional amine to be protonated as the counter ion for most salts tested.

Nitrate is expected to be a significant contaminant in solvent from both oxidation and absorption of NOx from the flue gas. Nitrate cannot be easily added to solvent as nitric acid due to the oxidative properties of the acid, which would potentially change the solvent alkalinity and add further degradation products. Instead, sodium nitrate was added to 7 m MEA. 7 m MEA with sodium formate was measured to quantify the difference between sodium and protonated MEA as the counter ion. As expected, sodium formate increased viscosity only 60% as much as formate with protonated MEA. Sodium is a more compact cation than the amine and should have less of an effect on viscosity. Surprisingly, sodium nitrate only increased viscosity by 25% as much as sodium formate, even though nitrate is a heavier anion than formate.

Table 2: Regressed coefficient for viscosity correlation for various heat stable salts (paired with protonated amine to maintain alkalinity unless otherwise noted)

Contaminant	7 m MEA	8 m PZ
Sulfate	0.94	0.83
Formate	0.40	0.27
Acetate	0.34	0.33
Propionate	0.47	
Oxalate		0.76
Glycolate	0.40	
Sodium Nitrate	0.06	
Sodium Formate	0.24	

In a typical pilot plant, formate, sulfate, acetate, and nitrate are the most significant heat stable salts to accumulate in the solvent (Nielsen, 2012). Oxalate is less thermally stable and will typically decompose to formate, limiting its concentration. Therefore, controlling formate, acetate, and sulfate accumulation is critical to limiting any increase in solvent viscosity. It is less critical to control nitrate, due to its weaker effect on viscosity.

Conclusions

- 0.03 moles of ammonia are initially produced per mole of peroxide reacted with PZ. Similar amounts of formate and ethylenediamine are also produced.
- Decreasing metal concentration and adding Inh A did not affect the initial rate of ammonia production via peroxide oxidation in PZ, but did reduce formate accumulation by a factor of 3.
- N_2O was also produced by peroxide oxidation, at 2 to 3 orders of magnitude less than ammonia.

- The effect of heat stable salts on solvent viscosity was quantified. Sulfate has the strongest effect, and longer-chained carboxylic acids have an increasing effect on viscosity.

Future Work

In the next quarter, the HTOR apparatus will be upgraded with an improved N_2 bubbler column to increase liquid depth and improve the removal of dissolved oxygen. An electrical resistance corrosion probe will be added to the high temperature section and an oxidation/reduction potential probe will be added downstream of the high pressure/temperature section. All this will be tested with 5 m PZ solvent with and without the addition of Inhibitor 8, a nonvolatile thermally-stable free radical scavenger designed to be recoverable from reclaimer waste.

The viscosity correlations for salt accumulation will be used to model the decrease in heat and mass transfer coefficients and thus the increased energy requirements put on the system. This will be used to determine the optimum balance between equivalent work and solvent reclaiming to maintain a tolerable solvent viscosity.

A new thermal reclaimer, designed to treat up to 1 drum (42 gallons) of solvent per day, will be used to reclaim degraded pilot plant PZ solvent from the SRP (mildly degraded) and Tarong facilities (moderately degraded).

References

Freeman SA. *Thermal Degradation and Oxidation of Aqueous Piperazine for Carbon Dioxide Capture*. The University of Texas at Austin. Ph.D. Dissertation. 2011.

Nielsen PT, Le L, Rochelle GT. "Piperazine degradation in pilot plants." *Energy Proc*. 2013;37:1912–1923.

Rochelle GT et al. "CO_2 Capture by Aqueous Absorption, Fourth Quarterly Progress Report 2013." Texas Carbon Management Program. The University of Texas at Austin. 2014.

Sexton AJ. *Amine Oxidation in CO_2 Capture Processes*. The University of Texas at Austin. Ph.D. Dissertation. 2008.

Voice AK. *Amine Oxidation in Carbon Dioxide Capture by Aqueous Scrubbing*. The University of Texas at Austin. Ph.D. Dissertation. 2013.

Weiland RH, Dingman JC, Cronin B, Browning GJ. "Density and Viscosity of Some Partially Carbonated Aqueous Alkanolamine Solutions and Their Blends." *J Chem Eng Data*. 1998;43(3):378–382.

A Techno-economic Evaluation of an NO_2 Polishing Scrubber with TEA for Solvent and Nitrosamine Management

Quarterly Report for October 1 – December 31, 2014

By Nathan A. Fine

Supported by the Texas Carbon Management Program

McKetta Department of Chemical Engineering

The University of Texas at Austin

January 31, 2015

Abstract

This quarter, a techno-economic evaluation was performed for simultaneously scrubbing NO_2 and SO_2 out of the flue gas upstream of the CO_2 scrubber using a NaOH scrubber with a triethanolamine (TEA) additive. Costs of NO_2 penetration into PZ are \$0.15–\$0.45/MT CO_2/ppm NO_2 due to the reaction of PZ with NO_2 as well as the cost of reclaiming and waste disposal. There is also an additional hidden cost for NO_2 penetration since n-nitrosopiperazine (PZNO), an intermediate product of NO_2 absorption, is carcinogenic. A base case NaOH scrubber at pH 8.0 with 7 m of Mellapak 250X and a gas superficial velocity of 1.5 m/s was analyzed with different TEA feed rates. As the feed rate of TEA increases, the concentration of TEA in the scrubber increases, which allows for greater NO_2 absorption. The optimal NO_2 removal occurs when the costs of increasing the TEA feed balance with diminishing returns on NO_2 removal. This corresponds to 86% removal and 80 mM circulating TEA for a gas inlet of 5 ppm NO_2 and 50 ppm SO_2. As inlet SO_2 increases, the purge rate must also increase so that sodium sulfate does not precipitate out of solution. The optimal TEA and removal decreases at higher purge rates, yielding 62% removal and 20 mM circulating TEA for a gas inlet of 5 ppm NO_2 and 300 ppm SO_2. Savings from NO_2 removal decrease with decreasing inlet NO_2, making pre-scrubbing economical only when inlet NO_2 is greater than around 2 ppm. Finally, analysis was performed with varying height and TEA at a constant 90% NO_2 removal. At 50 ppm inlet SO_2, the additional cost for TEA and height of the column balance with the savings of NO_2 removal, so PZNO concentration can decrease by a factor of 10 without any net cost to the process. At 300 ppm inlet SO_2, TEA scrubbing costs an additional \$1.20/MT CO_2, leaving room for technology improvement.

Nitrosamine Accumulation in Amine Scrubbing

Amine scrubbing is a mature and industrially proven method for carbon capture, but the amine solvents used can nitrosate in the desorber, forming hazardous, carcinogenic nitrosamines. In amine scrubbers, nitrosamine accumulation behaves as shown in Figure 1.

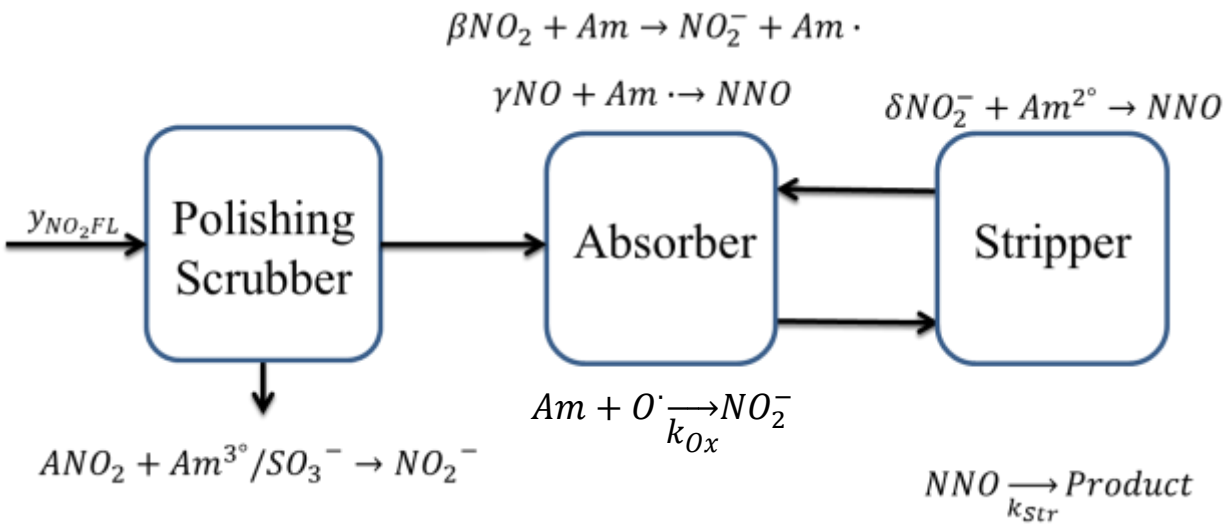

Figure 1: Nitrosamine Cycle

Flue gas containing NO_x, SO_2, and CO_2 gases enters a polishing scrubber where a fraction (A) of the NO_2 can be removed by reaction with sulfite or tertiary amine. The remaining NO_x then enters the absorber where a portion of the NO_2 (β) can be absorbed into the amine solution as nitrite. The NO can also be absorbed into solution (γ) by reacting with amine free radicals formed during NO_2 absorption. The rest of the NO_x will vent from the absorber along with the remaining scrubbed flue gas. Nitrite can also be formed from amine oxidation in solvents that are not oxidatively stable, such as MEA. The nitrite formed, from either NO_x absorption or amine oxidation, travels to the stripper where it can nitrosate a secondary amine with a yield of δ. This yield is determined by the concentration of secondary amines in the solution and their relative nitrosation rates compared to the principal amine. After nitrosating, the nitrosamines thermally decompose in the stripper sump, following pseudo-first-order nitrosation decomposition behavior with a rate constant, k_{str}. Nitrosamine sources from NO_x absorption and amine oxidation balance out with nitrosamine thermal decomposition, yielding a steady state nitrosamine concentration (Equation 1).

$$NNO_{Str} = \frac{(1-A)y_{NO_x}\frac{G}{L}(\delta\beta+\gamma) + \delta k_{Ox}\tau_{Tot}}{k_{Str}\tau_{Str}} \quad (1)$$

This report focuses on the economics of scrubbing NO_2 from the flue gas in the polishing scrubber with triethanolamine (TEA) in order to decrease the steady state nitrosamine concentration as well as manage solvent losses from amine nitrosation.

Economic Benefit of Polishing Scrubbers

In carbon capture from coal-fired power plants, a sodium hydroxide (NaOH) polishing scrubber is economically favorable to remove SO_2 before it reaches the main amine scrubber. A NaOH polishing scrubber works by absorbing SO_2 into NaOH to make sulfite (SO_3^{2-}). Under uninhibited conditions, SO_3^{2-} oxidizes immediately to sulfate, which is then purged from the system. NaOH scrubbing is economical because the reaction is k_g limited, allowing for small packing volumes, NaOH is 40 times cheaper than the amine by mole, negating the need for a regeneration system, and the waste is non-hazardous, simplifying disposal. Any SO_2 that does

make it through the polishing scrubber will react with the amine and form a sulfate salt, which will eventually cost \$0.10–\$0.30/MT CO_2/ppm SO_2 for a PZ solvent depending on reclaiming efficiency and cost of disposal (IEAGHG, 2014). Previous studies based on upgrading an existing limestone slurry scrubber before an MEA scrubber have reported an optimum removal to 10 ppm of SO_2 (Rao et al., 2002); more recent work based on a NaOH polishing scrubber before a proprietary solvent has targeted removal to 0–2 ppm of SO_2 (Gorset et al., 2013).

A similar economic analysis can be done with NO_2 pre-scrubbing to prevent amine nitrosation in the CO_2 absorption loop. NO_2 reacts with PZ with a final stoichiometry of 1:1.5 (Equations 2–6), costing \$0.15–\$0.45/MT CO_2/ppm NO_2. Depending on the rate of NO_2 absorption in the polishing scrubber and the cost of the sacrificial solvent, it may therefore be economical to remove NO_2 upstream of the absorber. Finally, carcinogenic n-nitrosopiperazine (PZNO) is an intermediate product of NO_2 absorption, providing further incentive for NO_2 pre-scrubbing.

$$NO_2 + PZ + OH^- \rightarrow NO_2^- + PZ\cdot + H_2O \quad (2)$$

$$PZ\cdot + 0.5H_2O \rightarrow 0.5PZOH + 0.5PZ \quad (3)$$

$$NO_2^- + PZ \rightarrow PZNO + OH^- \quad (4)$$

$$PZNO \xrightarrow{Base} PZOH + 0.5N_2O + 0.5H_2O \quad (5)$$

$$NO_2 + 1.5PZ \rightarrow 1.5PZOH + 0.5N_2O \quad \text{Sum} \quad (6)$$

Kinetics and Material Balances for NO_2 Scrubbing with TEA

Tertiary amines have been shown to rapidly absorb NO_2 at the pH and temperature in a polishing scrubber (Rochelle et al., 2013). The material balance for absorption is shown below. NaOH and TEA are fed to the polishing scrubber at a constant rate. The NaOH reacts with SO_2 to form sulfate and, with a small amount of CO_2, a sodium bicarbonate ($NaHCO_3$) buffer at pH = 7.5–9.0. The TEA will speciate to protonated TEA ($TEAH^+$) and free TEA depending on the pH; only the free TEA is active in absorbing NO_2. The free TEA absorbs NO_2 forming nitrite (NO_2^-) and a TEA radical (TEA•), which then oxidizes to byproducts. The overall stoichiometry of NO_2 absorption with TEA is approximately 1:1 (Rochelle et al, 2013). The purge rate is set so that the exit sodium sulfate will not precipitate out of solution. For this study, the sulfate concentration was set to a conservative 1.5 M since the effects of nitrite and TEA on the solid solubility of sodium sulfate have not been determined. The steady state material balances for NaOH and TEA are given in Equations 7–9.

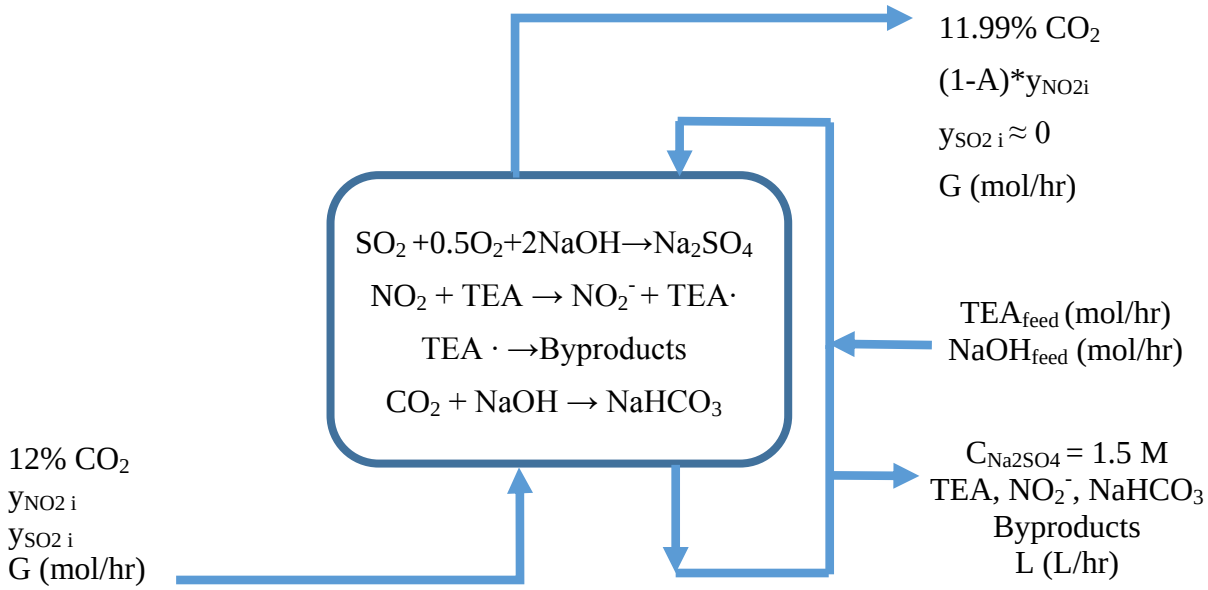

Figure 2: Material Balance for SO_2 and NO_2 Absorption in a Polishing Scrubber

$$\frac{dC_{Na_2SO_4}}{dt} = 0 = Gy_{SO_{2\,i}} - LC_{Na_2SO_4} \tag{7}$$

$$\frac{dC_{Na}}{dt} = 0 = \dot{n_{NaOH_{feed}}} - 2Gy_{SO_2} - LC_{NaHCO_3} \tag{8}$$

$$\frac{dC_{TEA}}{dt} = 0 = \dot{n_{TEA_{feed}}} - GAy_{NO_{2\,i}} - LC_{TEA} \tag{9}$$

Since the purge is set to 1.5 M Na_2SO_4, the ratio of purge flow to gas flow can be directly determined from Equation 7 to yield Equation 10. Any excess NaOH not used to neutralize the SO_2 will react with CO_2 and fix the pH (Equation 11). The steady state concentration of TEA in solution is given by Equation 12 with the concentration of free TEA determined using Henderson-Hasselbalch (Equation 13).

$$\frac{L}{G} = \frac{y_{SO_{2\,i}}}{C_{Na_2SO_4}} = \frac{y_{SO_{2\,i}}}{1.5\ M} \tag{10}$$

$$pH = 6.1 + log\frac{HCO_3^-}{p_{CO_2} * H_{CO_2}} = 6.1 + log\frac{HCO_3^-}{0.12\ atm * 0.018\ M/atm} \tag{11}$$

$$C_{TEA} = Ay_{NO_2} * \frac{G}{L} - \frac{\dot{n_{TEA_{feed}}}}{L} \tag{12}$$

$$TEA_{free} = C_{TEA} * \frac{10^{pH-pK_{a\,TEA}}}{1 + 10^{pH-pK_{a\,TEA}}} \tag{13}$$

The fraction of NO_2 absorbed (A) into the solvent is determined by the number of mass transfer units in the polishing scrubber (Equation 14), which is a function of the overall mass transfer coefficient for NO_2 absorption, the effective wetted area in the polishing scrubber, and the gas volumetric flow rate. An $\frac{a_e}{G}$ of 1.52 *10^6 s Pa m^2 mol^{-1} was used, representing a gas at 55 °C travelling through 7 m of Mellapak 250X with a superficial velocity of 1.5 m/s. This value is

roughly equal to polishing scrubber conditions at the Tarong and NCCC pilot plants. The gas side mass transfer coefficient (k_g) was taken to be $5*10^{-6}$ mol s^{-1} Pa^{-1} m^{-2} and the overall liquid side mass transfer coefficient (k_g') is assumed to be in the mass transfer with fast reaction regime (Equation 16).

$$A = 1 - e^{-N_{OG}} = 1 - e^{-K_g * \frac{a_e}{G}} \tag{14}$$

$$\frac{1}{K_g} = \frac{1}{k_g} + \frac{1}{k_g{}'} \tag{15}$$

$$k_g{}'[=] \frac{mol}{s\ Pa\ m^2} = 5.4 * 10^{-6} * \sqrt{TEA_{free}} \tag{16}$$

Safety

Whenever a new technology is considered, all of the risks associated with it should be carefully weighed. Scrubbing NO_2 with TEA is a relatively risk free method of removing NO_2 because the solvent is benign and NO_2 is fixed as nitrite instead of nitrosamine. Furthermore, the solvent is non-volatile, minimizing carryover from the polishing loop into the CO_2 absorption loop. The waste from the polishing scrubber will have to go to a wastewater treatment facility due to the high N content.

Economic Results

Effect of varying TEA

The economic benefit of removing NO_2 upstream of the absorber using TEA was analyzed for a flue gas containing 50 ppm SO_2 and 5 ppm NO_2. Any NO_2 not absorbed in the polishing scrubber is captured in the main absorber, costing a nominal \$0.23/MT CO_2/ppm NO_2. The polishing scrubber is assumed to be built for SO_2 absorption, so there is negligible additional capital cost associated with using TEA as an additive. The additional cost therefore, is the cost of the TEA (\$0.30/mol) added to the polishing scrubber. Savings are given by Equation 17 using the Tarong CO_2 capture rate as a basis.

$$Savings[=] \frac{\$}{MT\ CO_2} = \frac{\$0.23}{MT\ CO_2 \cdot ppm\ NO_2}(1 - A)5\ ppm\ NO_2 - \dot{n_{TEA}}_{feed} \frac{\$\ 0.30}{mol\ TEA} \frac{1\ hr}{0.684\ MT\ CO_2} \tag{17}$$

Figure 3 shows the performance of the scrubber as the concentration of total TEA varies. At low concentrations of TEA, NO_2 penetration is high, which limits the possible savings on PZ nitrosation. At high circulating TEA concentration, the feed rate of TEA ($\dot{n_{TEA}}_{feed}$) is dominated by the purge rate with diminishing additional savings from NO_2 removal. The economic optimum occurs where these two effects are balanced. However, the best operating condition is probably at higher concentrations of TEA due to the additional benefit of lower nitrosamine concentration in the PZ loop.

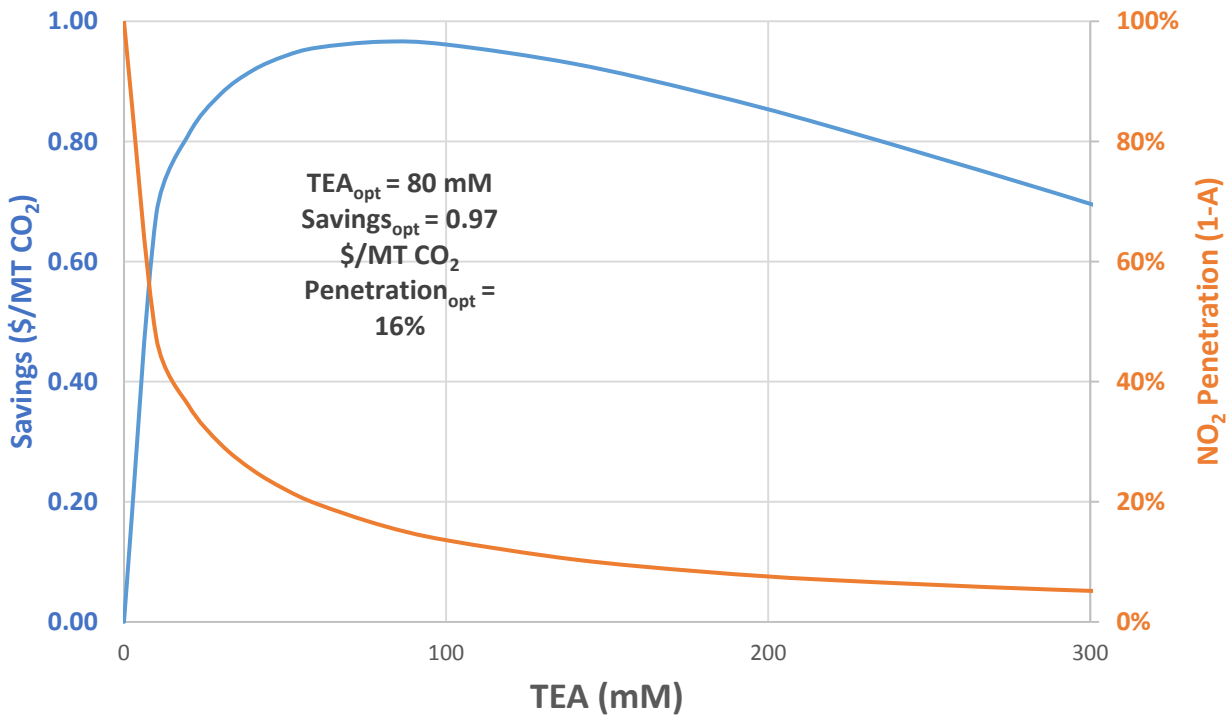

Figure 3: Polishing scrubber performance with varying TEA

pH = 8.0, T = 55 °C, $y_{NO2\,i}$ = 5ppm, $y_{SO2\,i}$ = 50 ppm, 7 m Mellapak 250X, u_{gas} = 1.5m/s

Effect of varying SO_2

The optimal TEA concentration was found for 10–300 ppm inlet SO_2 (Figure 4). As SO_2 increases, the purge rate must increase to keep a constant outlet concentration of Na_2SO_4. This decreases the possible savings since the TEA feed rate must be higher to keep the same concentration of TEA in the scrubber. Also, the optimal TEA decreases with increasing SO_2 since the purge rate begins to dominate the economics at lower TEA. Predictably, NO_2 penetration at optimal savings increases with increasing SO_2 due to lower circulating TEA. At high inlet SO_2 the economics could be improved further by upgrading the existing slurry scrubber to lower the purge rate in the polishing scrubber.

The analysis was repeated for a packing height of 3 meters instead of 7 meters, reflecting assumptions made in recent amine scrubbing techno-economic evaluations (Frailie, 2014). Overall savings decrease by approximately \$0.40/MT CO_2, and NO_2 penetration increases by 30%, as the packing height decreases from 7 meters to 3 meters. High NO_2 penetration in the 3 m column shows that more packing is needed to effectively remove NO_2 in the pre-scrubber. Thus, the height of the polishing scrubber will most likely be determined by the target NO_2 removal (k_g' limited) instead of the target SO_2 removal (k_g limited).

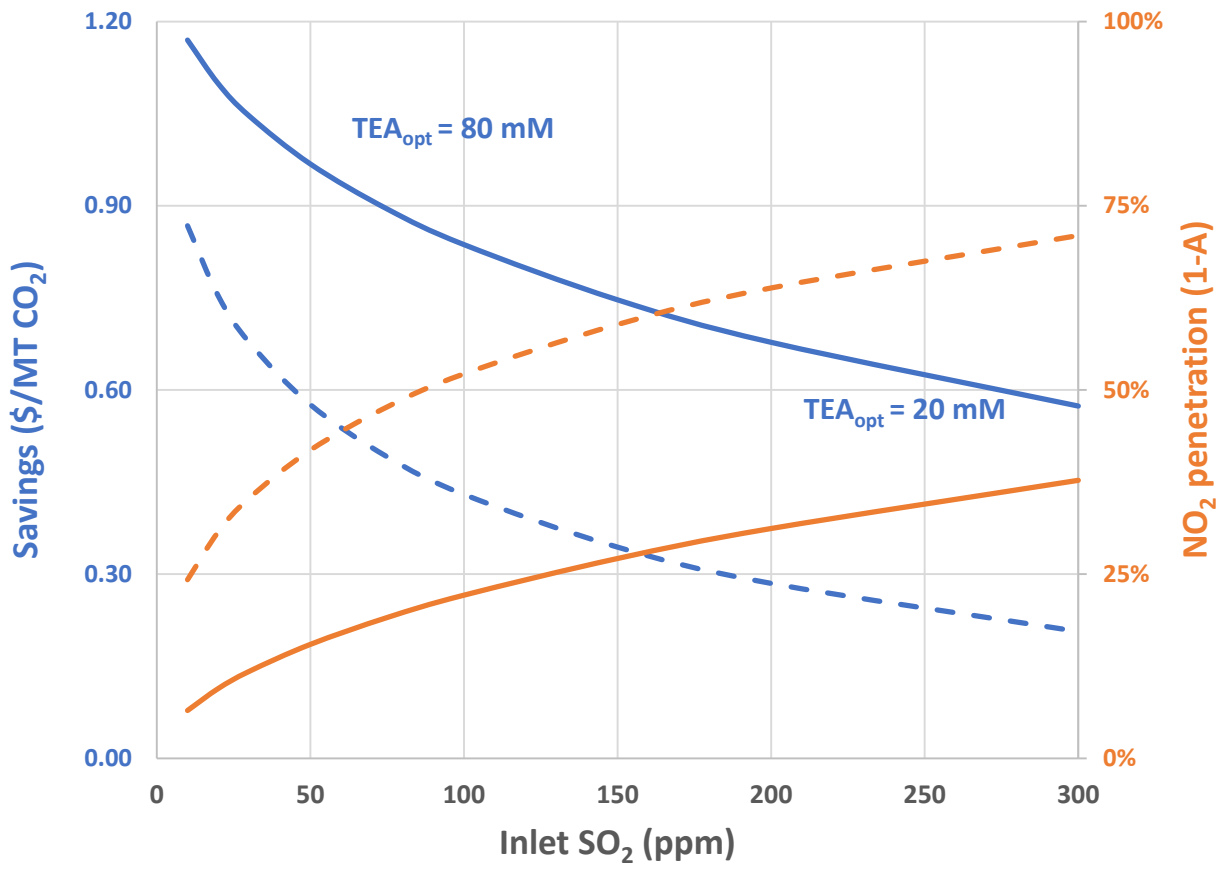

Figure 4: Savings and NO_2 penetration for 7 m (Solid) and 3 m (dashed) of packing pH = 8.0, T = 55 °C, $y_{NO2\,i}$ = 5ppm, u_{gas} = 1.5 m/s, optimal TEA

Effect of varying inlet NO_2

The economics of the 7 m polishing scrubber were evaluated as both NO_2 and SO_2 varied, with TEA optimized at each condition. As inlet NO_2 decreases, there is less overall PZ degradation through nitrosation, so there is less opportunity for saving through TEA scrubbing (Figure 5). Nitrosamine concentration is roughly proportional to inlet NO_2 (Equation 1), so nitrosamines become less important as inlet NO_2 decreases. Thus, NO_2 scrubbing will have diminishing returns as inlet NO_2 decreases and should only be pursued when inlet NO_2 is above approximately 2 ppm.

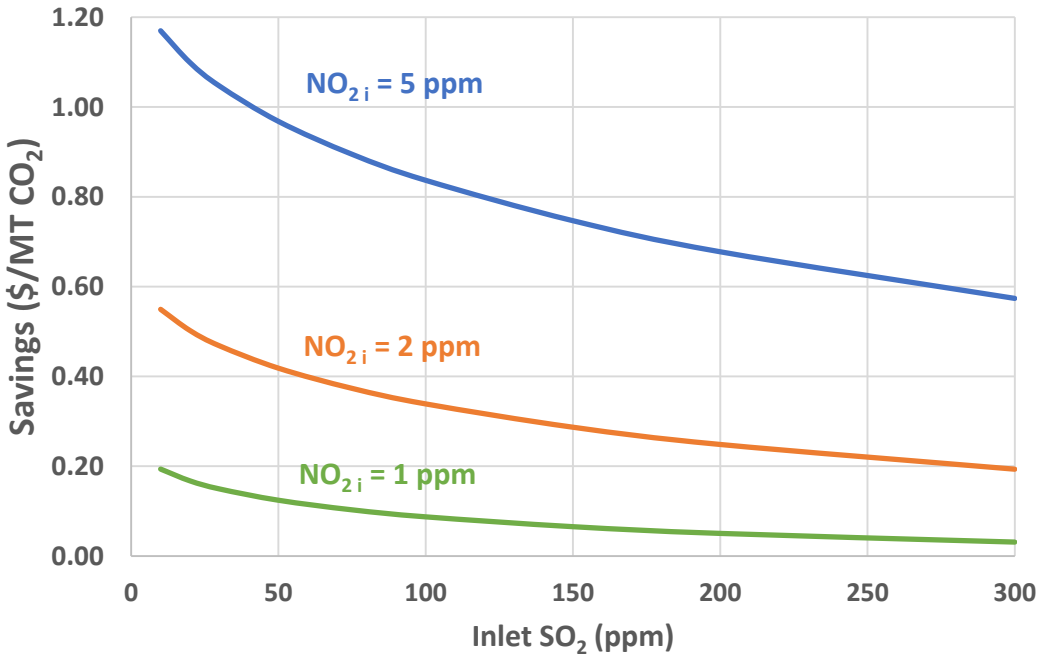

Figure 5: Savings from NO_2 scrubbing with varying inlet NO_2
pH = 8.0, T = 55 °C, 7 m Mellapak 250X, u_{gas} = 1.5m/s, optimal TEA

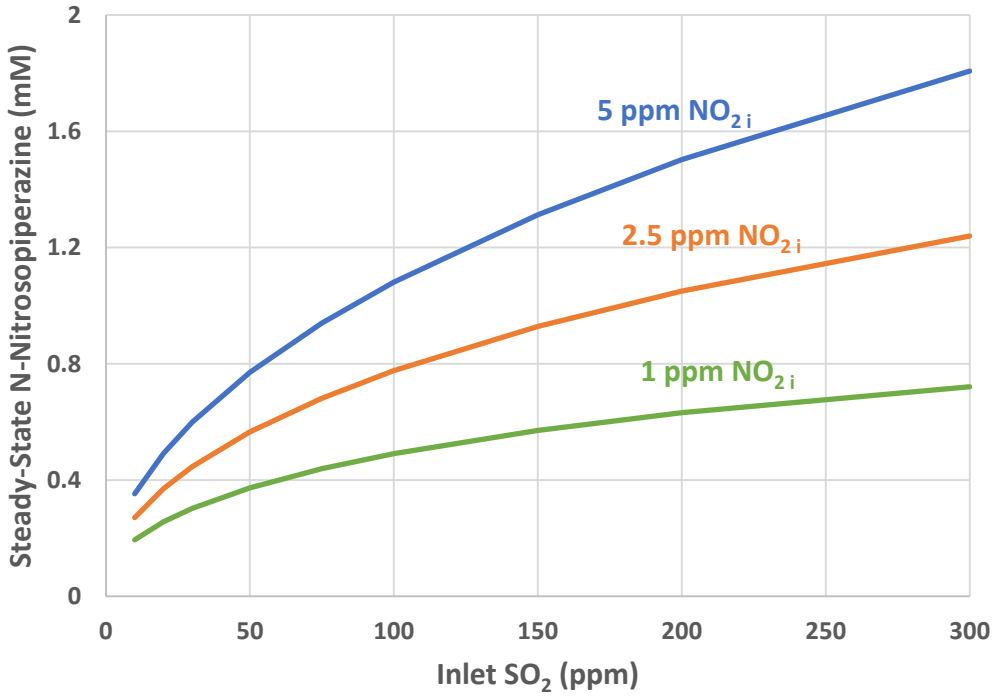

Figure 6: N-Nitrosopiperazine accumulation after NO_2 pre-scrubbing
Equation 1 constants from previous report (Rochelle et al., 2014)

Packing Height and TEA Optimization at Constant Penetration

The previous optimizations have focused on solvent management through NO_2 pre-scrubbing, but another goal is to limit nitrosamine accumulation in the main scrubber. TEA and packing height were both optimized to find the lowest-cost option for pre-scrubbing 5 ppm NO_2 to 0.5 ppm NO_2. The additional cost for NO_2 scrubbing is the additional height over the 3 meters already needed for SO_2 polishing and the cost of the TEA additive. Packing cost for Mellapak 250X constructed from 304 stainless steel is \$2000/m^3 (Equation 18) (Rochelle et al., 2014). Given a gas velocity of 1.5 m/s and 12% inlet CO_2, packing costs can be directly converted to an amortized capital cost (Equations 19–21) (Frailie, 2014).

$$Packing\ Cost\ [=]\frac{\$}{m^3} = 7.31 * a_p + 203.05 = 2031\frac{\$}{m^3} \tag{18}$$

$$Amortized\ Cost[=]\frac{\$}{MT\ CO_2} = \frac{Packing\ Cost * (V_{pack\ tot} - V_{pack\ SO_2}) * \alpha\beta}{MT\ CO_{2\ captured}/year} \tag{19}$$

$$Amortized\ Cost = \frac{2031\frac{\$}{m^3} * \pi {r_{col}}^2 * (h_{pack\ tot} - h_{pack\ SO_2}) * 0.2 * 5}{1.5\frac{m}{s} * \pi {r_{col}}^2 * 0.00019\frac{MT\ CO_{2\ captured}}{{m^3}_{Flue\ Gas}} * 2.8E7\frac{s}{oper\ year}} \tag{20}$$

$$Amortized\ Cost = 0.25\frac{\$}{MT\ CO_2 \cdot m} * \left(h_{pack\ tot} - 3\ m\right) \tag{21}$$

Additional blower, pump, and shell costs associated with the extra NO_2 scrubbing height were neglected in the analysis, but could add 0.10–0.20 \$/MT CO_2. No additional distributors or collectors are needed since NO_2 absorbs simultaneously with SO_2. Figure 7 shows how savings and packing height vary as inlet SO_2 increases. The maximum savings is at the lowest inlet SO_2 and requires an additional 1 m of packing to reach 90% NO_2 removal. Under these conditions, the purge rate is very low, allowing a very high TEA concentration (750 mM) before the purge rate dominates TEA losses. As inlet SO_2 increases, optimal TEA decreases and packing must increase to remove 90% CO_2. At 300 ppm inlet SO_2, total packing height reaches 9 m, costing an additional 1.20 \$/MT CO_2 over the base case without NO_2 scrubbing. Under these conditions sulfite scrubbing for NO_2 removal will be a more attractive technology.

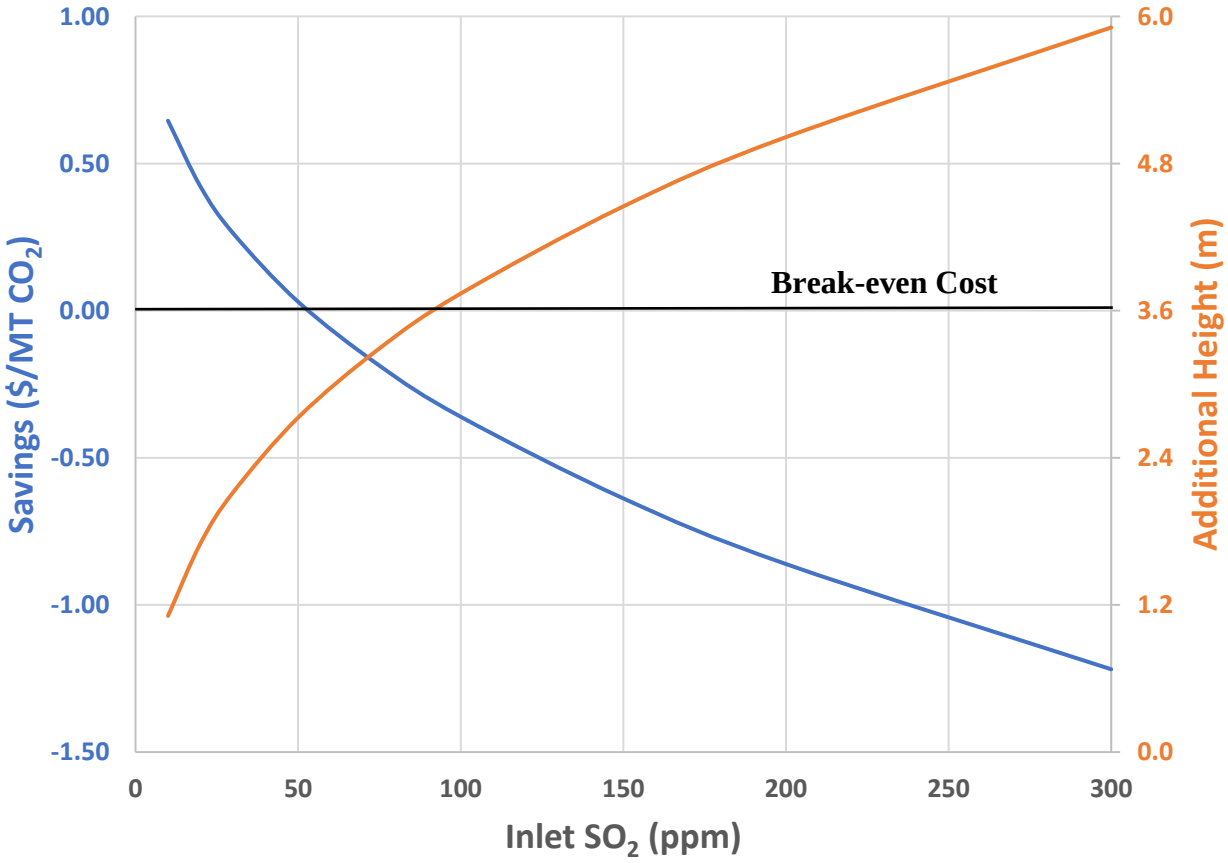

Figure 7: Savings for 90% NO_2 removal

pH = 8.0, $y_{NO2\,i}$ = 5ppm, T = 55 °C, u_{gas} = 1.5m/s, optimal TEA, optimal packing height

Conclusions

- NO_2 irreversibly reacts with PZ at a 1:1.5 stoichiometry.
- Inlet NO_2 costs 0.15–0.45 \$/MT CO_2/ppm NO_2 in PZ degradation and waste disposal costs.
- Pre-scrubbing NO_2 using the existing NaOH scrubber and a triethanolamine additive can save on degradation costs.
- Simultaneously scrubbing 5 ppm NO_2 and 50 ppm SO_2 with 80 mM TEA additive in a 7 m column saves 0.97 \$/MT CO_2.
- Savings decrease with increasing inlet SO_2 due to high purge rates.
- Savings increase with increasing column height due to higher absorption efficiency.
- Savings increase with increasing inlet NO_2 since the costs associated with PZ nitrosation increase.
- At 50 ppm inlet SO_2 and 5 ppm NO_2, n-nitrosopiperazine can be reduced by a factor of 10 with no net cost.

Future Work

- Perform a techno-economic analysis for NO_2 pre-scrubbing with sulfite.

References

Frailie PT. *Modeling of Carbon Dioxide Absorption/Stripping by Aqueous Methyldiethanolamine/Piperazine*. The University of Texas at Austin. Ph.D. Dissertation. 2014.

Gorset O, Knudsen JN, Bade OM, Askestad I. "Results from testing of Aker Solutions advanced amine solvents at CO_2 Technology Centre Mongstad." *Energy Proced.* 2014; 63:884–892.

IEAGHG. "Evaluation of Reclaimer Sludge Disposal from Post-Combustion CO_2 Capture Prepared by." *2014/02*. March 2014.

Rao AB, Rubin ES. "A Technical, Economic, and Environmental Assessment of Amine-Based CO_2 Capture Technology for Power Plant Greenhouse Gas Control." *Environ Sci Technol.* 2002;41(2):4467–4475.

Rochelle GT et al. "CO_2 Capture by Aqueous Absorption, Third Quarterly Progress Report 2013." Texas Carbon Management Program. The University of Texas at Austin. 2013.

Rochelle GT et al. "CO_2 Capture by Aqueous Absorption, First Quarterly Progress Report 2014." Texas Carbon Management Program. The University of Texas at Austin. 2014.

Corrosivity Screening of Amine Solutions in Thermal Cylinders

Quarterly Report for October 1 – December 31, 2014

by Kent Fischer

Supported by the Texas Carbon Management Program

McKetta Department of Chemical Engineering

The University of Texas at Austin

January 31, 2015

Abstract

A series of experiments was conducted to determine the relationships between amine structure and corrosivity. These experiments were conducted in 316 stainless steel Swagelok® cylinders, which were placed into 150 °C ovens and heated, causing corrosion of the cylinder and degradation of the amine. A series of linear amines was tested to determine the effect of chain length on amine corrosivity, and a series of hindered amines blended with piperazine (PZ) was screened. Corrosion was measured by determination of the amount of dissolved metal in solution using ICP-OES.

Introduction

The concentrated amine solutions used in post-combustion capture are corrosive to metal surfaces. Significant cost savings might be achieved if less corrosive solvents were discovered, allowing more construction with carbon steel instead of the more expensive stainless steel.
Corrosion occurs when a metal surface is oxidized, converting the oxidation state zero metal into a positively charged metal ion. Two corrosion examples are shown in Figure 1 below.

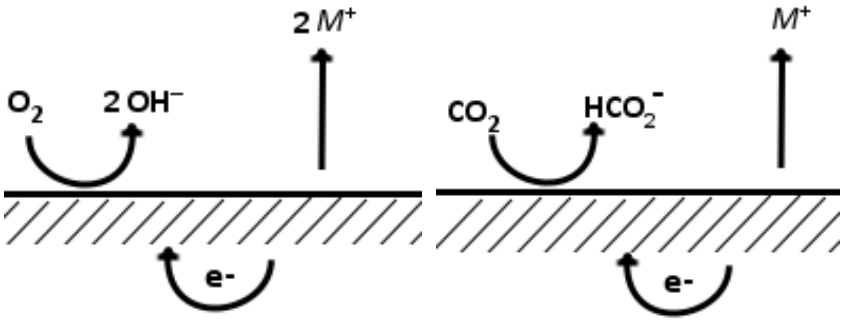

Figure 1: Corrosion in the presence of O_2 in solution (left) and in the presence of CO_2 and absence of O_2 (right)

The shaded area represents a metal surface in solution. In the oxygen-rich case, dissolved oxygen in the solution is reduced, producing hydroxide. In the oxygen-deficient case, carbon dioxide is reduced to formate. In both cases, the electrons are supplied by the oxidation of the metal.

Experimental Methods

A set of linear amines was screened to test for the effect of chain length on corrosivity, a series of hindered amines blended with PZ was screened to determine their corrosivity. The amines tested are given below in Table 1 along with their concentrations.

Table 1: Amines used in thermal cylinder experiments

Linear Amines		
Ethylenediamine (EDA)	**5 m**	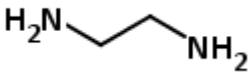
Monoethanolamine (MEA)	**10 m**	
Propylenediamine (PDA)	**5 m**	
Monopropanolamine (MPA)	**10 m**	
Putrescine or 1,4-diaminobutane (PUT or DAB)	**5 m**	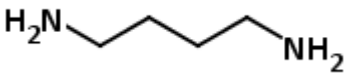
Jeffamine® EDR-104 or bis(aminoethyl)ether (JEFF or BAE)	**5 m**	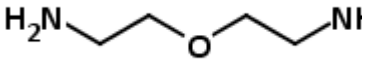
Hindered Amine/PZ blends		
2-Amino-2-methyl-propanol (AMP)	**2.67 m amine/1.33 m PZ**	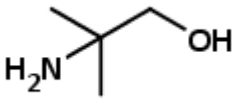
2-Amino-2-methyl-1,3-propanediol (AMPD)	**2.67 m amine/1.33 m PZ**	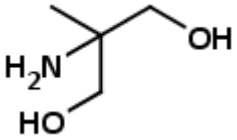

Tris(hydroxymethyl)aminomethane (TRIS)	**2.67 m amine/1.33 m PZ**	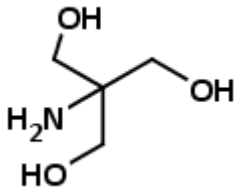
tert-butylaminoethanol (TBAE)	**2.67 m amine/1.33 m PZ**	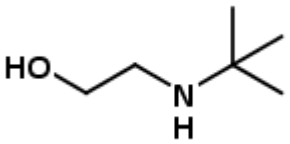
2-Piperidinemethanol (PM)	**2.67 m amine/1.33 m PZ**	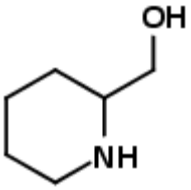
2-Piperidineethanol (PE)	**2.67 m amine/1.33 m PZ**	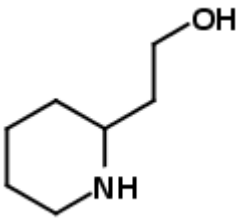

Thermal Cylinders for Corrosion Screening

All solutions were prepared to the specified concentration and then loaded with 0.4 mol CO_2/mol alkalinity. 4 mL of each solution was placed inside 3/8" Swagelok® stainless steel cylinders with volumes of 4.5 mL. The cylinders were sealed and heated to 150 ° C in a convection oven. Cylinders were removed at predetermined intervals and promptly cooled in a refrigerator to halt any further thermal degradation (Hatchell, 2013; Namjoshi, 2013).

After all cylinders had been removed from the oven and refrigerated, they were opened and sampled for metals analysis by ICP-OES. Each series of amines contained several time points with the final time point between 700 and 800 hours of heating. The analytical and experimental technique is similar to Freeman (Freeman, 2011).

ICP OES

All metals analysis was done by inductively coupled plasma optical emission spectroscopy using a Varian 710-ES instrument run in axial configuration. Samples were prepared by diluting to

30X through dilution with DDI water and acidified to 2% by mass with concentrated, low-metals grade nitric acid. Calibration curve standards were prepared from Fischer Chemicals 2000 ppm atomic absorption reference standards. Wavelengths analyzed are given in Table 2. Results for each wavelength were averaged with other wavelengths for the same ion.

Table 2: Wavelengths Analyzed in ICP OES analysis (nm)

Cr	Cr	Cr	Fe	Fe	Fe
205.560	206.158	267.716	234.350	238.204	259.940
Mn	Mn	Mn	Ni	Ni	Ni
257.610	259.372	260.568	216.555	221.648	231.604

Results

Screening of Linear Amines

Figure 3 highlights the marked difference in corrosivity between the two-carbon backboned species, MEA and EDA, and the three-carbon backboned species MPA and PDA. MEA and EDA both showed the highest levels of corrosion seen in these experiments. In the MEA sample, iron had accumulated to 27 mmol/kg solution, and in the EDA sample, iron had accumulated to 28 mmol/kg solution. The three-carbon backbone analogs MPA and PDA had negligible corrosivity in comparison. Iron had accumulated in the MPA sample to 0.8 mmol/kg solution, whereas PDA had accumulated iron to 0.3 mmol/kg solution. EDA is 93 times as corrosive as its 3-carbon analog, PDA, and MEA is 34 times as corrosive as its 3-carbon analog MPA.

There was no clear trend among the other linear amines. Figure 4 summarizes the corrosivity of the four- and five-carbon analogs of these linear amines. Putrescene (PUT or DAB), the four-carbon analog of EDA, showed low corrosivity, accumulating 3.1 mmol/kg solution of iron. BAE represents a longer chain analog of EDA, whereas DGA® represents a longer chain analog of MEA. If the ether groups in these molecules do not appreciably interact, then these molecules should behave similarly to the 5-carbon analogs of EDA and MEA. BAE showed moderate corrosivity, accumulating 11 mmol/kg solution of iron. DGA® showed low corrosivity, accumulating 1.4 mmol/kg solution of iron. There is a clear trend between the two- and three-carbon analogs where corrosivity drops sharply, but the four- and five-carbon analogs have no similar trend.

Figure 5 shows all time points for the EDA series of cylinders. It does not show a linear increase of metals, which would correspond to a constant rate of corrosion. Rather it shows most corrosion occurring in the first 200 hours of the experiment, with limited corrosion after that point. However, this may be due to the way the experiment was conducted. Cylinders were removed from convection ovens and kept in the refrigerator to be analyzed after all cylinders were completed. Additional corrosion may have occurred in the refrigerator after the cylinders were removed from the convection ovens. Future experiments will sample all cylinders immediately, without allowing additional time for the early time points to corrode in the refrigerator.

Screening of Hindered Amines/PZ blends

Figures 6, 7, and 8 show the accumulation of metals over time for the hindered amine experiments. Figure 6 shows iron accumulation, Figure 7 shows chromium accumulation, and Figure 8 shows nickel accumulation. Manganese was very near zero for all samples analyzed, so it could not be plotted. Certain hindered amines were more corrosive than others. There is a clear increasing trend in corrosivity from AMP to AMPD to TRIS. These amines are structural analogs with 1, 2, and 3 alcohol groups, respectively. The very hindered amine TBAE was very non-corrosive. PM accumulated 2.8 mmol/kg solution of iron, whereas 2-PE had only accumulated 0.03 mmol/kg solution of iron. This makes the PM solution 72 times more corrosive than the PE solution. There is a two-carbon backbone between the nitrogen and the alcohol functional group in PM, but a three-carbon backbone between the nitrogen and alcohol functional group in PE. This is the same trend of corrosivity decreasing with chain length seen in the linear amines.

Overall Trends in Corrosivity

Likely the two-carbon backbone species are able to form stable organometallic complexes that serve as catalysts for the reduction of CO_2 to HCO_2^-, which is accompanied by rapid oxidation and corrosion of the metal. The three-carbon backbone species are too long and labile to form a stable metal center, preventing metal-catalyzed oxidation. Figure 2 illustrates this effect with a stable MEA carbamate complex with iron, contrasted with an unstable MPA carbamate metal complex. The two-carbon backbone of MEA allows it to form a very stable octahedral complex with iron. The same complex cannot be formed with the three-carbon backbone of MPA, as it is too long and labile to easily form an octahedral complex.

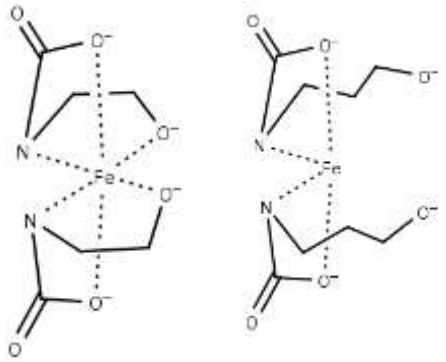

Figure 2: Stable MEA carbamate metal catalytic center (left) and unstable MPA carbamate metal catalytic center (right)

Figures 9, 10, 11, and 12 show the yearly corrosion of iron, chromium, nickel, and manganese, respectively. This attempts to directly compare the linear amine experiments and the hindered amine experiments. The linear amines MEA and EDA were the most corrosive.

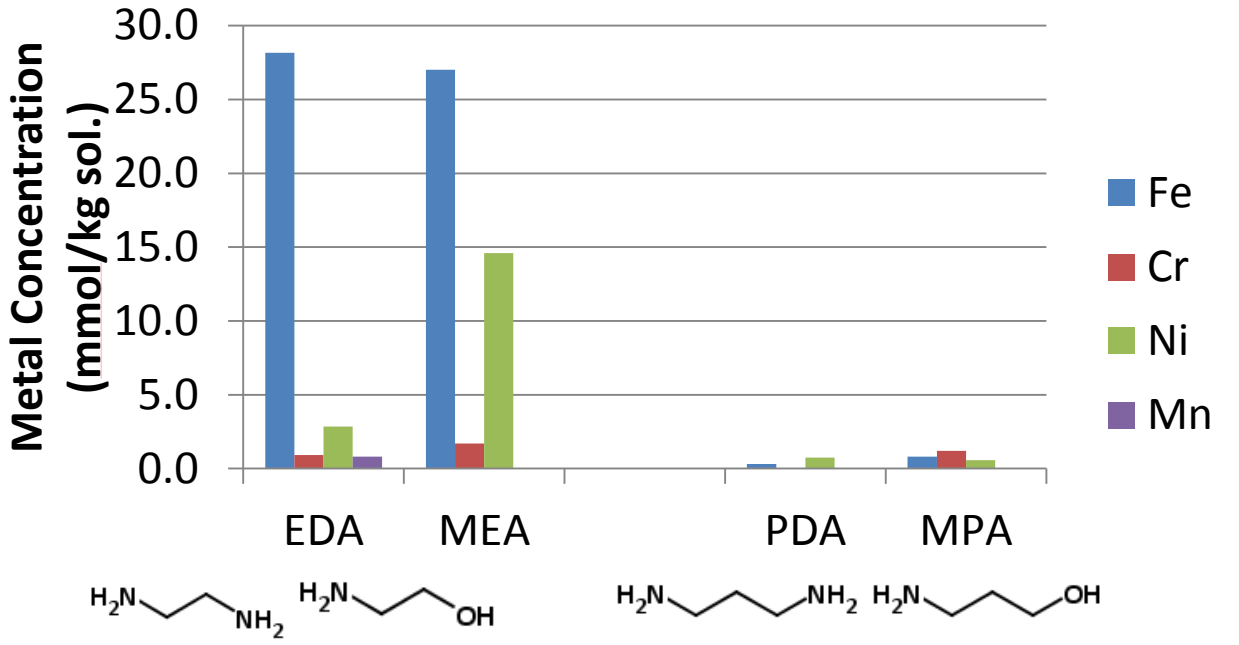

Figure 3: Metal accumulation after 670 hrs (EDA, PDA), 694 hrs (MEA), or 528 hrs (MPA) in thermal cylinders at 150 °C. EDA, PDA concentration is 5 molal. MEA and MPA concentration is 10 molal. α = 0.4.

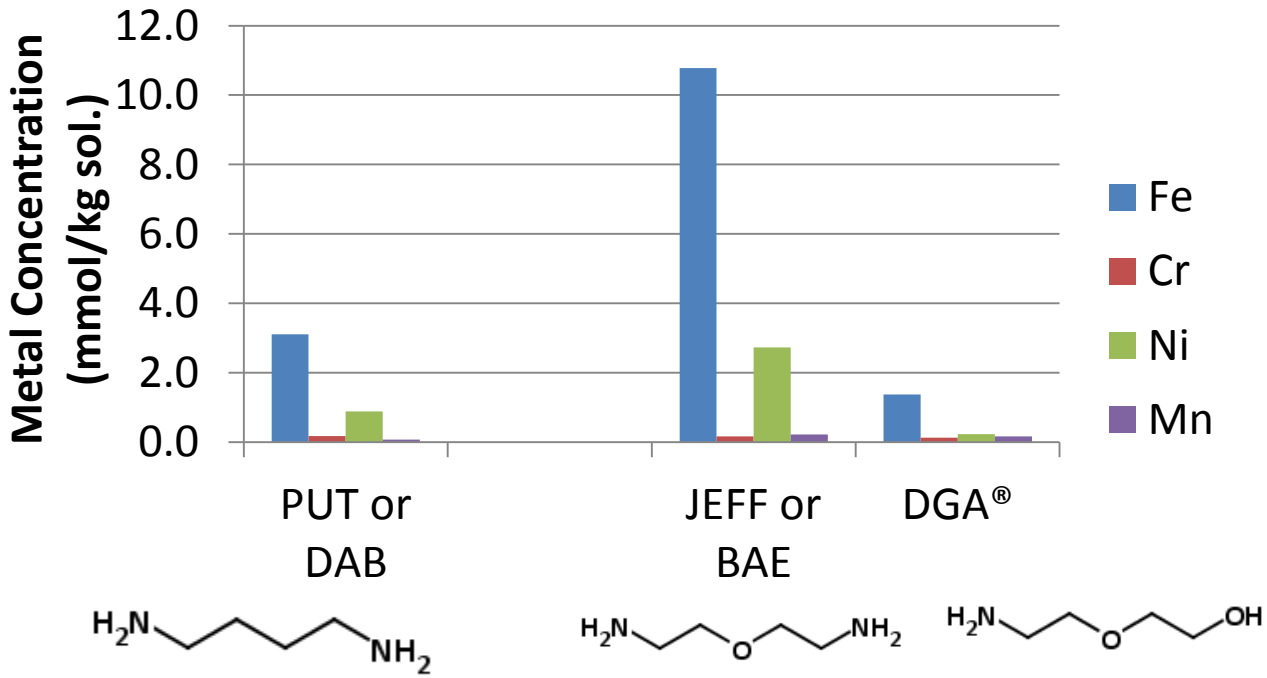

Figure 4: Metal accumulation after 670 hrs (PUT), 694 hrs (DGA®), or 810 hrs (JEFF) in thermal cylinders at 150 °C. DAB, BAE concentration is 5 molal. DGA® concentration is 10 molal. α = 0.4.

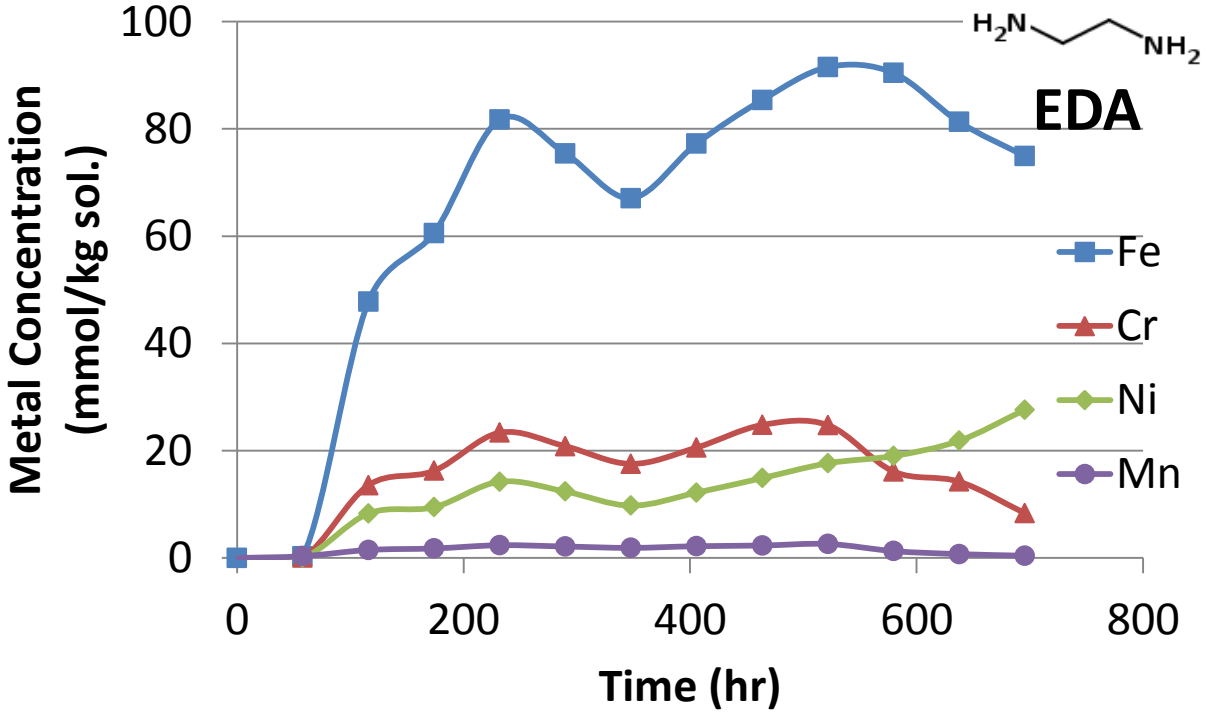

Figure 5: Accumulation of metals in 5 molal EDA in thermal cylinders at 150 °C. α = 0.4.

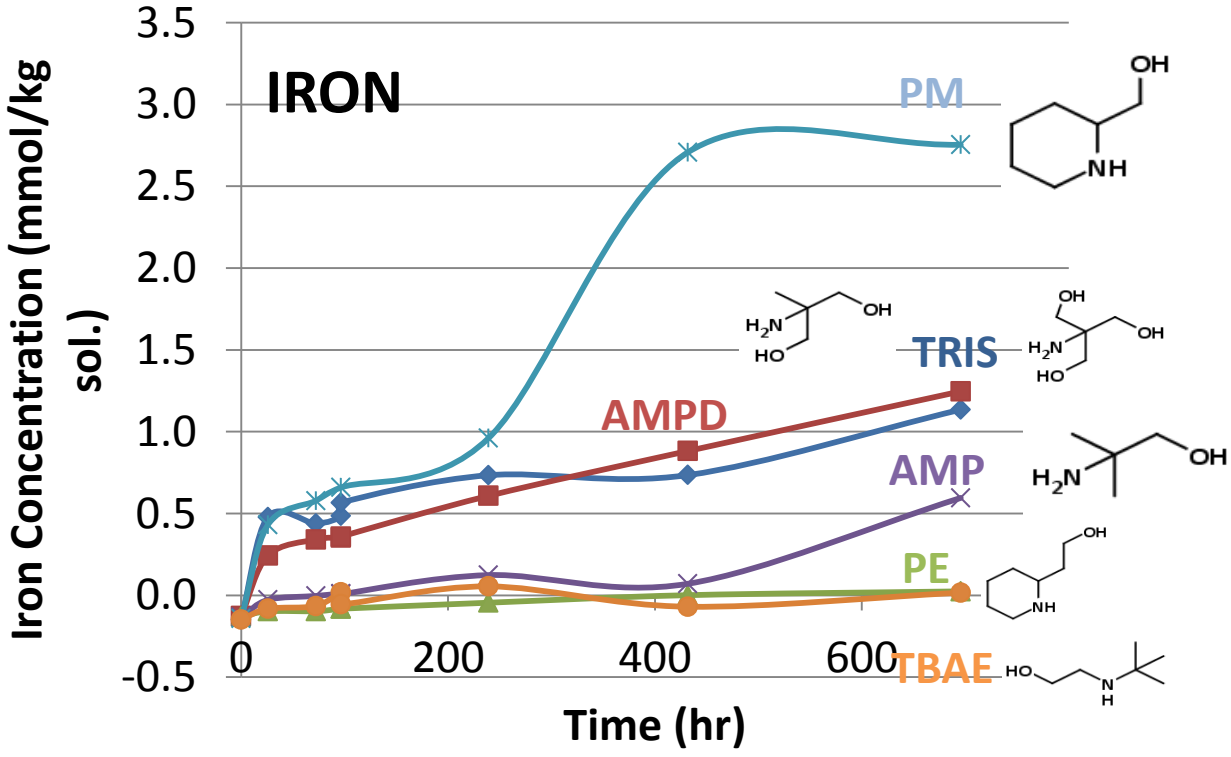

Figure 6: Accumulation of iron in hindered amine/PZ blends. Each experiment used 2.67 m hindered amine and 1.33 m PZ in thermal cylinders at 150°C. α = 0.4.

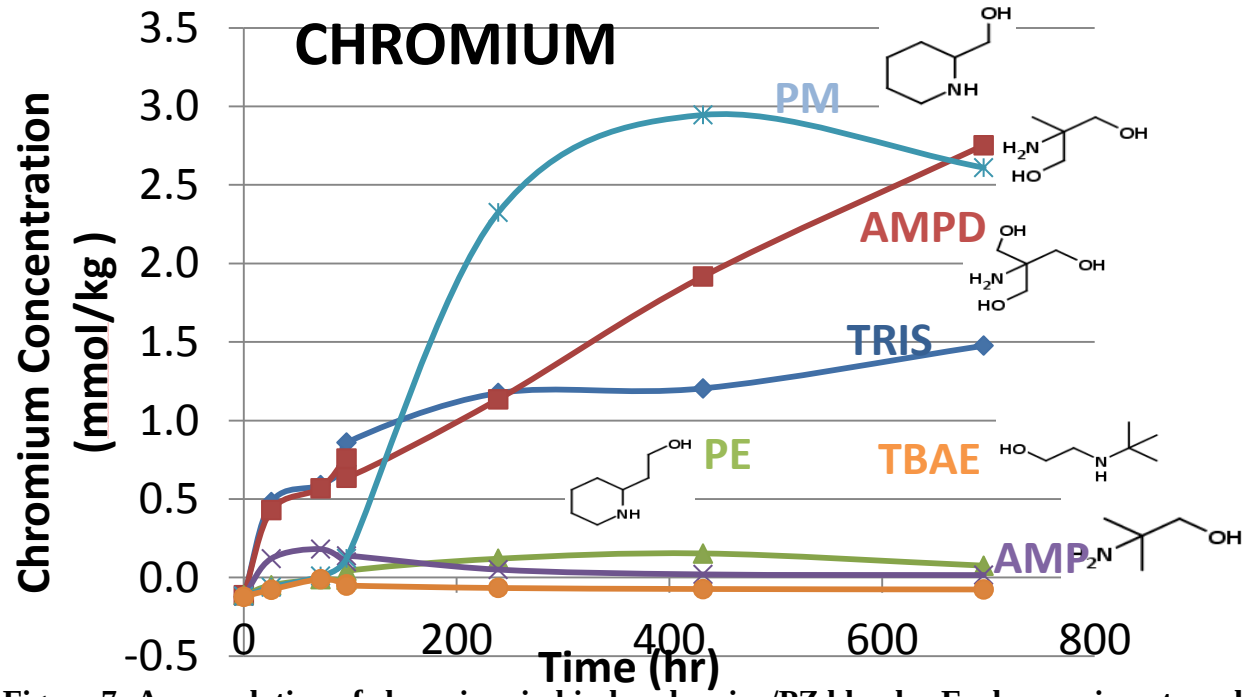

Figure 7: Accumulation of chromium in hindered amine/PZ blends. Each experiment used 2.67 m hindered amine and 1.33 m PZ in thermal cylinders at 150 °C. α = 0.4.

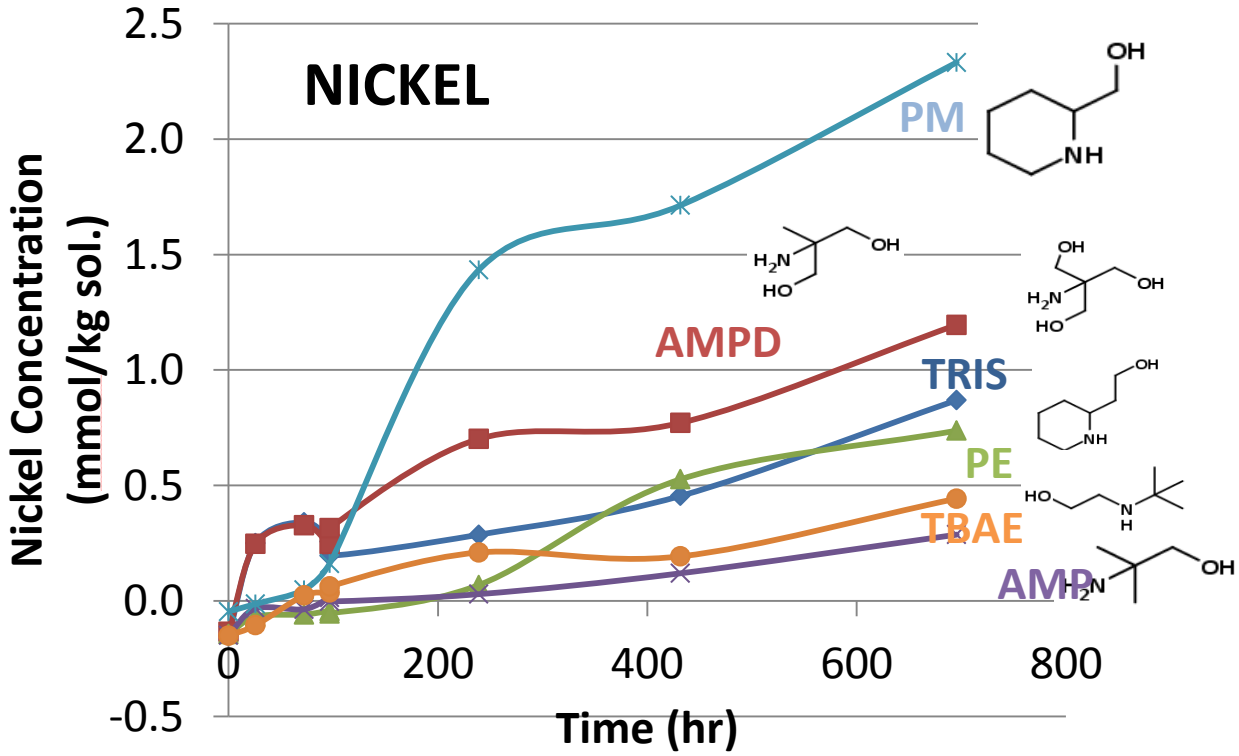

Figure 8: Accumulation of nickel in hindered amine/PZ blends. Each experiment used 2.67 m hindered amine and 1.33 m PZ in thermal cylinders at 150 °C. α = 0.4.

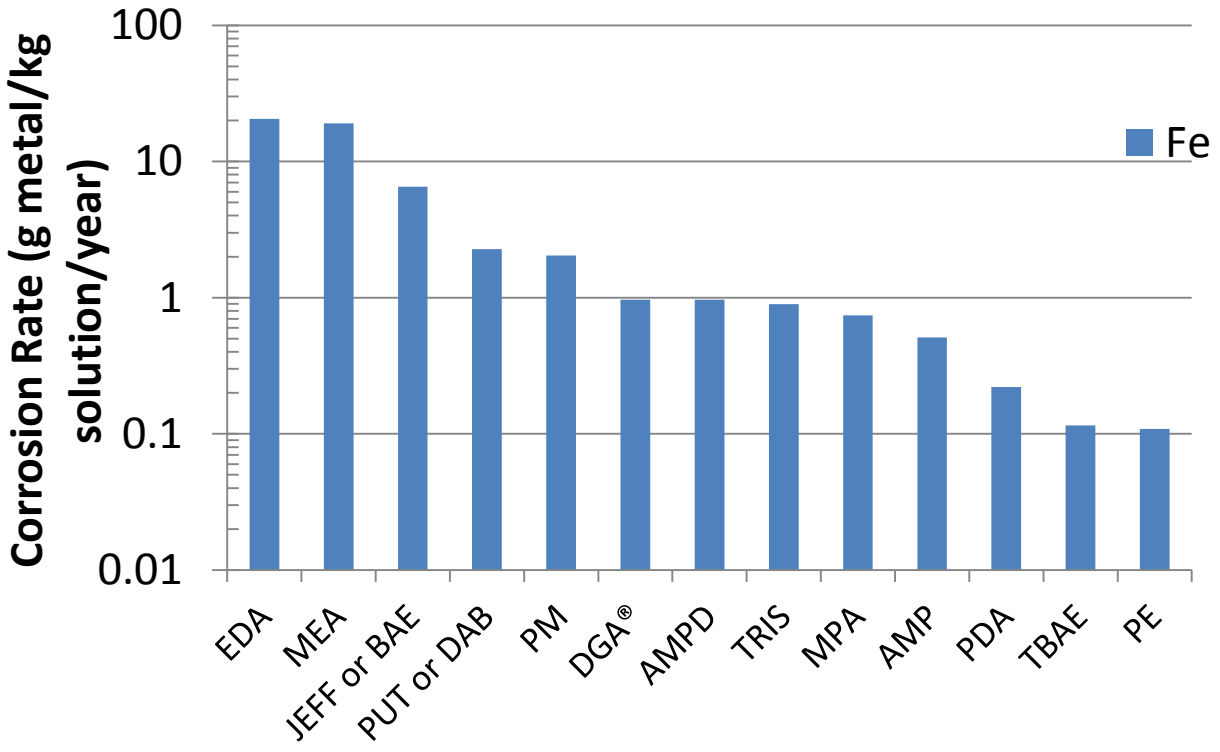

Figure 9: Yearly corrosion rate of iron

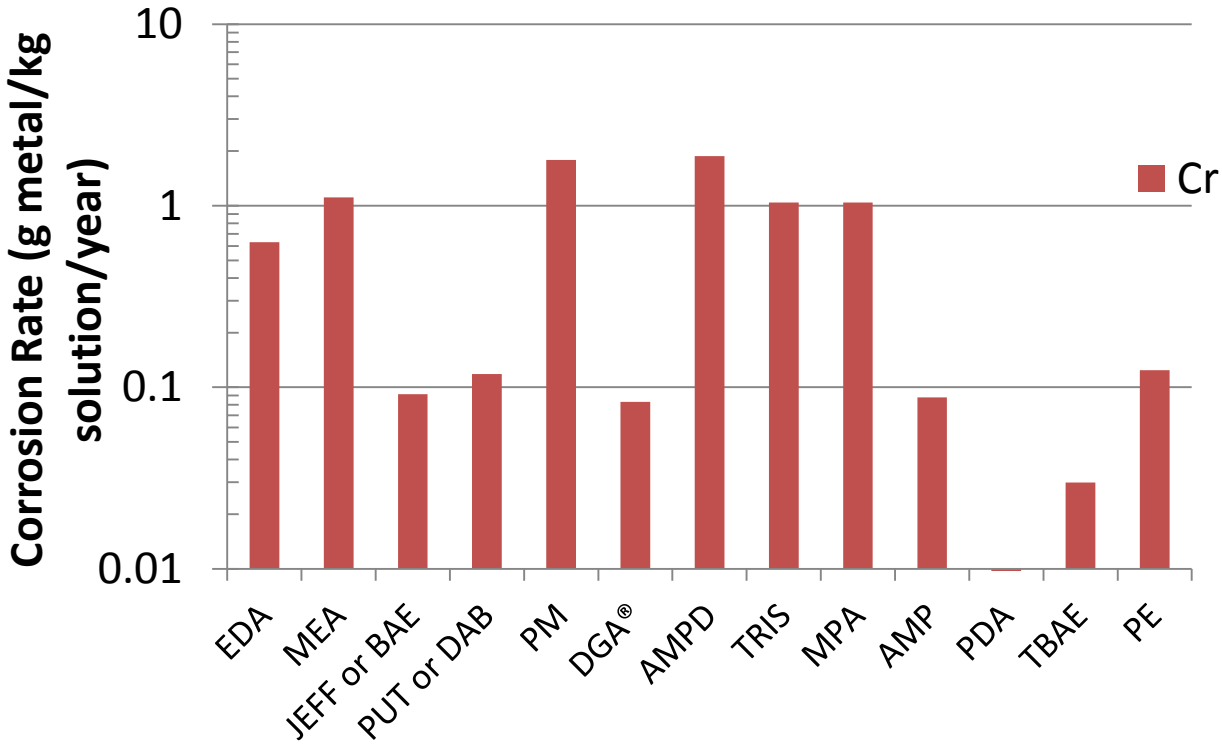

Figure 10: Yearly corrosion rate of chromium

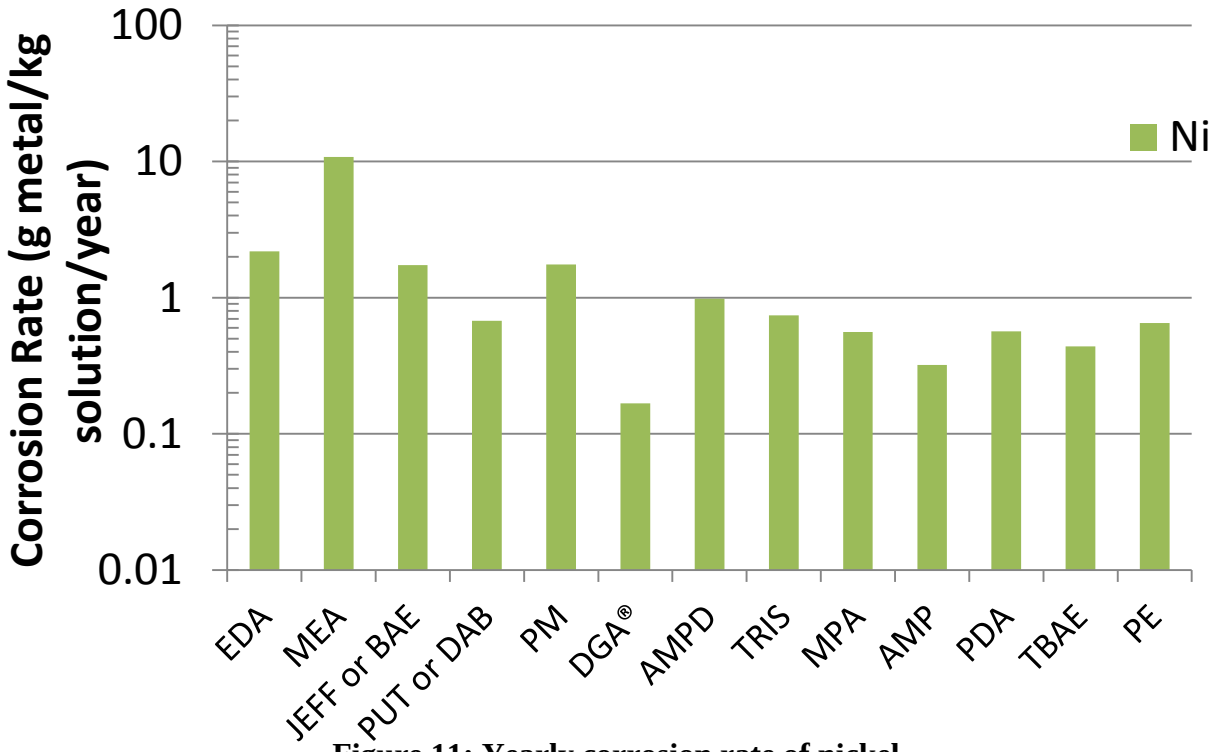

Figure 11: Yearly corrosion rate of nickel

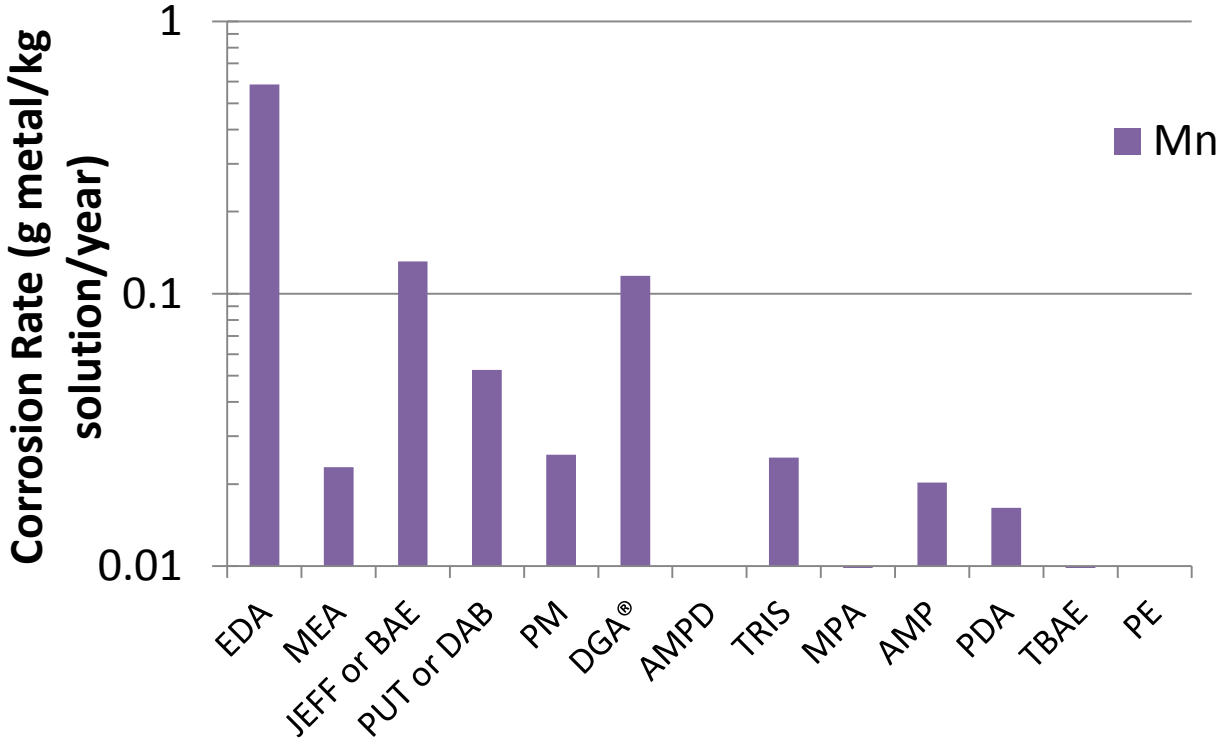

Figure 12: Yearly corrosion rate of manganese

Conclusions

In stainless steel 316 cylinders at 150 °C, 5 m ethylenediamine is 93 times as corrosive as its three-carbon analog, diaminopropane, and 10 m monoethanolamine is 34 times as corrosive as its three-carbon analog, aminopropanol.

In stainless steel 316 cylinders at 150 °C, a 2.67 m 2-piperidinemethanol (PM)/1.33 m PZ solution is 72 times more corrosive than a 2.67 m 2-piperidineethanol (PE)/1.33 m PZ solution. There is a two-carbon backbone between the nitrogen and the alcohol functional group in PM, whereas there is a three-carbon backbone between the nitrogen and alcohol functional group in PE. This is the same trend of corrosivity decreasing with chain length seen in the linear amines.

Likely the two-carbon backbone species are able to form stable organometallic complexes which serve as catalysts for the reduction of CO_2 to HCO_2^- which is accompanied by rapid oxidation and corrosion of the metal. The three-carbon backbone species are too long and labile to form a stable metal center, thus preventing metal-catalyzed oxidation.

References

Hatchell D, Namjoshi O, Fischer K, Rochelle GT. "Thermal degradation of linear amines for CO_2 capture." *Energy Proc.* 2014;63:1558-1568.

Namjoshi O, Hatchell D, Rochelle GT. "Thermal Degradation of PZ-Activated Tertiary and Hindered Amines." Presented at *GHGT-12*, Austin, October 59, 2014.

Freeman SA. *Thermal Degradation and Oxidation of Aqueous Piperazine for Carbon Dioxide Capture.* The University of Texas at Austin. Ph.D. Dissertation. 2011.